Active

Project #: E-16-M07 Cost share #: Rev #: 7
Center # : 10/24-6-R6997-0A0 Center shr #: OCA file #:
Work type : RES
Contract#: N62269-90-C-0246 Mod #: P00005 Document : CONT
Prime #: Contract entity: GTRC

Subprojects ? : Y CFDA:
Main project #: PE #:

Project unit: AERO ENGR Unit code: 02.010.110
Project director(s):
SANKAR N L AERO ENGR (404)894-3014
PRASAD J V R AERO ENGR (404)-

Sponsor/division names: NAVY / NAVAL AIR WARFARE CTR, PA
Sponsor/division codes: 103 / 010

Award period: 900713 to 951231 (performance) 960331 (reports)

Sponsor amount	New this change	Total to date
Contract value	0.00	210,099.00
Funded	0.00	193,811.00
Cost sharing amount		0.00

Does subcontracting plan apply ?: N

Title: UNSTEADY AERODYNAMIC ANALYSIS OF DUAL ELEMENT WING CONFIGURATIONS

PROJECT ADMINISTRATION DATA

OCA contact: E. Faith Gleason 894-4820

Sponsor technical contact	Sponsor issuing office
MR. DAVID B. FINDLAY / JOHN FUNK (215)441-1715	KENNETH SHERMAN, CONTRACTING SPECLST (215)441-1559
NAVAL AIR WARFARE CTR, AIRCRAFT DIV. CODE 6051 P.O. BOX 5152 WARMINSTER, PA 18974-0591	NAVAL AIR WARFARE CTR, AIRCRAFT DIV. MS 89 P.O. BOX 5152 WARMINSTER, PA 18974-0591 FAX: (215) 441-3763

Security class (U,C,S,TS) : U ONR resident rep. is ACO (Y/N): Y
Defense priority rating : DO-A1A supplemental sheet
Equipment title vests with: Sponsor X GIT

Administrative comments -
MODIFICATION NO. P00005 PROVIDES A NO-COST EXTENSION TO DECEMBER 31, 1995.
NOTE: CHANGE OF SPONSOR NAME AND ADDRESS AND ZIP CODE.

GEORGIA INSTITUTE OF TECHNOLOGY
OFFICE OF CONTRACT ADMINISTRATION

NOTICE OF PROJECT CLOSEOUT

Closeout Notice Date 05/02/96

Project No. E-16-M07 — Center No. 10/24-6-R6997-0A0

Project Director SANKAR N L — School/Lab AERO ENGR

Sponsor NAVY/NAVAL AIR WARFARE CTR, PA

Contract/Grant No. N62269-90-C-0246 — Contract Entity GTRC

Prime Contract No. ____________

Title UNSTEADY AERODYNAMIC ANALYSIS OF DUAL ELEMENT WING CONFIGURATIONS

Effective Completion Date 951231 (Performance) 960331 (Reports)

Closeout Actions Required:	Y/N	Date Submitted
Final Invoice or Copy of Final Invoice	Y	
Final Report of Inventions and/or Subcontracts	Y	
Government Property Inventory & Related Certificate	Y	
Classified Material Certificate	N	
Release and Assignment	Y	
Other ____________	N	

Comments ____________

Subproject Under Main Project No. ____________

Continues Project No. ____________

Distribution Required:

Project Director	Y
Administrative Network Representative	Y
GTRI Accounting/Grants and Contracts	Y
Procurement/Supply Services	Y
Research Property Managment	Y
Research Security Services	N
Reports Coordinator (OCA)	Y
GTRC	Y
Project File	Y
Other ____________	N
____________	N

NOTE: Final Patent Questionnaire sent to PDPI.

E-16-N07

1

UNSTEADY AERODYNAMIC ANALYSIS OF DUAL-ELEMENT WING CONFIGURATIONS

BI-MONTHLY PROGRESS LETTER
FOR THE PERIOD

JULY 13, 1990 - AUGUST 31, 1990

Submitted to the

NAVAL AIR DEVELOPMENT CENTER
WARMINSTER, PA
Attn: David Findlay

Prepared By

L. N. Sankar
Associate Professor
School of Aerospace Engineering
Georgia Institute of Technology, Atlanta, GA 30332

SEPTEMBER 1990

School of Aerospace Engineering

Georgia Institute of Technology
Atlanta, Georgia 30332-0150
404•894•3000
Fax: 404•894•2760

September 4, 1990

Mr. Dave Findlay
Code 6051
Naval Air Development Center
Warminster, PA 18974

Subject: BI-MONTHLY PROGRESS REPORT FOR THE PROJECT "UNSTEADY AERODYNAMIC ANALYSIS OF DUAL-ELEMENT WING CONFIGURATIONS"

Dear Mr. Findlay:

During the reporting period July 13, 1990- August 31, 1990, a 2-D compressible Navier-Stokes solver capable of handling multi-element airfoil configurations was developed. A user guide documenting the capabilities of the computer code has been prepared, and enclosed. An IBM PC Compatible diskette containing the Navier-Stokes solver and grid generator, sample input data set and sample output will be delivered to you, and an oral briefing given during your visit to Georgia Tech this month.

Sincerely,

LAKSHMI N. SANKAR
Associate Professor

USER GUIDE FOR

GTMEL2D (Version 1.0)
GEORGIA TECH
MULTI-ELEMENT AIRFOIL 2-D NAVIER-STOKES ANALYSIS PROGRAM

Written By

L. N. Sankar
Associate Professor
School of Aerospace Engineering
Georgia Institute of Technology, Atlanta, GA 30332

INTRODUCTION

The Multi-element airfoil code, in conjunction with the MFLGRD (Multi-foil grid generation) code may be used to study the subsonic and transonic aerodynamic characteristics of high lift configurations. Specifically,

* Any number of components may be present. The grid generator, as well as the flow solver can handle 2, 3 ,4 or 5 element airfoils. Thus airfoil-flap, airfoil-slat, airfoil-slat-flap combinations may be investigated.

* The program works in the Mach number range 0.1 < M , 1.0, for a large range of angles of attack (Angle of attack up to 90 degrees, flap deflection up to 90 degrees). The flow is assumed to be fully turbulent over the main airfoil and secondary elements.

MATHEMATICAL AND NUMERICAL FORMULATION

The GTMEL2D program solves the compressible full Navier-Stokes equations, and is based on the single element airfoil code GTNSE2D developed by Sankar and Tang in 1985, and later modified by Mr. Jiunn-Chi Wu at Georgia Tech as part of his Ph. D. thesis. It uses central differences to evaluate all spatial derivatives, and is therefore second order accurate in space. It uses a set of artificial viscosity terms proposed by Jameson and Turkel (AIAA Paper 81-1259). It uses a first order accurate implicit time marching scheme. The program can be used in the time accurate mode, or in the relaxation mode. If the relaxation mode is used, the program uses different values of time steps at the different node points, in order to relax the solution to the final converged values within 1000 time steps.

This program handles multi-element airfoils as follows. First, the flow field is divided into zones. If there are N elements, then the number of zones equals N+1. This is a user changeable value called NZO appearing in the parameter statements in every subroutine in the program. In each zone, a H- grid is used. The different zones communicate with each other in that flow properties are continuous across zone boundaries, except when the nodes on the zone boundaries correspond to solid points.

At every time step, the program performs the following calculations for each zone:

* It computes the metrics of transformation, which link the curvilinear H-grid in the physical plane to a uniformly spaced grid in the transformed plane. This is done in the main program.

* The main program calls the SLPS routine to advance the solution at all the interior points. This requires calls to RESI (which computes the inviscid contributions to the changes in the flow properties), to STRESS (which computes changes in flow properties due to viscous stresses, and calls EDDY to compute eddy viscosities), to DISS2 which computes the artificial viscosity terms needed to remove wiggles in the solution. The routine SLPS then assembles a penta-diagonal matrix system for the changes in the flow properties through calls to subroutines AMAT1 and AMAT2. SLPS further factors this penta-diagonal matrix into two tri-diagonal matrices, and solves for the changes in the flow properties through calls to MATRX1 and MATRX2. These routines are simply tri-diagonal matrix solvers, vectorized for efficient performance on a Cray XMP. The changes

in the flow properties are added to the old values to get flow properties at all interior nodes in a given zone.

After all the interior points in all the zones have been updated, the main program calls WALLBC, which updates the boundaries. At solid walls, the no slip condition is applied, and the pressure/density gradients are set to zero. At fluid boundaries that separate adjacent zones, the flow properties are averaged from above and below.

INPUT TO THE FLOW SOLVER

The input to the grid generation program is explained separately in a user guide. Here, the input to the flow solver are discussed.

The flow solver uses free format input everywhere. The first two cards in the input stream are comment cards used to document the case being considered. The program reads both cards, and echoes the second card.

The third card is a title card, read and ignored by the solver. Such title cards are used to document the data on the following card.

The fourth card specifies the number of time steps for the current run, the time step used, and a logical flag showing if the current run is time accurate. For multi-element airfoils, this logical flag may be set to FALSE. Then, the time step can vary from 1.0 to 5.0. The total number of time steps needed to achieve converged solution varies between 1000 and 2000 time steps.

The fifth card is a comment card.

The sixth card specifies the artificial viscosity coefficients used. The recommended values are WW=3, WWI=10, WW2X=WW2Y=1. and WW4X=WW4Y=0.1. These values should be adequate for most cases. Increase in this values improves convergence, at the expense of solution accuracy.

The seventh card is a comment card.

The eighth card is a logical card, stating if the current run is a RESTART run. If so, the program reads a previously saved solution from FORTRAN Unit 7. At the end of each run, the program automatically writes the solution to FORTRAN Unit 8.

The ninth card is a comment card.

The tenth card specifies the Mach number, the angle of attack, and the Reynolds number in Millions. If the Reynolds number is zero, then an inviscid Euler analysis is performed.

Note that the program expects the grid to be supplied as a file GRID.DAT, automatically generated by the MFLGRD program.

SAMPLE APPLICATION

As a sample application, the subsonic viscous flow past a GA(W)-1 airfoil with a flap deflected at 20 degree has been computed. The Mach number was 0.3, and the angle of attack was 5 degrees. The computed value of lift, equal to 2.62 (Perpendicular to the x- axis, the very last line of output) is in good agreement with the experimental value of 2.67. This airfoil has been studied extensively (e.g. Wentz and Seetharam, "Development of a Fowler Flap System for a General Aviation Airfoil," NASA CR 2443, November 1974). A sample input stream for the grid generator (File GAW130.DAT on the IBM PC diskette), and a sample input stream for the flow solver (File GTMEL2D.DAT on the diskette) are enclosed. Typical output from the flow solver is also enclosed. A plot of the body-fitted grid near the airfoil-flap combination, and a plot of Cp over the main airfoil and flap are also enclosed. The Cp distribution for the main airfoil also shows the measured Cp values.

FILES ON THE IBM PC DISKETTE

The IBM PC diskette contains

* The grid generation program source code (MFLGRD.FOR)

* The flow solver source code (GTMEL2D.FOR)

* Input data for the grid generator (GAW130.DAT)

* Input data for the flow solver (GTMEL2D.DAT).

CONCLUDING REMARKS

A general purpose multi-element airfoil code, capable of handling airfoil-flap, airfoil-slat and airfoil-slat-flap combinations has been developed. This solver can handle attached and separated flows, in the entire speed range of interest to aircraft and rotary wing designers.

User's Guide for Program
HLGRD
A grid Generation Program for Multiple
Component Airfoil Geometries

David M. Schuster
Aviation Technology Branch
GTRI/RAIL/TDD
October, 1989

HLGRD uses a Zonal approach to generate a two-dimensional body-fitted grid about multiple component airfoils. The program uses a H-Grid topology to break the overall grid into a number of zones conforming to the airfoil contours.

The geometry input format for the code is that of the NASA/Lockheed Multiple Airfoil Program (MAP)[1]. The basic topology used in the generation of multiple component airfoil grids is shown in Figure 1 for a two-element high lift airfoil. The user has complete control of the definition of the grid extents, and the spacing, placement and number of airfoil components. The user can control the number and spacing of the grid points along the boundaries of each zone, as well as the shape of the "wake" cuts ahead of and behind each airfoil component.

The two-dimensional grids are generated using a Succesive Line Over-Relaxation (SLOR) of Thompsons elliptic grid generation equations[2]. Source terms used to control the distribution of grid points interior to the boundaries are computed solely from the boundary information as suggested by Thomas[3]. The method maintains complete continuity across zonal interfaces by solving the grid generation equations across the interfaces. This option can be defeated for grids problems which do not require slope continuity across the zonal interfaces.

Input for the method consists of free-format input read from unit 5. Runtime output is to unit 6, while grids are written to unit 8. The input and output of the code will now be described in detail.

All input data is read in free-format from unit 5. Parameters controlling the distribution of points and the actual grid generation are read first, followed by the description of the geometry. Suggested values for some of the parameters are shown in parentheses.

Line 1 TITLE

TITLE	Title Descriptor for the grid generation case.

Line 2 NITR, OMEGA, MOVE, SRCCUT

NITR	Number of iterations to be performed in the SLOR iteration of the grid generation equations. (50) =0 Generates an algebraic grid.
OMEGA	Over-Relaxation Factor. (1.3)
MOVE	Determines whether zonal interfaces are to be updated during the grid generation. (1) =0 Interfaces will not be updated. (Slope Discontinuity) =1 Interfaces will be included in the solution of the grid generation equations. (Slope Continuity)

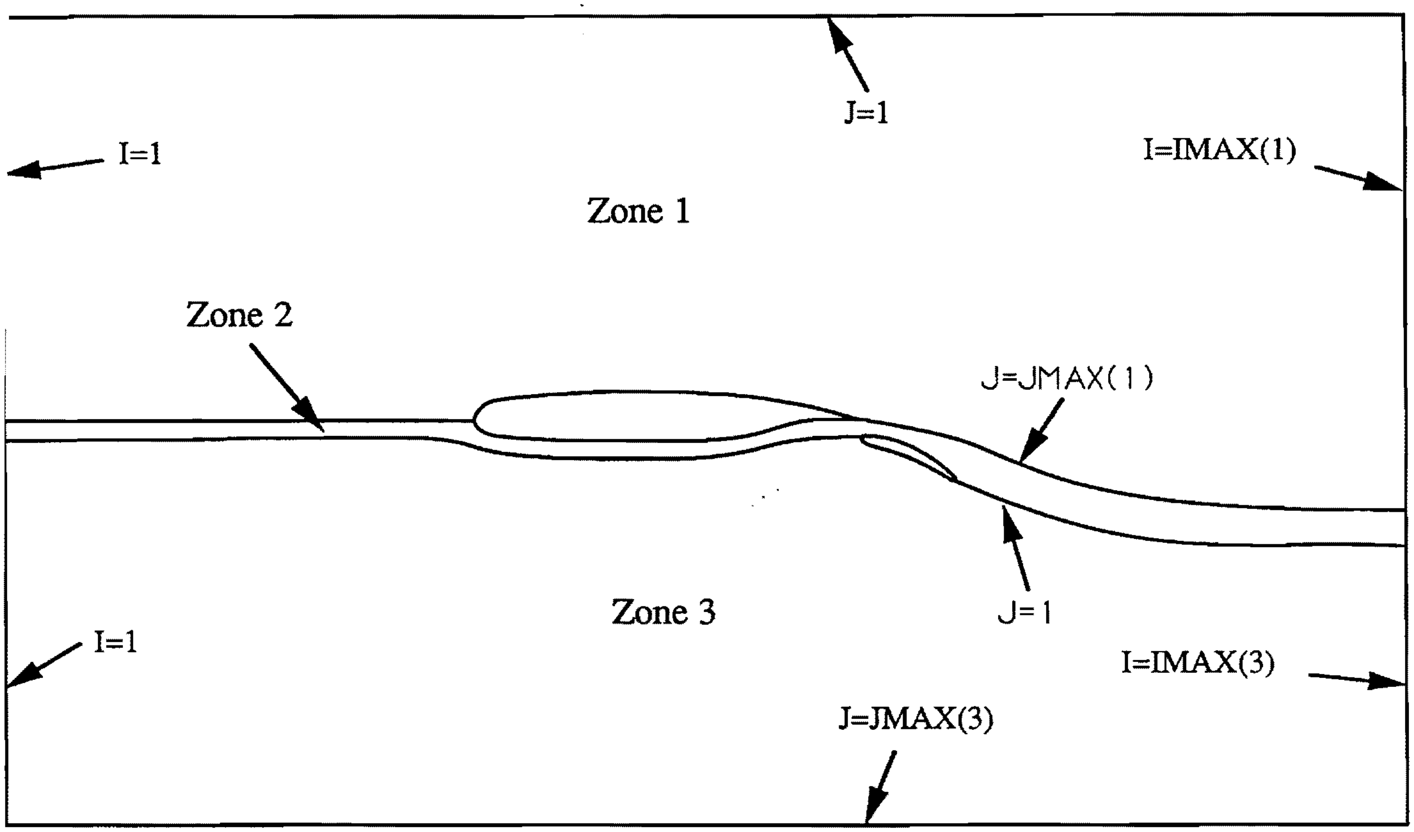

Figure 1. Grid Topology for a Two-Element Airfoil

SRCCUT Multiplier for the calculation of the source terms. (1.0)
=0.0 Source terms are not included in the grid generation.
>0.0 Source terms are pre-multiplied by the value of SRCCUT.

Line 3 NC

NC Number of airfoil components to be generated for this case. The total number of grid zones (NZONE) is set to NC+1.

Line 4 is repeated NZONE=NC+1 times.

Line 4 IMAX(N), JMAX(N)

IMAX Maximum number of points in the I, or ξ direction for zone N.

JMAX Maximum number of points in the J or η direction for zone N.

Line 5 Blank Line

Lines 6 through 17 are repeated NC times.

Line 6 NSEGU

NSEGU Number of segments the upper surface of component N is to be broken into.

Line 7 is repeated NSEGU times.

Line 7 ISU(M,N), IEU(M,N), SSU(M,N), SEU(M,N), DXSU(M,N), DXEU(M,N)

ISU Starting I-index for segment M on component N. If M=1, ISU is the index of the leading edge point for component N.

IEU Ending I-index for segment M on component N. If M=NSEGU, IEU is the trailing-edge index for the upper surface of component N.

SSU Fraction of the component N upper surface arc-length at which segment M begins. SSU(1,N) must equal zero.

SEU Fraction of the component N upper surface arc-length at which segment M ends. SEU(NSEGU,N) must equal 1.0.

DXSU Spacing of the first grid point along segment M as a fraction of the total arc-length of the upper surface. A value of 0.0 results in "free" spacing if M=1, or spacing will be obtained from the end of the previous segment if M>1.

DXEU Spacing of the last grid point along segment M as a fraction of the total arc-length of the upper surface. A value of 0.0 results in "free" spacing at the end of segment M.

Line 8 NSEGL

NSEGL Number of segments the lower surface of component N is to be broken into.

Line 9 is repeated NSEGL times.

Line 9 ISL(M,N), IEL(M,N), SSL(M,N), SEL(M,N), DXSL(M,N), DXEL(M,N)

ISL Starting I-index for segment M on component N. If M=1, ISL is the index of the leading edge point for component N and this value must equal ISU(1,N).

IEL	Ending I-index for segment M on component N. If M=NSEGL, IEL is the trailing-edge index for the lower surface of component N. At this point, it is necessary that IEU(NSEGU,N)=IEL(NSEGL,N).
SSL	Fraction of the component N lower surface arc-length at which segment M begins. SSL(1,N) must equal zero.
SEL	Fraction of the component N lower surface arc-length at which segment M ends. SEL(NSEGL,N) must equal 1.0.
DXSL	Spacing of the first grid point along segment M as a fraction of the total arc-length of the lower surface. A value of 0.0 results in "free" spacing if M=1, or spacing will be obtained from the end of the previous segment if M>1.
DXEL	Spacing of the last grid point along segment M as a fraction of the total arc-length of the lower surface. A value of 0.0 results in "free" spacing at the end of segment M.

Line 10 NPTSF(N)

NPTSF	Number of coordinates to be input to describe the shape of the forward wake. A cubic B-spline is used to generate the forward wake curve. The last point along the curve is assumed to be the leading edge point for component N, and this point does not need to be input in the definition of the curve. NPTSF must be greater than 2 to properly define the cubic B-spline. The curve coordinates must be input from the forward boundary to the leading edge of component N.

Line 11 is repeated NPTSF(N) times

Line 11 XFOR(M,N),YFOR(M,N)

XFOR	X-coordinate of point M on the forward wake of component N.
YFOR	Y-coordinate of point M on the forward wake of component N.

Line 12 NSEGF(N)

NSEGF	Number of segments the forward wake for component N is to be broken into.

Line 13 is repeated NSEGF times.

Line 13 ISF(M,N), IEF(M,N), SSF(M,N), SEF(M,N), DXSF(M,N), DXEF(M,N)

ISF	Starting I-index for segment M on the forward wake of component N. If M=1, ISF must equal 1.
IEF	Ending I-index for segment M on the forward wake of component N. If M=NSEGF, IEF must equal ISU(1,N).
SSF	Fraction of the arc-length along the forward wake at which segment M begins. SSF(1,N) must equal zero.
SEF	Fraction of the arc-length along the forward wake at which segment M ends. SEF(NSEGF,N) must equal 1.0.
DXSF	Spacing of the first grid point along segment M in the physical oordinates of the grid. A value of 0.0 results in "free" spacing if M=1, or spacing will be obtained from the end of the previous segment if M>1.
DXEF	Spacing of the last grid point along segment M in the physical coordinates of the grid. A value of 0.0 results in "free" spacing at the end of segment M.

Line 14 NPTSA(N)

NPTSA — Number of coordinates to be input to describe the shape of the aft wake for component N. A cubic B-spline is used to generate the aft wake curve. The first point along the curve is assumed to be the trailing edge point for component N, and this point is not required to be input in the definition of the curve. NPTSA must be greater than 2 to properly define the cubic B-spline. The curve coordinates must be input from the trailing edge of component N to the aft grid boundary.

Line 15 is repeated NPTSA(N) times

Line 15 XAFT(M,N),YAFT(M,N)

XAFT — X-coordinate of point M on the aft wake of component N.

YAFT — Y-coordinate of point M on the aft wake of component N.

Line 16 NSEGA(N)

NSEGA — Number of segments the aft wake for component N is to be broken into.

Line 17 is repeated NSEGA times.

Line 17 ISA(M,N), IEA(M,N), SSA(M,N), SEA(M,N), DXSA(M,N), DXEA(M,N)

ISA — Starting I-index for segment M on the aft wake of component N. If M=1, ISA must equal IEU(NSEGU,N).

IEA — Ending I-index for segment M on the aft wake of component N. If M=NSEGA, IEA must equal IMAX(N).

SSA — Fraction of the arc-length along the aft wake at which segment M begins. SSA(1,N) must equal zero.

SEA — Fraction of the arc-length along the aft wake at which segment M ends. SEA(NSEGA,N) must equal 1.0.

DXSA — Spacing of the first grid point along segment M in the <u>physical coordinates</u> of the grid. A value of 0.0 results in "free" spacing if M=1, or spacing will be obtained from the end of the previous segment if M>1.

DXEA — Spacing of the last grid point along segment M in the <u>physical coordinates</u> of the grid. A value of 0.0 results in "free" spacing at the end of segment M.

Line 18 Blank Line

Line 19 XMIN, XMAX, YMIN, YMAX

XMIN — X-coordinate of the forward grid boundary.

XMAX — X-coordinate of the aft grid boundary.

YMIN — Y-coordinate of the bottom grid boundary.

YMAX — Y-coordinate of the top grid boundary.

Line 20 NSEGT

NSEGT — Number of segments the top grid boundary is to be broken into.

Line 21 is repeated NSEGT times.

Line 21 IST(M,N), IET(M,N), SST(M,N), SET(M,N), DXST(M,N), DXET(M,N)

IST — Starting I-index for segment M on the top grid boundary. If M=1, IST must equal 1.

IET — Ending I-index for segment M on the top grid boundary. If M=NSEGT, IET must equal IMAX(1).

SST — Fraction of the arc-length along the top grid boundary at which segment M begins. SST(1,N) must equal zero.

SET — Fraction of the arc-length along the top grid boundary at which segment M ends. SET(NSEGT,N) must equal 1.0.

DXST — Spacing of the first grid point along segment M in the <u>physical coordinates</u> of the grid. A value of 0.0 results in "free" spacing if M=1, or spacing will be obtained from the end of the previous segment if M>1.

DXET — Spacing of the last grid point along segment M in the <u>physical coordinates</u> of the grid. A value of 0.0 results in "free" spacing at the end of segment M.

Line 22 NSEGB

NSEGB — Number of segments the bottom grid boundary is to be broken into.

Line 23 is repeated NSEGB times.

Line 23 ISB(M,N), IEB(M,N), SSB(M,N), SEB(M,N), DXSB(M,N), DXEB(M,N)

ISB — Starting I-index for segment M on the bottom grid boundary. If M=1, ISB must equal 1.

IEB — Ending I-index for segment M on the bottom grid boundary. If M=NSEGB, IEB must equal IMAX(NZONE).

SSB — Fraction of the arc-length along the bottom grid boundary at which segment M begins. SSB(1,N) must equal zero.

SEB — Fraction of the arc-length along the bottom grid boundary at which segment M ends. SEB(NSEGB,N) must equal 1.0.

DXSB — Spacing of the first grid point along segment M in the <u>physical coordinates</u> of the grid. A value of 0.0 results in "free" spacing if M=1, or spacing will be obtained from the end of the previous segment if M>1.

DXEB — Spacing of the last grid point along segment M in the <u>physical coordinates</u> of the grid. A value of 0.0 results in "free" spacing at the end of segment M.

Line 24 DSNU,DSNL

DSNU — Spacing of the first grid line normal to each component upper surface as a fraction of the components chord length.

DSNL — Spacing of the first grid line normal to each component lower surface as a fraction of the components chord length.

This concludes the input of the grid generation, grid size and spacing parameters for the grid generation. The geometry and placement information for each airfoil component is read next.

Lines 25 through 32 are repeated NC times.

Line 25 TITLE(N)

TITLE	Title descriptor for component N.

Line 26 SCALE(N)

SCALE	Scale factor for component N. Coordinates for component are multiplied by SCALE to obtain the final coordinates.

Line 27 NPP(N) (Not required for NC=1)

NPP	The number of pivot points to be defined for component N. Pivot points are used to place other airfoil components in relation to component N.

Line 28 is repeated NPP(N) times.

Line 28 XP(M,N), YP(M,N) (Not required for NC=1)

XP	X-coordinate of pivot point M referenced to component N.
YP	Y-coordinate of pivot point M referenced to component N.

Line 29 NU(N)

NU	Number of points to be input to define the upper surface of component N.

Line 30 is repeated NU(N) times.

Line 30 XU(M,N), YU(M,N)

XU	X-coordinate of upper surface point M on component N.
YU	Y-coordinate of upper surface point M on component N.

Line 31 NL(N)

NL	Number of points to be input to define the lower surface of component N.

Line 32 is repeated NL(N) times.

Line 32 XL(M,N), YL(M,N)

XL	X-coordinate of lower surface point M on component N.
YL	Y-coordinate of lower surface point M on component N.

Line 33 NM (Not required for NC=1)

NM	Index of the main component. This component is considered to be the reference component for the overall airfoil system.

Lines 34 and 35 are repeated NC-1 times. These lines place and deflect all of the components except the main component.

Line 34 IC,IPP,ICR,IPPR (Not required for NC=1)

ICC	Index of the component to be placed.
IPP	Index of the pivot point referenced to component IC to be used in the placement of the component.
ICR	Index of the component to be used as the reference component in the placement of component IC.
IPPR	Index of the pivot point referenced to component ICR to be used in the placement of component IC.

Line 35 DELTA (Not required for NC=1)

DELTA — Angle through which component IC is to be rotated. Measured from the horizontal, positive counter-clockwise.

Component IC is translated so that the coordinates of IPP are coincident with the coordinates of IPPR. Component IC is then rotated about the pivot point through the angle DELTA. This is done for each airfoil component. The angle DELTA is referenced to the horizontal for the individual component. However, this angle is added to the angle defined for the reference component, so DELTA is actually an increment to be added to the reference component. The order in which the component placement information is input to the program will not affect the final placement of the airfoil components. The program ensures that all reference components have been lofted before lofting each component.

Once the input data has been read, it is echoed to unit 6. The grid is generated and convergence information is printed. The final grid is then written to unit 8 using the following Fortran statements.

```
      OPEN(UNIT=8,FILE='FILE8.DAT',FORM='UNFORMATTED')
      WRITE(8) NZONE
      DO 10 K=1,NZONE
      WRITE(8) IMAX(K),JMAX(K)
      DO 10 J=1,JMAX(K)
      DO 10 I=1,IMAX(K)
      WRITE(8)  X(I,J,K),Y(I,J,K)
   10 CONTINUE
      CLOSE(UNIT=8)
```

The program dimensions are set through a PARAMETER statement at the beginning of the program and at the start of each subroutine. The values defined in this statement are as follows:

NCMX	Maximum number of components which can be input to the program.
NSMX	Maximum number of segments which can be defined for each of the component upper, lower, forward wake and aft wake surfaces, as well as for the top and bottom boundaries.
IMX	Maximum number of points in the I-direction (Streamwise) for any zone in the grid.
JMX	Maximum number of points in the J-direction (Vertical) for any zone in the grid.

The zonal grid is generated so that the top boundary and the upper surface of the first component input are located in Zone 1. The top boundary is located at J=1, and the upper surface is located at J=JMAX(1). The lower surface of the first input component is located at J=1 of Zone 2, while the upper surface of the second input component is located at J=JMAX(2). This pattern is followed until the lower surface of component NC is located at J=1 of Zone NZONE=NC+1 and the bottom boundary of the grid is located at J=JMAX(NZONE). The forward boundary is always located at I=1, while the aft boundary is located at I=IMAX for the respective zone. While the order of input of the components does not affect the overall set-up of the airfoil geometry, it does directly affect the definition of the resulting grid topology. Therefore, the user must be careful to input the airfoil component in a top-to-bottom order for the grid to be properly generated.

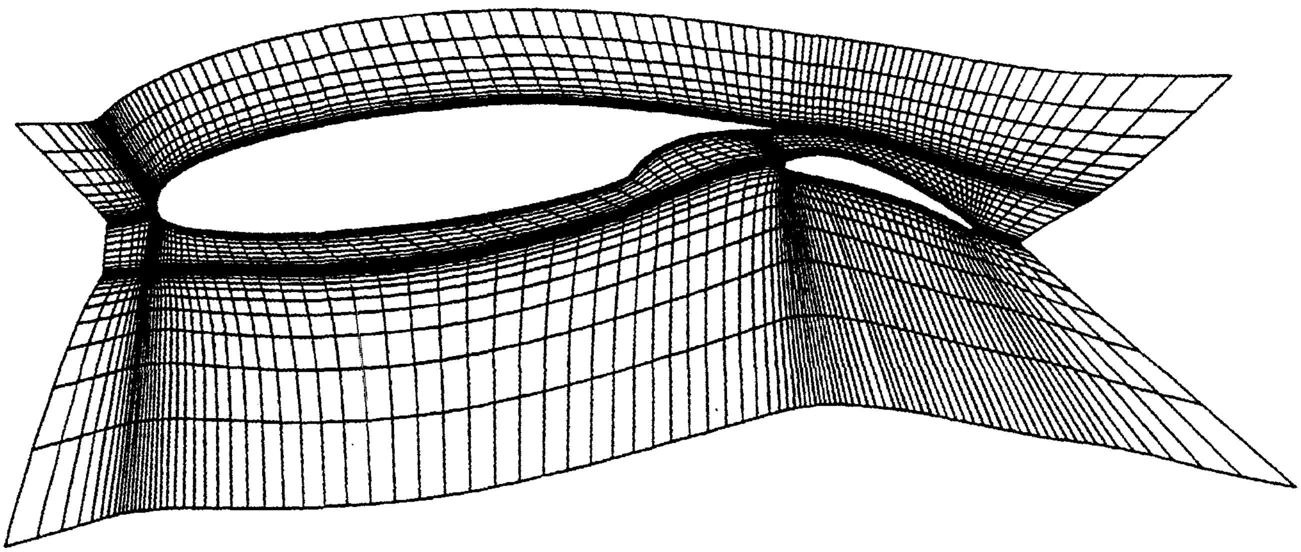

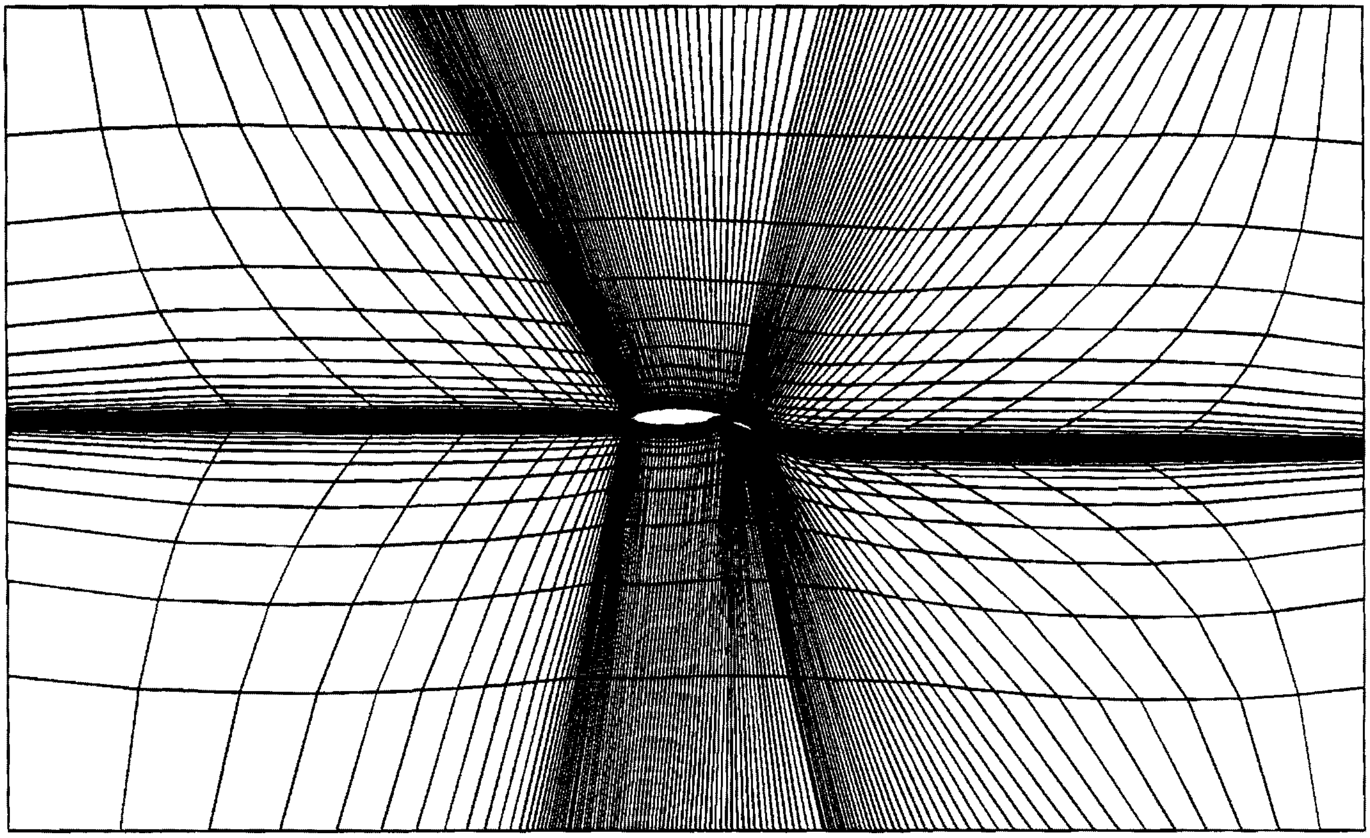

• Expt.

GAW-1 AIRFOIL, FLAP ANGLE 20 DEG.

MINF=0.3 2.2 Million Reynolds No.

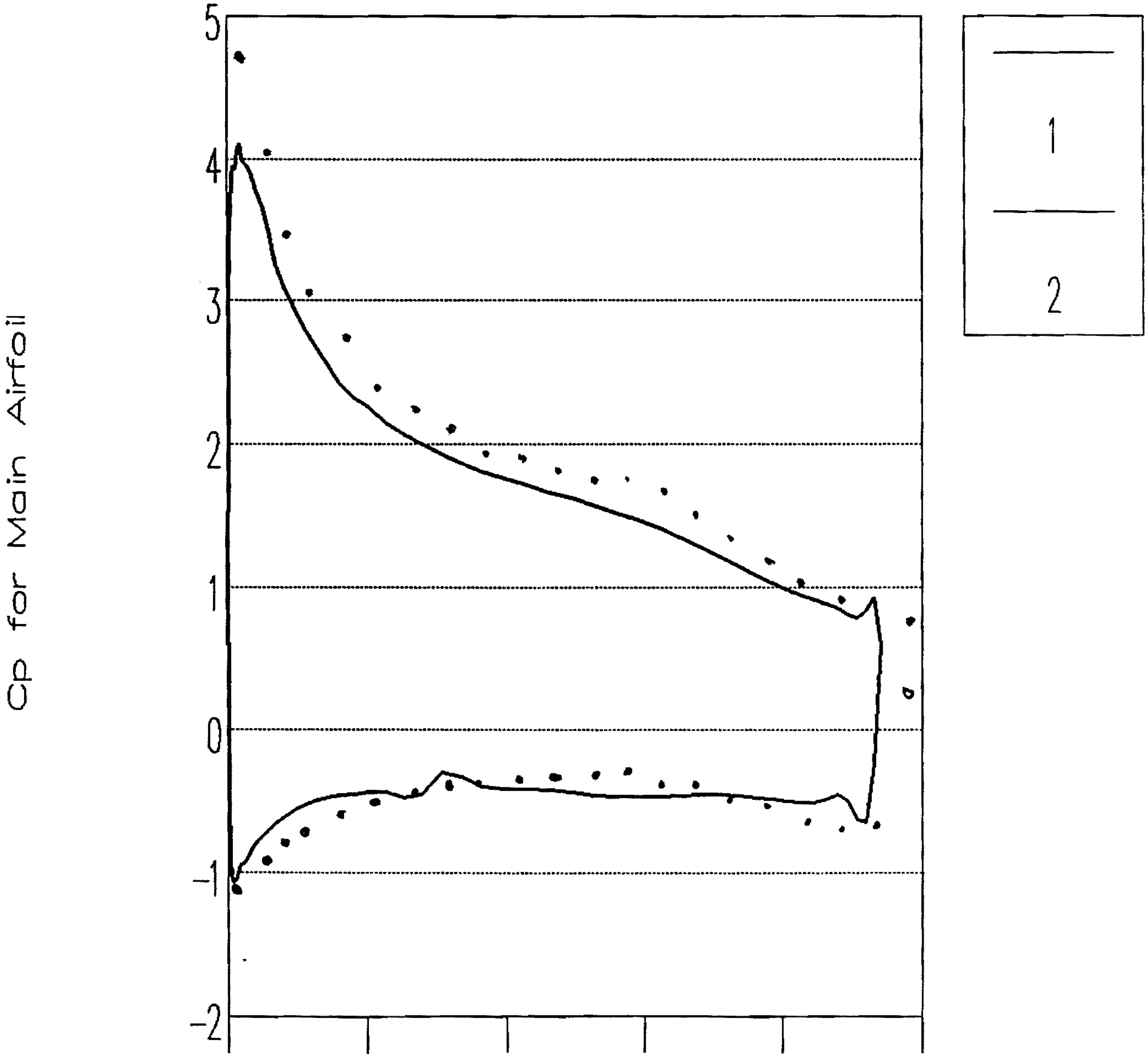

GAW-1 AIRFOIL, FLAP ANGLE 20 DEG.

MINF=0.3 2.2 Million Reynolds No.

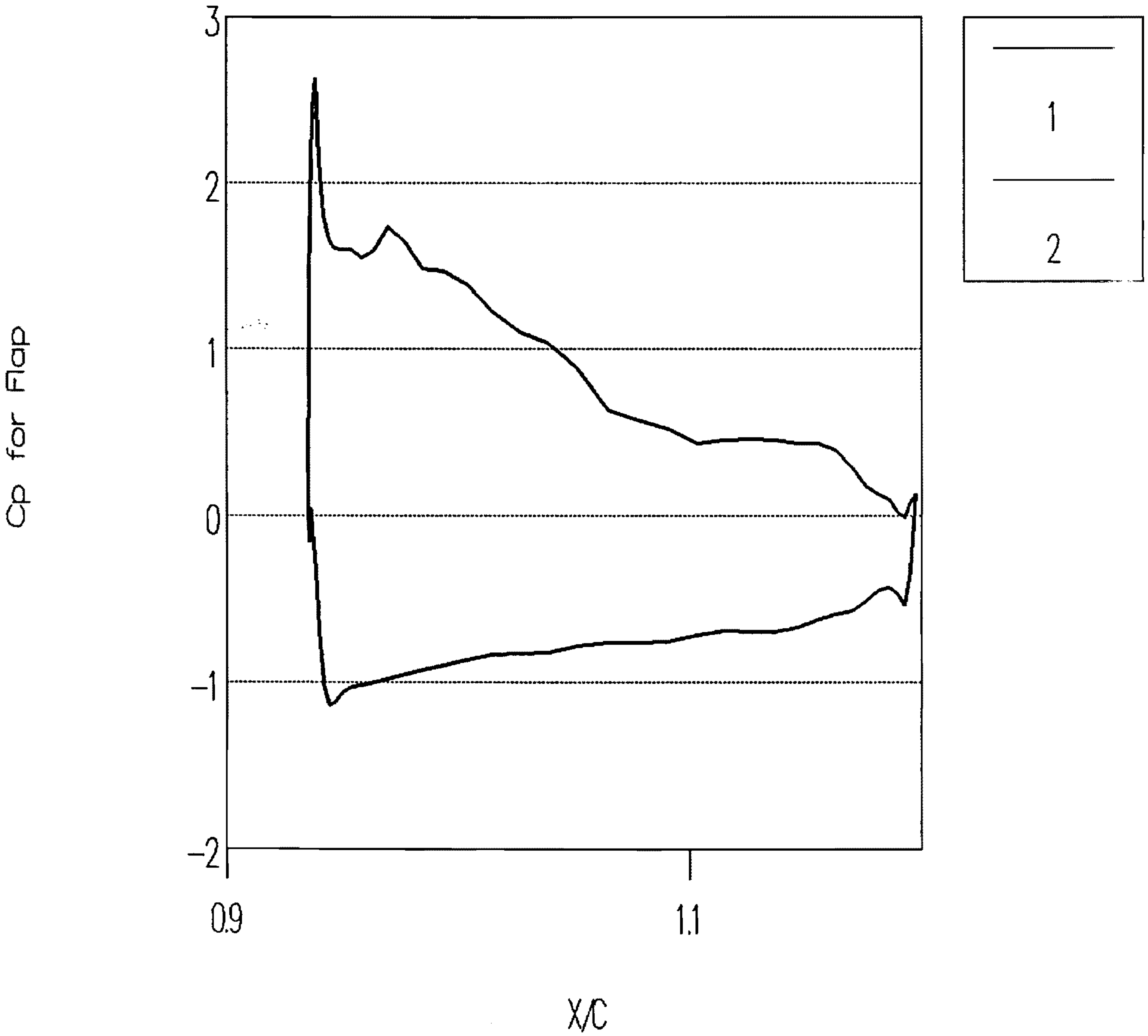

E-16-[illegible]
112

School of Aerospace Engineering

Georgia Institute of Technology
Atlanta, Georgia 30332-0150
404•894•3000
Fax: 404•894•2760

November 20, 1990

David Findlay
Code 6051
Naval Air Development Center
Warminster, PA 18974

Subject: Bi-Monthly Progress Report for the Period September 1 - October 30, 1990, for Contract N62269-90-C-0246

Dear Mr. Findlay:

During the reporting period September 1 - October 30, 1990, the following progress was made on the subject contract:

1. The two-dimensional multi-element airfoil code GTMEL2D (previously delivered to the sponsor) was modified to handle surface motion. The main airfoil as well as the second element (canard , flap or slat) is free to pitch and plunge. At each time step, the body-fitted grid must be regenerated. For small amplitude motions, the original grid developed by the Thompson-Thames-Mastin grid procedure can be modified by simple shearing transformations. For large amplitude motions, it is necessary to call the grid generator, and redistribute the grid. For rigid body rotations where the main airfoil and the second element both rotate about the same axis, by the same amount, the original grid may be simply rotated at every time step.

2. The modified flow solver with surface motion is being debugged through study of the dynamic stall characteristics of a Boeing Vertol VR-7 airfoil, with a leading edge slat made of a NACA 15320 profile. Experimental data for this configuration is available in the AIAA Paper 83-2533 titled "The Effect of a Leading Edge Slat on the Dynamic Stall of an Oscillating Airfoil," by Larry Carr and Ken McAlister.

Figure 1 shows the body-fitted grid, and figure 2 shows a close-up view of the grid in the vicinity of the slat.

To date, the following results have been obtained:

a) A steady state solution has been obtained for this configuration at Mach number 0.2, Mean Angle of Attack 5 degrees and a Reynolds number of 2.5 Million. The computed lift coefficient of 0.57 is in good agreement with the experimental data.

b) Unsteady variation of lift, drag and pitching moment for the early portion of the dynamic stall loop have also been obtained, but have not been compared with experimental data at this time.

We plan to brief you on the capabilities of the modified GTMEL2D code in December, and deliver the source code, sample data set and sample input/output information at that time.

Sincerely,

LAKSHMI N. SANKAR
Associate Professor

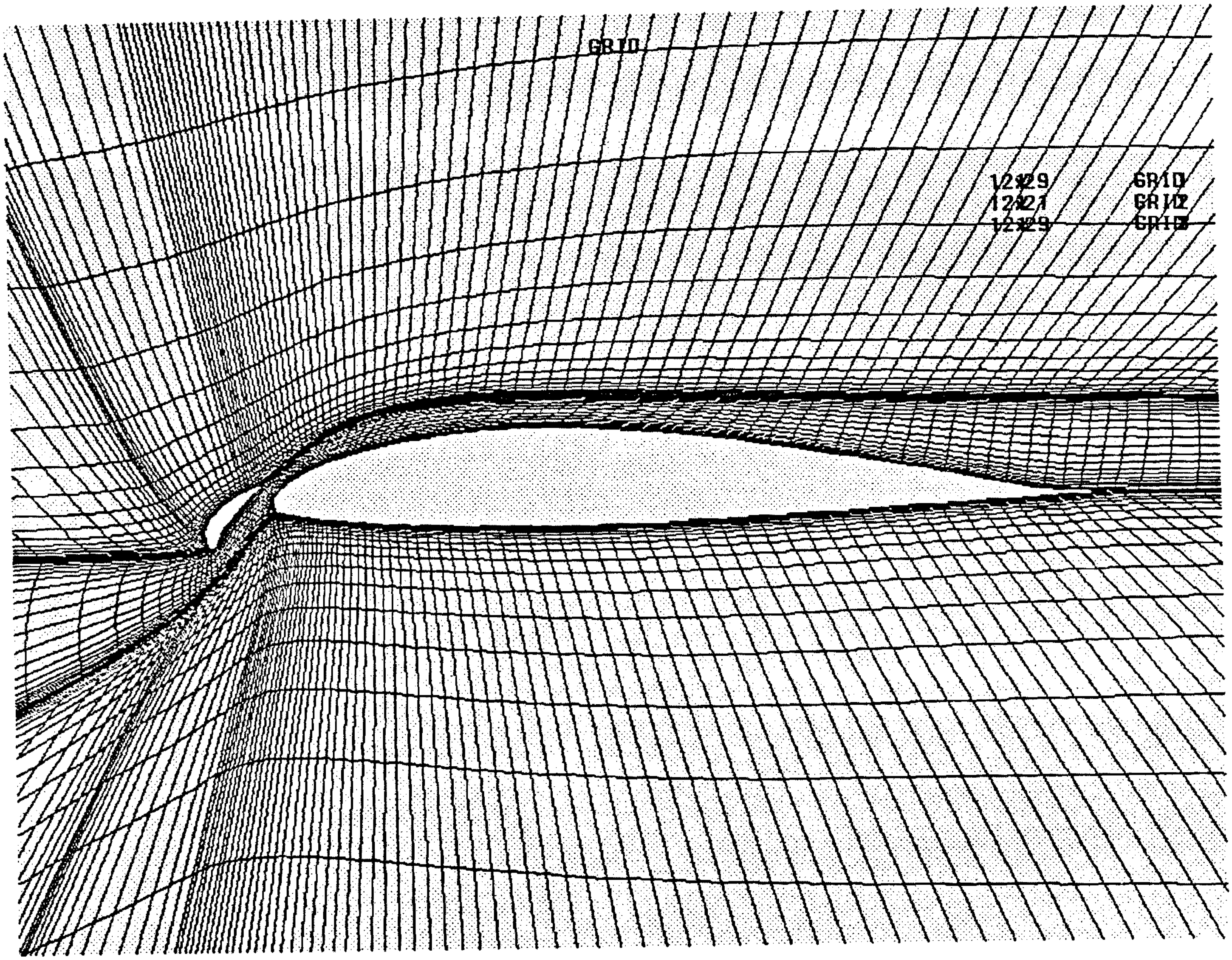
GRID

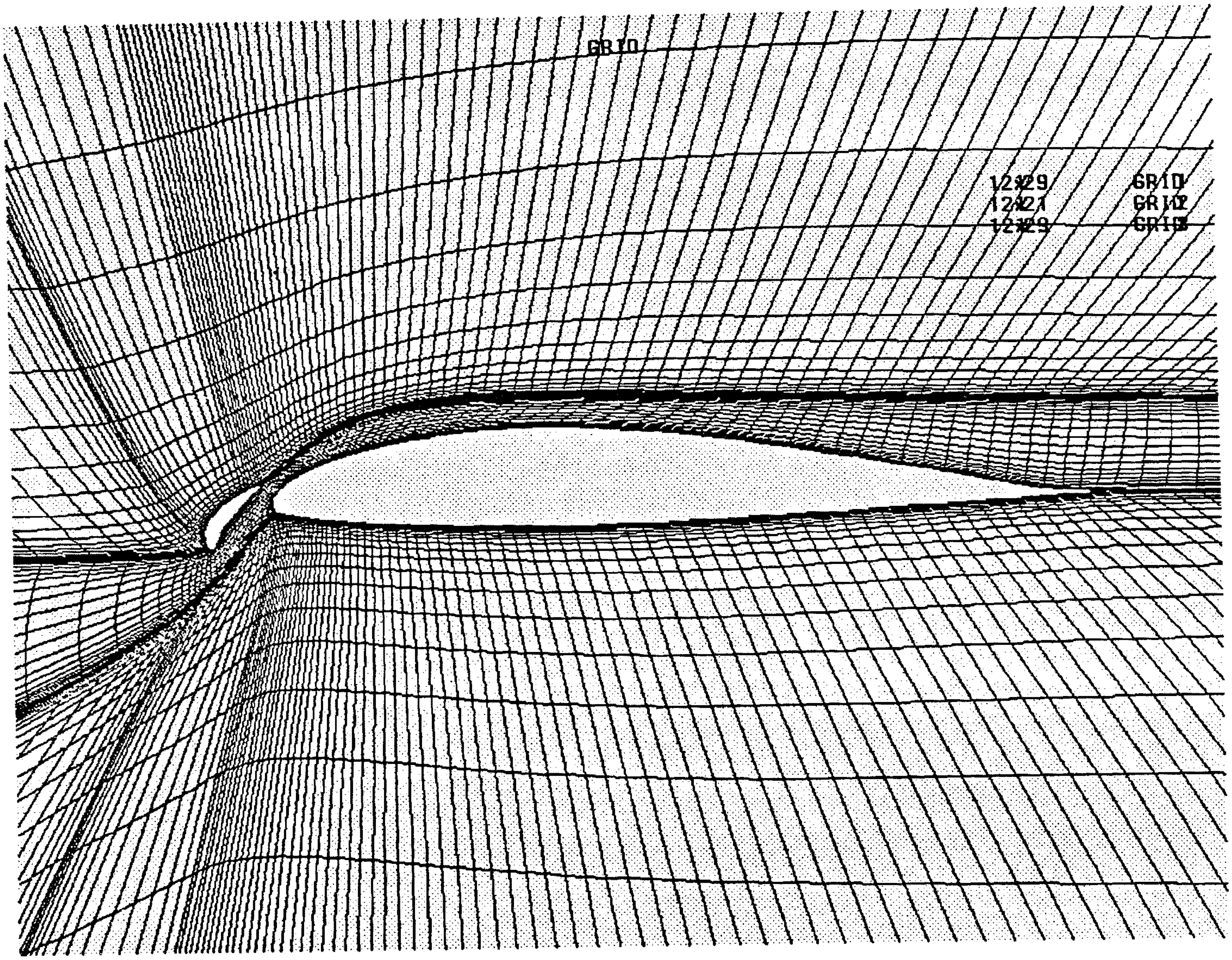
GRID
12X29 GRID
12X21 GRID2
12X29 GRID3

E-16-N07
3

UNSTEADY AERODYNAMIC ANALYSIS OF DUAL-ELEMENT WING CONFIGURATIONS

BI-MONTHLY PROGRESS LETTER FOR THE PERIOD

November 1, 1990 - December 31, 1990

Submitted to the

NAVAL AIR DEVELOPMENT CENTER
WARMINSTER, PA
Attn: David Findlay

Prepared By

L. N. Sankar
Associate Professor
School of Aerospace Engineering
Georgia Institute of Technology, Atlanta, GA 30332

January 1991

January 20, 1991

Mr. Dave Findlay
Code 6051
Naval Air Development Center
Warminster, PA 18974

Subject: BI-MONTHLY PROGRESS REPORT FOR THE PROJECT "UNSTEADY AERODYNAMIC ANALYSIS OF DUAL-ELEMENT WING CONFIGURATIONS"

Dear Mr. Findlay:

During the reporting period November 1, 1990- December 31, 1990, the following tasks were completed:

a) The 2-D compressible Navier-Stokes solver capable of handling multi-element airfoil configurations was calibrated by computing the flow field over a two-element Boeing Vertol VR-7 airfoil-slat configuration that has been tested at NASA by Larry Carr and Ken McAlister. In this study, the airfoil-slat combination undergoes large amplitude sinusoidal pitching oscillations, between 5 and 25 degrees. In the absence of the slat, a massively separated flow would arise at the end of the upstroke, giving rise to an abrupt stall and a slow recovery to attached flow conditions. The presence of the slat greatly reduces the separated flow region during the downstroke, and leads to smaller hysteresis loops.

Our calculations indicate that the multi-element airfoil solver correctly predicts the reduction in the size of the separated flow region, and leads to smaller hysteresis loops, when compared to a single element airfoil. Figure 1 shows the lift hysteresis loop computed using the Navier-Stokes solver, and figure 2 shows the surface pressure distribution over the slat and the main airfoil at a number of time levels.

While the computed hysteresis loop is in qualitative agreement with experiments, there are some discrepancies between the theory and measurements. The theory predicts that separation is triggered while the airfoil is pitching up, around 20 degrees. Experiments, and our single element airfoil analyses for comparable configurations indicate stall to begin around 25 degrees. The early separation appears to be a result of low eddy viscosities computed by the flow solver, over the upper region. Our experience in the past with single element airfoil analyses indicates that low computed eddy viscosities frequently arise when the gird density normal to the airfoil is not fine enough.

These calculations are being repeated on a finer grid, to determine if improvements in the computed hysteresis loops are possible, and to assess the effects of grid spacing on the computed loads.

b) A series of calculations to study the effects of blowing at the surface of low aspect ratio wings on the high-alpha stall characteristics are in progress. These calculations are done jointly with Dave Findlay of NADC. Preliminary results on the effects of blowing on the vortex-twin tail interactions of fighter aircraft will be presented at the forthcoming AIAA Fluids and Plasma Dynamics Conference.

c) The Georgia Tech 3-D compressible Navier-Stokes code is being modified to study multi-element surfaces such as wing-canard combinations. To calibrate this code, we plan to use a generic wing-canard-fuselage combination recently studied at the NASA Ames Research Center. Figure 3 shows the configuration geometry, and details of the surface grid.

Sincerely,

LAKSHMI N. SANKAR
Associate Professor

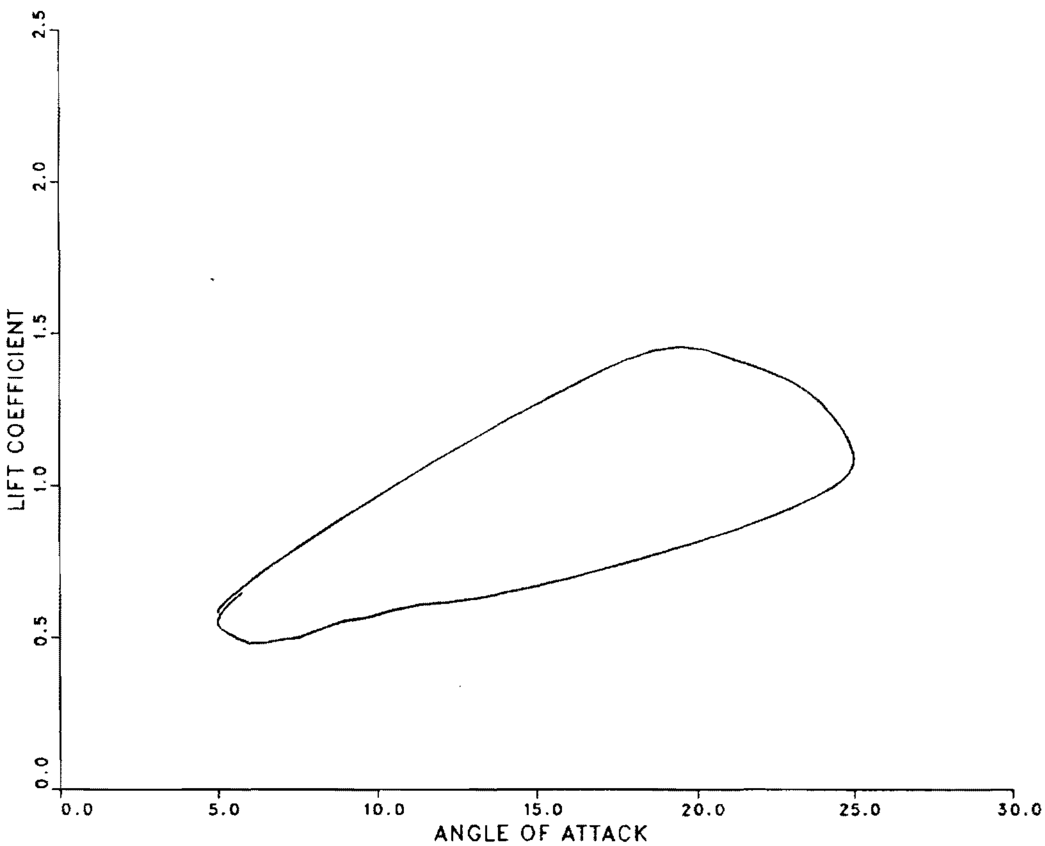

lbm run, dt = 0.01

Fig. 1 Lift hysteresis loop for a Boeing Vertol VR-7-Slat combination.

Fig. 2 Surface pressure distributions for airfoil-slat combination at different time levels.

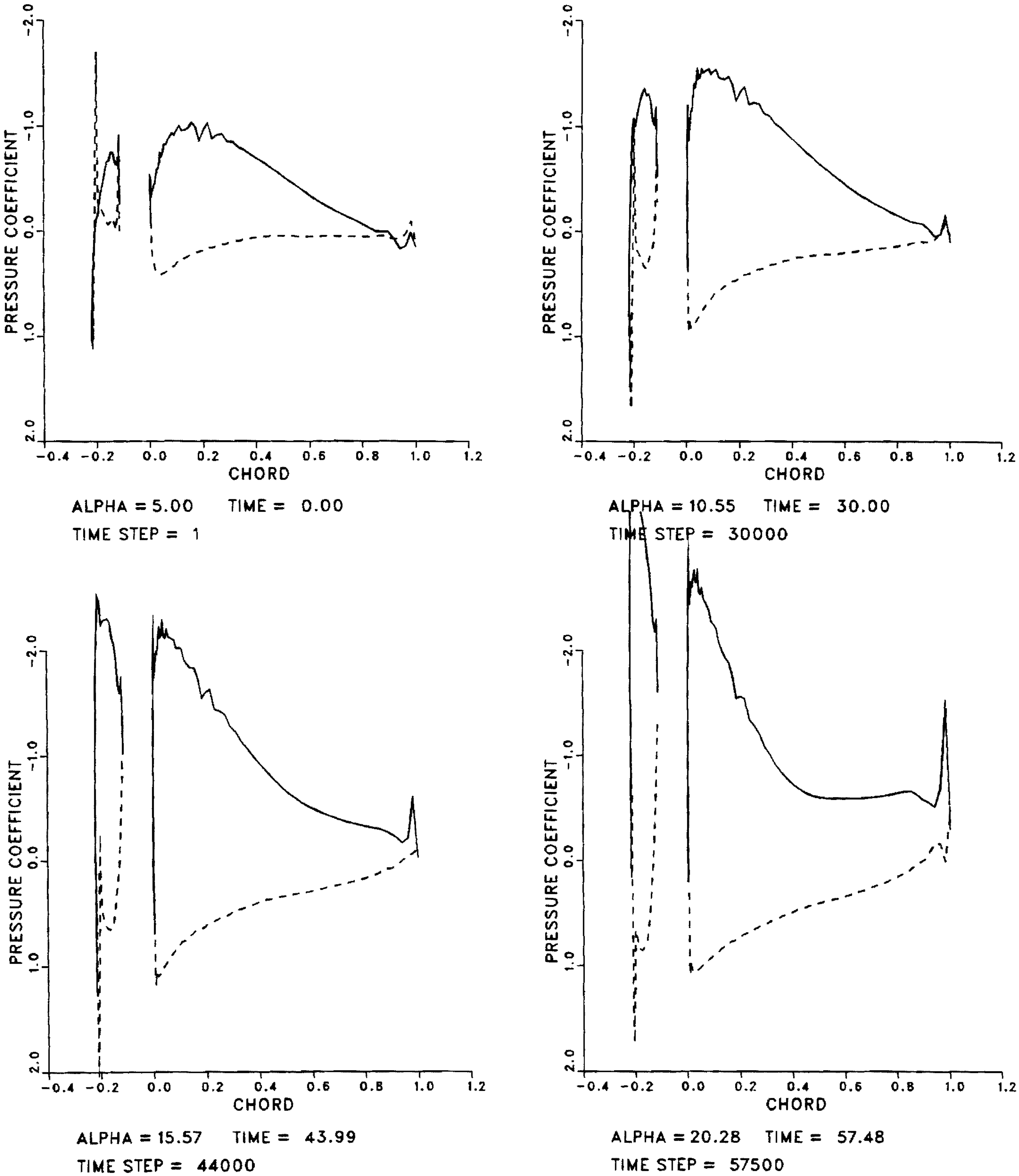

Ibm run, dt = 0.01

Fig. 2 (continued)

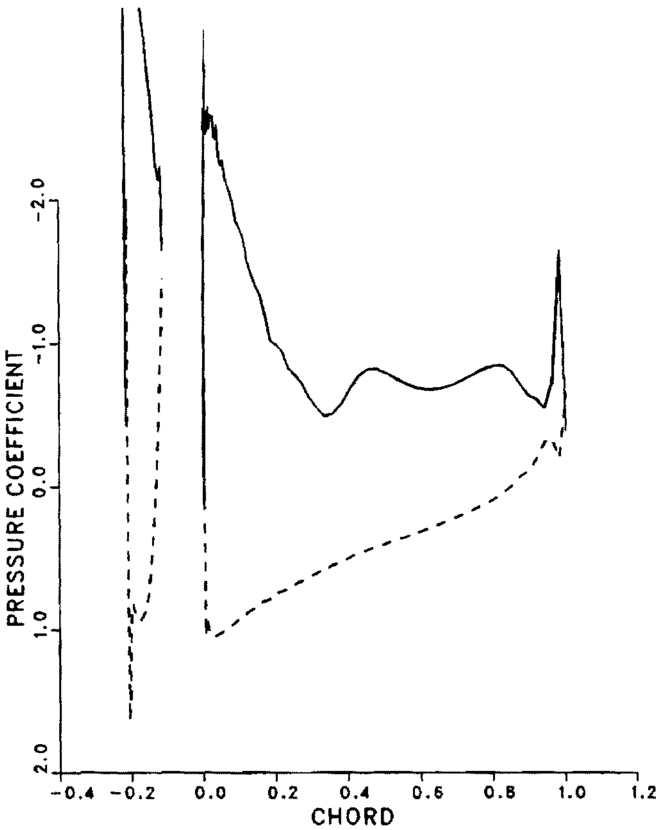

ALPHA = 23.51   TIME = 69.97

TIME STEP = 70000

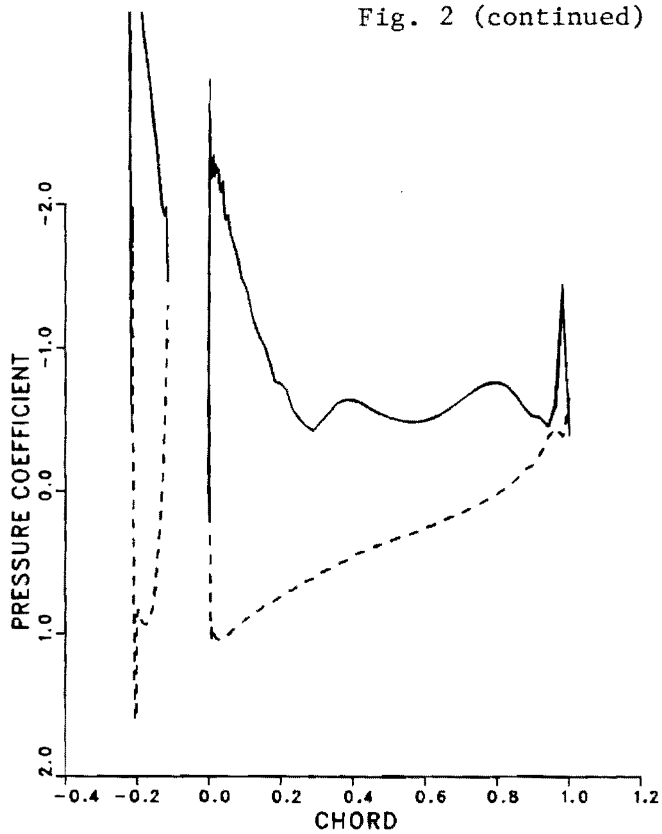

ALPHA = 25.00   TIME = 84.96

TIME STEP = 85000

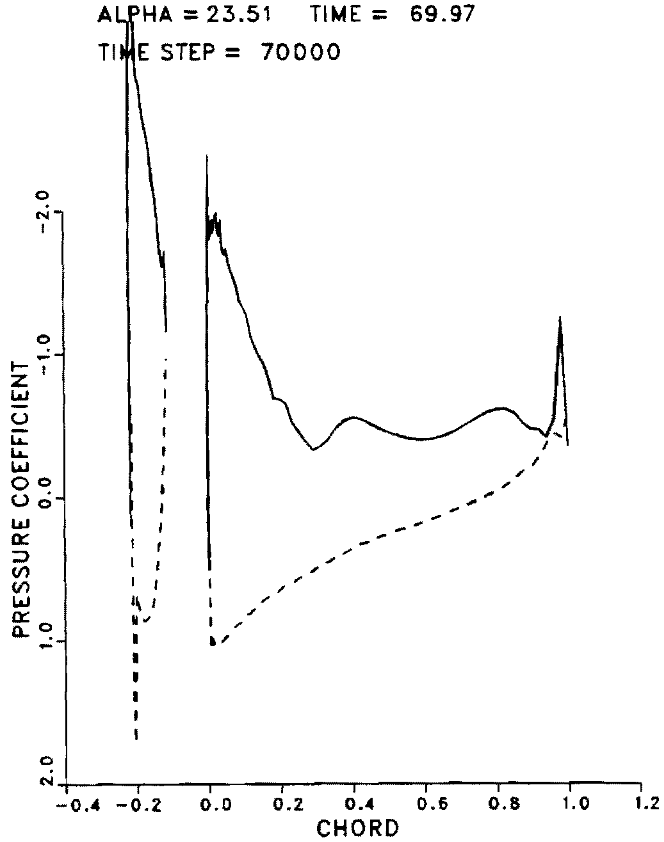

ALPHA = 22.97   TIME = 102.46

TIME STEP = 102500

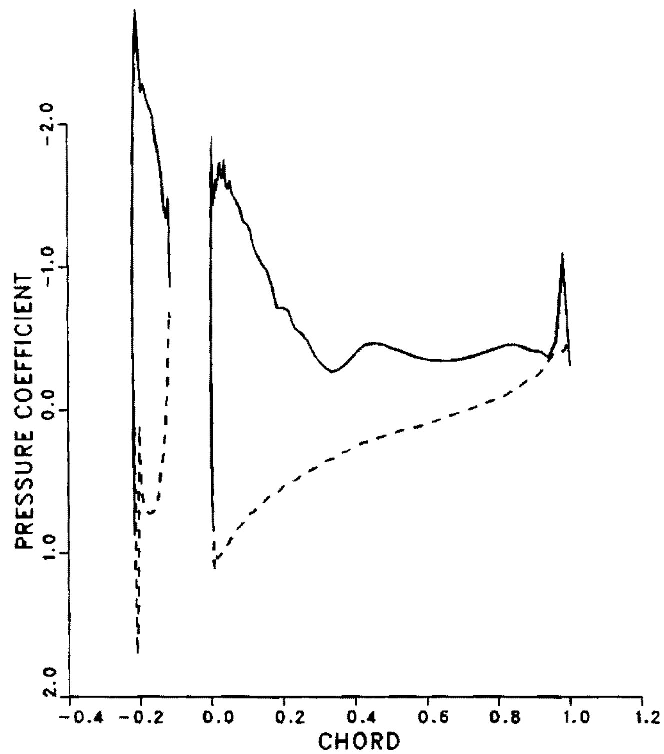

ALPHA = 19.43   TIME = 114.95

TIME STEP = 115000

lbm run, dt = 0.01

Fig. 2 (continued)

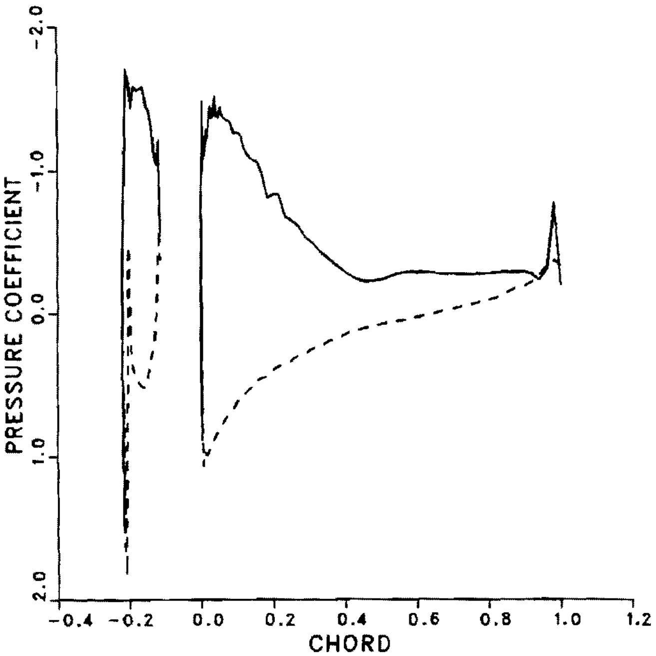

ALPHA = 14.97 TIME = 127.44

TIME STEP = 127500

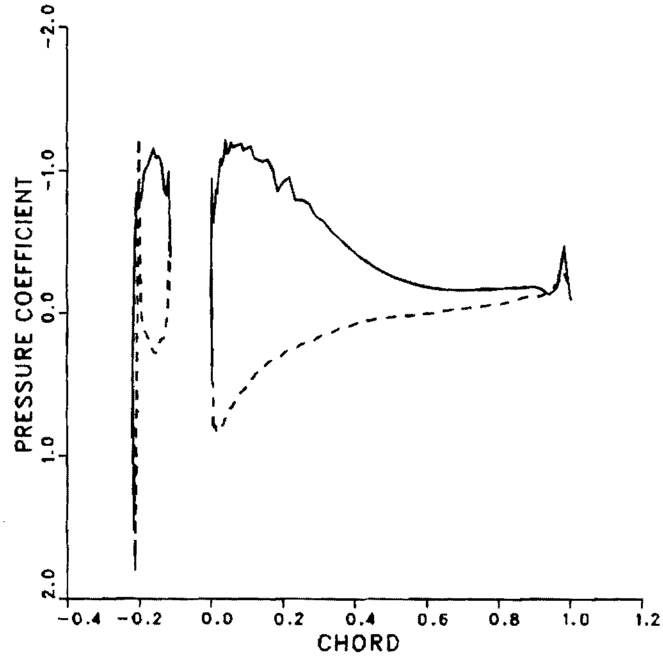

ALPHA = 10.48 TIME = 140.03

TIME STEP = 140000

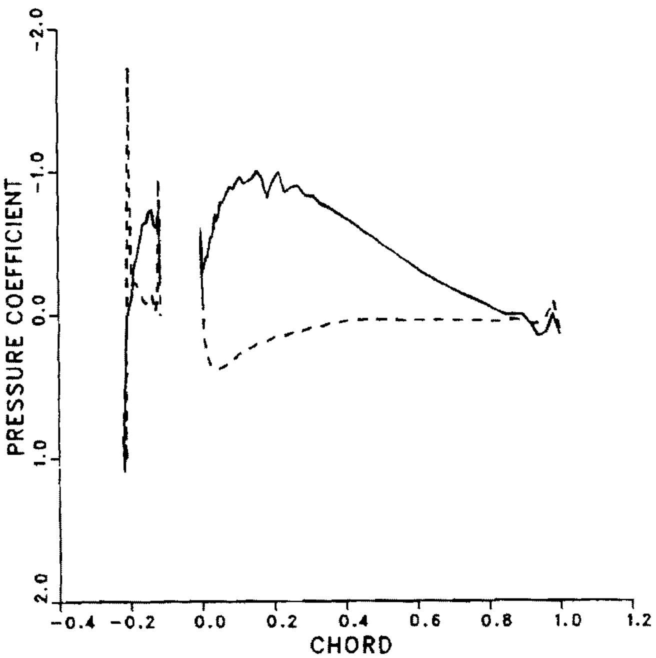

ALPHA = 5.00 TIME = 170.24

TIME STEP = 170000

lbm run, dt = 0.01

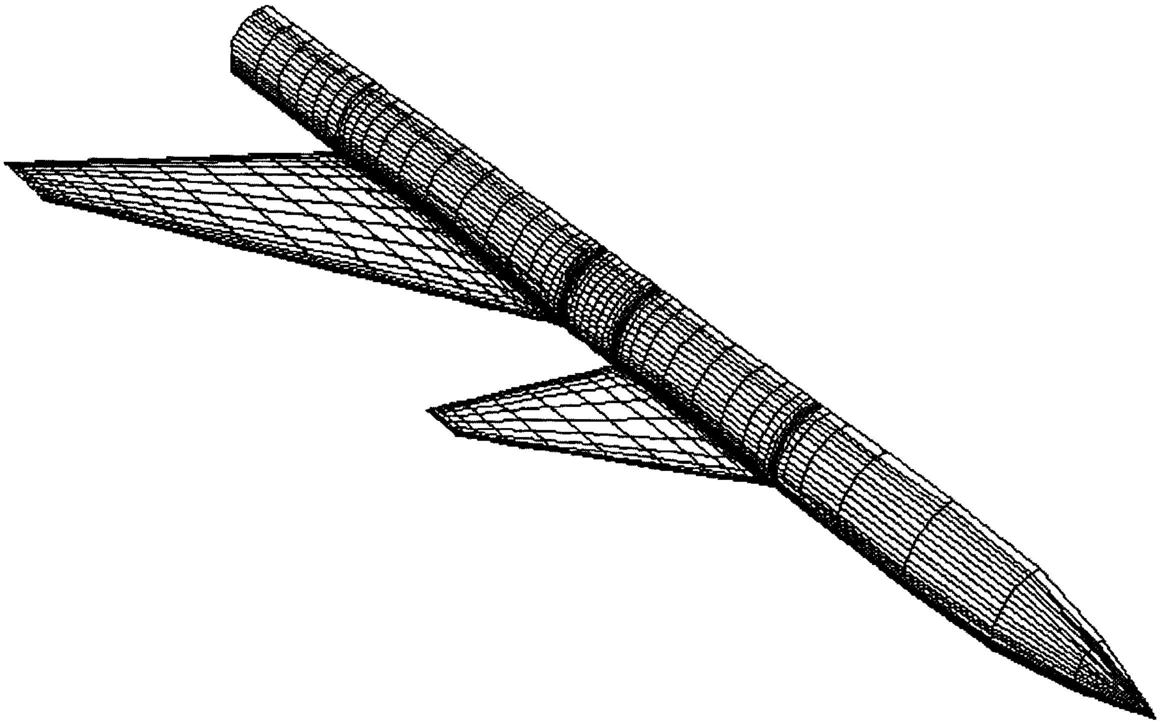

Fig. 3a Geometry definition for a generic wing-body-canard configuration.

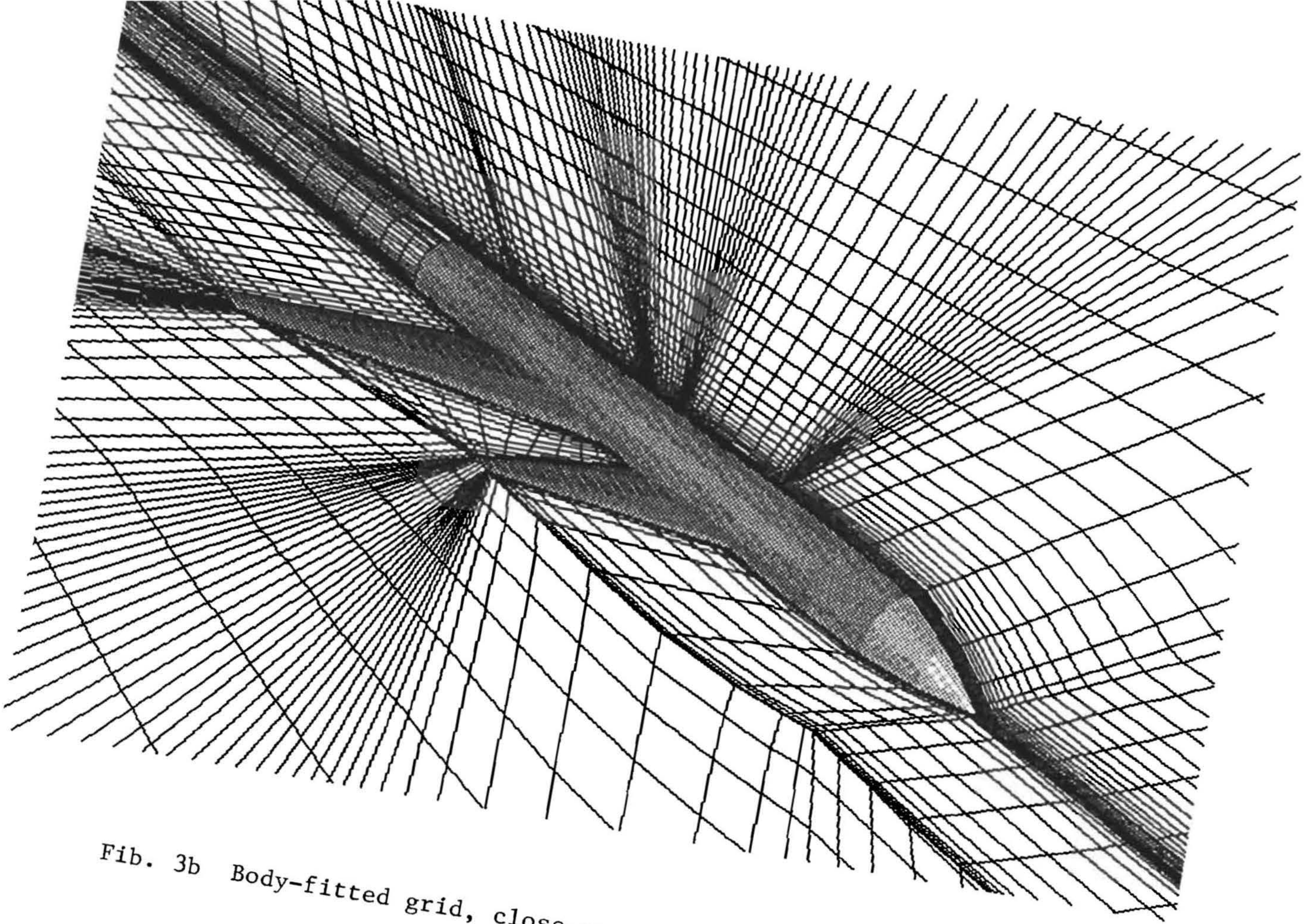

Fib. 3b Body-fitted grid, close-up view.

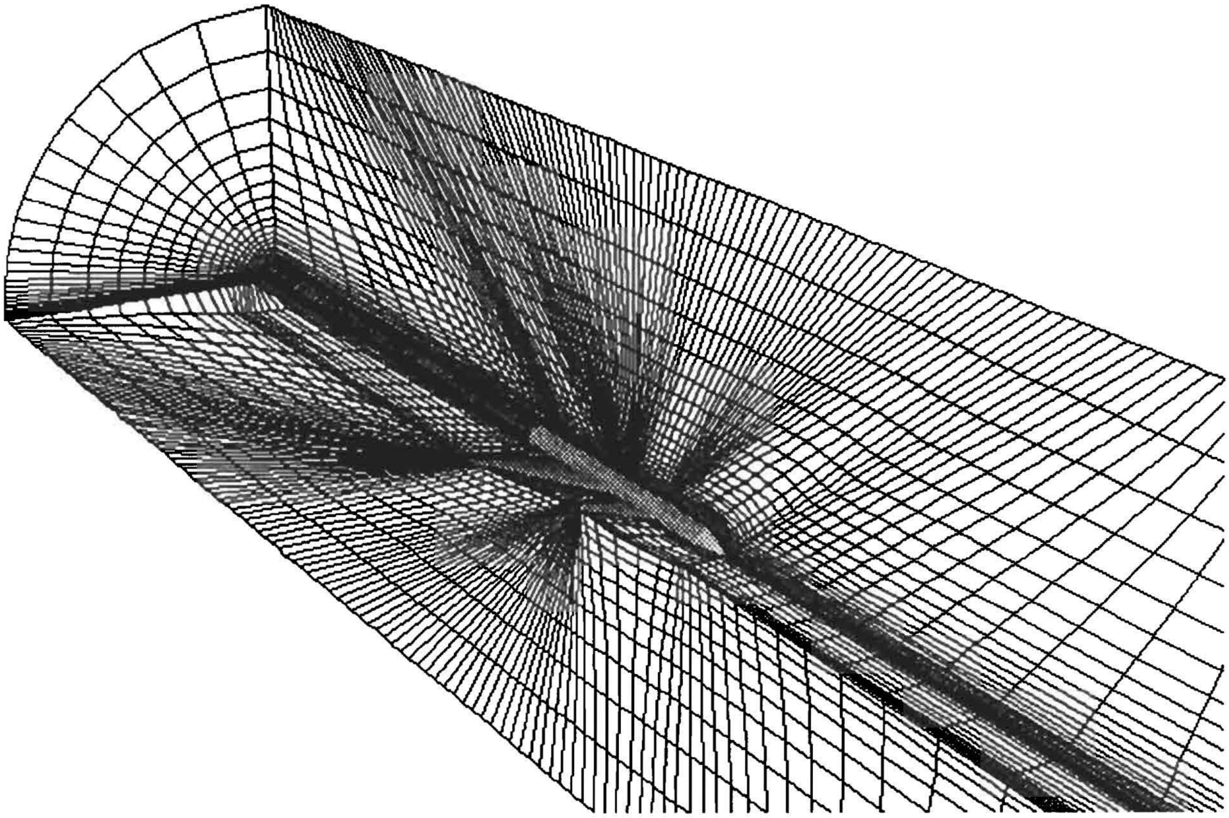

Fig. 3c Body-fitted grid, including far field boundaries.

E-16-607

4

UNSTEADY AERODYDYNAMIC ANALYSIS OF DUAL-ELEMENT WING CONFIGURATIONS

BI-MONTHLY PROGRESS LETTER
FOR THE PERIOD

JANUARY 1, 1991 - FEBURARY 28, 1991

Submitted to the

NAVAL AIR DEVELOPMENT CENTER
WARMINSTER, PA

Attn: David Findlay

Prepared by

L. N. Sankar
Associate Professor
O. J. Kwon
Post-Doctoral Fellow
School of Aerospace Engineering
Georgia Institute of Technology,
Atlanta, GA 30332

March 1991

School of Aerospace Engineering

Georgia Institute of Technology
Atlanta, Georgia 30332-0150
404•894•3000
Fax: 404•894•2760

March 31, 1991

Mr. Dave Findlay
Code 6051
Naval Air Development Center
Warminster, PA 18974

Subject: BI-MONTHLY PROGRESS REPORT FOR THE PROJECT "UNSTEADY AERODYNAMIC ANALYSIS OF DUAL-ELEMENT WING CONFIGURATIONS"

Dear Mr. Findlay:

During the reporting period January 1, 1991 - February 28, 1991, the following tasks were completed:

a) The Georgia Tech 3-D compressible, unsteady Navier-Stokes code capable of handling 3-D wings and helicopter rotors has been modified to study the flow over the F-15 wing-body-inlet configuration at high angles of attack. Calculations were performed for the cases with and without spanwise blowing and suction at wing leading-edge and fuselage forebody to study the effect of flow control on the overall flowfield, vortex trajectory, and the aerodynamic loading behavior at 20 deg. angle of attack and freestream Mach number of 0.15. The results were obtained in a time accurate mode so that the inherent unsteadiness of the flow at this high angle of attack can be captured properly.

Fig. 1 shows the F-15 wing-body-inlet configuration with wing leading edge blowing region (shown as a dark strip on the figure) which stretches through the entire wing span. The intensity of blowing or suction (negative blowing) was assumed to be 15% of the freestream velocity in the direction normal to the wing leading edge at each spanwise section. Figs. 2 and 3 show the top and side views of the particle trajectories for the cases with and without blowing. In the case of wing leading edge blowing (Fig. 2 a), the vortex over the wing has a more organized structure and tighter vortex core than without blowing (Fig. 2 b). This is expected to delay the vortex bursting as a result. The vortex core trajectory for the blowing case is located much closer to the fuselage and the vertical tail than that without blowing. The time history of the local lift coefficient at several spanwise stations with and without blowing is compared in Fig. 4. The result shows that the lift coefficient without blowing has an inherent unsteady nature represented by the repeated pattern of lift variation at about 5 Hz, especially on the wing. This is most likely due to the vortex bursting near the wing trailing edge. Since the blowing adds energy to the flow and delays the vortex bursting, the lift behavior for the blowing case shows much less unsteadiness than without blowing.

In case of wing leading edge suction, the particle trajectory simulation in Fig. 2 c shows an early vortex bursting on the wing surface at about 40% of the chord at the wing tip region. The lift behavior plotted on Fig. 5 shows that the magnitude of flow unsteadiness is much larger than that without blowing on the wing surface. Thus suction appears to promote early vortex bursting.

During the next reporting period, this study will be continued for several different blowing intensities and for different blowing locations over the wing and body, and the aerodynamic loading on the vertical tail due to the vortex-vertical tail interactions will be estimated.

(b) A modification of the 3-D Georgia Tech Navier-Stokes code is under progress to study multi-element surfaces such as canard-wing-body combinations both in steady and unsteady flight conditions. The flow solver has been restructured so that a multi-block flow simulation is possible. This solver is being coupled to the elliptic multi-block grid generator, which was reported in the previous progress report. The code debugging and test runs will continue for the next several reporting periods.

Sincerely,

LAKSHMI N. SANKAR
Associate Professor.

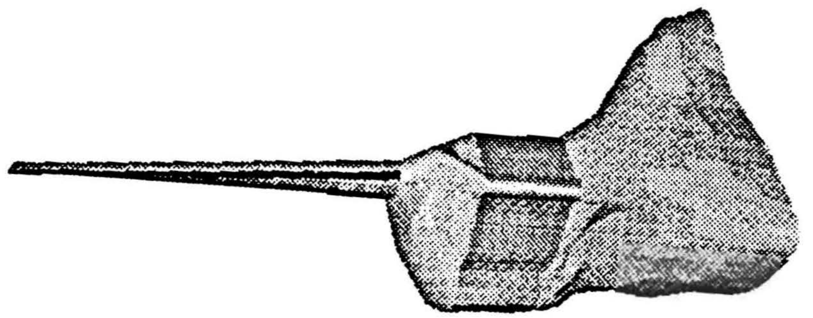

Fig. 1 F-15 Wing-Body-Inlet Configuration

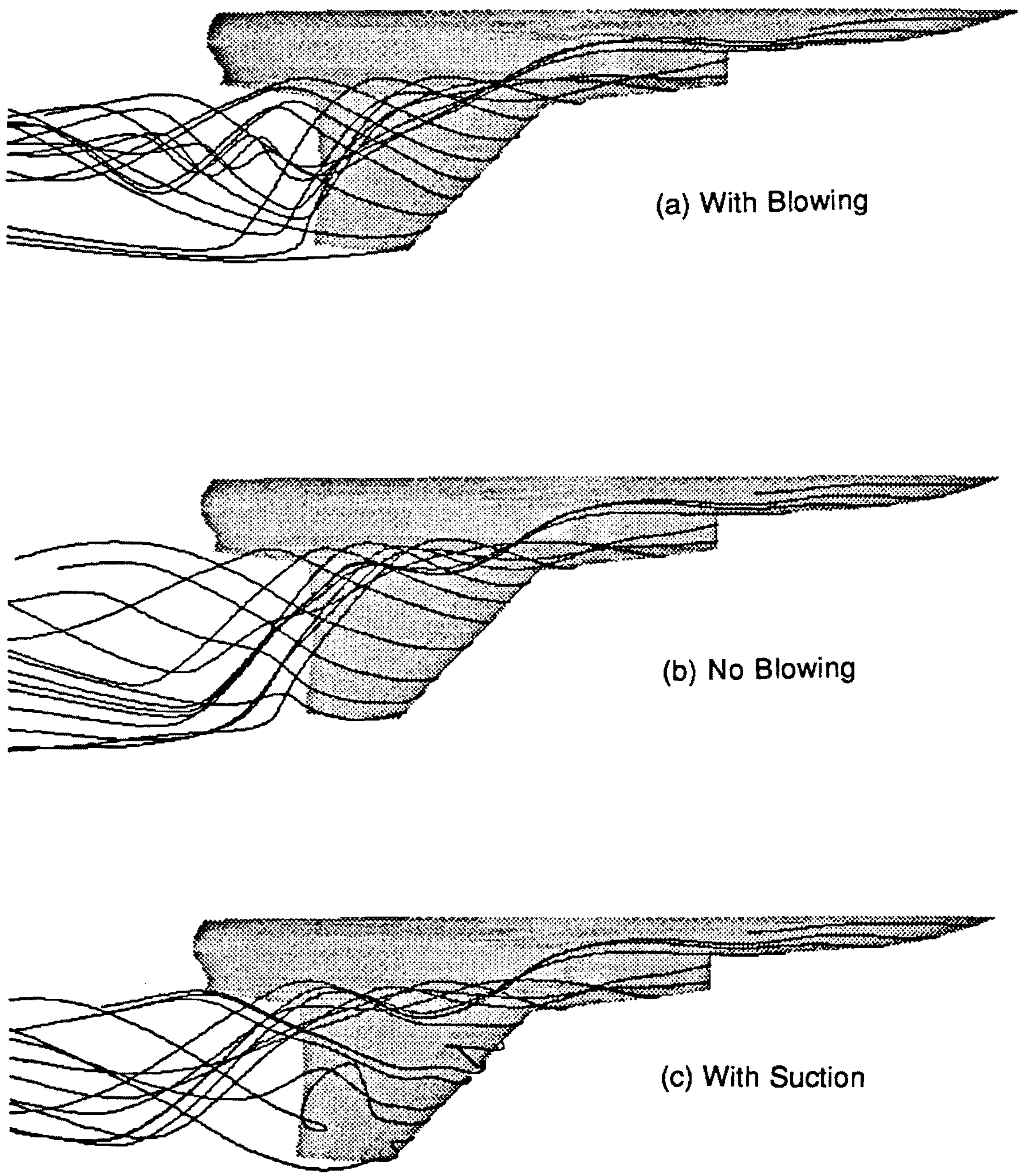

Fig. 2 Particle Trajectory Simulation (Top View)

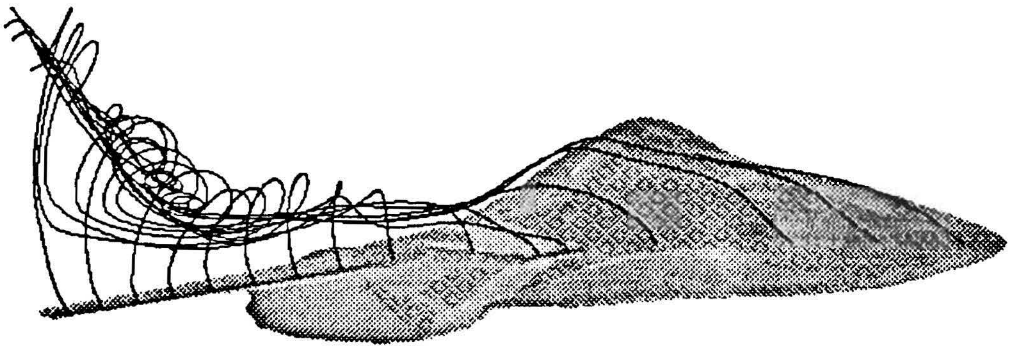

(a) With Blowing

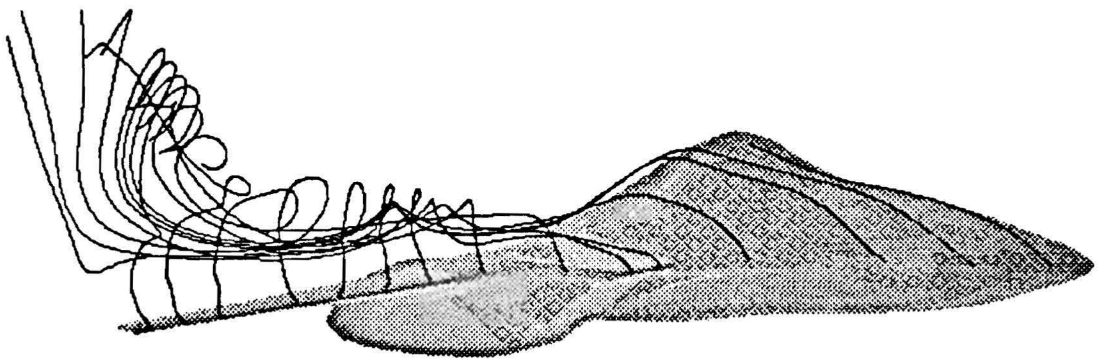

(b) No Blowing

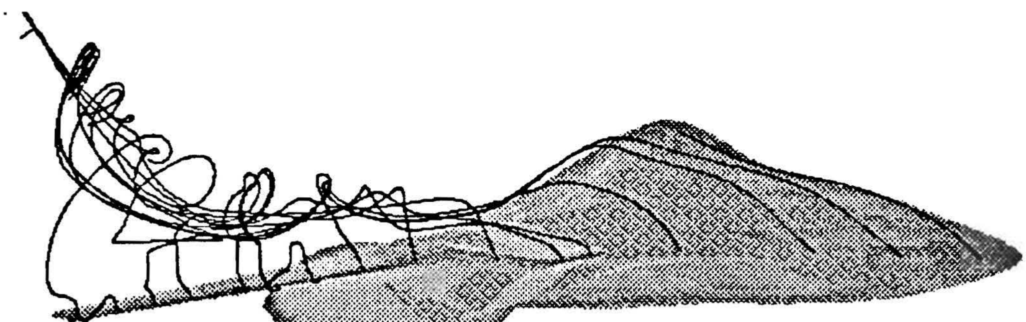

(c) With Suction

Fig. 3 Particle Trajectory Simulation (Side View)

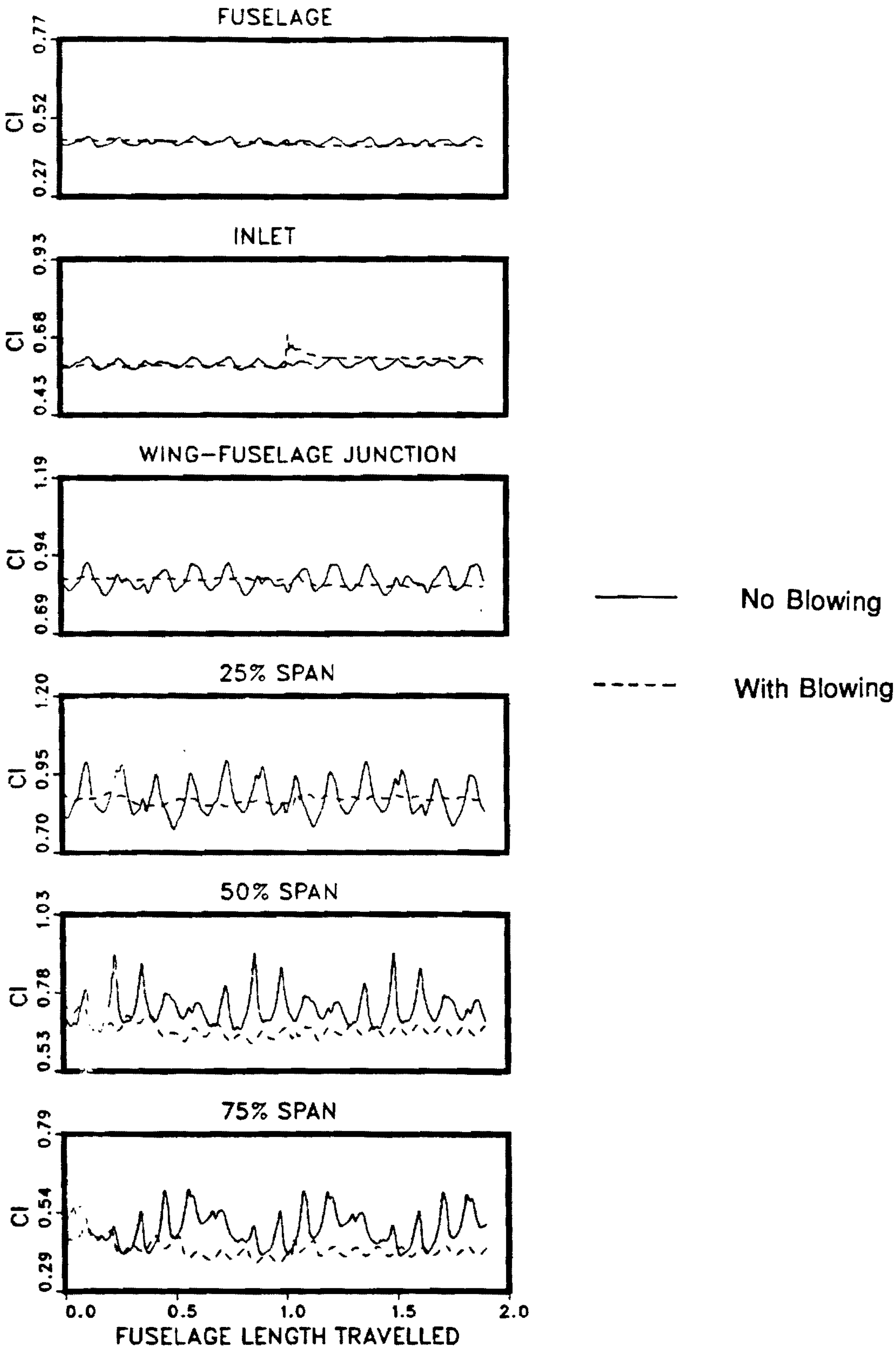

Fig. 4 Comparison of Lift vs. Time Between With and Without Blowing

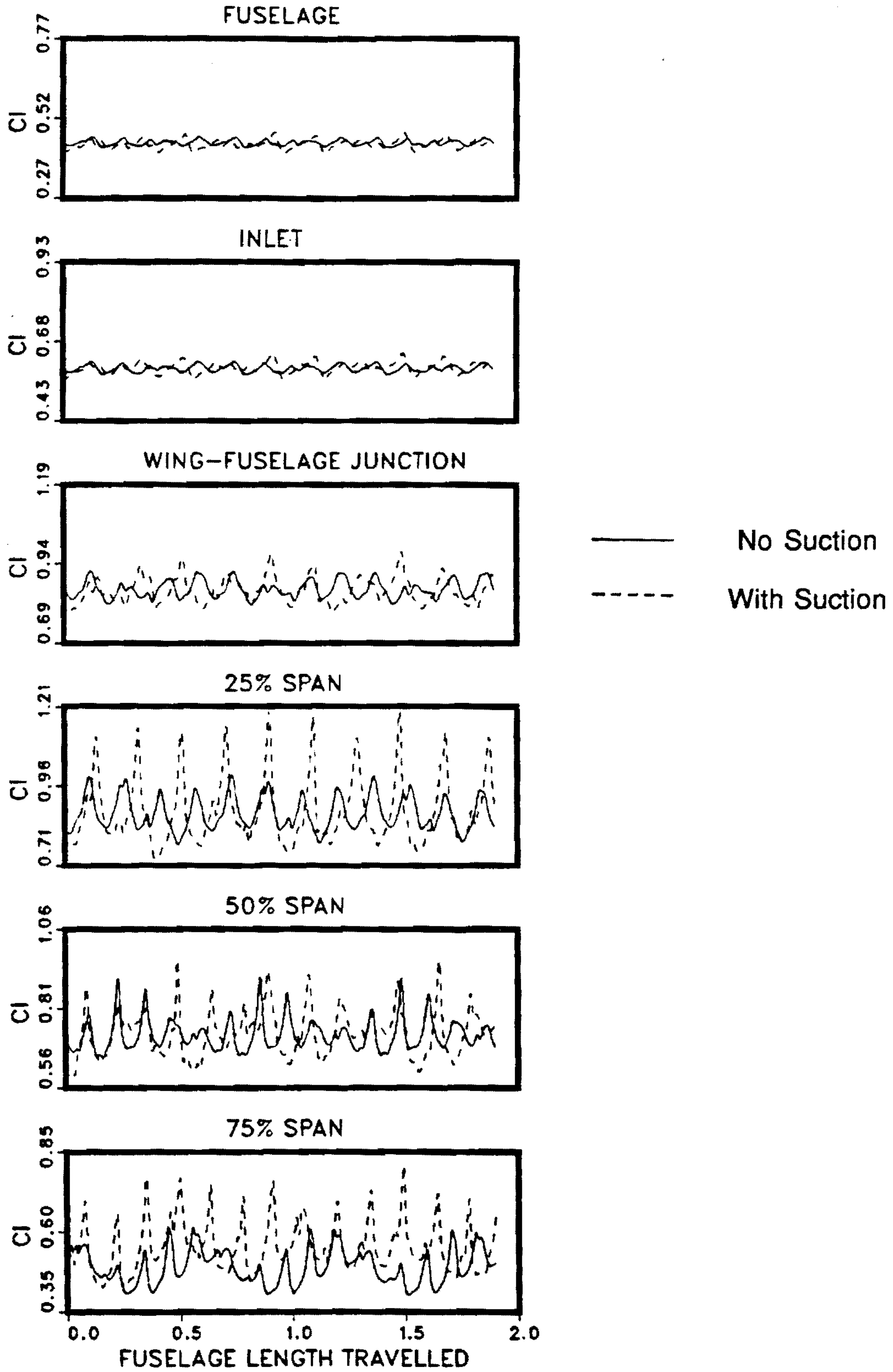

Fig. 5 Comparison of Lift vs. Time Between With and Without Suction

5

UNSTEADY AERODYNAMIC ANALYSIS OF DUAL-ELEMENT WING CONFIGURATIONS

BI-MONTHLY PROGRESS LETTER
FOR THE PERIOD

March 1, 1991 - April 30, 1991

Submitted to the

NAVAL AIR DEVELOPMENT CENTER
WARMINSTER, PA
Attn: David Findlay

Prepared By

L. N. Sankar
Professor
School of Aerospace Engineering
Georgia Institute of Technology, Atlanta, GA 30332

May 1991

May 20, 1991

Mr. Dave Findlay
Code 6051
Naval Air Development Center
Warminster, PA 18974

Subject: BI-MONTHLY PROGRESS REPORT FOR THE PROJECT "UNSTEADY AERODYNAMIC ANALYSIS OF DUAL-ELEMENT WING CONFIGURATIONS"

Dear Mr. Findlay:

During the reporting period March 1, 1991 - April 30, 1991, the following tasks were completed:

a) Calculations for the effects of blowing on an F-15 wing-body-inlet configuration were completed. These results will be presented at the AIAA Fluids and Plasma Dynamics Conference, in June 1991. Final Plots showing particle traces generated using PLOT3D were generated. These plots will be shown to you, and hand-delivered to you, during your trip to Atlanta in June 1991.

b) Modifications to the Georgia Tech 3-D compressible Navier-Stokes code to study multi-element surfaces such as wing-canard combinations continued. Preliminary results for the surface pressure distribution over a generic wing-body of revolution-canard configuration have been obtained, and will be presented to you during your visit in June. The program diverges if large time steps are taken, over the wing and canard upper surface where high fluid velocities and low pressures occur. We are investigating modifications to the numerical viscosity terms in the 3-D solver to improve the stability of the solution procedure.

Sincerely,

LAKSHMI N. SANKAR
Professor

L 76 1

6

UNSTEADY AERODYDYNAMIC ANALYSIS OF DUAL-ELEMENT WING CONFIGURATIONS

BI-MONTHLY PROGRESS LETTER
FOR THE PERIOD

May 1, 1991 - June 30, 1991

Submitted to the

NAVAL AIR DEVELOPMENT CENTER
WARMINSTER, PA

Attn: David Findlay

Prepared by

L. N. Sankar
Professor
and
O. J. Kwon
Post-Doctoral Fellow

School of Aerospace Engineering
Georgia Institute of Technology,
Atlanta, GA 30332

July 1991

School of Aerospace Engineering

Georgia Institute of Technology
Atlanta, Georgia 30332-0150
404•894•3000
Fax: 404•894•2760

July 17, 1991

Mr. Dave Findlay
Code 6051
Naval Air Development Center
Warminster, PA 18974

Subject: BI-MONTHLY PROGRESS REPORT FOR THE PROJECT "UNSTEADY AERODYNAMIC ANALYSIS OF DUAL-ELEMENT WING CONFIGURATIONS"

Dear Mr. Findlay:

During the reporting period May 1, 1991 - June 30, 1991, the following tasks were completed:

a) The 3-D elliptic grid generator developed at Georgia Tech has been modified for multi-element configurations and the multi-block grid generation for a typical canard-wing-body combination has been completed. The baseline grid for this configuration is generated as a two-block H-O topology grid with 139 streamwise, 39 radial, and 78 circumferential points. The surface grid distribution and the flowfield grid of the upper block are illustrated in Fig. 1 and Fig. 2. A similar grid for the bottom half of the canard-wing-body configuration completes the second block. The grid points are clustered near the fuselage forebody, wing and canard leading and trailing edges.

b) A modification of the 3-D Navier-Stokes code to study multi element surfaces has been completed. The flow solver has been restructured so that a multi-block flow simulation is possible. This solver has been coupled to the elliptic multi-block grid system described earlier.

An initial test calculation has been performed for the flow about a typical canard-wing-body configuration at a transonic Mach number of 0.95 and at an angle of attack of 13 deg. Fig. 3 to Fig. 6 show the chordwise pressure distributions at several wing spanwise stations. It is shown that the calculated pressures do not correlate well with the experiment, especially on the upper surface of the wing. It is believed that the number of grid points (approximately 400,000) is still not enough to resolve the vortical flow over the wing and canard, especially when there exists a close coupled interaction of the flow between the canard and the wing. Other researchers (e.g., E. Tu, "Navier-Stokes Simulation of a Close-Coupled Canard-Wing-Body Configuration," AIAA Paper 91-0070) also found a need to use a large number of nodes (over 1.5 million) to capture the upper surface features. Fig. 7 shows the particle trajectory simulation of the flow at this flight condition.

We are investigating grid embedding (i.e., computation of flow just over the upper surface of the wing on a dense grid) with the global solution providing boundary conditions and initial condition. Additional test cases for different Mach numbers and at different angles of attack will be performed during the next reporting period.

Sincerely,

LAKSHMI N. SANKAR
Professor

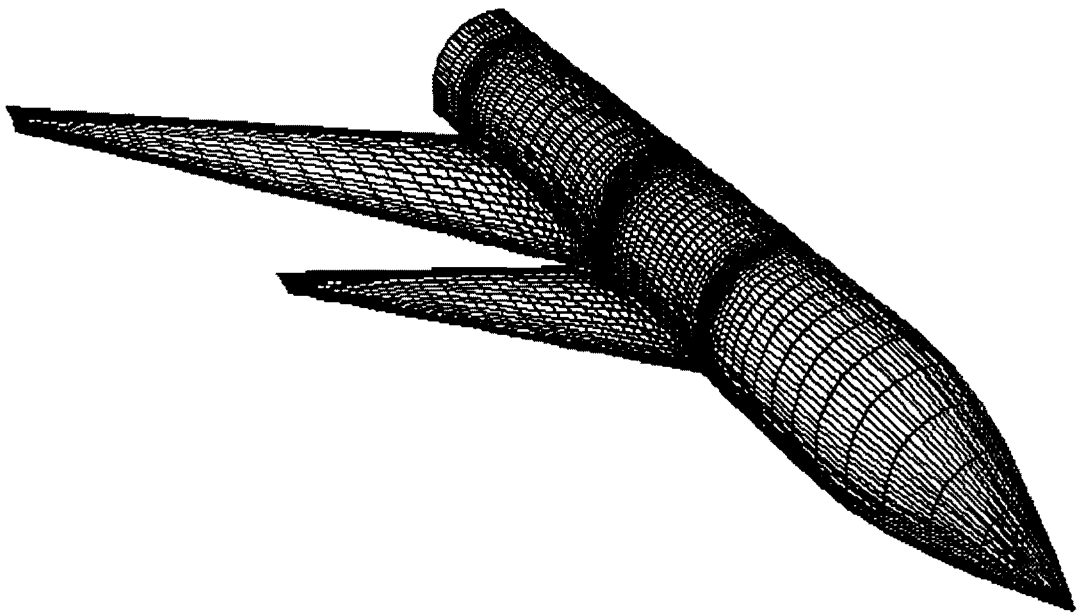

Fig.1 Surface Grid Distribution of a Canard-Wing-Body Configuration

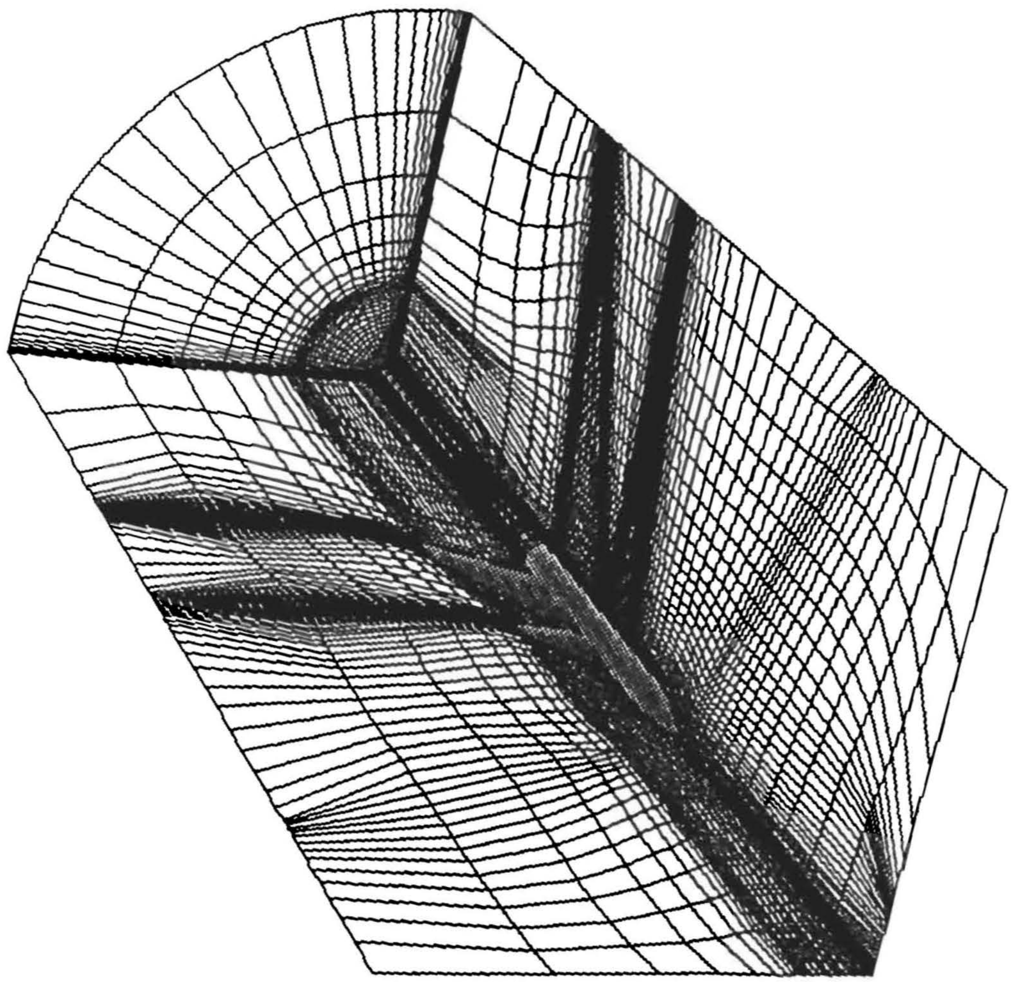

Fig. 2 H-O Grid Topology for a Canard-Wing-Body Configuration

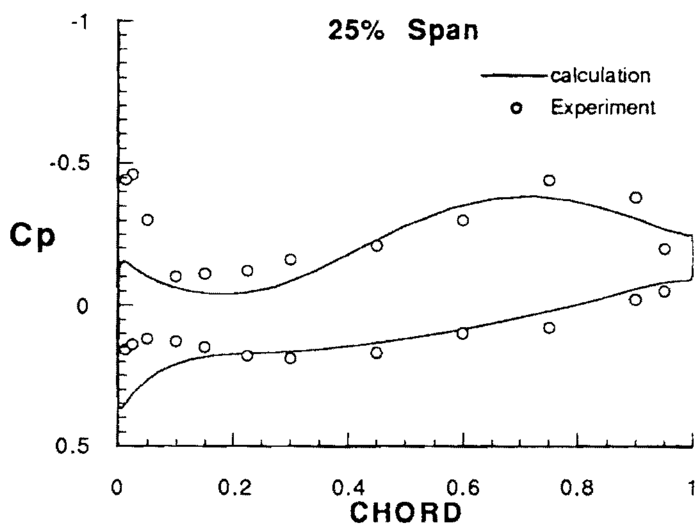

Fig. 3 Chordwise Pressure Distribution of a Canard-Wing-Body Configuration at 25% Wing Span

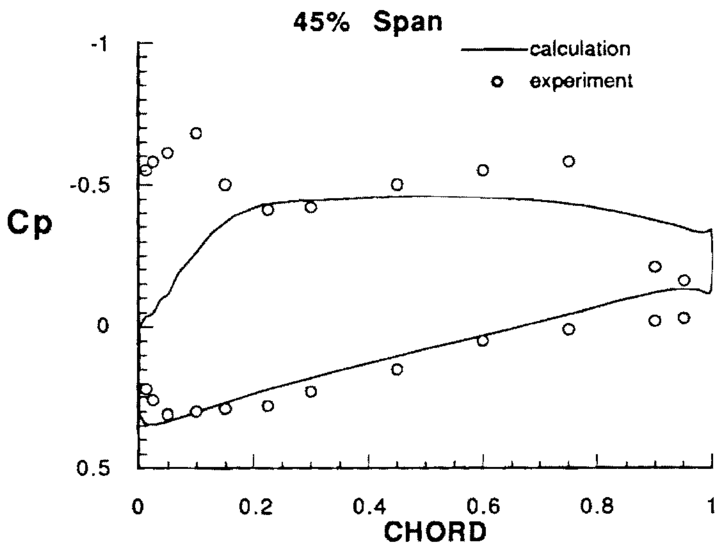

Fig. 4 Chordwise Pressure Distribution of a Canard-Wing-Body Configuration at 45% Wing Span

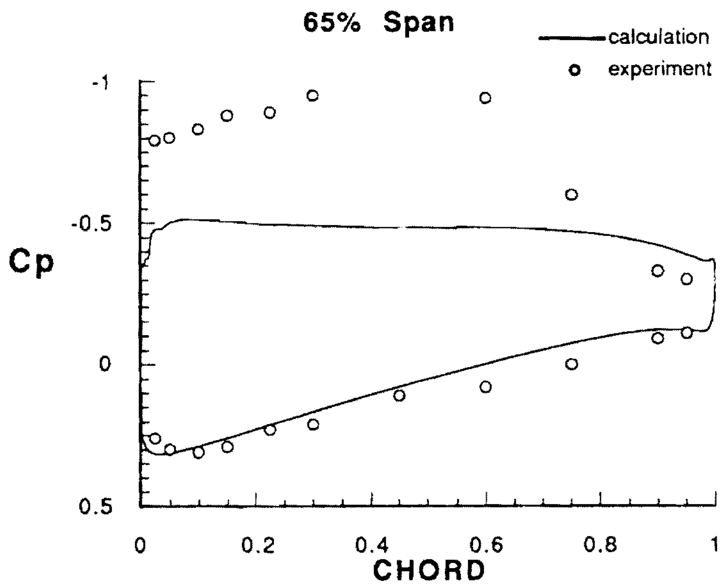

Fig. 5 Chordwise Pressure Distribution of a Canard-Wing-Body Configuration at 65% Wing Span

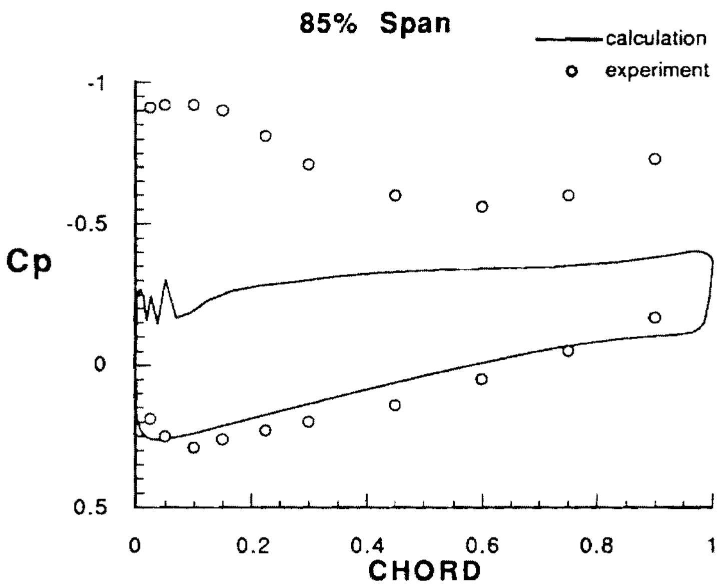

Fig. 6 Chordwise Pressure Distribution of a Canard-Wing-Body Configuration at 85% Wing Span

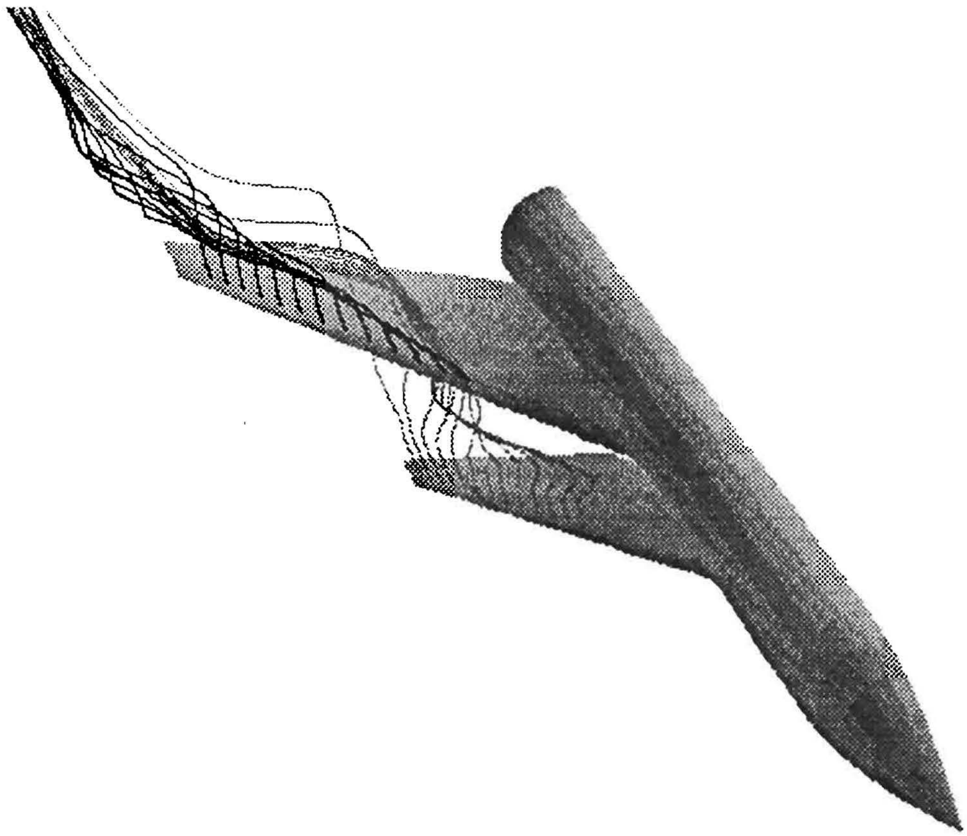

Fig. 7 Particle Trajectory Simulation over a Canard-Wing-Body Configuration at 13 deg. Angle of Attack

7

UNSTEADY AERODYDYNAMIC ANALYSIS OF DUAL-ELEMENT WING CONFIGURATIONS

BI-MONTHLY PROGRESS LETTER
FOR THE PERIOD

July 1, 1991 - Aug. 30, 1991

Submitted to the

NAVAL AIR DEVELOPMENT CENTER
WARMINSTER, PA

Attn: Marvin M. Walters

Prepared by

L. N. Sankar
Professor
and
O. J. Kwon
Post-Doctoral Fellow

School of Aerospace Engineering
Georgia Institute of Technology,
Atlanta, GA 30332

September 1991

School of Aerospace Engineering

Georgia Institute of Technology
Atlanta, Georgia 30332-0150
404•894•3000
Fax: 404•894•2760

September 30, 1991

Mr. Marvin M. Walters
Code 6051
Naval Air Development Center
Warminster, PA 18974

Subject: BI-MONTHLY PROGRESS REPORT FOR THE PROJECT "UNSTEADY AERODYNAMIC ANALYSIS OF DUAL-ELEMENT WING CONFIGURATIONS"

Dear Mr. Findlay:

During the reporting period July 1, 1991 - August 30, 1991, the following tasks were completed:

a) The 3-D elliptic grid generator developed at Georgia Tech has been modified for multi-element configurations and the multi-block grid generation for a typical canard-wing-body combination has been completed. The grid for this configuration is generated as a two-block H-O topology grid with 174 streamwise, 49 radial, and 98 circumferential points, which is about twice more points than the cases included in the previous progress report. The surface grid distribution and the flowfield grid of the upper block are illustrated in Fig. 1 and Fig. 2. A similar grid for the bottom half of the canard-wing-body configuration completes the second block. The surface grid points are clustered near the fuselage forebody, wing and canard leading and trailing edges. Also, the grid normal spacing is redistributed so that the first point away from the surface can be a user input. Presently, the spacing for the first normal grid point is 0.0001 of the wing root chord.

b) A modification of the 3-D Navier-Stokes code to study multi element surfaces has been completed. The flow solver has been restructured so that a multi-block flow simulation is possible. This solver has been coupled to the elliptic multi-block grid system described earlier. Calculations have been performed for the flow about a typical canard-wing-body configuration at a transonic Mach number of 0.7 and at angles of attack of 4 and 12 degs. The Reynolds number for the calculations is 1.35 million based on the wing mean geometric chord.

Fig. 3 shows the chordwise pressure distribution at several wing spanwise stations for 4 deg. angle of attack. It is shown that the calculated pressures correlate very well with the experiment. The leading-edge suction of the pressure due to the leading-edge vortex is well predicted. Fig. 4 shows the canard and wing upper surface pressure contours at 4 deg. angle of attack. It clearly indicates well defined vortex passages which originate from the leading edge and travels toward the tip on both wing and canard. Fig. 5 shows a particle trajectory simulation of the vortices.

Fig. 6 shows the chordwise pressure distribution at several wing spanwise stations for 12 deg. angle of attack. It is seen that the calculated pressures again correlate very well with the experiment. The leading-edge suction of the pressure due to the leading-edge vortex is also well predicted. Fig. 7 shows the canard and wing upper surface pressure contours at 12 deg. angle of attack. It is observed that the leading-edge vortex on the canard breaks down at about 50% of the span near the mid chord. The particle trajectory simulation in Fig. 8 also shows this vortex breakdown phenomena. The vortex on the wing does not break down and remains well organized.

Sincerely,

LAKSHMI N. SANKAR
Professor

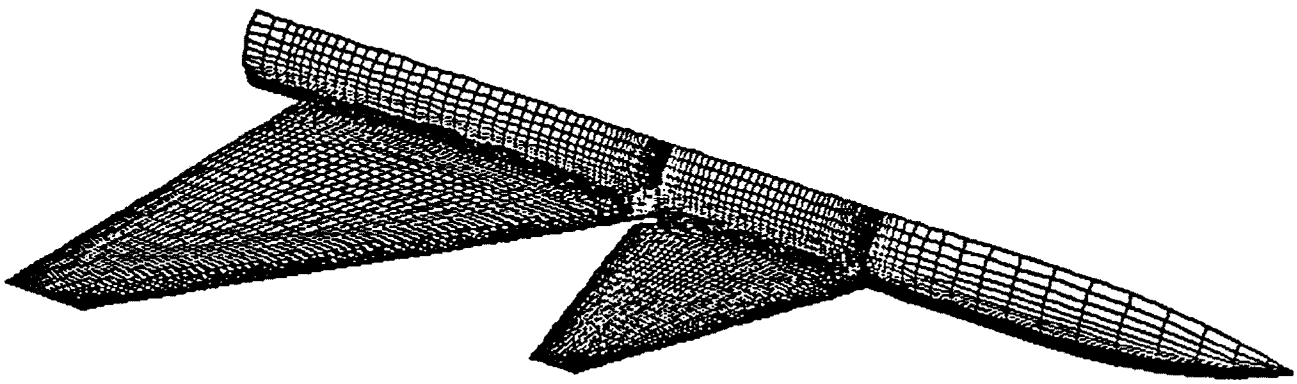

Fig. 1 Surface Grid Distribution of Canard-Wing-Body Configuration

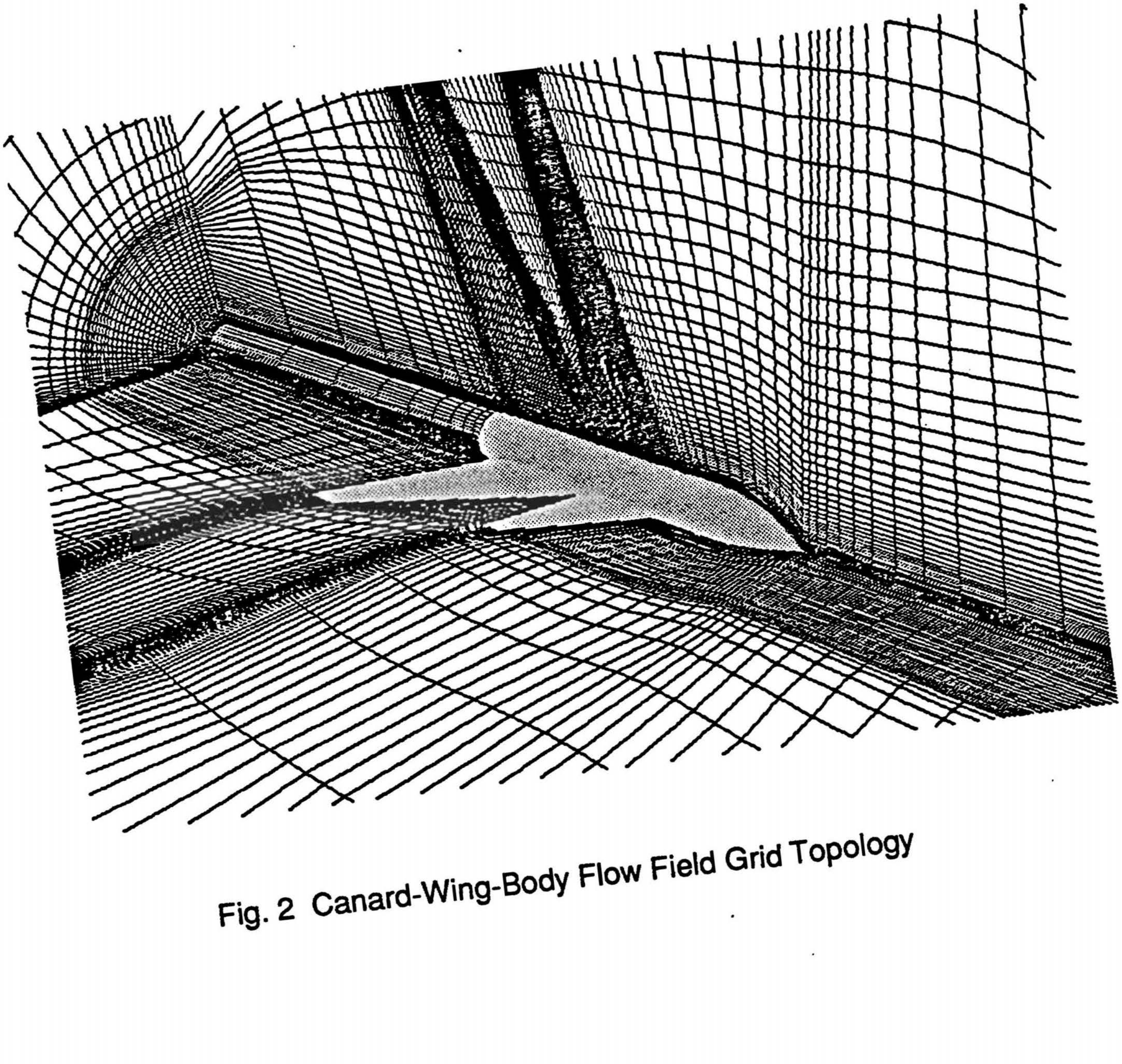

Fig. 2 Canard-Wing-Body Flow Field Grid Topology

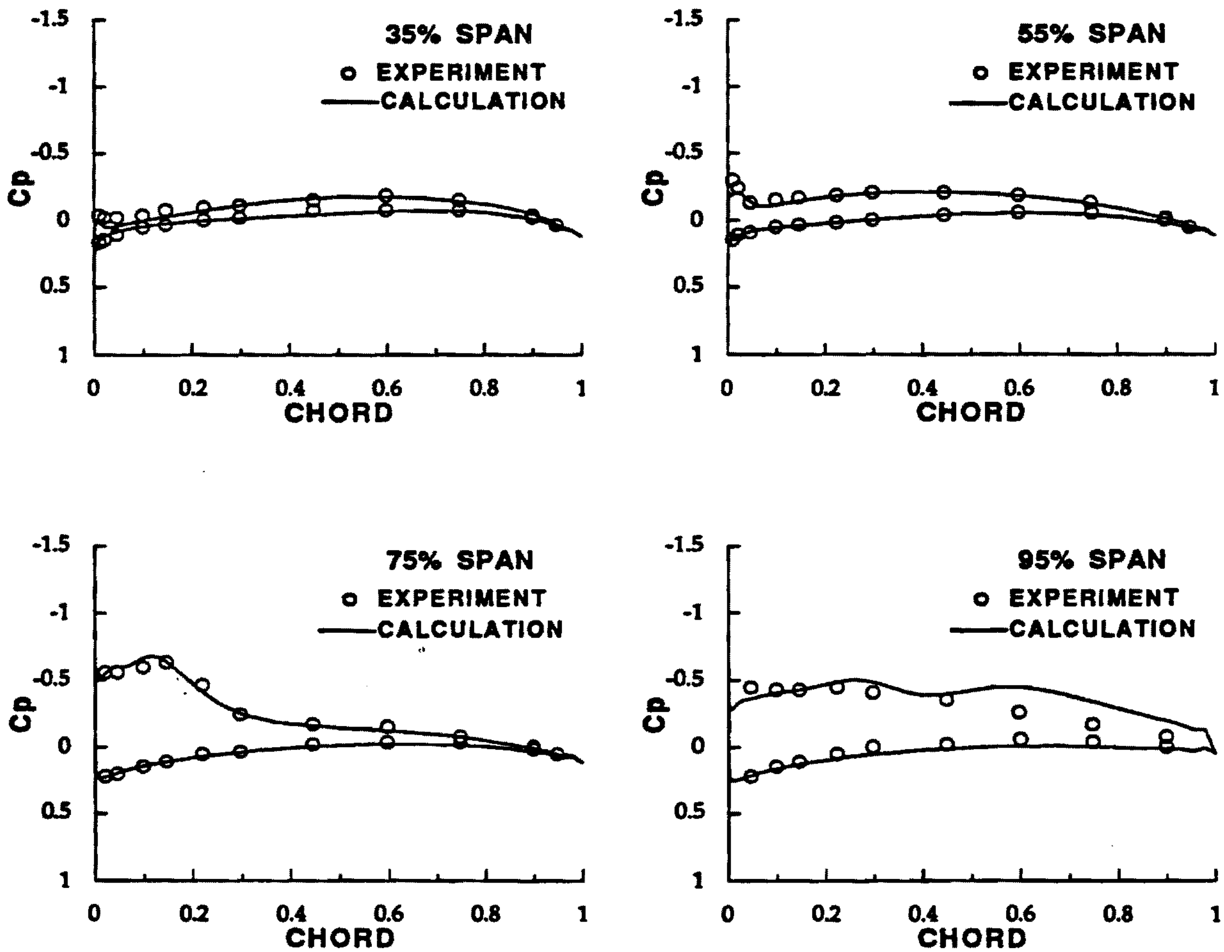

Fig. 3 Surface Pressure Distribution of the Canard-Wing-Body Configuration at M_∞=0.7, α=4 deg.

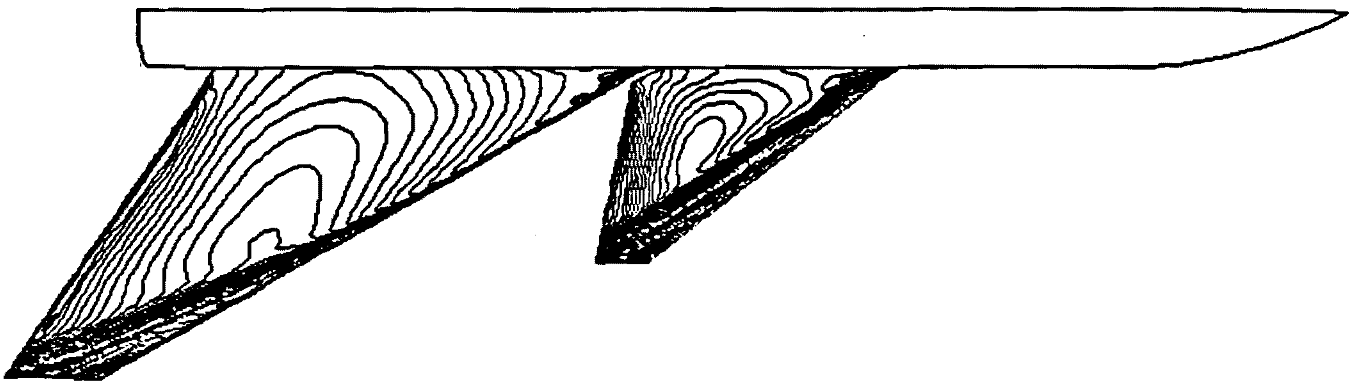

Fig. 4 Upper Surface Pressure Contour for the Canard-Wing-Body Configuration at M_{∞}=0.7, α=4 deg.

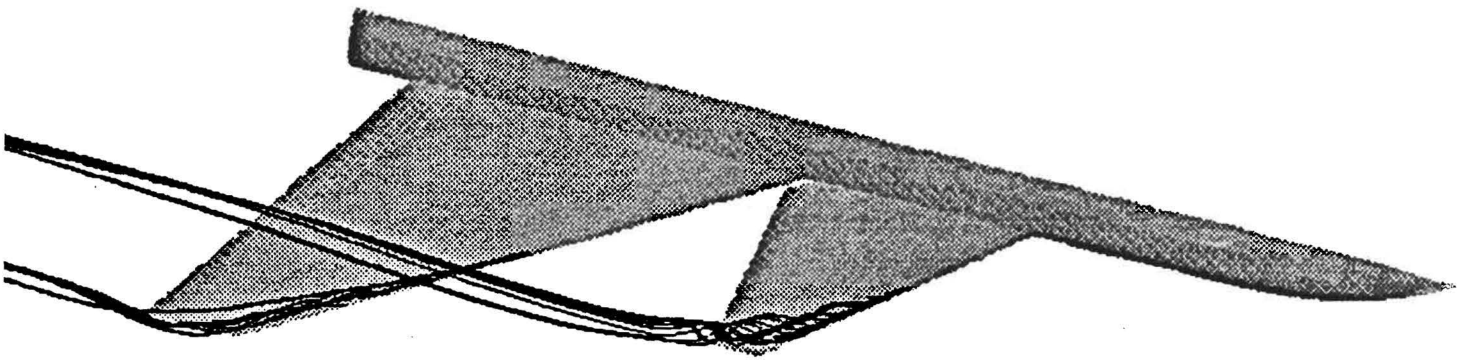

Fig. 5 Particle Trajectory Simulation of the Canard-Wing-Body Configuration at M_∞=0.7, α=4 deg.

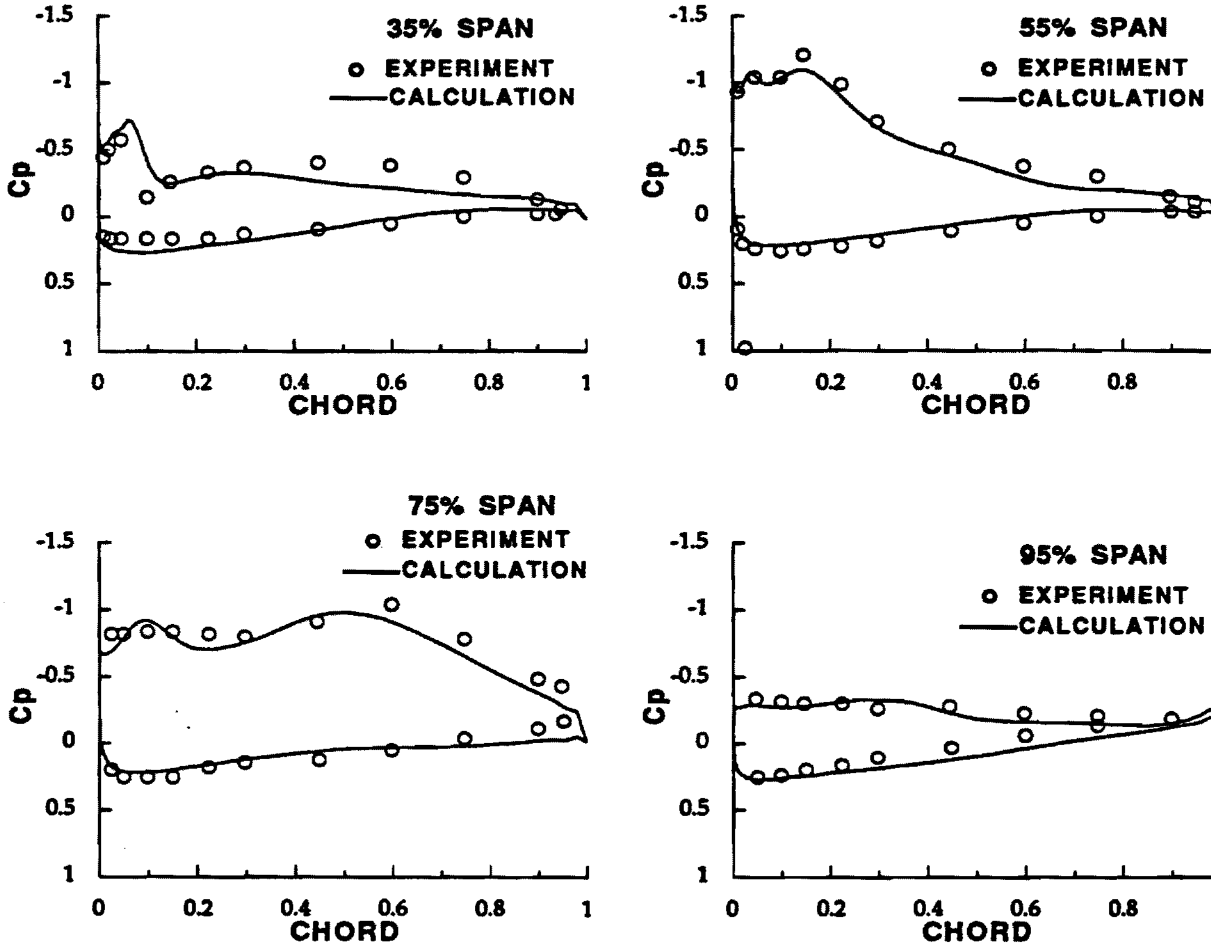

Fig. 6 Surface Pressure Distribution of the Canard-Wing-Body Configuration at M_∞=0.7, α=12 deg.

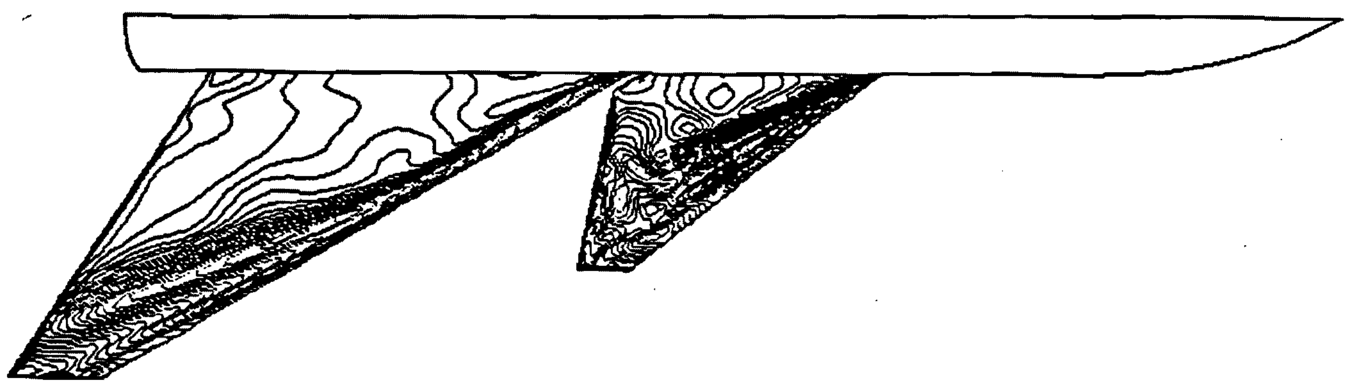

Fig. 7 Upper Surface Pressure Contour for the Canard-Wing-Body Configuration at M_{∞}=0.7, α=12 deg.

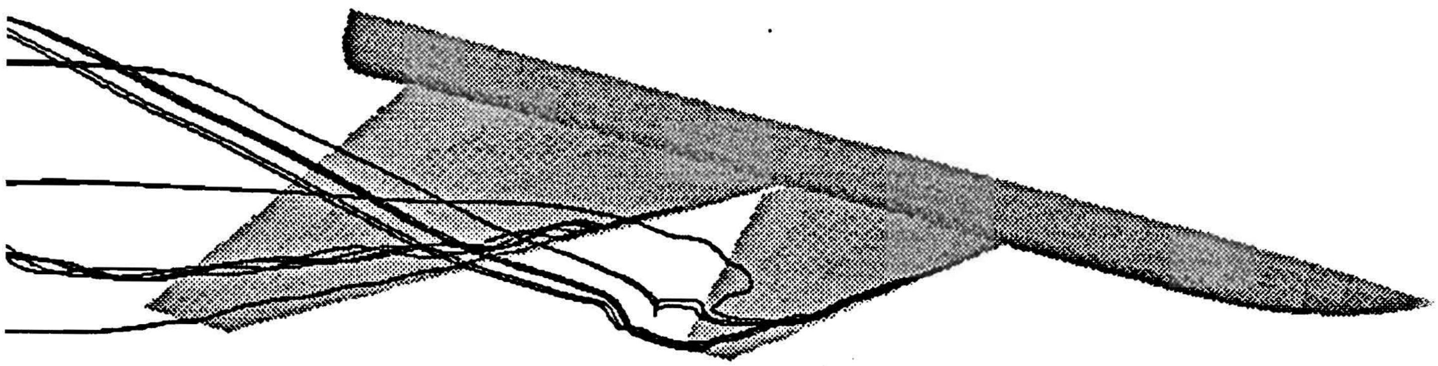

Fig. 8 Particle Trajectory Simulation of the Canard-Wing-Body Configuration at M_{∞}=0.7, α=12 deg.

2 / ... 1
8

UNSTEADY AERODYNAMIC ANALYSIS OF DUAL-ELEMENT WING CONFIGURATIONS

BI-MONTHLY PROGRESS LETTER
FOR THE PERIOD

September 1, 1991 - October 31, 1991

Submitted to the

NAVAL AIR DEVELOPMENT CENTER
WARMINSTER, PA
Attn: Mr. Marvin M. Walters

Prepared By

L. N. Sankar
Professor
School of Aerospace Engineering
Georgia Institute of Technology, Atlanta, GA 30332

November 1991

November 15, 1991

Mr. Marivin M. Walters
Code 6051
Naval Air Development Center
Warminster, PA 18974

Subject: BI-MONTHLY PROGRESS REPORT FOR THE PROJECT "UNSTEADY AERODYNAMIC ANALYSIS OF DUAL-ELEMENT WING CONFIGURATIONS"

Dear Mr. Walters:

During the reporting period September 1, 1991 - October 31, 1991, the following tasks were completed:

a) The 3-D multi-element wing-body-canard code development was completed. It may be recalled that sample results from this computer code were included in the previous progress report (July 1 - August 31, 1991). This program, and sample data sets were delivered to NADC researchers during my recent visit to ther Naval Air Development Center.

b) The 3-D wing-body analysis (used by Mr. Dave Findlay to study the effects of suction on vortical flow over F-15 like configurations), was modified to simulate the unsteady aerodynamics of wing-body configurations, undergoing a ramp motion. This program can handle wing-alone and wing-body configurations. An algebraic grid generator for wing-alone configurations is built into this solver. For complex geometries such as a wing-body configuration, a separate grid generator was provided. The ramp motion is specified as a starting angle of attack α_0, ending angle of attack α_1, and the number of time steps over which the angle of attack linearly changes from α_0 to α_1. This program, and the grid generation program were also delivered to NADC personnel during my recent visit.

I plan to work closely with Dr. Tseng in the validation of the wing-body ramp motion simulation. I understand that the initial code validation will be for a untapered, swept/unswept wing subjected to ramp motion, recently tested by researchers at United Technologies Research Center.

With best wishes,

Sincerely,

LAKSHMI N. SANKAR
Professor

UNSTEADY AERODYNAMIC ANALYSIS OF DUAL-ELEMENT WING CONFIGURATIONS

BI-MONTHLY PROGRESS LETTER
FOR THE PERIOD

November 1, 1991 - December 31, 1991

Submitted to the

NAVAL AIR DEVELOPMENT CENTER
WARMINSTER, PA
Attn: Mr. Marvin M. Walters

Prepared By

L. N. Sankar
Professor
School of Aerospace Engineering
Georgia Institute of Technology, Atlanta, GA 30332

January 1992

School of Aerospace Engineering

Georgia Institute of Technology
Atlanta, Georgia 30332-0150
404•894•3000
Fax: 404•894•2760

January 15, 1992

Mr. Marvin M. Walters
Code 6051
Naval Air Development Center
Warminster, PA 18974

Subject: BI-MONTHLY PROGRESS REPORT FOR THE PROJECT "UNSTEADY AERODYNAMIC ANALYSIS OF DUAL-ELEMENT WING CONFIGURATIONS"

Dear Mr. Walters:

During the reporting period (November 1, 1991 - December 31, 1991), the following tasks were completed:

1) The validation of the 2-D multi-element airfoil code has been completed. This code has been applied to a Boeing Vertol VR-7 airfoil/slat configuration, to assess the effects of the slat on the main airfoil stall characteristics. We plan to present this work as an AIAA paper at the forthcoming AIAA Structural Dynamics and Dynamics Specialists Conference, in April 1992. A copy of the AIAA paper is enclosed.

2) We have modified the 3-D Navier-Stokes solver to accept leading edge and trailing edge control surface motion. The user may prescribe the amplitude of oscillations, flap/slat hinge location and the frequency of oscillations. A simple algebraic grid shearing scheme has been implemented, which allows the original body-fitted grid to move with the flap/leading edge slat motion. Sample grids for an F-15 wing equipped with a leading edge and trailing edge control surfaces at a number of span stations, including span stations beyond the wing tip are enclosed. It may be noted that the algebraic deformation does not cause grid cross-over, even for very large flap deflections.

3) We are applying the 3-D Navier-Stokes solver with oscillating leading/trailing edge control surfaces to an F-5 wing equipped with a trailing edge flap. This configuration was tested by Tijdeman at NLR, for a variety of Mach numbers. The mean flow conditions are: Mach number = 0.95, wing angle of attack = 0 degrees. Navier-Stokes solutions for this mean flow have already been obtained, and are enclosed. Calculations are now in progress for the oscillating flap case, and will be reported in the next progress report.

With best wishes,

Sincerely,

LAKSHMI N. SANKAR
Professor

UNSTEADY AERODYNAMIC CHARACTERISTICS OF A DUAL-ELEMENT AIRFOIL

Ismail. H. Tuncer*　　Lakshmi N. Sankar†

School of Aerospace Engineering
Georgia Institute of Technology
Atlanta, Georgia 30332

ABSTRACT

Unsteady aerodynamic behavior and load characteristics of a VR-7 slat/airfoil combination oscillating sinusoidally between 5 and 25 degrees have been studied. The unsteady, compressible Navier-Stokes equations are solved on a multi-block grid using an approximate factorization Finite Difference scheme. In the case of a single airfoil, a massive flow separation and formation of a strong vortex is observed. The vortex induced suction and the shedding of the vortex into the wake is responsible for high aerodynamic loads and the subsequent stall of the airfoil. In the case of a slat/airfoil combination, the suction peak at the leading edge of the airfoil is reduced significantly in comparison to the single airfoil. Flow separation is confined to the trailing edge of the main airfoil and the formation of a strong vortical structure is not observed. The slat/airfoil combination does not experience a massive flow separation and the aerodynamic lift does not undergo the characteristic deep dynamic stall hysteresis loops.

INTRODUCTION

In recent years, there has been an increased interest in exploiting the large unsteady lift generated by wings during pitch up to enhance the maneuver capabilities of fighter aircraft. Generation of high unsteady lift without the adverse effects of dynamic stall is also a critical design consideration in helicopters. The unsteady loads generated during the dynamic stall of helicopter blades limit the flight speed and reduce maneuverability.

*Post-Doctoral Fellow, Member AIAA.
†Professor, Member AIAA.

Slats are currently being used in fighter aircraft primarily to enhance take-off and landing performance. There is a need to investigate whether the use of those devices may be used to enhance the lift generated during pitch-up maneuvers and postpone stall. In helicopter applications, slats are almost never used because of the mechanical complexity and weight considerations. Nevertheless, they may provide improved maneuverability and increase forward flight speed achievable. Work is needed to understand the dynamic lift generation characteristics of dual-element (slat/airfoil) configurations.

Dynamic stall characteristics of airfoils undergoing high amplitude pitching motions and mechanisms to delay or to suppress dynamic stall have been studied experimentally as well as numerically by many researchers in the last decade[1,2,3,4]. McCroskey et al.[1] conducted an extensive experimental study on dynamic stall characteristics of several airfoils. They have observed that deep dynamic stall is rather insensitive to airfoil profile, Reynolds number and flow Mach number, but it is a strong function of the reduced frequency of the pitching motion and the maximum angle of attack. In a later study, Carr and McAlister[2] observed that a leading edge slat postpones the dynamic stall angle well beyond that of the single airfoil. They hypothesized that this behavior is attributable to the shifting of the flow acceleration onto the slat from the main airfoil. Also, the formation of the leading edge vortex may be suppressed due to the energizing effect of the vortical wake of the slat on the boundary layer of the main airfoil.

In earlier numerical studies of multi-element airfoils, inviscid flow approximations using panel methods[5] or solving potential/Euler flow equations[6] were employed. Recently, Wang[7] investigated high angle of attack, separated flows around a VR-7 slat/airfoil combination by solving a velocity-vorticity formulation of the incompressible Navier-Stokes equations.

In this study, dynamic stall characteristics of a VR-7 airfoil with and without a leading edge slat are investigated using an unsteady, compressible Navier-Stokes solver. In the past, several versions of this solver have been employed successfully to compute subsonic and transonic, steady and unsteady, viscous flows past such diverse configurations as helicopter rotors, high speed propellers and fighter wing and bodies[4,8,9]. For investigating flowfields around multi-element airfoils, the computational domain is divided into blocks to facilitate the discretization. The Navier-Stokes solver then sweeps the computational blocks. The flow is assumed to be fully turbulent. The computed results are analyzed through a study of computed surface pressure distributions, unsteady lift vs. angle of attack behavior, and instantaneous mass-flux contours.

UNSTEADY NAVIER-STOKES EQUATIONS

The unsteady flowfields around oscillating airfoils is modeled by the Reynolds averaged, full Navier-Stokes equations. The well-known, conservative form of these equations in an inertial Cartesian coordinate system reads as follows:

$$\vec{q}_t + \vec{F}_x + \vec{G}_y = \vec{R}_x + \vec{S}_y \qquad (1)$$

where $\vec{q}$ is the conservative flow variables, (ρ, ρu, ρv, E_T). E_T is the total energy per unit volume which is given by

$$E_T = \rho(e + (u^2 + v^2)/2) \qquad (2)$$

and e is the internal energy per unit mass. $\vec{F}$ and $\vec{G}$ are the inviscid and $\vec{R}$ and $\vec{S}$ are the viscous flux vectors, respectively. The subscripts denote partial derivatives.

The above governing equations may be transformed into a general curvilinear coordinate system; ($\xi(x,y,t), \eta(x,y,t), \tau(t)$). This transformation allows the solution of the equations on body-fitted, non-orthogonal computational grids. The transformed governing equations can also be expressed in the same conservative form as the Equation 1, however, the transformed flux terms are now related to their Cartesian counterparts through the metrics of transformation. For a detailed description of flux vectors in the Cartesian and transformed coordinate systems, the reader is referred to Reference 9.

In the solution of the governing equations, boundary conditions are applied on the solid surfaces and the far-field boundaries. On the solid surfaces, the *no slip* condition is applied which simply states that the fluid velocity on the solid surface is equal to the velocity of the solid surface. In the case of a constant angle of attack, surface boundary velocities are set to zero. For oscillating airfoils, they are set to the solid surface velocities which are based on the reduced frequency of the motion. At the far-field boundary, free-stream values of the flow variables are applied.

Turbulence Model

In this formulation, the turbulence in high Reynolds number flows is treated with Reynolds stresses. They are similar to the viscous stresses in that they contribute to the transport of momentum. The Reynolds stresses are similarly modeled as proportional to the strain. And the eddy viscosity coefficient, μ_t, is employed as the proportionality constant. In this work, we have used a two layer Baldwin-Lomax eddy viscosity model. This model treats the eddy viscosity in two layers; namely *inner* and *outer* layers and employs different length scales and empirical constants in each of these layers. For a detailed discussion of this model, the reader is referred to Reference 9.

Although use of such a simple algebraic eddy viscosity model in massively separated flows may be questionable, earlier studies with higher order models[4], did not show any significant improvements in numerical predictions. Thus, we have employed this model in separated flow and wake regions.

NUMERICAL METHOD

The governing equations expressed in the transformed domain are first discretized and then integrated in time. Standard second order accurate central differences are used to approximate the spacial derivatives, and to compute the metrics of transformation. The instabilities due to growth of high frequency errors in the numerical solution, which is caused by the odd-even coupling of the standard central differencing, are controlled by adding a set of artificial dissipation terms to the discretized equations. These dissipation terms consists of second and forth order differences of the flow properties as suggested by Jameson[10]. The highly non-linear inviscid flux terms in $\vec{F}$ and $\vec{H}$ are linearized about their values at a previous time level. The viscous flux terms are also evaluated at a previous time level and are applied explicitly on the right hand side of the governing equations. The resulting linear equations, which are expressed in *delta* quantity, $(\vec{q}^n - \vec{q}^{n-1})$ form a penta-diagonal matrix system of simultaneous equations. For an efficient solution of these linear equations, the penta-diagonal matrix system is approximately factored into a product of tridiagonal matrices using the Beam-Warming approximate factorization scheme. The details of the numerical formulation are discussed in detail in Reference 9.

The computational domain is discretized by employing multiple blocks and generating computational grids in each block. The Governing equations are solved in each block as described above. At the block interfaces, the continuity of the flow variables across the block boundaries is enforced. In the computation of eddy viscosity values, care is taken near the block boundaries in the direction normal to the solid surfaces, so that inner and outer eddy viscosity values are computed across the block boundaries and assigned correctly.

Numerical solution of the discretized governing equations is based on the numerical integration of these equations in space and in time. For a steady state solution at a constant angle of attack, the flowfield is first initialized with the free-stream conditions and the appropriate boundary conditions. Then, the equations are integrated by marching in time till a converged solution is reached. In steady flow computations, in which the final solution is independent of time, a local time step which varies in space may be used. Local time stepping increases the convergence rates and efficiency of the computations. In this study, we used a geometric variation of the time step, Δt, proportional to the grid spacing:

$$\Delta t = \frac{\Delta T}{1+\sqrt{J}} \tag{3}$$

where J is the Jacobian of the grid cell and $\sqrt{J}$ represents the width of the grid cell. ΔT is set to 1.

The computation of the unsteady flowfields takes a steady state solution already computed as the initial condition. The equations are then integrated in time with a global, constant time step, which conserves the time accuracy of the solution. Unsteady boundary conditions are updated at every time step. The flow variables at the block boundaries are updated after every sweep by averaging the values at the first inner grid nodes next to the block boundary in neighboring blocks.

Multi-block Grid Generation

The multi-block grid generation scheme is based on the division of a multiply connected computational domain into simple, simply connected rectangular blocks and the generation of a near orthogonal grid in each block individually. Airfoil profiles, block boundaries and grid distribution along the block boundaries in terms of the first and the last grid spacing are user defined. With these given boundary conditions, an elliptic solver is employed for generating near orthogonal grids in each block. Grid spacing along the directions normal to the solid surfaces is then redistributed according to the first grid spacing off the solid surface specified as input. This procedure enables a sufficient number of grid points to be placed within the boundary layer zone of the flow. Continuity of a global grid across block boundaries is satisfied by averaging the coordinates on either side of the common block boundaries.

Figure 1 shows the definition of blocks for a slat/airfoil combination. The distribution of grid points around the slat/airfoil combination and a close-up view of leading edge region are given in Figure 2a and 2b. In Figure 2a, only every other horizontal grid line is shown for clarity.

NUMERICAL RESULTS AND DISCUSSION

Previous Validation Studies

In the past, the present methodology has been used for a number of steady and unsteady flow problems, and some of the previously published work is reproduced here to demonstrate the ability of this technique. Figure 3 shows the steady surface pressure distribution computed over a GAW-130 airfoil/flap combination[11]. The total computed C_l value of 2.62 is in good agreement with the measured value of 2.67 for this case. Figure 4 shows the dynamic stall hysteresis loop for a single element NACA0012 airfoil for a reduced frequency of 0.15 at $M = 0.283$[12]. Additional code validation studies are presented in Reference[4].

Present Results

The Finite Difference methodology mentioned previously was applied to an oscillating single VR-7 airfoil as a baseline study. The calculations were then repeated for a leading edge slat/airfoil combination. In these cases, the oscillatory pitching motion is about the quarter chord of the main airfoil and of a sinusoidal type described by $\alpha = 15° - 10° \cos(\omega t)$. The frequency of the motion, ω, is based on the non-dimensional reduced frequency parameter, k, which is defined as $k = \omega c / 2U_\infty$. c is the chord length. For both the airfoil, and the slat/airfoil combination , the unsteady flowfields and dynamic stall characteristics are computed at $k = 0.10$, $Re = 2.5x10^6$ and $M = 0.185$. Unsteady flowfields over the VR-7 slat/airfoil configuration have also been tested at NASA by Carr and McAlister[2] for the flow conditions mentioned above.

Single Airfoil

In this case, two grid blocks with 121x49 and 121x41 in size on the upper and lower sides of the airfoil, respectively, were employed. 128 grid points were placed over the airfoil (upper and lower surfaces) and the first grid point was placed at 0.00001 chord length off of the solid surface boundary. The steady state solution at $\alpha = 5°$ was obtained using a local time stepping. The computed flowfield in terms of Mach number and mass-flux contours around the airfoil is depicted in Figure 5. The computed lift coefficient is 0.69, which compares well with the experimental value of 0.7 [1]. Figure 6 shows the distribution of surface pressures.

The unsteady flowfield along the oscillatory motion was then computed by advancing this solution in time with time dependent boundary conditions. The computed unsteady flowfields along the pitching motion is depicted in Figure 7. Figure 8 also shows the corresponding distribution of the pressure coefficient around the airfoil. The variation of lift with respect to angle of attach is given in Figure 9. It is seen that, the flowfield stays mostly attached up to the static stall angle, which is about 12°. Separated flow regions and the formation of a vortex at the trailing edge is evident as a suction peak induced by the vortex, in the pressure distribution. At around $\alpha = 17° \uparrow$, (the $\uparrow$ sign denotes pitch-up) the flow separation reaches the leading edge and a completely separated vortical region covers the upper surface. The suction induced on the upper airfoil surface by the vortex is also noticeable. At this stage, before the vortex starts moving off the airfoil surface and the vortex induced low pressure region decreases, the maximum lift equal to 2.13 is attained. At angles of attack beyond $\alpha = 20° \uparrow$, the vortex lifts off the surface and is shed into the wake. The lift drops drastically and the airfoil stalls. At $\alpha = 21.5° \uparrow$, the suction peaks in the pressure distribution reveal the presence of weak secondary vortical structures. However, the pressure distribution on the upper surface flattens out subsequently.

The flowfield remains mostly separated along the return cycle. Around $\alpha = 12° \downarrow$, the flow reattachment starts from the leading edge downward. However, the aerodynamic lift stays well below the attached flow values attained during the pitch up. The lift finally recovers back to attached flow values as the minimum angle of attack is reached and the second pitch-up cycle starts.

Slat/Airfoil Combination

In this case, the computational grid consisted of 3 blocks with 121x49, 121x29 and 121x31 points from top to the bottom as seen in Figure 1. 128 grid points over the main airfoil surface and 40 points over the slat were placed. The steady state solution is depicted in Figure 10. The pressure distribution on the slat and the airfoil is given in Figure 11. It should be noted that the suction peak at the leading edge of the airfoil is not as much pronounced as it is in the single airfoil case. The lift coefficient on the main airfoil was found to be 0.59. This may be attributed in part to the downwash over the main airfoil caused by the bound circulation around the slat.

The computed unsteady flowfields and the corresponding pressure distributions are given in Figures 12 and 13. It is readily observed that the massive flow separation experienced in the single airfoil does not occur. The flowfield stays attached well beyond the static stall angle of the single airfoil. As the maximum angle of attack is reached, the thickened boundary layer over the upper surface separates at the trailing edge. However, the separated region is confined to the rear portion of the airfoil and it does not progress towards the leading edge. The lack of a suction peak on the upper surface around the trailing edge also suggests that a trailing edge vortex does not form.

In comparison to the single airfoil case, the suction peak values at the leading edge at around $\alpha = 15° \uparrow$ are smaller. The fact that the adverse pressure gradient is not as great may explain the delayed separation of the flow. On the other hand, the suction peaks reached at around the maximum angle attack is quite comparable to the maximum values experienced in the single airfoil case prior to the flow separation. Yet, the flow at the leading edge still stays attached. It may be argued at this point that the accelerated flow over the slat energizes the boundary layer on the main airfoil, and prevents it from being separated.

The variation of lift coefficient on the main airfoil is given in Figure 14. It is also clearly seen that the dynamic stall is completely eliminated. It may be noted that experimental load data for the main airfoil alone was measured by Carr et al. for VR-7 slat/airfoil combination. These loads were artificially corrected to match the lift-curve slope of the basic airfoil[2]. Since rationale for such adjustments is not clear in an unsteady flow environment, these measured data are not included in the present study.

CONCLUDING REMARKS

A numerical procedure for the computation of the dynamic stall characteristics of multi-element airfoils has been developed and applied to a VR-7 slat/airfoil configuration. The computations clearly demonstrate the beneficial effects of slat on the airfoil loads at very large angles of attack.

This method may be used in systematic studies of slat shape, slat clearance etc. needed in aerodynamic design of high lift devices. The two-dimensional static and dynamic loads computed in this work may also be used in helicopter performance analyses (such as CAMRAD) as table look-up values to assess the effects of slat on rotor performance, and vibrating airloads.

ACKNOWLEDGEMENTS

This work was supported by NADC under Contract No. N62269-90-C-0246. The authors would like to thank Mr. Dave Findlay for his stimulating interest in this work.

REFERENCES

1. McCroskey, W.J., McAlister, K.W., Carr, L.W. and Pucci, S.L., *An Experimental Study of Dynamic Stall on Advanced Airfoil Sections*, Vol. 1-2, NASA TM 84245, July 1982.

2. Carr, L.W. and MacAlister K.W, *The Effect of a Leading-edge Slat on the Dynamic Stall of an Oscillating Airfoil*, AIAA paper 83-2533.

3. Tuncer, I.H, Wu, J.C. and Wang, C.M., *Theoretical and Numerical Studies of Oscillating Airfoils*, AIAA Journal, September 1990.

4. Wu, Jiunn-Chi, Huff, D. and Sankar, L.N., *Evaluation of Three Turbulence Models in Static Airloads and Dynamic Stall Predictions*, Journal of Aircraft, Vol. 27, No. 4, April 1990.

5. Dutt, H.N.V., *Analysis of Multi-element Airfoils by Vortex Panel Method*, AIAA J., Vol. 27, No. 5, pp. 658-660, 1989.

6. Hall, I.M. and Suddhoo, A., *Inviscid Compressible Flow Past a Multi-element Aerofoil*, AGARD-CP-365, 1984.

7. Wang, C. Wu, J.C. and Tung, C., *A Numerical Study of General Viscous Flows Around Multi-Element Airfoils*, AIAA Paper 90-0572.

8. Sankar, L.N. and Tang, W., *Numerical Solution of Unsteady Viscous Flow Past Rotor Sections* , AIAA Paper 85-0129.

9. Wake, B.E., *Solution Procedure for the Navier-Stokes Equations Applied to Rotors*, Ph.D. Thesis, School of Aerospace Engineering, Georgia Institute of Technology, April 1987.

10. Jameson, A., Schmidt, W., and Turkel, E., *Numerical Solution of the Euler Equations by Finite Volume Methods using Runge-Kutta Time Stepping Schemes*, AIAA Paper 81-1259.

11. Narramore, J.C. and Sankar, L.N., *Numerical Simulation of Multizone Two-Dimensional Transonic Flows Using the Full Navier-Stokes Equations*, International Technical Specialists' Meeting on Rotorcraft Basic Research of the American Helicopter Society, at the Georgia Institute of Technology, March 25-27, 1991.

12. Hixon, R. and Sankar, L.N., *Minimal Residual Method for Application of a Generalized Two-Dimensional Unsteady Flow*, AIAA Paper 92-0430, Aerospace Sciences Meeting and Exhibit, Reno, Nevada, January 1992.

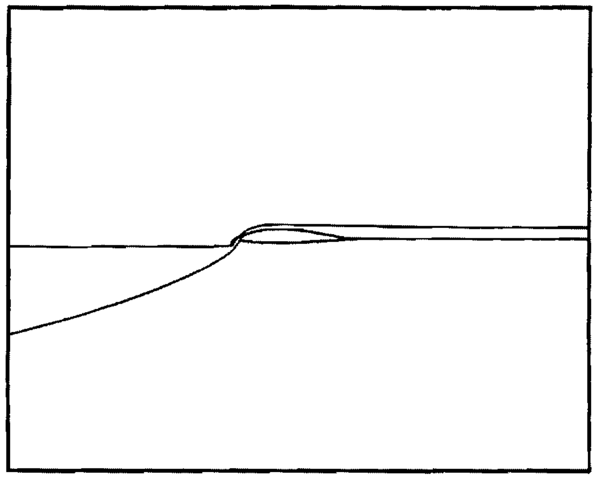

Fig. 1. Definition of a multi-block grid.

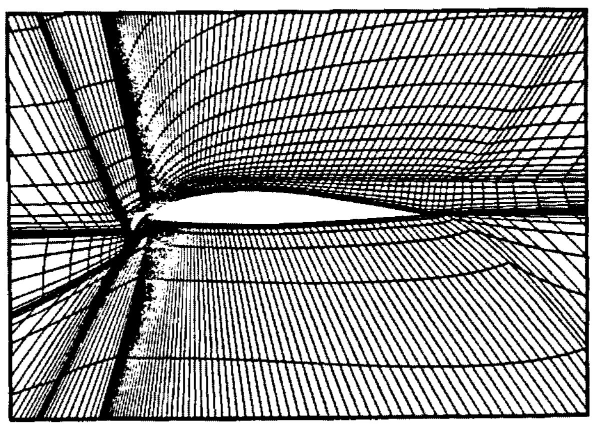

Fig. 2a Grid distribution near a slat/airfoil combination.

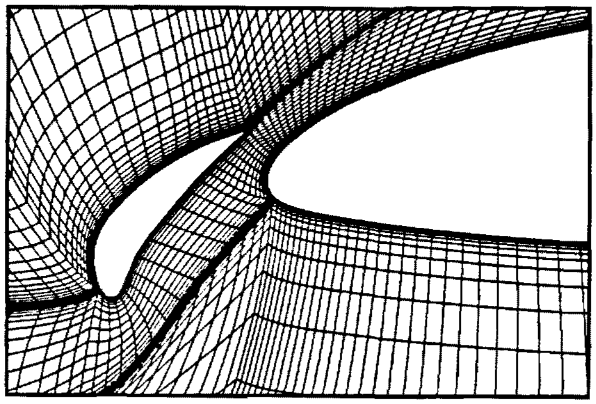

Fig. 2b. Close-up view of the grid distribution around slat and airfoil leading edge.

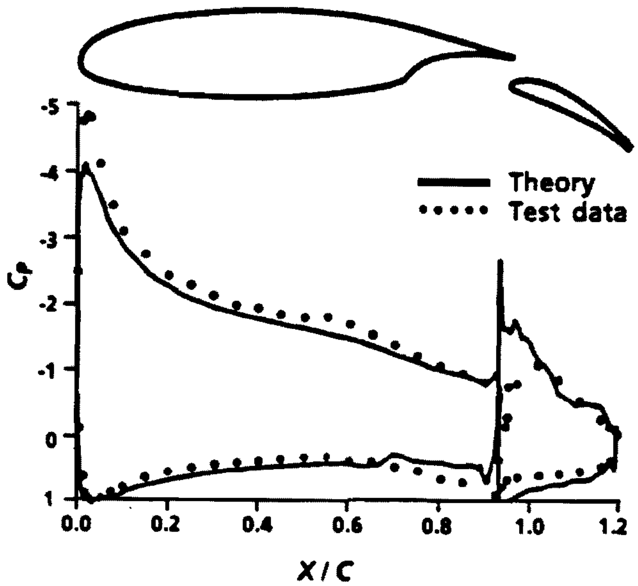

Fig. 3. Pressure distribution - GAW-130 airfoil, flap angle 20°, $M = 0.3$, $Re = 2.2x10^6$.

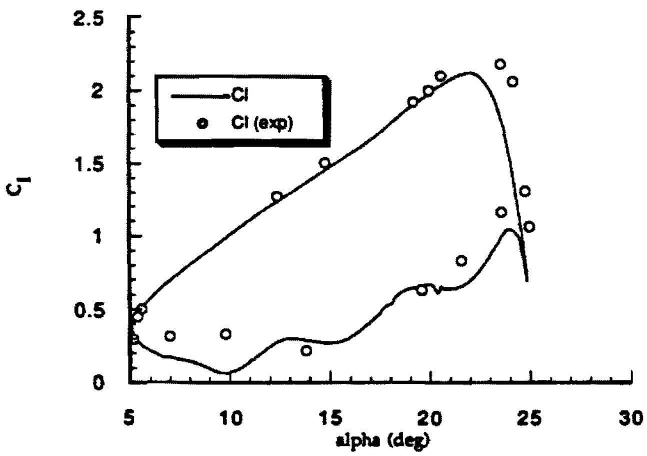

Fig. 4. Unsteady lift - oscillating NACA0012 airfoil, $k = 0.151$, $M = 0.283$

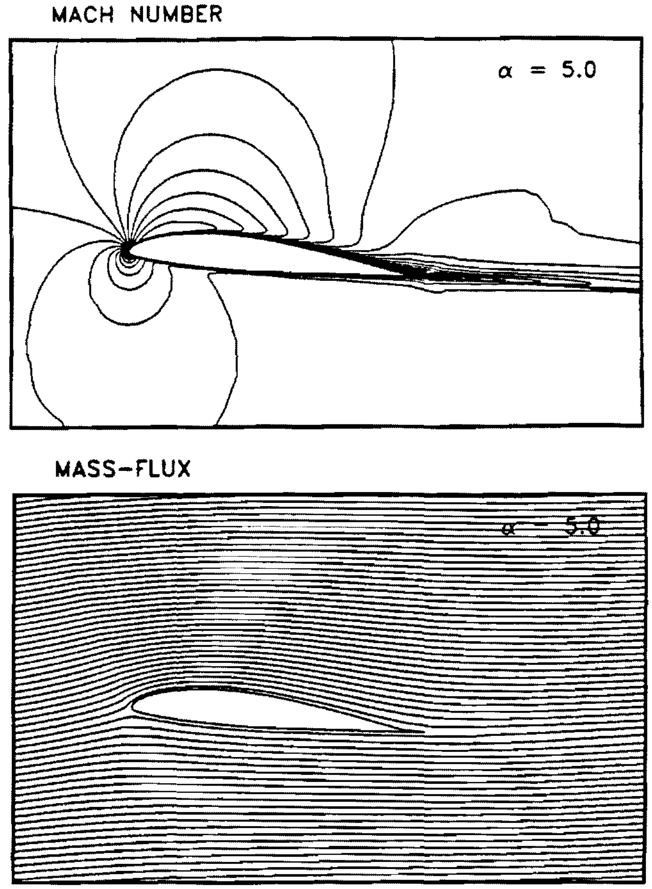

Fig. 5. Mach number and mass-flux contours - $\alpha = 5°$, single element.

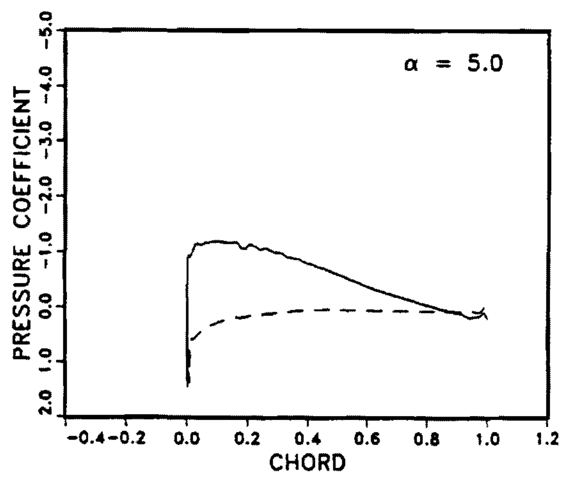

Fig. 6 Pressure distribution - $\alpha = 5°$, single element.

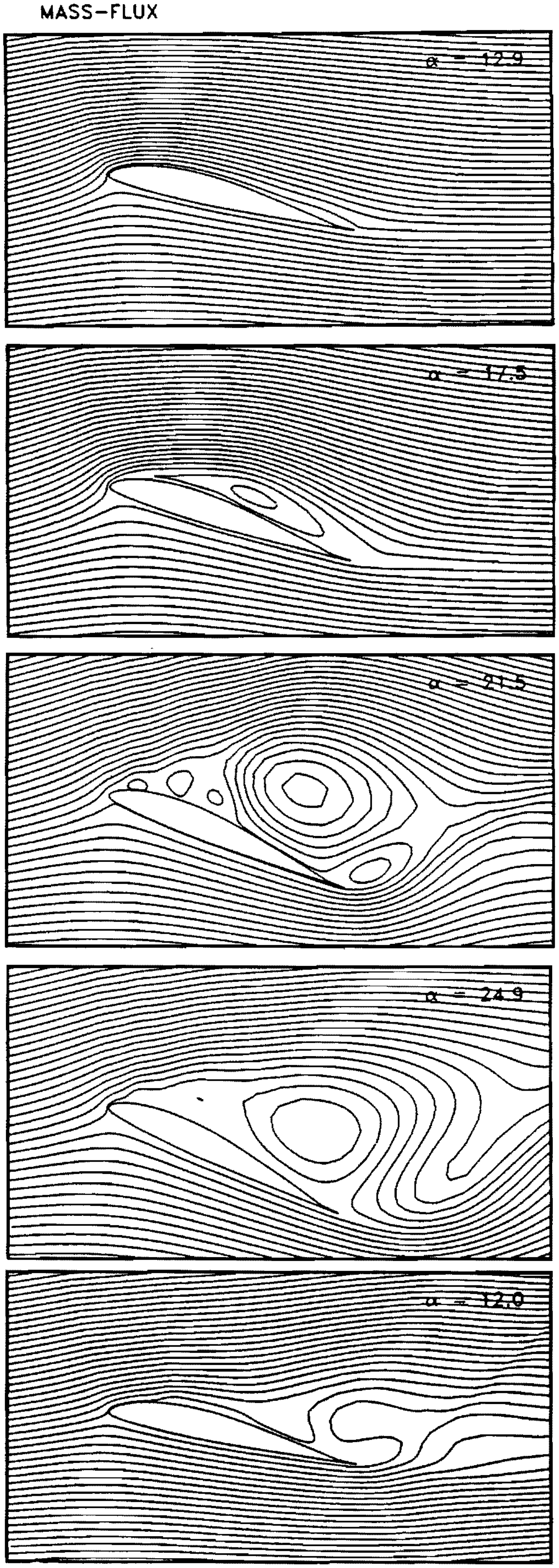

Fig. 7. Instantaneous mass-flux contours - $\alpha = 15° - 10° \cos(\omega t)$, single element.

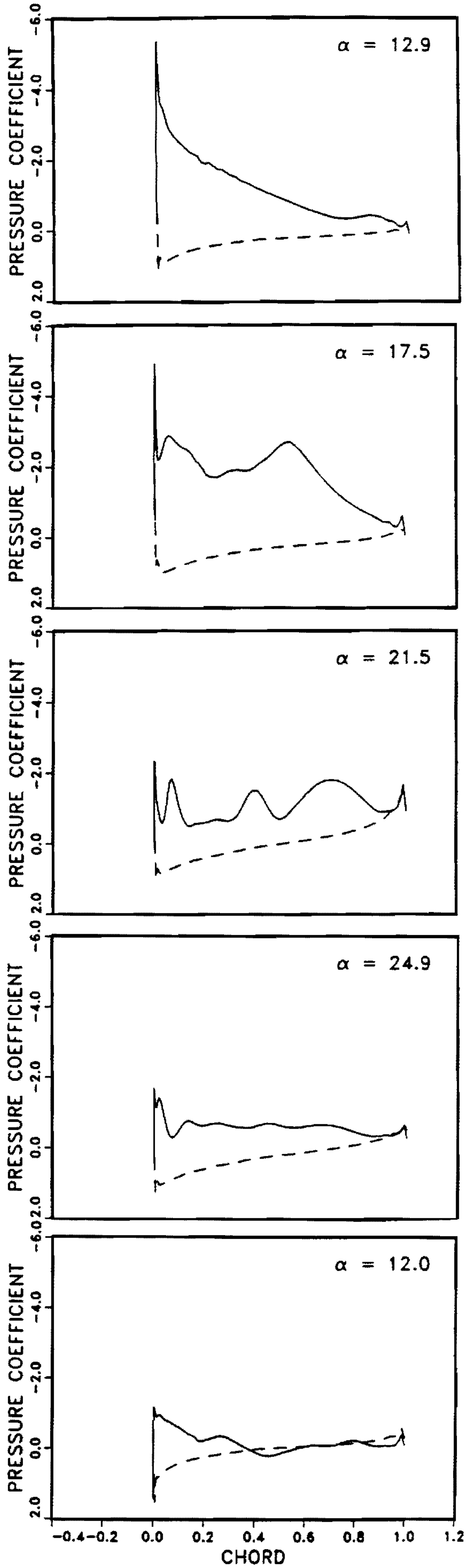

Fig. 8. Pressure distribution - $\alpha = 15° - 10° \cos(\omega t)$, single element.

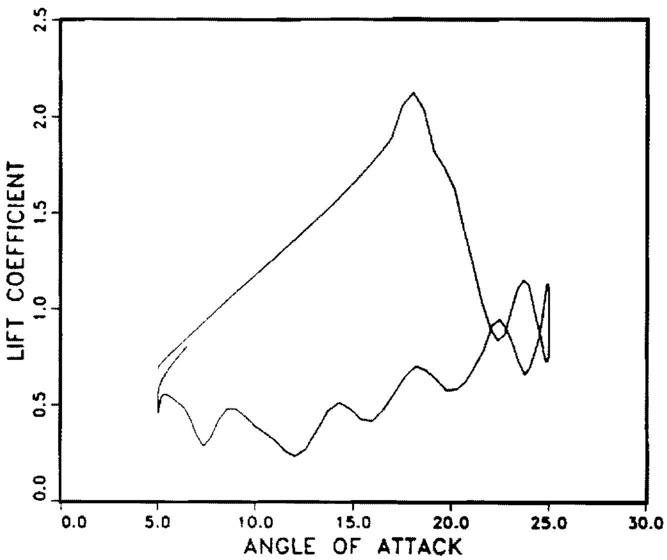

Fig. 9. Unsteady lift - $\alpha = 15° - 10° \cos(\omega t)$, single element.

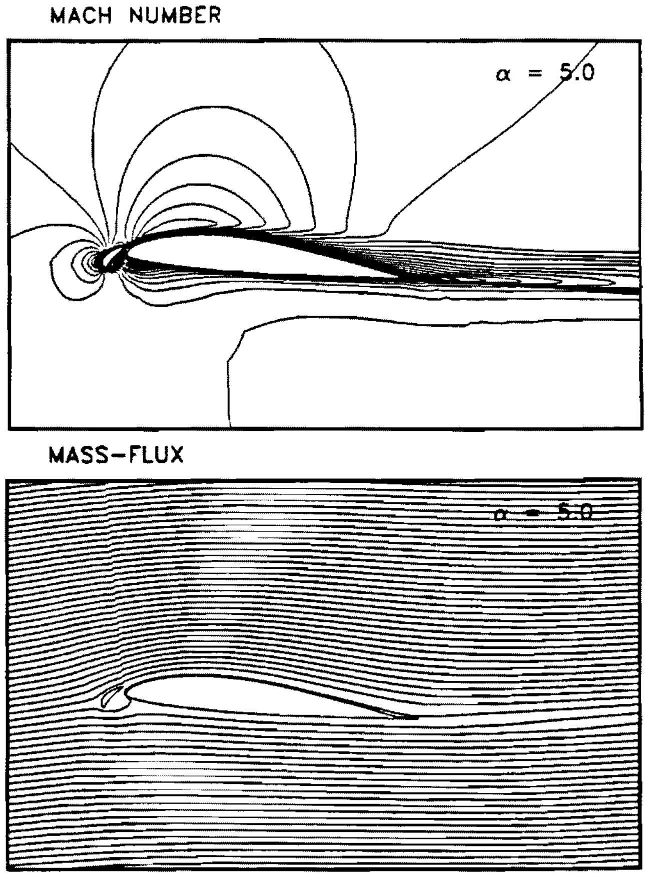

Fig. 10. Mach number and mass-flux contours - $\alpha = 5°$, slat/airfoil.

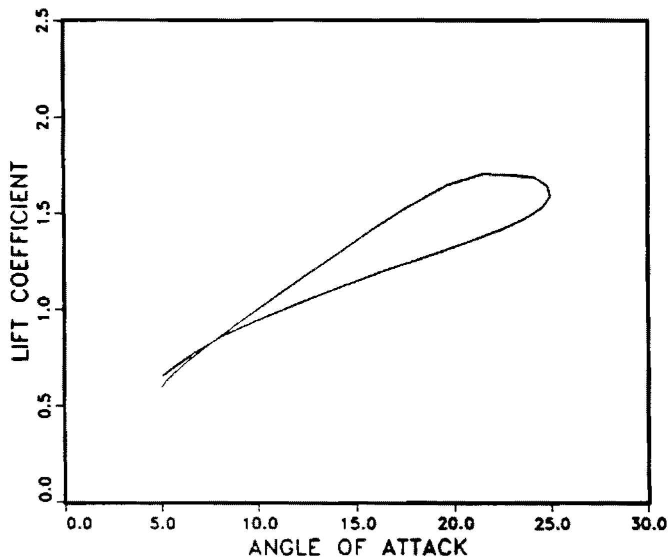

Fig. 14. Unsteady lift - $\alpha = 15° - 10° \cos(\omega t)$, slat/airfoil.

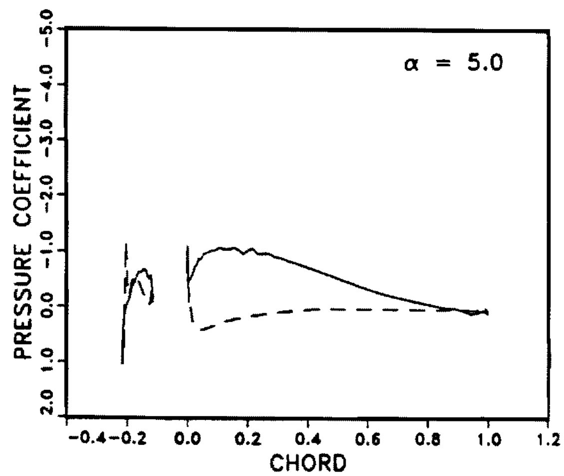

Fig. 11. Pressure distribution - $\alpha = 5°$, slat/airfoil.

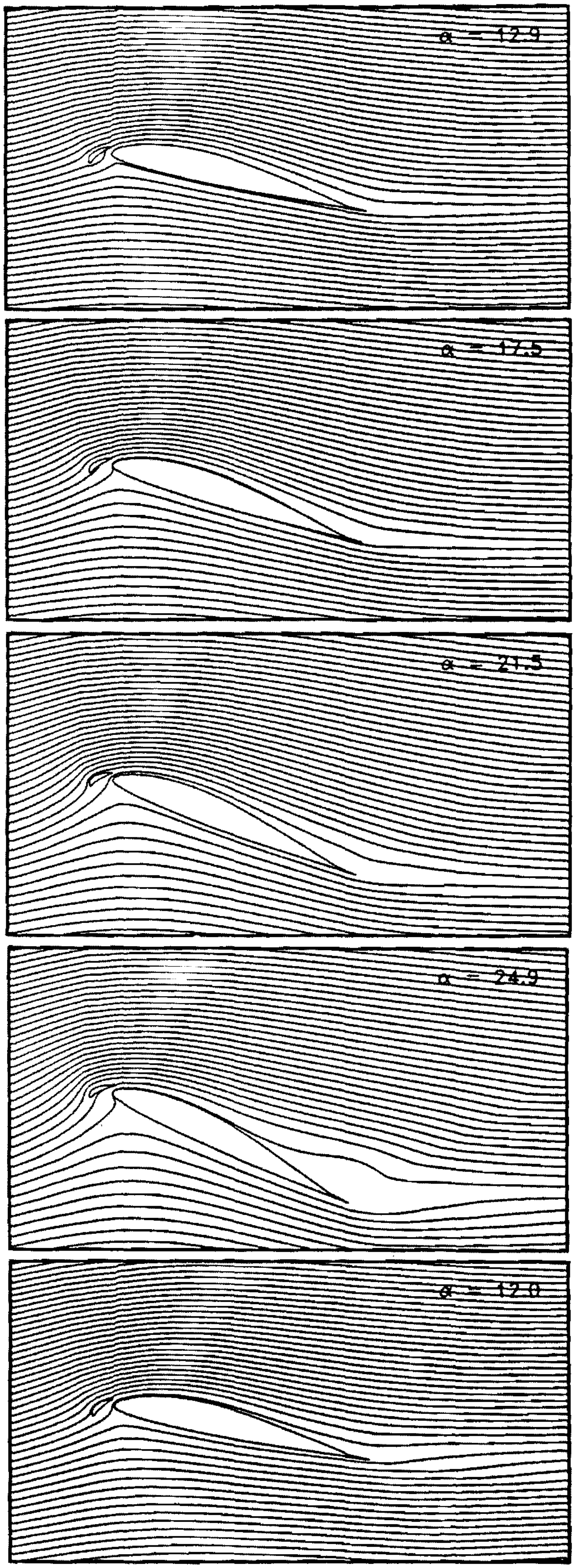

Fig. 12. Instantaneous mass-flux contours - $\alpha = 15° - 10° \cos(\omega t)$, slat/airfoil.

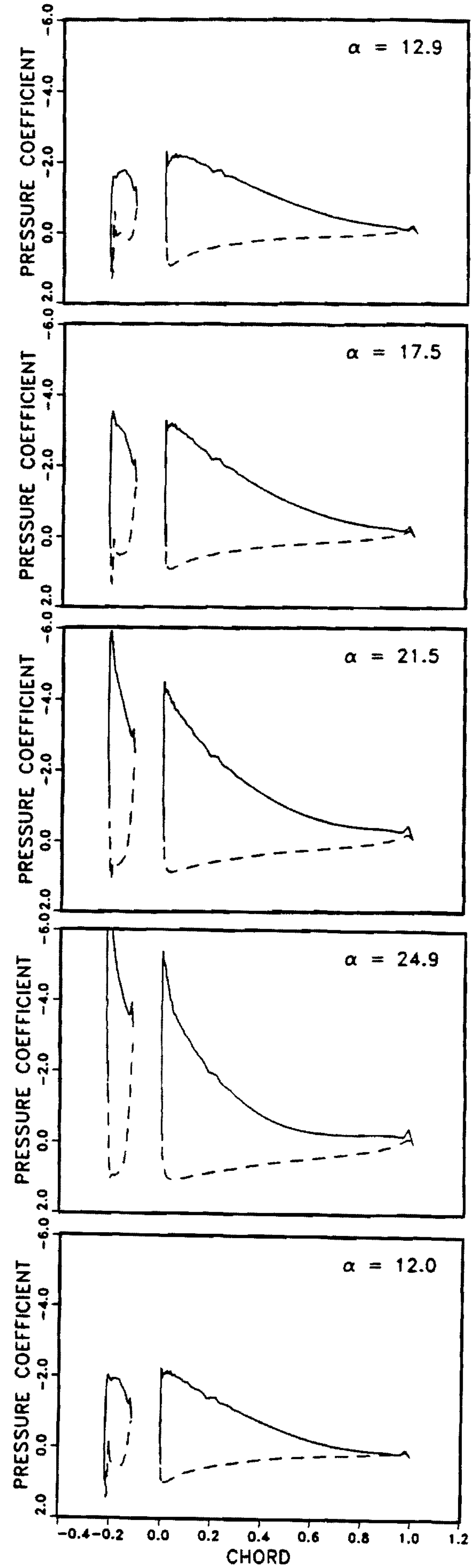

Fig. 13. Pressure distribution - $\alpha = 15° - 10° \cos(\omega t)$, slat/airfoil.

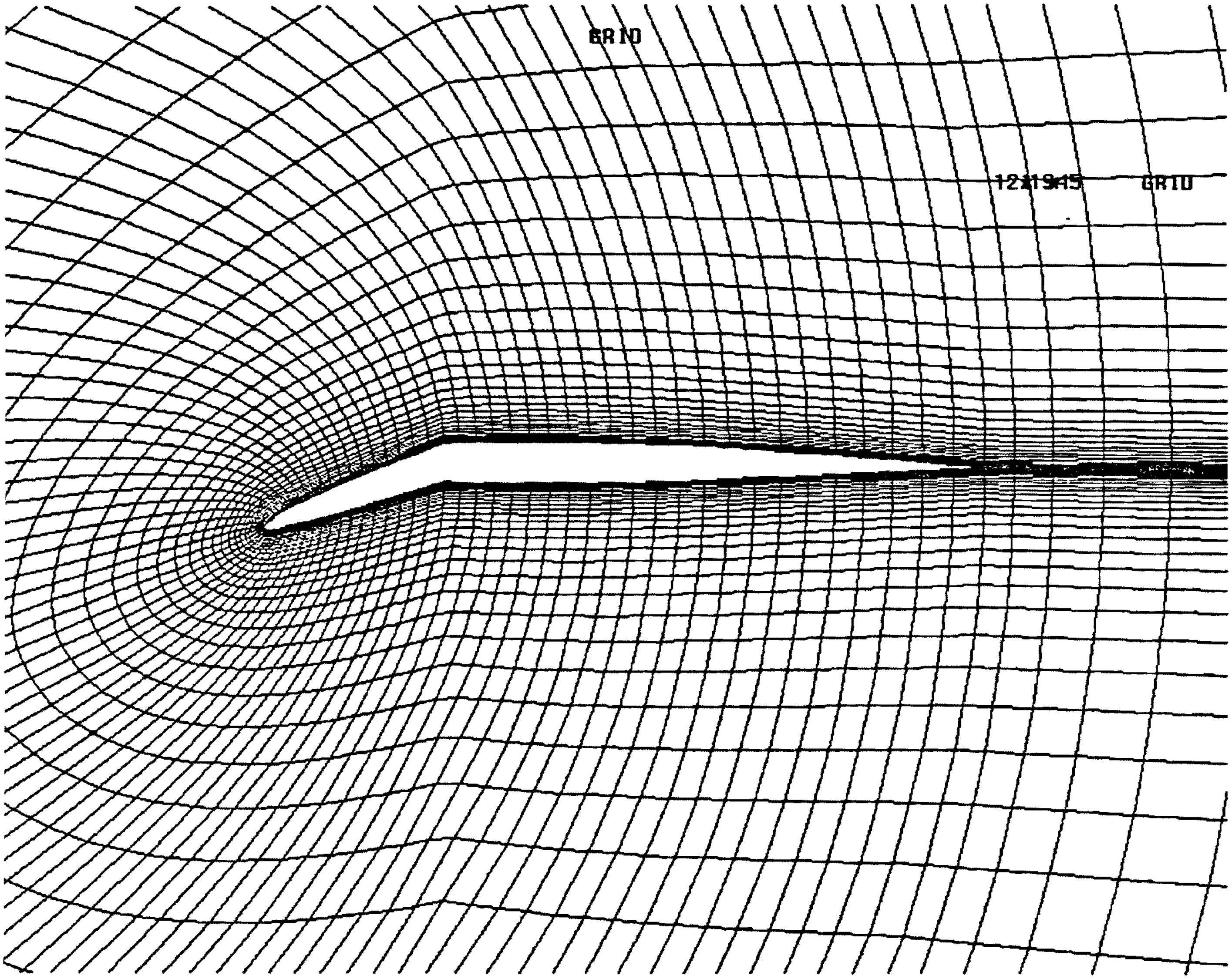
GRID
12:19:45
GRID

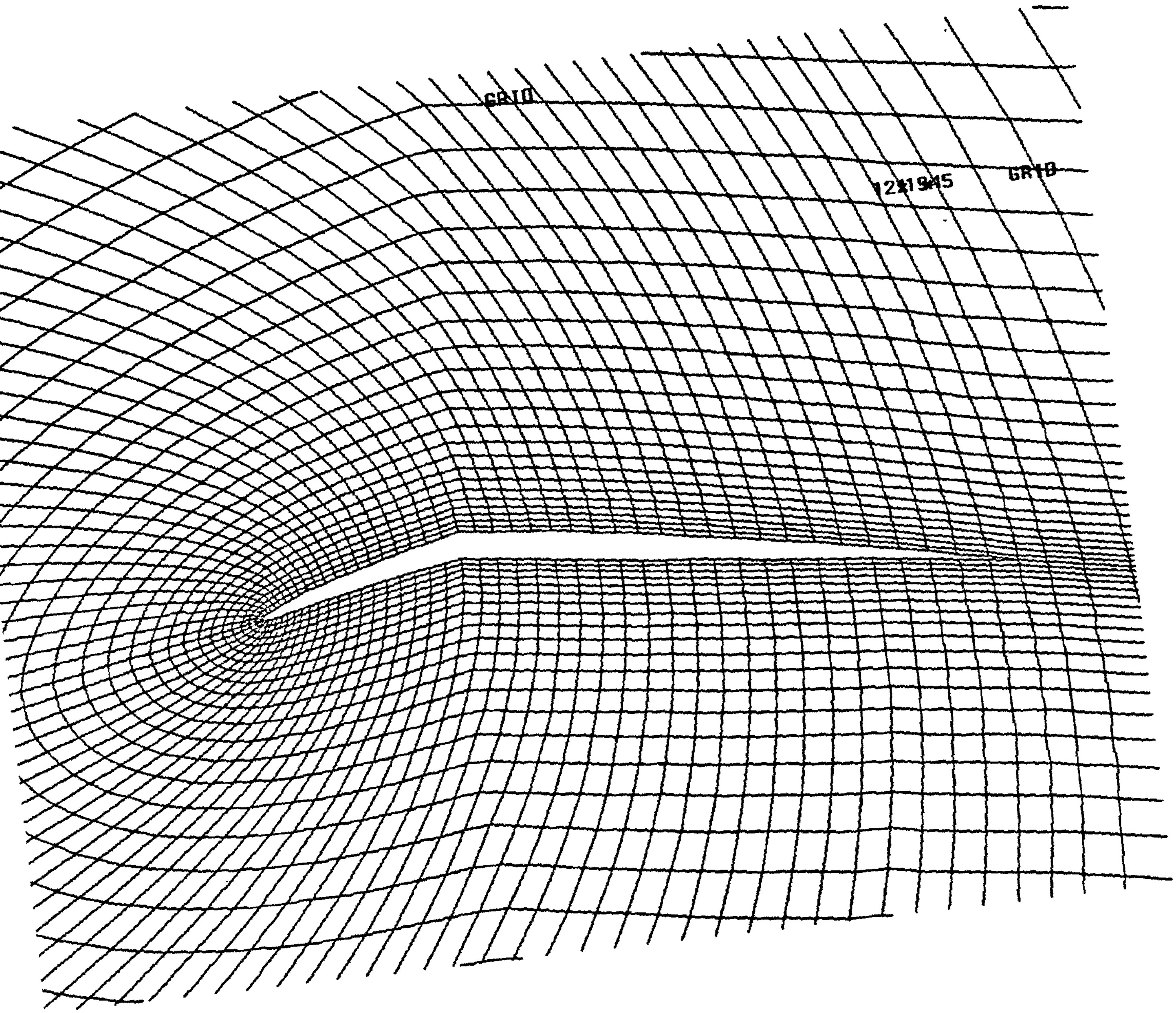
GRID
12219845
GRID

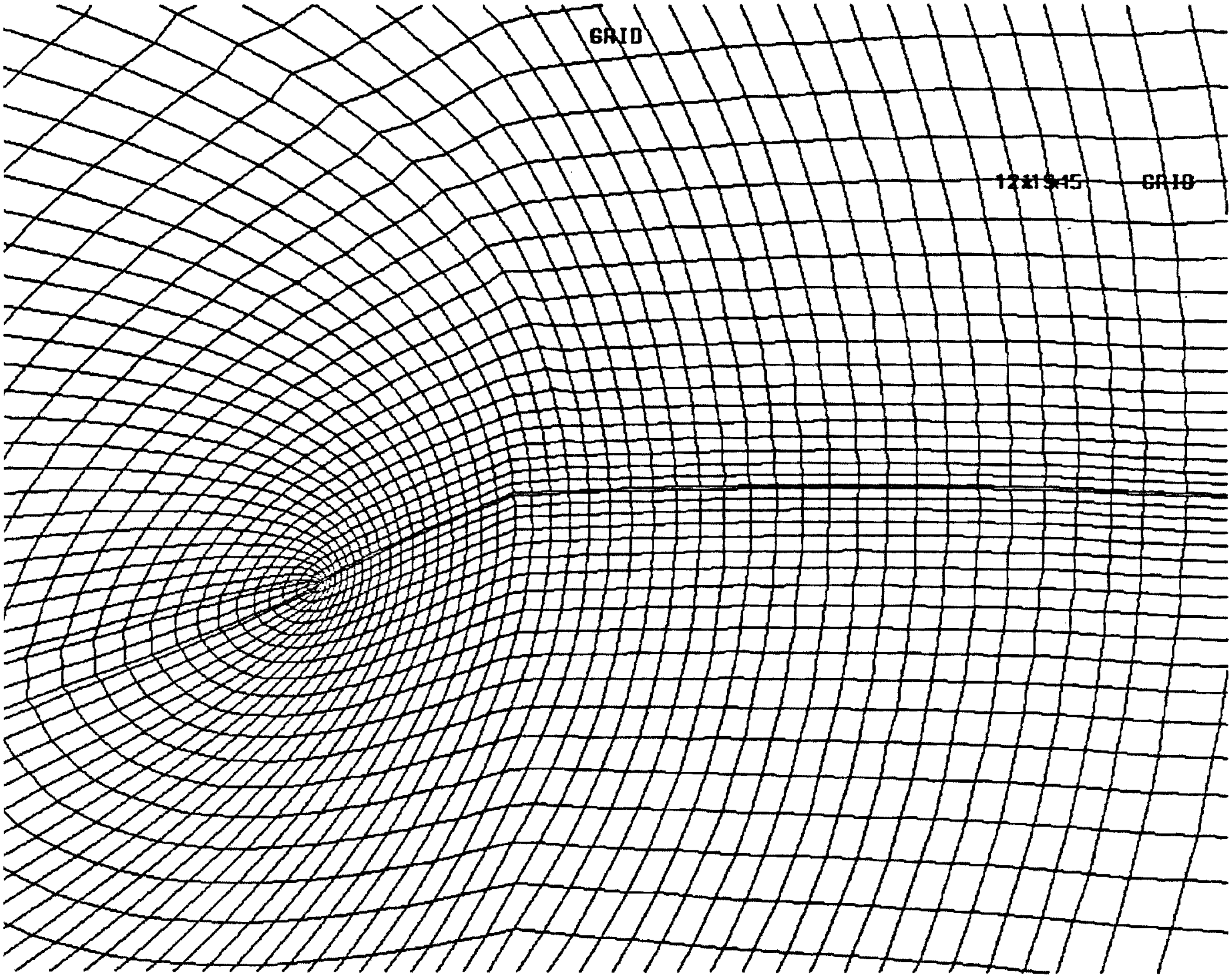
GRID
GRID

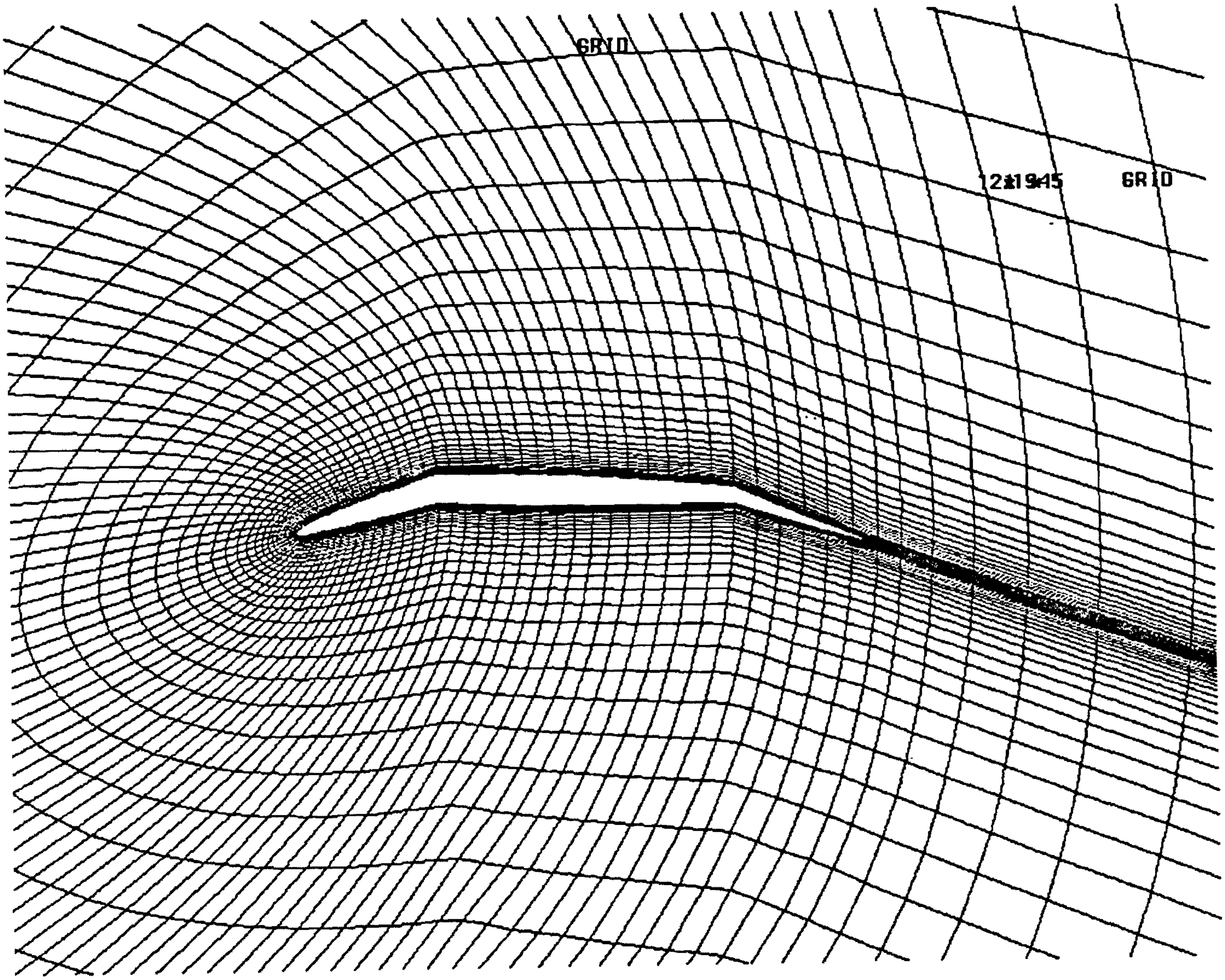
GRID
12:19:45
GRID

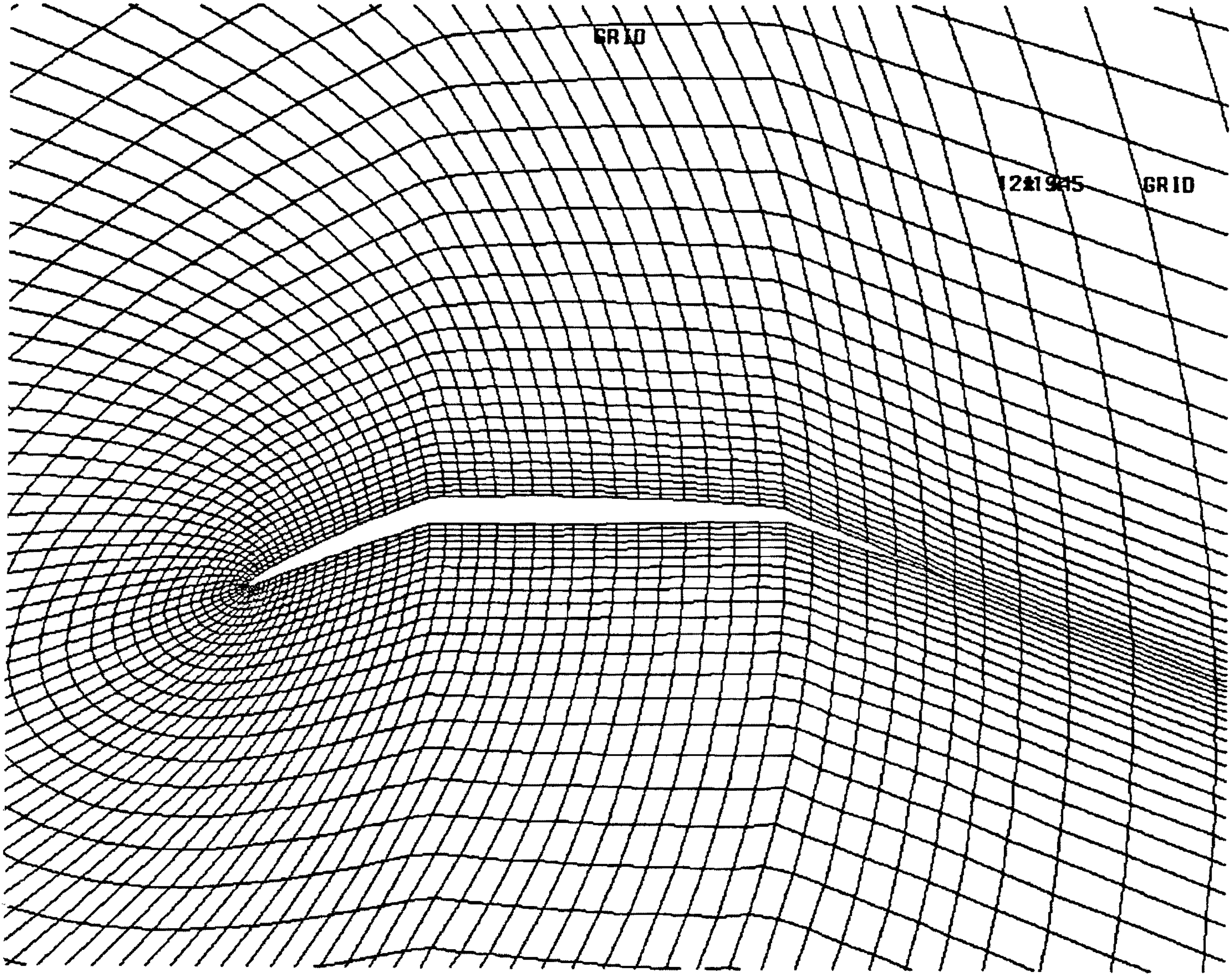
GRID
GRID

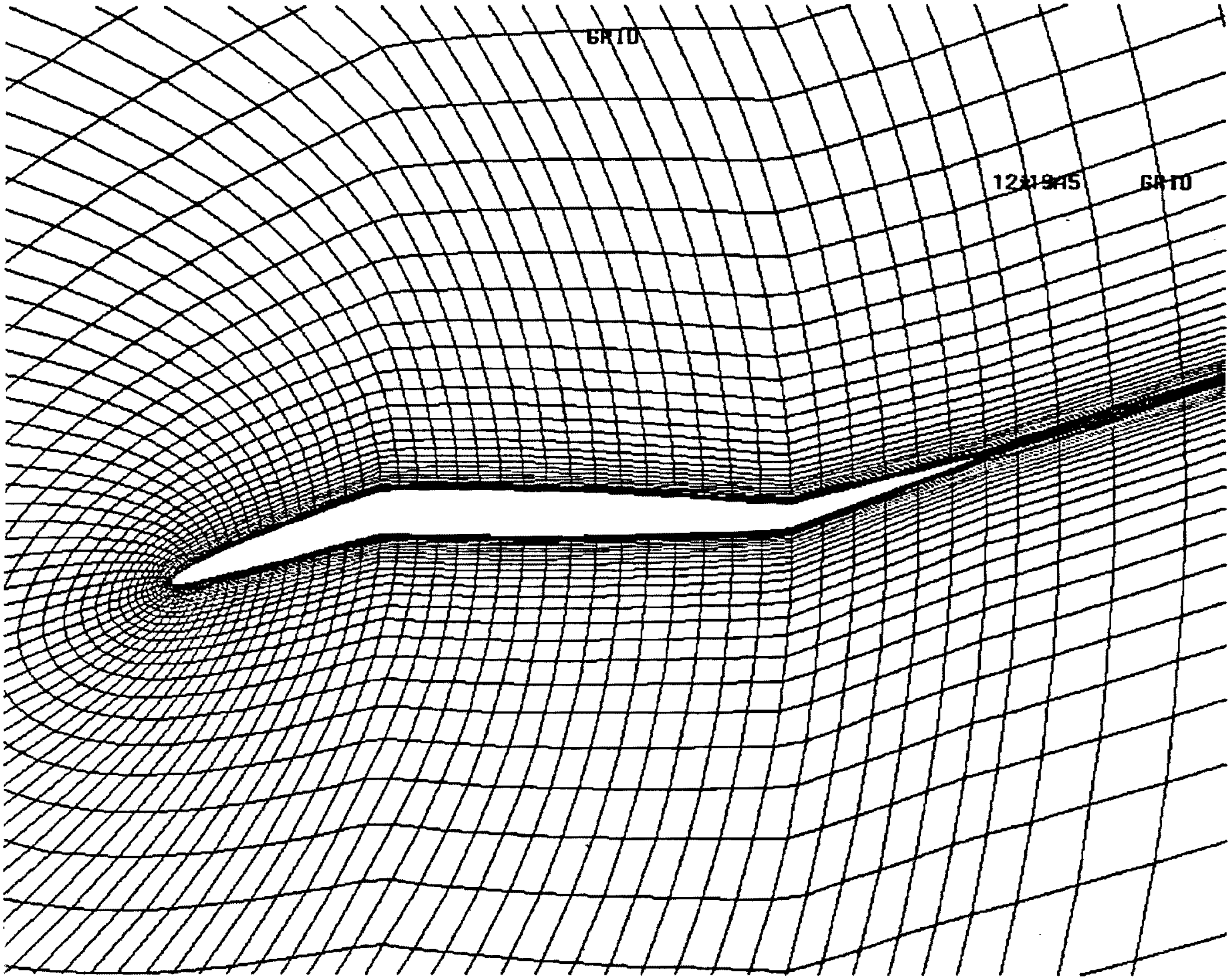
GRID
GRID

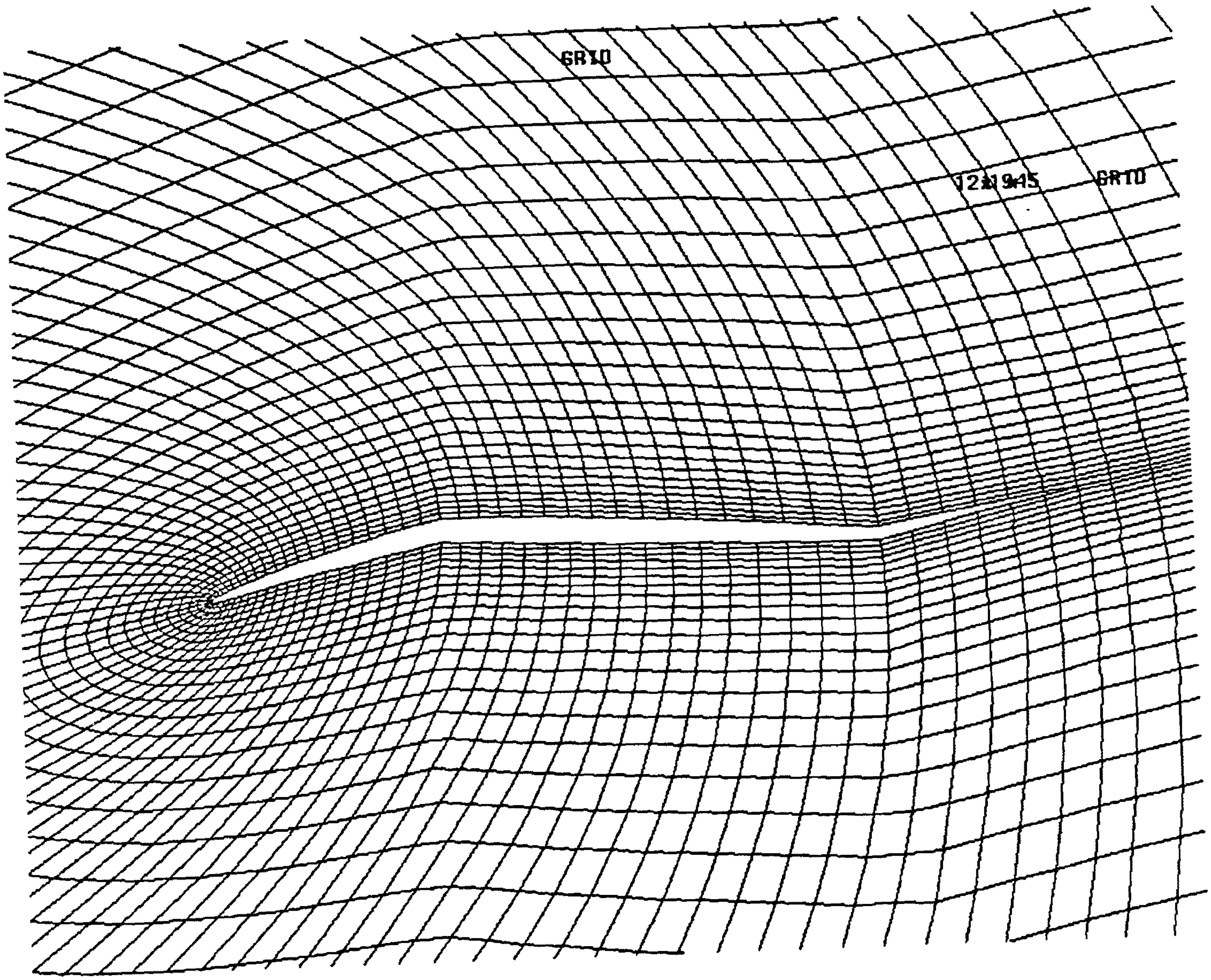
GRID
12x19x15
GRID

F5 wing

$M_\infty = 0.95 \qquad Re = 11.0\text{x}10^6$

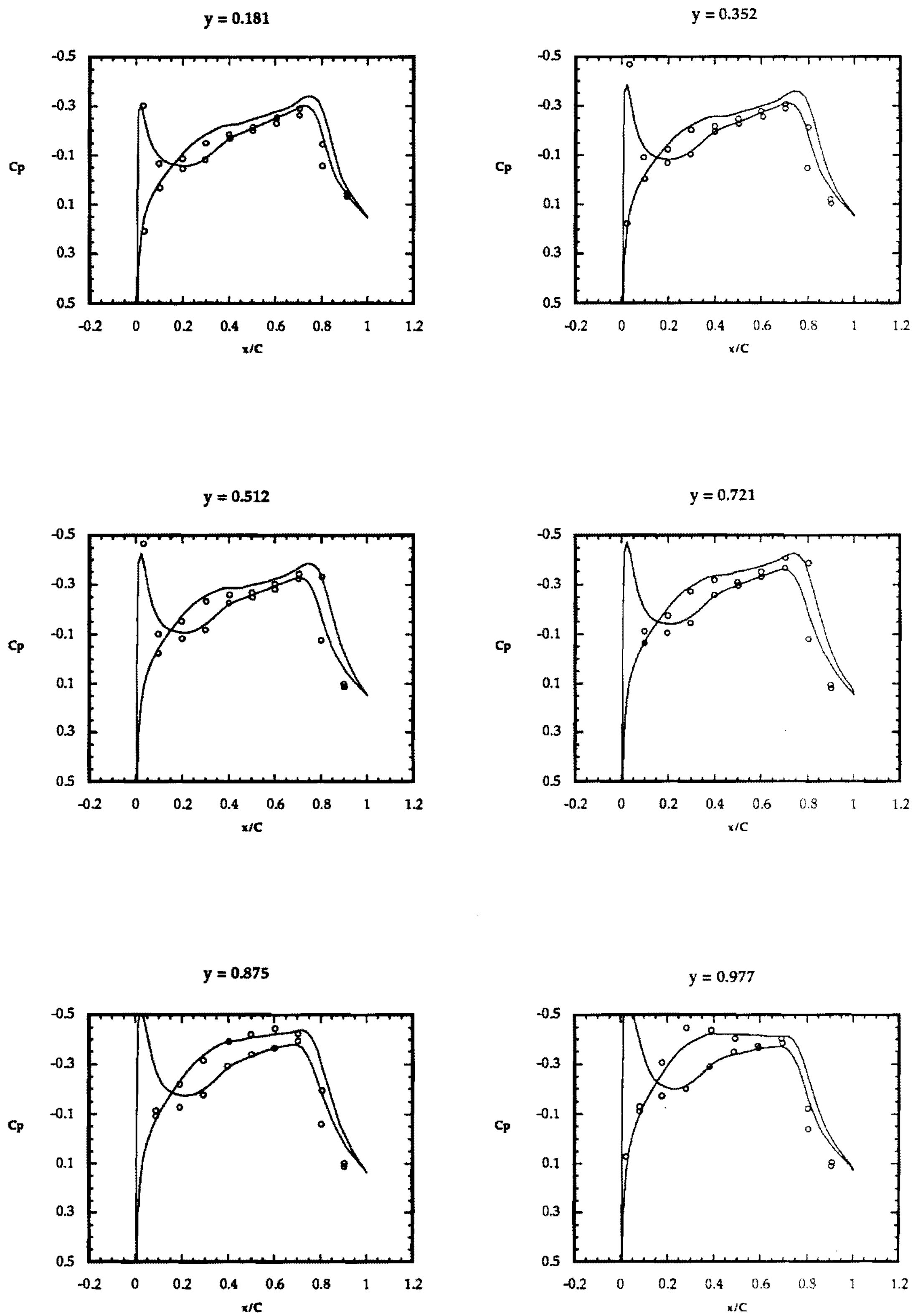

E 16-N01,
/0

UNSTEADY AERODYNAMIC ANALYSIS OF DUAL-ELEMENT WING CONFIGURATIONS

BI-MONTHLY PROGRESS LETTER FOR THE PERIOD

January 1 - February 29, 1992

Submitted to the

NAVAL AIR DEVELOPMENT CENTER
WARMINSTER, PA

Attn: Mr. Marvin M. Walters

Prepared By

L. N. Sankar
Professor
School of Aerospace Engineering
Georgia Institute of Technology, Atlanta, GA 30332

March 1992

School of Aerospace Engineering

Georgia Institute of Technology
Atlanta, Georgia 30332-0150
404•894•3000
Fax: 404•894•2760

March 18, 1992

Mr. Marvin M. Walters
Code 6051
Naval Air Development Center
Warminster, PA 18974

Subject: BI-MONTHLY PROGRESS REPORT FOR THE PROJECT "UNSTEADY AERODYNAMIC ANALYSIS OF DUAL-ELEMENT WING CONFIGURATIONS"

Dear Mr. Walters:

During the reporting period (January 1, 1992 - February 29, 1992), the following tasks were completed:

1) It may be recalled that the 3-D Navier-Stokes solver has already been modified to accept leading edge and trailing edge control surface motion. In the previous report, the dynamic grid generation methodology was described. Sample grids were shown for an F-15 wing equipped with a leading edge and trailing edge control surfaces at a number of span stations, including span stations beyond the wing tip.

The above 3-D Navier-Stokes solver was applied to an F-5 wing equipped with a trailing edge flap. This configuration was tested by Tijdeman at NLR, for a variety of Mach numbers. The mean flow conditions are: Mach number = 0.95, wing angle of attack = 0 degrees. The flap was allowed to sinusoidally oscillate with an amplitude of 0.5 degrees at a frequency of 20 Hz.

The enclosed figure shows the surface pressure distribution at two span stations. Both the in-phase and out-of-phase components of pressure fluctuations are shown, normalized with respect to the amplitude of flap oscillations. In general, reasonable agreement is observed, except in the vicinity of the shock, at 80% chord, where the present shock capturing scheme does not adequately predict the large pressure spikes typical of unsteady shock motion.

The residual history (a measure of the error in the solution of the discretized form of the governing equations at every time step) indicates that the governing equations are satisfied to a high level of tolerance at every time step.

The computer code used to produce these results was made available to Mr. Tseng during his recent trip to Georgia Tech.

With best wishes,

Sincerely,

LAKSHMI N. SANKAR
Professor

F-5 Wing Computations with Unsteady Flap Motion

$M_\infty = 0.9, \alpha = 0°, \alpha_{flap} = \pm 0.5°, f = 20$ Hz

Data are for 1st Cycle of Flap Motion

Cp_{upper} for y = 0.181

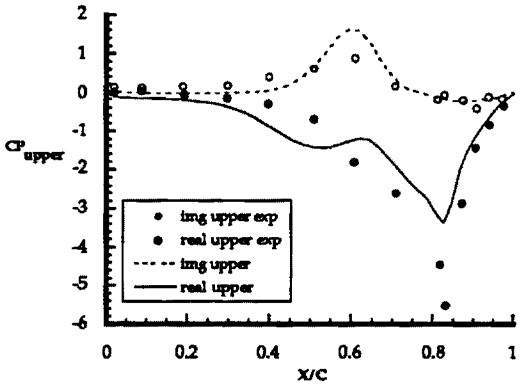

Cp_{lower} for y = 0.181

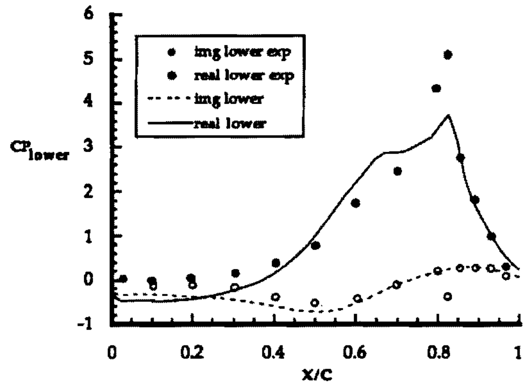

Cp_{upper} for y = 0.512

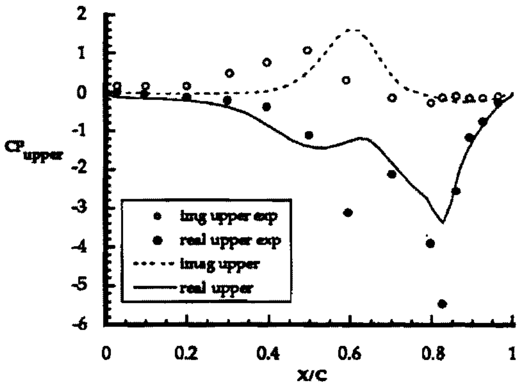

Cp_{lower} for y = 0.512

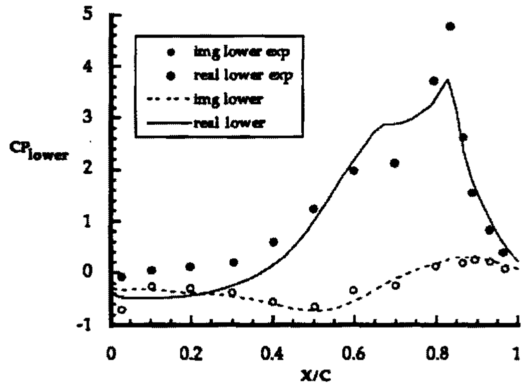

Sectional Cl at Two Spanwise Stations for the First Cycle

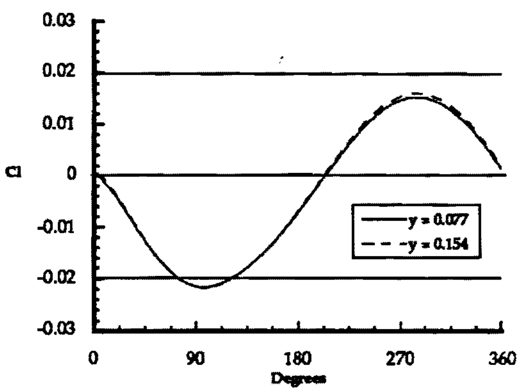

Residual History for the 1st Cycle

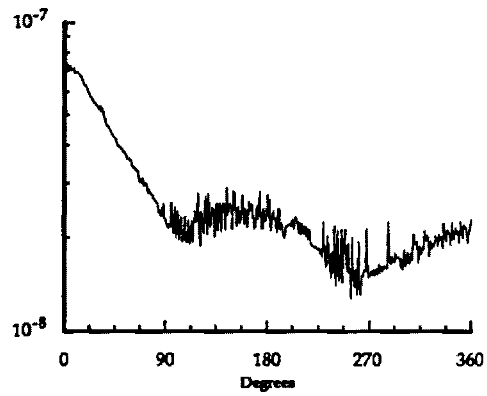

2nd Cycle

f5 flap exp data

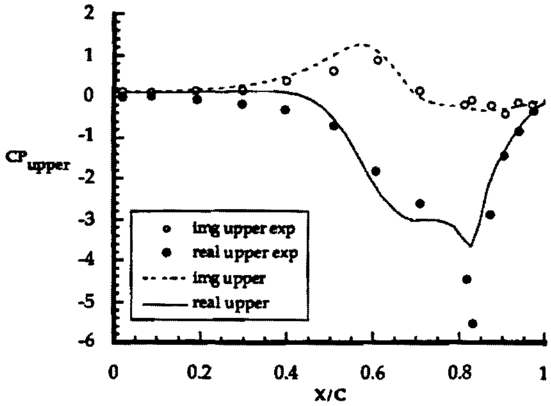

f5 flap exp data

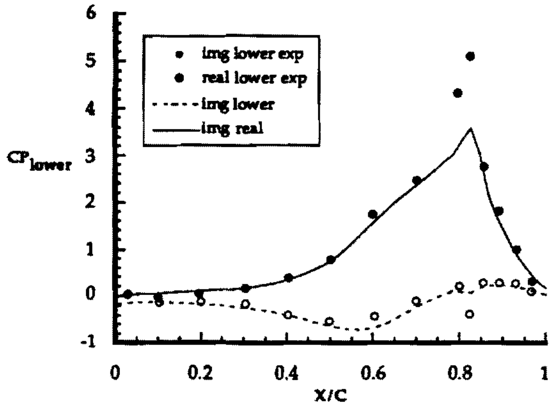

18.1%

f5 flap exp data

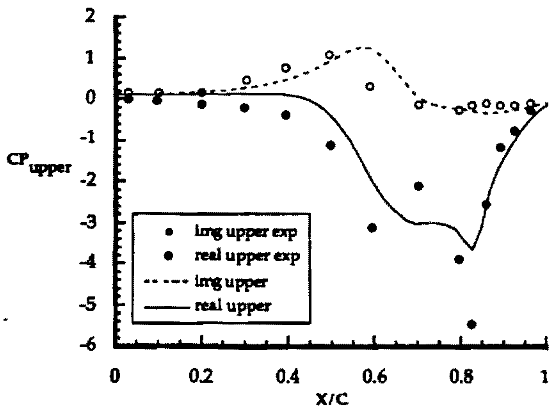

f5 flap exp data

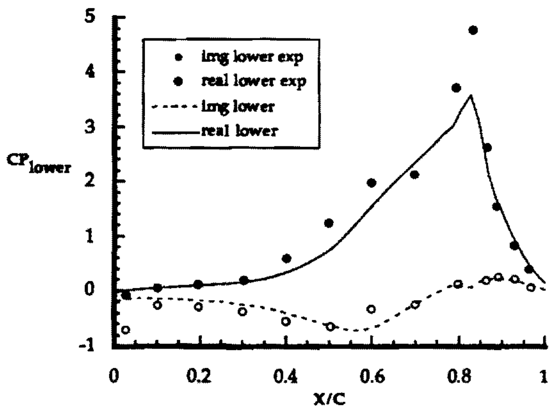

51.2%

11

UNSTEADY AERODYNAMIC ANALYSIS OF DUAL-ELEMENT WING CONFIGURATIONS

BI-MONTHLY PROGRESS LETTER FOR THE PERIOD

March 1 - April 30, 1992

Submitted to the

NAVAL AIR DEVELOPMENT CENTER
WARMINSTER, PA

Attn: Mr. Marvin M. Walters

Prepared By

L. N. Sankar
Professor
School of Aerospace Engineering
Georgia Institute of Technology, Atlanta, GA 30332

May 1992

School of Aerospace Engineering

Georgia Institute of Technology
Atlanta, Georgia 30332-0150
404•894•3000
Fax: 404•894•2760

May 22, 1992

Mr. Marvin M. Walters
Code 6051
Naval Air Development Center
Warminster, PA 18974

Subject: BI-MONTHLY PROGRESS REPORT FOR THE PROJECT "UNSTEADY AERODYNAMIC ANALYSIS OF DUAL-ELEMENT WING CONFIGURATIONS"

Dear Mr. Walters:

During the reporting period (March 1, 1992 - April 30, 1992), the following tasks were completed:

1) The development of the 3-D Navier-Stokes solver modified to accept leading edge and trailing edge control surface motion is now complete. A manual describing the theory, and programmer's guide documenting the computer code are now in preparation.

2) We are assisting Dr. Wei Tseng in your group in the validation of the above solver, and application of this solver to the problem of dynamic lift enhancement of an F-18 wing subjected to leading edge control surface motion. The abstract of a paper submitted to the forthcoming AIAA 31st Aerospace Sciences Meeting is enclosed.

With best wishes,

Sincerely,

LAKSHMI N. SANKAR
Professor

Numerical Simulation of Dynamic Lift Enhancement Using Oscillatory Leading Edge Flaps

Wei W. Tseng
Code 6051
Naval Air Development Center
Warmister, PA

Fu Lin Tsung, Graduate Student
and
Lakshmi N. Sankar ,Professor
School of Aerospace Engineering
Georgia Institute of Technology
Atlanta, GA 30332-0150

(404)-894-3014

INTRODUCTION

Fighter aircraft such as the F-18 employed by the U. S. Navy often require large amounts of lift for relatively short periods of time. For example, the availability of large amounts of lift during the landing on an aircraft carrier can significantly reduce the landing speed, and reduce the loads on the vehicle by the arresting mechanism as it is brought to rest. A fighter aircraft can use a variety of mechanisms, e.g. vectored thrust, high vehicle angle of attack, deployment of leading edge and trailing edge control surfaces to achieve the required lift.

One of the interesting concepts for lift generation that has been experimentally studied under NADC funding involves a rapid sinusoidal pitching motion by the leading edge control surfaces. Experimental studies done by B. Smith [Ref. 1] indicates that a dynamic lift enhancement may be possible using oscillating leading edge control surfaces.

To our knowledge, this problem has not been numerically investigated before. There is a need to systematically investigate the origin of 3-D dynamic lift for this situation, and investigate the associated drag and pitching moment penalties. There is also the need to quantitatively assess the relative merits of the leading edge control motion concept, in comparison to other concepts mentioned above. Finally, a capability for the quantitative simulation is necessary for parametric design/trade-off studies of flap size, oscillation amplitude and oscillation frequency.

In the present work, this problem is studied using a three-dimensional compressible Navier-Stokes solver developed by the present investigators [Ref. 2]. This solver is validated as part of the present work through steady 3-D Navier-Stokes simulations of flow over an F-5 fighter wing, and 3-D unsteady flow over an F-5 wing with an oscillating trailing edge control surface. It is subsequently applied to a numerical study of the dynamic lift generation over an F-18 wing at subsonic Mach numbers through leading edge flap motion.

MATHEMATICAL AND NUMERICAL FORMULATION

The 3-D unsteady, compressible Reynolds-averaged Navier-Stokes equations may formally be written as

$$q_t + F_x + G_y + H_z = R_x + S_y + T_z \qquad (1)$$

Here q is vector containing the unknown flow properties such as density, velocity and temperature. The quantities F, G and H are inviscid flux vectors and contain information related to the convective transport of mass, momentum and energy and pressure forces. The terms R, S and T contain viscous (laminar and turbulent) stress contributions to mass, momentum and energy transport.

To facilitate the computation of flow past arbitrary shaped configurations such as wings and wing-bodies, and to account for the flap rotation these equations are transformed to a new coordinate system (ξ,η,ζ,τ), in which the solid surfaces such as the wing or fuselage maps on to surfaces such as ζ= constant or ξ = constant. In such a coordinate system, the governing equations may formally be written as

$$\mathbf{q}_\tau + \mathbf{F}_\xi + \mathbf{G}_\eta + \mathbf{H}_\zeta = \mathbf{R}_\xi + \mathbf{S}_\eta + \mathbf{T}_\zeta \qquad (2)$$

The quantities **q** , **F** , **G** , **H** etc. depend on their Cartesian counterparts q, F, G and H through the metrics of transformation.

The objective of calculation is then to integrate these equations numerically, starting from an initial guess for the flow vector q, by marching in time. At every time step, appropriate boundary conditions for the flow properties must be imposed. In viscous flows, the appropriate boundary conditions are that the fluid and solid have the same velocity, and that the temperature and density gradients at the solid surface vanish. At the boundaries that are sufficiently far away from the solid surfaces, the flow properties have been computed by prescribing or extrapolating 1-D Riemann variables in the present work.

A finite difference procedure has been used to approximate the various derivatives appearing in equation (2). Although second order accuracy and fourth order accuracy in space are possible with the present formulation, for the sake of clarity only the simplest first order temporal-second order spatial formulation is described here. The finite difference analog of equation (2) at a time level 'n' is then

$$\Delta \mathbf{q}^{n+1}/\Delta t + \delta_\eta \mathbf{F}^{n+1} + \delta_\eta \mathbf{G}^* + \delta_\zeta \mathbf{H}^{n+1} = (\delta_\xi \mathbf{R} + \delta_\eta \mathbf{S} + \delta_\zeta \mathbf{T})^n \quad (3)$$

Here δ_ξ, δ_η and δ_ζ are standard symmetric central difference operators. The quantity $\Delta \mathbf{q}^{n+1}$ is the change in $\mathbf{q}$ during adjacent time levels and Δt is the time step. Note that the viscous terms at the right side are evaluated explicitly (at the previous time level, n) while the quantities **F** and **H** are evaluated implicitly at the new time level 'n+1'. The spanwise derivative $\delta_\eta \mathbf{G}^*$ is evaluated semi-implicitly, that is using old time level values and new time level values as they become available.

Equation (3) in its present form is a set of non-linear algebraic equations for the change in flow property $\Delta \mathbf{q}$. In order to solve for $\Delta \mathbf{q}$, the non-linear vectors **F** and **H** at time level 'n+1' are linearized at every time level about their values at the previous time level 'n' as follows:

$$\mathbf{F}^{n+1} = \mathbf{F}^n + A\,\Delta \mathbf{q} \quad (4a)$$

$$\mathbf{H}^{n+1} = \mathbf{H}^n + B\,\Delta \mathbf{q} \quad (4b)$$

where A is a 5 x 5 matrix, given by $d\mathbf{F}/d\mathbf{q}$, and B is $d\mathbf{H}/d\mathbf{q}$, evaluated at time level 'n'.

The linearized system of algebraic equations may formally be written in the following operator form, as a system of equations involving the unknown $\Delta\mathbf{q}$:

$$[I + \Delta t\, \delta_\xi A + \Delta t\, \delta_\zeta B]\, \{\Delta\mathbf{q}\}^{n+1} = R^{n,n+1} \quad (5)$$

where the right hand side contains known information from the previous time level about **F,G,H,R,S** and **T**. This term is called the residual. In steady state applications, a solution to the 3-D Navier-Stokes equations requires that this quantity R be driven to zero, in an iterative fashion. In an unsteady problem, R is of the order of the time step Δt and need not necessarily go to zero after several time steps.

Equation (5) couples the quantity $\Delta\mathbf{q}$ at every point in the flow field with its 4 neighbor nodes, and is a block penta-diagonal system. A direct inversion of the penta-diagonal system is costly, and some type of approximation is required to reduce the CPU time. The conventional techniques require strategies such as incomplete LU decomposition, or an alternating direction approximate factorization (AF) {Ref. 3-5]. The AF scheme is used here, and requires factorization of the matrix operator on the left side of equation (5) into two smaller operators leading to the solution of the following equation:

$$[I + \Delta t\, \delta_\xi A\,]\,[\,I + \Delta t\, \delta_\zeta B]\, \{\Delta\mathbf{q}\}^{n+1} = R^{n,n+1} \quad (6)$$

It may be shown that equation (6) requires solving at every node two tri-diagonal matrix equations than a single penta-diagonal matrix equation. Solution of tri-diagonal matrix systems may be performed efficiently using the well known Thomas algorithm, and may also be easily vectorized.

The above temporal differencing scheme is called a hybrid time differencing scheme, and has several advantages over fully explicit schemes and fully implicit schemes. Specifically,

a) The flow property vector q need be stored at only one time level. Most schemes require the flow properties (or changes in q) to be stored at several time levels. Thus, the present approach is memory efficient.

b) The above scheme requires a single evaluation of the residual at a node per time step, and two tridiagonal matrix inversions. Fully explicit schemes require residual calculations to be performed two or four times per node per time step. Fully implicit schemes require three tri-diagonal matrix inversions and are computationally expensive.

c) The present approach can be coded such that the flow variables at five η= constant planes need be in memory at a given time. Flow variables at the other planes may reside on secondary storage devices. Thus, this approach works well on virtual memory machines.

In high Reynolds number flows, use of standard central differences can cause wiggles to appear at every time step. These high frequency spatial oscillations can grow if unchecked, and can lead to catastrophic failure of the solution. To avoid this, at every time step, the solution is smoothed using a weighted formula linking a node to its four neighbors. For enhanced stability, the correction Δq is also smoothed. In viscous flows, it is necessary to augment the laminar viscosity coefficient with an eddy viscosity coefficient using the Baldwin-Lomax algebraic model. Two types of numerical viscosity terms, the first based on the work of Jameson, Turkel and Schmidt as modified by Radspiel et al. and a second based on a third order upwind Roe scheme have been implemented, and tested. The results presented here were computed using the Jameson-Schmidt-Turkel form.

RESULTS AND DISCUSSION

The above 3-D Navier-Stokes solver was applied to an F-5 wing equipped with/without a trailing edge flap. This configuration was tested by Tijdeman at NLR, for a variety of Mach numbers. The mean flow conditions are: Mach number = 0.95, wing angle of attack = 0 degrees. The Reynolds number was 11 Million.

Figure 1 shows the surface pressure distribution obtained on a 121 x 45 x 24 grid after several thousand iterations. It is seen that the solver accurately captures the flow characteristics, including the leading edge pressure spike due to the drooped leading edge of the F-5 wing, and the trailing edge shock. The flap was allowed to sinusoidally oscillate with an amplitude of 0.5 degrees at a frequency of 20 Hz.

Figure 2 shows the surface pressure distribution when the trailing edge flap is oscillated sinusoidally up or down by 1/2 degree at a frequency of 0 Hz. Both the in-phase and out-of-phase components of pressure fluctuations are shown, normalized with respect to the amplitude of flap oscillations. In general, reasonable agreement is observed, except in the vicinity of the shock, at 80% chord, where the present shock capturing scheme does not adequately predict the large pressure spikes typical of unsteady shock motion.

Following the above code validation studies, the flow solver was applied to an F-18 wing equipped with a leading edge flap. The 3-D Navier-Stokes solver can accept a fairly general small or large amplitude leading edge and trailing edge control surface motion. The user may prescribe the amplitude of oscillations, flap/slat hinge location and the frequency of oscillations. A simple algebraic grid shearing scheme has been implemented, which allows the original body-fitted grid to move with the flap/leading edge slat motion. Sample grids for an F-18 wing equipped with a leading edge control surface are enclosed as figure 3. It may be noted that the algebraic deformation does not cause grid cross-over, even for very large flap deflections.

The flow conditions for the F-18 dynamic lift enhancement study are as follows. The mean flow Mach number and angle of attack were 0.15 and 40 degrees, respectively. A 121 x 17 x 45 grid was used, with 90 points on the wing surface. A constant time step, equal to 0.02 (based on wing root chord, and freestream speed of sound) was used. The Reynolds number was 200,000, The leading edge flap oscillation amplitude was 2 degrees, about a mean deflected position. The frequency of oscillation was and all the above parameters were chosen in order to conform as closely to the data given in Ref. 1 as possible.

Figure 4 shows the total pressure contours at the midspan, at several time levels during the oscillations. The intensity of the color (blue to red) indicates total pressure losses, which usually occur near the core of a vortex. It is seen that a significant amount of vorticity is being shed into the wake by the control surface. In the full paper these results will be compared with the flow visualization data from Ref. 1.

Finally, figure 5 shows the variation in sectional lift at mid-chord as a function of time. These results, considered preliminary because a grid sensitivity analysis has not been done yet, indicate significant rises in lift values even for a small 1/2 flap oscillation amplitude.

The full paper will give full details of the calculations, surface pressure distribution and grid sensitivity results. Wherever possible, we plan to give a detailed one-to-one comparisons with the studies given in Ref. 1.

CONCLUSIONS

An existing 3-D unsteady Navier-Stokes solver has been modified to handle leading and trailing edge control surface motions of fighter aircraft wings. The solver was first validated through numerical studies of flow over an F-5 wing. Subsequently, calculations were done for an F-18 wing with an oscillating leading edge control surface were done. Preliminary flow visualization and load histories indicate that the leading edge surface motion may be effective in enhancing the lift generated by the wing.

REFERENCES

1. Smith, B., "Dynamic Lift Enhancement Using Oscillating Leading Edge Flaps," AIAA paper 92-2625, to be presented at the 10th AIAA Applied Aerodynamics Conference, Palo Alto, CA, June 22-24, 1992.

2. Sankar N. L. and Kwon, O. J., Viscous Flow Simulations of a Fighter Aircraft, Proceedings of the High Alpha Aerodynamics Conference, NASA Langley Research center, 1990.

3. Rizk Y.M., and Chaussee, D.S., Three dimensional viscous flow computations using a directionally hybrid implicit-explicit procedure , AIAA paper 83-1910.

4. Beam R.M., Warming R.F., An implicit factor scheme for the compressible Navier Stokes equation , AIAA journal, vol. 16, no 4, 1978.

5. Steger J.L., and Kutler P., Implicit finite differencing procedures for computation of vortex wake , AIAA journal, vol 15, no. 4, April 1977.

F-5 Wing

$M_\infty = 0.95$, $Re = 11.0 \times 10^6$, $\alpha_{wing} = 0°$

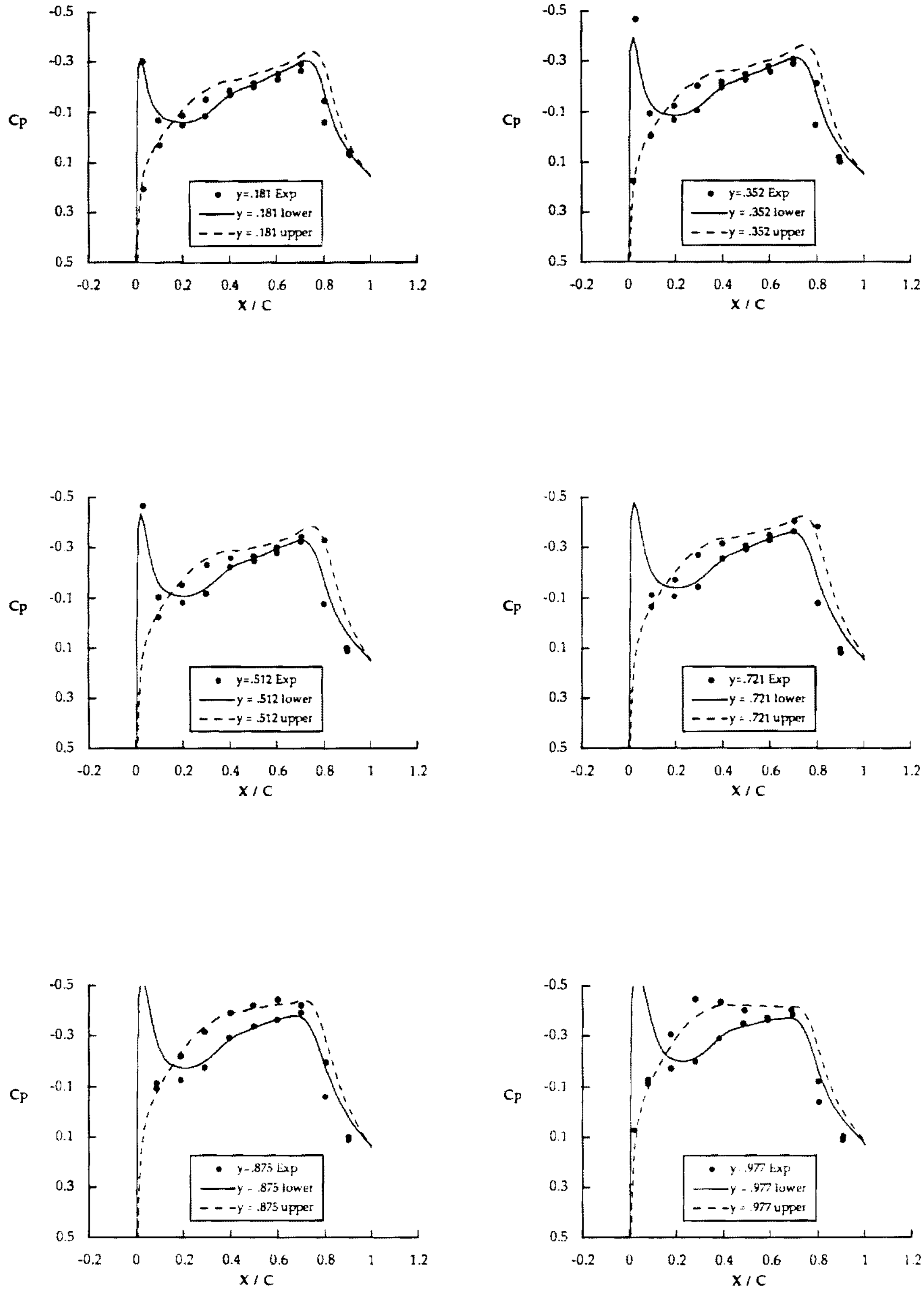

Figure 1. Comparison of ADI scheme with experimental data

F-5 Wing Computation with Unsteady Trailing Edge Flap Motion

$M_\infty = 0.90$, $\alpha_{wing} = 0°$, $\alpha_{flap} = \pm 0.5°$, $f = 20Hz$

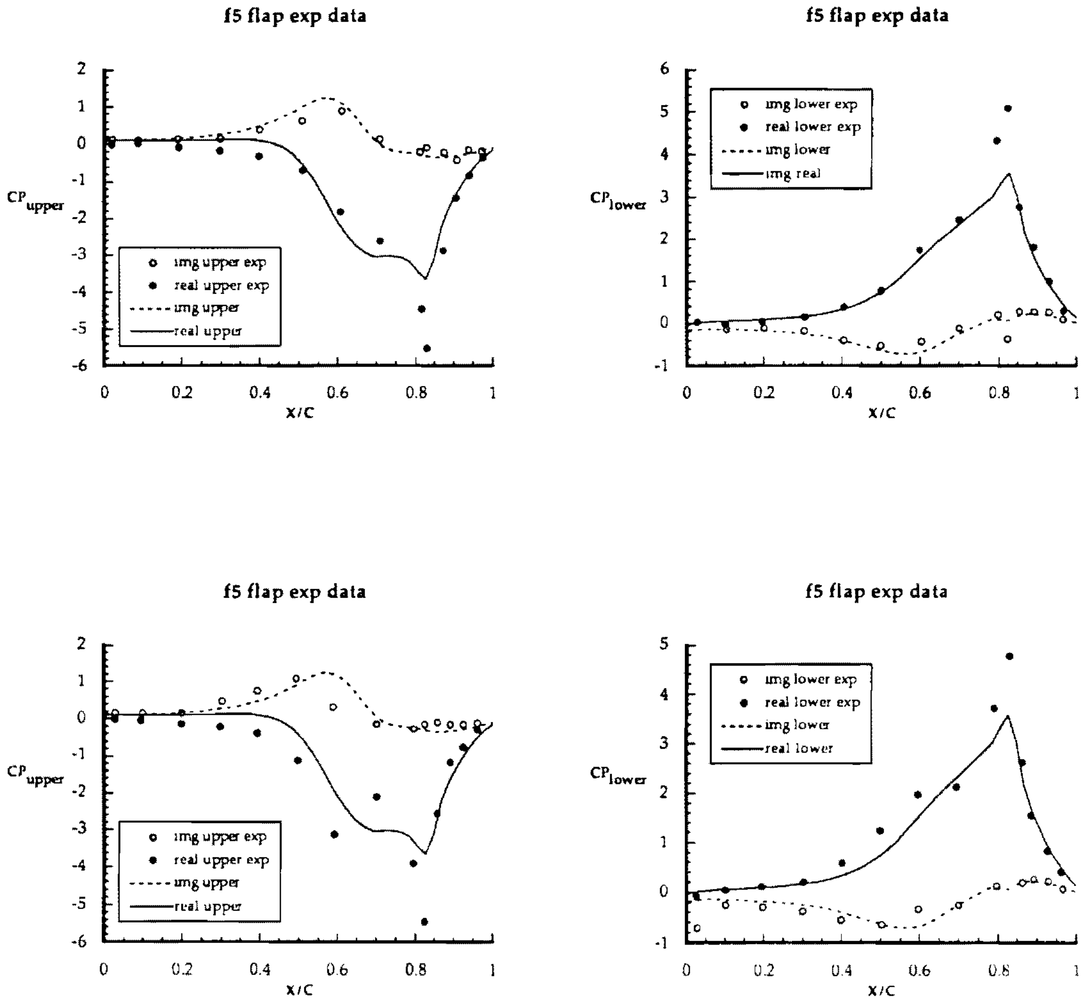

Figure 2. Comparison of ADI scheme with experimental data

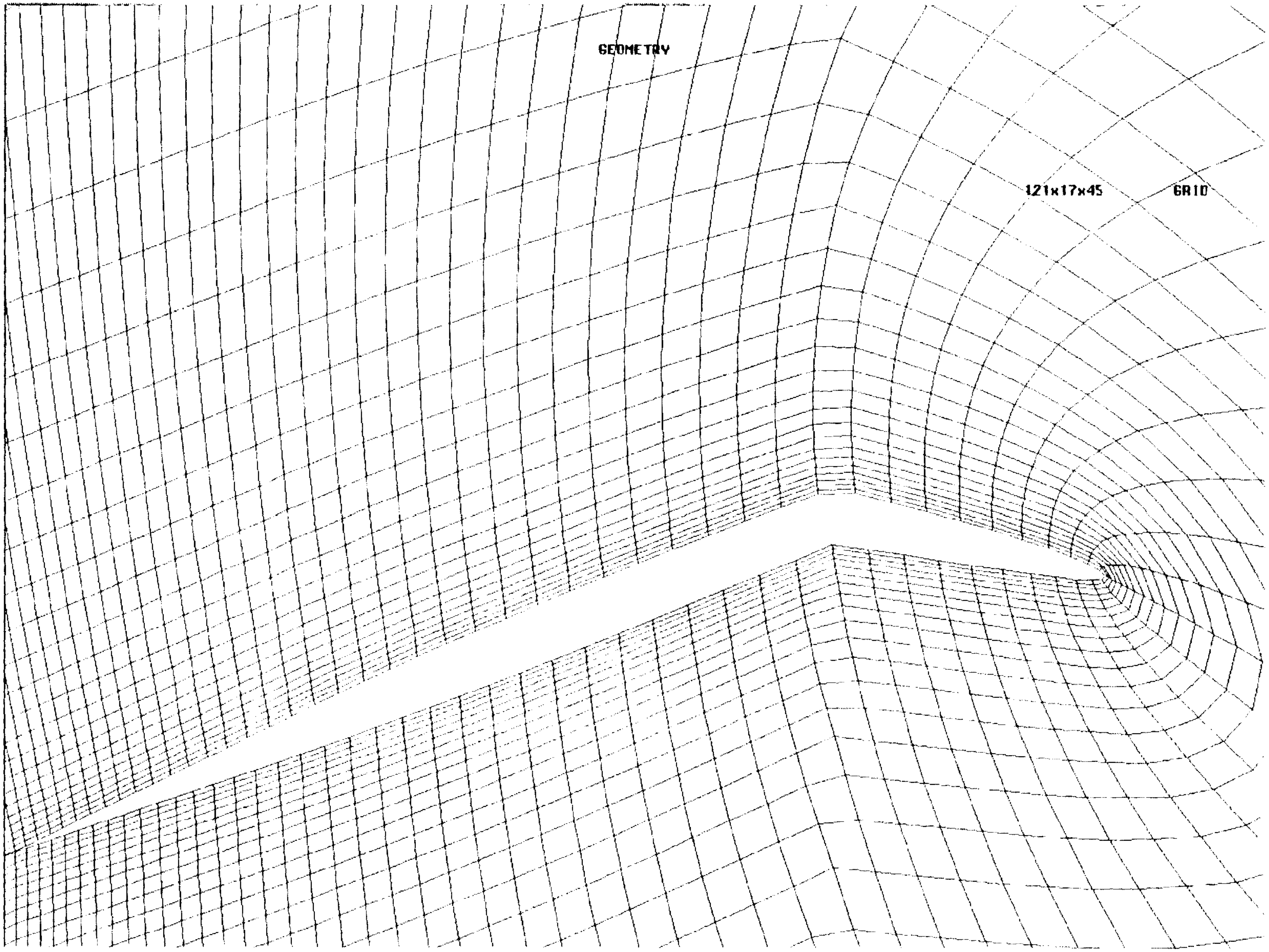
GEOMETRY
121x17x45
GRID

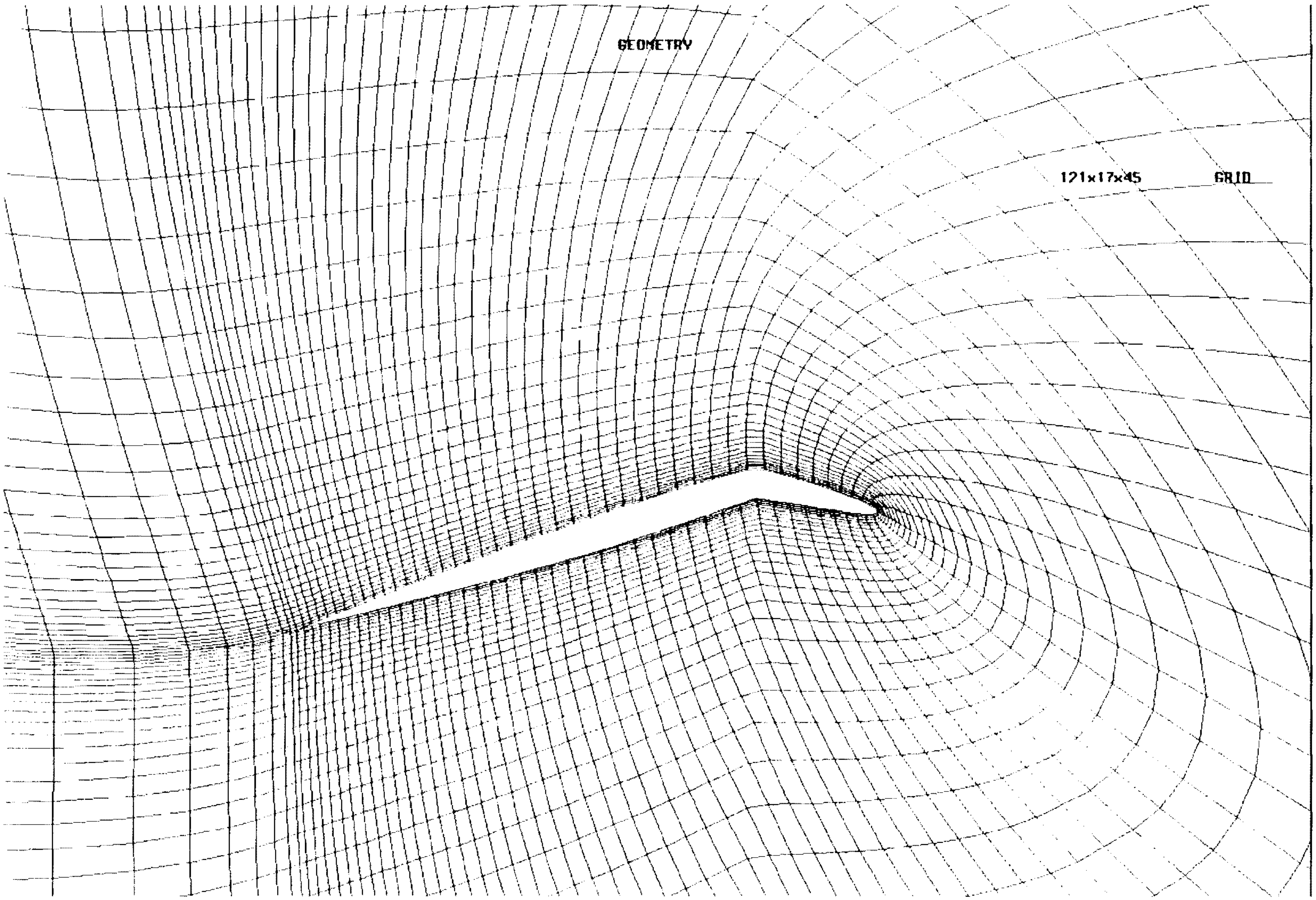

GEOMETRY
121x17x45
GRID

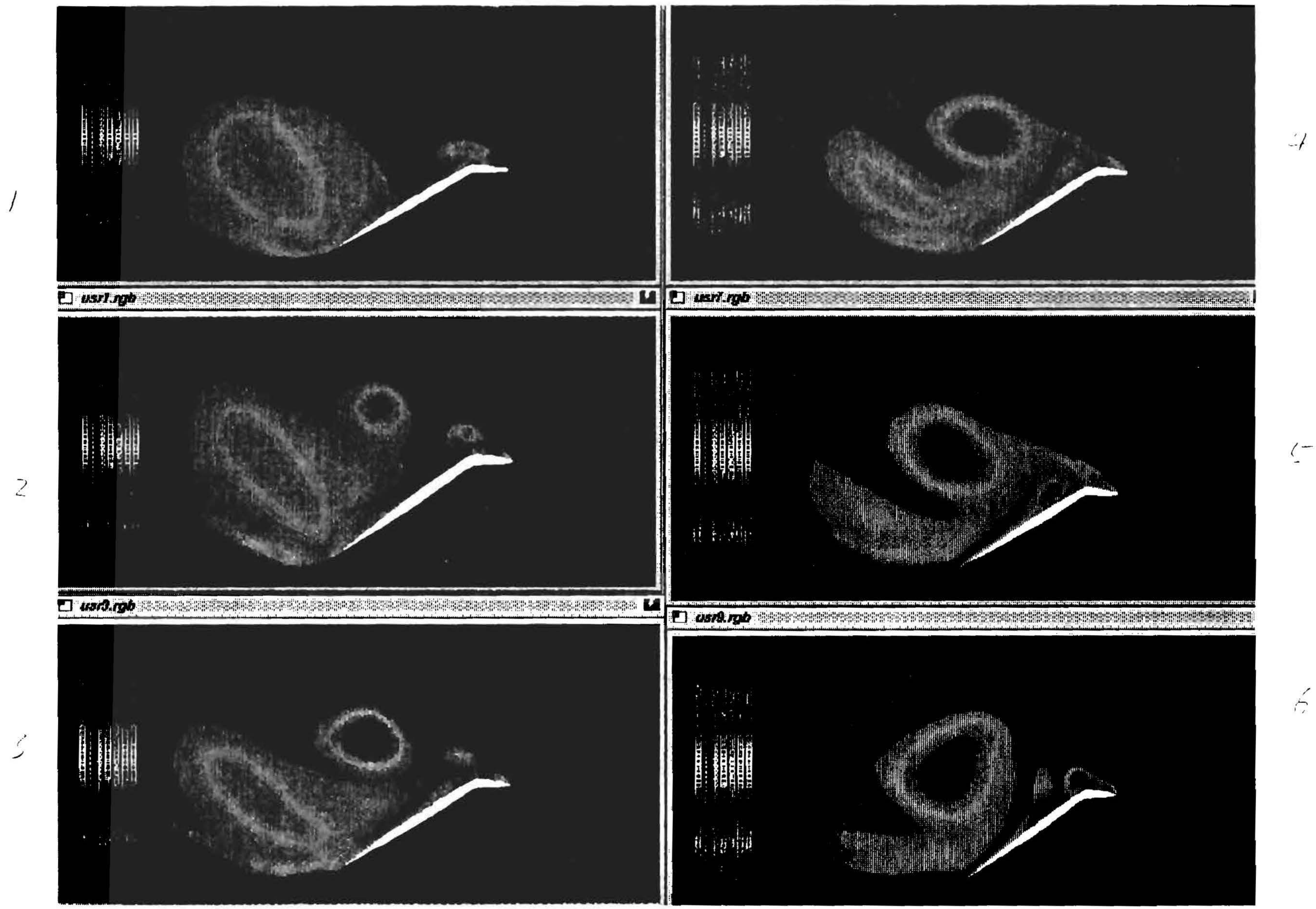

Fig 4. Total Pressure Contours at Selected Time Levels

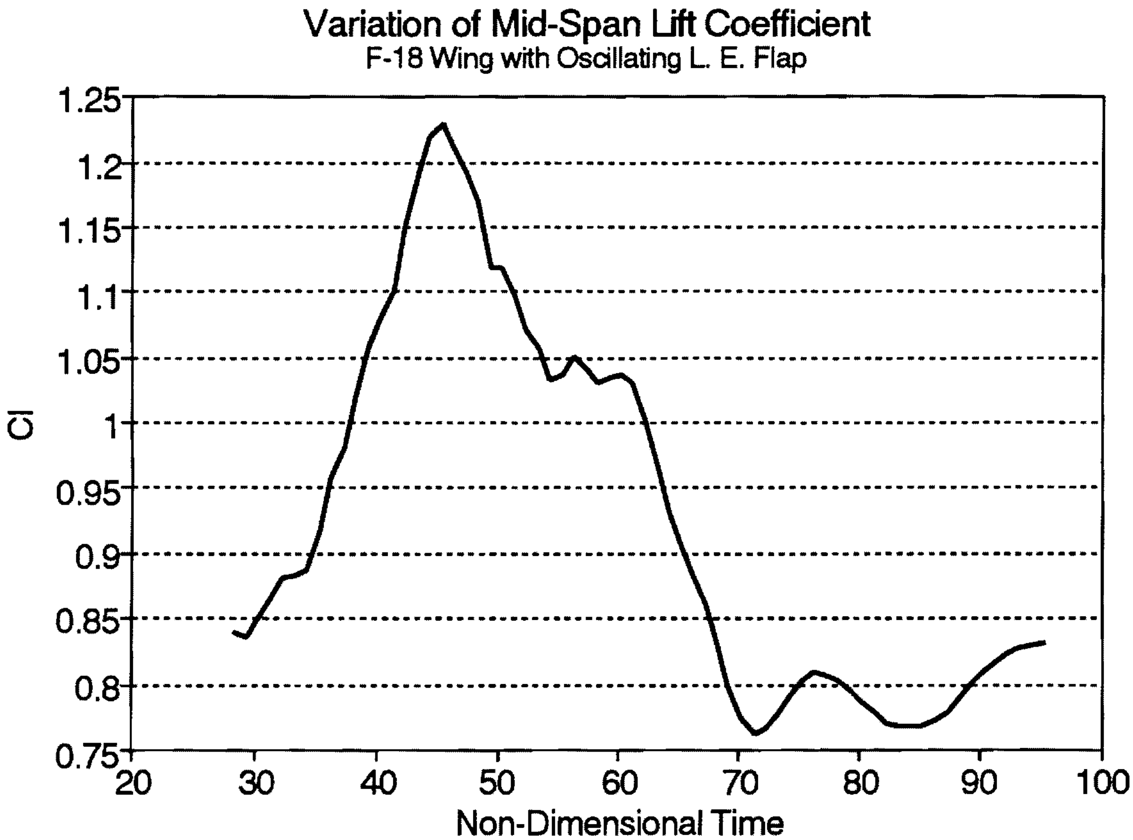

Fig 5 Cl vs time

12

UNSTEADY AERODYNAMIC ANALYSIS OF DUAL-ELEMENT WING CONFIGURATIONS

BI-MONTHLY PROGRESS LETTER
FOR THE PERIOD

May 1 - June 30, 1992.

Submitted to the

NAVAL AIR DEVELOPMENT CENTER
WARMINSTER, PA

Attn: Mr. Marvin M. Walters

Prepared By

L. N. Sankar
Professor
School of Aerospace Engineering
Georgia Institute of Technology, Atlanta, GA 30332

August 1992

School of Aerospace Engineering

Georgia Institute of Technology
Atlanta, Georgia 30332-0150
404•894•3000
Fax: 404•894•2760

August 2, 1992

Mr. Marvin M. Walters
Code 6051
Naval Air Development Center
Warminster, PA 18974

Subject: BI-MONTHLY PROGRESS REPORT FOR THE PROJECT "UNSTEADY AERODYNAMIC ANALYSIS OF DUAL-ELEMENT WING CONFIGURATIONS"

Dear Mr. Walters:

During the reporting period (May 1, 1992 - June 30, 1992), the following tasks were completed:

As stated in our previous progress report, we are assisting Dr. Wei Tseng in your group in the validation of a 3-D Navier-Stokes solver, and application of this solver to the problem of dynamic lift enhancement of an F-18 wing subjected to leading edge control surface motion. We performed an independent set of calculations at Georgia Tech for the above wing, for a case where the leading edge flap pitches up and down three times per reference chord length of travel. Figure 1 shows the pressure contours at a representative spanwise station on the wing, at a typical time level. Three well defined vortical structures are evident on the wing upper surface. This is to be expected, because the leading edge has undergone three cycles of motion, releasing three pockets of organized vortical structures into the flow. The vortical structures appear to lift off the wing upper surface. These features are in good agreement with the water tunnel visualizations done for the same wing, reported in AIAA Paper 92-2625.

Our calculations revealed a new, surprising feature. As these vortical structures reached the wing trailing edge, a new vortex of opposite sign was released from the wing trailing edge. The effect of this trailing edge vortex is to reduce the wing lift, offsetting any gains in the lift achieved by the formation of the leading edge vortices. In other words, the bound circulation over the wing sections can not indefinitely increase. Once every 14 chord lengths or so of travel, the wing will unload itself, through a shedding of a strong trailing edge vortex. Figure 2 shows the time variation of sectional loads at two spanwise stations for sixty chord lengths of travel, and a detailed enlarged view for time periods $36 < t < 38$. It is seen that a low frequency oscillation of the airloads exists, with a wave length equal to 14 chord lengths of travel, superposed over high frequency oscillations in the airloads that occur three times per chord length of travel.

With best wishes,

Sincerely,

LAKSHMI N. SANKAR
Professor

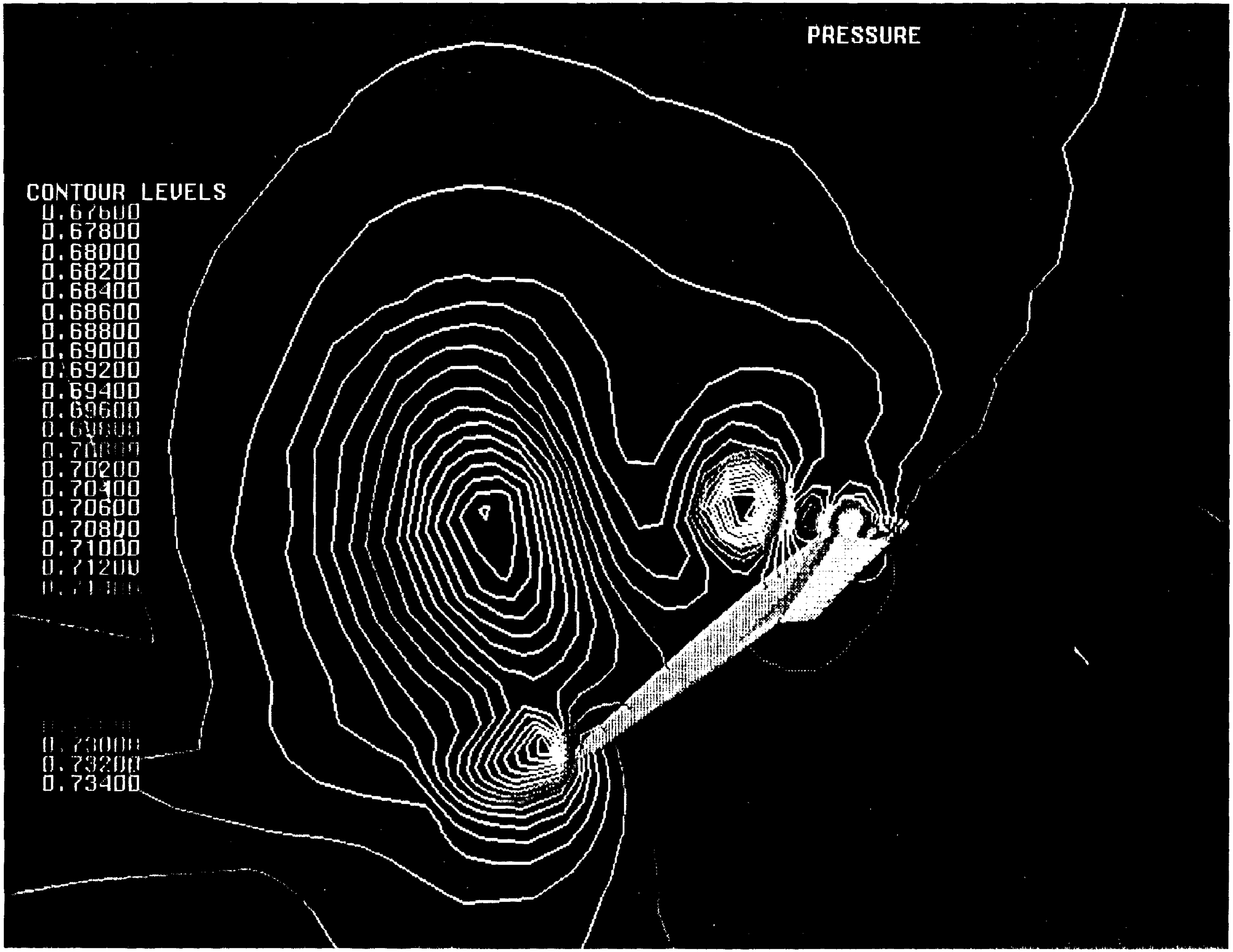
PRESSURE
CONTOUR LEVELS
0.67600
0.67800
0.68000
0.68200
0.68400
0.68600
0.68800
0.69000
0.69200
0.69400
0.69600
0.69800
0.70000
0.70200
0.70400
0.70600
0.70800
0.71000
0.71200
0.73000
0.73200
0.73400

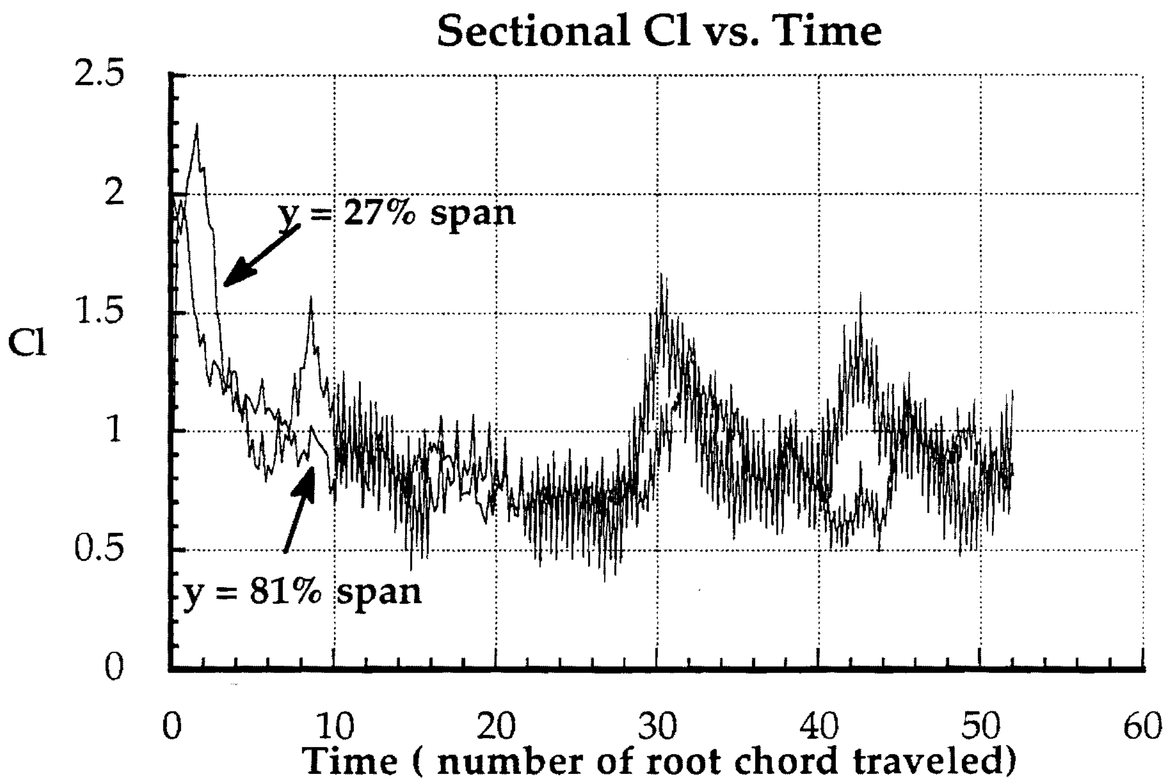

Sectional Cl vs. Time
Cl
2.5
2
1.5
1
0.5
0
y = 27% span
y = 81% span
0
10
20
30
40
50
60
Time (number of root chord traveled)

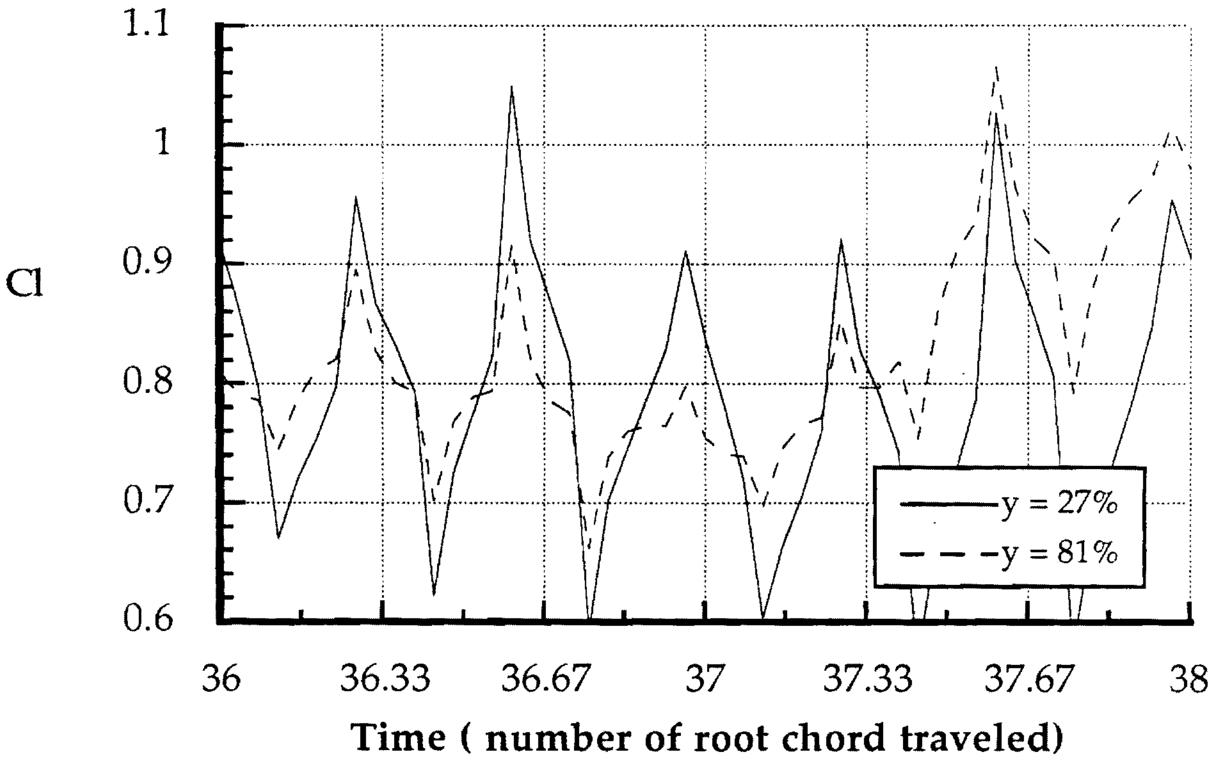

Cl
1.1
1
0.9
0.8
0.7
0.6
y = 27%
y = 81%
36
36.33
36.67
37
37.33
37.67
38
Time (number of root chord traveled)

Georgia Institute of Technology
School of Aerospace Engineering

November 2, 1992

Mr. Marvin M. Walters
Code 6051
Naval Air Development Center
Warminster, PA 18974

Subject: BI-MONTHLY PROGRESS REPORT FOR THE PROJECT "UNSTEADY AERODYNAMIC ANALYSIS OF DUAL-ELEMENT WING CONFIGURATIONS"

Dear Mr. Walters:

During the reporting period (July 1, 1992 - August 31, 1992), the following tasks were completed:

1. Work began on the development of a computer code that can model the performance of a helicopter rotor, operating in the vicinity of a ship deck. A copy of a report co-authored by Mr. Olympio Mello, one of my graduate students, describing work done to date is enclosed. I will be briefing Dr. Tseng on the capabilities of this code during his trip to Georgia Tech next week.

2. In Reno, we will be presenting a paper documenting our 3-D compressible Navier-Stokes solver, and our recent attempts to improve its stability and robustness. Some of the results shown for an F-5 wing with an oscillating trailing edge flap were done under your sponsorship. A copy of this paper is enclosed.

With best wishes,

Sincerely,

LAKSHMI N. SANKAR
Professor

UNSTEADY AERODYNAMIC ANALYSIS OF DUAL-ELEMENT WING CONFIGURATIONS

BI-MONTHLY PROGRESS LETTER FOR THE PERIOD

July 1 - August 30, 1992

Submitted to the

NAVAL AIR WARFARE CENTER
AIRCRAFT DIVISION
WARMINSTER, PA

Attn: Mr. Marvin M. Walters

Prepared By

L. N. Sankar
Professor
School of Aerospace Engineering
Georgia Institute of Technology, Atlanta, GA 30332

November 1992

NUMERICAL SIMULATION OF HELICOPTER LANDING ON SHIP DECKS

Lakshmi N. Sankar, Professor
and
Olympio A. F. Mello, Graduate Student

School of Aerospace Engineering
Georgia Institute of Technology
Atlanta, GA 30332-0150

(404) 894-3014

INTRODUCTION

The problem of helicopter landing on ship decks is analyzed for inclusion in a general helicopter simulation code (GENHEL). In the past, the problem of helicopter/ship interference has received limited theoretical attention, due to its complexity. Healey [1] discusses the several aspects that should be taken into account for a comprehensive analysis of the problem, namely:

1. Sea and ship motion;
2. Atmospheric turbulence;
3. Ship aerodynamics;
4. Helicopter motion itself.

It is beyond the scope of this work to analyze all of these aspects in detail. Additionally, detailed simulation of these effects would result in an excessively time-consuming simulation. The present approach will be to build a relatively simple helicopter model which is capable of including all of the relevant effects, albeit approximately.

General Approach

An in-house developed vortex-lattice code is used for the computation of the blade loading. The computation is performed at a number of azimuth locations. Subsequently, an azimuth-wise averaging is performed to yield the thrust. The effect of the wake is taken into account by introducing the inflow though the rotor tip-path-plane as an input to the vortex-lattice code. A simple non-uniform inflow distribution is introduced, as well as a simple correction for ground effect. This treatment of the wake effects greatly simplifies the computational chore, by avoiding costly free-wake computations, since a rigid-wake model would be unrealistic due to the sea/ship proximity.

The current vortex-lattice approach is also suitable for inclusion of the relevant interaction effects, as follows:

1. The presence of the fuselage may be taken into account by a simple model (e.g., sources/sinks) which generate an additional inflow at the rotor disk;

2. The sea and ship motions — which are considered as inputs — simply affect the ground effect correction in the wake inflow;

3. If necessary, the atmospheric turbulence may be directly input in the vortex lattice code: perturbations normal to the rotor disk would result in an additional inflow term, while perturbations in the rotor disk plane would result in an additional term included in the local velocity.

4. The inflow correction for ground effect does not include the "ground vortex" [2] at this time. However, this effect may be included by a simple model of the ground vortex [3] which would result in an additional inflow term;

5. The ground effect correction may be computed locally, in order to simulate the effect of the front portion of the rotor disk coming into the influence of the ship;

6. The ship aerodynamics may be taken into account by a simple vortex-shedding model from which an additional inflow term would be obtained.

Ground Effect

As an initial step, the ground effect in forward flight is analyzed. The first analysis of ground effect in hover is probably due to Betz [4], who used the method of images. Subsequent analyses for forward flight (e.g. [5], [6]) used the same concept. Cheeseman and Bennett [5] derived an expression for the inflow correction and compared their results with flight test data, reaching a good correlation.

Further experimental investigations provided more insight into the physics of ground effect. In particular, the experiments carried out by Sheridan and Wiesner [2] and Curtiss et al. [3] showed the need for the modeling of the ground vortex generated by the forward portion of the rotor wake impinging on the ground. A simple model for taking this effect into account was suggested in the latter reference.

More recently, Curtiss et al. [7] performed another experimental and analytical analysis of the problem. They used force and moment measurements in order to obtain harmonic inflow coefficients, with limited success.

In the present approach, the simple correction first proposed by Cheeseman and Bennett [5] is used, as it was shown to give reasonable results, is simple and suitable for a local correction as discussed above. Note that a similar ground effect correction is used in the 2GCHAS code [8].

MATHEMATICAL FORMULATION

Local Velocity

As mentioned above, a vortex-lattice code is used for the computation of the blade loading. At a given azimuth location ψ, the blade is analyzed as a lifting surface for which the local forward velocity V varies spanwise as:

$$V = \Omega\, r + V_\infty \sin\psi \qquad \text{or} \qquad V/\Omega R = r/R + \mu \sin\psi \qquad (1)$$

where Ω is the rotor rotational speed, r is the local radius, V_∞ is the free-stream velocity and $\mu = V_\infty/\Omega R$ is the advance ratio.

Local Downwash

As usual in the vortex-lattice method, the vorticity at each panel on the blade is obtained from the solution of a linear system of equations resulting from the application of the non-penetration boundary condition at the center of each panel. The right-hand side of this system of equations is the downwash at the center of the panel:

$$w/\Omega R = -(V/\Omega R)\sin\alpha_{TPP} + \lambda_{TPP} \qquad (2)$$

where α_{TPP} is the is the tip-path-plane (TPP) angle of attack and λ_{TPP} is the inflow ratio through the TPP. Note that:

$$\alpha = \theta_0 + \theta_{1c}\cos\psi + \theta_{1s}\sin\psi + \theta_{tw}(r/R - 0.75) \qquad (3)$$

where θ_0 is the collective pitch considered as the setting at $(r/R = 0.75)$, θ_{1c} and θ_{1s} are the cyclic pitch settings, and θ_{tw} is the blade twist. Also,

$$\lambda_{TPP} = \lambda_i - \mu\tan\alpha_{TPP} \qquad (4)$$

where λ_i is the induced inflow ratio, an input to the method which may be found from a simple trim analysis.

Non-Uniform Inflow Correction

A simple non-uniform inflow correction is introduced as:

$$(\lambda_i)_{local} = \lambda_{i0}\,[1 + (r/R)(k_1\cos\psi + k_2\cos 2\psi)\,] \qquad (5)$$

where λ_{i0} is the inflow ratio for uniform inflow. The above expression is similar to other inflow models [9], with the addition of a term on $\cos 2\psi$. The constants k_1 and k_2 are inputs to the method. Here we use $k_1 = 1.2$ (after [9]) and $k_2 = -0.5$, which appear to give reasonable results.

Ground Effect Correction

A ground effect correction factor, K_{GE}, is introduced as [8]:

$$K_{GE} = 1 - \frac{1}{16\ (z/R)^2} \cos^2 (\chi - \alpha_{TPP}) \tag{6}$$

Note that this correction is applies to the total inflow ratio through the TPP, while the non-uniform inflow correction is applied only to the induced inflow. Therefore, the final expression for the local inflow is:

$$(\lambda_{TPP})_{local} = \{ \lambda_{i0} [1 + (r/R) \tan (\chi/2) \cos \psi] - \mu \tan \alpha_{TPP} \} K_{GE} \tag{7}$$

Local Lift Coefficient

In this type of vortex lattice configuration, the bound circulation Γ at a given spanwise section is simply the vorticity at the last chordwise panel. The blade section lift coefficient is computed by using the Kutta-Joukowski theorem:

$$c_l = \frac{l}{0.5\ \rho\ V^2\ c} = \frac{\rho\ V\ \Gamma}{0.5\ \rho\ V^2\ c} = \frac{2\ (\Gamma/\Omega R c)}{(r/R) + \mu \sin \psi} \tag{8}$$

Rotor Thrust Coefficient

As mentioned before, the computation is performed at a number of azimuth locations. Subsequently, an azimuth-wise averaging is performed to yield the thrust:

$$T = \frac{N_b}{2\pi} \int_0^{2\pi} L_b (\psi)\ d\psi \approx \frac{N_b}{2\pi} \sum L_b (\psi)\ \Delta\psi \tag{9}$$

where L_b (ψ) is the blade lift at the azimuth ψ, obtained by integration along the radius.

NUMERICAL IMPLEMENTATION

In the numerical implementation, priority is given to a cost-effective code. Specifically, the tasks that demand most computational time are the assembly of the influence coefficient matrix for the vortex-lattice method (which is done only once, since the relative position of blade panels do not change) and the solution of the linear system of equations. Since the system has to be solved as many times as the number of azimuth locations used, a LU-factorization of the influence matrix is performed only once and subsequently a corresponding back-substitution is employed [10].

The source code is presented in the Appendix.

RESULTS AND DISCUSSION

The aerodynamic loading on the rotor blade of a Sikorsky S-58 helicopter in forward flight was computed and compared with the flight test data tabulated in Ref. [11]. The flight conditions correspond to flight no. 11 (table no. 14) in that reference. The section loading at r/R 0.75 is presented for a complete rotor revolution in Fig. 1 and at azimuth locations near $\psi = 60^{\circ}$ along the blade span in Fig. 2. It can be seen that the general trends are well predicted. A notable exception is seen in Fig. 2, where a second increase in section loading very near the tip is observed in the flight test results. This is due to blade-vortex interaction, which cannot be modeled by the present method.

A more complete validation of the code is currently in progress, however the results obtained so far indicate that the present method is adequate for the purposes of simulation, since it captures the main features of the flow while still keeping the computational cost low.

REFERENCES

1. Healey, J. Val., "The Prospects for Simulating the Helicopter/Ship Interface," *Naval Engineers Journal*, March 1987, pp. 45-63.

2. Sheridan, P. F., and Wiesner, W., "Aerodynamics of Helicopter Flight Near the Ground," 33rd Annual Forum of the American Helicopter Society, May 1977.

3. Curtiss, H. C., Jr., Sun, M., Putman, W. F., and Hanker, E. J., Jr., "Rotor Aerodynamics in Ground Effect at Low Advance Ratios," 37th Annual Forum of the American Helicopter Society, New Orleans, LA, May 1981. (Also *Journal of the American Helicopter Society*, January 1984).

4. Betz, A., "The Effect of the Ground on Lifting Propellers," NACA TM 836, April 1937.

5. Cheeseman, I. C., and Bennett, W. E., "The Effect of the Ground on a Helicopter Rotor in Forward Flight," ARC R&M No. 3021, September 1955.

6. Heyson, H. H., "Ground Effect for Lifting Rotors in Forward Flight," NASA TN D-234, May 1960.

7. Curtiss, H. C., Jr., Erdman, W., and Sun, M., "Ground Effect Aerodynamics," *Vertica*, Vol. 11, No. 1/2, 1987, pp. 29-42.

8. U.S. Department of the Army — Aeroflightdynamics Directorate, "2GCHAS Theory Manual," (Second Generation Comprehensive Helicopter Analysis System, Version 2.1), Vol. II, Chapter 5 – Airloads and Induced Velocity, Ames Research Center, Moffett Field, CA, July 1992.

9. Bramwell, A. R. S., *Helicopter Dynamics*, Edward Arnold, London, 1976, pp. 125-126.

10. Press, W. H., Flannery, B. P., Teukolsky, S. A. and Vetterling, W. T., *Numerical Recipes — The Art of Scientific Computing (FORTRAN Version)*, Cambridge University Press, 1989.

11. Scheiman, J., "A Tabulation of Helicopter Rotor-Blade Differential Pressures, Stresses and Motions as Measured in Flight," NASA TM X-952, March 1964.

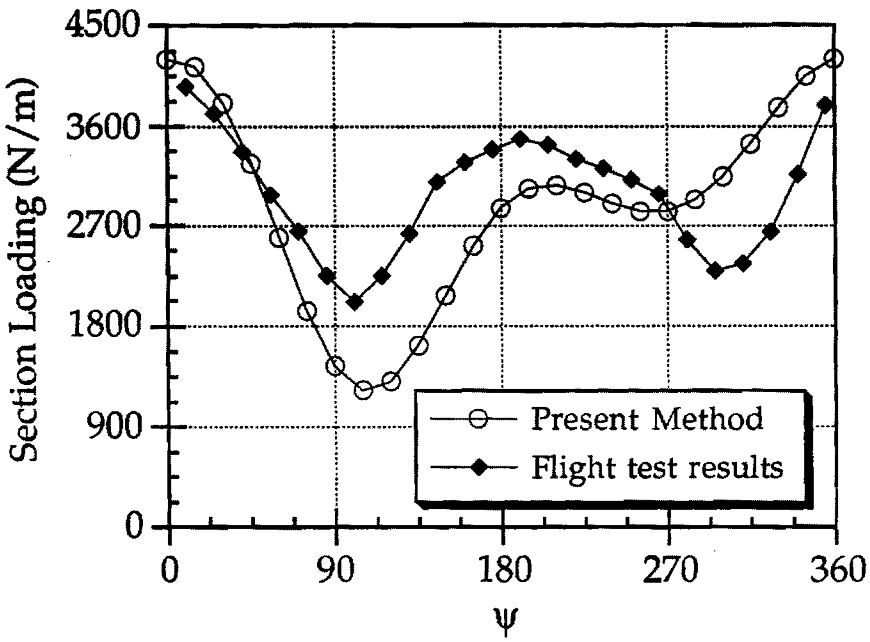

Fig. 1: Blade section aerodynamic loading at r/R = 0.75, flight conditions of Flight no. 11 in Ref. [11].

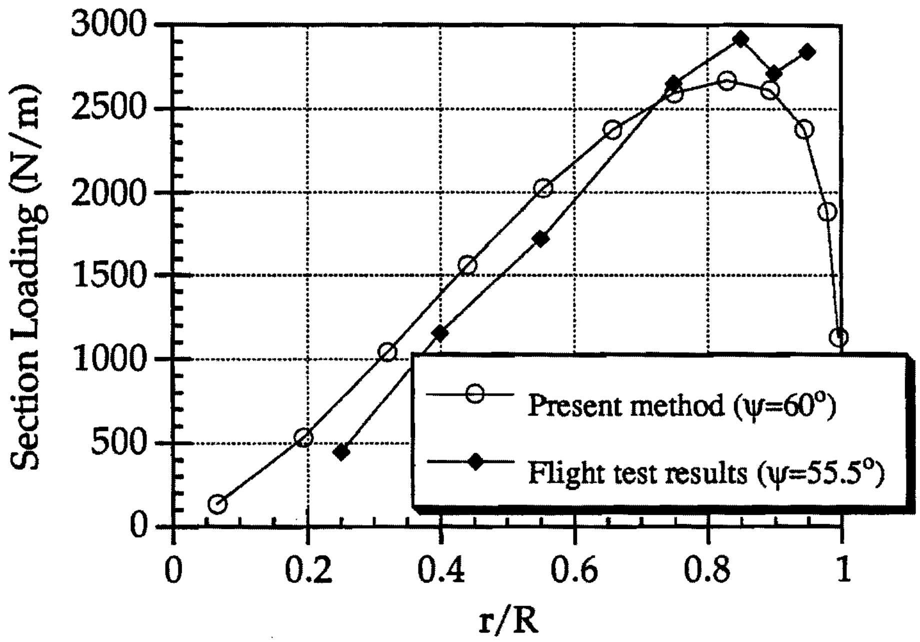

Fig. 2: Blade section aerodynamic loading near $\psi = 60^\circ$, flight conditions of Flight no. 11 in Ref. [11].

APPENDIX: SOURCE CODE

```
c
c Program to compute incompressible inviscid flow past helicopter rotor
c using Vortex-Lattice Method
c The lift distribution along the blade radius at each azimuth
c is computed and printed during the process. Finally, the lift is
c integrated to yield the rotor thrust coefficient
c
      program vorlat
      parameter(imaxp=10,jmaxp=20,nmaxp=imaxp*jmaxp,npsip=75)
      real lami,lamv,lam,kge,klamc,klam2c,laml
      character tab*1
      integer indx(nmaxp)
      common/grid1/x(imaxp+1),y(jmaxp+1)
      common/amat1/a(nmaxp,nmaxp)
      common/vort/gamma(nmaxp)
      common/azim/psi(0:npsip)
      common/par/imax,jmax
      common/rotor/advr,btwt,lami,lamv,lam,kge,klamc,klam2c,colp,cosp,
     &sinp
      common/blade/yrel(jmaxp),laml(jmaxp),vlocal(jmaxp),alfal(jmaxp)
      tab=char(9)
      pi=4.*atan(1.)
      raddeg=180.0/pi
      degrad=1./raddeg
c
c Open input and output files
c
      OPEN(5,FILE='vorlat.dat',STATUS='OLD')
      OPEN(6,FILE='vorlat.out',STATUS='NEW')
c
c Total no. of vortex lattice panels can not exceed nmaxp
c
      read (5,*) imax , jmax
      write(6,*) 'IMAX=',imax,' ; JMAX=',jmax
      nmax=imax*jmax
      if(nmax.gt.nmaxp) then
        write (6,*) 'Total No. of Panels Exceeds ',nmaxp
        stop
      end if
c
c Read rotor data:
c
c Blade aspect ratio ar=R/c
      read (5,*) ar
c No. of blades
      read (5,*) nblades
c Advance Ratio advr = vinf / (Omega * R)
      read (5,*) advr
c Air density (kg/m3)
      read (5,*) rho
c Rotor rotational speed Omega (in RPM)
      read (5,*) omega
```

```
      omega=omega/30.0*pi
c Rotor blade radius (m)
      read (5,*) bldr
c Root cut out as a fraction of R
      read (5,*) root
c Blade twist (in degrees)
      read (5,*) btw
      btwt = (btw * (1.0-root)) * degrad
c
c Read control settings, CT and induced velocity
c
c Tip path plane (TPP) angle of attack alphad (in degrees)
      read (5,*) alphad
      alphad = alphad * degrad
c Thrust coefficient CT
      read (5,*) CT1
c Induced inflow ratio Lambda_i = vi/(Omega*R)
c  (positive for induced velocity downwards)
      read (5,*) lami
      lamv= -advr * tan(alphad)
      lam = lamv + lami
c Collective pitch (in degrees)
      read (5,*) colp
      colp=colp*degrad
c Cosine component of cyclic pitch (in degrees)
      read (5,*) cosp
      cosp=cosp*degrad
c Sine component of cyclic pitch (in degrees)
      read (5,*) sinp
      sinp=sinp*degrad
c Number of azimuth locations used for computation
      read(5,*) npsi
c Height of rotor above the ground, as a fraction of the rotor radius
      read(5,*) hg
c Coefficients of rotor airfoil drag polar
      read(5,*) cd0
      read(5,*) cd1
      read(5,*) cd2
c Non-uniform inflow correction factors
      read(5,*) klamc
      read(5,*) klam2c
      CLOSE(5)
c
c Compute chord and helicopter forward velocity
c
      chord=bldr/ar
      vinf=advr*omega*bldr
      fac0 = 0.5 * rho * (omega*bldr)**2 * chord
      arpi=ar*pi
      ar2pi=arpi*2
c
c Print out input data
c
      write(6,*) 'imax=',imax,' ; jmax=',jmax,' ; npsi=',npsi
      write(6,*) 'AR=',ar,' ; Nb=',nblades,' ; Mu=',ADVR
      write(6,*) 'rho=',rho,' kg/m3 ; omega=',omega,' rad/s'
      write(6,*) 'R=',bldr,' m ; chord=',chord,' m ; Vinf=',vinf,' m/s'
      write(6,*) 'Cutout=',root,' ; Twist=',btw,' deg.'
```

```
      write(6,*) 'AlphaD=',alphad*raddeg,' deg.'
      write(6,*) 'ct=', ct1,' ; Lambda i=',lami,' ; Lambda=',lam
      write(6,*) 'Theta0=',colp*raddeg,' deg; Thetac=',cosp*raddeg,
     &           ' deg'
      write(6,*) 'Thetas=',sinp*raddeg,' deg'
      write(6,*) 'klamc=',klamc,' ; klam2c=',klam2c
c
c Compute the grid
c
      call grid(x,y,imax,jmax,ar)
c
c Compute azimuth angles
c
      delpsi = 2.0*Pi/npsi
      DO 129 i = 0, npsi
        psi(i) = i * delpsi
 129  continue
c
c Compute influence matrix
c
      call amat(x,y,a,imax,jmax)
c
c Perform LU decomposition of influence matrix
c
      call LUDCMP(a,nmax,nmaxp,indx,dlu)
c
c Iteration for CT
c
      do 200 itct=1,10
        write(6,*)
      write(6,*) 'Iteration no. ',itct,' on CT:'
      write(6,*)
c
c Correction of inflow ratio for ground effect
c
      kge=1.0-0.0625*(cos(atan(advr/lami)-alphad)/hg)**2
      lam=lam*kge
      write(6,*) 'z/R=',hg,' ; Kge=',kge,' ; Lambda (corrected)=',lam
c
c Initialize CT, CH and CQ before azimuth-wise integration
c
      ct = 0.0
      ch = 0.0
      cq = 0.0
c
c For each azimuth location...
c
      do 138 k = 0, npsi-1
        write(6,*)
        write(6,*)
        write (6,*) 'psi= ', psi(k) * raddeg,' deg'
        cpsi=cos(psi(k))
        spsi=sin(psi(k))
        write(6,*)
c
c Compute right hand side
c
        call right(imax,jmax,cpsi,spsi)
```

```
c
c Solve for bound vortex distribution
c
        call LUBKSB(a,nmax,nmaxp,indx,gamma)
        write(6,*)
        write(6,*) 'j',tab,'y',tab,'yrel',tab,'vlocal',tab,'alphal',
     &                tab,'lift',tab,'cl'
        write(6,*)
c
c Initialize ctb, chb and cqb before spanwise integration
c
        ctb = 0.0
        chb = 0.0
        cqb = 0.0
c
c At each spanwise location...
c
        do 1 j = 1 , jmax
c
c Circulation around blade section is equal to vorticity at last
c chordwise panel
c
          bvort=gamma(j*imax)
c
c Use Kutta-Joukowski theorem (l = rho * V * Gamma) to compute blade
c section lift coefficient
c
          cl = 2.0 * bvort / vlocal(j)
c
c Write out results at this spanwise location
c
          facl = fac0 * vlocal(j)**2
          write(6,*) j,tab,0.5*(y(j)+y(j+1)),tab,yrel(j),tab,vlocal(j),
     &                tab,alfal(j),tab,cl*facl,tab,cl
c
c Contribution from this section to CT
c
          dyrel = ( y(j+1) - y(j) ) / y(jmax+1)
          ctb = ctb +  bvort * vlocal(j) * dyrel
c
c Contribution to H-force and Torque
c
          phi = atan( laml(j) / (yrel(j) + advr ) )
          alfaef = alfal(j) - phi
          cd = cd0 + cd1*alfaef + cd2*alfaef**2
c          write(6,*) j,alfal(j),phi,alfaef,cd
          dch = (cd*cos(phi) + cl*sin(phi)) * dyrel * vlocal(j)**2
          chb = chb + dch * spsi
          cqb = cqb + dch * yrel(j)
    1   continue
        ctb = ctb / arpi
        chb = chb / ar2pi
        cqb = cqb / ar2pi
        write(6,*)
        write (6,*) 'Contribution from this blade to CT =' , ctb
        write (6,*) 'Contribution from this blade to CH =' , chb
        write (6,*) 'Contribution from this blade to CQ =' , cqb
        ct = ct + ctb * delpsi
```

```
        ch = ch + chb * delpsi
        cq = cq + cqb * delpsi
 138  continue
c
c Compute CT: Average contribution from blade at each azimuth location
c and multiply by number of blades
c
      ct = float(nblades) * ct / 2. / pi
      ch = float(nblades) * ch / 2. / pi
      cq = float(nblades) * cq / 2. / pi
      write(6,*)
      write(6,*)
      write (6,*) 'CT =' , ct
      write(6,*)
      write (6,*) 'CH =' , ch
      write(6,*)
      write (6,*) 'CQ =' , cq
c
c Check if computed CT value matches with input CT; if not,
c recalculate Lambda
c
        errct=Ct/Ct1-1.0
        write(6,*)
        write(6,*) 'Iteration no. ',itct,' ; Error in Ct = ',errct*100.,
     &  ' %'
        write(9,*) 'Iteration no. ',itct,' ; Error in Ct = ',errct*100.,
     &  ' %'
        write(6,*)
        if (abs(errct).lt.1e-3) go to 201
        if (itct.eq.1) then
          plami=lami
          lami=Ct/2./Sqrt(advr**2+lam**2)
        else
          clami=lami+(lami-plami)*(Ct1-Ct)/(Ct-pct)
          plami=lami
          lami=clami
        endif
        pct=ct
  200 continue
  201 continue
      CLOSE(6)
      stop
      end
c
c Subroutine to compute the right-hand-side
c
      subroutine right(imax,jmax,cpsi,spsi)
      parameter(imaxp=10,jmaxp=20,nmaxp=imaxp*jmaxp,npsip=75)
      real lami,lamv,lam,kge,klamc,klam2c,laml
      common/grid1/x(imaxp+1),y(jmaxp+1)
      common/azim/psi(0:npsip)
      common/rotor/advr,btwt,lami,lamv,lam,kge,klamc,klam2c,colp,cosp,
     &sinp
      common/vort/gamma(nmaxp)
      common/blade/yrel(jmaxp),laml(jmaxp),vlocal(jmaxp),alfal(jmaxp)
      raddeg=57.29578
      c2psi=cpsi**2-spsi**2
      alfa = colp + cosp * cpsi + sinp * spsi
```

```
      write (6,*) 'alpha=',alfa*raddeg,' deg'
      l    = 0
c
c Spanwise scan
c
      do 100 j = 1 , jmax
c
c Non-uniform induced inflow correction
c
        laml(j)=lamv+lami*(1.0+yrel(j)*(klamc*cpsi
     &                                   +klam2c*c2psi))
c
c Correction of inflow ratio for ground effect
c
        laml(j)=laml(j)*kge
c
c Local velocity (non-dimensionalized with respect to Omega*R)
c
        vlocal(j)=yrel(j)+advr*spsi
c
c Local blade pitch
c Note: Blade pitch control setting is considered as the pitch
c at 3/4 radius. Therefore, the linear twist is computed with
c respect to this location.
c
        alfal(j)=alfa+btwt*(yrel(j)-0.75)
c
c Right-hand side is sum of contribution due to local pitch and
c contribution due to inflow through rotor disk
c
        rhsj = - sin(alfal(j)) * vlocal(j) + laml(j)
c
c Chordwise scan
c
        do 100 i = 1 , imax
          l = l + 1
          gamma(l) = rhsj
  100 continue
      return
      end
c
c Subroutine to compute the grid for the vortex-lattice method
c
      subroutine grid(imax,jmax,ar)
      parameter(imaxp=10,jmaxp=20,nmaxp=imaxp*jmaxp)
      common/grid1/x(imaxp+1),y(jmaxp+1)
      common/blade/yrel(jmaxp),laml(jmaxp),vlocal(jmaxp),alfal(jmaxp)
      dy = 0.8 * ar / (jmax)
      dth= 2. * atan(1.) / jmax
      pi2 = 2. * atan(1.)
      dx = 1.0/(imax)
      do 10 j = 1 , jmax+1
   10 y(j) =ar * sin((j-1)*dth)
      do 20 i = 1 , imax+1
   20 x(i) = (i-1) * dx - 0.25
c
      do 30 j = 1 , jmax
c
```

```
c Relative spanwise location
c
         yrel(j)=0.5*(y(j)+y(j+1))/y(jmax+1)
   30 continue
      return
      end
c
c subroutine to compute the influence coefficients
c
      subroutine amat(imax,jmax)
      parameter(imaxp=10,jmaxp=20,nmaxp=imaxp*jmaxp)
      common/grid1/x(imaxp+1),y(jmaxp+1)
      common/amat1/a(nmaxp,nmaxp)
      m = 0
      do 1000 k = 1 , jmax
      do 100  l = 1 , imax
      m     = m + 1
c    m is the control point
      xmid = x(l) + 0.5 * (x(l+1)-x(l))
      ymid = 0.5*(y(k)+y(k+1))
      n    = 0
      do 200 j = 1 , jmax
      do 200 i = 1 , imax
      n    = n + 1
c    n is the panel being considered
      xa   = x(i) - xmid
      xb   = x(i) - xmid
      ya   = y(j) - ymid
       yb   = y(j+1) - ymid
       za   = 0.0
       zb   = 0.0
       call vorinf(xa,ya,xb,yb,fact)
       a(m,n) = fact
       xa      = x(i) - xmid
       ya      = y(j+1) - ymid
       xb      = x(i+1) - xmid
c      if(i.eq.imax) xb = 100. - xmid
       yb      = y(j+1) - ymid
       za      = 0.0
       zb      = 0.0
       call vorinf(xa,ya,xb,yb,fact)
       a(m,n) = fact + a(m,n)
       if(i.eq.imax) goto 555
       xa      = x(i+1) - xmid
       xb      = x(i+1) - xmid
       ya      = y(j+1) - ymid
       yb      = y(j) - ymid
       za      = 0.0
       zb      = 0.0
       call vorinf(xa,ya,xb,yb,fact)
       a(m,n) =fact  + a(m,n)
555    xa    = x(i+1) - xmid
c      if(i.eq.imax) xa = 100. - xmid
       ya = y(j) - ymid
       za  = 0.0
       xb  = x(i) - xmid
       yb = y(j) - ymid
       zb = 0.0
```

```
       call vorinf(xa,ya,xb,yb,fact)
       a(m,n) = fact + a(m,n)
  200 continue
  100 continue
 1000 continue
      return
      end
c
      subroutine vorinf(xa,ya,xb,yb,fact)
      term1 = xa * yb - xb * ya
      x0    = xa - xb
      y0    = ya - yb
      sa    = sqrt(xa * xa + ya * ya)
      sb    = sqrt(xb * xb + yb * yb)
      term2 = x0 * (xa/sa - xb/sb) + y0 * (ya/sa-yb/sb)
      fact  = 1./ (16. * atan(1.0)) * term2/term1
      return
      end
c
c Subroutine for LU Decomposition including pivoting
c **Note** The decomposition is done 'in place' so the input matrix is
c destroyed.
c From Press, W. H., et. al., Numerical Recipes - The Art of Scientific
c Computing (FORTRAN Version), Cambridge University Press, 1989,
c pp. 35-36
c
      SUBROUTINE LUDCMP(A,N,NP,INDX,D)
      PARAMETER (NMAX=100,TINY=1.0E-20)
      DIMENSION A(NP,NP),INDX(N),VV(NMAX)
      D=1.
      DO 12 I=1,N
        AAMAX=0.
        DO 11 J=1,N
          IF (ABS(A(I,J)).GT.AAMAX) AAMAX=ABS(A(I,J))
11      CONTINUE
        IF (AAMAX.EQ.0.) PAUSE 'Singular matrix.'
        VV(I)=1./AAMAX
12    CONTINUE
      DO 19 J=1,N
        IF (J.GT.1) THEN
          DO 14 I=1,J-1
            SUM=A(I,J)
            IF (I.GT.1)THEN
              DO 13 K=1,I-1
                SUM=SUM-A(I,K)*A(K,J)
13            CONTINUE
              A(I,J)=SUM
            ENDIF
14        CONTINUE
        ENDIF
        AAMAX=0.
        DO 16 I=J,N
          SUM=A(I,J)
          IF (J.GT.1)THEN
            DO 15 K=1,J-1
              SUM=SUM-A(I,K)*A(K,J)
15          CONTINUE
            A(I,J)=SUM
```

```
          ENDIF
          DUM=VV(I)*ABS(SUM)
          IF (DUM.GE.AAMAX) THEN
            IMAX=I
            AAMAX=DUM
          ENDIF
16      CONTINUE
        IF (J.NE.IMAX)THEN
          DO 17 K=1,N
            DUM=A(IMAX,K)
            A(IMAX,K)=A(J,K)
            A(J,K)=DUM
17        CONTINUE
          D=-D
          VV(IMAX)=VV(J)
        ENDIF
        INDX(J)=IMAX
        IF(J.NE.N)THEN
          IF(A(J,J).EQ.0.)A(J,J)=TINY
          DUM=1./A(J,J)
          DO 18 I=J+1,N
            A(I,J)=A(I,J)*DUM
18        CONTINUE
        ENDIF
19    CONTINUE
      IF(A(N,N).EQ.0.)A(N,N)=TINY
      RETURN
      END
c
c Subroutine for Solving a Linear System of Equations Given the
c (pivoted) LU Decomposition of the matrix of coefficients
c From Press, W. H., et. al., Numerical Recipes - The Art of Scientific
c Computing (FORTRAN Version), Cambridge University Press, 1989,
c pp. 36-37
c
      SUBROUTINE LUBKSB(A,N,NP,INDX,B)
      DIMENSION A(NP,NP),INDX(N),B(N)
      II=0
      DO 12 I=1,N
        LL=INDX(I)
        SUM=B(LL)
        B(LL)=B(I)
        IF (II.NE.0)THEN
          DO 11 J=II,I-1
            SUM=SUM-A(I,J)*B(J)
11        CONTINUE
        ELSE IF (SUM.NE.0.) THEN
          II=I
        ENDIF
        B(I)=SUM
12    CONTINUE
      DO 14 I=N,1,-1
        SUM=B(I)
        IF(I.LT.N)THEN
          DO 13 J=I+1,N
            SUM=SUM-A(I,J)*B(J)
13        CONTINUE
        ENDIF
```

```
      B(I)=SUM/A(I,I)
14    CONTINUE
      RETURN
      END
```

UNSTEADY AERODYNAMIC ANALYSIS OF DUAL-ELEMENT WING CONFIGURATIONS

BI-MONTHLY PROGRESS LETTER FOR THE PERIOD

September 1 - October 31, 1992

Submitted to the

NAVAL AIR WARFARE CENTER
AIRCRAFT DIVISION
WARMINSTER, PA

Attn: Mr. Marvin M. Walters

Prepared By

L. N. Sankar
Professor
School of Aerospace Engineering
Georgia Institute of Technology, Atlanta, GA 30332

December 1992

Georgia Institute of Technology
School of Aerospace Engineering

December 14, 1992

Mr. Marvin M. Walters
Code 6051
Naval Air Development Center
Warminster, PA 18974

Subject: BI-MONTHLY PROGRESS REPORT FOR THE PROJECT "UNSTEADY AERODYNAMIC ANALYSIS OF DUAL-ELEMENT WING CONFIGURATIONS"

Dear Mr. Walters:

During the reporting period (September 1, 1992 - October 30, 1992), the following tasks were completed:

1. Work continued on the development of a computer code that can model the performance of a helicopter rotor, operating in the vicinity of a ship deck. We have acquired the source version of the GENHEL computer code that will form the basis of this study, and have made the code opeartional on one of the Unix workstations within our department. The modlues that compute the inflow into the rotor disk have been identified. These modules are being modified so that they will accept the dynamic inflow from a dynamic inflow theory developed by Prof. David Peters of George Washington University.

   A revised copy of a report co-authored by Mr. Olympio Mello, one of my graduate students, describing work done to date is enclosed. This report supercedes the report enclosed in our previous progress report, and incorporates corrections to some equations found on pages 4 and 5.

2. We continue to work wirh Dr. Tseng on our joint paper to be presented at the 31st AIAA Aerospace Sciences Meeting.

With best wishes,

Sincerely,

LAKSHMI N. SANKAR
Professor

NUMERICAL SIMULATION OF HELICOPTER LANDING ON SHIP DECKS

Lakshmi N. Sankar, Professor
and
Olympio A. F. Mello, Graduate Student

School of Aerospace Engineering
Georgia Institute of Technology
Atlanta, GA 30332-0150

(404) 894-3014

INTRODUCTION

The problem of helicopter landing on ship decks is analyzed for inclusion in a general helicopter simulation code (GENHEL). In the past, the problem of helicopter/ship interference has received limited theoretical attention, due to its complexity. Healey [1] discusses the several aspects that should be taken into account for a comprehensive analysis of the problem, namely:

1. Sea and ship motion;
2. Atmospheric turbulence;
3. Ship aerodynamics;
4. Helicopter motion itself.

It is beyond the scope of this work to analyze all of these aspects in detail. Additionally, detailed simulation of these effects would result in an excessively time-consuming simulation. The present approach will be to build a relatively simple helicopter model which is capable of including all of the relevant effects, albeit approximately.

General Approach

An in-house developed vortex-lattice code is used for the computation of the blade loading. The computation is performed at a number of azimuth locations. Subsequently, an azimuth-wise averaging is performed to yield the thrust. The effect of the wake is taken into account by introducing the inflow though the rotor tip-path-plane as an input to the vortex-lattice code. A simple non-uniform inflow distribution is introduced, as well as a simple correction for ground effect. This treatment of the wake effects greatly simplifies the computational chore, by avoiding costly free-wake computations, since a rigid-wake model would be unrealistic due to the sea/ship proximity.

The current vortex-lattice approach is also suitable for inclusion of the relevant interaction effects, as follows:

1. The presence of the fuselage may be taken into account by a simple model (e.g., sources/sinks) which generate an additional inflow at the rotor disk;

2. The sea and ship motions — which are considered as inputs — simply affect the ground effect correction in the wake inflow;

3. If necessary, the atmospheric turbulence may be directly input in the vortex lattice code: perturbations normal to the rotor disk would result in an additional inflow term, while perturbations in the rotor disk plane would result in an additional term included in the local velocity.

4. The inflow correction for ground effect does not include the "ground vortex" [2] at this time. However, this effect may be included by a simple model of the ground vortex [3] which would result in an additional inflow term;

5. The ground effect correction may be computed locally, in order to simulate the effect of the front portion of the rotor disk coming into the influence of the ship;

6. The ship aerodynamics may be taken into account by a simple vortex-shedding model from which an additional inflow term would be obtained.

Ground Effect

As an initial step, the ground effect in forward flight is analyzed. The first analysis of ground effect in hover is probably due to Betz [4], who used the method of images. Subsequent analyses for forward flight (e.g. [5], [6]) used the same concept. Cheeseman and Bennett [5] derived an expression for the inflow correction and compared their results with flight test data, reaching a good correlation.

Further experimental investigations provided more insight into the physics of ground effect. In particular, the experiments carried out by Sheridan and Wiesner [2] and Curtiss et al. [3] showed the need for the modeling of the ground vortex generated by the forward portion of the rotor wake impinging on the ground. A simple model for taking this effect into account was suggested in the latter reference.

More recently, Curtiss et al. [7] performed another experimental and analytical analysis of the problem. They used force and moment measurements in order to obtain harmonic inflow coefficients, with limited success.

In the present approach, the simple correction first proposed by Cheeseman and Bennett [5] is used, as it was shown to give reasonable results, is simple and suitable for a local correction as discussed above. Note that a similar ground effect correction is used in the 2GCHAS code [8].

MATHEMATICAL FORMULATION

Local Velocity

As mentioned above, a vortex-lattice code is used for the computation of the blade loading. At a given azimuth location ψ, the blade is analyzed as a lifting surface for which the local forward velocity V varies spanwise as:

$$V = \Omega r + V_\infty \sin\psi \qquad \text{or} \qquad V/\Omega R = r/R + \mu \sin\psi \qquad (1)$$

where Ω is the rotor rotational speed, r is the local radius, V_∞ is the free-stream velocity and $\mu = V_\infty/\Omega R$ is the advance ratio.

Local Downwash

As usual in the vortex-lattice method, the vorticity at each panel on the blade is obtained from the solution of a linear system of equations resulting from the application of the non-penetration boundary condition at the center of each panel. The right-hand side of this system of equations is the downwash at the center of the panel:

$$w/\Omega R = - (V/\Omega R) \sin \alpha_{local} + \lambda_{TPP} \qquad (2)$$

where α_{local} is the local geometric angle of attack and λ_{TPP} is the inflow ratio through the TPP. Note that:

$$\alpha_{local} = \theta_0 + \theta_{1c} \cos \psi + \theta_{1s} \sin \psi + \theta_{tw} (r/R - 0.75) \qquad (3)$$

where θ_0 is the collective pitch considered as the setting at ($r/R = 0.75$), θ_{1c} and θ_{1s} are the cyclic pitch settings, and θ_{tw} is the blade twist. Also,

$$\lambda_{TPP} = \lambda_i - \mu \tan \alpha_{TPP} \qquad (4)$$

where λ_i is the induced inflow ratio, an input to the method which may be found from a simple trim analysis, and α_{TPP} is the is the tip-path-plane (TPP) angle of attack.

Non-Uniform Inflow Correction

A simple non-uniform inflow correction is introduced as:

$$(\lambda_i)_{local} = \lambda_{i0} [1 + (r/R) (k_1 \cos \psi + k_2 \cos 2\psi)] \qquad (5)$$

where λ_{i0} is the inflow ratio for uniform inflow. The above expression is similar to other inflow models [9], with the addition of a term on $\cos 2\psi$. The constants k_1 and k_2 are inputs to the method. Here we use $k_1 = 1.2$ (after [9]) and $k_2 = -0.5$, which appear to give reasonable results.

Ground Effect Correction

A ground effect correction factor, K_{GE}, is introduced as [8]:

$$K_{GE} = 1 - \frac{1}{16\,(z/R)^2}\cos^2\left(\tan^{-1}(\mu/\lambda_{i0}) - \alpha_{TPP}\right) \tag{6}$$

Note that this correction is applies to the total inflow ratio through the TPP, while the non-uniform inflow correction is applied only to the induced inflow. Therefore, the final expression for the local inflow is:

$$(\lambda_{TPP})_{local} = [\,(\lambda_i)_{local} - \mu \tan \alpha_{TPP}\,]\,K_{GE} \tag{7}$$

with $(\lambda_i)_{local}$ given by (5).

Local Lift Coefficient

In this type of vortex lattice configuration, the bound circulation Γ at a given spanwise section is simply the vorticity at the last chordwise panel. The blade section lift coefficient is computed by using the Kutta-Joukowski theorem:

$$c_l = \frac{l}{0.5\,\rho\,V^2\,c} = \frac{\rho\,V\,\Gamma}{0.5\,\rho\,V^2\,c} = \frac{2\,(\Gamma/\Omega Rc)}{(r/R) + \mu \sin\psi} \tag{8}$$

Rotor Thrust Coefficient

As mentioned before, the computation is performed at a number of azimuth locations. Subsequently, an azimuth-wise averaging is performed to yield the thrust:

$$T = \frac{N_b}{2\pi} \int_0^{2\pi} L_b(\psi)\, d\psi \approx \frac{N_b}{2\pi} \sum L_b(\psi)\, \Delta\psi \qquad (9)$$

where $L_b(\psi)$ is the blade lift at the azimuth ψ, obtained by integration along the radius.

NUMERICAL IMPLEMENTATION

In the numerical implementation, priority is given to a cost-effective code. Specifically, the tasks that demand most computational time are the assembly of the influence coefficient matrix for the vortex-lattice method (which is done only once, since the relative position of blade panels do not change) and the solution of the linear system of equations. Since the system has to be solved as many times as the number of azimuth locations used, a LU-factorization of the influence matrix is performed only once and subsequently a corresponding back-substitution is employed [10].

The source code is presented in the Appendix.

RESULTS AND DISCUSSION

The aerodynamic loading on the rotor blade of a Sikorsky S-58 helicopter in forward flight was computed and compared with the flight test data tabulated in Ref. [11]. The flight conditions correspond to flight no. 11 (table no. 14) in that reference. The section loading at r/R 0.75 is presented for a complete rotor revolution in Fig. 1 and at azimuth locations near $\psi = 60^\circ$ along the blade span in Fig. 2. It can be seen that the general trends are well predicted. A notable exception is seen in Fig. 2, where a second increase in section loading very near the tip is observed in the flight test results. This is due to blade-vortex interaction, which cannot be modeled by the present method.

A more complete validation of the code is currently in progress, however the results obtained so far indicate that the present method is adequate for the purposes of simulation, since it captures the main features of the flow while still keeping the computational cost low.

REFERENCES

1. Healey, J. Val., "The Prospects for Simulating the Helicopter/Ship Interface," *Naval Engineers Journal*, March 1987, pp. 45-63.

2. Sheridan, P. F., and Wiesner, W., "Aerodynamics of Helicopter Flight Near the Ground," 33rd Annual Forum of the American Helicopter Society, May 1977.

3. Curtiss, H. C., Jr., Sun, M., Putman, W. F., and Hanker, E. J., Jr., "Rotor Aerodynamics in Ground Effect at Low Advance Ratios," 37th Annual Forum of the American Helicopter Society, New Orleans, LA, May 1981. (Also *Journal of the American Helicopter Society*, January 1984).

4. Betz, A., "The Effect of the Ground on Lifting Propellers," NACA TM 836, April 1937.

5. Cheeseman, I. C., and Bennett, W. E., "The Effect of the Ground on a Helicopter Rotor in Forward Flight," ARC R&M No. 3021, September 1955.

6. Heyson, H. H., "Ground Effect for Lifting Rotors in Forward Flight," NASA TN D-234, May 1960.

7. Curtiss, H. C., Jr., Erdman, W., and Sun, M., "Ground Effect Aerodynamics," *Vertica*, Vol. 11, No. 1/2, 1987, pp. 29-42.

8. U.S. Department of the Army — Aeroflightdynamics Directorate, "2GCHAS Theory Manual," (Second Generation Comprehensive

Helicopter Analysis System, Version 2.1), Vol. II, Chapter 5 – Airloads and Induced Velocity, Ames Research Center, Moffett Field, CA, July 1992.

9. Bramwell, A. R. S., *Helicopter Dynamics*, Edward Arnold, London, 1976, pp. 125-126.

10. Press, W. H., Flannery, B. P., Teukolsky, S. A. and Vetterling, W. T., *Numerical Recipes — The Art of Scientific Computing (FORTRAN Version)*, Cambridge University Press, 1989.

11. Scheiman, J., "A Tabulation of Helicopter Rotor-Blade Differential Pressures, Stresses and Motions as Measured in Flight," NASA TM X-952, March 1964.

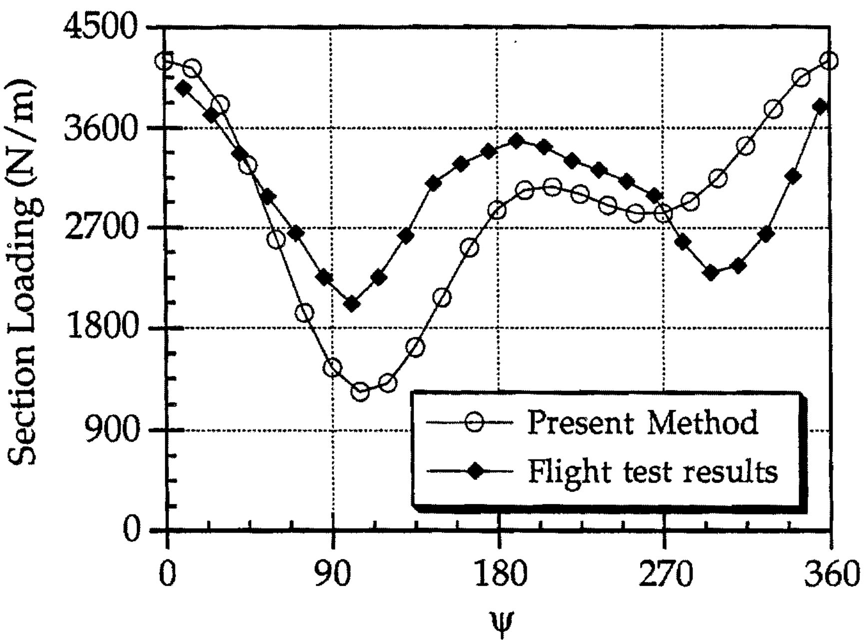

Fig. 1: Blade section aerodynamic loading at r/R = 0.75, flight conditions of Flight no. 11 in Ref. [11].

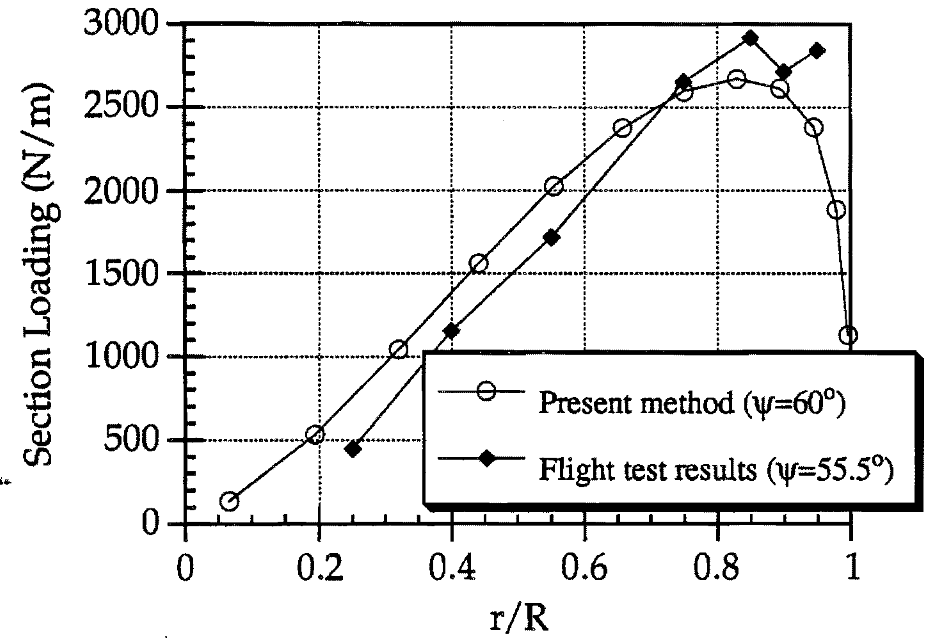

Fig. 2: Blade section aerodynamic loading near $\psi = 60^\circ$, flight conditions of Flight no. 11 in Ref. [11].

APPENDIX: SOURCE CODE

```
c
c Program to compute incompressible inviscid flow past helicopter rotor
c using Vortex-Lattice Method
c The lift distribution along the blade radius at each azimuth
c is computed and printed during the process. Finally, the lift is
c integrated to yield the rotor thrust coefficient
c
      program vorlat
      parameter(imaxp=10,jmaxp=20,nmaxp=imaxp*jmaxp,npsip=75)
      real lami,lamv,lam,kge,klamc,klam2c,laml
      character tab*1
      integer indx(nmaxp)
      common/grid1/x(imaxp+1),y(jmaxp+1)
      common/amat1/a(nmaxp,nmaxp)
      common/vort/gamma(nmaxp)
      common/azim/psi(0:npsip)
      common/par/imax,jmax
      common/rotor/advr,btwt,lami,lamv,lam,kge,klamc,klam2c,colp,cosp,
     &sinp
      common/blade/yrel(jmaxp),laml(jmaxp),vlocal(jmaxp),alfal(jmaxp)
      tab=char(9)
      pi=4.*atan(1.)
      raddeg=180.0/pi
      degrad=1./raddeg
c
c Open input and output files
c
      OPEN(5,FILE='vorlat.dat',STATUS='OLD')
      OPEN(6,FILE='vorlat.out',STATUS='NEW')
c
c Total no. of vortex lattice panels can not exceed nmaxp
c
      read (5,*) imax , jmax
      write(6,*) 'IMAX=',imax,' ; JMAX=',jmax
      nmax=imax*jmax
      if(nmax.gt.nmaxp) then
        write (6,*) 'Total No. of Panels Exceeds ',nmaxp
        stop
      end if
c
c Read rotor data:
c
c Blade aspect ratio ar=R/c
      read (5,*) ar
c No. of blades
      read (5,*) nblades
c Advance Ratio advr = vinf / (Omega * R)
      read (5,*) advr
c Air density (kg/m3)
      read (5,*) rho
c Rotor rotational speed Omega (in RPM)
      read (5,*) omega
```

```
      omega=omega/30.0*pi
c Rotor blade radius (m)
      read (5,*) bldr
c Root cut out as a fraction of R
      read (5,*) root
c Blade twist (in degrees)
      read (5,*) btw
      btwt = (btw * (1.0-root)) * degrad
c
c Read control settings, CT and induced velocity
c
c Tip path plane (TPP) angle of attack alphad (in degrees)
      read (5,*) alphad
      alphad = alphad * degrad
c Thrust coefficient CT
      read (5,*) CT1
c Induced inflow ratio Lambda_i = vi/(Omega*R)
c  (positive for induced velocity downwards)
      read (5,*) lami
      lamv= -advr * tan(alphad)
      lam = lamv + lami
c Collective pitch (in degrees)
      read (5,*) colp
      colp=colp*degrad
c Cosine component of cyclic pitch (in degrees)
      read (5,*) cosp
      cosp=cosp*degrad
c Sine component of cyclic pitch (in degrees)
      read (5,*) sinp
      sinp=sinp*degrad
c Number of azimuth locations used for computation
      read(5,*) npsi
c Height of rotor above the ground, as a fraction of the rotor radius
      read(5,*) hg
c Coefficients of rotor airfoil drag polar
      read(5,*) cd0
      read(5,*) cd1
      read(5,*) cd2
c Non-uniform inflow correction factors
      read(5,*) klamc
      read(5,*) klam2c
      CLOSE(5)
c
c Compute chord and helicopter forward velocity
c
      chord=bldr/ar
      vinf=advr*omega*bldr
      fac0 = 0.5 * rho * (omega*bldr)**2 * chord
      arpi=ar*pi
      ar2pi=arpi*2
c
c Print out input data
c
      write(6,*) 'imax=',imax,' ; jmax=',jmax,' ; npsi=',npsi
      write(6,*) 'AR=',ar,' ; Nb=',nblades,' ; Mu=',ADVR
      write(6,*) 'rho=',rho,' kg/m3 ; omega=',omega,' rad/s'
      write(6,*) 'R=',bldr,' m ; chord=',chord,' m ; Vinf=',vinf,' m/s'
      write(6,*) 'Cutout=',root,' ; Twist=',btw,' deg.'
```

```
      write(6,*) 'AlphaD=',alphad*raddeg,' deg.'
      write(6,*) 'ct=', ct1,' ; Lambda i=',lami,' ; Lambda=',lam
      write(6,*) 'Theta0=',colp*raddeg,' deg; Thetac=',cosp*raddeg,
     &           ' deg'
      write(6,*) 'Thetas=',sinp*raddeg,' deg'
      write(6,*) 'klamc=',klamc,' ; klam2c=',klam2c
c
c Compute the grid
c
      call grid(x,y,imax,jmax,ar)
c
c Compute azimuth angles
c
      delpsi = 2.0*Pi/npsi
      DO 129 i = 0, npsi
        psi(i) = i * delpsi
 129  continue
c
c Compute influence matrix
c
      call amat(x,y,a,imax,jmax)
c
c Perform LU decomposition of influence matrix
c
      call LUDCMP(a,nmax,nmaxp,indx,dlu)
c
c Iteration for CT
c
      do 200 itct=1,10
        write(6,*)
      write(6,*) 'Iteration no. ',itct,' on CT:'
      write(6,*)
c
c Correction of inflow ratio for ground effect
c
      kge=1.0-0.0625*(cos(atan(advr/lami)-alphad)/hg)**2
      lam=lam*kge
      write(6,*) 'z/R=',hg,' ; Kge=',kge,' ; Lambda (corrected)=',lam
c
c Initialize CT, CH and CQ before azimuth-wise integration
c
      ct = 0.0
      ch = 0.0
      cq = 0.0
c
c For each azimuth location...
c
      do 138 k = 0, npsi-1
        write(6,*)
        write(6,*)
        write (6,*) 'psi= ', psi(k) * raddeg,' deg'
        cpsi=cos(psi(k))
        spsi=sin(psi(k))
        write(6,*)
c
c Compute right hand side
c
        call right(imax,jmax,cpsi,spsi)
```

```
c
c Solve for bound vortex distribution
c
       call LUBKSB(a,nmax,nmaxp,indx,gamma)
       write(6,*)
       write(6,*) 'j',tab,'y',tab,'yrel',tab,'vlocal',tab,'alphal',
     &            tab,'lift',tab,'cl'
       write(6,*)
c
c Initialize ctb, chb and cqb before spanwise integration
c
       ctb = 0.0
       chb = 0.0
       cqb = 0.0
c
c At each spanwise location...
c
       do 1 j = 1 , jmax
c
c Circulation around blade section is equal to vorticity at last
c chordwise panel
c
         bvort=gamma(j*imax)
c
c Use Kutta-Joukowski theorem (l = rho * V * Gamma) to compute blade
c section lift coefficient
c
         cl = 2.0 * bvort / vlocal(j)
c
c Write out results at this spanwise location
c
         fac1 = fac0 * vlocal(j)**2
         write(6,*) j,tab,0.5*(y(j)+y(j+1)),tab,yrel(j),tab,vlocal(j),
     &              tab,alfal(j),tab,cl*fac1,tab,cl
c
c Contribution from this section to CT
c
         dyrel = ( y(j+1) - y(j) ) / y(jmax+1)
         ctb = ctb +  bvort * vlocal(j) * dyrel
c
c Contribution to H-force and Torque
c
         phi = atan( laml(j) / (yrel(j) + advr ) )
         alfaef = alfal(j) - phi
         cd = cd0 + cd1*alfaef + cd2*alfaef**2
c         write(6,*) j,alfal(j),phi,alfaef,cd
         dch = (cd*cos(phi) + cl*sin(phi)) * dyrel * vlocal(j)**2
         chb = chb + dch * spsi
         cqb = cqb + dch * yrel(j)
    1  continue
       ctb = ctb / arpi
       chb = chb / ar2pi
       cqb = cqb / ar2pi
       write(6,*)
       write (6,*) 'Contribution from this blade to CT =' , ctb
       write (6,*) 'Contribution from this blade to CH =' , chb
       write (6,*) 'Contribution from this blade to CQ =' , cqb
       ct = ct + ctb * delpsi
```

```
        ch = ch + chb * delpsi
        cq = cq + cqb * delpsi
 138  continue
c
c Compute CT: Average contribution from blade at each azimuth location
c and multiply by number of blades
c
      ct = float(nblades) * ct / 2. / pi
      ch = float(nblades) * ch / 2. / pi
      cq = float(nblades) * cq / 2. / pi
      write(6,*)
      write(6,*)
      write (6,*) 'CT =' , ct
      write(6,*)
      write (6,*) 'CH =' , ch
      write(6,*)
      write (6,*) 'CQ =' , cq
c
c Check if computed CT value matches with input CT; if not,
c recalculate Lambda
c
        errct=Ct/Ct1-1.0
        write(6,*)
        write(6,*) 'Iteration no. ',itct,' ; Error in Ct = ',errct*100.,
     &  ' %'
        write(9,*) 'Iteration no. ',itct,' ; Error in Ct = ',errct*100.,
     &  ' %'
        write(6,*)
        if (abs(errct).lt.1e-3) go to 201
        if (itct.eq.1) then
          plami=lami
          lami=Ct/2./Sqrt(advr**2+lam**2)
        else
          clami=lami+(lami-plami)*(Ct1-Ct)/(Ct-pct)
          plami=lami
          lami=clami
        endif
        pct=ct
  200 continue
  201 continue
      CLOSE(6)
      stop
      end
c
c Subroutine to compute the right-hand-side
c
      subroutine right(imax,jmax,cpsi,spsi)
      parameter(imaxp=10,jmaxp=20,nmaxp=imaxp*jmaxp,npsip=75)
      real lami,lamv,lam,kge,klamc,klam2c,laml
      common/grid1/x(imaxp+1),y(jmaxp+1)
      common/azim/psi(0:npsip)
      common/rotor/advr,btwt,lami,lamv,lam,kge,klamc,klam2c,colp,cosp,
     &sinp
      common/vort/gamma(nmaxp)
      common/blade/yrel(jmaxp),laml(jmaxp),vlocal(jmaxp),alfal(jmaxp)
      raddeg=57.29578
      c2psi=cpsi**2-spsi**2
      alfa = colp + cosp * cpsi + sinp * spsi
```

```
      write (6,*) 'alpha=',alfa*raddeg,' deg'
      l    = 0
c
c Spanwise scan
c
      do 100 j = 1 , jmax
c
c Non-uniform induced inflow correction
c
        laml(j)=lamv+lami*(1.0+yrel(j)*(klamc*cpsi
     &                                  +klam2c*c2psi))
c
c Correction of inflow ratio for ground effect
c
        laml(j)=laml(j)*kge
c
c Local velocity (non-dimensionalized with respect to Omega*R)
c
        vlocal(j)=yrel(j)+advr*spsi
c
c Local blade pitch
c Note: Blade pitch control setting is considered as the pitch
c at 3/4 radius. Therefore, the linear twist is computed with
c respect to this location.
c
        alfal(j)=alfa+btwt*(yrel(j)-0.75)
c
c Right-hand side is sum of contribution due to local pitch and
c contribution due to inflow through rotor disk
c
        rhsj = - sin(alfal(j)) * vlocal(j) + laml(j)
c
c Chordwise scan
c
        do 100 i = 1 , imax
          l = l + 1
          gamma(l) = rhsj
  100 continue
      return
      end
c
c Subroutine to compute the grid for the vortex-lattice method
c
      subroutine grid(imax,jmax,ar)
      parameter(imaxp=10,jmaxp=20,nmaxp=imaxp*jmaxp)
      common/grid1/x(imaxp+1),y(jmaxp+1)
      common/blade/yrel(jmaxp),laml(jmaxp),vlocal(jmaxp),alfal(jmaxp)
      dy = 0.8 * ar / (jmax)
      dth= 2. * atan(1.) / jmax
      pi2 = 2. * atan(1.)
      dx = 1.0/(imax)
      do 10 j = 1 , jmax+1
   10 y(j) =ar * sin((j-1)*dth)
      do 20 i = 1 , imax+1
   20 x(i) = (i-1) * dx - 0.25
c
      do 30 j = 1 , jmax
c
```

```
c Relative spanwise location
c
        yrel(j)=0.5*(y(j)+y(j+1))/y(jmax+1)
   30 continue
      return
      end
c
c subroutine to compute the influence coefficients
c
      subroutine amat(imax,jmax)
      parameter(imaxp=10,jmaxp=20,nmaxp=imaxp*jmaxp)
      common/grid1/x(imaxp+1),y(jmaxp+1)
      common/amat1/a(nmaxp,nmaxp)
      m = 0
      do 1000 k = 1 , jmax
      do 100  l = 1 , imax
      m      = m + 1
c    m is the control point
      xmid = x(l) + 0.5 * (x(l+1)-x(l))
      ymid = 0.5*(y(k)+y(k+1))
      n     = 0
      do 200 j = 1 , jmax
      do 200 i = 1 , imax
      n     = n + 1
c     n is the panel being considered
      xa    = x(i) - xmid
      xb    = x(i) - xmid
      ya    = y(j) - ymid
       yb    = y(j+1) - ymid
       za    = 0.0
       zb    = 0.0
       call vorinf(xa,ya,xb,yb,fact)
       a(m,n) = fact
       xa      = x(i) - xmid
       ya      = y(j+1) - ymid
       xb      = x(i+1) - xmid
c      if(i.eq.imax) xb = 100. - xmid
       yb      = y(j+1) - ymid
       za      = 0.0
       zb      = 0.0
       call vorinf(xa,ya,xb,yb,fact)
       a(m,n) = fact + a(m,n)
       if(i.eq.imax) goto 555
       xa      = x(i+1) - xmid
       xb      = x(i+1) - xmid
       ya      = y(j+1) - ymid
       yb      = y(j) - ymid
       za      = 0.0
       zb      = 0.0
       call vorinf(xa,ya,xb,yb,fact)
       a(m,n) =fact   + a(m,n)
 555   xa    = x(i+1) - xmid
c      if(i.eq.imax) xa = 100. - xmid
       ya = y(j) - ymid
       za  = 0.0
       xb  = x(i) - xmid
       yb = y(j) - ymid
       zb = 0.0
```

```
       call vorinf(xa,ya,xb,yb,fact)
       a(m,n) = fact + a(m,n)
  200 continue
  100 continue
 1000 continue
      return
      end
c
      subroutine vorinf(xa,ya,xb,yb,fact)
      term1 = xa * yb - xb * ya
      x0    = xa - xb
      y0    = ya - yb
      sa    = sqrt(xa * xa + ya * ya)
      sb    = sqrt(xb * xb + yb * yb)
      term2 = x0 * (xa/sa - xb/sb) + y0 * (ya/sa-yb/sb)
      fact  = 1./ (16. * atan(1.0)) * term2/term1
      return
      end
c
c Subroutine for LU Decomposition including pivoting
c **Note** The decomposition is done 'in place' so the input matrix is
c destroyed.
c From Press, W. H., et. al., Numerical Recipes - The Art of Scientific
c Computing (FORTRAN Version), Cambridge University Press, 1989,
c pp. 35-36
c
      SUBROUTINE LUDCMP(A,N,NP,INDX,D)
      PARAMETER (NMAX=100,TINY=1.0E-20)
      DIMENSION A(NP,NP),INDX(N),VV(NMAX)
      D=1.
      DO 12 I=1,N
        AAMAX=0.
        DO 11 J=1,N
          IF (ABS(A(I,J)).GT.AAMAX) AAMAX=ABS(A(I,J))
11      CONTINUE
        IF (AAMAX.EQ.0.) PAUSE 'Singular matrix.'
        VV(I)=1./AAMAX
12    CONTINUE
      DO 19 J=1,N
        IF (J.GT.1) THEN
          DO 14 I=1,J-1
            SUM=A(I,J)
            IF (I.GT.1)THEN
              DO 13 K=1,I-1
                SUM=SUM-A(I,K)*A(K,J)
13            CONTINUE
              A(I,J)=SUM
            ENDIF
14        CONTINUE
        ENDIF
        AAMAX=0.
        DO 16 I=J,N
          SUM=A(I,J)
          IF (J.GT.1)THEN
            DO 15 K=1,J-1
              SUM=SUM-A(I,K)*A(K,J)
15          CONTINUE
            A(I,J)=SUM
```

```
          ENDIF
          DUM=VV(I)*ABS(SUM)
          IF (DUM.GE.AAMAX) THEN
            IMAX=I
            AAMAX=DUM
          ENDIF
16      CONTINUE
        IF (J.NE.IMAX)THEN
          DO 17 K=1,N
            DUM=A(IMAX,K)
            A(IMAX,K)=A(J,K)
            A(J,K)=DUM
17        CONTINUE
          D=-D
          VV(IMAX)=VV(J)
        ENDIF
        INDX(J)=IMAX
        IF(J.NE.N)THEN
          IF(A(J,J).EQ.0.)A(J,J)=TINY
          DUM=1./A(J,J)
          DO 18 I=J+1,N
            A(I,J)=A(I,J)*DUM
18        CONTINUE
        ENDIF
19    CONTINUE
      IF(A(N,N).EQ.0.)A(N,N)=TINY
      RETURN
      END
c
c Subroutine for Solving a Linear System of Equations Given the
c (pivoted) LU Decomposition of the matrix of coefficients
c From Press, W. H., et. al., Numerical Recipes - The Art of Scientific
c Computing (FORTRAN Version), Cambridge University Press, 1989,
c pp. 36-37
c
      SUBROUTINE LUBKSB(A,N,NP,INDX,B)
      DIMENSION A(NP,NP),INDX(N),B(N)
      II=0
      DO 12 I=1,N
        LL=INDX(I)
        SUM=B(LL)
        B(LL)=B(I)
        IF (II.NE.0)THEN
          DO 11 J=II,I-1
            SUM=SUM-A(I,J)*B(J)
11        CONTINUE
        ELSE IF (SUM.NE.0.) THEN
          II=I
        ENDIF
        B(I)=SUM
12    CONTINUE
      DO 14 I=N,1,-1
        SUM=B(I)
        IF(I.LT.N)THEN
          DO 13 J=I+1,N
            SUM=SUM-A(I,J)*B(J)
13        CONTINUE
        ENDIF
```

```
        B(I)=SUM/A(I,I)
14    CONTINUE
      RETURN
      END
```

E16-M07
15

UNSTEADY AERODYNAMIC ANALYSIS OF DUAL-ELEMENT WING CONFIGURATIONS

BI-MONTHLY PROGRESS LETTER FOR THE PERIOD

November 1 - December 31, 1992

Submitted to the

NAVAL AIR WARFARE CENTER
AIRCRAFT DIVISION
WARMINSTER, PA

Attn: Mr. Marvin M. Walters

Prepared By

L. N. Sankar
Professor
School of Aerospace Engineering
Georgia Institute of Technology, Atlanta, GA 30332

January 1993

Georgia Institute of Technology
School of Aerospace Engineering

January 20, 1993

Mr. Marvin M. Walters
Code 6051
Naval Air Development Center
Warminster, PA 18974

Subject: BI-MONTHLY PROGRESS REPORT FOR THE PROJECT "UNSTEADY AERODYNAMIC ANALYSIS OF DUAL-ELEMENT WING CONFIGURATIONS"

Dear Mr. Walters:

During the reporting period (November 1, 1992 - December 31, 1992), the following tasks were completed:

Work continued on the development of a computer code that can model the performance of a helicopter rotor, operating in the vicinity of a ship deck. We have modified the GENHEL computer code so that the inflow through the rotor disk may be modeled using a dynamic inflow theory developed by Prof. David Peters of George Washington University.

A report co-authored by Mr. Olympio Mello, one of my graduate students, describing the dynamic flow modeling is enclosed.

With best wishes,

Sincerely,

LAKSHMI N. SANKAR
Professor

IMPLEMENTATION OF A DYNAMIC INFLOW MODEL IN A GENERAL HELICOPTER SIMULATION PROGRAM

Lakshmi N. Sankar, Professor
and
Olympio A. F. Mello, Graduate Student

School of Aerospace Engineering
Georgia Institute of Technology
Atlanta, GA 30332-0150

(404) 894-3014

INTRODUCTION

The present report concerns the implementation of a Dynamic Inflow model [1–3] in a general helicopter simulation code (GENHEL) [4] in order to improve its aerodynamic modeling and allow it to more accurately simulate complex flight conditions, in particular the problem of helicopter landing on ship decks.

He and Lewis [5] have recently performed a parametric study in which they included first- and second-order dynamic inflow modeling in the FLIGHTLAB real-time rotorcraft flight simulation environment. They concluded that the first-order dynamic inflow model consistently improved the correlation between the simulation and flight test data over an uniform inflow model, while the second-order model improved the correlation in some cases but underestimated transient response in others.

The dynamic inflow model used in this work is the first-order model described by Peters and HaQuang [3], which is expected to provide a significant improvement in the aerodynamic modeling in GENHEL while retaining a level of sophistication — and computational cost — consistent with the other components of the simulation code.

MATHEMATICAL FORMULATION

Brief Description of the Inflow Model

A throughout description of dynamic inflow modeling, including bibliography and higher-order modeling, is given by He in Ref. [2]. The first-order dynamic inflow model used here is described by Peters and HaQuang in Ref. [3]. Therefore, only a brief description will be presented here.

The rotor aerodynamics computation in GENHEL is based on the blade-element model, in which the blades are divided into a finite number of segments. Local angle of attack, yaw and Mach number are computed and used to obtain lift and drag coefficients from airfoil experimental data, approximately given in equation form. This is an "instantaneous steady" approach in the sense that no pitch rate terms or unsteady wake effects are taken into account. The downwash (inflow) induced by the rotor wake system is also represented in an instantaneous manner as an additional term in the angle of attack computation. In the current GENHEL implementation, the inflow model has a first harmonic variation over the rotor disk (Glauert downwash factors).

In order to more accurately represent the unsteady nature of the flow over the rotor blade, the pitch rate term should be included in the local effective angle of attack and the effect of the unsteady wake should be taken into account in the inflow. While the effect of the wake for unsteady two-dimensional airfoil motion has been known for many years, its application to rotors is not straightforward, not only because of the three-dimensional effect, but mainly because of the distorted helical wake generated by the rotor.

Efforts to construct a suitable unsteady aerodynamics model for rotors have been numerous (see Ref. [2] for a review of the most significant models). Among those, the dynamic inflow model emerged as a very adequate model for aeroelastic and flight dynamics applications, because it is simple to implement and represents to an acceptable accuracy the main unsteady rotor wake effects. The wake vorticity depends on the rotor aerodynamic loads and in turn induces a non-uniform inflow over the rotor disk. This non-uniform inflow distribution is represented by a sum of a finite number of harmonics of blade azimuth, of which the multiplying coefficients are time-dependent and radial variations are accounted for by shape functions, i.e.,

$$\lambda\,(r,\psi,t) = \nu_0\,(t) + \sum_{n=1}^{N} \chi_n\,(r)\left[\nu_{ns}\,(t)\sin(n\psi) + \nu_{nc}\,(t)\cos(n\psi)\right] \qquad (1)$$

By expressing the pressure distribution over the rotor disk in terms of an acceleration potential, which is expanded in Legendre functions in terms of ellipsoidal coordinates, and integrating the momentum equation along the streamwise direction [2], the coefficients in the inflow expansion (1) can be related to the aerodynamic loads by a system of first-order ordinary differential equations:

$$[M]\frac{1}{\Omega}\{\dot{\nu}\} + [L]^{-1}\{\nu\} = \{\tau\} \qquad (2)$$

where the dot in $\{\dot{\nu}\}$ denotes time derivative and $\{\tau\}$ is a vector obtained from integrals of the pressure distribution over the rotor disk. In the first-order dynamic inflow used here [3], the inflow expansion reduces to

$$\lambda\,(r,\psi,t) = \lambda_0\,(t) + \lambda_s\,(t)\frac{r}{R}\sin(\psi) + \lambda_c\,(t)\frac{r}{R}\cos(\psi) \qquad (3)$$

and the system of equations (2) becomes

$$[M]\frac{1}{\Omega}\begin{Bmatrix}\dot{\lambda}_0\\ \dot{\lambda}_s\\ \dot{\lambda}_c\end{Bmatrix} + [\hat{L}]^{-1}\begin{Bmatrix}\lambda_0\\ \lambda_s\\ \lambda_c\end{Bmatrix} = \begin{Bmatrix}C_T\\ -C_1\\ -C_2\end{Bmatrix}_{aero} \qquad (4)$$

where C_T, C_1 and C_2 are the instantaneous rotor thrust, and rolling and pitching moment coefficients, respectively. The subscript "aero" denotes that only aerodynamic contributions are considered in these coefficients. Note that equations (3) and (4) are expressed in the tip-path-plane axes system. The matrices $[M]$ and $[\hat{L}]$ are given in Ref. [3].

Transformations Needed to Implement the Dynamic Inflow Model in GENHEL

In order to time-integrate the inflow-state equation (4), the rotor aerodynamic forces and moments are needed. These are computed by the same expressions as in pages 5.1-34 and 5.1-35 of Ref. [4], but taking into account only the aerodynamic contributions. The resulting forces and moments are denoted as in Ref. [4], with the addition of a subscript "A", i.e., forces T_{HA}, H_{HA} and J_{HA} and moments M_{HA}, L_{HA} and Q_{HA}. As mentioned above, equations (3) and (4) are expressed in the tip-path-plane axes system. GENHEL, in turn, uses the fixed shaft axes system. The corresponding transformation of coordinates is:

$$\begin{bmatrix} H_{HA} & L_{HA} \\ J_{HA} & M_{HA} \\ T_{HA} & Q_{HA} \end{bmatrix}_{TPP} = [T]_{STPP} \begin{bmatrix} H_{HA} & L_{HA} \\ J_{HA} & M_{HA} \\ T_{HA} & Q_{HA} \end{bmatrix}_{S} \qquad (5)$$

where

$$[T]_{STPP} = \begin{bmatrix} \cos\beta_{1c} & 0 & \sin\beta_{1c} \\ \sin\beta_{1c}\sin\beta_{1s} & \cos\beta_{1s} & -\cos\beta_{1c}\sin\beta_{1s} \\ -\sin\beta_{1c}\cos\beta_{1s} & \sin\beta_{1s} & \cos\beta_{1c}\cos\beta_{1s} \end{bmatrix} \qquad (6)$$

is the transformation matrix between shaft and tip-path-plane axes and β_{1c} and β_{1s} are the first harmonics flapping coefficients. Referring to the notation used in Ref [4], p. 5.1-18, $\beta_{1c} = -$ A1FMR and $\beta_{1s} = -$ B1FMR. The nondimensional coefficients needed in Eq. (4) may be now computed as:

$$C_T = \frac{T_{HA}}{\rho\,\pi\,R^2(\Omega R)^2} \; ; \; C_l = \frac{-L_{HA}}{\rho\,\pi\,R^3(\Omega R)^2} \; ; \; C_2 = \frac{M_{HA}}{\rho\,\pi\,R^3(\Omega R)^2} \qquad (7)$$

The nondimensional translational velocity components, μ_{XS}, μ_{YS} and μ_{ZS} in the shaft axes are also transformed to the tip-path-plane axes as needed in the computation of the matrices [M] and $[\hat{L}]$:

$$\begin{Bmatrix} \mu_1 \\ -\mu_2 \\ \mu_3 \end{Bmatrix} = [T]_{STPP} \begin{Bmatrix} \mu_{XS} \\ \mu_{YS} \\ \mu_{ZS} \end{Bmatrix} \qquad (8)$$

where μ_1, μ_2 and μ_3 are the nondimensional translational velocities in the tip-path-plane axes system according to the notation of Ref. [3].

During each simulation frame computation, the nondimensional thrust and moment coefficients are computed according to Eqs. (5) and (7). At the end of the simulation frame, the matrices [M] and $[\hat{L}]$ are computed using the translational velocities computed during the frame and transformed using Eq. (8). Then the new inflow states λ_0, λ_s and λ_c corresponding to the end of the simulation frame are obtained from explicit first-order integration of Eq. (4). These new inflow states will be used for the computation of inflow distribution over the disk at the next simulation frame. Since GENHEL uses all velocities in the shaft axes system, the inflow must be transformed as:

$$\begin{Bmatrix} U_{WX} \\ U_{WY} \\ U_{WZ} \end{Bmatrix}_S = [T]^{-1}_{STPP} \begin{Bmatrix} 0 \\ 0 \\ \lambda\,(r,\psi) \end{Bmatrix} = \begin{Bmatrix} -\lambda \sin\beta_{1c}\cos\beta_{1s} \\ \lambda \sin\beta_{1s} \\ \lambda \cos\beta_{1c}\cos\beta_{1s} \end{Bmatrix} \qquad (9)$$

When the inflow is transformed to the blade axes according to Ref. [4], the resulting total downwash contributions at the rotor disk [4, p.5.1-21] become:

$$\begin{aligned} UPDMR_I = \left(\lambda_\xi + y_{2IS}\,\lambda_y\right) \Big[& -\sin\beta\cos(\psi+\delta)\sin\beta_{1c}\cos\beta_{1s} \\ & -\sin\beta\sin(\psi+\delta)\sin\beta_{1s} - \cos\beta\cos\beta_{1c}\cos\beta_{1s} \Big] \end{aligned} \qquad (10)$$

$$UTDMR_I = \left(\lambda_\xi + y_{2IS}\,\lambda_y\right)\left[\sin(\psi+\delta)\sin\beta_{1c}\cos\beta_{1s} - \cos(\psi+\delta)\sin\beta_{1s}\right] \qquad (11)$$

$$\begin{aligned} URDMR_I = \left(\lambda_\xi + y_{2IS}\,\lambda_y\right) \Big[& \cos\beta\cos(\psi+\delta)\sin\beta_{1c}\cos\beta_{1s} \\ & +\cos\beta\sin(\psi+\delta)\sin\beta_{1s} - \sin\beta\cos\beta_{1c}\cos\beta_{1s} \Big] \end{aligned} \qquad (12)$$

where

$$\lambda_\xi = \lambda_0 + \xi\left(\lambda_s \sin\psi + \lambda_c \cos\psi\right) \qquad (13)$$

$$\lambda_y = \lambda_s \sin\left(\psi + \delta\right) + \lambda_c \cos\left(\psi + \delta\right) \qquad (14)$$

These inflow contributions are used to compute the local angle of attack as described in Ref. [4]. In addition, the pitch rate term must be included in the effective angle of attack. Following the notation in Ref. [4]:

$$\Delta\alpha_{\text{pitch rate}} = \frac{c_{YIS}}{2}\frac{\dot{T}_{H0AMR_{IB}}}{U_{T_I}} = \frac{c_{YIS}}{2\,U_{T_I}}\,\Omega\left[A_{1S}\sin\left(\psi_R + \Delta_{SP}\right)_{IB} - B_{1S}\cos\left(\psi_R + \Delta_{SP}\right)_{IB}\right] \quad (15)$$

NUMERICAL IMPLEMENTATION

The integration of inflow states through first-order explicit integration of Eq. (4) is performed at the beginning of each simulation frame, before the blade loop is started and using the inflow derivatives computed at the end of the previous frame. The inflow states λ_0, λ_s and λ_c are denoted by XLAM0, XLAMS and XLAMC, respectively.

The downwash contributions UPD1, UPD2, URD1, URD2, UTD1 and UTD2 are computed using Eqs. (10–14) for use in the subroutine RADIAL. Note the addition of UTD1 and UTD2 which were not needed in the original code. This requires a modification of RADIAL to include these coefficients in the list of arguments and in the computation of local velocities.

For the inclusion of the pitch rate term, an additional coefficient (denoted by THETAD) including the terms in Eq. (15) not dependent on the blade segment is computed prior to calling RADIAL and used as input to that routine, which is also modified to include Eq. (15).

The aerodynamic forces and moments needed in Eq. (5) are denoted by FHHA, FJHA, FTHA, TMHA, TLHA and TQHA and are computed during the blade loop in ROTOR. After the blade loop is completed, the subroutine DYNINF is called to perform the transformations needed (5),(8), compute C_T,

C_1 and C_2 and the matrices [M] and $[\hat{L}]$ in Eq.(4), and finally to compute the inflow state derivatives $\dot{\lambda}_0$, $\dot{\lambda}_s$ and $\dot{\lambda}_c$, denoted by DXLAM0, DXLAMS and DXLAMC in the code. Note that DYNINF uses the flapping coefficients from the previous simulation frame.

The inflow states and their time derivatives and the average inflow λ_m (needed in DYNINF to compute the matrices [M] and $[\hat{L}]$ and computed according to Ref. [3] from the inflow states) need to be stored from frame to frame. This is accomplished through EQUIVALENCE statements, by storing them in RC(330) through RC(336).

RESULTS AND DISCUSSION

Preliminary results obtained with the present implementation showed no noticeable increase in computational time over the original rotor code. Trim results agreed well with the original code, which has been show to agree well with flight test trim data [6]. The most important effect to be expected of the current implementation is an improvement in the helicopter transient response [5]. This result is expected to emerge from the validation efforts currently underway.

REFERENCES

1. Gaonkar, G. H., and Peters, D. A., "Review of Dynamic Inflow Modeling for Rotorcraft Flight Dynamics," *Vertica,* Vol. 12, No. 3, 1988, pp. 213–242.

2. He, Chengjian, "Development and Application of a Generalized Dynamic Wake Theory for Lifting Rotors," Ph.D. Dissertation, Georgia Institute of Technology, 1989.

3. Peters, D. A., and HaQuang, N., "Dynamic Inflow for Practical Applications," *Journal of the American Helicopter Society,* October 1988, pp. 64–68.

4. Howlett, J. J., "UH-60A Black Hawk Engineering Simulation Program: Volume I — Mathematical Model," NASA CR-166309, 1981.

5. He, C., and Lewis, W. D., "A Parametric Study of Real Time Mathematical Modeling Incorporating Dynamic Wake and Elastic Blades," 48th Annual Forum of the American Helicopter Society, Washington, DC, June 1992.

6. Ballin, M. G., "Validation of Real-Time Engineering Simulation of the UH-60A Helicopter," NASA TM-88360, February 1987.

E 16-P137
/16

UNSTEADY AERODYNAMIC ANALYSIS OF DUAL-ELEMENT WING CONFIGURATIONS

BI-MONTHLY PROGRESS LETTER
FOR THE PERIOD

January 1 - February 28, 1993

Submitted to the

NAVAL AIR WARFARE CENTER
AIRCRAFT DIVISION
WARMINSTER, PA

Attn: Mr. Marvin M. Walters

Prepared By

L. N. Sankar
Professor
School of Aerospace Engineering
Georgia Institute of Technology, Atlanta, GA 30332

March 1993

Georgia Institute of Technology
School of Aerospace Engineering

March 18, 1993

Mr. Marvin M. Walters
Code 6051
Naval Air Development Center
Warminster, PA 18974

Subject: BI-MONTHLY PROGRESS REPORT FOR THE PROJECT "UNSTEADY AERODYNAMIC ANALYSIS OF DUAL-ELEMENT WING CONFIGURATIONS"

Dear Mr. Walters:

During the reporting period (January 1, 1993 - February 28, 1993), the following tasks were completed:

Work continued on the validation of a computer code that can model the performance of a helicopter rotor, operating in the vicinity of a ship deck. We have modified the GenHel computer code so that the inflow through the rotor disk may be modeled using a dynamic inflow theory developed by Prof. David Peters of George Washington University.

A report co-authored by Mr. Olympio Mello, one of my graduate students, describing the validation effort is enclosed.

With best wishes,

Sincerely,

LAKSHMI N. SANKAR
Professor

VALIDATION OF A DYNAMIC INFLOW MODEL IMPLEMENTATION IN A GENERAL HELICOPTER SIMULATION PROGRAM

Lakshmi N. Sankar, Professor

and

Olympio A. F. Mello, Graduate Student

School of Aerospace Engineering
Georgia Institute of Technology
Atlanta, GA 30332-0150

(404) 894-3014

INTRODUCTION

The present report describes the validation of a Dynamic Inflow model [1–4] implementation, described in our previous report, in a general helicopter simulation code (GENHEL) [5] in order to improve its aerodynamic modeling and allow it to more accurately simulate complex flight conditions, in particular the problem of helicopter landing on ship decks. The next steps in the helicopter/ship interaction simulation are briefly discussed.

VALIDATION

The dynamic inflow implementation described in our previous report has been validated by comparing the static trim results with uniform inflow and flight test results presented in Appendix B of Ref. [6] and by comparing the transient response with uniform inflow results. The transient response cases were chosen so as to coincide with some of the test cases used in Ref. [7].

The static trim correlations are presented in Figs. 1–7. No significant changes were observed in collective, longitudinal cyclic and pedal controls and on pitch attitude. Some additional left lateral cyclic was observed when using the dynamic inflow model, with corresponding changes in roll angle and sideslip. These effects can be attributed to non-uniformity of inflow between the forward and aft portions of the rotor disk which requires the additional lateral cyclic pitch [7]. Note that these effects are not as dramatic as when verified in Ref. [7], probably due to the fact that the uniform inflow version of GenHel was able to trim the aircraft at values much closer to the flight test data than the test case presented in Ref. [7].

The transient response correlations are presented in Figs. 8–10. Note that flight test data are not presented here because our validation used simply "perfect" step control inputs, not the actual control time histories as used in Ref. [7]. However, the results obtained herein demonstrate improvements in the transient response similar to those obtained in Ref. [7].

CONSIDERATIONS REGARDING THE IMPLEMENTATION OF A HIGHER-ORDER DYNAMIC INFLOW MODEL

When the inflow model to be implemented in GenHel for the current effort was being considered, higher-order models were analyzed. However, we opted for a first-order model for the following reasons:

1. Since the final objective is real-time simulation, the method is expected to be as fast as possible while giving sufficient accuracy;

2. The structural model presently implemented in GenHel uses rigid blades, which is a "zeroth-order" elastic model. It would seem that using a higher-order inflow model while retaining the lower-order elastic model would be inconsistent and most likely no improvement would be obtained over the first-order model. The higher-order inflow models are consistent with higher-order elastic models, which are needed when one is interested in vibrations and aeroelastic studies.

These considerations are supported by extensive studies performed by Dr. William D. Lewis for his Ph.D. research at Georgia Tech [8]. His results are summarized in Ref. [7]. Drs. Lewis and He investigated the effect of inflow models of zeroth to second order coupled with rigid and elastic blade models in Georgia Tech's flight simulator program (FLIGHTSIM). From their findings, we conclude that the most important modifications in order to improve GenHel's rotor module are first-harmonic dynamic inflow and an elastic blade model.

For the actual implementation of a higher-order model, the following additional steps will be required:

1. Additional computation of second-order inflow forcing functions, and inclusion of second-harmonic inflow state variables will be required.

2. An additional transformation of coordinates will be needed, since the dynamic inflow equations are usually expressed in the wind-axes system, while GenHel uses the fixed shaft axes. In our current first-order implementation, dynamic inflow expressions in the tip-path-plane axes system were used [3], therefore our implementation does not include the transformation from wind-axes to tip-path-plane axes;

3. The addition of radial shape functions would require further modifications in the subroutine RADIAL and in the inflow coefficients (UPD1, UPD2, URD1, URD2, UTD1, UTD2) to reflect the modified radial inflow variation.

UPCOMING STEPS IN THE HELICOPTER/SHIP INTERACTION ANALYSIS

The upcoming steps in the helicopter/ship interaction analysis are the addition of a specialized ground effect module to take into account the presence of the ship and the inclusion of the ship's wake turbulence in the inflow experienced by the rotor. The former is currently being analyzed. For the latter problem, we are currently in contact with Dr. Prasad's research group at Georgia Tech regarding the possibility of using subroutines developed by that group for use in Georgia Tech's flight simulator program.

REFERENCES

1. Gaonkar, G. H., and Peters, D. A., "Review of Dynamic Inflow Modeling for Rotorcraft Flight Dynamics," *Vertica,* Vol. 12, No. 3, 1988, pp. 213–242.

2. He, Chengjian, "Development and Application of a Generalized Dynamic Wake Theory for Lifting Rotors," Ph.D. Thesis, Georgia Institute of Technology, 1989.

3. Peters, D. A., and HaQuang, N., "Dynamic Inflow for Practical Applications," *Journal of the American Helicopter Society,* Vol. 33, No. 4, October 1988, pp. 64–68.

4. Peters, D. A., and He, C. J., "Correlation of Measured Induced Velocities with a Finite-State Inflow Model," *Journal of the American Helicopter Society,* Vol. 36, No. 3, July 1991, pp. 59–70.

5. Howlett, J. J., "UH-60A Black Hawk Engineering Simulation Program: Volume I — Mathematical Model," NASA CR-166309, 1981.

6. Ballin, M. G., "Validation of Real-Time Engineering Simulation of the UH-60A Helicopter," NASA TM-88360, February 1987.

7. He, C., and Lewis, W. D., "A Parametric Study of Real Time Mathematical Modeling Incorporating Dynamic Wake and Elastic Blades," 48th Annual Forum of the American Helicopter Society, Washington, DC, June 1992.

8. Lewis, W. D., "An Aeroelastic Model Structure Investigation for a Manned Real-Time Rotorcraft Simulation," Ph.D. Thesis, Georgia Institute of Technology, 1992.

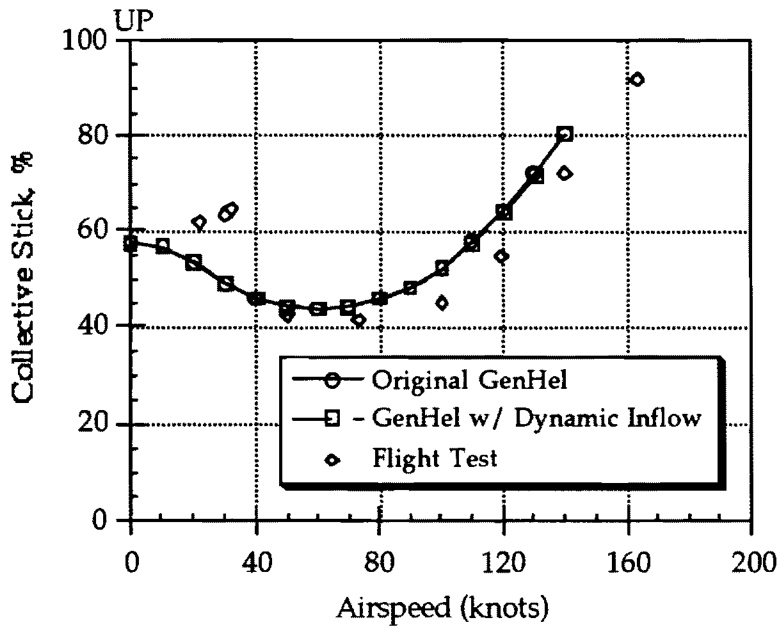

Fig. 1: Comparison of Collective Stick Position with Uniform and Dynamic Inflow

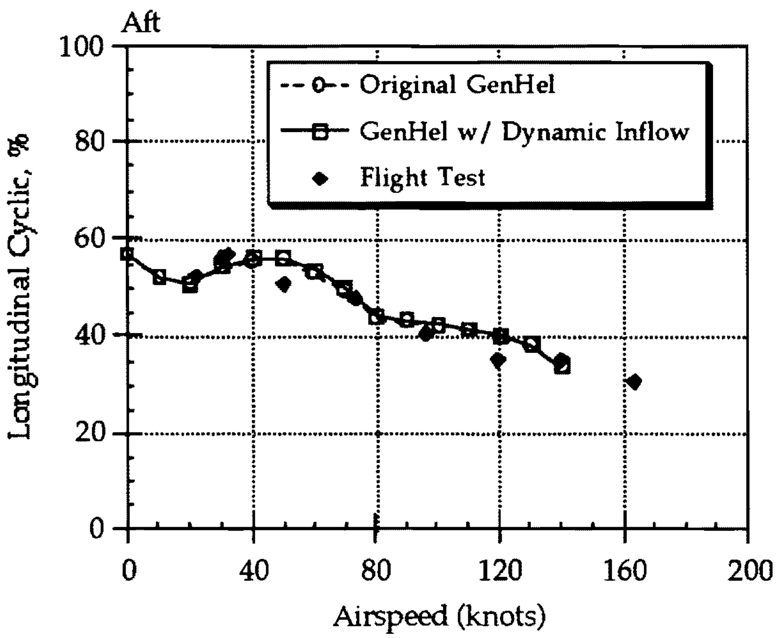

Fig. 2: Comparison of Longitudinal Cyclic Pitch with Uniform and Dynamic Inflow

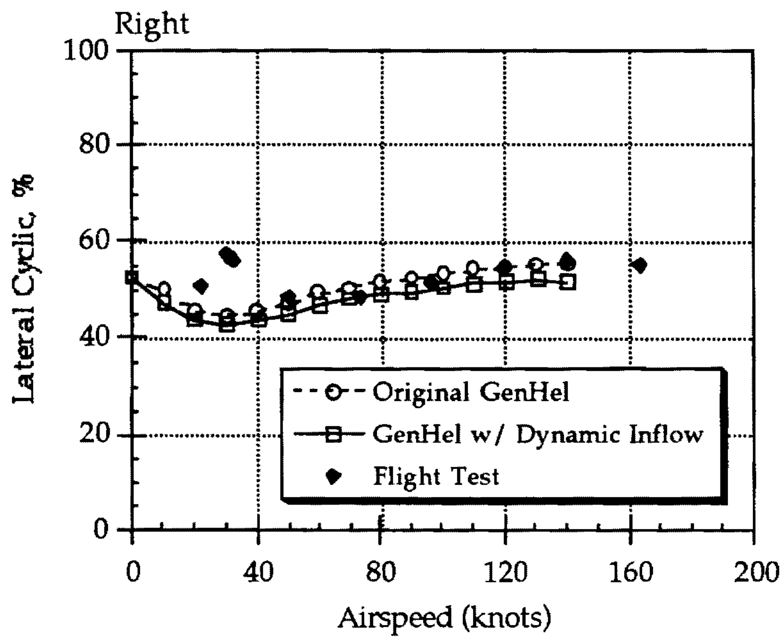

Fig. 3: Comparison of Lateral Cyclic Pitch with Uniform and Dynamic Inflow

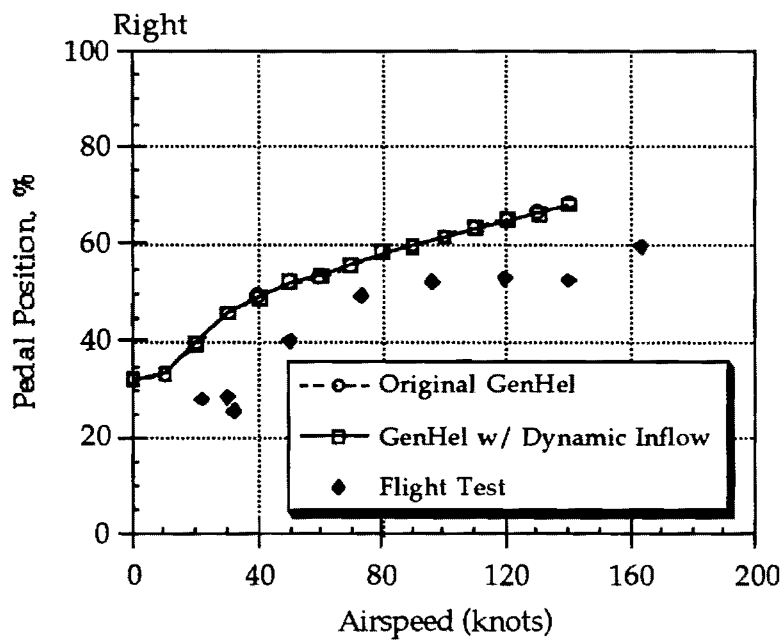

Fig. 4: Comparison of Pedal Position with Uniform and Dynamic Inflow

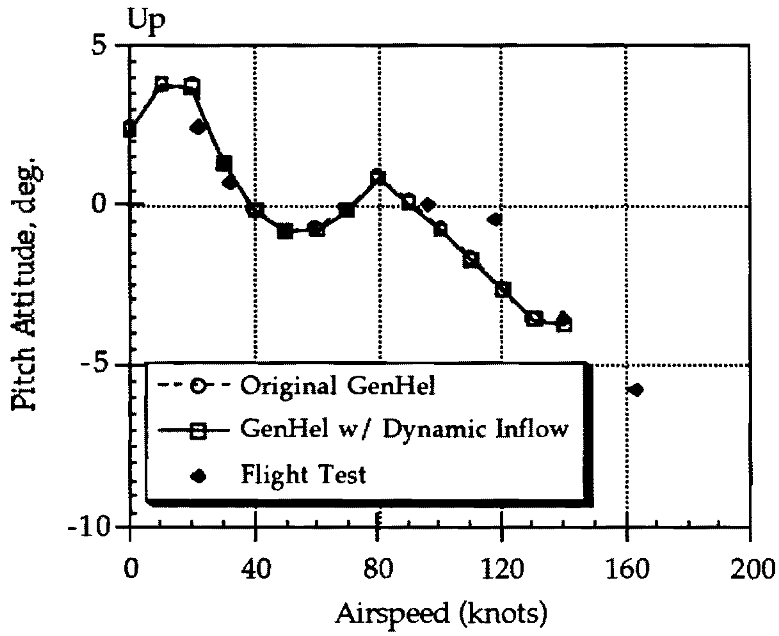

Fig. 5: Comparison of Pitch Attitude with Uniform and Dynamic Inflow

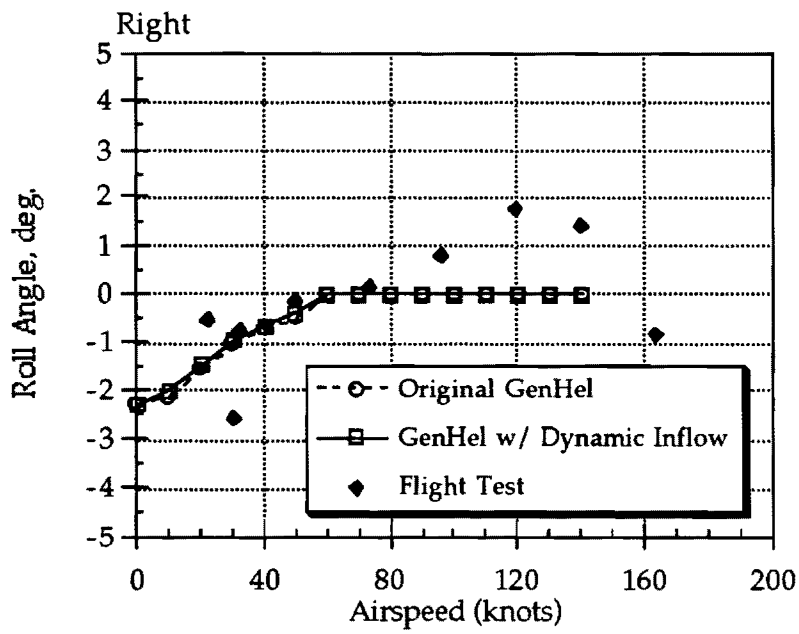

Note: Below 60 kts, GenHel trims the aircraft at zero sideslip and nonzero roll angle; at or above 60 kts, GenHel trims at zero roll angle and nonzero sideslip.

Fig. 6: Comparison of Roll Angle with Uniform and Dynamic Inflow

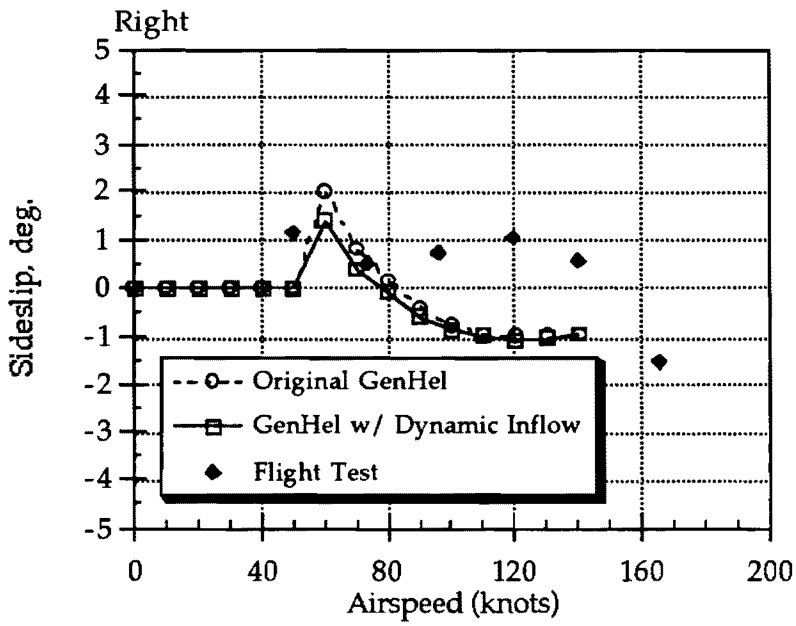

Note: Below 60 kts, GenHel trims the aircraft at zero sideslip and nonzero roll angle; at or above 60 kts, GenHel trims at zero roll angle and nonzero sideslip.

Fig. 7: Comparison of Sideslip with Uniform and Dynamic Inflow

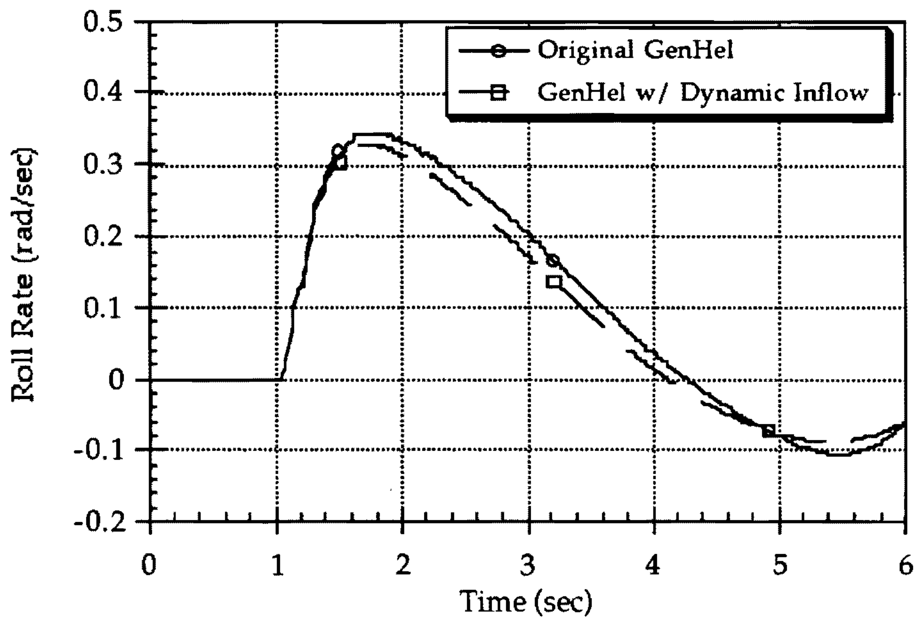

Fig. 8: Comparative Response Due to a 1 in. Lateral Cyclic Step in Hover

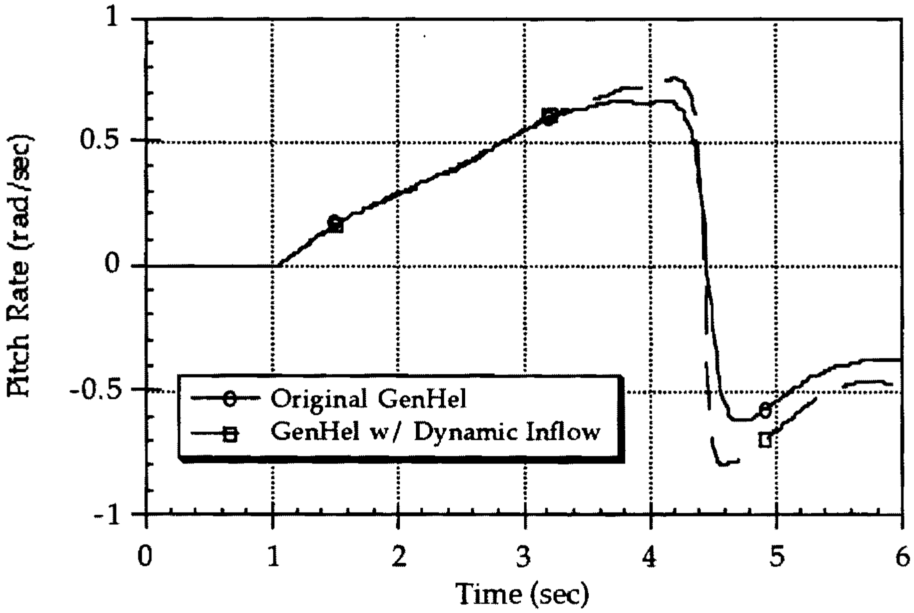

Fig. 9: Comparative Response Due to a 1 in. Aft Longitudinal Cyclic Step at 60 kts

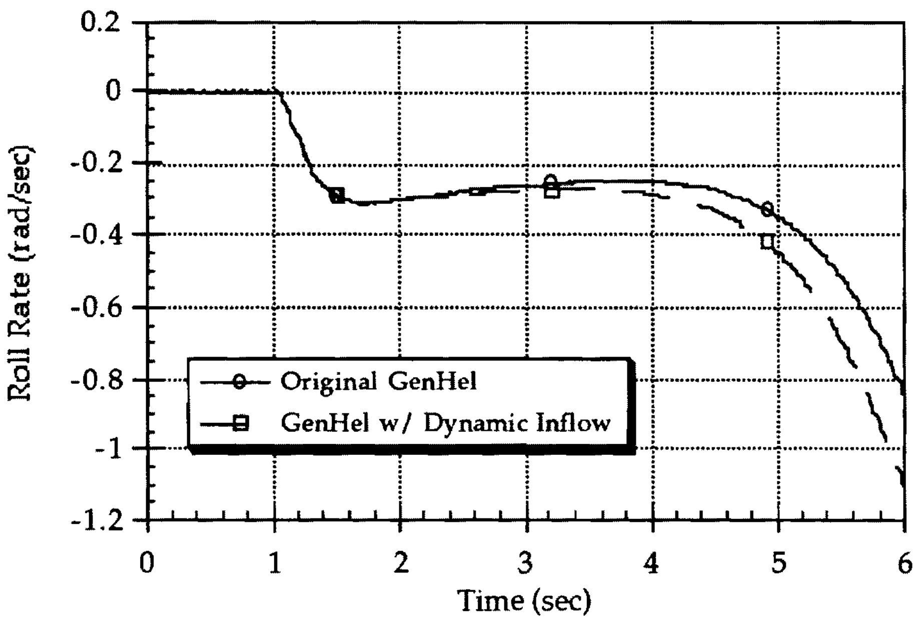

Fig. 10: Comparative Response Due to a 1 in. Left Lateral Cyclic Step at 60 kts

E 16-M09
17

UNSTEADY AERODYNAMIC ANALYSIS OF DUAL-ELEMENT WING CONFIGURATIONS

BI-MONTHLY PROGRESS LETTER FOR THE PERIOD

March 1 - April 30, 1993

Submitted to the

NAVAL AIR WARFARE CENTER
AIRCRAFT DIVISION
WARMINSTER, PA

Attn: Mr. Marvin M. Walters

Prepared By

L. N. Sankar
Professor
School of Aerospace Engineering
Georgia Institute of Technology, Atlanta, GA 30332

May 1993

Georgia Institute of Technology
School of Aerospace Engineering

May 25, 1993

Mr. Marvin M. Walters
Code 6051
Naval Air Development Center
Warminster, PA 18974

Subject: BI-MONTHLY PROGRESS REPORT FOR THE PROJECT "UNSTEADY AERODYNAMIC ANALYSIS OF DUAL-ELEMENT WING CONFIGURATIONS"

Dear Mr. Walters:

During the reporting period (March 1, 1993 - April 30, 1993), the following tasks were completed:

1) We began modification of the Georgia Tech 3-D Navier-Stokes solver to account for the presence of partial span flaps. This required conversion of the original solver into a multi-zone solver. At the zone boundaries, the nodes from adjacent zones may not have the same (x,y,z) values. Special interpolation of the flow properties are therefore needed to transfer information from one zone to the next. We have used a simple linear interpolation of information from adjacent zones in the present version of the multi-zone solver.

Encouraging preliminary results for an F-18 wing with a partial span flap have been obtained. An abstract describing the formulation of the multizone solver has been submitted to the forthcoming AIAA meeting. This abstract is enclosed.

2) Mr. Olympio Mello is continuing to work on the numerical simulation of helicopter rotors operating in the vicinity of an aircraft carrier deck. There are a number of ways the effects of the carrier deck can be modeled. In a simulation code such as the GENHEL code, the presence of the ship deck, and the rolling motion of the ship can be modeled as modifications to the inflow through the rotor disk. While such a

simple phenomenological model is computationally efficient, it can not handle in a first principles basis details of the ship geometry, clearance between the ship deck and the sea surface, and presence of superstructures. We have developed a panel method that can account for these effects, and can model the rolling motion of the ship. This method uses a source panel representation of the ship structure, and a vortex lattice representation of the rotor blades. We anticipate completion of this code by the end of the next reporting period.

With best wishes,

Sincerely,

LAKSHMI N. SANKAR
Professor

A MULTIZONE NAVIER-STOKES ANALYSIS OF DYNAMIC LIFT ENHANCEMENT CONCEPTS

A.Bangalore and L.N.Sankar
School of Aerospace Engineering
Georgia Institute of Technology, Atlanta, GA 30332
and
Wei Tseng
Naval Air Warfare Center, Aircraft Division
Warminster, PA

An Abstract presented to the
Applied Aerodynamics Session
32nd AIAA Aerospace Sciences Meeting, Reno, NV

INTRODUCTION

Recent studies indicate that one of the viable concepts for improving the maneuverability and low speed characteristics of tactical fighter aircraft at high angles of attack well beyond static stall is by partial flap oscillation.The physical phenomenon involves vortex generation by flap oscillation at a particular frequency, the movement of the vortices over the wing resulting in dynamic lift enhancement. Dynamic lift studies has been done in the past over helicopter blades and highly swept sharp edge delta wings, However little has been done to study similar phenomena over fighter aircraft wings with moderate aspect ratio.

CFD analysis can provide a good physical insight into the dynamic lift phenomena of oscillating leading edge and/or trailing edge flaps. Such an analysis will be a valuable tool in the design of wing planform shapes with oscillating flaps to satisfy certain specific performance requirements, such as low speed landing characteristics.

This work is an extension of a previous study done by W.Tseng, F.Tsung and Sankar (Ref 1). They presented results for a F-18 wing with a full span flap. Their computational results were compared with experimental results presented by Smith (Ref 2) for a F-18 aircraft at high angles of attack with a full span oscillating flap.

In an actual aircraft, full span flaps (leading edge or trailing edge) are seldom used because of the weight considerations and the need for housing actuators and motors on the wing. Partial span slats and flaps are much more common, and are already in use to enhance takeoff and landing performance. If these existing devices are dynamically used (i.e. oscillated), will they generate additional lift over and above the static lift ?. This work attempts to address this issue.

A time dependent Reynolds averaged Navier-Stokes solver, originally developed in Refs 1,3,4 is modified in to a multizone solver. The original code has already been extensively validated for several wing alone and complete aircraft configuration studies.

The main emphasis of this paper is to describe the multizone methodology to study unsteady flow over a complex arrangement of leading edge and trailing edge oscillating flaps. At this writing the multizone solver has been developed and is operational. Some results for flow over a F-18 wing at high angle of atttack with a stationary deflected flap are presented. The final paper will contain these results and additional results for an oscillating flap.

NUMERICAL FORMULATION

The three dimensional unsteady compressible Navier-Stokes equations are written in the generalised co-ordinates as

$$q_\tau + F_\xi + G_\eta + H_\zeta = R_\xi + S_\eta + T_\zeta$$

where q is the vector containing unknown flow properties such as density, velocity and temperature. The quantities F, G and H are the inviscid flux vectors. R, S and T contain the viscous stress contributions to mass, momentum and energy transport. These governing equations are integrated in time numerically starting from an initial guess for the flow vector q. At every time step appropriate boundary conditions are applied at all the boundaries of the computational domain and the zonal interfaces. At the body surface the noslip condition is imposed and at far-field boundaries the freestream conditions are prescribed or the 1-D Reimann variables are extrapolated depending on whether the boundary is inflow or outflow.

The finite difference representation of the above equation at time level 'n' is

$$\Delta q^{n+1}/\Delta\tau + \delta\xi F^{n+1} + \delta\eta G^{*} + \delta\zeta H^{n+1} = (\delta\xi R + \delta\eta S + \delta\zeta T)^{n}$$

where $\delta\xi$, $\delta\eta$ and $\delta\zeta$ are the standard central difference operators. Δq^{n+1} is the change in q during adjacent time levels and $\Delta\tau$ is the time step. The viscous terms are evaluated explicitly and the inviscid flux vectors F and H are calculated implicitly at time level n+1. The spanwise derivative $\delta\eta G^{*}$ is evaluated semi-implicitly, that is using new time level values as they become available. The nonlinear flux vectors F and H at time level n+1 are linearized at every time level about their values at their previous time level 'n'. The resulting linearized implicit system of algebraic equations are

$$[I + \Delta\tau\delta\xi A + \Delta\tau\delta\zeta B]\ \{\Delta q\}^{n+1} = R^{n,n+1}$$

where $A = \partial F/\partial q$ and $B = \partial H/\partial q$ are the flux jacobian matrices. The right hand side R contains information from the previous time level about F,G,H,R,S and T. In steady state applications the residual R is driven to zero. Approximate factorization is used to factorize the implicit coefficient matrix operator in to two operators which results in tri-diagonal matrices. The factorized system of equations look like

$$[I + \Delta\tau\delta\xi A]\ [I + \Delta\tau\ \delta\zeta\ B]\ \{\Delta q\}^{n+1} = R^{n,n+1}$$

The solution of the tri-diagonal matrix systems are done efficiently using Thomas algorithm. The above time differencing scheme is called a hybrid time differencing scheme which has several advantages over fully explicit and fully implicit schemes. Numerical viscosity terms, based on the work by Jameson, Turkel and Schmidt are used in these calculations to prevent the high frequency oscillations from blowing up.

MULTIZONE METHODOLOGY

This approach is very powerful for solving flow over complex geometries. A similar approach was used by the present authors to solve flow over a multi-element airfoil (Ref 6). To generate a single block grid which is body conforming for complicated geometries such as partial span flaps is very difficult and impractical. Using multizone approach, the wing is divided in to a number of spanwise zones and each zone is solved independently on a simply connected grid. Adjacent zones communicate with each other via the interfaces.

The multizone grid used in the present application is shown in Fig 1 and Fig 2. The boundary condition at the interface involves transfer of data between the adjacent zones. As shown in the grid the flap is deflected in zone 2 and there are no flaps in the other zones. This results in a shearing between the grids. The grid with an oscillating flap will be moving with respect to the other stationary grids. At present a simple bilinear interpolation technique is used to transfer data between the zones. The sketch below shows the typical grid points at any zonal interface.

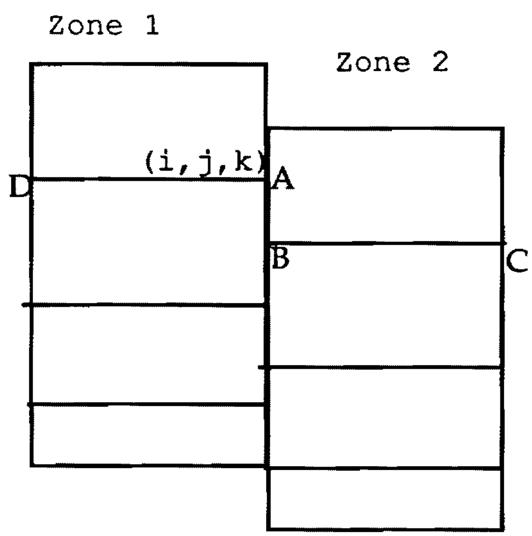

Grid points A and D in the sketch above belong to zone 1, B, C belong to zone 2. The points A,B are along the interface.

$$q_A = (\Delta S_1\, q_C + \Delta S_2\, q_D) / (\Delta S_1 + \Delta S_2)$$

$$q_B = (\Delta S_3\, q_C + \Delta S_4\, q_D) / (\Delta S_3 + \Delta S_4)$$

ΔS_1 = distance between gridpoints A and D, ΔS_2 = distance between gridpoints A and C, ΔS_3 = distance between gridpoints B and D, ΔS_4 = distance between gridpoints B and C. 'q' represents the vector containing the flow variables as explained in the previous section. The 'q' vector is updated at the interface at every time step using the above expression. Higher order interpolation schemes involving more number of grid points will be investigated in the final paper. The multizone code can handle any number of zones in the spanwise direction. This feature is particularly useful in the case of leading and trailing edge flaps located at different positions along the span.

RESULTS AND DISCUSSION

The results presented here are for a F-18 wing planform with a partial span leading edge flap. The freestream Mach number and Reynolds number are 0.2 and 20,000 respectively. The partial span flap is at 34 degrees to the main wing. The calculations done at present are for the flap kept steady with no oscillation. The flow conditions correspond to the one used in Ref 2 .

Fig 1 and Fig 2 show the computational grid sections in the X-Z plane at 27% and 73% span stations respectively. The planform is divided in to three zones along the span. The first zone consists of 40% of the span from the root. The second zone spans from 50% to 80% of the span and has the leading edge flap. The third zone starts from 80% span and extends all the way till the outermost span station(JMAX) which is about a chord length beyond the tip. The grid dimensions used in these calculations are 141 x 7 x 61, 141 x 5 x 61, 141 x 8 x 61 in zones 1,2 and 3 respectively.

Fig 3 and Fig 4 shows the total pressure contours in the x-z plane on the upper side of the wing at 27% and 73% span stations. The angle of attack of the main wing is 40 degrees. The leading edge flap is located in zone 2 and the hinge line of the flap is at 19% chord. At this high angle of attack, we can observe streamwise seperation even in zone 2 where the flap is present. Similar type of seperation was observed by Smith (Ref 2) in their water tunnel experiments. Spanwise flow particle traces are shown in Fig 5 and Fig 6. We observe complicated flow pattern in the flap region and the flowfield needs to be investigated further. Fig 6 shows the spanwise particle traces for a clean wing.

Fig 7 shows the variation of lift coefficient along the span with and without partial span flap. A 10% increase in lift coefficient is observed at the flap portion of the wing. These Cl values are taken after 30 time units where each time unit correspond to the time taken by air particles with freestream speed to travel one chord length. A better way to compare would be to compute the time averaged lift coefficient.

The final paper will include flow cases with several leading and trailing edge flap arrangements oscillating at different frequencies. A grid resolution study and other interpolation techniques will be included in the final paper.

REFERENCES

1. Tseng,W., Tsung,F.L. and Sankar,L.N. " Numerical simulation of dynamic lift enhancement using oscillatory leading edge flaps",AIAA-93-0177, Jan 1993.
2. Smith, B., " Dynamic lift enhancement using oscillating leading edge flaps," AIAA paper 92-2625.
3. Sankar,L.N. and Kwon, O.J., " Viscous flow simulation of fighter aircraft," AIAA paper 91-0278, Jan 1991.
4. Wake, B.E. and Sankar, L.N. " Solution of Navier-Stokes equations for the flow about a rotor blade, " Journal of the American Helicopter Society, April 1989.
5. Tsung, F.L. and Sankar, L.N., "Numerical simulation of flow seperation for rotors and fixed wings," AIAA paper 92-0635.
6. Sankar, L.N., Phaengsook, N. and Bangalore, A. " Effects of icing on the Aerodynamic performance of high lift airfoils," AIAA 93-0026, Jan 1993.

Fig 1 Computational grid section inX-Z plane, y/b = 0.27

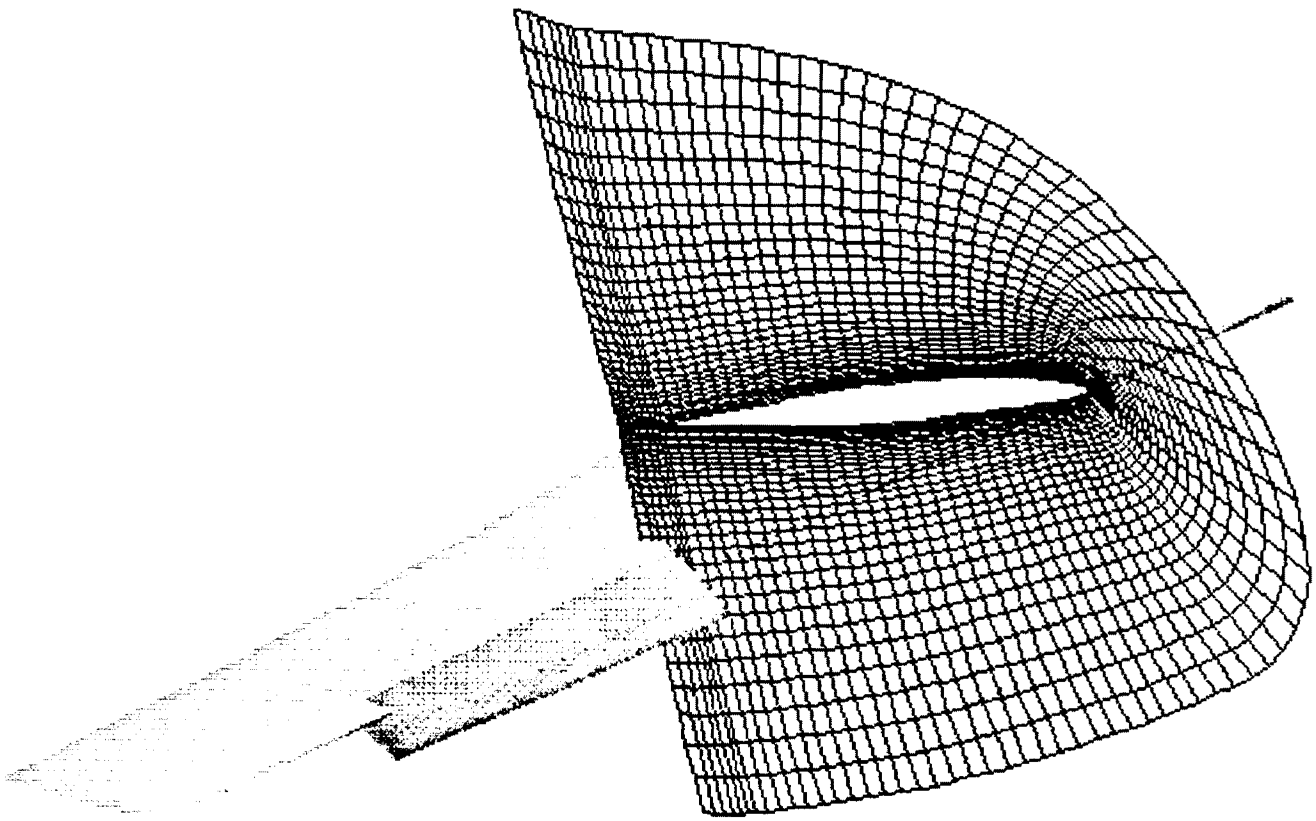

Fig 2 Computational grid section in X-Z plane, y/b = 0 73

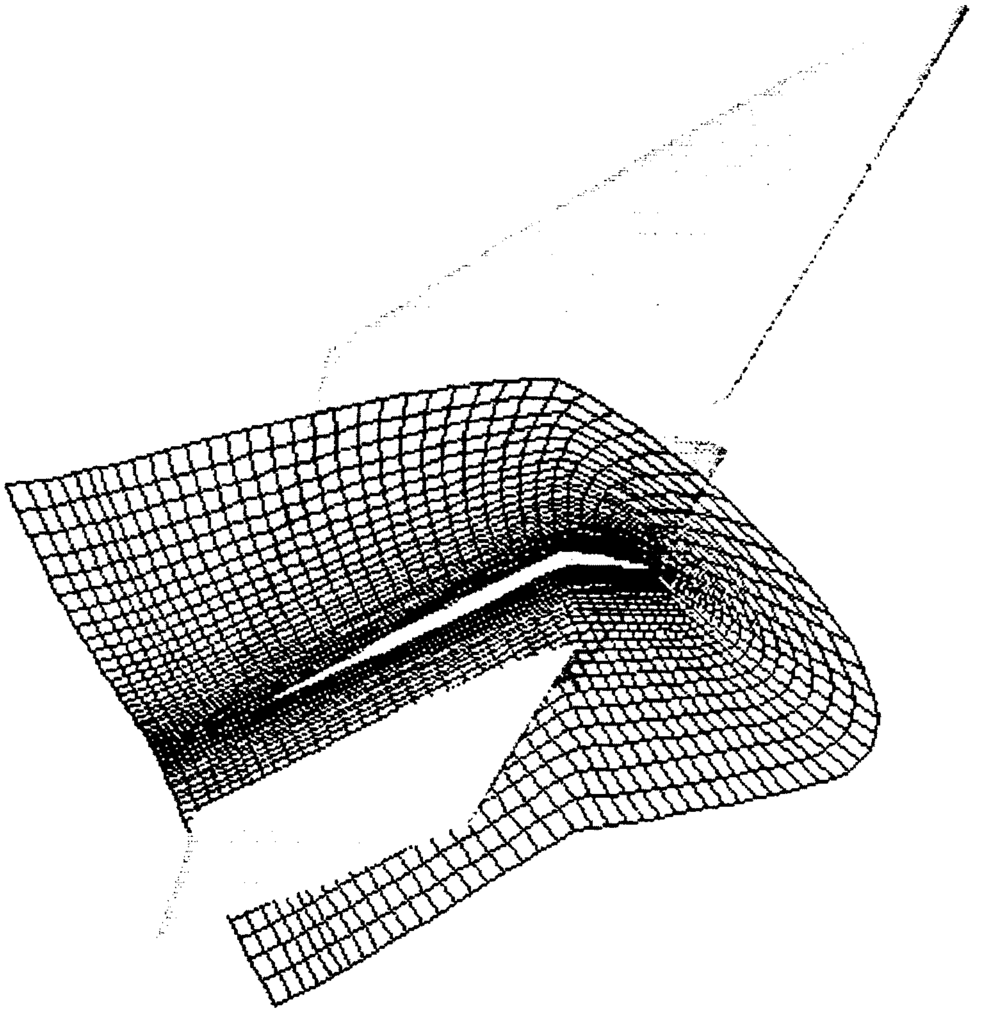

Fig 3: Stagnation pressure contours, y/b = 0.27

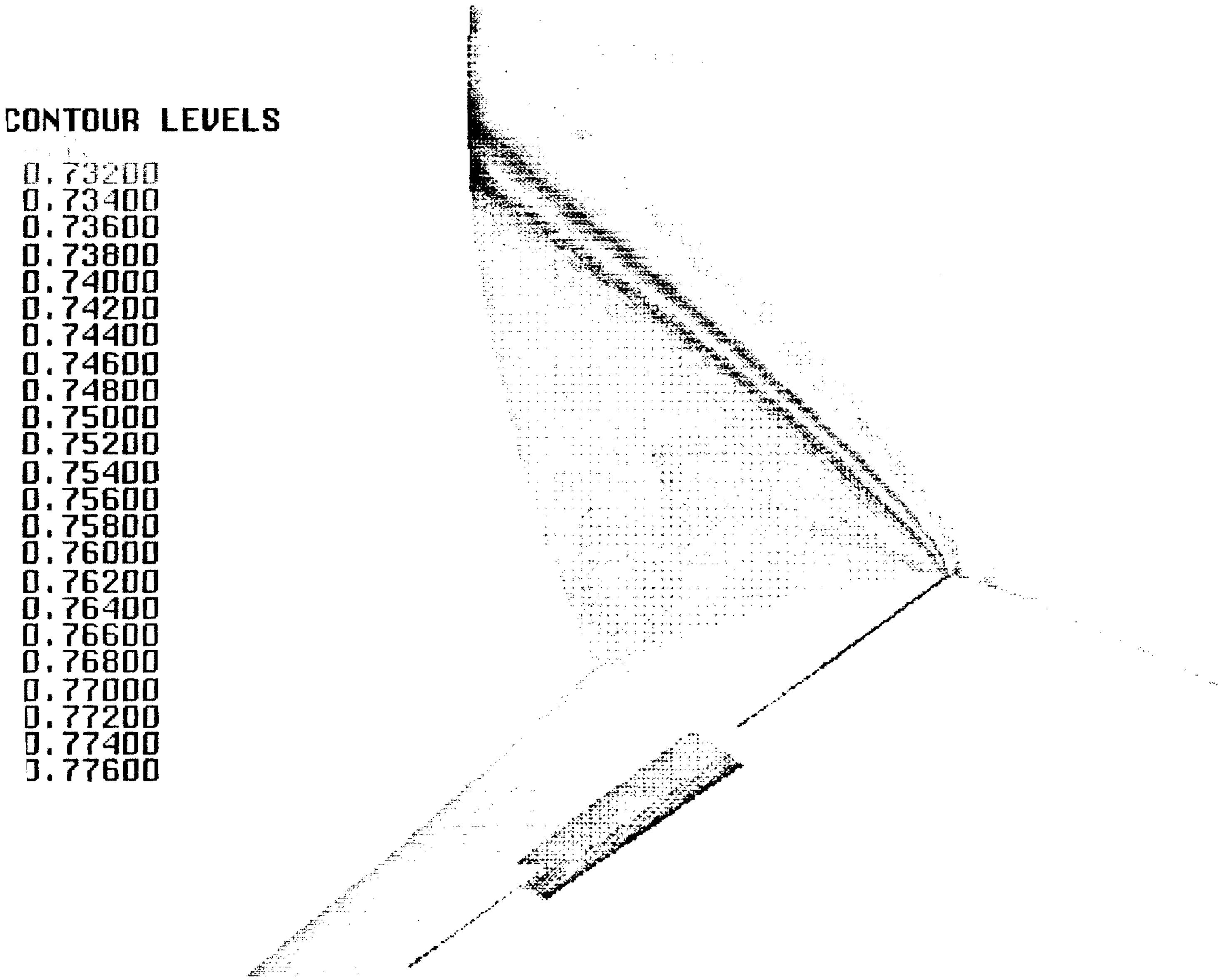

Fig 4: Stagnation pressure contours, y/b =0.73

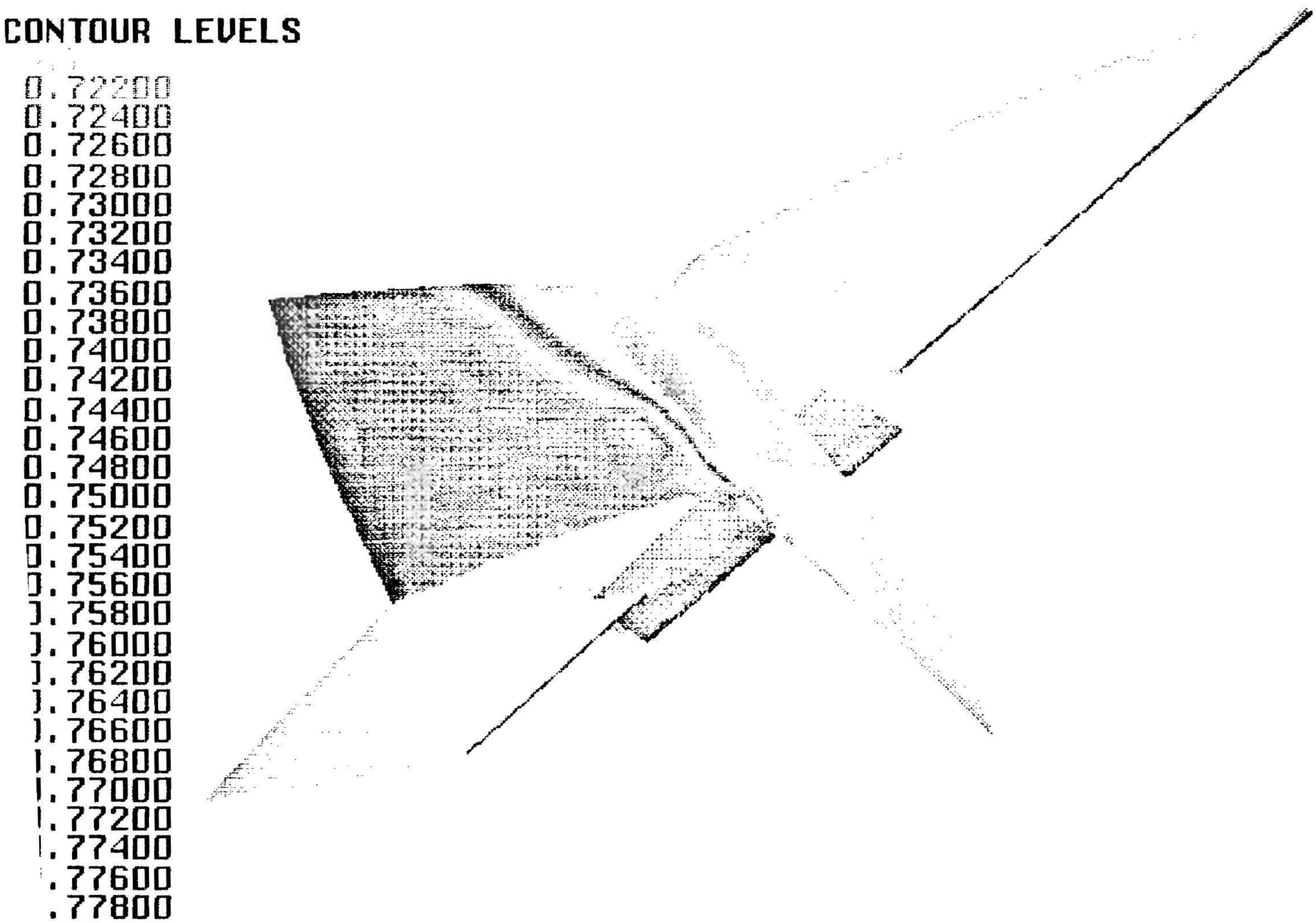

Fig 5: Spanwise flow visualization, with flap deflected

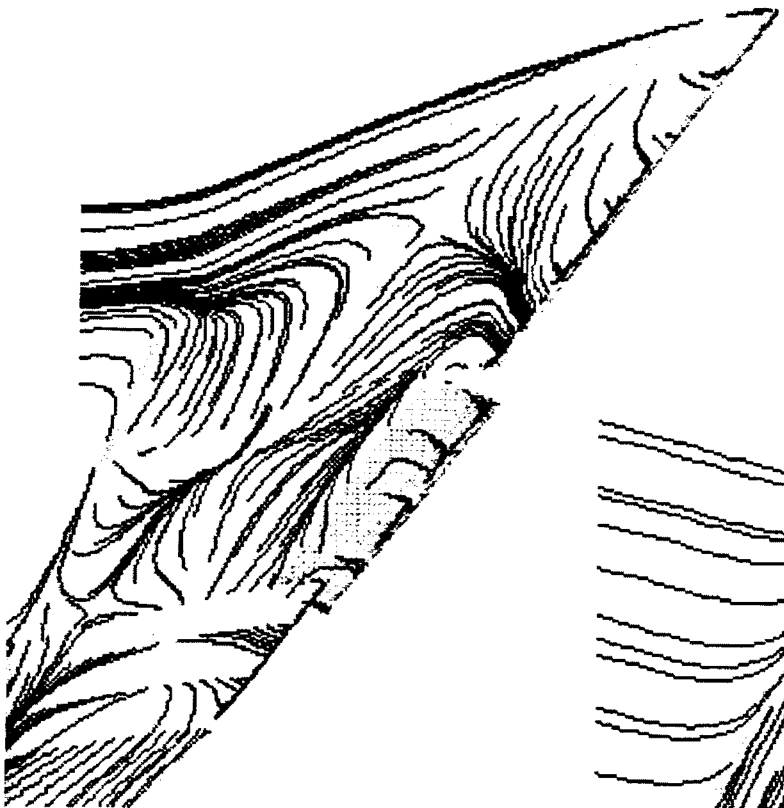

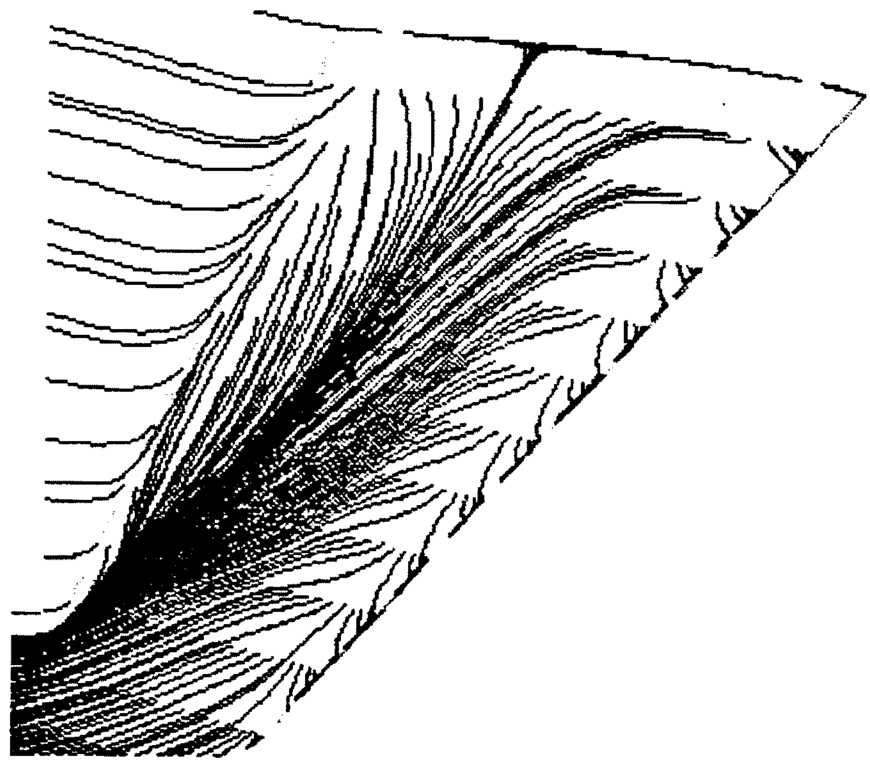

Fig 6: Spanwise flow visualization, clean wing

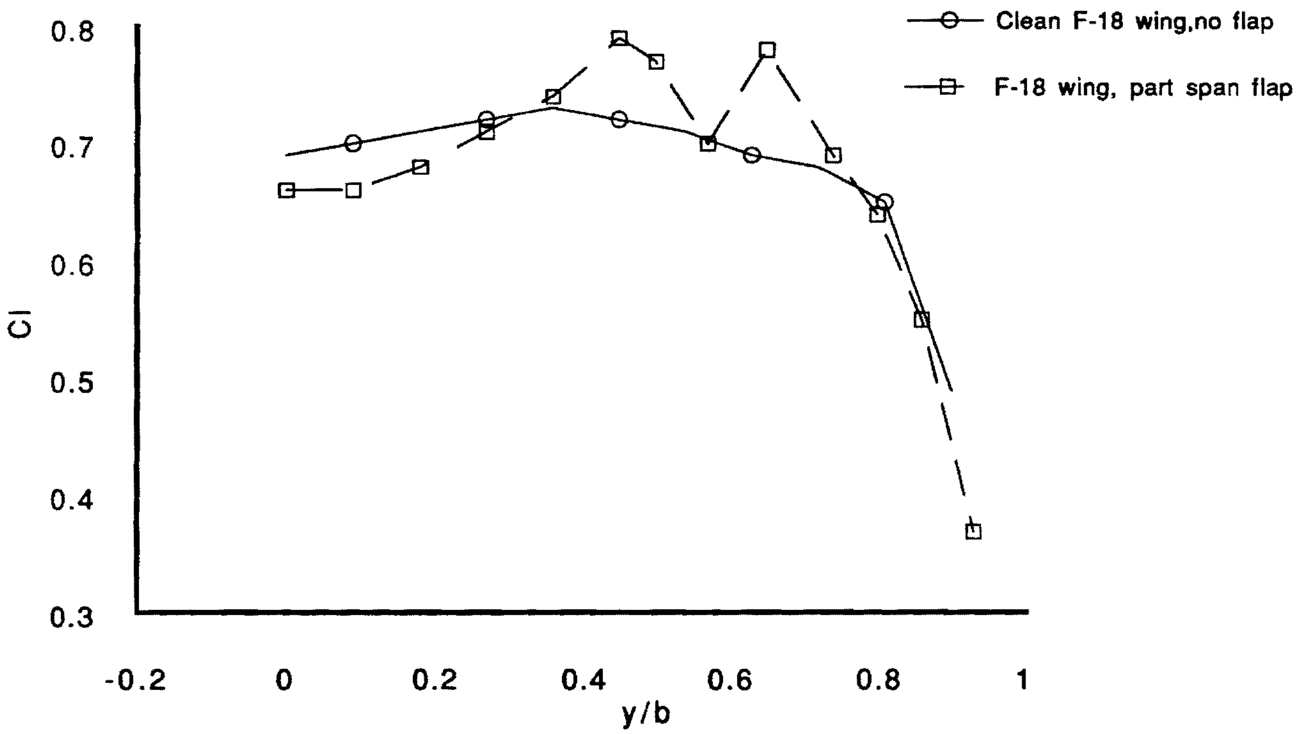

Fig : 7 Spanwise lift distribution, F-18 wing,
alpha = 40 degrees, Re = 20,000., time = 30 units

E16-M07
18

UNSTEADY AERODYNAMIC ANALYSIS OF DUAL-ELEMENT WING CONFIGURATIONS

BI-MONTHLY PROGRESS LETTER FOR THE PERIOD

May 1 - June 30, 1993

Submitted to the

NAVAL AIR WARFARE CENTER
AIRCRAFT DIVISION
WARMINSTER, PA

Attn: Mr. Marvin M. Walters

Prepared By

L. N. Sankar
Professor
School of Aerospace Engineering
Georgia Institute of Technology, Atlanta, GA 30332

July 1993

Georgia Institute of Technology
School of Aerospace Engineering

July 23, 1993

Mr. Marvin M. Walters
Code 6051
Naval Air Development Center
Warminster, PA 18974

Subject: BI-MONTHLY PROGRESS REPORT FOR THE PROJECT "UNSTEADY AERODYNAMIC ANALYSIS OF DUAL-ELEMENT WING CONFIGURATIONS"

Dear Mr. Walters:

During the reporting period (May 1, 1993 - June 30, 1993), the following tasks were completed:

1) As discussed in the previous report, a multi-zone Navier-Stokes solver has been developed to study dynamic lift enhancement concepts. An abstract regarding this work was sent to AIAA Aerospace meeting, Reno 1994 in May 1993 and a copy of the abstract was attached in the previous report.

During the present reporting period some calculations were performed over a F-18 wing for a part span oscillating leading edge flap. The freestream Mach number and Reynolds number are 0.2 and 20,000 respectively. The angle of attack of the wing is 40 degrees and the partial span flap is initially set at 34 degrees relative to the main wing. The flap oscillates at a reduced frequency of 9.424. Fig 1 shows a typical computational grid section in the X-Z plane. The planform is divided in to three spanwise zones. Fig 2 and Fig 3 show the total pressure contours in the X-Z plane on the upper side of the wing at 20% and 50% span stations. Figures 4 (a),(b),(c),(d) and (e) show the time history of the sectional lift coefficient at different span stations. As seen in Figs 4(b) and (c), the lift coefficient peaks at a regular frequency in the flap region due to the vortices generated by flap oscillation. The secondary effect of flap oscillation is felt on the other span sections where there is no flap. This is reflected in the small oscillations in the lift coefficient as in Fig 4 (a),(b). The Figures 5 (a), (b), (c), (d) and (e) show the variation of Cl over a longer period of time of about 50 convective time units. As expected no significant variation of the mean lift coefficient with time is seen.

The time variation of sectional lift coefficient at different span stations was plotted for the case of a stationary flap and the results are shown in Figures 7 (a),(b)..(e). The other flow parameters like Mach number, Reynolds number and angle of attack were the same as in the first case. The mean lift coefficient was compared in the two cases, one being the stationary flap and the other an oscillating flap and is shown in Fig 6. No significant enhancement in the mean lift coefficient was seen by oscillating the flap, though there were intermittent peaks in lift coefficient at a regular frequency. Some of these results were faxed to Dr. W.Tseng during June-July '93.

At present this Navier-Stokes solver has an algebraic Baldwin-Lomax turbulence model to simulate turbulence effects. As seen in other calculations this algebraic model works well for attached flows or flows with small separation, but for massively separated flows a better turbulence model like the K-e model may be required. A two equation K-ε turbulence model has been incorporated in to the present solver. We are working on improving the stability characteristics of the k-e solver, and to ensure that the computed k and ε fields are independent of the arbitrary initial levels prescribed by the user.

We are also in the process of calibrating the present version of the multizone code with some existing experimental data and numerical calculations for oscillating control surfaces given in the AIAA paper 93-3363. We anticipate that these calibration studies will be completed in time for the Aerospace Sciences Meeting in Reno in January 1994.

2) Mr. Olympio Mello has nearly completed work on the numerical simulation of helicopter rotors operating in the vicinity of an aircraft carrier deck. In the appendix, a report summarizing all the work done to date is enclosed, along with an abstract we have submitted to an American Helicopter Society

Aeromechanics Meeting to be held in January 1994. This report includes the following new results:

(a) We have validated the prescribed wake portion of the rotor-ship-airwake interaction code by comparing the induced velocities near the rotor disk for some representative configurations, with measured data. Good agreement is observed.

(b) The correction to the rotor inflow due to the presence of the ship has been modeled from first principles, using a source panel representation of the ship.

With best wishes,

Sincerely,

LAKSHMI N. SANKAR
Professor

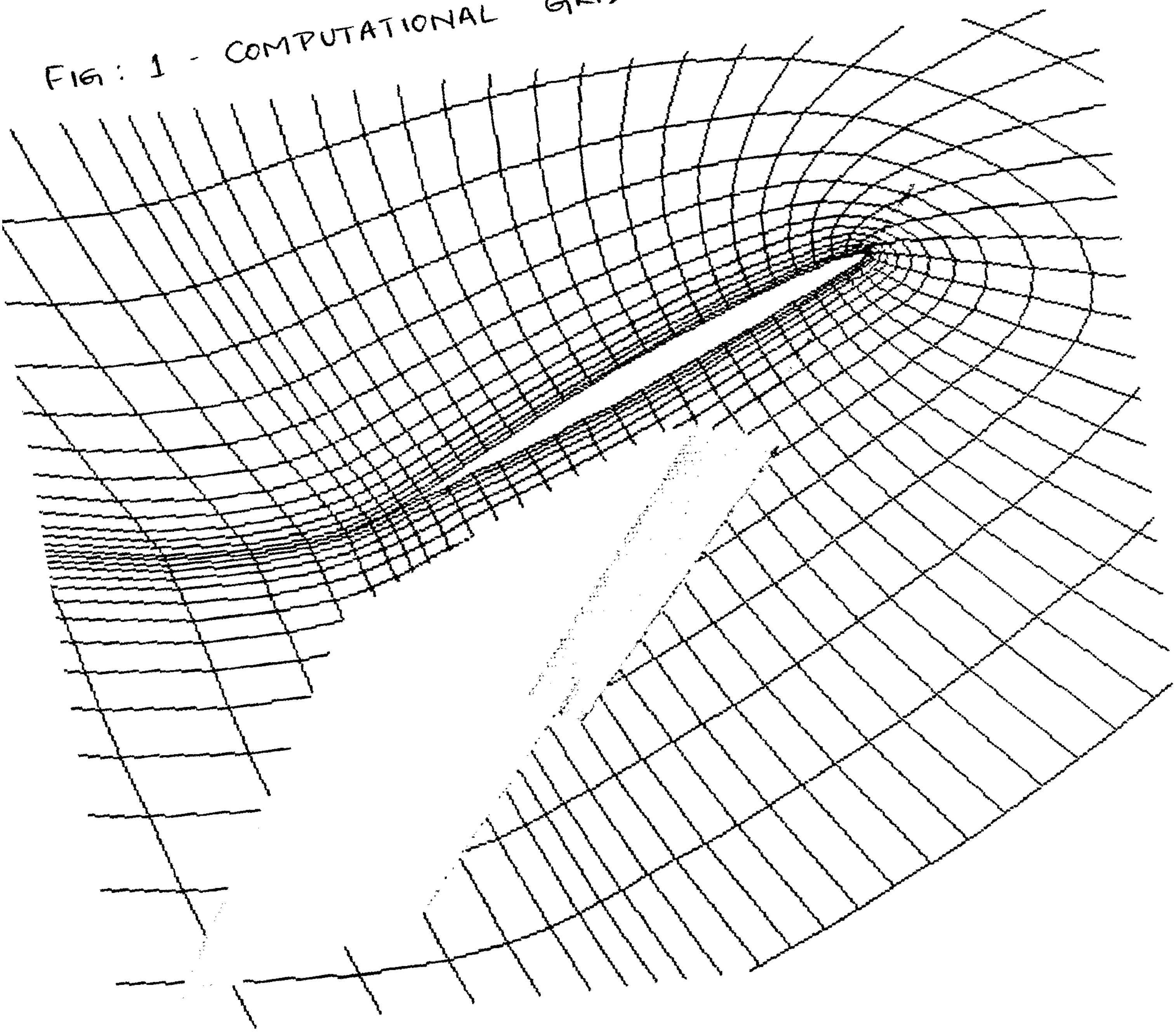

FIG: 1 - COMPUTATIONAL GRID IN X-Z PLANE

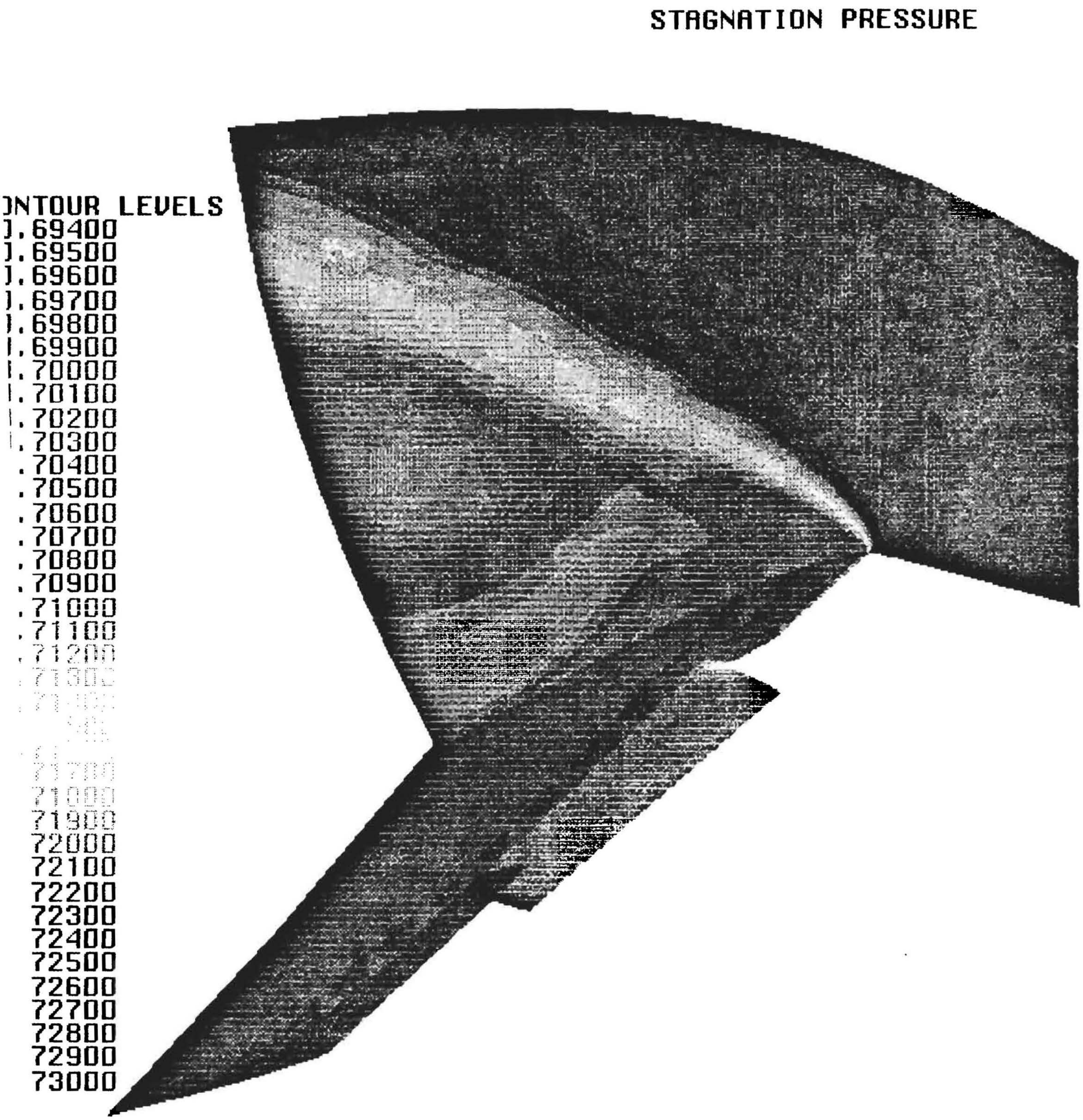
STAGNATION PRESSURE
NTOUR LEVELS
.69400
.69500
.69600
.69700
.69800
.69900
.70000
.70100
.70200
.70300
.70400
.70500
.70600
.70700
.70800
.70900
.71000
.71100
.71200
.71300
71700
71900
72000
72100
72200
72300
72400
72500
72600
72700
72800
72900
73000

FIG: 2.

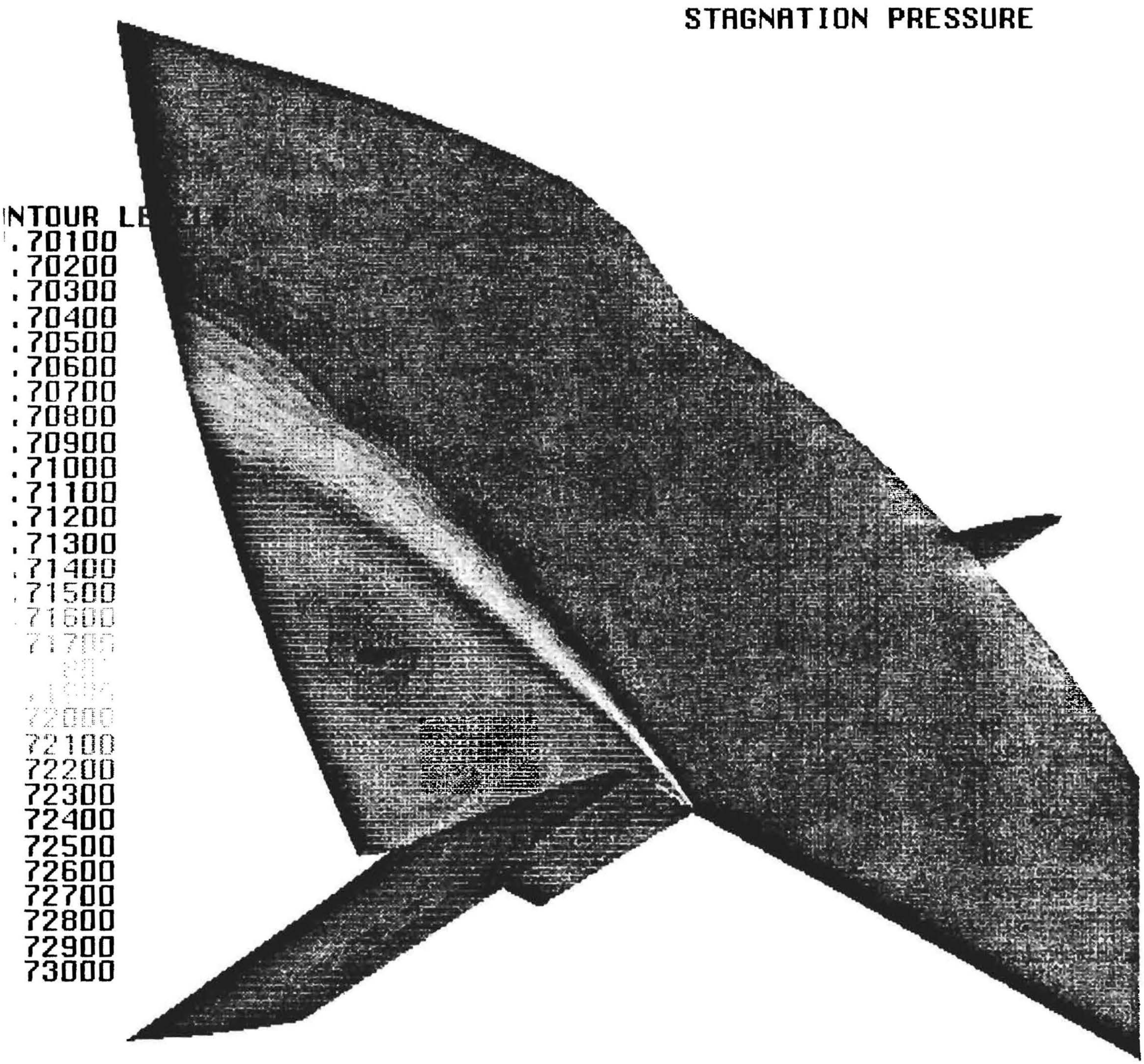
STAGNATION PRESSURE
.70100
.70200
.70300
.70400
.70500
.70600
.70700
.70800
.70900
.71000
.71100
.71200
.71300
.71400
.71500
.71600
72000
72100
72200
72300
72400
72500
72600
72700
72800
72900
73000

FIG: 3.

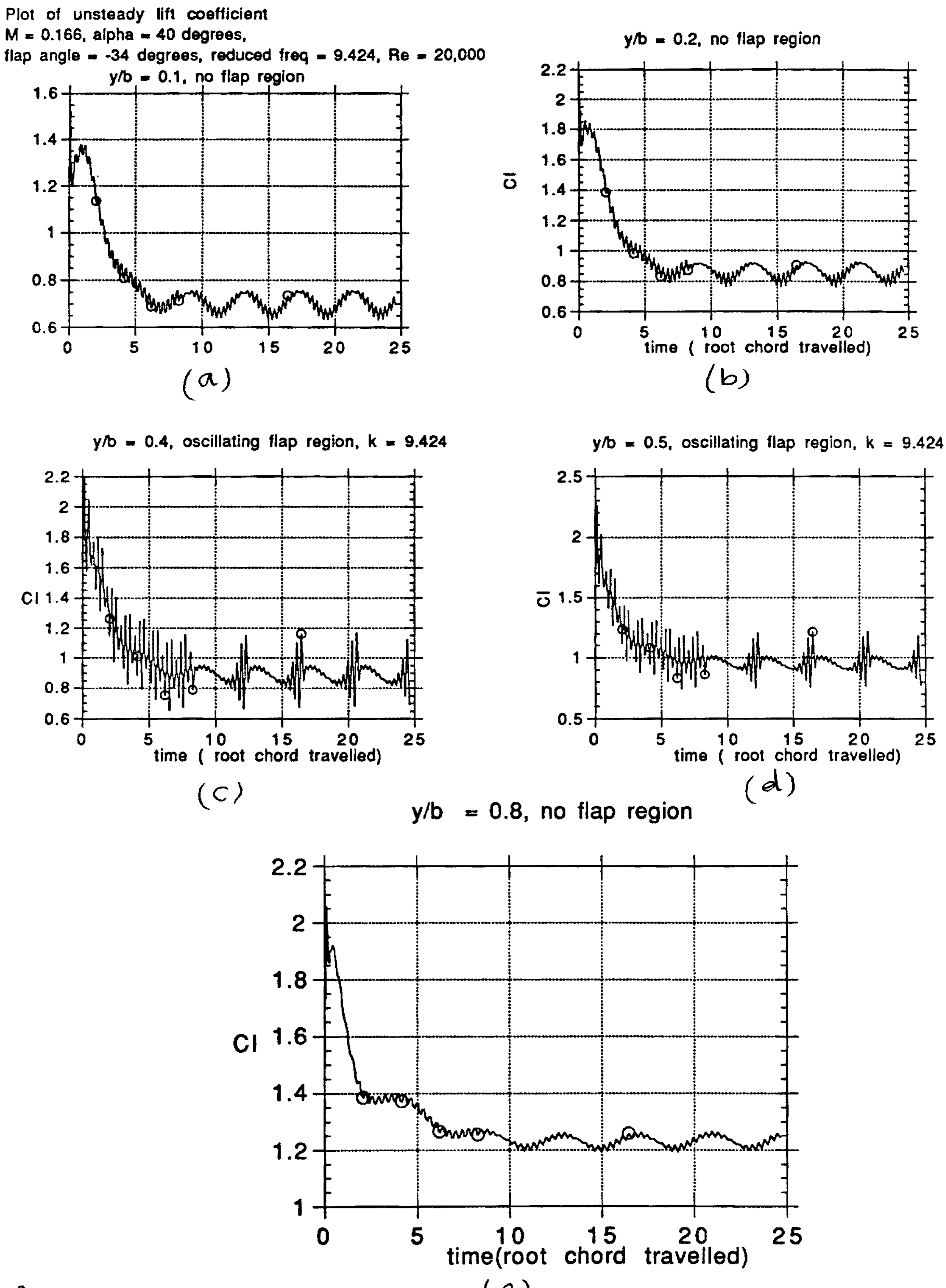
Plot of unsteady lift coefficient
M = 0.166, alpha = 40 degrees,
flap angle = -34 degrees, reduced freq = 9.424, Re = 20,000
y/b = 0.1, no flap region
(a)
y/b = 0.2, no flap region
Cl
time (root chord travelled)
(b)
y/b = 0.4, oscillating flap region, k = 9.424
Cl
time (root chord travelled)
(c)
y/b = 0.5, oscillating flap region, k = 9.424
Cl
time (root chord travelled)
(d)
y/b = 0.8, no flap region
Cl
time(root chord travelled)
(e)

FIG : 4

TIME HISTORY OF SECTIONAL LIFT COEFFICIENT
M = 0.1666, ALPHA = 40.0 DEGREES,FLAP ANGLE = -34.0 DEGREES
Re = 20,000, REDUCED FREQUENCY = 9.424

y/b = 0.0

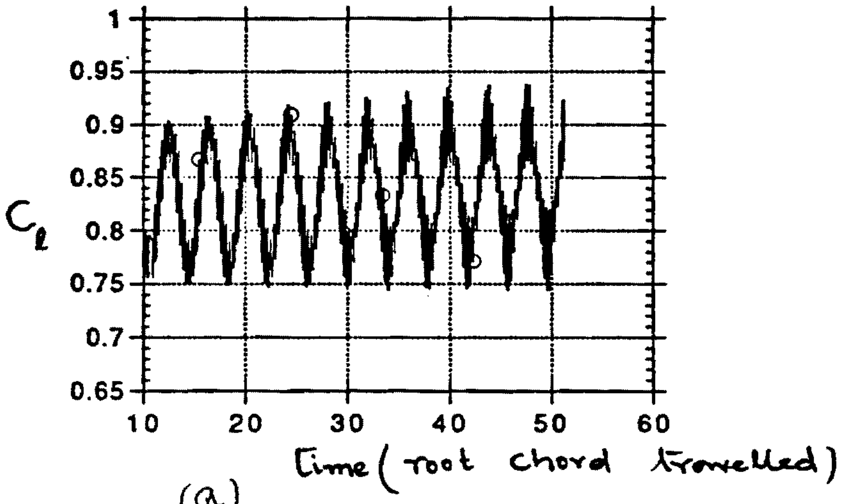

(a)

y/b = 0.3

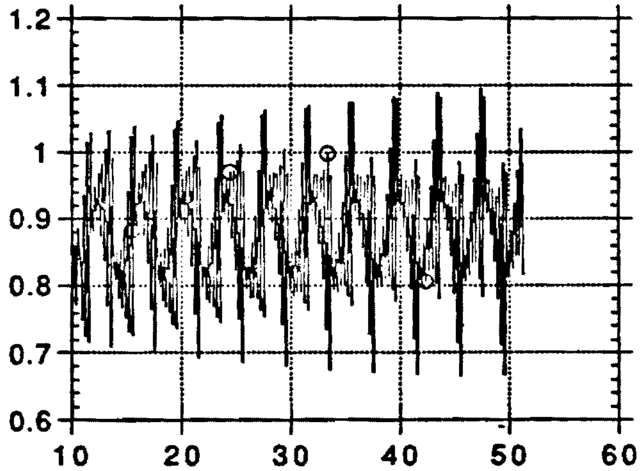

(b)

y/b = 0.7

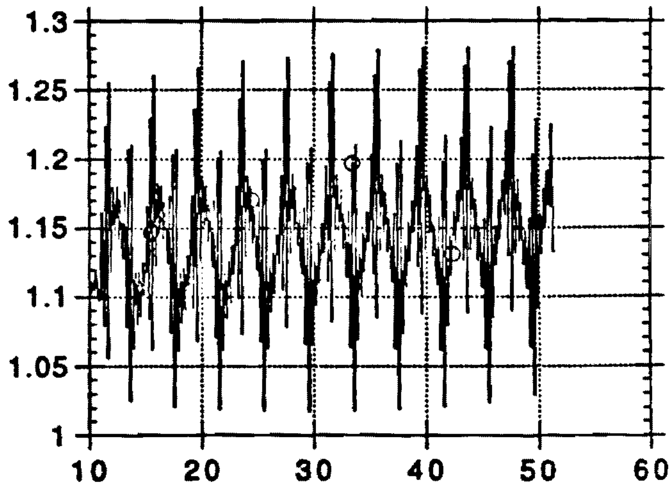

FIG : 5

(c)

Cl vs time, dt = 0.01, multi zone solver

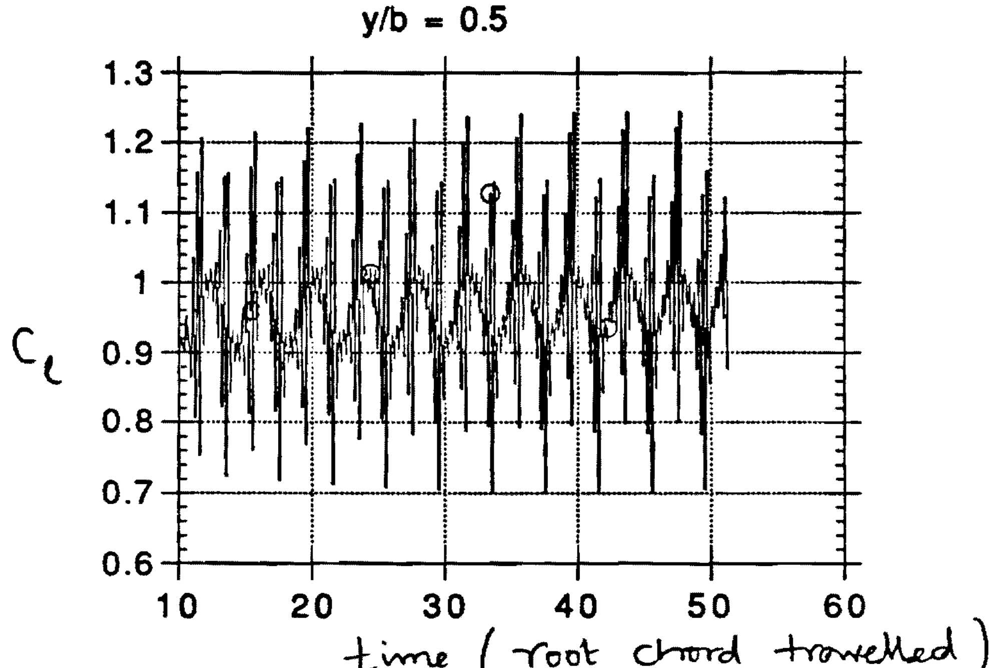

(e)

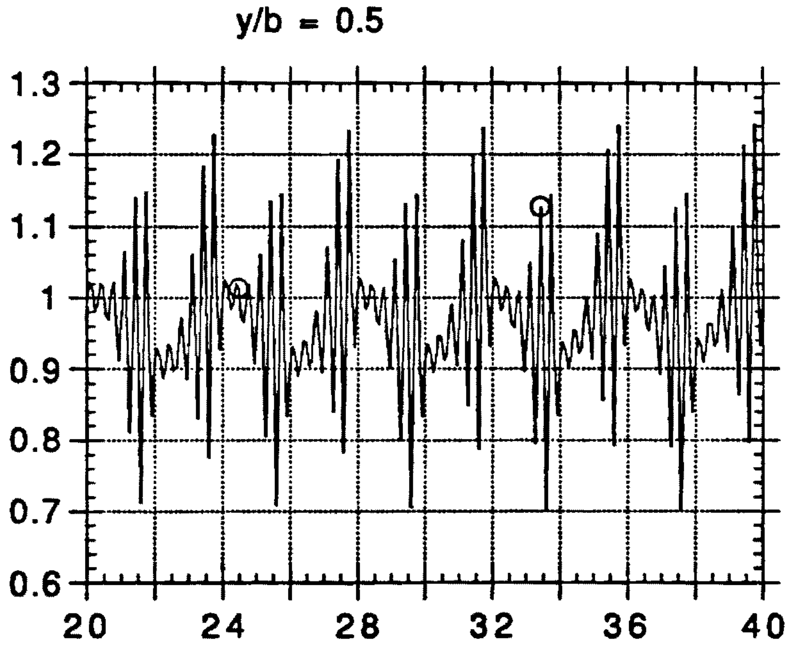

(f)

FIG: 5

COMPARISON OF MEAN SPANWISE LIFT COEFFICIENT BETWEEN OSCILLATORY AND STEADY PARTIAL SPAN FLAP, M = 0.16, ALPHA = 40 DEGREES,F-18 WING

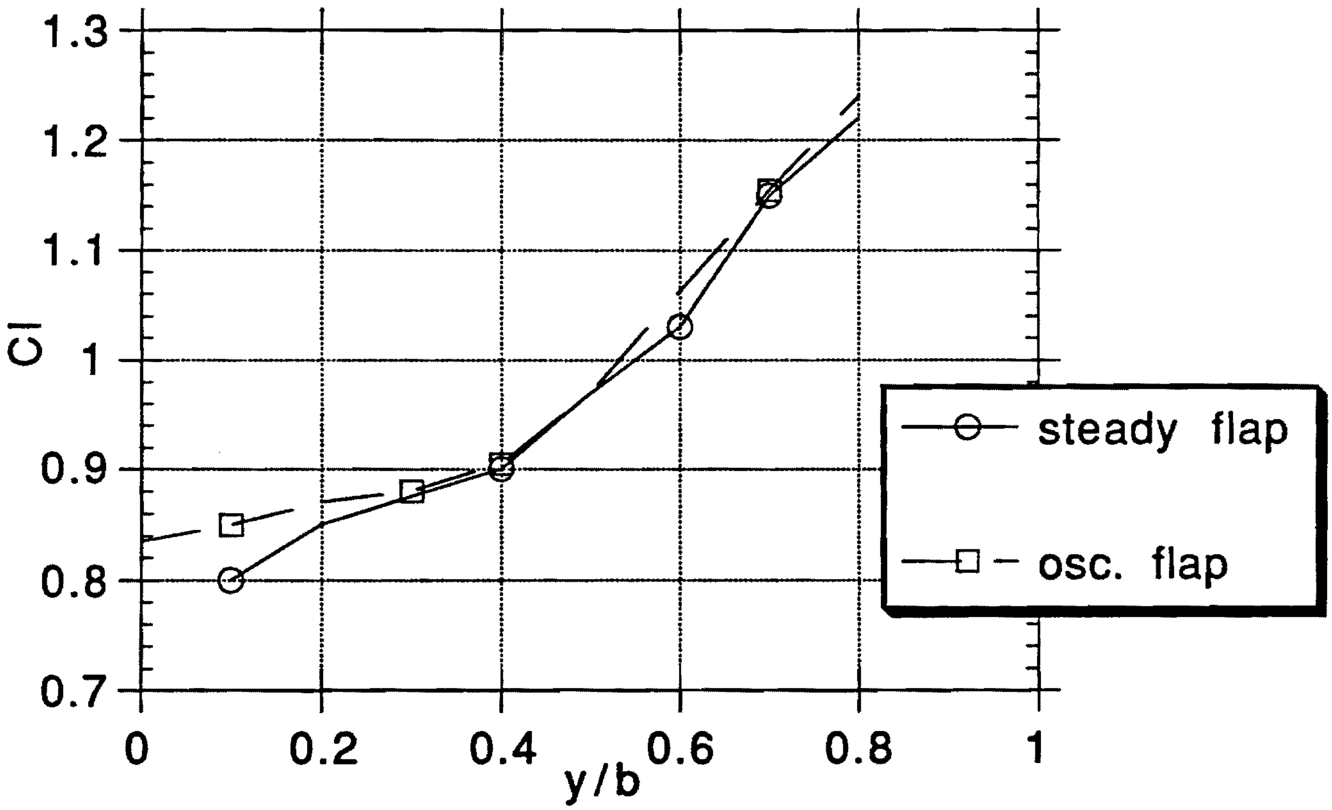

FIG: 6

TIME HISTORY OF SECTIONAL LIFT COEFFICIENT
M = 0.1666, ALPHA = 40.0 DEGREES,FLAP ANGLE = -34.0 DEGREES
Re = 20,000, STATIONARY FLAP

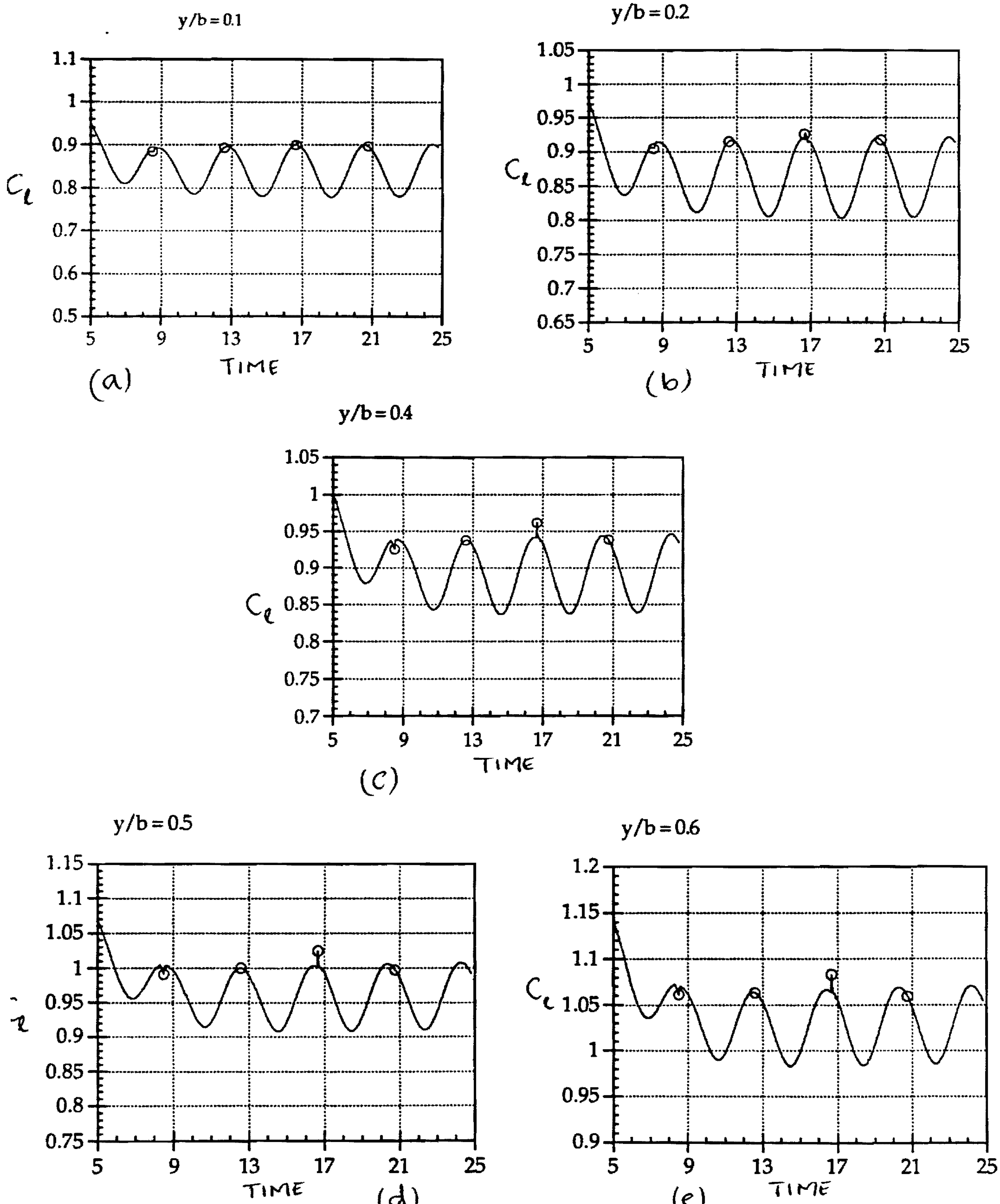

FIG: 7

APPENDIX

NUMERICAL SIMULATION OF HELICOPTER / SHIP AIRWAKE INTERACTIONS

by

Olympio A. F. Mello
Graduate Research Assistant

and

Lakshmi N. Sankar
Professor

School of Aerospace Engineering
Georgia Institute of Technology
Atlanta, GA 30332-0150

July 1993

1. Introduction

Landing a helicopter on a ship deck can be a hazardous process. The determination of safe operating envelopes has been done at sea by the Naval Air Test Center in a lengthy and expensive process [1]. This fact suggests a need for an appropriate helicopter/ship interference model to be incorporated into rotorcraft simulation codes.

There are several aspects that contribute to the complexity of the problem, namely:

1. Sea and ship motions;
2. Atmospheric turbulence;
3. Ship aerodynamics;
4. Helicopter motion itself, in the presence of the ship.

The sea and ship motions can be modeled to a reasonable degree [1]. Their effects on the helicopter have to be investigated. The only effect of the sea motion on the helicopter would be in the extent that it modifies the ground effect, but this change may be regarded as negligible with respect to the other factors involved. The ship motion will have a more significant effect on the ship/helicopter interference and has to be considered.

Statistical atmospheric turbulence models are also available, and may be considered as user-prescribed for simulation purposes.

The ship aerodynamics is very complex. The flow around the superstructure is characterized by turbulence and vortex shedding. The turbulence level in the atmosphere also affects the flow. The knowledge about this type of flow is mostly empirical and based on building aerodynamics. Few wind-tunnel investigations have been performed to measure the flow about ships [2]. For the purposes of analysis, the effects of ship aerodynamics on the helicopter can be divided into the "airmass displacement effect" due to the proximity between the rotor and the ship surface, and the ship-induced turbulence effect. The ship airmass displacement effect may be modeled under the assumption of attached flow around the ship, which in turn is modified by the helicopter presence. The turbulence effect has to be modeled statistically, and included in the simulation as an additional turbulent air velocity contribution to be added to the helicopter model.

The simulation of helicopter motion can be carried out by a standard helicopter simulation code, if the effects discussed above are included. The simulation program must therefore be able to:

1. Include the ground effect due to the sea, with the sea surface considered as fixed;

2. Include air velocity contributions due to the atmospheric turbulence and ship-induced turbulence, which combine to form the turbulent ship airwake, considered to be prescribed. This influence may be taken into account as an additional inflow term, which in turn implies that a non-uniform, time-dependent inflow model such as a dynamic inflow model [3] is necessary for consistency;

3. Include the ship airmass displacement effect, as discussed above. For this purpose, a panel method representation of the ship surface may be used, and the effect of the ship on the rotor is modeled by the induced velocity field produced by the ship's panels. It must be noted that for the computation of the flow around the ship using a panel method, the flow due to the rotor and its wake have to be considered.

In this report, these three aspects will be discussed in more detail concerning their implementation in a helicopter simulation code. More specifically, our discussion will emphasize the implementation on the GENHEL simulation code [4].

2. Ground Effect

As an initial effort, the ground effect in forward flight was analyzed. The first analysis of ground effect in hover is probably due to Betz [5], who used the method of images. Subsequent analyses for forward flight (e.g. [6], [7]) used the same concept. Cheeseman and Bennett [6] derived an expression for the inflow correction and compared their results with flight test data, reaching a good correlation. In this model, a ground effect correction factor, K_{GE}, is introduced as:

$$K_{GE} = 1 - \frac{1}{16\,(z/R)^2}\cos^2\left(\tan^{-1}(\mu/\lambda_{i0}) - \alpha_{TPP}\right) \qquad (2.1)$$

where z is the height of the rotor above the ground, R is the rotor radius, μ is the non-dimensional forward velocity, λ_{i0} is the induced inflow ratio when the helicopter is away from the ground and α_{TPP} is the Tip-Path-Plane (TPP) angle of attack. This correction factor is applied to the total inflow ratio through the TPP as a multiplication factor, yielding the inflow ratio in ground effect.

Further experimental investigations provided more insight into the physics of ground effect. In particular, the experiments carried out by Sheridan and Wiesner [8] and Curtiss et al. [9] showed the need for the modeling of the ground vortex generated by the forward portion of the rotor wake impinging on the ground. A simple model for taking this effect into account was suggested in the latter reference. It should be noted that the experiments have shown that the ground vortex appears for a specific range of forward velocities, and of course when the helicopter is close enough to the ground.

More recently, Curtiss et al. [10] performed another experimental and analytical analysis of the problem. They used force and moment measurements in order to obtain harmonic inflow coefficients, with limited success.

As a first approximation, the simple correction first proposed by Cheeseman and Bennett [6] may be used, as it was shown to give reasonable results, is simple and suitable for a local correction as discussed above. Note that a similar ground effect correction is used in the 2GCHAS code [11]. If flight test data are available for the specific helicopter, a semi-empirical expression may be used instead of Eq. (2.1). This is the approach used in the helicopter simulation code GENHEL [4], where flight test data obtained for the UH-60 are used. The ground vortex is not particularly relevant in this case because the helicopter would approach the ship at a height above the sea for which the ground vortex would not have been formed, and when the helicopter is close enough to the ship to see its deck as the "ground", its velocity would have been reduced and again the conditions for the formation of the ground vortex would not be met.

Although this simple correction is suitable for local application, its accuracy for this purpose has not been well established. Since a rotor wake model is necessary to obtain the velocities induced by the rotor and its wake on the ship, a better choice may be to modify the wake model to include the ground effect, at the expense of additional computational effort, but providing a more consistent overall model.

3. Dynamic Inflow Model

As discussed above, a non-uniform, time-dependent inflow model such as a dynamic inflow model [3] is indicated in order to provide a consistent treatment where time-dependent turbulent inflow contributions are included. Therefore, our second effort was implementing such a dynamic inflow model into the GENHEL simulation code [4].

In the derivation of the dynamic inflow model [12-15], the rotor is considered as an actuator disk, around which an acceleration potential solution is found analytically in terms of associated Legendre functions expressed in ellipsoidal coordinates. The velocity field is related to the acceleration potential using the continuity and momentum equations. The resulting relations between the inflow through the disk and the pressure distribution are then used to obtain the matrices of coefficients of a system of first order ordinary differential equations involving the coefficients of the assumed harmonic inflow representation and its time derivatives. Details of the derivation are given in the cited references.

The inflow model to be used may be of arbitrary order, a higher-order model in general providing higher accuracy but being more computationally expensive. In the present work, we opt for a first-order model for the following reasons:

1. Since the final objective is real-time simulation, the method is expected to be as fast as possible while giving sufficient accuracy;

2. The structural model presently implemented in GENHEL uses rigid blades, which is a "zeroth-order" elastic model. It would seem that using a higher-order inflow model while retaining the lower-order elastic model would be inconsistent and most likely no improvement would be obtained over the first-order model. The higher-order inflow models are consistent with higher-order elastic models, which are needed when one is interested in vibrations and aeroelastic studies.

These considerations are supported by extensive studies performed by Dr. William D. Lewis for his Ph.D. research at Georgia Tech [16]. His results are summarized in Ref. [17]. Drs. Lewis and He investigated the effect of inflow models of zeroth to second order coupled with rigid and elastic blade models in Georgia Tech's flight simulator program

(FLIGHTSIM). They concluded that the first-order dynamic inflow model consistently improved the correlation between the simulation and flight test data over an uniform inflow model, while the second-order model improved the correlation in some cases but underestimated transient response in others. From their findings, we conclude that the most important modifications in order to allow a helicopter simulation code to consistently treat time-dependent inflow effects are first-harmonic dynamic inflow and an elastic blade model.

The dynamic inflow model used in this work is the first-order model described by Peters and HaQuang [3], which is expected to provide a significant improvement in the aerodynamic modeling in a helicopter simulation code such as GENHEL while retaining a level of sophistication — and computational cost — consistent with the other components of the simulation code.

3.1. Mathematical Formulation

A throughout description of dynamic inflow modeling, including bibliography and higher-order modeling, is given by He [14]. The first-order dynamic inflow model used here is described by Peters and HaQuang in Ref. [3]. Therefore, only a brief description will be presented here.

The rotor aerodynamics computation in GENHEL is based on the blade-element model, in which the blades are divided into a finite number of segments. Local angle of attack, yaw and Mach number are computed and used to obtain lift and drag coefficients from airfoil experimental data, approximately given in equation form. This is an "instantaneous steady" approach in the sense that no pitch rate terms or unsteady wake effects are taken into account. The downwash (inflow) induced by the rotor wake system is also represented in an instantaneous manner as an additional term in the angle of attack computation. In the current GENHEL implementation, the inflow model has a first harmonic variation over the rotor disk (Glauert downwash factors).

In order to more accurately represent the unsteady nature of the flow over the rotor blade, the pitch rate term should be included in the local effective angle of attack and the effect of the unsteady wake should be taken into account in the inflow. While the effect of the wake for unsteady two-dimensional airfoil motion has been known for many years, its application to rotors is not straightforward, not only because of the three-dimensional effect, but mainly because of the distorted helical wake generated by the rotor.

Efforts to construct a suitable unsteady aerodynamics model for rotors have been numerous (see Ref. [14] for a review of the most significant models). Among those, the dynamic inflow model emerged as a very adequate model for aeroelastic and flight dynamics applications, because it is simple to implement and represents to an acceptable accuracy the main unsteady rotor wake effects. The wake vorticity depends on the rotor aerodynamic loads and in turn induces a non-uniform inflow over the rotor disk. This non-uniform inflow distribution is represented by a sum of a finite number of harmonics of blade azimuth, of which the multiplying coefficients are time-dependent and radial variations are accounted for by shape functions, i.e.,

$$\lambda\,(r,\psi,t) = \nu_0\,(t) + \sum_{n=1}^{N} \chi_n\,(r)\left[\nu_{ns}\,(t)\sin(n\psi) + \nu_{nc}\,(t)\cos(n\psi)\right] \tag{3.1}$$

By expressing the pressure distribution over the rotor disk in terms of an acceleration potential, which is expanded in Legendre functions in terms of ellipsoidal coordinates, and integrating the momentum equation along the streamwise direction [14], the coefficients in the inflow expansion (3.1) can be related to the aerodynamic loads by a system of first-order ordinary differential equations:

$$[M]\frac{1}{\Omega}\{\dot{\nu}\} + [L]^{-1}\{\nu\} = \{\tau\} \tag{3.2}$$

where the dot in $\{\dot{\nu}\}$ denotes time derivative and $\{\tau\}$ is a vector obtained from integrals of the pressure distribution over the rotor disk. In the first-order dynamic inflow used here [3], the inflow expansion reduces to

$$\lambda\,(r,\psi,t) = \lambda_0\,(t) + \lambda_s\,(t)\frac{r}{R}\sin(\psi) + \lambda_c\,(t)\frac{r}{R}\cos(\psi) \tag{3.3}$$

and the system of equations (3.2) becomes

$$[M]\frac{1}{\Omega}\begin{Bmatrix}\dot{\lambda}_0\\ \dot{\lambda}_s\\ \dot{\lambda}_c\end{Bmatrix} + [\hat{L}]^{-1}\begin{Bmatrix}\lambda_0\\ \lambda_s\\ \lambda_c\end{Bmatrix} = \begin{Bmatrix}C_T\\ -C_1\\ -C_2\end{Bmatrix}_{aero} \tag{3.4}$$

where C_T, C_1 and C_2 are the instantaneous rotor thrust, and rolling and pitching moment coefficients, respectively. The subscript "aero" denotes that only aerodynamic contributions are considered in these coefficients. Note that equations (3.3) and (3.4) are expressed in the tip-path-plane axes system. The matrices [M] and $[\hat{L}]$ are given in Ref. [3]. The matrix [M] is given as:

$$[M] = \begin{bmatrix} \frac{8}{3\pi}(*) & 0 & 0 \\ 0 & \frac{16}{45\pi} & 0 \\ 0 & 0 & \frac{16}{45\pi} \end{bmatrix} \tag{3.5}$$

(*) $\frac{128}{75\pi}$ for twisted rotors

The matrix $[\hat{L}]^{-1}$ was obtained analytically as:

$$[\hat{L}]^{-1} = \frac{1}{EF} \begin{bmatrix} V_T DE & V_T BE \sin\Delta & V_T BE \cos\Delta \\ -VBE\sin\Delta & V\left(F\cos^2\Delta + \frac{E}{2}\sin^2\Delta\right) & -VG\sin\Delta\cos\Delta \\ -VBE\cos\Delta & -VG\sin\Delta\cos\Delta & V\left(F\sin^2\Delta + \frac{E}{2}\cos^2\Delta\right) \end{bmatrix} \tag{3.6}$$

where we follow the notation used in Ref. [3], i.e., Δ is the angle between the projection of the forward velocity on the rotor disk and the zero-azimuth line, $V_T = \sqrt{\lambda^2 + \mu^2}$ is the total nondimensional inflow through the disk, V is a mass-flow parameter defined by

$$V = \frac{\mu^2 + \lambda(\lambda+\lambda_m)}{V_T} \tag{3.7a}$$

with λ_m being defined as the average induced inflow over the rotor disk. If we denote by α the wake angle with respect to the rotor disk, the remaining quantities in Eq. (3.6) are defined as:

$$B = \frac{15\pi}{64}\sqrt{\frac{1-\sin\alpha}{1+\sin\alpha}} \; ; \; D = \frac{4\sin\alpha}{1+\sin\alpha} \; ; \; E = \frac{4}{1+\sin\alpha} \tag{3.7b,c,d}$$

$$F = B^2 + \frac{D}{2} \quad ; \quad G = F - \frac{E}{2} \tag{3.7e,f}$$

3.2. Transformations Needed to Implement the Dynamic Inflow Model in GENHEL

In order to time-integrate the inflow-state equation (3.4), the rotor aerodynamic forces and moments are needed. These are computed by expressions similar to those used in Ref. [4], but taking into account only the aerodynamic contributions. The resulting forces and moments are denoted as in Ref. [4], with the addition of a subscript "A", i.e., forces T_{HA}, H_{HA} and J_{HA} and moments M_{HA}, L_{HA} and Q_{HA}. As mentioned above, equations (3.3) and (3.4) are expressed in the tip-path-plane axes system. GENHEL, in turn, uses the fixed shaft axes system. The corresponding transformation of coordinates is:

$$\begin{bmatrix} H_{HA} & L_{HA} \\ J_{HA} & M_{HA} \\ T_{HA} & Q_{HA} \end{bmatrix}_{TPP} = [T]_{STPP} \begin{bmatrix} H_{HA} & L_{HA} \\ J_{HA} & M_{HA} \\ T_{HA} & Q_{HA} \end{bmatrix}_{S} \tag{3.8}$$

where

$$[T]_{STPP} = \begin{bmatrix} \cos\beta_{1c} & 0 & \sin\beta_{1c} \\ \sin\beta_{1c}\sin\beta_{1s} & \cos\beta_{1s} & -\cos\beta_{1c}\sin\beta_{1s} \\ -\sin\beta_{1c}\cos\beta_{1s} & \sin\beta_{1s} & \cos\beta_{1c}\cos\beta_{1s} \end{bmatrix} \tag{3.9}$$

is the transformation matrix between shaft and tip-path-plane axes and β_{1c} and β_{1s} are the first harmonics flapping coefficients. Referring to the notation used in Ref [4], $\beta_{1c} = -$ A1FMR and $\beta_{1s} = -$ B1FMR. The nondimensional coefficients needed in Eq. (3.4) may be now computed as:

$$C_T = \frac{T_{HA}}{\rho\,\pi\,R^2(\Omega R)^2} \quad ; \quad C_l = \frac{-L_{HA}}{\rho\,\pi\,R^3(\Omega R)^2} \quad ; \quad C_2 = \frac{M_{HA}}{\rho\,\pi\,R^3(\Omega R)^2} \tag{3.10}$$

The nondimensional translational velocity components, μ_{XS}, μ_{YS} and μ_{ZS} in the shaft axes are also transformed to the tip-path-plane axes as needed in the computation of the matrices [M] and $[\hat{L}]^{-1}$:

$$\begin{Bmatrix} \mu_1 \\ -\mu_2 \\ \mu_3 \end{Bmatrix} = [T]_{STPP} \begin{Bmatrix} \mu_{XS} \\ \mu_{YS} \\ \mu_{ZS} \end{Bmatrix} \tag{3.11}$$

where μ_1, μ_2 and μ_3 are the nondimensional translational velocities in the tip-path-plane axes system according to the notation of Ref. [3].

During each simulation frame computation, the nondimensional thrust and moment coefficients are computed according to Eqs. (3.8) and (3.10). At the end of the simulation frame, the matrices [M] and $[\hat{L}]^{-1}$ are computed using the translational velocities computed during the frame and transformed using Eq. (3.11). Then the new inflow states λ_0, λ_s and λ_c corresponding to the end of the simulation frame are obtained from explicit first-order integration of Eq. (3.4). These new inflow states will be used for the computation of inflow distribution over the disk at the next simulation frame. Since GENHEL uses all velocities in the shaft axes system, the inflow must be transformed as:

$$\begin{Bmatrix} U_{WX} \\ U_{WY} \\ U_{WZ} \end{Bmatrix}_S = [T]^{-1}_{STPP} \begin{Bmatrix} 0 \\ 0 \\ \lambda\,(r,\psi) \end{Bmatrix} = \begin{Bmatrix} -\lambda \sin\beta_{1c} \cos\beta_{1s} \\ \lambda \sin\beta_{1s} \\ \lambda \cos\beta_{1c} \cos\beta_{1s} \end{Bmatrix} \tag{3.12}$$

When the inflow is transformed to the blade axes according to Ref. [4], the resulting total downwash contributions at the rotor disk [4, p.5.1-21] become:

$$\begin{aligned} UPDMR_I = \left(\lambda_\xi + y_{2IS}\,\lambda_y\right) \Big[&-\sin\beta \cos(\psi+\delta) \sin\beta_{1c} \cos\beta_{1s} \\ &-\sin\beta \sin(\psi+\delta) \sin\beta_{1s} - \cos\beta \cos\beta_{1c} \cos\beta_{1s} \Big] \end{aligned} \tag{3.13}$$

$$UTDMR_I = \left(\lambda_\xi + y_{2IS}\,\lambda_y\right)\left[\sin(\psi+\delta) \sin\beta_{1c} \cos\beta_{1s} - \cos(\psi+\delta) \sin\beta_{1s}\right] \tag{3.14}$$

$$\begin{aligned} URDMR_I = \left(\lambda_\xi + y_{2IS}\,\lambda_y\right) \Big[&\cos\beta \cos(\psi+\delta) \sin\beta_{1c} \cos\beta_{1s} \\ &+\cos\beta \sin(\psi+\delta) \sin\beta_{1s} - \sin\beta \cos\beta_{1c} \cos\beta_{1s} \Big] \end{aligned} \tag{3.15}$$

where

$$\lambda_\xi = \lambda_0 + \xi\left(\lambda_s \sin\psi + \lambda_c \cos\psi\right) \tag{3.16}$$

$$\lambda_y = \lambda_s \sin(\psi + \delta) + \lambda_c \cos(\psi + \delta) \tag{3.17}$$

These inflow contributions are used to compute the local angle of attack as described in Ref. [4]. In addition, the pitch rate term must be included in the effective angle of attack. Following the notation of Ref. [4]:

$$\Delta\alpha_{\text{pitch rate}} = \frac{c_{y_{IS}}}{2}\frac{\dot{T}_{H0AMR_{IB}}}{U_{T_I}} = \frac{c_{y_{IS}}}{2\,U_{T_I}}\Omega\left[A_{1S}\sin(\psi_R + \Delta_{SP})_{IB} - B_{1S}\cos(\psi_R + \Delta_{SP})_{IB}\right] \tag{3.18}$$

3.3. Numerical Implementation

The integration of inflow states through first-order explicit integration of Eq. (3.4) is performed at the beginning of each simulation frame, before the blade loop is started and using the inflow derivatives computed at the end of the previous frame. The inflow states λ_0, λ_s and λ_c are denoted by XLAM0, XLAMS and XLAMC, respectively.

The downwash contributions UPD1, UPD2, URD1, URD2, UTD1 and UTD2 are computed using Eqs. (3.13–3.17) for use in the subroutine RADIAL. Note the addition of UTD1 and UTD2 which were not needed in the original code. This requires a modification of RADIAL to include these coefficients in the list of arguments and in the computation of local velocities.

For the inclusion of the pitch rate term, an additional coefficient (denoted by THETAD) including the terms in Eq. (3.18) not dependent on the blade segment is computed prior to calling RADIAL and used as input to that routine, which is also modified to include Eq. (3.18).

The aerodynamic forces and moments needed in Eq. (3.8) are denoted by FHHA, FJHA, FTHA, TMHA, TLHA and TQHA and are computed during the blade loop in ROTOR. After the blade loop is completed, the subroutine DYNINF is called to perform the transformations needed (3.8),(3.11), compute C_T, C_1 and C_2 and the matrices [M] and $[\hat{L}]^{-1}$ using Eqs.(3.5),(3.6), and finally to compute the inflow state derivatives $\dot{\lambda}_0$, $\dot{\lambda}_s$ and

$\dot{\lambda}_c$, denoted by DXLAM0, DXLAMS and DXLAMC in the code. Note that DYNINF uses the flapping coefficients from the previous simulation frame.

The inflow states and their time derivatives and the average inflow λ_m (needed in DYNINF to compute the matrices [M] and $[\hat{L}]^{-1}$ and computed according to Ref. [3] from the inflow states) need to be stored from frame to frame. This is accomplished through EQUIVALENCE statements, by storing them in RC(330) through RC(336).

3.4. Validation

The dynamic inflow implementation described above has been validated by comparing the static trim results with uniform inflow and flight test results presented in Appendix B of Ref. [18] and by comparing the transient response with uniform inflow results. The transient response cases were chosen so as to coincide with some of the test cases used in Ref. [17].

The static trim correlations are presented in Figs. 3.1–3.7. No significant changes were observed in collective, longitudinal cyclic and pedal controls and on pitch attitude. Some additional left lateral cyclic was observed when using the dynamic inflow model, with corresponding changes in roll angle and sideslip. These effects can be attributed to non-uniformity of inflow between the forward and aft portions of the rotor disk which requires the additional lateral cyclic pitch [17]. Note that these effects are not as dramatic as when verified in Ref. [17], probably due to the fact that the uniform inflow version of GENHEL was able to trim the aircraft at values much closer to the flight test data than the test case presented in Ref. [17].

The transient response correlations are presented in Figs. 3.8–3.10. Note that flight test data are not presented here because our validation used simply "perfect" step control inputs, not the actual control time histories as used in Ref. [17]. However, the results obtained herein demonstrate improvements in the transient response similar to those obtained in Ref. [17].

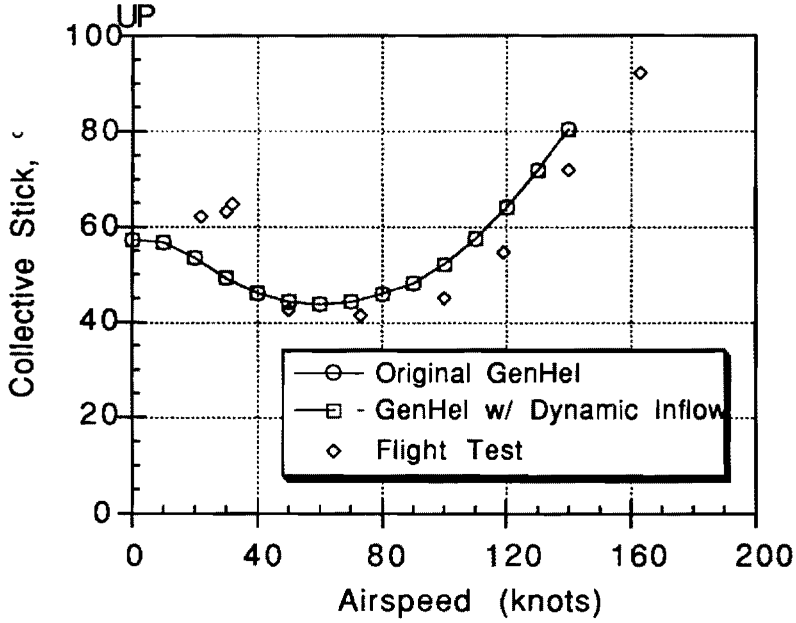

Fig. 3.1: Comparison of Collective Stick Position with Uniform and Dynamic Inflow

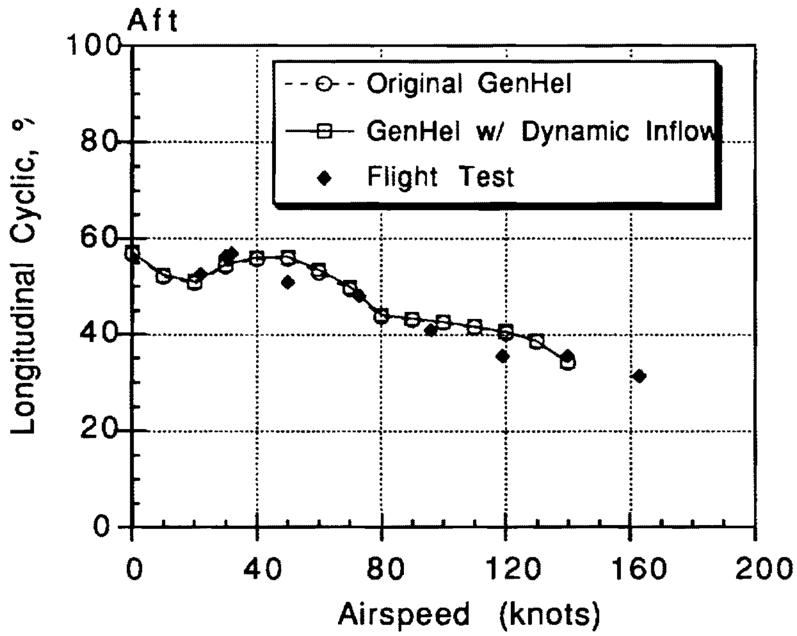

Fig. 3.2: Comparison of Longitudinal Cyclic Pitch with Uniform and Dynamic Inflow

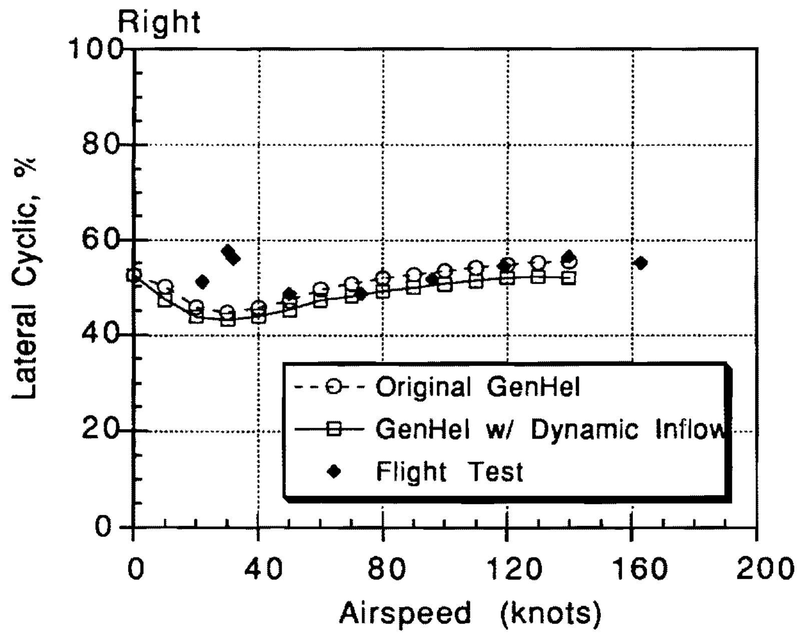

Fig. 3.3: Comparison of Lateral Cyclic Pitch with Uniform and Dynamic Inflow

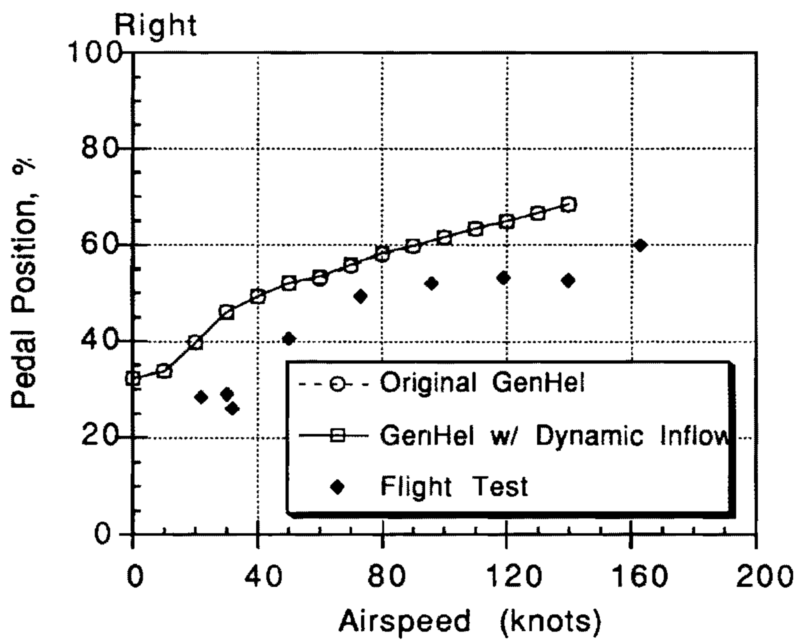

Fig. 3.4: Comparison of Pedal Position with Uniform and Dynamic Inflow

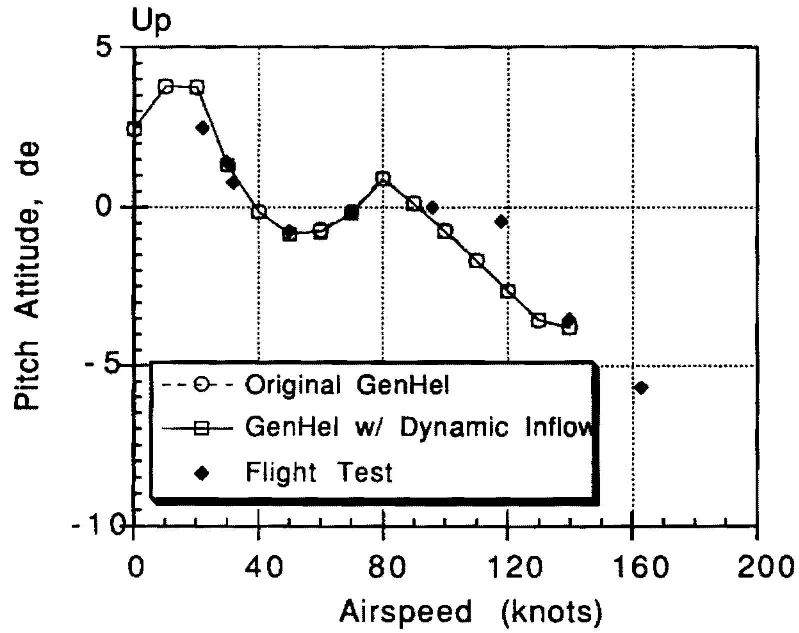

Fig. 3.5: Comparison of Pitch Attitude with Uniform and Dynamic Inflow

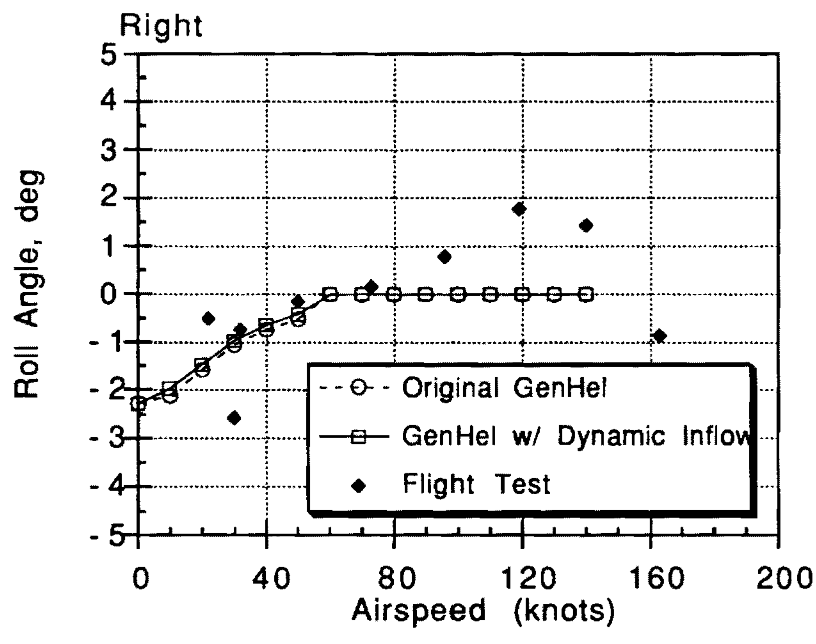

Note: Below 60 kts, GenHel trims the aircraft at zero sideslip and nonzero roll angle; at or above 60 kts, GenHel trims at zero roll angle and nonzero sideslip.

Fig. 3.6: Comparison of Roll Angle with Uniform and Dynamic Inflow

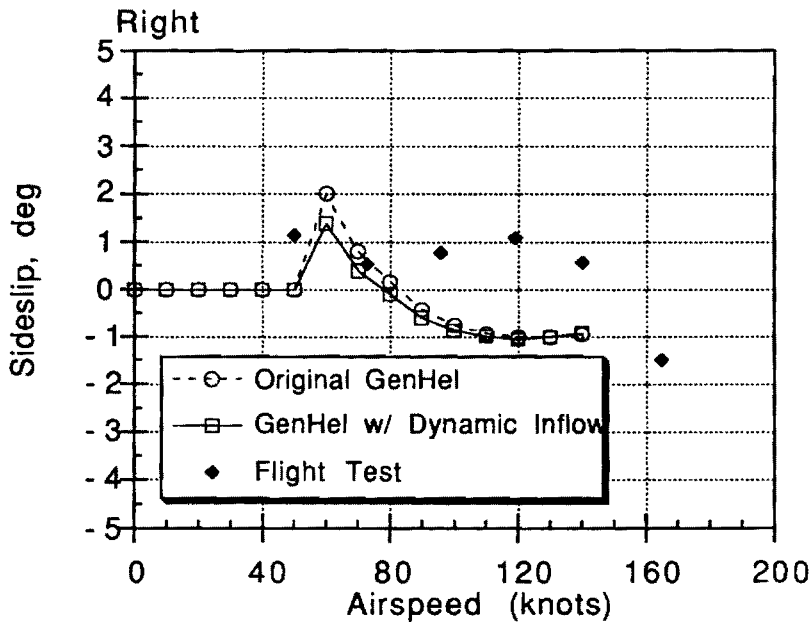

Note: Below 60 kts, GenHel trims the aircraft at zero sideslip and nonzero roll angle; at or above 60 kts, GenHel trims at zero roll angle and nonzero sideslip.

Fig. 3.7: Comparison of Sideslip with Uniform and Dynamic Inflow

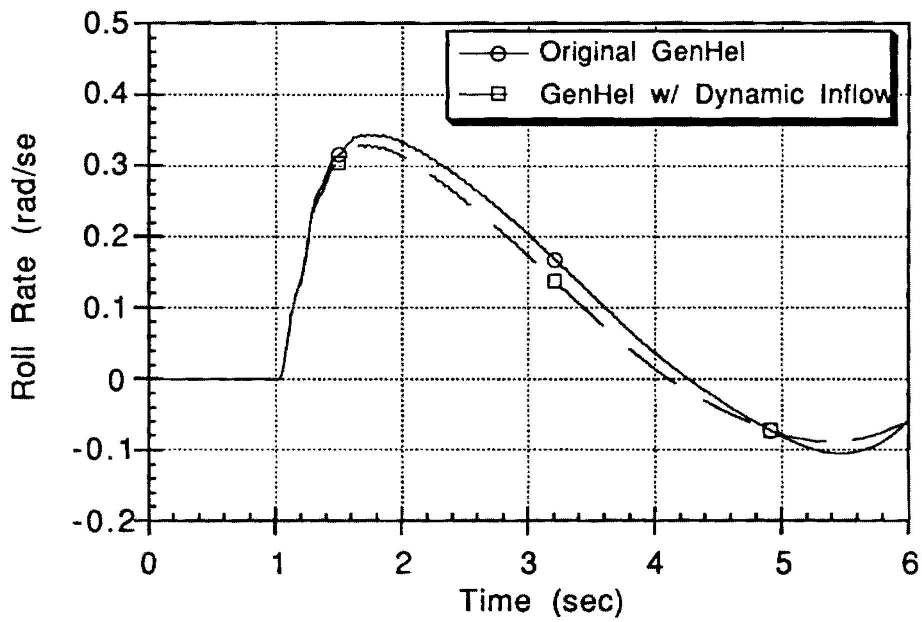

Fig. 3.8: Comparative Response Due to a 1 in. Lateral Cyclic Step in Hover

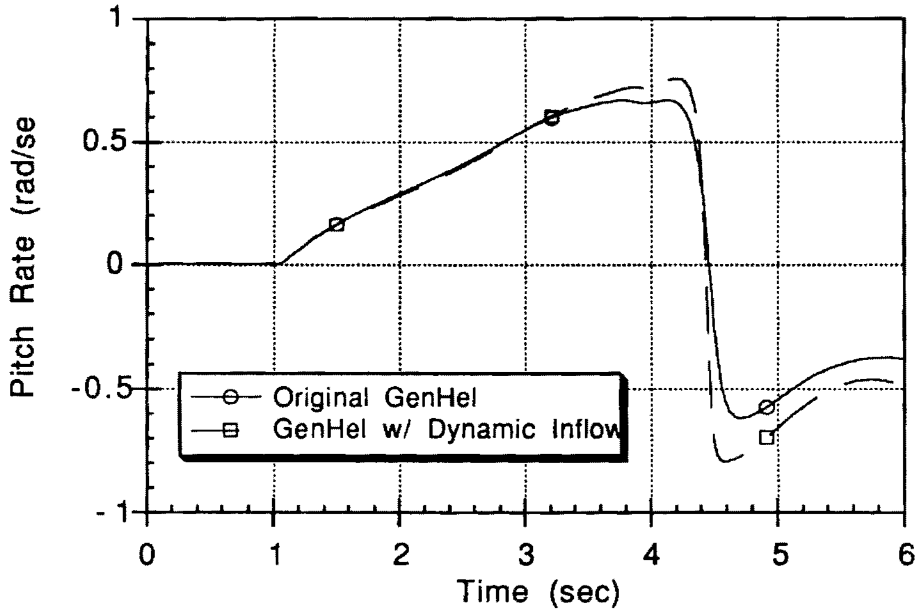

Fig. 3.9: Comparative Response Due to a 1 in. Aft Longitudinal Cyclic Step at 60 kts

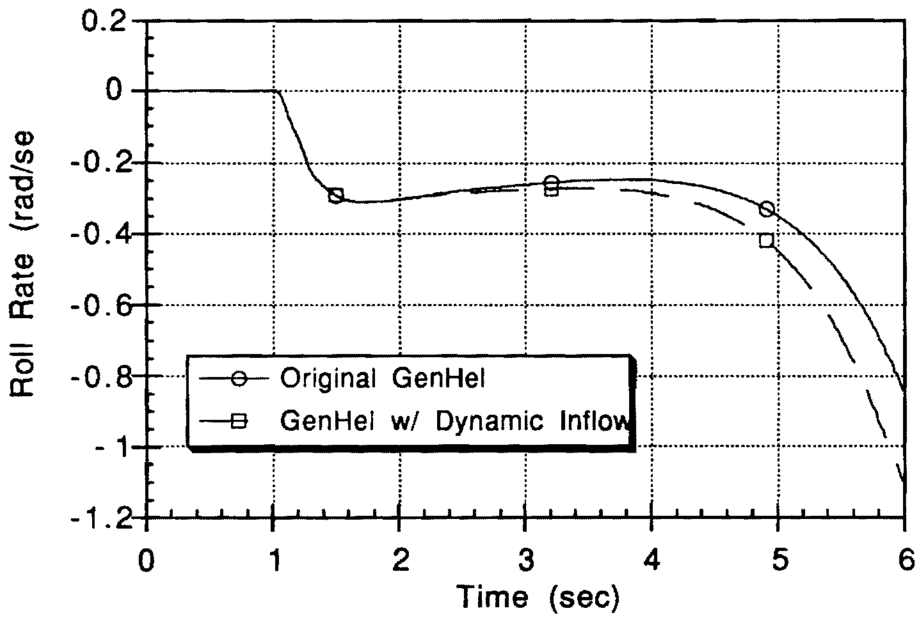

Fig. 3.10: Comparative Response Due to a 1 in. Left Lateral Cyclic Step at 60 kts

4. Ship Airmass Displacement Effect

The effect of the ship proximity to the helicopter is modeled by using a standard panel method, based on the classical solution by Hess and Smith [19]. The ship is modeled by source panels which allow a good geometric representation. The effect of the ship on the rotor is given by the induced velocities on the rotor disk due to the ship panels. For the computation of the strengths of the sources, it is necessary to take into account both the ship velocity and the velocity field on the ship due to the rotor wake. This velocity field is computed using a rigid helical wake model. The strength of the rotor wake vortices depends on the circulation around the rotor blade, which, in turn, depends on the ship effects. Therefore, an iterative process would be needed. However, for the simulation problem, it may be assumed that changes in circulation around the blade and the flow about the ship are not too rapid and consequently the iterative process may be intrinsically performed during the simulation process.

In order to model the ground effect due to the sea surface, the method of images is used. An image rotor wake and an image ship panel system are placed below the sea surface and the influence of these images are taken into account in the computation of the downwash induced by the rotor and in the computation of the coefficient matrix for the ship panel method. Note that, since an image rotor wake is used for this purpose, it may also be used for the purposes of ground effect correction for the inflow on the rotor disk, instead of the simple correction discussed in Item 1.

4.1. Ship Formulation

The ship surface is approximately represented by plane source panels with constant distributed strength. The strength of the sources are determined by enforcing the non-penetration condition at the centroid of each panel. In this implementation, both the normal component of the ship's motion and the normal component of the downwash induced by the rotor are taken into account. The details of the ship source panel method are given in Ref. [19] and therefore will not be repeated here. This formulation results in a linear system of equations to be solved for the ship panel source strengths σ:

$$[A]\{\sigma\} = [B] \qquad (4.1)$$

where [A] is the matrix of influence coefficients, $\{\sigma\}$ is the vector of unknown source strengths and [B] is the right-hand side which includes the normal component of the velocities on the ship surface due to the free-stream and due to the rotor and its wake. The system of equations (4.1) is solved by a standard linear equations solver. The resulting source panel strengths are then used to compute the velocities induced by the ship source panel system on the rotor disk.

4.2. Rotor Wake Formulation

In order to compute the induced velocity due to the rotor and its wake on the ship, as well the rotor disk inflow distribution in ground effect, a rigid wake model is used. This model is a modified version of the model described in [20] and allows the computation of the instantaneous induced velocities both on the rotor disk and on the ship surface, which is adequate for simulation purposes, as discussed before.

The following assumptions are made:

1) Blade flapping angles are small and their higher harmonics are negligible;

2) The rotor blade is modeled by a lifting line of bound vorticity; this bound vorticity is assumed to have a prescribed variation both radially and azimuth-wise;

3) The wake has a prescribed geometry, which is basically a classical skewed helical wake, with a limited wake contraction model;

4) The wake is divided into a "near" wake, composed of trailing and shed vortices and a "far" wake composed of trailing tip vortices only. The strength of the trailing and shed vortices are given by the radial and azimuth-wise variations of the bound vorticity, respectively, while the strength of the far wake tip vortex is assumed as equal to the maximum bound vorticity at the azimuth location where the vortex filament leaves the blade;

5) The rotor wake is convected downstream with a velocity which is equal to the vector sum of the free stream velocity and the averaged (momentum theory value) induced velocity over the disk.

4.2.1. Vorticity Distribution

The blade bound vorticity distribution is assumed to be a known function of the non-dimensional radial location $\bar{r} = r/R$ and azimuth ψ. The radial variation is assumed to be of the form:

$$f(\bar{r}) = \bar{r}\sqrt{1 - \bar{r}^2} \tag{4.2}$$

which is characteristic of a typical radial variation of circulation. The azimuth-wise variation is assumed to be such that no thrust offset is produced, by imposing the condition that the total blade moment be constant over the disk. Under this assumption and for radially uniform circulation, the resulting azimuth-wise variation can be shown to be [21]:

$$g(\psi) = \frac{1}{1 + \frac{3}{2}\mu \sin\psi} \tag{4.3}$$

For non-uniform circulation variation along the radius, the above result is slightly modified:

$$g(\psi) = \frac{1}{1 + \frac{3}{2}\, k_T\, \mu \sin\psi} \tag{4.4}$$

It can be shown that for the radial variation assumed here, k_T has the value of $15\pi/16$ or approximately 0.982.

With the assumptions (4.2) and (4.4), the bound vorticity distribution along the blade and disk results of the form:

$$\Gamma_b(\bar{r},\psi) = \Gamma_0\, \bar{r}\sqrt{1 - \bar{r}^2}\, \frac{1}{1 + \frac{3}{2}\, k_T\, \mu \sin\psi} \tag{4.5}$$

The constant Γ_0 which appears in Eq. (4.5) may be related to the thrust coefficient by applying Kutta-Joukowski theorem for a section of the rotor blade:

$$l = \rho\, V\, \Gamma = \rho\, (\Omega R)(\bar{r} + \mu \sin \psi)\, \Gamma_b(\bar{r},\psi) \tag{4.6}$$

The rotor thrust is given by:

$$T = \frac{N_b\, R}{2\pi} \int_{\psi=0}^{2\pi} \int_{\bar{r}=0}^{1} l\,(\bar{r},\psi)\, d\bar{r}\, d\psi \tag{4.7}$$

where N_b is the number of blades. The thrust coefficient is given by:

$$C_T = \frac{T}{\rho\, \pi R^2 (\Omega R)^2} \tag{4.8}$$

Applying (4.5) and (4.6) in (4.7), carrying out the integration and using (4.8) gives:

$$\tilde{\Gamma}_0 = \frac{\Gamma_0}{R\,(\Omega R)} = C_T \frac{\pi}{N_b} \frac{\sqrt{1 - a^2}}{\frac{\pi}{16} + \frac{4}{9k_T}\left(\sqrt{1 - a^2} - 1\right)} \tag{4.9}$$

where $a = 1.5\, k_T\, \mu$.

4.2.2. Velocity Induced by Blade Bound Vortices

From the above described bound vorticity distribution, the velocity induced by the blade bound vortices can be obtained by application of the Biot-Savart law:

$$v_b = \frac{1}{4\pi} \int_{\bar{r}=0}^{1} \Gamma_b \frac{d\vec{s}_b \times \Delta\vec{R}_{Pb}}{|\Delta\vec{R}_{Pb}|^3} \tag{4.10}$$

where $d\vec{s}_b$ is the elementary vector in the direction of the vortex filament and $\Delta\vec{R}_{Pb}$ is the position vector of the point in question with respect to the bound vortex element. Denoting by $\vec{R}_b$ the position vector of a blade bound vortex element as expressed in the tip-path-plane (TPP) reference frame:

$$\vec{R}_b = r\left\{\left[-\cos\psi\,\hat{i}_T - \sin\psi\,\hat{j}_T\right]\cos\beta_0 + \sin\beta_0\,\hat{k}_T\right\} \qquad (4.11)$$

Then the elementary vector $d\vec{s}_b$ can be obtained from:

$$d\vec{s}_b = \frac{\dfrac{\partial\vec{R}_b}{\partial r}}{\left|\dfrac{\partial\vec{R}_b}{\partial r}\right|}\,dr \qquad (4.12)$$

with

$$\frac{\partial\vec{R}_b}{\partial r} = \left[-\cos\psi\,\hat{i}_T - \sin\psi\,\hat{j}_T\right]\cos\beta_0 + \sin\beta_0\,\hat{k}_T = \frac{\vec{R}_b}{r} \qquad (4.13)$$

Given a point with coordinates (x_P, y_P, z_P) in the tip-path-plane reference frame, the vector $\Delta\vec{R}_{Pb}$ is then:

$$\Delta\vec{R}_{Pb} = \vec{R}_P - \vec{R}_b = \left(x_P\,\hat{i}_T + y_P\,\hat{j}_T + z_P\,\hat{k}_T\right) - \vec{R}_b \qquad (4.14)$$

4.2.3. Near Wake

As mentioned above, the near wake is assumed to be composed of trailing and shed vortices, with strength given by the radial and azimuth-wise variations of the bound vorticity, respectively, at the azimuth location where the vortex filament leaves the blade. Let us first consider an element of a trailing vortex filament of length $r\,d\nu$, which left the blade at the radial location r, and is located at a wake age ν. This element has left the blade when it was at an azimuth location $\psi-\nu$, ψ being the current azimuth location of the blade. Therefore, the vorticity of the element is given by $\Gamma_t(\bar{r},\psi-\nu)\,r\,d\nu$, where $\Gamma_t(\bar{r},\psi)$ is the trailing vortex vorticity, equal to the radial variation of Γ_b. From (4.5):

$$\Gamma_t(\bar{r},\psi) = \frac{\partial \Gamma_b}{\partial \bar{r}} = \Gamma_0 \frac{1 - 2\bar{r}^2}{\sqrt{1-\bar{r}^2}} \frac{1}{1 + \frac{3}{2}\ k_T\, \mu \sin\psi} \tag{4.15}$$

The velocity induced by the entire filament at a point is given by integration of elementary induced velocities obtained from the Biot-Savart law:

$$dv_t = \frac{1}{4\pi} \int_{\nu=0}^{\nu_{nw}} \Gamma_t \frac{d\vec{s}_t \times \Delta\vec{R}_{Pt}}{|\Delta\vec{R}_{Pt}|^3} \tag{4.16}$$

where $d\vec{s}_t$ is the elementary vector in the direction of the vortex filament and $\Delta\vec{R}_{Pt}$ is the position vector of the point in question with respect to the vortex element. Note that the integration is performed only along the "near" wake. Note also that Eq.(4.16) gives only the velocity induced by a single trailing vortex filament. To obtain the total induced velocity due to all trailing vortex filaments, one has to integrate Eq.(4.16) along the blade, i.e.:

$$v_t = \frac{1}{4\pi} \int_{\bar{r}=0}^{1} \int_{\nu=0}^{\nu_{nw}} \Gamma_t \frac{d\vec{s}_t \times \Delta\vec{R}_{Pt}}{|\Delta\vec{R}_{Pt}|^3} \tag{4.17}$$

Denoting by $\vec{R}_s$ the position vector of the trailing vortex element as expressed in the tip-path-plane (TPP) reference frame and using the assumption that the wake is convected downstream with a velocity which is equal to the vector sum of the free stream velocity and the averaged induced velocity over the disk, we have:

$$\vec{R}_s = r\left\{\left[-\cos(\psi-\nu)\,\hat{i}_T - \sin(\psi-\nu)\,\hat{j}_T\right]\cos\beta_0 + \sin\beta_0\,\hat{k}_T\right\} + \frac{\vec{v}_{i_0} - \vec{V}_{H_T}}{\Omega}\,\nu \tag{4.18}$$

where β_0 is the coning angle, Ω is the rotor rotational speed, $\vec{V}_{H_T}$ is the helicopter velocity vector in the TPP reference frame, $\hat{i}_T$, $\hat{j}_T$ and $\hat{k}_T$ are the unit vectors corresponding to the TPP axes, and $\vec{v}_{i_0}$ is the averaged induced inflow vector, given by:

$$\vec{v}_{i_0} = -(\Omega R)\,\lambda_{i_0}\,\hat{k}_T \tag{4.19}$$

where λ_{i_0} is the induced inflow ratio. The elementary vector in the direction of the filament, $d\vec{s}_t$, can be obtained as:

$$d\vec{s}_t = \frac{\dfrac{\partial \vec{R}_s}{\partial \nu}}{\left|\dfrac{\partial \vec{R}_s}{\partial \nu}\right|} r \, d\nu \tag{4.20}$$

with

$$\frac{\partial \vec{R}_s}{\partial \nu} = r\left[- \sin(\psi\text{-}\nu)\,\hat{i}_T + \cos(\psi\text{-}\nu)\,\hat{j}_T\right] \cos \beta_0 + \frac{\vec{v}_{i_0} - \vec{V}_{H_T}}{\Omega} \tag{4.21}$$

Given a point with coordinates (x_P, y_P, z_P) in the tip-path-plane reference frame, the vector $\Delta\vec{R}_{Pt}$ is then:

$$\Delta\vec{R}_{Pt} = \vec{R}_P - \vec{R}_s = \left(x_P\,\hat{i}_T + y_P\,\hat{j}_T + z_P\,\hat{k}_T\right) - \vec{R}_s \tag{4.22}$$

Equations (4.15)–(4.22) allow us to obtain the induced velocity at any point due to the trailing vortex system.

Now, let us consider an element of a shed vortex filament of length dr, which left the blade at the radial location r, and is located at a wake age ν. This element has left the blade when it was at an azimuth location $\psi-\nu$, ψ being the current azimuth location of the blade. Therefore, the vorticity of the element is given by $\Gamma_S(\bar{r},\psi-\nu)\,dr$, where $\Gamma_S(\bar{r},\psi)$ is the shed vortex vorticity, equal to the azimuthal variation of Γ_b. From (4.5):

$$\Gamma_s(\bar{r},\psi) = \frac{\partial \Gamma_b}{\partial \psi} = - \Gamma_0\, \bar{r}\sqrt{1 - \bar{r}^2}\, \frac{\frac{3}{2}\, k_T\, \mu \cos\psi}{\left(1 + \frac{3}{2}\, k_T\, \mu \sin\psi\right)^2} \tag{4.23}$$

The velocity induced by the entire shed vortex system at a point is given by radial integration of elementary induced velocities obtained from the Biot-Savart law, and subsequent integration along the wake to account for all the shed vortices:

$$v_s = \frac{1}{4\pi} \int_{\nu=0}^{\nu_{nw}} \int_{\bar{r}=0}^{1} \Gamma_s \frac{d\vec{s}_s \times \Delta\vec{R}_{Ps}}{|\Delta\vec{R}_{Ps}|^3} \tag{4.24}$$

Note that the integration is performed only along the "near" wake. The position vector of the shed vortex element, $\vec{R}_s$, is given again by Eq. (4.18), therefore the vector $\Delta\vec{R}_{Ps}$ is equal to $\Delta\vec{R}_{Pt}$ and is accordingly given by Eq. (4.22). The elementary vector in the direction of the shed vortex filament, $d\vec{s}_s$, can be obtained as:

$$d\vec{s}_s = \frac{\dfrac{\partial\vec{R}_s}{\partial r}}{\left|\dfrac{\partial\vec{R}_s}{\partial r}\right|} dr \tag{4.25}$$

with

$$\frac{\partial\vec{R}_s}{\partial r} = \left[- \cos(\psi\text{-}\nu)\,\hat{i}_T - \sin(\psi\text{-}\nu)\,\hat{j}_T\right] \cos\beta_0 + \sin\beta_0\,\hat{k}_T \tag{4.26}$$

4.2.4. Far Wake

As mentioned above, the far wake is assumed to be composed of trailing tip vortices only, with strength assumed as equal to the maximum bound vorticity at the azimuth location where the vortex filament leaves the blade. Considering an element of wake filament of length $r_{tv}\,d\nu$ (where r_{tv} corresponds to the radial location where the tip vortex has rolled up) and at a wake age ν, this element has left the blade when it was at an azimuth location $\psi-\nu$, ψ being the current azimuth location of the blade. Therefore, the vorticity of the element is given by $\Gamma_T(\psi-\nu)\, r_{tv}\, d\nu$, where $\Gamma_T(\psi)$ is the trailing tip vortex vorticity, equal to the radial maximum of Γ_b. From (4.5):

$$\Gamma_T(\psi) = \frac{1}{2}\Gamma_0 \frac{1}{1 + \frac{3}{2}\, k_T\, \mu \sin\psi} \tag{4.27}$$

The velocity induced by the wake at a point is given by integration of elementary induced velocities obtained from the Biot-Savart law:

$$v_T = \frac{1}{4\pi}\int_{v=v_{ftw}}^{\infty} \Gamma_T \frac{d\vec{s}_T \times \Delta\vec{R}_{PT}}{|\Delta\vec{R}_{PT}|^{\beta}} \tag{4.28}$$

where $d\vec{s}_T$ is the elementary vector in the direction of the vortex filament and $\Delta\vec{R}_{PT}$ is the position vector of the point in question with respect to the vortex element. Denoting by $\vec{R}_T$ the position vector of the tip vortex element as expressed in the tip-path-plane (TPP) reference frame and using the assumption that the wake is convected downstream with a velocity which is equal to the vector sum of the free stream velocity and the averaged induced velocity over the disk, we have:

$$\vec{R}_T = r_{tv}\left\{\left[-\cos(\psi\text{-}v)\,\hat{i}_T - \sin(\psi\text{-}v)\,\hat{j}_T\right]\cos\beta_0 + \sin\beta_0\,\hat{k}_T\right\} + \frac{\vec{v}_{i_0} - \vec{V}_{H_T}}{\Omega}\,v \tag{4.29}$$

The elementary vector in the direction of the tip vortex filament, $d\vec{s}_T$, can be obtained as:

$$d\vec{s}_T = \frac{\dfrac{\partial\vec{R}_T}{\partial v}}{\left|\dfrac{\partial\vec{R}_T}{\partial v}\right|}\, r_{tv}\, dv \tag{4.30}$$

with

$$\frac{\partial\vec{R}_T}{\partial v} = r_{tv}\left[-\sin(\psi\text{-}v)\,\hat{i}_T + \cos(\psi\text{-}v)\,\hat{j}_T\right]\cos\beta_0 + \frac{\vec{v}_{i_0} - \vec{V}_{H_T}}{\Omega} \tag{4.31}$$

Given a point with coordinates (x_P, y_P, z_P) in the tip-path-plane reference frame, the vector $\Delta\vec{R}_{PT}$ is then:

$$\Delta\vec{R}_{PT} = \vec{R}_P - \vec{R}_T = \left(x_P\,\hat{i}_T + y_P\,\hat{j}_T + z_P\,\hat{k}_T\right) - \vec{R}_T \tag{4.32}$$

Equations (4.27)–(4.32) allow us to obtain the induced velocity at any point due to the far wake.

4.2.5. Root Cut-Out

To account for blade root cut-out, all radial integrations above are started from the nondimensional location $\bar{r}_i$ corresponding to the blade root cut-out, except as noted below regarding wake contraction.

4.2.6. Wake Contraction

A crude wake contraction model is applied, such that the near wake initially starts from the blade root cut-out location $\bar{r}_i$ and extends to the blade tip and after a wake age ν_{ctr} is contracted such as to start from the hub (r=0) and extend to the radial location r_{tv}. Between $\nu=0$ and $\nu=\nu_{ctr}$, a linear interpolation is used to determine the starting and end radial locations.

4.2.7. Vortex Core Model

A Rankine vortex core model [11] with radius of one tenth of the blade chord is used. This model is illustrated in Fig. 4.1, and is applied by scaling the induced velocity due to the elementary vortex filament by the square of the ratio between the distance to the filament and the core radius, whenever the point where the induced velocity is being calculated lies within the vortex core.

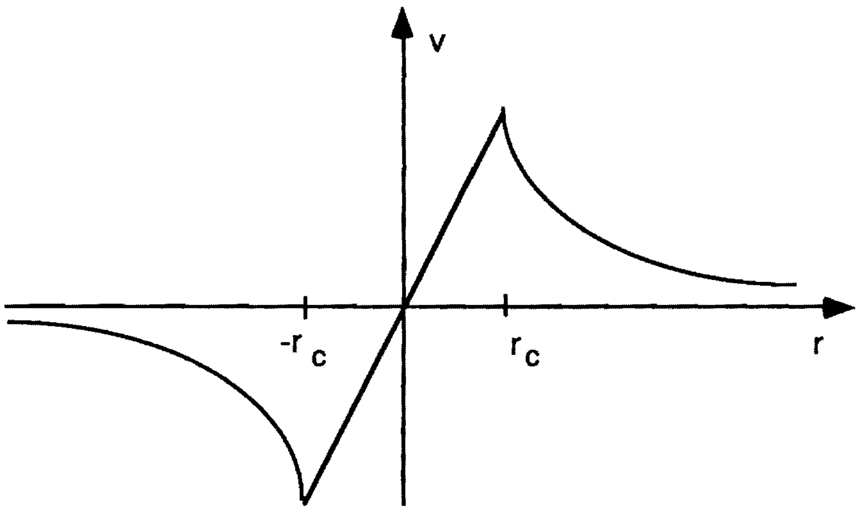

Fig. 4.1: Rankine Vortex Core Model

4.2.8. Validation

For the validation of the present wake model, our numerical results were compared to experimental data presented in Ref. [22]. The time-average velocities induced by the rotor and its wake, non-dimensionalized by the average (momentum theory value) of the induced velocity are shown in Figs. 4.2-4.6.

Figs. 4.2-4.4 show the induced velocities for an advance ratio $\mu = 0.095$, at the cross-flow sections $x/R = 0$, $x/R = 0.5$ and $x/R = 1.07$, respectively (i.e., at the disk lateral line of symmetry and at two sections behind it) and at heights $z/R = -0.07$, $z/R = -0.05$ and $z/R = -0.01$, respectively (i.e., all below the disk). A good agreement can be observed for most points, although sharp variations are not well predicted.

Figs. 4.5-4.6 show the induced velocities for an advance ratio $\mu = 0.232$, at the cross-flow sections $x/R = 0$ and $x/R = 1.07$, respectively and at heights $z/R = -0.08$ and $z/R = -0.19$, respectively. The agreement is still reasonable, but not as good as for the lower advance ratio, probably due to the more pronounced wake distortion, which is not modeled in our method. However, since for our purposes (landing on a ship deck) the advance ratios to be encountered are low, the present method is adequate.

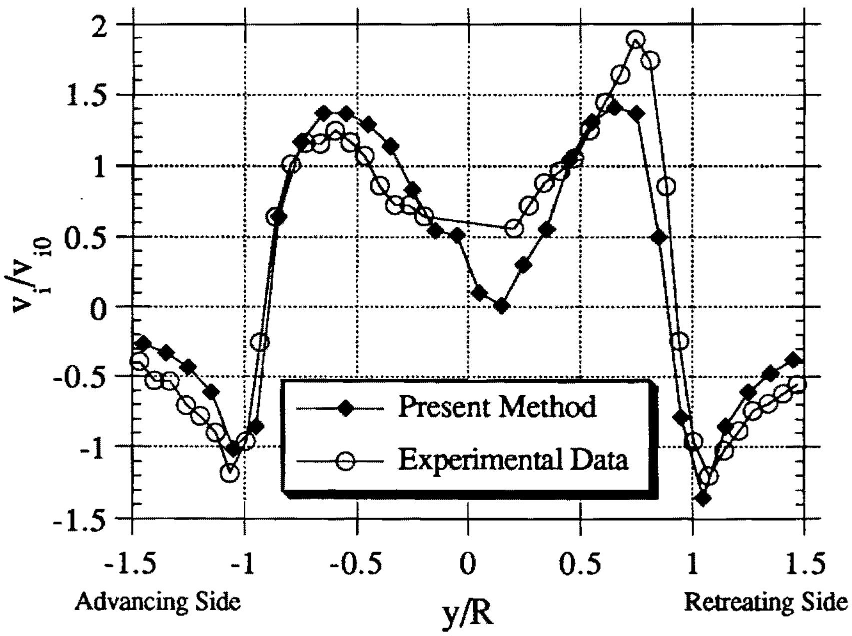

Fig. 4.2: Nondimensional Induced Velocities for $\mu = 0.095$; $x/R = 0$; $z/R = -0.07$

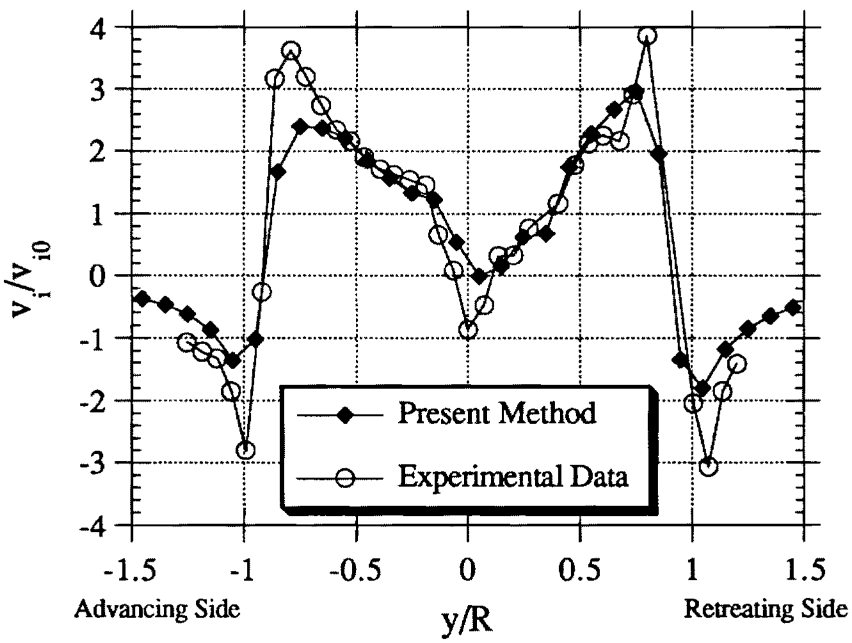

Fig. 4.3: Nondimensional Induced Velocities for $\mu = 0.095$; $x/R = 0.5$; $z/R = -0.05$

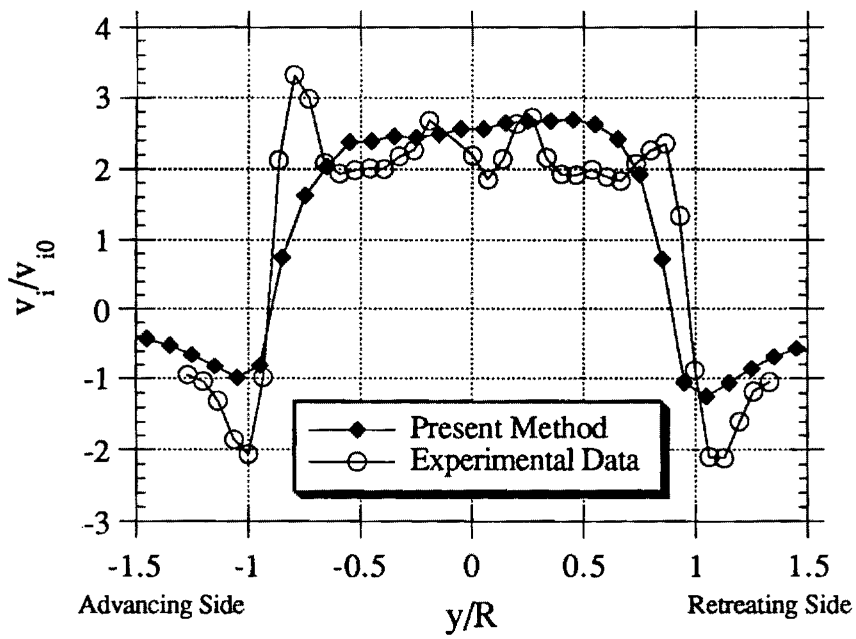

Fig. 4.4: Nondimensional Induced Velocities for $\mu = 0.095$; $x/R = 1.07$; $z/R = -0.01$

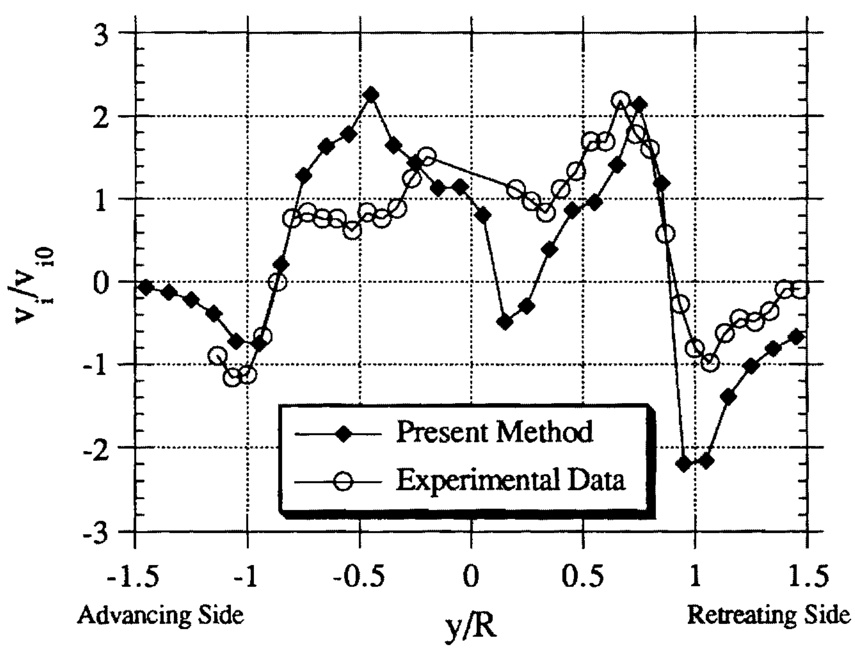

Fig. 4.5: Nondimensional Induced Velocities for $\mu = 0.232$; $x/R = 0$; $z/R = -0.08$

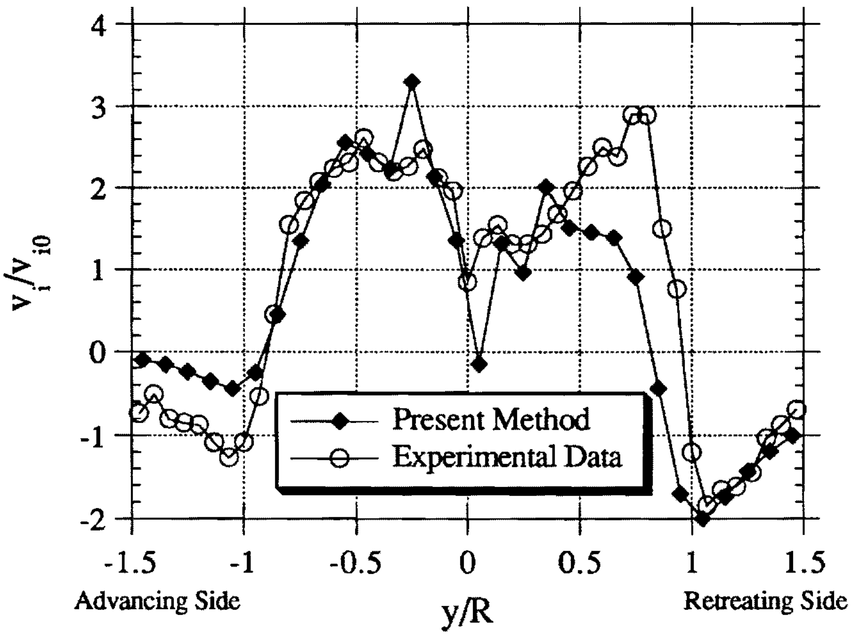

Fig. 4.6: Nondimensional Induced Velocities for $\mu = 0.232$; $x/R = 1.07$; $z/R = -0.19$

4.3. Numerical Results

The above described helicopter/ship interaction method has been applied to a SH-60 Sea Hawk helicopter at an advance ratio of $\mu = 0.05$ at one rotor radius above the landing deck of a Oliver Hazard Perry-class frigate. Only the ship airmass displacement effect has been computed, i.e., no ship-induced turbulence effects have been included. The instantaneous induced velocities at the rotor blades due to the ship and sea at the rotor disk longitudinal and lateral planes of symmetry are shown in Figs. 4.7 and 4.8, respectively, non-dimensionalized by the momentum-theory value of induced inflow. For comparison purposes, the velocities induced by the ship deck (which could represent a crude model of the complete ship) and sea are presented, as well as the upflow at the rotor blades due to a mirror image wake only, for a rotor one revolution above the ground (i.e., without the presence of the ship).

It can be observed that the ship airmass displacement effect can be substantial, and it cannot be accurately represented by assuming that the helicopter has an infinite ground below it at the same height as it is above the deck. A crude representation such as modeling the deck only is also inadequate, and therefore the superstructure should be included in the model.

It can also be noted that the airmass displacement effect is more pronounced around the center and in the aft portion of the disk. The first phenomenon can be explained by observing that the velocity field induced by a rotor far from the disk resembles one due to a vortex pair, which implies higher induced velocities near the center, which in turn results in stronger ship upflow in that region. The second phenomenon is to be expected because the rotor wake is being washed aft of the disk and consequently the part of the ship deck near the rear of the disk is more affected by the rotor presence.

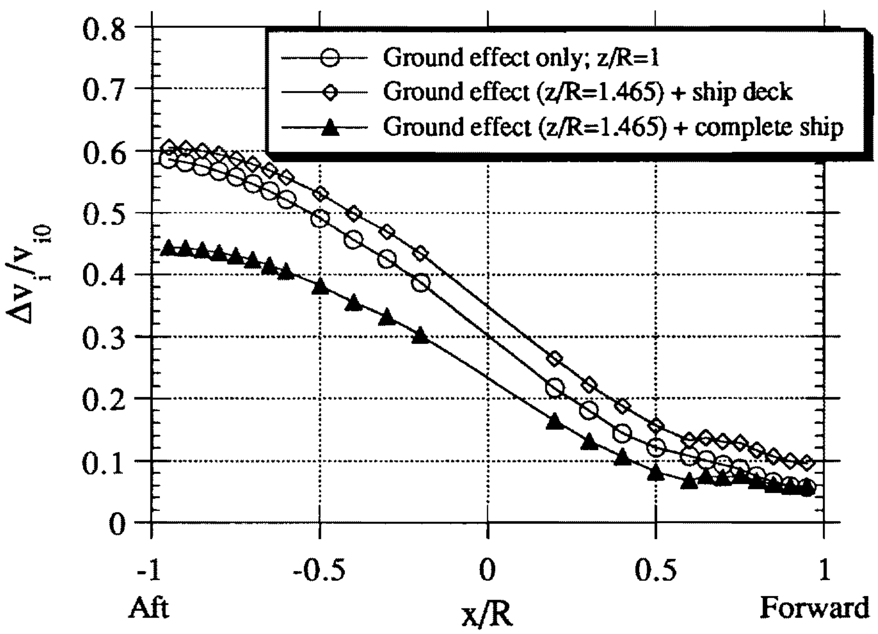

Fig. 4.7: Instantaneous induced velocities at the rotor blades due to the ship and sea at the rotor disk longitudinal plane of symmetry of a SH-60 at one rotor radius above the landing deck of a Oliver Hazard Perry-class frigate ($\mu = 0.05$)

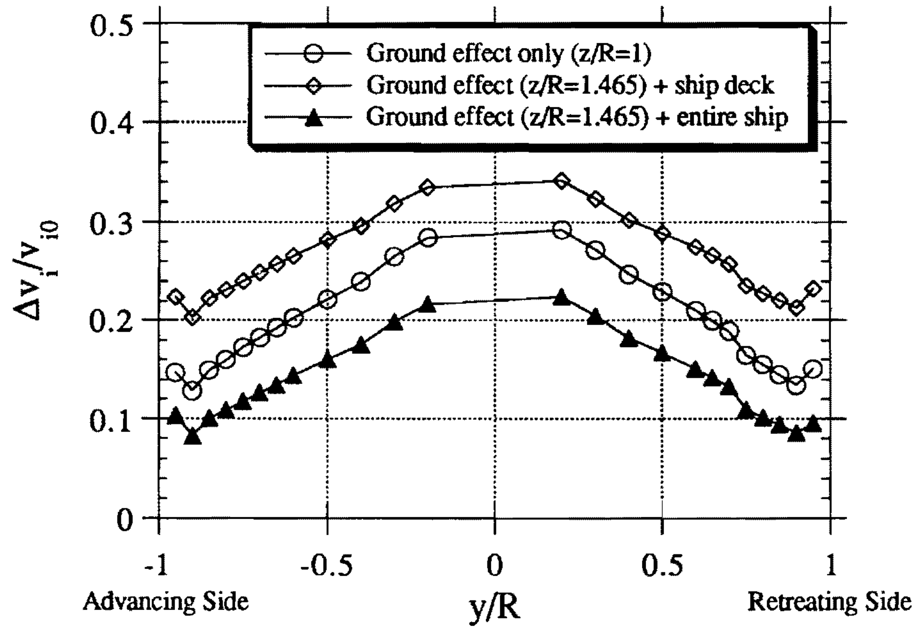

Fig. 4.8: Instantaneous induced velocities at the rotor blades due to the ship and sea at the rotor disk lateral plane of symmetry of a SH-60 at one rotor radius above the landing deck of a Oliver Hazard Perry-class frigate ($\mu = 0.05$)

5. Ship Airwake Turbulence

The atmospheric turbulence velocities experienced by non-rotating helicopter components and the rotating blades can be substantially different [23]. The differences are due to the spatial motion of the blades, which move fore and aft through the gust waves. Body-fixed atmospheric turbulence refers to the atmospheric turbulence experienced by a fixed (non-rotating) point of the helicopter, while blade-fixed atmospheric turbulence refers to the atmospheric turbulence experienced by an element of the rotating rotor blade. The simulation of the latter involves treatment of cyclostationary processes, for which a specific formulation has been developed by Prasad et al. [23-25]. For simulation purposes, it is assumed that the body-fixed ship airwake turbulence is given. This body-fixed turbulence field should be then transformed into a blade-fixed turbulence field for implementation in the simulator code as an additional time-dependent inflow term.

6. Conclusions

The problem of simulating the helicopter/ship airwake interaction for the purposes of simulating helicopter landing on ship decks has been discussed. The following aspects which contribute to the complexity of the problem have been specifically analyzed:

1. The ground effect due to the sea surface may be approximated by applying a multiplicative factor to the inflow through the disk, or by using a mirror image wake system. The first method is much simpler but may not be accurate locally. The second method is computationally expensive but is consistent with the use of a wake model for rotor/ship interaction analysis. The ground vortex is not particularly relevant in this case because the helicopter would approach the ship at a height above the sea for which the ground vortex would not have been formed, and when the helicopter is close enough to the ship to see its deck as the "ground", its velocity would have been reduced and again the conditions for the formation of the ground vortex would not be met.

2. The effects of ship aerodynamics on the helicopter can be divided into the ship airmass displacement effect due to the proximity between the rotor and the ship surface, and the ship-induced turbulence effect.

3. The ship-induced turbulence effect has to be modeled statistically, in addition to the atmospheric turbulence. For the analysis of both turbulence contributions, one has to take into account the fact that the turbulent velocities experienced by the rotating blades are modified due to the spatial motion of the blades, which requires specific modeling which is available in the literature.

4. Due to the time-dependent and local nature of the turbulence effects, a time-dependent inflow model is necessary for theoretical consistency. A first-order dynamic inflow model has been successfully implemented in the GENHEL simulation code.

5. The ship airmass displacement effect may be modeled under the assumption of attached flow around the ship, which in turn is modified by the helicopter presence. This can be accomplished by standard panel representation of the ship surface coupled with a rigid helical wake model for the rotor wake. Such a method has been successfully developed in the present work.

6. Results from the rotor/ship interaction model show that the ship airmass displacement effect can be substantial, and it cannot be accurately represented by assuming that the helicopter has an infinite ground below it at the same height as it is above the deck. A crude representation such as modeling the deck only is also inadequate, and therefore the superstructure should be included in the panel representation of the ship.

7. References

1. Healey, J. Val., "The Prospects for Simulating the Helicopter/Ship Interface," *Naval Engineers Journal*, March 1987, pp. 45-63.

2. Hurst, D. W., and Newman, S. J., "Wind Tunnel Measurements of Ship Induced Turbulence and the Prediction of Helicopter Rotor Blade Response," *Vertica*, Vol. 12, No. 3, 1988, pp. 267-278.

3. Peters, D. A., and HaQuang, N., "Dynamic Inflow for Practical Applications," *Journal of the American Helicopter Society*, October 1988, pp. 64–68.

4. Howlett, J. J., "UH-60A Black Hawk Engineering Simulation Program: Volume I — Mathematical Model," NASA CR-166309, 1981.

5. Betz, A., "The Effect of the Ground on Lifting Propellers," NACA TM 836, April 1937.

6. Cheeseman, I. C., and Bennett, W. E., "The Effect of the Ground on a Helicopter Rotor in Forward Flight," ARC R&M No. 3021, September 1955.

7. Heyson, H. H., "Ground Effect for Lifting Rotors in Forward Flight," NASA TN D-234, May 1960.

8. Sheridan, P. F., and Wiesner, W., "Aerodynamics of Helicopter Flight Near the Ground," 33rd Annual Forum of the American Helicopter Society, May 1977.

9. Curtiss, H. C., Jr., Sun, M., Putman, W. F., and Hanker, E. J., Jr., "Rotor Aerodynamics in Ground Effect at Low Advance Ratios," 37th Annual Forum of the

American Helicopter Society, New Orleans, LA, May 1981. (Also *Journal of the American Helicopter Society*, January 1984).

10. Curtiss, H. C., Jr., Erdman, W., and Sun, M., "Ground Effect Aerodynamics," *Vertica*, Vol. 11, No. 1/2, 1987, pp. 29-42.

11. U.S. Department of the Army — Aeroflightdynamics Directorate, "2GCHAS Theory Manual," (Second Generation Comprehensive Helicopter Analysis System, Version 2.1), Vol. II, Chapter 5 – Airloads and Induced Velocity, Ames Research Center, Moffett Field, CA, July 1992.

12. Pitt, D. M., and Peters, D. A., "Theoretical Prediction of Dynamic-Inflow Derivatives," *Vertica*, Vol. 5, No. 1, 1981, pp. 21-34.

13. Gaonkar, G. H., and Peters, D. A., "Review of Dynamic Inflow Modeling for Rotorcraft Flight Dynamics," *Vertica,* Vol. 12, No. 3, 1988, pp. 213–242.

14. He, Chengjian, "Development and Application of a Generalized Dynamic Wake Theory for Lifting Rotors," Ph.D. Dissertation, Georgia Institute of Technology, 1989.

15. Peters, D. A., and He, C. J., "Correlation of Measured Induced Velocities with a Finite-State Inflow Model," *Journal of the American Helicopter Society,* Vol. 36, No. 3, July 1991, pp. 59–70.

16. Lewis, W. D., "An Aeroelastic Model Structure Investigation for a Manned Real-Time Rotorcraft Simulation," Ph.D. Thesis, Georgia Institute of Technology, 1992.

17. He, C., and Lewis, W. D., "A Parametric Study of Real Time Mathematical Modeling Incorporating Dynamic Wake and Elastic Blades," 48th Annual Forum of the American Helicopter Society, Washington, DC, June 1992.

18. Ballin, M. G., "Validation of Real-Time Engineering Simulation of the UH-60A Helicopter," NASA TM-88360, February 1987.

19. Hess, J. L., and Smith, A. M. O., "Calculation of Potential Flow about Arbitrary Bodies," *Progress in Aeronautical Sciences*, Vol. 8. Edited by D. Küchemann. Pergamon Press, Oxford, England, 1967.

20. Mello, O. A. F., "*Unsteady Loads on Helicopter Lifting Surfaces*," M.S. Thesis, University of Maryland, College Park, UMAERO 88-21, July 1988.

21. Stepniewski, W. Z. and Keys, C. N., *Rotary-Wing Aerodynamics*, Dover, 1984.

22. Heyson, H. H., and Katzoff, S., "Induced Velocities Near a Lifting Rotor with Nonuniform Disk Loading," NACA Report 1319, 1957.

23. Costello, M., Prasad, J. V. R., Schrage, D. P., and Gaonkar, G. H., "Some Issues on Modeling Atmospheric Turbulence Experienced by Helicopter Rotor Blades," *Journal of the American Helicopter Society*, Vol. 37, No. 2, April 1992, pp. 71–75.

24. Riaz, J., Prasad, J. V. R., Schrage, D. P., and Gaonkar, G. H., "New Method for Simulating Atmospheric Turbulence for Rotorcraft Applications," 47th Annual Forum of the American Helicopter Society, Phoenix, Arizona, 1991.

25. Prasad, J. V. R., Mavris, D. N., and Schrage, D. P., "Ship Airwake Modeling and Simulation, Phase I — Methodology Development," Research Report submitted to Naval Air Warfare Center, School of Aerospace Engineering, Georgia Institute of Technology, Atlanta, August 1992.

Analysis of Helicopter / Ship Aerodynamic Interactions

O. A. F. Mello*, J. V. R. Prasad§ and L. N. Sankar¶

School of Aerospace Engineering
Georgia Institute of Technology
Atlanta, Georgia 30332

An abstract submitted to the AHS Aeromechanics
Specialists Conference, San Francisco, CA, 1994

SUMMARY

A method for analysis of the aerodynamic interactions between a helicopter and a ship is presented. The complex flow problem is decomposed into two: The first effect is the ship "airmass displacement effect", consisting of the changes in the flowfield in the vicinity of the ship so that the airflow contours the ship surface. This effect is modeled by a panel representation of the ship surface, taking into account the downwash induced by the rotor. The second effect is the ship-induced turbulence effect, which is modeled statistically. Results for the ship airmass displacement effect on a SH-60 rotor due a frigate are presented and indicate that this effect has to be considered in simulations. The full paper will contain additional results for the ship air displacement effect and will include the ship-induced turbulence effects.

INTRODUCTION

Landing a helicopter on a ship deck can be a hazardous process. The determination of safe operating envelopes has been done at sea by the Naval Air Test Center in a lengthy and expensive process[1]. This fact suggests a need for an appropriate helicopter/ship aerodynamic interaction model to be incorporated into rotorcraft simulation codes.

There are several aspects that contribute to the complexity of the problem, namely:

1. Sea and ship motions;
2. Atmospheric turbulence;
3. Ship aerodynamics;
4. Helicopter motion itself, in the presence of the ship.

The sea and ship motions can be modeled to a reasonable degree[1]. Their effects on the helicopter have to be investigated. The only effect of the sea motion on the helicopter would be in the extent that it modifies the ground effect, but this change may be regarded as negligible with respect to the other factors involved. The ship motion will have a more significant effect on the ship/helicopter interference and has to be considered.

---

* Graduate Research Assistant, School of Aerospace Engineering

§ Associate Professor, School of Aerospace Engineering.

¶ Professor, School of Aerospace Engineering.

Statistical atmospheric turbulence models are also available, and may be considered as user-prescribed for simulation purposes.

The ship aerodynamics is very complex. The flow around the superstructure is characterized by turbulence and vortex shedding. The turbulence level in the atmosphere also affects the flow. The knowledge about this type of flow is mostly empirical and based on building aerodynamics. Few wind-tunnel investigations have been performed to measure the air flow about ships[2]. For the purposes of analysis, the effects of ship aerodynamics on the helicopter can be divided into the "airmass displacement effect" due to the proximity between the rotor and the ship surface, and the ship-induced turbulence effect. The ship airmass displacement effect may be modeled under the assumption of attached flow around the ship, which in turn is modified by the helicopter presence. The turbulence effect has to be modeled statistically[3], and included in the simulation as an additional turbulent air velocity contribution to be added to the helicopter model.

The simulation of helicopter motion can be carried out by a standard helicopter simulation code, if the effects discussed above are included. The simulation program must therefore be able to:

1. Include the ground effect due to the sea, with the sea surface considered as fixed;

2. Include air velocity contributions due to the ship airwake, considered to be prescribed. This influence may be taken into account as an additional inflow term, which in turn implies that a non-uniform, time-dependent inflow model is necessary for consistency;

3. Include the ship airmass displacement effect, as discussed above. For this purpose, a panel method representation of the ship surface may be used, and the effect of the ship on the rotor is modeled by the induced velocity field produced by the ship's panels. It must be noted that for the computation of the flow around the ship using a panel method, the flow due to the rotor and its wake have to be considered.

The remaining of this abstract is organized as follows: First, a brief description of the mathematical formulation of the rotor wake and ship panel methods is given. Next, results for the airmass displacement effect on a SH-60 rotor due to a frigate are presented. The abstract concludes with a list of additional results to be presented in the full paper.

MATHEMATICAL FORMULATION

Rotor Wake Formulation

In order to compute the downwash on the ship surface due to the rotor, a rigid, skewed helical wake model consisting of trailing tip vortices is used. It is assumed that the tip vortices are created by the roll-up of the trailing vortex sheet which is shed from the blade. Consequently, the strength of the trailing vortex is equal to the spanwise maximum strength of the blade bound vortex at the azimuthal location where each vortex filament was shed from the blade. The bound vortex radial and azimuth-wise functional variations over the rotor disk are prescribed, and consequently the strength of the trailing vortices results as a prescribed function of the blade azimuth and wake age, times a constant which can be related to the rotor thrust by application of the Kutta-Joukowski theorem for the local blade section lift and integration over the rotor disk. Details are given in Ref. 4. The resulting trailing vortex strength distribution is of the form:

$$\Gamma_T = \Gamma_0 \, f(\psi - \nu) \tag{1}$$

where $\Gamma_0 = \Gamma_0 (C_T)$ is the constant mentioned above, ψ is the blade azimuth and ν is the wake age.

Using the above described model, the velocities induced by the rotor and its wake on the ship surface are computed by applying the Biot-Savart law and integrating over the blades (bound vortices) and over the wake (trailing tip vortices). The total induced velocities are then resolved for the component normal to the surface for input in the ship model.

Ship Formulation

The ship is modeled by a source panel method[5] common in aeronautical applications. The ship surface is approximately represented by plane source panels with constant distributed strength. The strength of the sources are determined by enforcing the non-penetration condition at the centroid of each panel. In this implementation, both the normal component of the ship's motion and the normal component of the downwash induced by the rotor are taken into account. This formulation results in a linear system of equations which is solved for the source strengths, which are then used to compute the induced velocity at the rotor disk due to the ship.

Effect of Sea Surface

In order to model the ground effect due to the sea surface, the method of images is used. An image rotor wake and an image ship panel system are placed below the sea surface and the influence of these images are taken into account in the computation of the downwash induced by the rotor and in the computation of the coefficient matrix for the ship panel method.

RESULTS AND DISCUSSION

The above described helicopter/ship interaction method has been applied to a SH-60 Sea Hawk helicopter at an advance ratio of μ=0.05 one rotor radius above the landing deck of a Oliver Hazard Perry-class frigate. Only the ship airmass displacement effect has been computed, i.e., no ship-induced turbulence effects have been included. Although in the actual simulation the computations are performed at a fixed blade azimuth (corresponding to a given time), for validation purposes the average over one rotor revolution of the induced velocities due to the ship at the rotor disk lateral and longitudinal planes of symmetry are shown in Figs. 1 and 2, respectively, non-dimensionalized by the momentum-theory value of induced inflow.

It can be observed that the ship airmass displacement effect can be substantial, reaching locally up to 20% of the momentum-theory value of the induced inflow, and therefore should be included in any helicopter/ship interaction simulation. It can also be noted that this effect is more pronounced around the center and in the aft portion of the disk. This is to be expected because the rotor wake is being washed aft of the disk and consequently the part of the ship deck near the rear of the disk is more affected by the rotor presence.

ADDITIONAL RESULTS TO BE FOUND IN THE FULL PAPER

The final paper will contain additional results for the ship air displacement effect and will include the ship-induced turbulence effects.

REFERENCES

1. Healey, J. Val., "The Prospects for Simulating the Helicopter/Ship Interface," *Naval Engineers Journal*, March 1987, pp. 45-63.

2. Hurst, D. W., and Newman, S. J., "Wind Tunnel Measurements of Ship Induced Turbulence and the Prediction of Helicopter Rotor Blade Response," *Vertica*, Vol. 12, No. 3, 1988, pp. 267-278.

3. Prasad, J. V. R., Mavris, D. N., and Schrage, D. P., "Ship Airwake Modeling and Simulation, Phase I — Methodology Development," Research Report submitted to Naval Air Warfare Center, School of Aerospace Engineering, Georgia Institute of Technology, Atlanta, August 1992.

4. Mello, O. A. F., "Unsteady Loads on Helicopter Lifting Surfaces," M.S. Thesis, University of Maryland, College Park, Report No. UMAERO 88-21, July 1988.

5. Hess, J. L., and Smith, A. M. O., "Calculation of Potential Flow about Arbitrary Bodies," *Progress in Aeronautical Sciences*, Vol. 8. Edited by D. Küchemann. Pergamon Press, Oxford, England, 1967.

Figures:

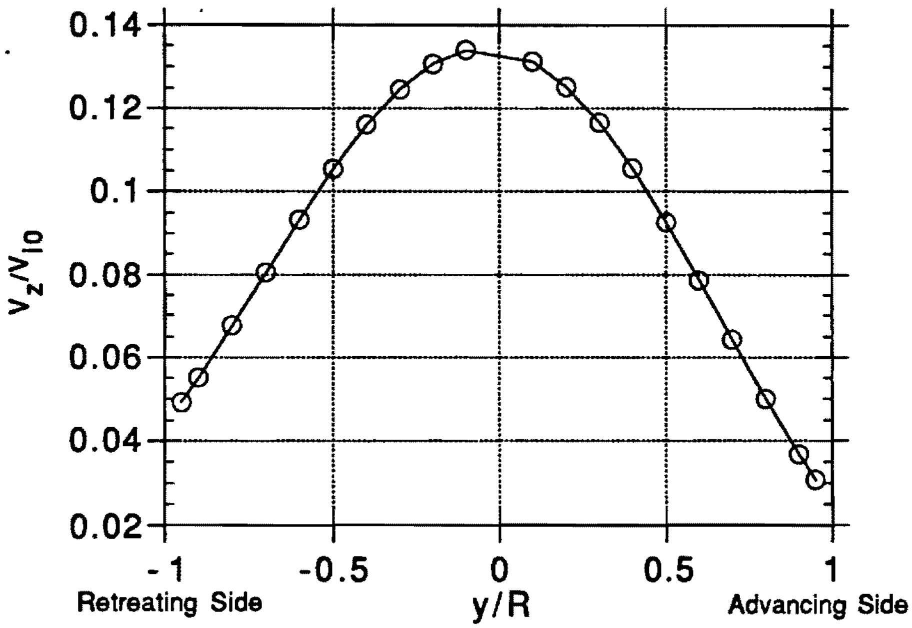

Fig. 1: Lateral Variation of Upwash on the Rotor Disk Due to Ship (h/R=1; μ=0.05)

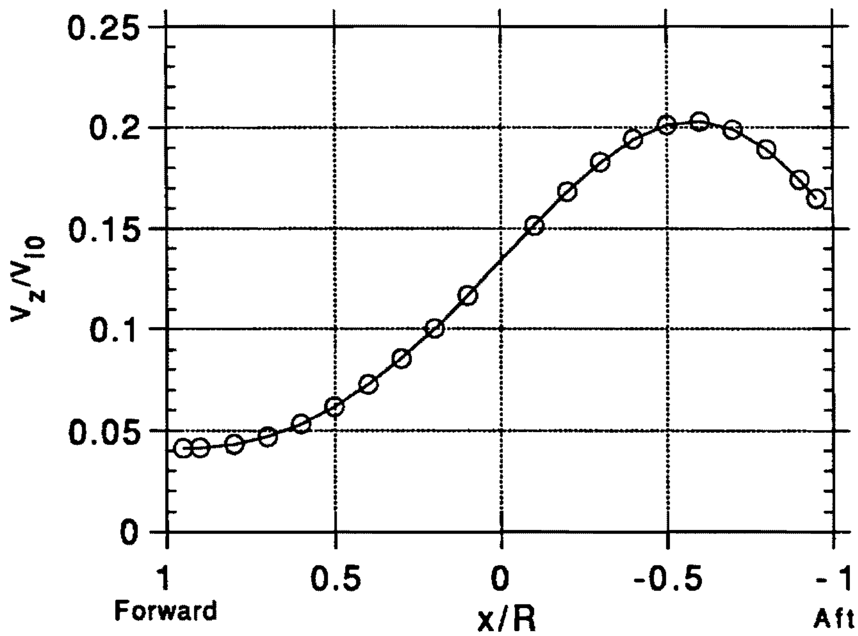

Fig. 2: Longitudinal Variation of Upwash on the Rotor Disk Due to Ship (h/R=1; μ=0.05)

E-15-M07
19

UNSTEADY AERODYNAMIC ANALYSIS OF DUAL-ELEMENT WING CONFIGURATIONS

BI-MONTHLY PROGRESS LETTER FOR THE PERIOD

July 1 - August 31, 1993

Submitted to the

NAVAL AIR WARFARE CENTER
AIRCRAFT DIVISION
WARMINSTER, PA

Attn: Mr. Marvin M. Walters

Prepared By

L. N. Sankar
Professor
School of Aerospace Engineering
Georgia Institute of Technology, Atlanta, GA 30332

March 1994

Georgia Institute of Technology
School of Aerospace Engineering

March 21, 1994

Mr. Marvin M. Walters
Code 6051
Naval Air Development Center
Warminster, PA 18974

Subject: BI-MONTHLY PROGRESS REPORT FOR THE PROJECT "UNSTEADY AERODYNAMIC ANALYSIS OF DUAL-ELEMENT WING CONFIGURATIONS"

Dear Mr. Walters:

During the reporting period (July 1, 1993 - August 31, 1993), the following tasks were completed:

1) As discussed in the previous report, a multi-zone Navier-Stokes solver has been developed to study dynamic lift enhancement concepts. During the reporting period, an AIAA paper regarding this work was prepared. A copy of this paper is enclosed.

2) Mr. Olympio Mello has completed work on the numerical simulation of helicopter rotors operating in the vicinity of an aircraft carrier deck. During the reporting period, he prepared a paper titled "Analysis of Helicopter/Ship Aerodynamic Interactions" for the AHS Aeromechanics Specialists Conference that was held in January 1994. In the appendix, viewgraphs summarizing this work are enclosed.

With best wishes,

Sincerely,

LAKSHMI N. SANKAR
Professor

APPENDIX

AIAA 94-0164
A Multizone Navier-Stokes Analysis of Dynamic Lift Enhancement Concepts

Ashok Bangalore
Georgia Institute of Technology
Atlanta, GA
Wei Tseng
Naval Air Warfare Center
Warminster, PA
Lakshmi N. Sankar
Georgia Institute of Technology
Atlanta, GA

32nd Aerospace Sciences Meeting & Exhibit
January 10-13, 1994 / Reno, NV

A MULTI-ZONE NAVIER-STOKES ANALYSIS OF DYNAMIC LIFT ENHANCEMENT CONCEPTS

Ashok Bangalore*
School of Aerospace Engineering
Georgia Institute of Technology, Atlanta, GA

Wei Tseng**
Naval Air Warfare Center, Aircraft Division
Warminster, PA

Lakshmi N. Sankar‡
School of Aerospace Engineering
Georgia Institute of Technology, Atlanta, GA

ABSTRACT

A 3-D unsteady multi-block Navier-Stokes solver capable of handling partial span leading and trailing edge flaps is described. The flow solver is validated through numerical simulations of flow over a cropped delta wing at a low angle of attack, with an oscillating trailing edge flap. The flow solver is next applied to the flow past a F-18 wing-alone configuration at a high angle of attack. Oscillating leading edge flaps are employed in an attempt to alter the leading edge vortex over the wing and to enhance the vortex lift. Sectional airload histories reveal two characteristic frequencies, one corresponding to the vortex shedding frequency of the basic wing with stationary flaps, and the other corresponding to the flap oscillation frequency. The time averaged sectional airloads for the cases with moving leading edge flaps are virtually identical to the loads where the flaps are deployed and held fixed. The present calculations indicate that the oscillatory motion of leading edge flaps does not significantly enhance the vortex lift, or the unsteady flow behavior of the baseline configuration.

INTRODUCTION

Modern fighter aircraft use highly swept wings because of their low drag characteristics at supersonic speeds, and their ability to develop high lift at low speed, high angle of attack conditions. At sufficiently high angles of attack, the leading edge vortex that forms over the wing upper surface gives rise to an additional mechanism for lift known as the vortex lift. Fighter aircraft make use the vortex lift, and an additional component known as the dynamic lift, during maneuvers. Military aircraft, and even the commercial aircraft such as the Concorde and the proposed high speed civil transport aircraft, can take advantage of vortex lift during low speed-take-off and landing.

As the angle of attack increases, the leading edge vortex becomes unstable, lifts off the wing surface, and vortex bursting occurs. The vortex burst phenomenon results in a loss in vortex lift, and leads to several other undesirable side effects. The vortex burst process may not occur simultaneously on both wings, and the resulting rolling moment can lead to the wing rock phenomenon. The vertical tail and other control surfaces in the wake of the main wing may experience buffeting, and structural fatigue. In extreme cases, a loss in yaw control due to the loss in the dynamic pressure over the vertical tail can occur.

Much work has been done in the United States during the past two decades on vortex lift generation, enhancement and control. Passive control devices such as leading edge extensions (LEX), forebody strakes and vortex flaps have been studied. Work has also gone into active vortex control strategies such as blowing and suction. A recent NASA conference on high angle of attack technology summarizes ongoing work in this area [Ref. 1].

During the past four years, a joint research effort between researchers at Georgia Tech and the Naval Air Warfare Center has been underway on the topic of dynamic lift enhancement, i.e. the stabilization and enhancement of the leading edge vortex using active control concepts. Early studies concentrated on the F-15 aircraft, because of the researchers' prior experience with this aircraft [Ref. 2,3] and the availability of good quality experimental data for this aircraft [Ref. 4,5]. The F-15 aircraft has a higher leading edge sweep than the F-18 configuration, and has no leading edge extension devices. The high angle of attack characteristics of the aircraft are dominated by the roll up a vortex sheet off the wing leading edge into a large core vortex that spans the entire upper surface of the wing. At sufficiently high angles of attack, a self-excited unsteady phenomenon associated with the vortex burst and its reformation occurs. The joint studies indicated that this vortex may be stabilized, and the vortex burst avoided using a small amount of blowing over the wing upper surface, in the vicinity of the leading edge [Ref. 6].

Blowing control requires the supply of high pressure air from the engines, that reduce their propulsive efficiency. The overall weight of the system is increased due to the

---

* Graduate Student
** Aerospace Engineer, Member AIAA
‡ Professor, School of Aerpspace Engineering

hardware needed to deliver the high pressure air to slots over the wing surface. For these reasons, The present researchers began to look at other active control strategies that require very small amounts of energy, and a small weight penalty.

One of the strategies explored was a concept that has been previously studied by Smith et al. [Ref. 7] through water tunnel flow visualization studies of an F-18 wing-alone configuration. In this approach, integral leading edge flaps are used, that oscillate $\pm 2^{\circ}$ about their mean downward deflected position. Such small amplitudes are necessary in order to keep the power consumed by the actuators low. The goal is not to significantly alter the tip vortex strength, but to stabilize it with small amounts of vorticity injected into the vortex core. It was anticipated that this may be accomplished with small amplitude flap motions.

Numerical studies by the present investigators for the configuration studied in Ref. 7 focused on full span flaps [Ref. 8]. Several interesting conclusions were drawn from the numerical studies. It was found that the flow over the wing surface was highly three-dimensional, containing substantial amounts of spanwise flow. The flow visualization studies of the numerical results showed large concentrated packets of vorticity resulting from the leading edge flap motion, that appeared to interact with the existing leading edge vortex. The airload time history showed a different story. Sectional and total airload history showed high frequency fluctuations associated with the flap motion, as expected. These time histories also showed that a low frequency oscillation in loads associated with the vortex burst and regeneration was still present. In other words, the vorticity generated by the leading edge flap motion did not suppress the basic stall characteristics of the wing.

In an actual aircraft, full span flaps (leading edge or trailing edge) are seldom used because of the weight considerations and the need for housing actuators and motors on the wing. Partial span slats and flaps are much more common, and are already in use to enhance takeoff and landing performance. The present study is a continuation of the studies reported in Ref. 8, and focuses on the following questions: (a) can partial span flaps be used in their static downward deployed position, or in sinusoidal motion about a mean position, to control vortex burst? (b) where should the flaps be located over the wing leading edge for optimum effect, if any?

The present study uses the same configuration used in Ref. 7 and 8. The Mach number is set to 0.15, and the Reynolds number based on wing root chord was set to 20,000 to closely mimic the experimental conditions. At these Reynolds numbers, the flow is expected to be transitional and can not be modeled using existing turbulence models, that are tuned for high Reynolds numbers. For these reasons, laminar flow simulations were done in the present study.

This paper is organized as follows. First, modifications to the flow solver described in Ref. 8, needed to model partial span flap oscillations are discussed. Some code validation studies performed to gain confidence in the modified solver are next discussed. Finally, results are presented for the F-18 wing, where the partial span flaps were located at two locations: inboard near the wing root, and outboard near the wing tip. Results are presented primarily in the form of time history of sectional loads.

NUMERICAL FORMULATION

The flow solver used here has been documented extensively in literature [e.g. Ref. 2,3, 8] , and only its basic characteristics are described here.

This solver integrates in time the 3-D compressible Navier-Stokes equations on a curvilinear body-fitted coordinate system (ξ,η,ζ,τ). Second or fourth order accurate central difference formulas are used to approximate the spatial derivatives that appear in the governing equations as well as the metrics of transformation that link the physical domain (x,y,z,t) with the transformed domain (ξ,η,ζ,τ). The time derivative that appears in the flow equations are approximated by a first order accurate, two-point difference scheme.

When these approximations are used, a system of nonlinear algebraic equations result for the flow properties at a number of points in the flow domain. As is common with the Newton's method for solving nonlinear equations, these equations are linearized about their values at a previous time level. The matrix of the resulting system of equations contain 5x5 matrix elements, but may be shown to be sparse, banded, and diagonally dominant. This matrix may be approximately factored into two or more tri-diagonal matrices, that may be easily inverted. In some instances, using a strategy proposed by Pulliam and Chaussee [Ref. 9], these factored matrices may be reduced to scalar tridiagonal matrices prior to their inversion.

The effects of turbulence may be modeled in the flow solver using the classical Baldwin-Lomax model, or a two-equation k-ε model. As stated earlier, the F-18 wing calculations shown here were done assuming the flow to be fully laminar.

The accuracy and stability characteristics of this baseline methodology are now well understood. The present authors have studied a number of configurations such as unsteady flow over an F-5 wing with an oscillating trailing edge flap [Ref. 8], helicopter rotors [Ref. 10] and high speed propellers [Ref. 11] with this baseline code with success.

MULTI-ZONE METHODOLOGY

Whenever a configuration that is more complex than an isolated wing is considered, new complications arise. The partial span flaps considered here can not be easily solved by mapping the flow filed surrounding the wing/flap into a single block. Such a single block would have resulted in a highly sheared, discontinuous grid at the wing-flap interface.

Techniques for solving complex flows using a multi-block strategy are highly developed, and a number of flow solvers, including a counter-rotating propeller analysis developed by the present investigators use the multi-block strategy. In this approach, the body-fitted grids over individual components align neatly at the block interface [e.g. Ref. 12,13]. Other researchers have resorted to unstructured strategies [e.g. Ref. 14, 15] , or an overset grid strategy [e.g. Ref. 16]. In many instances, the flow field and/or the grid is steady and the governing equations may be solved, and the mass, momentum and energy fluxes conserved both in a local cell-by-cell sense and the global sense.

Block structured grid analyses of unsteady flows require more care. If the boundary conditions are not properly implemented at the block interface, false reflections may occur, contaminating the temporal behavior. In unsteady flows, there is always a time lag between the surface motion and the resulting lift force. This lag is due to the finite time required for the vorticity field and the acoustic waves to travel in space. In an unsteady flow, these unsteady waves may travel across zone boundaries, say from root to tip. If care is not taken in handling the transfer of this information, both the airload magnitude and phase may be affected.

To our knowledge, the boundary conditions at the interface of a moving flap and a fixed wing section have been rigorously implemented only in Ref. 17 . These researchers used a variation of the Chimera scheme. The Chimera scheme requires interpolation of the flow properties at a grid point on a given grid, based on its neighbors on a second grid. A search is usually needed to locate the closest neighbors to a grid point. Ref. 17 describes several sophisticated schemes for implementing the search process.

A sample multi-zone grid used in the present calculations is shown in Fig 1. The wing is divided into two or three spanwise blocks depending on the configuration involved. In the present work, we have considered two different partial span flap configurations. In the first case the leading edge flap is located between 50% and 100% of the semi-span of the wing , and the overall flow field is divided into two zones. In the second case the partial span flap is located between 38% and 66% of the semi-span. A built-in algebraic grid generator is used to generate the C-H grid. The grid in the flap region moves in time according to the flap oscillation.

The following strategy is used for handling the boundary conditions at the wing-flap interface. The flow is first updated in each zone by the time marching scheme described earlier. During this phase, the boundary conditions at the block interface are lagged by one time step. The flow properties at the interface boundaries are next updated using a simple linear interpolation. The sketch below shows the typical grid points at the block interface.

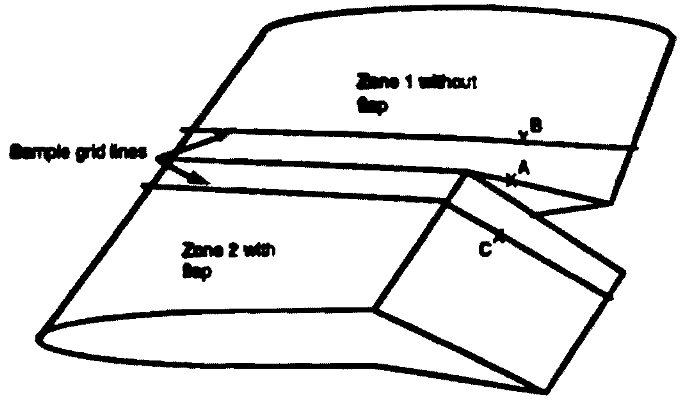

Grid points A and B in the sketch above belong to zone 1, while the points A and C belong to zone 2. The flow properties at the point A on the interface are computed from the interior points B and C as follows:

$$q_A = \frac{\Delta s_1 q_C + \Delta s_2 q_B}{\Delta s_1 + \Delta s_2}$$

Here ΔS_1 is the distance between grid points A and B, ΔS_2 is the distance between grid points A and C. Similarly the interface points located on the lower surface of the wing use the neighboring lower surface grid points to update the flow information. On uniformly spaced grids, ($\Delta S_1 = \Delta S_2$) it is seen that this interpolation reduces to simple averages.

CODE VALIDATION STUDIES

As stated earlier, the baseline single block solver has been validated for a number of applications. The code validation studies here focused on multi-block simulations, where the block interface boundary conditions vary as a function of time.

The wing studied is a clipped delta wing with a 6% thick circular arc airfoil section. A trailing edge flap is located between 56.6% and 82.9% of the semispan as shown in Fig 2. The wing leading edge sweep Λ is 50.4°. The freestream Mach number is chosen to be 0.4 and the mean angle of attack is 0.05°. The hinge line of the flap is located at 80% chord, and the flap frequency of oscillation is 8 Hertz. The flow Reynolds number is 1.5 million. The above configuration and flight conditions were chosen because of the availability of experimental data [Ref. 18]. The Baldwin-Lomax turbulence model is used to calculate eddy viscosity.

The computational domain is divided into three spanwise blocks. The inboard block covers the region from the root to 56.6% of the semispan. The second zone encloses the trailing edge flap, and the third zone covers the region outboard of the flap. The grids used have 121 X 8 X 45,121 X 7 X 45 and 121 X 9 X 45 nodes in zones 1 , 2 and 3 respectively.

Figure 3 shows the comparison of the amplitude of upper surface pressure coefficient with the experiment. As expected, much of the lift production for the oscillating flap case occurs in the aft region of the wing, downstream of 60% chord. In the vicinity of the hinge line large spikes in the pressure coefficient are observed both in the experiment and the calculations. The phase lag between the flap motion and the upper surface pressure is shown in Figure 4 . In compressible flows, there is a phase lag between the surface pressure, and the flap motion due to the finite speed of sound, and the finite speed at which vorticity is carried away by the wake. This lag will be expected to increase with the distance measured from the flap hinge line. Fair agreement can be seen between the experiment and the computed phase lag. The discrepancies between the measurements and the predictions are due to the rather coarse grid used in the simulations, with less than 7 points over the flap in the chordwise direction. Some differences in the leading edge region are attributable to the fact that the wing with a sharp leading edge was analyzed using a wrap-around C- grid.

F-18 WING SIMULATIONS

The F-18 Wing planform is chosen here with an aspect ratio of 3.5, leading edge sweep angle 26.7°and a taper ratio of 0.42. The freestream Mach number, Reynolds number and the angle of attack are 0.1666, 20,000 and 40° respectively. These flow conditions are identical to the water tunnel experiments conducted by Smith (Ref. 7].

Two sets of grid dimensions 121X24X45 and 141X24X45 were used in the calculations, to assess the effect of grid density on the solutions. The coarser grid was not adequately able to capture the low frequency oscillation in the spanwise loading, due to the vortex burst phenomenon. All the results presented here are for the 141X24X45 grid.

The built-in algebraic C-H grid generator with an elliptic smoothing routine has been used in all the simulations. The grid near the leading edge flap conforms to the flap setting and moves with the flap during the oscillations. The three different flap configurations considered here are

i) Oscillating flap between 50% and 100% semispan

ii) Oscillating flap between 33% and 66% semispan

iii) Oscillating flap between the root and 50% semispan

For all these cases 'k',the reduced frequency of the flap oscillation is 9.4 or three cycles per time unit. The reduced frequency k is defined as

$$k = c\omega/2U_\infty$$

where c is the root chord, ω is the flap frequency in radians per second and U_∞ is the Freestream speed.

The flap goes through three cycles of saw tooth motion per root chord length of travel. The initial flap setting is -34° with respect to the main wing, and the flap is allowed to move up and down by 4° in a saw-tooth fashion. That is, the flap moves between -34 degrees and -30 degrees of deflection, in a saw tooth fashion. These conditions correspond to the values used by Smith et al (Ref. 17) in their water tunnel studies for the F-18 wing a full span leading edge flap.

The calculations in all the three cases were carried out for several hundred cycles of flap oscillation, in order to ensure their repeatability. Because of the large volume of flow field data such 3-D unsteady simulations generate, it was not practical to analyze in detail the flow field using scientific visualization techniques. Instead, the interpretation of the flow field was carried out using the sectional airload time history.

Case 1. Flap between 50% and 100% semi-span:

Figure 5 shows the sectional airloads (normalized by freestream dynamic pressure and local chord) for case (i). Results are presented at four locations: 31% , 45%, 60% and 86% semi-span. The time loads at all these stations show a low frequency oscillation, over which a high frequency oscillation is superposed. The time period T_1 for the low frequency oscillation is seen to be 4 units, based on root chords traveled, regardless of the spanwise location. Because the frequency of this long wave length does not vary from span station to span station, we conclude that this is a fundamental vortex burst frequency of the entire wing. This fundamental frequency was present in all the three cases studied.

Figure 5 shows a second, high frequency variation in the sectional airload at the four stations. The time period, T_2, associated with this high frequency oscillation is 1/3 which corresponds to 'k', the reduced frequency being equal to 9.4. Since there are three cycles of flap motion per root chord travel, this frequency is easily identified as the frequency of flap motion.

Figure 5 also reveals that these two basic phenomena do not nonlinearly interact with each other. In other words, the amplitude of the high frequency motion does not seem to depend on where it is located in the low frequency cycle. We therefore conclude that the load variation due to the flap motion does not fundamentally alter, or is influenced by, the fundamental vortex burst activity.

Figure 5 also shows that the magnitude of the high frequency fluctuations do depend on the spanwise location. In the outboard region the high frequency fluctuations have a higher magnitude than near the root, and dominate over the fundamental low frequency fluctuations. This is likely due to the fact that the flap was located in the outboard station.

Several large spikes in the high frequency oscillations are seen, particularly in the outboard region. These spikes may be traced to the discontinuity in the slope of the saw tooth motion employed in this study.

Case 2. Flap between 33% and 66% semispan

Figure 6 shows the sectional airloads for this case at four representative span locations. In this case, calculations were also carried out with the flaps deployed, but without the oscillatory motion, and are shown. Many of the features of this calculations are identical to case (1) above. The fundamental low frequency variation in lift is clearly seen both for the oscillatory flap case, and the stationary flap case. The time-averaged values, as well as the amplitude of the low frequency oscillations of the sectional loads are identical for the stationary and moving flap case, reinforcing our earlier observation that the flap motion does not significantly alter the unsteady aerodynamic characteristics of the basic wing. As in case 1, over the portion of the span where the flap is located, the amplitude of the high frequency oscillations is much higher than over the rest of the wing, although the entire wing experiences the high frequency fluctuations.

Case 3. Flap between 0% and 50% semispan:

Figure 7 shows the sectional airloads for this case. As in the previous two cases, both the low frequency and high frequency oscillations are evident. At the inboard stations, the magnitude of the high frequency fluctuations approaches very high values (ΔC_l of the order of 0.3 or higher) and is significant compared to the mean C_l values (C_l around 0.8). Given the fact that the wing has a significant amount of taper, this would indicate that the inboard flaps are the most effective in changing the overall C_L levels of the wing, if only in a transient manner. Away from the flap, the high frequency fluctuations drop to about 3% of the local load, although the effects of the flap oscillation are felt all the way to the wing tip.

CONCLUSIONS

An existing single block three dimensional unsteady Navier-Stokes solver has been modified into a multi-block flow solver is capable of analyzing partial span leading edge and trailing edge flap motions. This solver was used to determine if oscillating leading edge flap devices may be used to increase the lift generated by a F-18 wing. The calculations indicate that the low frequency fundamental oscillations associated with the vortex burst phenomenon would not be altered by the presence of the flaps, or their spanwise placement. There was very little aerodynamic coupling between the high frequency oscillations associated with the flaps, and the fundamental unsteady flow behavior of the wing.

Other approaches for the stabilization of the vortical flow over the wing, and lift enhancement should be explored. Tangential blowing in the vicinity of the vortex core may be a worthwhile concept to explore, despite the structural weight penalties associated with this approach.

ACKNOWLEDGEMENTS

The Authors wish to express their appreciation to Mr. Marvin Walters for his support and also NASA Ames Research Center for providing Cray-YMP for computations.

REFERENCES

1. Proceedings of the High-Angle-of-Attack Technology Conference, Vol. I-III, NASA CP-3149, October 1990.

2. Sankar, L. N. and Kwon, O. J., "High Alpha Simulation of Fighter Aircraft," NASA CP-3149, October 1990, pp689-702.

3. Kwon, O. J. and Sankar, L. N., " Viscous flow simulation of fighter aircraft," *Journal of Aircraft*, Vol. 29, No. 5, September-October 1992, pp886-891.

4. Komerath, N. M., Schwartz, R. J., Kim, J. M. and Percival, S., "Unsteady Flowfield Measurements over Twin-Tailed Fighters," NASA CP-3149, October 1990, pp1061-1087.

5. Komerath, N. M., McMahon, H. M., Scwartz, R. J., Liou, S. G. and Kim, J. M., "Flowfield Measurements near a Fighter Model at High Angles of Attack," AIAA Paper 90-1431, June 1990.

6. Findlay, D, Kwon. O.J. and Kern. F.,"Numerical Investigation of the effect of Blowing on High Angle of Attack flow over Delta wings", AIAA paper 91-1809, June 1991.

7. Smith, B., " Dynamic lift enhancement using oscillating leading edge flaps," AIAA paper 92-2625.

8. Tseng, W., Tsung, F. L. and Sankar, L. N. " Numerical simulation of dynamic lift enhancement using oscillatory leading edge flaps", AIAA-93-0177, January 1993.

9. Pulliam, T. and Chaussee, D., "A Diagonal Form of an Implicit Approximate Factorization Algorithm," *Journal of Computational Physics*, Vol. 39, pp. 347-363, 1981.

10. Wake, B. E. and Sankar, L. N. "Solution of Navier-Stokes equations for the flow about a rotor blade," *Journal of the American Helicopter Society*, April 1989.

11. Srivastava. R., Sankar, L. N. and Reddy, T.S.R., "Application of an Efficient Hybrid Scheme for Aeroelastic Analysis of Advanced Propellers," *Journal of Propulsion and Power*, September-October 1991, pp 767-775.

12. Biedron, R. T. and Thomas, J. L., "Navier-Stokes Computations for an F-18 Forebody with Actuated Control Strake," NASA CP-3149, October 1990, pp481-506.

13. Thomas, J. L., Walters, R. W., Reu, T., Ghaffari, F., Weston, R. P. and Luckring, J. M., "A Patched-Grid Algorithm for Complex Configurations Directed Towards the F/A-18 Aircraft," *Journal of Aircraft*, Vol. 27, No. 9, 1990, pp. 749-756.

14. Batina, J. T., "A Fast Implicit Upwind Solution Algorithm for Three-Dimensional Unstructured Dynamic meshes," AIAA Paper 92-0447, January 1992.

15. Jameson, A., Baker, T. J., and Weatherhill, N. P., "Calculation of Inviscid Flow over a Complete Aircraft," AIAA paper 86-0103, January 1983.

16. Benek, J. A., Buning, P. G. and Steger, J. L., "A 3-D Chimera Grid Embedding Technique," AIAA paper 85-1523, July 1985.

17. Klopfer, G. H. and Obayashi, S., "Virtual zone Navier-Stokes computations for oscillating control surfaces", AIAA paper 93-3363-CP, July 1993.

18. Hess, R. W., Cazier, F. W. Jr. and Wynne, E. C, "Steady and unsteady transonic pressure measurements on a clipped delta wing for pitching and control surface oscillations," NASA TP -2594, October 1986.

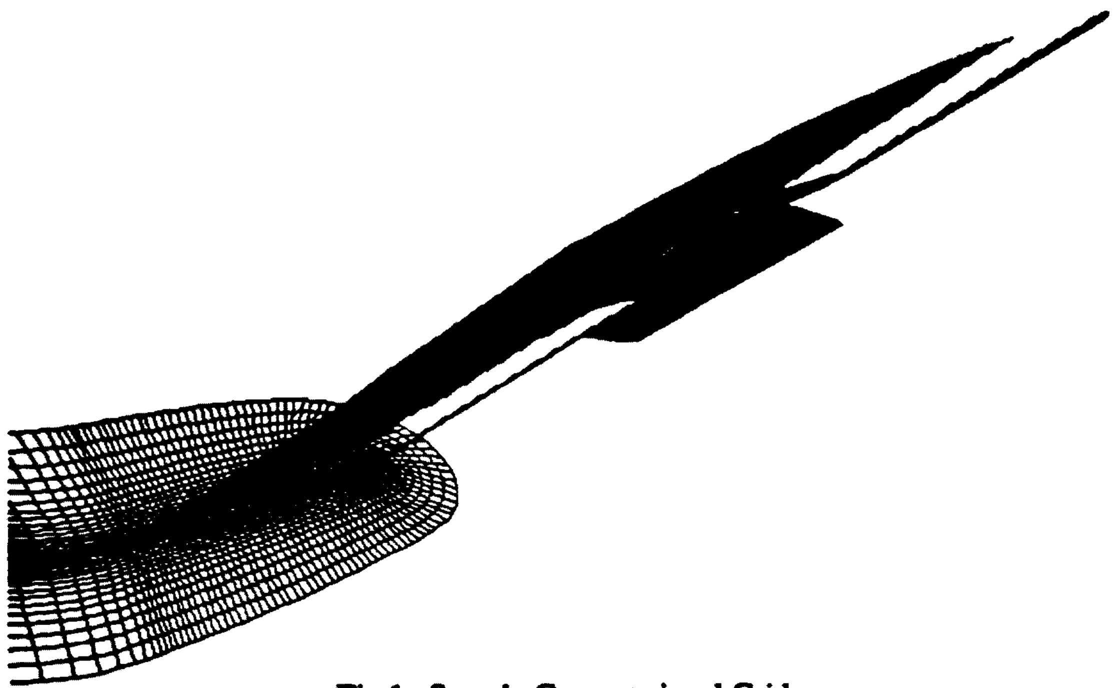

Fig 1 : Sample Computational Grid

CLIPPED DELTA WING WITH TRAILING EDGE FLAP

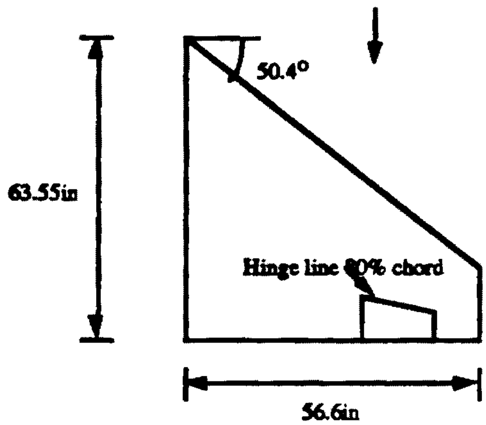

Fig 2 : Delta Wing Planform

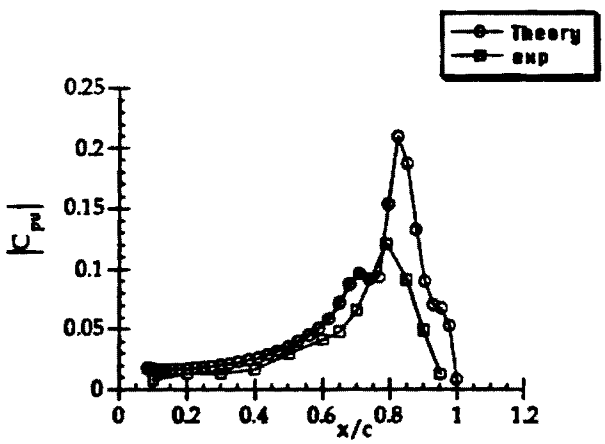

Fig 3: Amplitude of Unsteady Upper Surface Pressure Coefficient, M = 0.4, flap frequency = 8Hertz

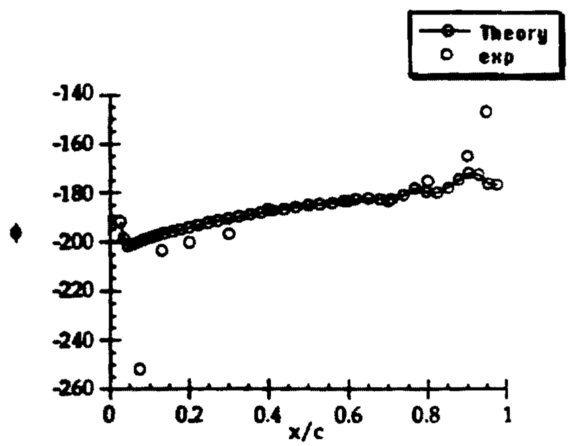

Fig 4: Phase Angle of Upper Surface Pressure Coefficient

F-18 Wing Planform, L.E.Flap 50% - 100%

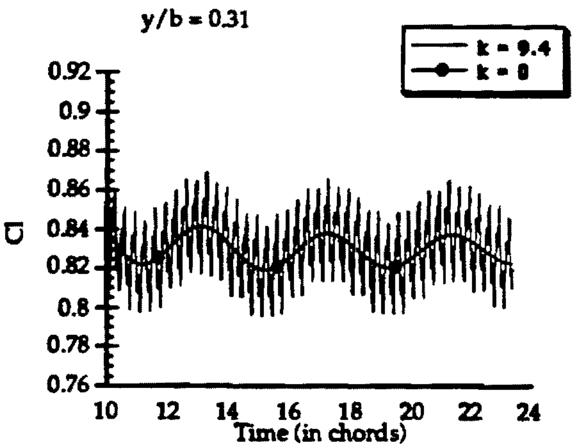

(a)

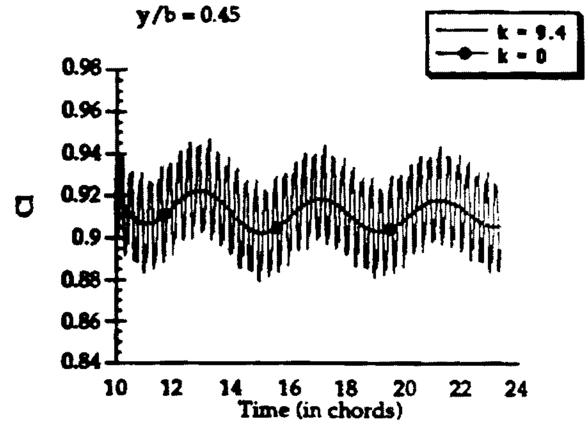

(b)

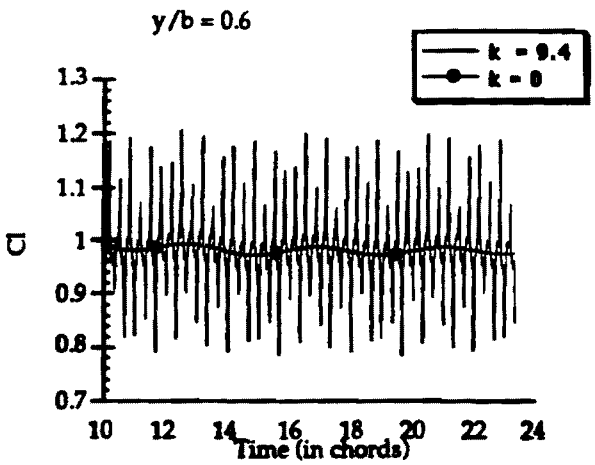

(c)

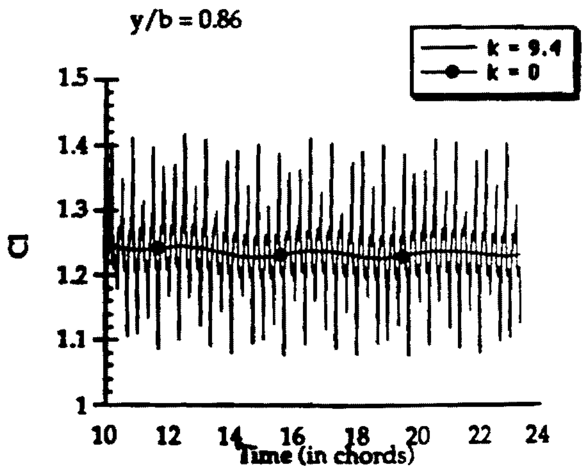

(d)

Fig 5 : Sectional Lift History at Different Span Stations
case(i), L.E.Flap 50% - 100%

F-18 Wing Planform, L.E. Flap 33%-66%

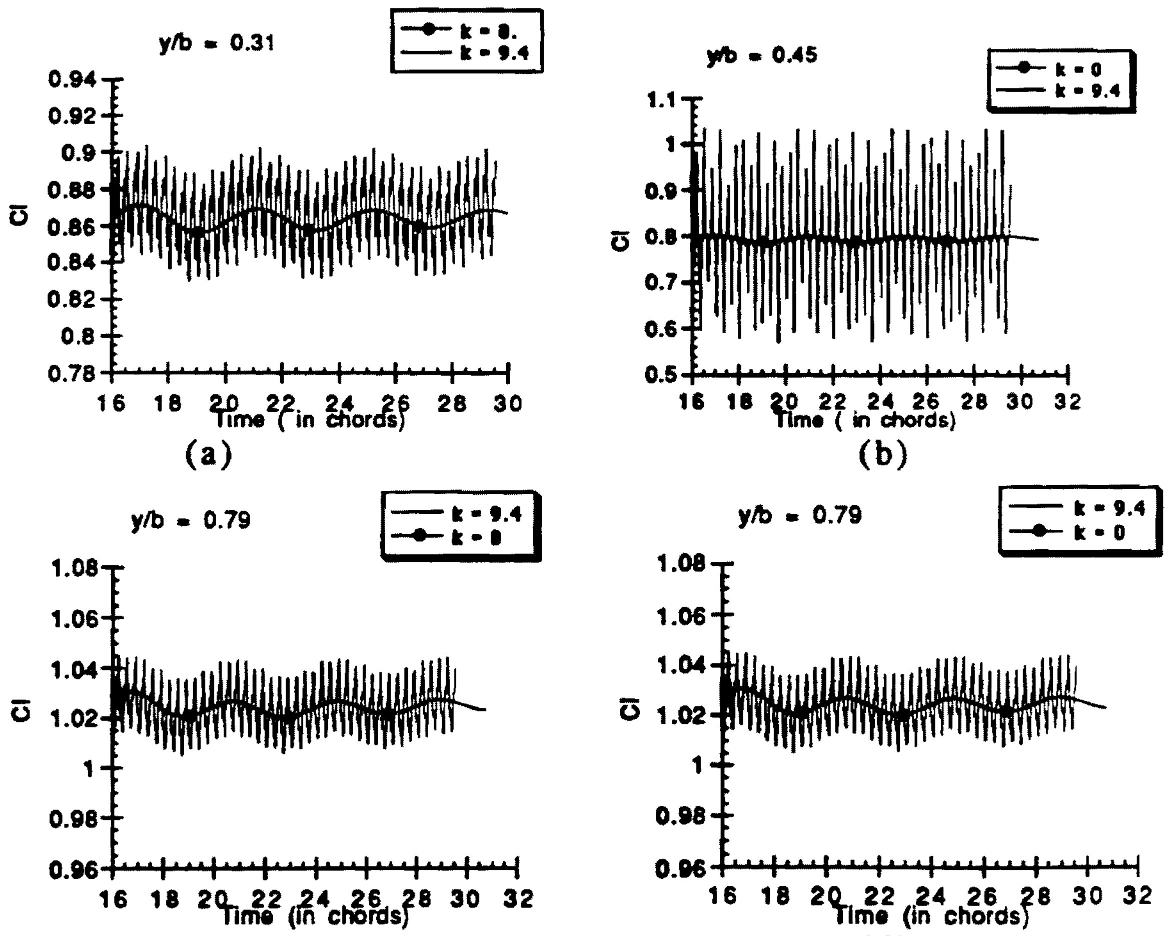

Fig 6 : Sectional Lift History at Different Span Stations
case(ii) L.E.Flap 33% - 66%

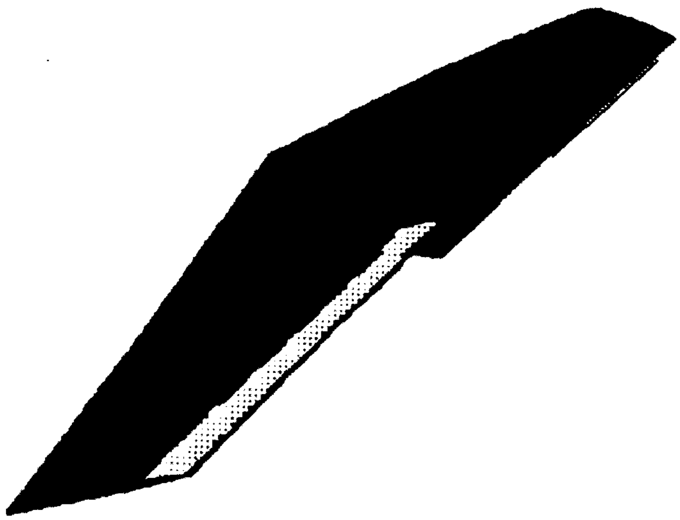

F-18 Wing Planform, L.E.Flap 0% - 50%

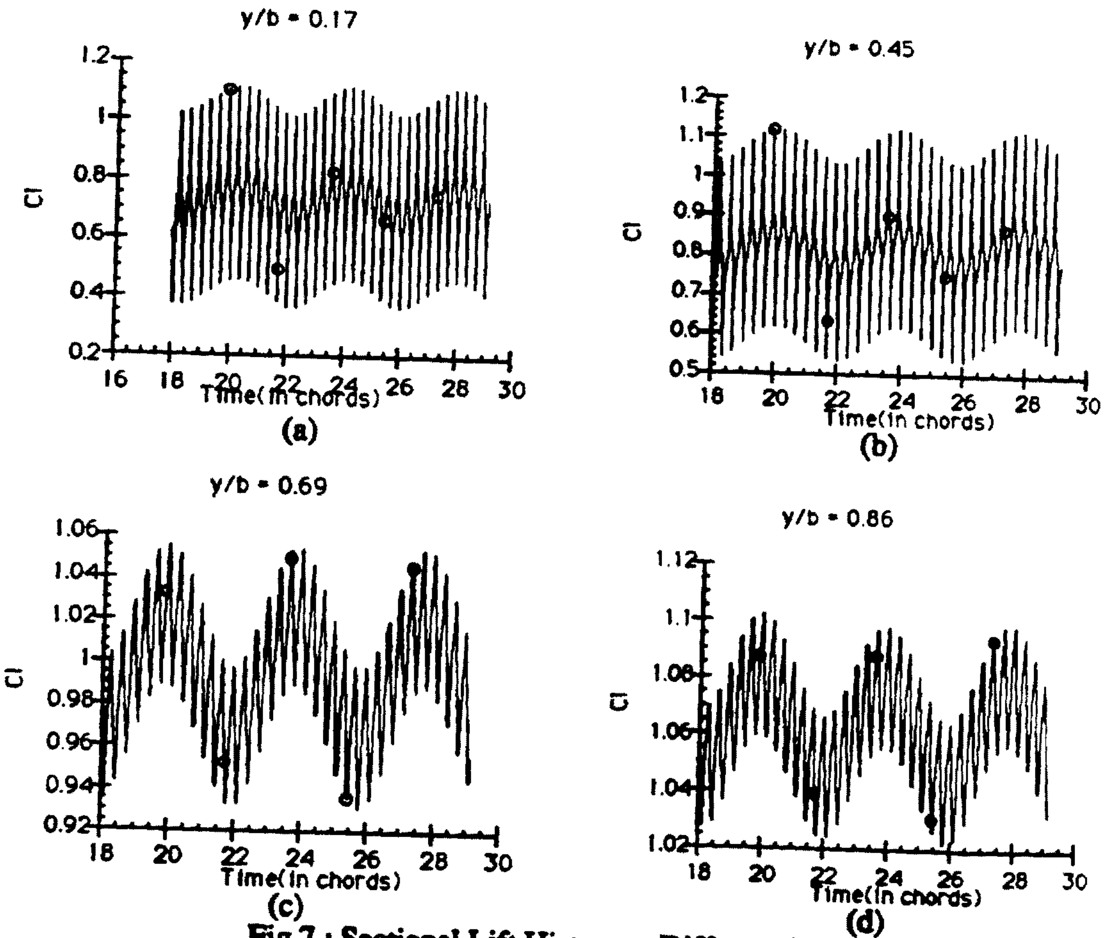

Fig 7 : Sectional Lift History at Different Span Stations
case(iii), L.E.Flap 0% - 50%

Analysis of Helicopter/Ship Aerodynamic Interactions

by

O.A.F. Mello, J.V.R. Prasad, L.N. Sankar
School of Aerospace Engineering
Georgia Institute of Technology
Atlanta, GA

and

W. Tseng
Naval Air Warfare Center
Aircraft Division
Warminster, PA

AHS Aeromechanics Specialists Conference
San Francisco, CA
January1994

Introduction

- Motivation: Determination of safe operating environment for landing helicopters on non-aviation ship decks
- Current sea trial process is long and expensive
- Need an appropriate helicopter/ship aerodynamic interaction model to be incorporated into simulation codes

Past Efforts

- Ship Airwake
  - Wind tunnel visualization;
  - Characterized by large separation, vortex shedding and turbulence;
  - Wind tunnel and full-scale tests: Mean velocities and turbulence spectra;
  - Navier-Stokes computations.

Past Efforts (cont'd)

- Ship "Ground Effect"
  - Simple semi-empirical correction factor applied to inflow, based only on distance from ground;
  - No "partial" ground effect;
  - Does not take into account presence of superstructure.

Present Approach

- Ship Airwake (after Prasad et al.)
  - Mean velocities from system identification techniques using full-scale test results (Australian Navy);
  - Turbulent components from statistical model contructed from full-scale tests;
  - Rotatory sampling for incorporation of turbulent components.

Present Approach (cont'd)

- Ship "Ground Effect"
  - Panel representation for the ship; use sources/sinks from panel solution to compute resulting velocities on rotor disk;
  - RHS of panel method system computed using a rigid helical wake model;
  - Mirror image to account for sea surface.

Ship Panel Representation

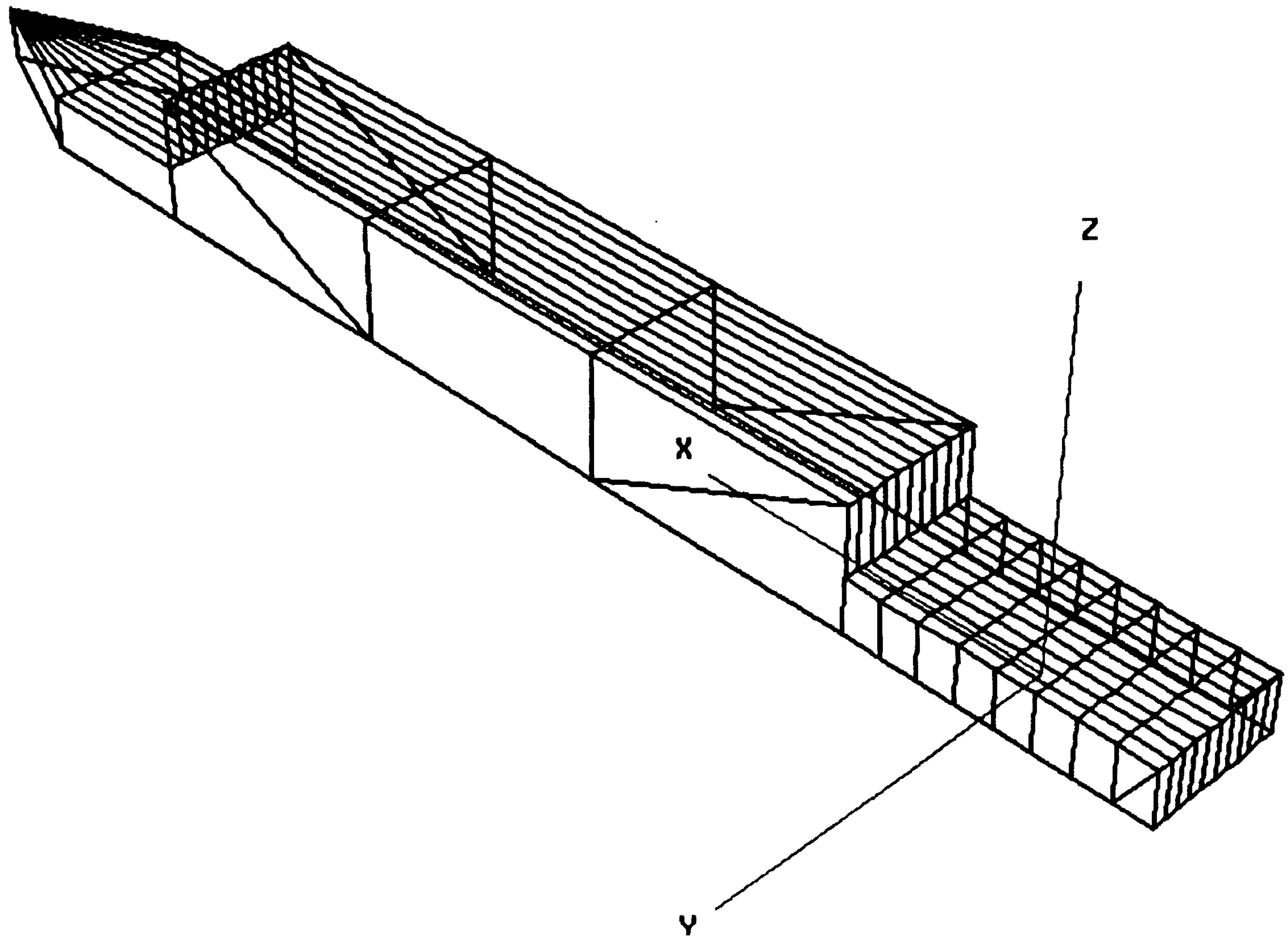

Present Approach (cont'd)

- **Rotor/Wake Formulation**
  - Skewed helical wake model;
  - Near wake and far wake (tip vortices only);
  - Assumed wake vorticity distribution:

$$\Gamma_b(\bar{r},\psi) = \Gamma_0 \, \bar{r} \sqrt{1 - \bar{r}^2} \, \frac{1}{1 + \frac{3}{2} \, k_T \, \mu \sin \psi}$$

  - Mirror image to account for sea surface.

Rotor/Wake Formulation

- **Vorticity Related to Thrust Coefficient:**

$$\tilde{\Gamma}_0 = \frac{\Gamma_0}{R\left(\Omega R\right)} = C_T \frac{\pi}{N_b} \frac{\sqrt{1 - a^2}}{\frac{\pi}{16} + \frac{4}{9k_T}\left(\sqrt{1 - a^2} - 1\right)}$$

- **Near Wake:**

$$\Gamma_t(\bar{r},\psi) = \frac{\partial \Gamma_b}{\partial \bar{r}} = \Gamma_0 \frac{1 - 2\,\bar{r}^2}{\sqrt{1 - \bar{r}^2}} \frac{1}{1 + \frac{3}{2}\; k_T\, \mu \sin \psi}$$

$$\Gamma_s(\bar{r},\psi) = \frac{\partial \Gamma_b}{\partial \psi} = -\,\Gamma_0\, \bar{r} \sqrt{1 - \bar{r}^2}\, \frac{\frac{3}{2}\; k_T\, \mu \cos \psi}{\left(1 + \frac{3}{2}\; k_T\, \mu \sin \psi\right)^2}$$

- **Far Wake:** $\Gamma_T(\psi) = \frac{1}{2} \Gamma_0 \frac{1}{1 + \frac{3}{2}\; k_T\, \mu \sin \psi}$

Implementation into Simulation Code (GENHEL)

- Blade element method
- Ship airwake and "ground effect" contributions are added to total blade velocities;
- Panel code incorporated as additional module;
- Compute influence coefficients only once and store a LU decomposition of coefficient matrix for efficient backsubstitution;
- Not suitable for real-time simulation.

Results and Discussion

- Method applied to a SH-60 near a FFG-7 class frigate, both at 15 kts;
- Aircraft was trimmed with and without ship present;
- Ship airwake turbulent component was not used;
- Ship airwake mean velocities were computed from panel method for comparison with full-scale data;
- Aircraft was positioned above center of deck, above edge of deck and just outside deck, all one rotor radius above deck

Helicopter Positioning with Respect to Ship Deck

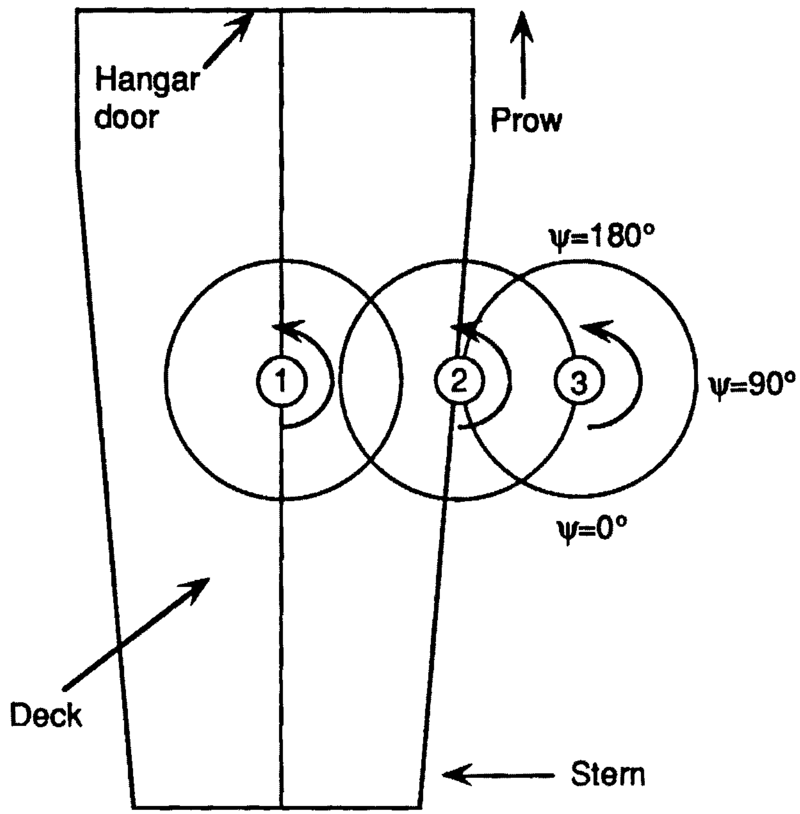

Ship Ground Effect, Helicopter Above Center of Deck

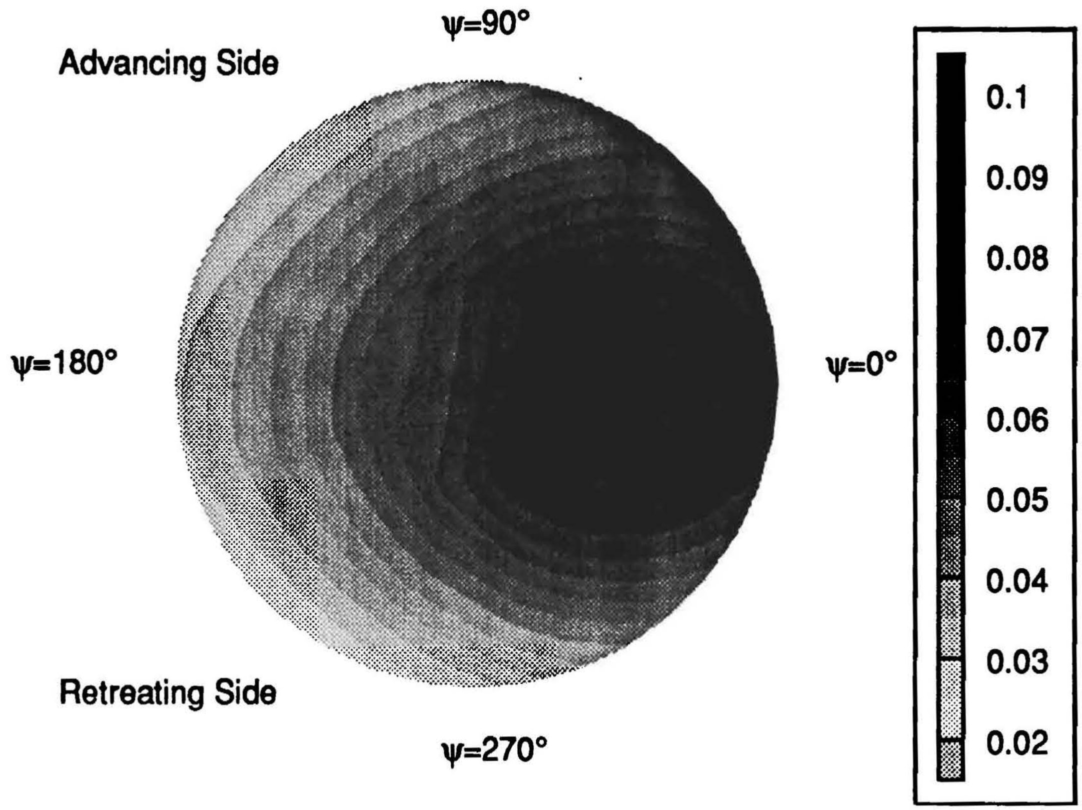

Ship Ground Effect, Helicopter Above Edge of Deck

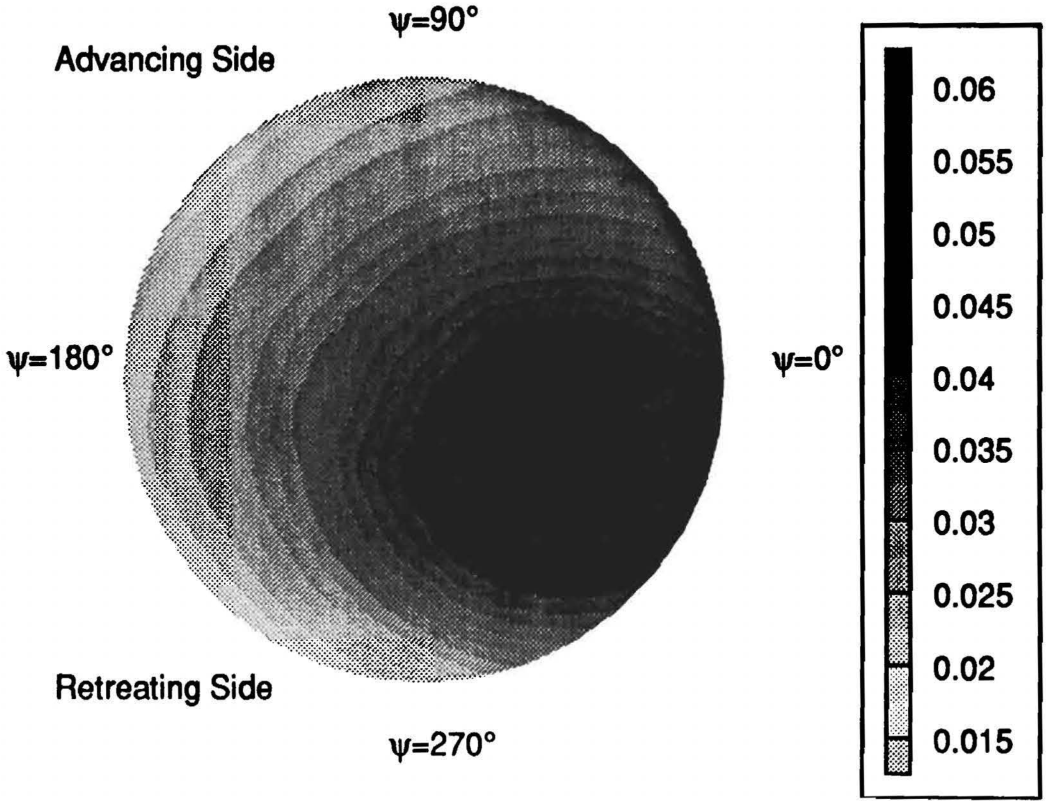

Ship Ground Effect, Helicopter Outside Deck

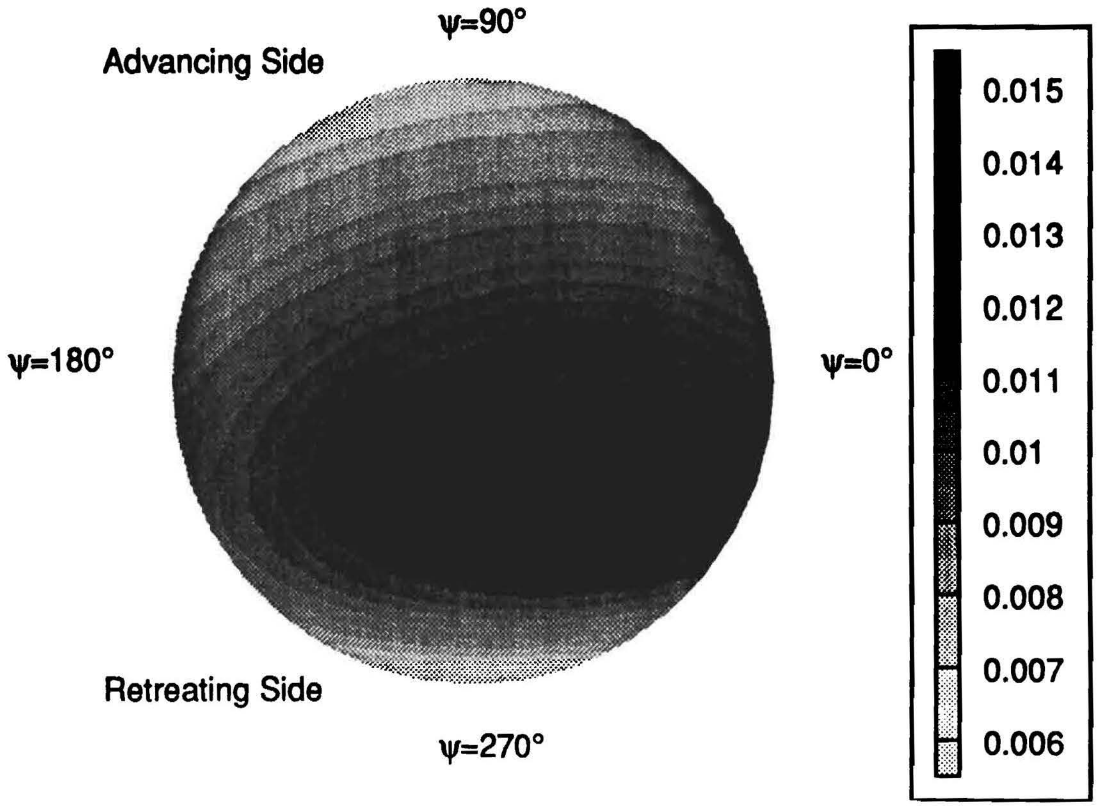

Ship Ground Effect: Variations with Helicopter Position

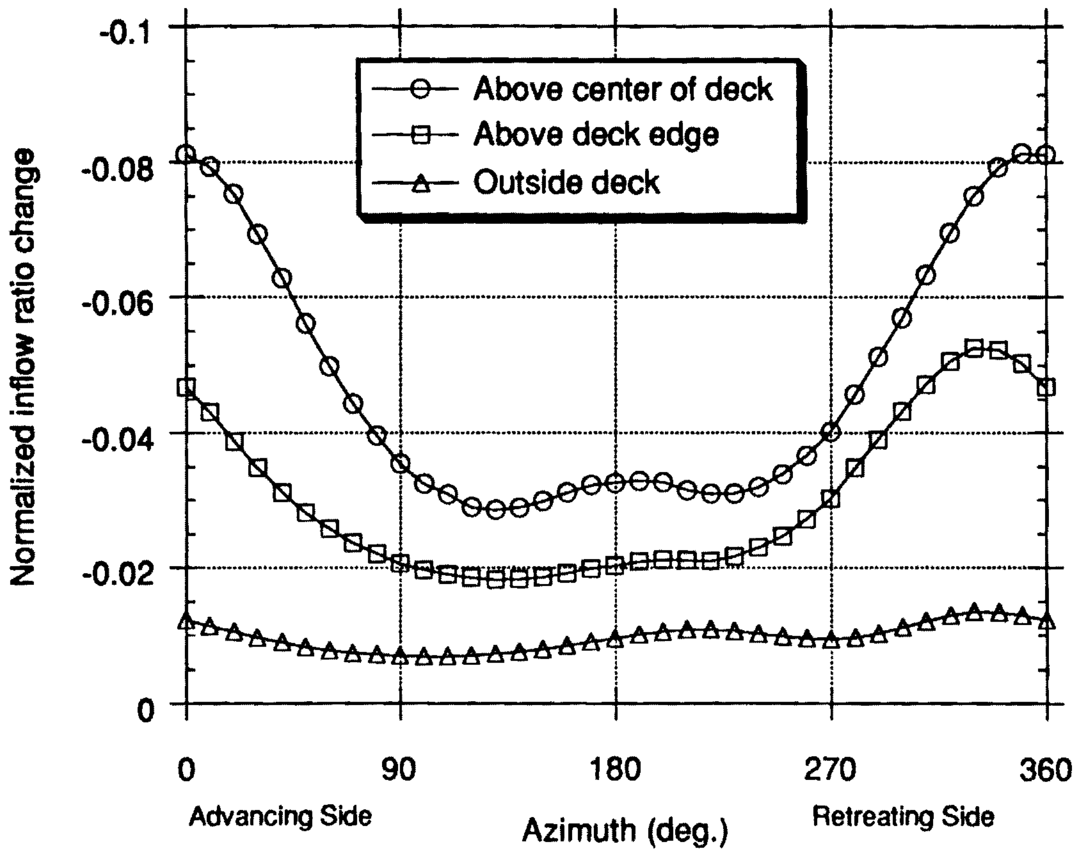

Ship Ground Effect: Local Inflow Correction

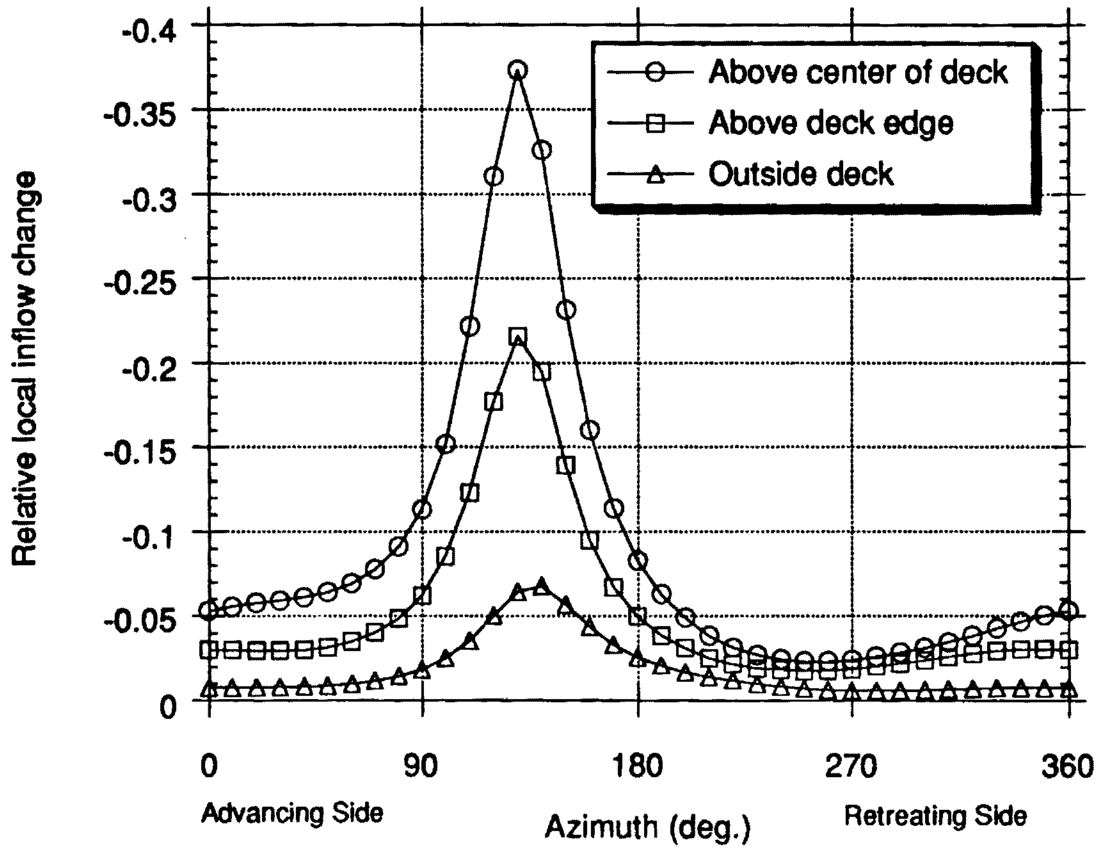

Partial Ground Effect

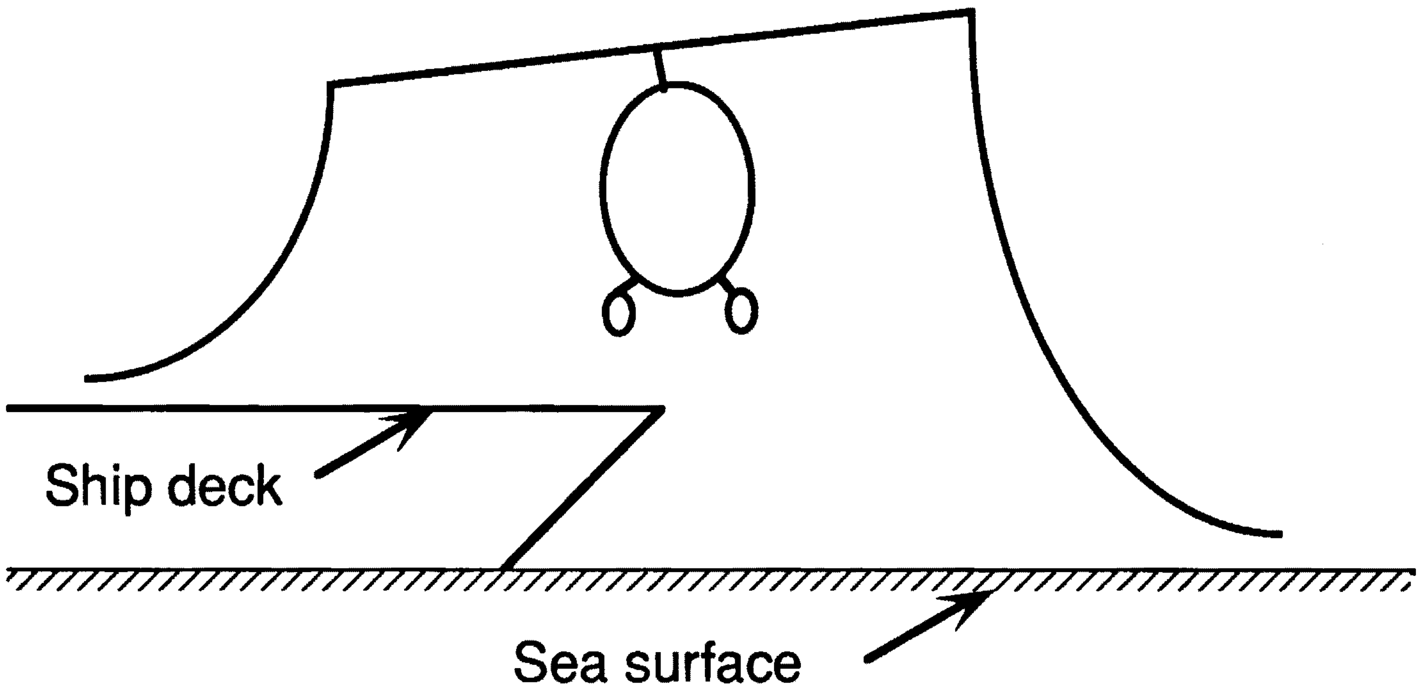

Ship Airwake Effect on Blade Normal Velocity

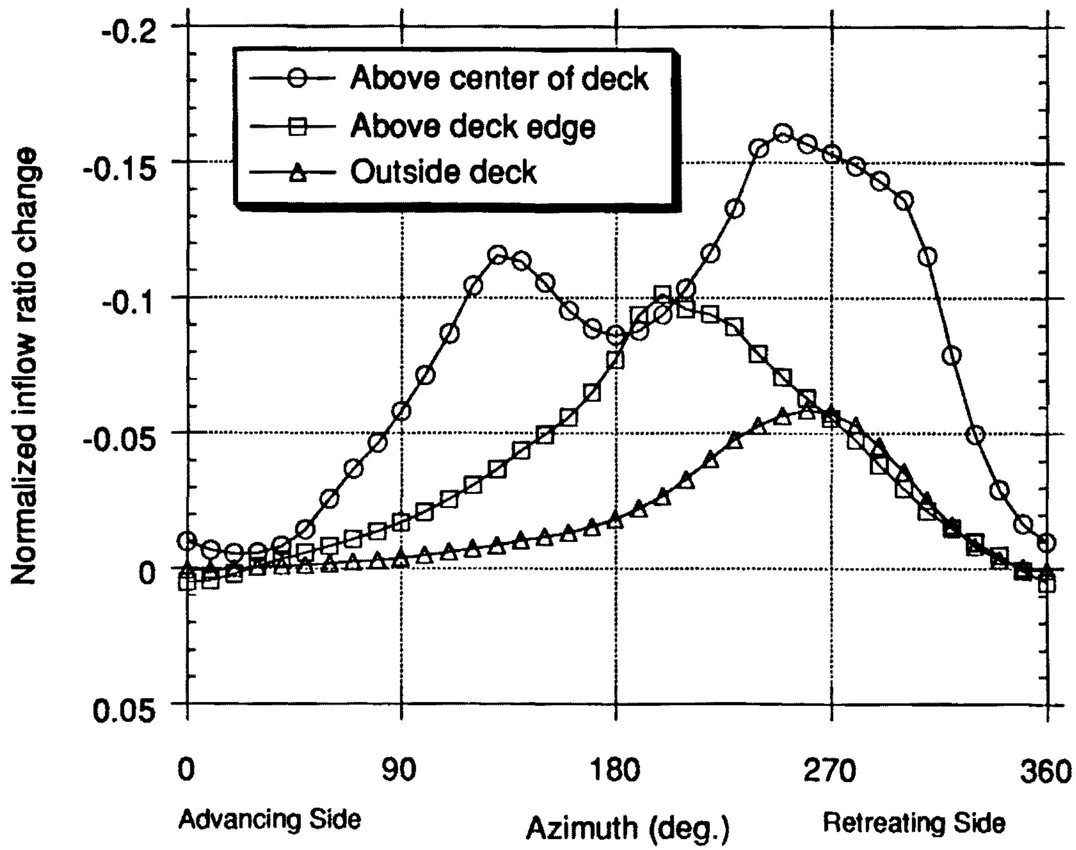

Ship Airwake Effect on Blade Normal Velocity (cont'd)

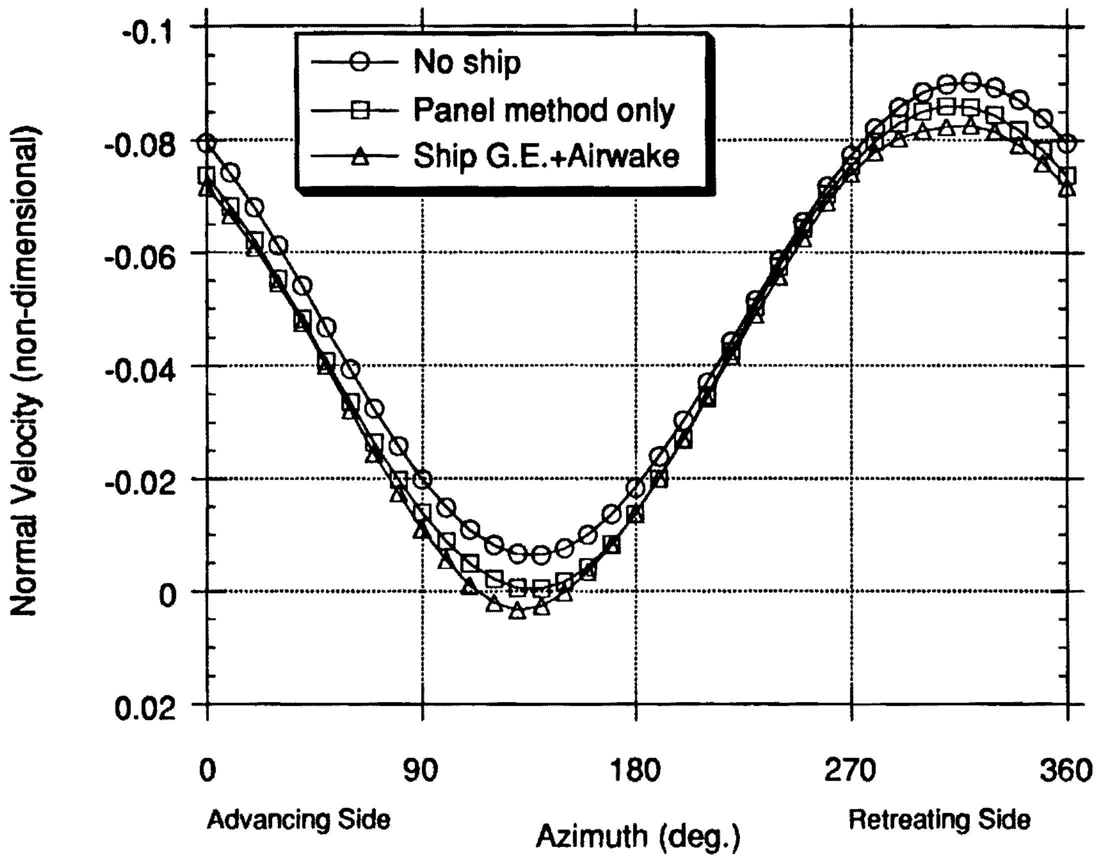

Ship Airwake Effect on Blade Tangential Velocity

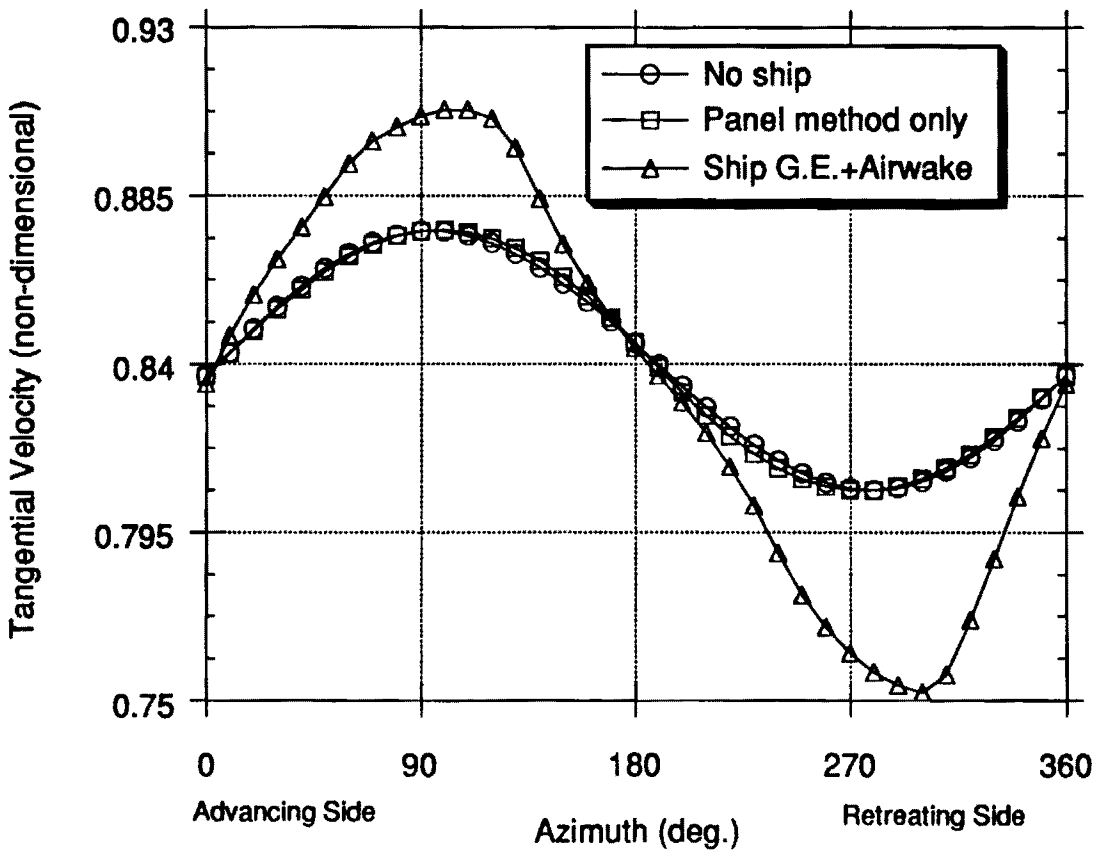

Ship Airwake Effect on Blade Radial Velocity

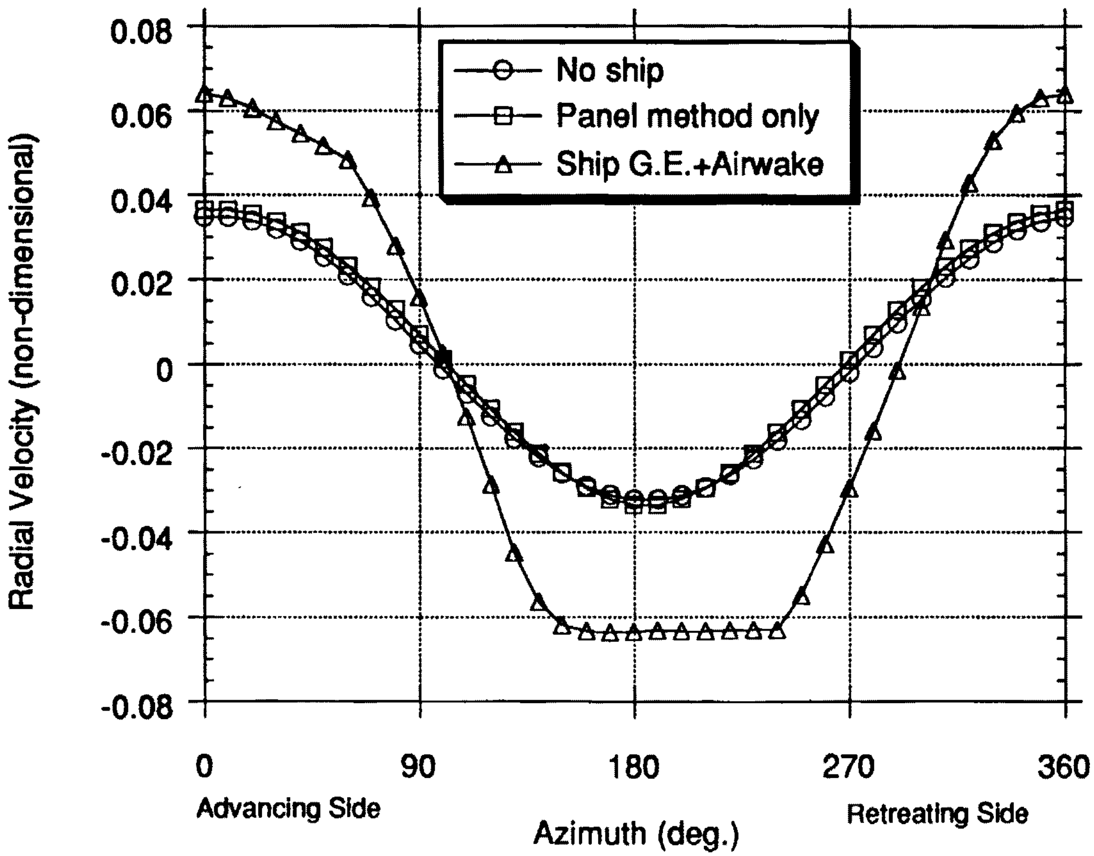

Effect of Helicopter Position on Controls

Configuration	Lat.Cyc.	Long.Cyc.	Collective	Pedal
No ship / no G.E.	4.595	4.466	5.137	2.008
No ship / G.E.	4.595	4.469	5.135	2.010
Hel. deck center	4.563	4.196	4.946	2.084
Hel. deck edge	4.622	4.301	5.083	2.072
Hel. outside	4.599	4.414	5.138	2.037

Concluding Remarks

- Local ship "ground effect" is significant; simple correction factor not appropriate;
- Ship airwake cannot be adequately approximated by panel representation; a ship airwake database is needed;
- Instrumented flight tests are needed to validate the approach;
- First step towards the construction of a suitable model for real-time simulation.

Directions for Future Work

- Allow for non-prescribed rotor wake vorticity distribution;
- Incorporate the rotor wake and ship models into Georgia Tech's FLIGHTLAB code;
- Conduct landing simulations incorporating ship airwake turbulent component;
- Use present method as a building block for a modified dynamic inflow model to be incorporated into real-time simulation codes.

Progress Report
on
Aerodynamic Modeling of Ground Effect for Helicopter/Ship Interaction Studies
Period covered: June - August 1994

During the past three months work has been underway on modifying the existing rotor/wake model to include a ship ground effect.

(a) <u>CFD effort</u>:

1) The prescribed geometry/prescribed vorticity distribution wake model has been modified to account for changes in wake vorticity due to the redistribution of lift over the disk and corresponding redistribution of bound circulation.

2) The prescribed wake geometry has been modified so that instead of simply truncating the wake revolutions near the ground, a "flat wake" is used for wake ages beyond that corresponding to a wake location that places the vortex filament at a user-specified clearance above the ground.

3) A partial parametric investigation has been performed in order to investigate the effect of wake parameters such as near wake age, number of wake revolutions and wake clearance above the ground on the rotor required power in ground effect. It was observed that for low speeds the total number of revolutions is the major factor influencing the computed ground effect. This is not the case for moderate to high speeds, since the wake is quickly washed away from the rotor.

4) A preliminary investigation on the adequacy and feasibility of extending the current prescribed helical geometry model to that of a distorted or free wake model is underway.

(b) <u>Inflow Modeling effort:</u>

During this period, the effort has concentrated on the development of methodology for identifying the modified [L] matrix. From CFD, the upwash due to the presence of the ground is computed, which is a function of radial station, azimuth angle and height of the rotor above the ground (ship deck) for a given rotor position with respect to the deck (x,y). The analysis is carried out using the following four steps:

1) Using least square fitting techniques, the upwash for a given hub position in space (x,y,h) is decomposed into the variations in uniform inflow, the first and second harmonic variations.

(2) An analytical function to represent the variation of the various inflow components, i.e., uniform, first harmonic and second harmonic, as a function of rotor height above the deck has been obtained.

(3): A bi-variate spline representation is used to capture the variation of inflow components as functions of (x,y) location around the ship deck.

(4): For steady flight conditions, the RHS forcing terms in the dynamic model for in-ground effect are approximately the same as those for out-of-ground effect. Hence, we can modify the [L] matrix, once we know the variations of the inflow components due to the ground.

Currently work is in progress on:

1) Developing the CFD code using free wake theory
2) Obtaining an explicit expression for the modified [L] matrix for a given flight condition.

Progress Report
on
Aerodynamic Modeling of Ground Effect for Helicopter/Ship Interaction Studies
Period covered: September-October 1994

During the past two months work has been underway on extending the existing rigid wake model for the ground effect modeling to a free wake code. The results of this investigation showed that wake instability is a major problem and substantial additional work would be needed to achieve a stable and reliable code. Therefore, our emphasis has shifted towards the modification of CAMRAD's free wake code to include ground effect modeling and incorporating the resulting code into the helicopter/ship interaction analysis.

Also, during this period extensive computations were carried out to compute the inflow velocity distribution over the disk at various heights ranging from 0.5R to 3R above the ground, and at different locations with respect to the ship deck. This step generated the needed data base for estimating the dynamic inflow model parameters. For a specific advance ratio, the [L] matrix including ground effect is modified as a function of (x,y,h) as well as the wake skew angle. Although the wake skew angle reflects the advance ratio to some degree, the effect of advance ratio on the inflow distribution is currently being studied in detail in order to make the [L] matrix of the inflow model an explicit function of advance ratio.

Progress Report
on
Aerodynamic Modeling of Ground Effect for Helicopter/Ship Interaction Studies
Period covered: November-December 1994

During the two months, as one of the graduate students working on the project, Olympio Mello, was graduating in December '94, the focus of the effort was directed towards documenting all the modifications that were made to the GENHEL program as part of the project. The resulting document is attached as Appendix I. Also, during this time we had interacted with Dr. Peters of Washington University for his comments on the theoretical work that was carried out on modeling of ground effect by extending the 'Peters-He generalized wake theory' by including an image rotor system in the formulation. We are continuing the work on studying the effect of advance ratio on the in-ground effect inflow distribution in order to make the [L] matrix of the inflow model an explicit function of advance ratio.

APPENDIX - I

1. INTRODUCTION

This report describes the modifications made in the helicopter simulation code GENHEL, in order to investigate helicopter/ship interactions. The theoretical formulation for the GENHEL code is given in Refs. 1 and 2 and will not be discussed here.

The effect of the ship proximity to the helicopter is modeled by using a standard panel method, based on the classical solution by Hess and Smith[7]. The ship is modeled by source panels which allow a good geometric representation. The effect of the ship on the rotor is given by the induced velocities on the rotor disk due to the ship panels. For the computation of the strengths of the sources, it is necessary to take into account both the ship velocity and the velocity field on the ship due to the rotor wake. This velocity field is computed using a rigid helical wake model. The strength of the rotor wake vortices depends on the circulation around the rotor blade, which, in turn, depends on the ship effects. Therefore, an iterative process would be needed. However, for the simulation problem, it may be assumed that changes in circulation around the blade and the flow about the ship are not too rapid and consequently the iterative process may be intrinsically performed during the simulation process.

For the computation of wake vorticity, two approaches have been employed: The first approach was to assume a prescribed vorticity distribution along the rotor disk. This allows all vorticity strengths on the disk and in the wake to be related to the thrust coefficient. Details on this approach were given in Ref. 4. The second approach was to compute the local vorticity at the rotor disk from the section lift. This approach requires numerical differentiation of the resulting vorticity distribution in order to obtain the wake vorticity strengths. Details on this latter approach are given in the Appendix.

In order to model the ground effect due to the sea surface, the method of images is used. An image rotor wake and an image ship panel system are placed below the sea surface and the influence of these images are taken into account in the computation of the downwash induced by the rotor and in the computation of the coefficient matrix for the ship panel method.

The remaining of this report is organized as follows: First, brief instructions on compiling and running GENHEL are given; Next the modifications and additions to GENHEL are described, including the first-order dynamic inflow model and the helicopter/ship interaction code using both the prescribed wake vorticity and computed wake vorticity models. Finally, an attempt to extend the rotor wake code to a free wake model is described.

2. COMPILING AND RUNNING GENHEL

The source code for the original version of GENHEL is divided into five FORTRAN files: bhawk.f, bhawka.f, bhawkb.f, bhawkc.f and bhawkd.f. The subroutine ROTOR is included in the file bhawkd.f and contains the blade-element model. In addition, several *.DAT files and a "Makefile" file are needed. The compilation is achieved by issuing the command Makefile twice to compile and link. This results in an executable file called bhawk. The execution is then performed by simply running bhawk. All the input files have their names pre-defined. The main input file is BHAWK.DAT. The input parameters in BHAWK.DAT are described in Ref. 1. Ref. 2 contains test cases that may be useful for validation of changes made to the original code.

3. FIRST-ORDER DYNAMIC INFLOW

The first order dynamic inflow model from Ref. 3 was implemented in GENHEL, as described in Ref. 4. These modifications were made mainly in the subroutines `ROTOR` and `RADIAL`, and a new subroutine called `DYNINF` was added. These changes were made in `bhawkd.f`, resulting in a new file called `bhawkd2.f`. Minor changes were made to the file `bhawkc.f`, for output of variables of interest, but this file was not renamed. A new `Makefile2` file was used to compile and link this dynamic inflow version. Note that these files also include the turbulence modifications made by Riaz (Refs. 5,6).

4. HELICOPTER/SHIP INTERACTION: PRESCRIBED VORTICITY VERSION

The first version of the helicopter/ship interaction model was developed using a rigid helical wake model with prescribed vorticity distribution in the wake, as described in Ref. 4. The ship model was the panel method of Ref. 7. The rotor wake and ship models were included in the file `bhawke.f`. Changes were made in the file `bhawkd2.f`, resulting in a new file `bhawkd3.f`. Minor changes were also made in `bhawk.f` and `bhawkb.f`, resulting in `bhawk2.f` and `bhawkb2.f`, respectively. This version should be compiled and linked by issuing the command `Makefile3` twice, which generates the executable file `bhawk2`. The changes are significantly commented (one can search for them by searching for the string `MELLO`).

4.1. Subroutines

The subroutines and function subprograms included in `bhawke.f` are as follows:

`RSHIP` Main module for computation of the interaction between the rotor and the ship; calls other needed routines.

`GETSHC` Reads ship coordinates and computes unit vectors.

`EUL3` Constructs a matrix of coordinate transformations after 3 Euler rotations α about y, β about z' and γ about x".

`MATMUL`, `MTMUL`, `MTMUL2` Subroutines for matrix multiplication.

`CONV` Contains the convergence procedure for the integration which gives the velocity induced by the rotor wake at a given point.

`AINTT` Function to be integrated along the wake coordinate to give total induced velocity due to wake tip vortex filaments.

GAMATV Functional variation of trailing vorticity as a function of the sine and cosine of blade azimuth when the filament left the blade.

AINTB Function to be integrated along the radius to give total induced velocity due to blade bound vortices on a given point.

GAMABV Functional variation of bound vorticity as a function of the radius and sine and cosine of blade azimuth.

AINTNW Function to be integrated along the near wake to give total induced velocity due to blade shed and trailing vortices on a given point; for a given wake age, it uses a radial integration of AINWR.

AINWR Function to be integrated along the radius to give total induced velocity due to a blade shed vortex filament and due to the sum of trailing vortex elements at that near wake location on a given point.

GSHEDV Functional variation of shed vorticity as a function of the radius and sine and cosine of blade azimuth.

GTRAV Functional variation of trailing vorticity as a function of the radius and sine and cosine of blade azimuth.

GAULEG Computes abscissas and weights for Gauss-Legendre quadrature (from Ref. 8).

QGAUS, QGAUSR Integrate a function using Gauss-Legendre quadrature (from Ref. 8).

PANEL Contains the panel method procedure; calls subroutines for the several coordinate transformations and induced velocity computations. It computes the influence coefficients for induced velocities due to a ship panel on other ship panels and due to a ship panel on the rotor blade elements.

PANVEL Computes the velocities induced by a ship panel, in the panel axes, on a point given in the same panel axes.

TRAFP Performs coordinate transformations from ship axes to panel axes.

TRAPF Performs coordinate transformations from panel axes to ship axes.

TRAFPM Performs coordinate transformations from ship axes to mirror panel axes.

TRAPFM Performs coordinate transformations from mirror panel axes to ship axes.

LUDCMP Performs an LU decomposition of the ship influence coefficient matrix (from Ref. 8).

LUBKSB Performs a back-substitution for solution of the system of equations, given the LU decomposition of the matrix of coefficients.

4.2. Input Parameters

The input parameters for the rotor/ship interaction computation are included in the file BHAWK.DAT and in a new file called rship.dat. The format of this latter file is as follows:

```
0.95  0.5   0.0   1.0   1.0  0.02  36  10  3    10
Rtv   Fnw   Xn0fr Fnctr Kt   Eps   Nqn Nqr Nmin Nmax
```

The above parameters have the following meaning:

Rtv Radial location of the tip vortex
Fnw Length of near wake, in number of revolutions
Xn0fr Wake age for starting of integration
Fnctr Wake age for wake contraction, in number of revolutions
Kt Factor used in vorticity distribution (see Ref. 4)
Eps Tolerance for convergence in wake integration
Nqn Number of points along the wake for Gauss quadrature

`Nqr`	Number of points along the radius for Gauss quadrature
`Nmin`	Minimum number of revolutions for wake integration
`Nmax`	Maximum number of revolutions for wake integration

The additions to `BHAWK.DAT` are as follows: The following flags are added to `$RUNFLAG`:

`IGNDEF`	Ground effect flag (0 for no ground effect)
`ISHIP`	Ship flag (0 for no ship)
`IRRW`	Rotor induced velocity flag: If set to 1, rotor wake is used to compute inflow on rotor disk; if set to 0, dynamic inflow is used. Recommended setting is 0.
`ISHMV`	Ship mean velocities flag: If set to 1, the ship airwake mean velocities are obtained from polynomial fitting of test data; if set to 0, the panel method is used. Recommended setting is 1.

and the following inputs are included in `$RUNIC`:

`ALSHIP`	Ship attitude (deg)
`PHSHIP`	Ship bank angle (deg)
`VSHKT`	Ship velocity (knots)
`XSHIP0`, `YSHIP0`, `ZSHIP0`	Initial ship location in inertial reference frame.
`VWIND`	Wind velocity (knots)
`PSIWND`	Wind direction (deg)
`NSS`	Number of blade elements (was fixed in the code in the original version).

5. HELICOPTER/SHIP INTERACTION: COMPUTED VORTICITY VERSION

Another version of the helicopter/ship interaction model was developed using the same rigid helical wake model as above, but with the vorticity distribution in the wake computed from the section lift coefficients. Details on this model are given in the Appendix.

The changes in the rotor wake model resulted in a new file `bhawke2.f`, which replaced `bhawke.f`. Changes were also made in `bhawkd3.f`, resulting in a new file `bhawkd4.f`, primarily to compute the section lift and pass it to the rotor wake code. This version should be compiled and linked by issuing the command `Makefile4` twice, which generates the executable file `bhawk3`.

For all versions of the helicopter/ship interaction code discussed so far, the rotor wake was simply truncated at a small height above the ship deck. It was observed that this procedure resulted in unrealistic ground effect modeling at very low heights. Consequently, a new version was developed in which the wake was not truncated, but assumed to be "flat", i.e., in a plane parallel to the ground, just above it, for wake ages above the wake age for which the vortex wake filaments were at a specified minimum distance from the deck (see Fig. 1). These changes were implemented in a new file `bhawke3.f`, which replaced `bhawke2.f`. This version should be compiled and linked by issuing the command `Makefile6` twice, which generates the executable file `bhawk6`. This is to be considered the current production version.

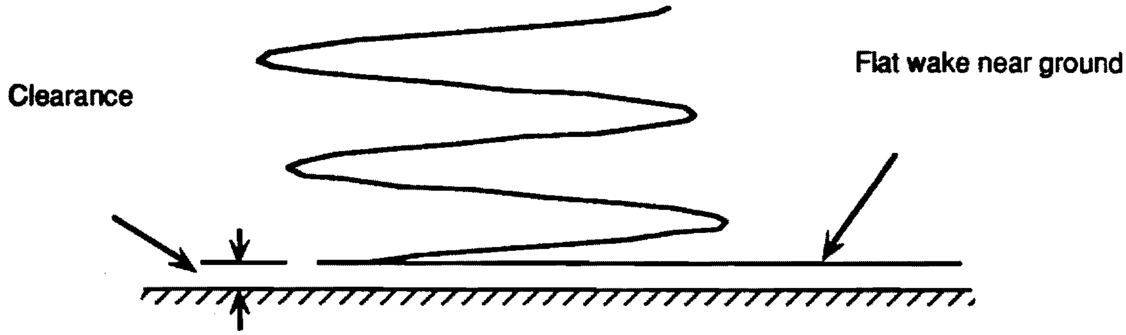

Fig. 1: Modified Wake Geometry

5.1. Subroutines

The subroutines and function subprograms in `bhawke2.f` and `bhawke3.f` are essentially the same as in `bhawke.f` and are listed below:

`RSHIP` Main module for computation of the interaction between the rotor and the ship; calls other needed routines.

`GETSHC` Reads ship coordinates and computes unit vectors.

`EUL3` Constructs a matrix of coordinate transformations after 3 Euler rotations α about y, β about z' and γ about x''.

`MATMUL`, `MTMUL`, `MTMUL2` Subroutines for matrix multiplication.

`GAMABV` Functional variation of bound vorticity as a function of the radius and sine and cosine of blade azimuth.

`GSHEDV` Functional variation of shed vorticity as a function of the radius and sine and cosine of blade azimuth.

`GTRAV` Functional variation of trailing vorticity as a function of the radius and sine and cosine of blade azimuth.

GAMATV Functional variation of trailing vorticity as a function of the sine and cosine of blade azimuth when the filament left the blade.

BVINT Subroutine for integration of bound vortices' contribution using trapezoidal rule.

AINTB Function to be integrated along the radius to give total induced velocity due to blade bound vortices on a given point.

NWINT Subroutine for integration along near wake.

AINTNW Function to be integrated along the near wake to give total induced velocity due to blade shed and trailing vortices on a given point; for a given wake age, it uses a radial integration of AINWR.

AINWR Function to be integrated along the radius to give total induced velocity due to a blade shed vortex filament and due to the sum of trailing vortex elements at that near wake location on a given point.

FWINT Subroutine for integration along far wake.

AINTT Function to be integrated along the wake coordinate to give total induced velocity due to wake tip vortex filaments.

CONV GAULEG, QGAUS, QGAUSR Integration routines not used in these versions

PANEL Contains the panel method procedure; calls subroutines for the several coordinate transformations and induced velocity computations. It computes the influence coefficients for induced velocities due to a ship panel on other ship panels and due to a ship panel on the rotor blade elements.

PANVEL Computes the velocities induced by a ship panel, in the panel axes, on a point given in the same panel axes.

TRAFP Performs coordinate transformations from ship axes to panel axes.

TRAPF Performs coordinate transformations from panel axes to ship axes.

TRAFPM Performs coordinate transformations from ship axes to mirror panel axes.

TRAPFM Performs coordinate transformations from mirror panel axes to ship axes.

LUDCMP Performs an LU decomposition of the ship influence coefficient matrix (from Ref. 8).

LUBKSB Performs a back-substitution for solution of the system of equations, given the LU decomposition of the matrix of coefficients.

5.2. Input Parameters

As in the prescribed vorticity version, the input parameters for the rotor/ship interaction computation are included in the file BHAWK.DAT and in a new file called rship.dat. The format of this latter file is as follows:

```
0.95  0.5   0.0   1.0   1.0  0.02  36  10  3    10   0.1
Rtv   Fnw   Xn0fr Fnctr Kt   Eps   Nqn Nqr Nmin Nmax Gndclf
```

The above parameters have the following meaning:

Rtv Radial location of the tip vortex
Fnw Length of near wake, in number of revolutions
Xn0fr Wake age for starting of integration
Fnctr Wake age for wake contraction, in number of revolutions
Kt Factor used in vorticity distribution (not used in this version)
Eps Tolerance for convergence in wake integration (not used in this version)
Nqn Number of points along the wake for Gauss quadrature (not used in this version)
Nqr Number of points along the radius for Gauss quadrature (not used in this version)

Nmin Minimum number of revolutions for wake integration

Nmax Maximum number of revolutions for wake integration

Gndclf Wake clearance above deck (minimum distance between wake filaments and deck), non-dimensionalized by the rotor radius.

Note that the format of the input file is the same as in the previous version, with the addition of Gndclf. The unused input parameters were maintained for compatibility with the previous version.

The additions to BHAWK.DAT are as in the previous version: The following flags are added to $RUNFLAG:

IGNDEF Ground effect flag (0 for no ground effect)

ISHIP Ship flag (0 for no ship)

IRRW Rotor induced velocity flag: If set to 1, rotor wake is used to compute inflow on rotor disk; if set to 0, dynamic inflow is used. Recommended setting is 0.

ISHMV Ship mean velocities flag: If set to 1, the ship airwake mean velocities are obtained from polynomial fitting of test data; if set to 0, the panel method is used. Recommended setting is 1.

and the following inputs are included in $RUNIC:

ALSHIP Ship attitude (deg)

PHSHIP Ship bank angle (deg)

VSHKT Ship velocity (knots)

XSHIP0, YSHIP0, ZSHIP0 Initial ship location in inertial reference frame.

VWIND Wind velocity (knots)

PSIWND Wind direction (deg)

NSS Number of blade elements (was fixed in the code in the original version).

5.3. Parametric Investigation

A limited parametric investigation was performed to determine the effect of number of revolutions and wake clearance above the ground on the ground effect modeling. Representative results are shown in Figs. 2 and 3. In these figures the power required is non-dimensionalized by the hover out-of-ground effect (OGE) power required and plotted as a function of the reduced advance ratio, $\mu/(C_T/2)^{1/2}$. These non-dimensionalizations allow a more meaningful comparison with the experimental data in Ref. 10, which were obtained for the Boeing-Vertol YUH-61, a helicopter of the same class as the UH-60.

From the parametric investigation, it may be concluded that the clearance above the ground is a minor factor, at least in the range investigated. The number of revolutions is a major factor at low speeds, and a minor factor at high speeds, because as the speed is increased, the wake is washed away from the deck.

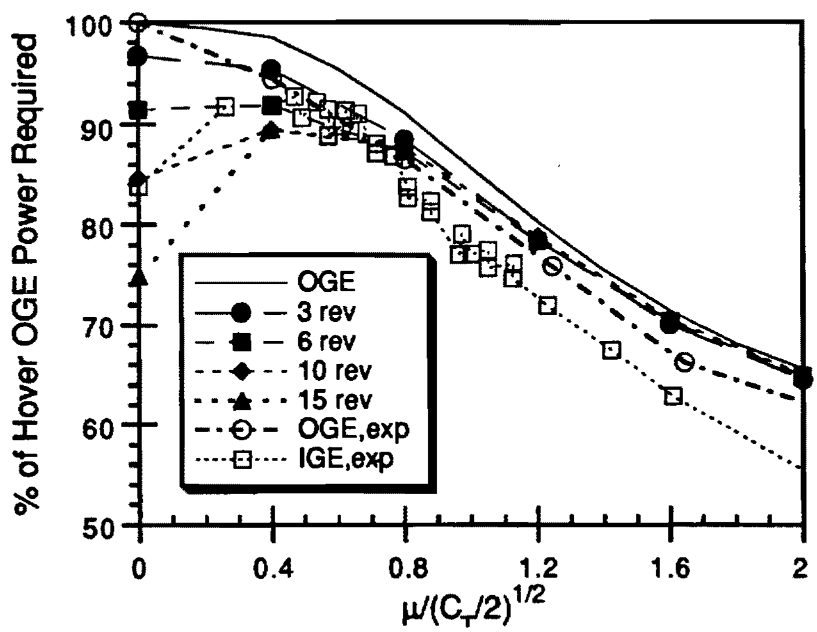

Fig. 2: Parametric Investigation: Effect of Number of Wake Revolutions.

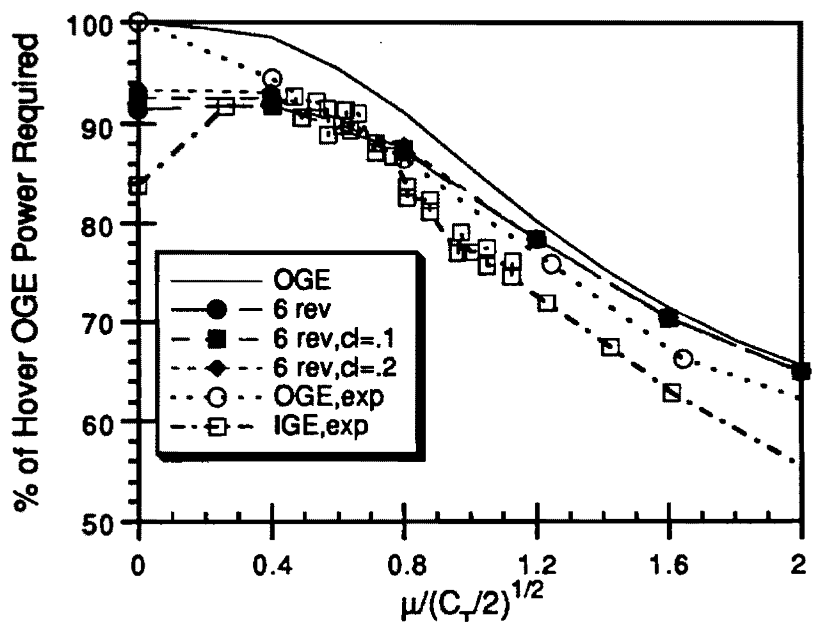

Fig. 3: Parametric Investigation: Effect of Clearance above Ground.

6. HELICOPTER/SHIP INTERACTION: FREE WAKE MODEL

In order to increase the code fidelity at very low speeds, an extension of the current code to a free wake model has been attempted. The changes in the rotor wake model resulted in a new file `bhawke4.f`. Preliminary runs showed that the wake was unstable, even though relaxation techniques were used. This is illustrated in Fig. 4, where side views of a wake filament from one blade is shown at four iteration levels. This unstable behavior has been observed during the development of other free wake codes. From these preliminary computations, it became apparent that the further development of a free wake code would require a substantial effort by itself, in a deviation from the main objective at hand, which is the helicopter/ship interaction study. Therefore, it is recommended that the emphasis be shifted towards the adaptation of the existing free wake module in CAMRAD for application to the helicopter/ship interaction study.

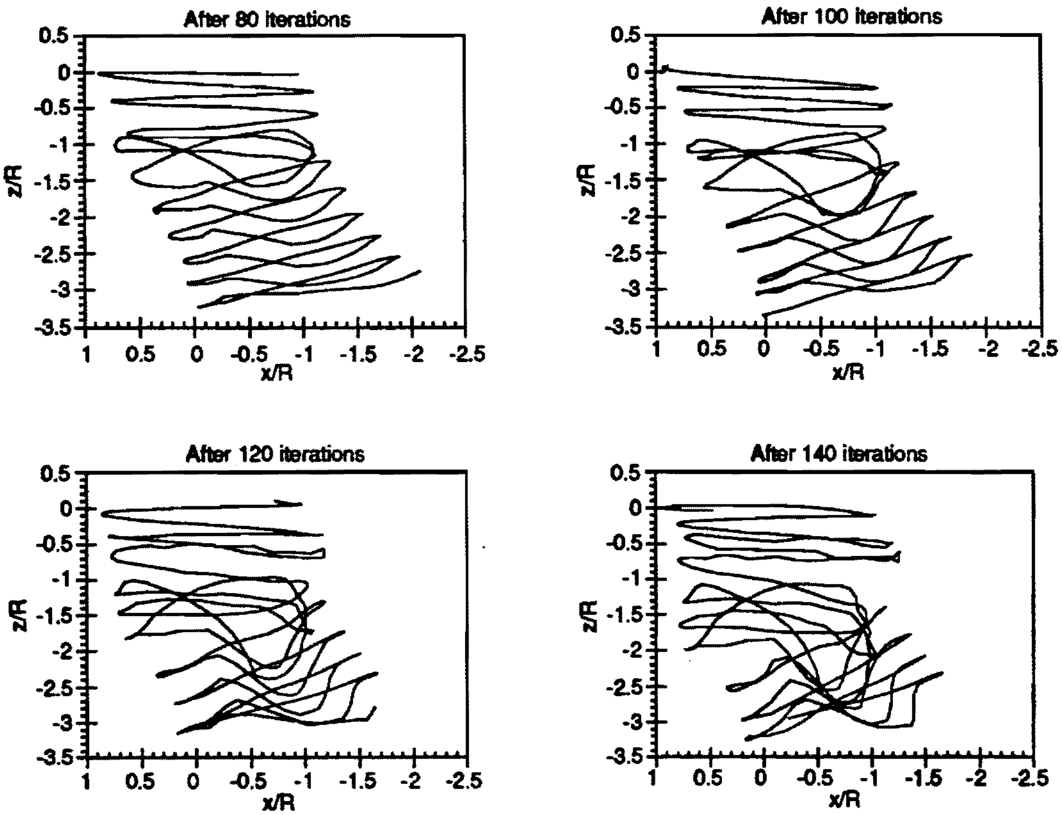

Fig. 4: Free Wake Instability

APPENDIX

SHIP GROUND EFFECT MODELING USING PRESCRIBED WAKE GEOMETRY WITH COMPUTED WAKE VORTICITY DISTRIBUTION

The effect of the ship proximity to the helicopter is modeled by using a standard panel method, based on the classical solution by Hess and Smith[7]. The ship is modeled by source panels which allow a good geometric representation. The effect of the ship on the rotor is given by the induced velocities on the rotor disk due to the ship panels. For the computation of the strengths of the sources, it is necessary to take into account both the ship velocity and the velocity field on the ship due to the rotor wake. This velocity field is computed using a rigid helical wake model. The strength of the rotor wake vortices depends on the circulation around the rotor blade, which, in turn, depends on the ship effects. Therefore, an iterative process would be needed. However, for the simulation problem, it may be assumed that changes in circulation around the blade and the flow about the ship are not too rapid and consequently the iterative process may be intrinsically performed during the simulation process.

In order to model the ground effect due to the sea surface, the method of images is used. An image rotor wake and an image ship panel system are placed below the sea surface and the influence of these images are taken into account in the computation of the downwash induced by the rotor and in the computation of the coefficient matrix for the ship panel method.

A.1. Ship Formulation

The ship surface is approximately represented by plane source panels with constant distributed strength. The strengths of the sources are determined by enforcing the non-penetration condition at the centroid of each panel. In this implementation, both the normal component of the ship's motion and the normal component of the downwash induced by the rotor are taken into account. The details of the ship source panel method are given in Ref. 7 and therefore will not be repeated here. This formulation results in a linear system of equations to be solved for the ship panel source strengths σ:

$$[A]\{\sigma\}=[B] \tag{A.1}$$

where [A] is the matrix of influence coefficients, $\{\sigma\}$ is the vector of unknown source strengths and [B] is the right-hand side which includes the normal component of the velocities on the ship surface due to the free-stream and due to the rotor and its wake. The system of equations (A.1) is solved by a standard linear equations solver. The resulting source panel strengths are then used to compute the velocities induced by the ship source panel system on the rotor disk.

A.2. Rotor Wake Formulation

In order to compute the induced velocity due to the rotor and its wake on the ship, as well the rotor disk inflow distribution in ground effect, a rigid wake model is used. This model is a modified version of the model described in Ref. 4 and allows the computation of the instantaneous induced velocities both on the rotor disk and on the ship surface. In Ref. 4 a prescribed vorticity distribution was assumed. In the current version, the vorticity distribution is computed from the blade section lift, as described in more detail in Section A.2.1. It should also be noted that in the present work the rotor wake model is used only for computation of the induced velocities on the ship surface. Numerical experimentation has shown that using the current model for computation of induced velocities on the rotor disk is computationally time-consuming while presenting no clear advantage over a dynamic inflow model.

The following assumptions are made:

1) Blade flapping angles are small and their higher harmonics are negligible;

2) The rotor blade is modeled by a lifting line of bound vorticity; this bound vorticity is related to the blade section lift by Kutta-Joukowski's theorem;

3) The wake has a prescribed geometry, which is basically a classical skewed helical wake, with a limited wake contraction model;

4) The wake is divided into a "near" wake, composed of trailing and shed vortices and a "far" wake composed of trailing tip vortices only. The strengths of the trailing and shed vortices are given by the radial and azimuth-wise variations of the bound vorticity, respectively, while the strength of the far wake tip vortex is assumed as equal to the maximum bound vorticity at the azimuth location where the vortex filament leaves the blade;

5) The rotor wake is convected downstream with a velocity which is equal to the vector sum of the free stream velocity and the averaged (momentum theory value) induced velocity over the disk.

A.2.1. Vorticity Distribution

The blade bound vorticity distribution is obtained through an iterative process from the blade section lift. Let the blade section bound vorticity be $\Gamma_{b_{ij}} = \Gamma_b(r_i, \psi_j)$. From Kutta-Joukowski theorem:

$$l_{ij} = \rho \, V_{ij} \, \Gamma_{ij} = \rho \, (\Omega R)(\bar{r}_i + \mu \sin \psi_j) \, \Gamma_{b_{ij}} \tag{A.2}$$

or:

$$\Gamma_{b_{ij}} = \frac{\ell_{ij}}{\rho(\Omega R)(\bar{r}_i + \mu \sin \psi_j)} \tag{A.3}$$

A.2.2. Velocity Induced by Blade Bound Vortices

From the computed bound vorticity distribution, the velocity induced by the blade bound vortices can be obtained by application of the Biot-Savart law:

$$v_b = \frac{1}{4\pi} \int_{\bar{r}=0}^{1} \Gamma_b \frac{d\vec{s}_b \times \Delta \vec{R}_{Pb}}{|\Delta \vec{R}_{Pb}|^3} \tag{A.4}$$

where $d\vec{s}_b$ is the elementary vector in the direction of the vortex filament and $\Delta\vec{R}_{Pb}$ is the position vector of the point in question with respect to the bound vortex element. Denoting by $\vec{R}_b$ the position vector of a blade bound vortex element as expressed in the tip-path-plane (TPP) reference frame:

$$\vec{R}_b = r\left\{\left[-\cos\psi\,\hat{i}_T - \sin\psi\,\hat{j}_T\right]\cos\beta_0 + \sin\beta_0\,\hat{k}_T\right\} \tag{A.5}$$

Then the elementary vector $d\vec{s}_b$ can be obtained from:

$$d\vec{s}_b = \frac{\dfrac{\partial\vec{R}_b}{\partial r}}{\left|\dfrac{\partial\vec{R}_b}{\partial r}\right|}dr \tag{A.6}$$

with

$$\frac{\partial\vec{R}_b}{\partial r} = \left[-\cos\psi\,\hat{i}_T - \sin\psi\,\hat{j}_T\right]\cos\beta_0 + \sin\beta_0\,\hat{k}_T = \frac{\vec{R}_b}{r} \tag{A.7}$$

Given a point with coordinates (x_P, y_P, z_P) in the tip-path-plane reference frame, the vector $\Delta\vec{R}_{Pb}$ is then:

$$\Delta\vec{R}_{Pb} = \vec{R}_P - \vec{R}_b = \left(x_P\,\hat{i}_T + y_P\,\hat{j}_T + z_P\,\hat{k}_T\right) - \vec{R}_b \tag{A.8}$$

The discretization of Eqs (A.5–A.8) is straightforward. Eq. (A.4) then reduces to a summation over the blade:

$$v_b\left(\psi_j, \vec{R}_P\right) = v_{b_j} = \frac{1}{4\pi}\sum_{i=1}^{N_r}\Gamma_{b_{ij}}\frac{\Delta\vec{s}_{b_j}\times\Delta\vec{R}_{Pb_{ij}}}{\left|\Delta\vec{R}_{Pb_{ij}}\right|^3} \tag{A.9}$$

A.2.3. <u>Near Wake</u>

As mentioned above, the near wake is assumed to be composed of trailing and shed vortices, with strength given by the radial and azimuth-wise variations of the bound vorticity, respectively, at the azimuth location where the vortex filament leaves the blade. Let us first consider an element of a trailing vortex filament of length $r_i\,\Delta v$, which left the blade at the radial location r_i, and is located at a wake age v_k. This element has left the blade when it was at an azimuth location $\psi_j - v_k$, ψ_j being the current azimuth location of the blade. Therefore, the vorticity of the element is given by $\Gamma_t\,(\bar{r}_i, \psi_j - v_k)\, r_i\,\Delta v$, where $\Gamma_{t_{i,j,k}} = \Gamma_t\,(\bar{r}_i, \psi_j - v_k)$ is the trailing vortex vorticity, equal to the radial variation of Γ_b:

$$\Gamma_{t_{ijk}} = \Gamma_t\left(\bar{r}_i, \psi_j - v_k\right) = \frac{\partial \Gamma_b}{\partial \bar{r}} \approx \frac{\Gamma_b\left(\bar{r}_i, \psi_j - v_k\right) - \Gamma_b\left(\bar{r}_{i-1}, \psi_j - v_k\right)}{\bar{r}_i - \bar{r}_{i-1}} \tag{A.10}$$

The velocity induced by the entire filament at a point is given by integration of elementary induced velocities obtained from the Biot-Savart law:

$$dv_t = \frac{1}{4\pi} \int_{v=0}^{v_{nw}} \Gamma_t \frac{\vec{ds}_t \times \Delta \vec{R}_{Pt}}{|\Delta \vec{R}_{Pt}|^3} \tag{A.11}$$

where $\vec{ds}_t$ is the elementary vector in the direction of the vortex filament and $\Delta\vec{R}_{Pt}$ is the position vector of the point in question with respect to the vortex element. Note that the integration is performed only along the "near" wake. Note also that Eq.(A.11) gives only the velocity induced by a single trailing vortex filament. To obtain the total induced velocity due to all trailing vortex filaments, one has to integrate Eq.(A.11) along the blade, i.e.:

$$v_t = \frac{1}{4\pi} \int_{\bar{r}=0}^{1} \int_{v=0}^{v_{nw}} \Gamma_t \frac{\vec{ds}_t \times \Delta \vec{R}_{Pt}}{|\Delta \vec{R}_{Pt}|^3} \tag{A.12}$$

Denoting by $\vec{R}_s$ the position vector of the trailing vortex element as expressed in the tip-path-plane (TPP) reference frame and using the assumption that the wake is convected downstream with a velocity which is equal to the vector sum of the free stream velocity and the averaged induced velocity over the disk, we have:

$$\vec{R}_s = r\left\{\left[-\cos(\psi - v)\,\hat{i}_T - \sin(\psi - v)\,\hat{j}_T\right]\cos\beta_0 + \sin\beta_0\,\hat{k}_T\right\} + \frac{\vec{v}_{i_0} - \vec{V}_{H_T}}{\Omega}\, v \tag{A.13}$$

where β_0 is the coning angle, Ω is the rotor rotational speed, $\vec{V}_{H_T}$ is the helicopter velocity vector in the TPP reference frame, $\hat{i}_T$, $\hat{j}_T$ and $\hat{k}_T$ are the unit vectors corresponding to the TPP axes, and $\vec{v}_{i_0}$ is the averaged induced inflow vector, given by:

$$\vec{v}_{i_0} = -\left(\Omega R\right)\lambda_{i_0}\,\hat{k}_T \tag{A.14}$$

where λ_{i_0} is the induced inflow ratio. The elementary vector in the direction of the filament, $d\vec{s}_t$, can be obtained as:

$$d\vec{s}_t = \frac{\dfrac{\partial \vec{R}_s}{\partial v}}{\left|\dfrac{\partial \vec{R}_s}{\partial v}\right|}\, r\, dv \tag{A.15}$$

with

$$\frac{\partial \vec{R}_s}{\partial v} = r\left[-\sin(\psi - v)\,\hat{i}_T + \cos(\psi - v)\,\hat{j}_T\right]\cos\beta_0 + \frac{\vec{v}_{i_0} - \vec{V}_{H_T}}{\Omega} \tag{A.16}$$

Given a point with coordinates (x_P, y_P, z_P) in the tip-path-plane reference frame, the vector $\Delta\vec{R}_{Pt}$ is then:

$$\Delta\vec{R}_{Pt} = \vec{R}_P - \vec{R}_s = \left(x_P\,\hat{i}_T + y_P\,\hat{j}_T + z_P\,\hat{k}_T\right) - \vec{R}_s \tag{A.17}$$

The discretization of Eqs (A.13–A.17) is straightforward. Eq. (A.12) then reduces to a double summation over the radial and wake coordinates along the near wake:

$$v_t\left(\psi_j, \vec{R}_P\right) = v_{t_j} = \frac{1}{4\pi}\sum_{k=1}^{N_{nw}}\sum_{i=1}^{N_r}\Gamma_{t_{ijk}}\,\frac{\Delta\vec{s}_{t_{ijk}} \times \Delta\vec{R}_{Pt_{ijk}}}{\left|\Delta\vec{R}_{Pt_{ijk}}\right|^3} \tag{A.18}$$

Now, let us consider an element of a shed vortex filament of length Δr_i, which left the blade at the radial location r_i, and is located at a wake age v_k. This element has left the blade when it was at an azimuth location $\psi_j - v_k$, ψ_j being the current azimuth location of the blade. Therefore, the vorticity of the element is given by $\Gamma_s(\bar{r}_i, \psi_j - \nu_k)\, \Delta r_i$, where $\Gamma_s(\bar{r}_i, \psi_j - \nu_k)$ is the shed vortex vorticity, equal to the azimuthal variation of Γ_b:

$$\Gamma_{s_{ijk}} = \Gamma_s(\bar{r}_i, \psi_j - \nu_k) = \frac{\partial \Gamma_b}{\partial \psi} \approx \frac{\Gamma_b(\bar{r}_i, \psi_j - \nu_k) - \Gamma_b(\bar{r}_i, \psi_{j-1} - \nu_k)}{\Delta \psi} \qquad \text{(A.19)}$$

The velocity induced by the entire shed vortex system at a point is given by radial integration of elementary induced velocities obtained from the Biot-Savart law, and subsequent integration along the wake to account for all the shed vortices:

$$v_s = \frac{1}{4\pi} \int_{\nu=0}^{\nu_{nw}} \int_{\bar{r}=0}^{1} \Gamma_s \frac{d\vec{s}_s \times \Delta \vec{R}_{P_s}}{|\Delta \vec{R}_{P_s}|^3} \qquad \text{(A.20)}$$

Note that the integration is performed only along the "near" wake. The position vector of the shed vortex element, $\vec{R}_s$, is given again by Eq. (A.13), therefore the vector $\Delta\vec{R}_{P_s}$ is equal to $\Delta\vec{R}_{P_t}$ and is accordingly given by Eq. (A.17). The elementary vector in the direction of the shed vortex filament, $d\vec{s}_s$, can be obtained as:

$$d\vec{s}_s = \frac{\dfrac{\partial \vec{R}_s}{\partial r}}{\left|\dfrac{\partial \vec{R}_s}{\partial r}\right|} dr \qquad \text{(A.21)}$$

with

$$\frac{\partial \vec{R}_s}{\partial r} = \left[- \cos(\psi-\nu)\, \hat{i}_T - \sin(\psi-\nu)\, \hat{j}_T\right] \cos\beta_0 + \sin\beta_0\, \hat{k}_T \qquad \text{(A.22)}$$

The discretization of Eq (A.22) is straightforward. Eq. (A.20) then reduces to a double summation over the radial and wake coordinates along the near wake:

$$v_s(\psi_j, \vec{R}_P) = v_{s_j} = \frac{1}{4\pi} \sum_{k=1}^{N_{nw}} \sum_{i=1}^{N_r} \Gamma_{s_{ijk}} \frac{\Delta\vec{s}_{s_{ijk}} \times \Delta \vec{R}_{P_{s_{ijk}}}}{|\Delta \vec{R}_{P_{s_{ijk}}}|^3} \qquad \text{(A.23)}$$

A.2.4. Far Wake

As mentioned above, the far wake is assumed to be composed of trailing tip vortices only, with strength assumed as equal to the maximum bound vorticity at the azimuth location where the vortex filament leaves the blade. Considering an element of wake filament of length $r_{tv}\,\Delta\nu$ (where r_{tv} corresponds to the radial location where the tip vortex has rolled up) and at a wake age ν_k, this element has left the blade when it was at an azimuth location $\psi_j-\nu_k$, ψ_j being the current azimuth location of the blade. Therefore, the vorticity of the element is given by $\Gamma_{T_{jk}}\, r_{tv}\,\Delta\nu = \Gamma_T\,(\psi_j-\nu_k)\, r_{tv}\,\Delta\nu$, where $\Gamma_T\,(\psi_j-\nu_k)$ is the trailing tip vortex vorticity, equal to the radial maximum of Γ_b:

$$\Gamma_{T_{jk}} = \Gamma_T\left(\psi_j-\nu_k\right) = \max_i \Gamma_b\left(\bar{r}_i, \psi_j-\nu_k\right) \qquad \text{(A.24)}$$

The velocity induced by the wake at a point is given by integration of elementary induced velocities obtained from the Biot-Savart law:

$$v_T = \frac{1}{4\pi}\int_{wake}^{\infty} \Gamma_T \frac{\vec{ds}_T \times \Delta\vec{R}_{PT}}{\left|\Delta\vec{R}_{PT}\right|^3} \qquad \text{(A.25)}$$

where $\vec{ds}_T$ is the elementary vector in the direction of the vortex filament and $\Delta\vec{R}_{PT}$ is the position vector of the point in question with respect to the vortex element. Denoting by $\vec{R}_T$ the position vector of the tip vortex element as expressed in the tip-path-plane (TPP) reference frame and using the assumption that the wake is convected downstream with a velocity which is equal to the vector sum of the free stream velocity and the averaged induced velocity over the disk, we have:

$$\vec{R}_T = r_{tv}\left\{\left[-\cos(\psi-\nu)\,\hat{i}_T - \sin(\psi-\nu)\,\hat{j}_T\right]\cos\beta_0 + \sin\beta_0\,\hat{k}_T\right\} + \frac{\vec{v}_{i_0} - \vec{V}_{H_T}}{\Omega}\,\nu \qquad \text{(A.26)}$$

The elementary vector in the direction of the tip vortex filament, $\vec{ds}_T$, can be obtained as:

$$d\vec{s}_T = \frac{\dfrac{\partial \vec{R}_T}{\partial \nu}}{\left|\dfrac{\partial \vec{R}_T}{\partial \nu}\right|} r_{tv}\, d\nu \tag{A.27}$$

with

$$\frac{\partial \vec{R}_T}{\partial \nu} = r_{tv}\left[-\sin(\psi-\nu)\,\hat{i}_T + \cos(\psi-\nu)\,\hat{j}_T\right]\cos\beta_0 + \frac{\vec{v}_{i_0} - \vec{V}_{H_T}}{\Omega} \tag{A.28}$$

Given a point with coordinates (x_P, y_P, z_P) in the tip-path-plane reference frame, the vector $\Delta\vec{R}_{PT}$ is then:

$$\Delta\vec{R}_{PT} = \vec{R}_P - \vec{R}_T = \left(x_P\,\hat{i}_T + y_P\,\hat{j}_T + z_P\,\hat{k}_T\right) - \vec{R}_T \tag{A.29}$$

The discretization of Eqs (A.26–A.29) is straightforward. Eq. (A.25) then reduces to a summation over the wake coordinate along the far wake:

$$v_T\left(\psi_j, \vec{R}_P\right) = v_{T_j} = \frac{1}{4\pi} \sum_{k=N_{nw}+1}^{N_w} \Gamma_{T_{jk}} \frac{\Delta\vec{s}_{T_{jk}} \times \Delta\vec{R}_{PT_{jk}}}{\left|\Delta\vec{R}_{PT_{jk}}\right|^{\beta}} \tag{A.30}$$

A.2.5. Vortex Core Model

A Rankine vortex core model[9] with radius of one tenth of the blade chord is used. This model is illustrated in Fig. A.1, and is applied by scaling the induced velocity due to the elementary vortex filament by the square of the ratio between the distance to the filament and the core radius, whenever the point where the induced velocity is being calculated lies within the vortex core.

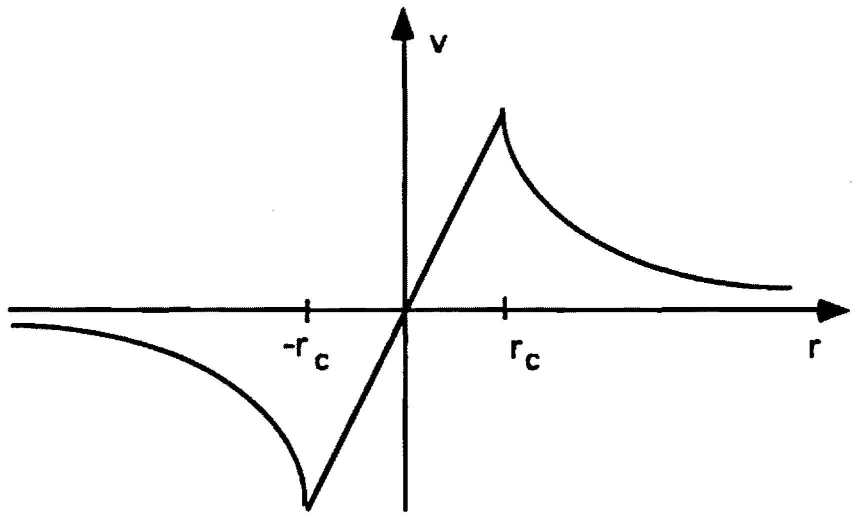

Fig. A.1: Rankine Vortex Core Model

REFERENCES

1. Howlett, J. J., "UH-60A Black Hawk Engineering Simulation Program: Volume I — Mathematical Model," NASA CR-166309, 1981.

2. Ballin, M. G., "Validation of Real-Time Engineering Simulation of the UH-60A Helicopter," NASA TM-88360, February 1987.

3. Peters, D. A., and HaQuang, N., "Dynamic Inflow for Practical Applications," *Journal of the American Helicopter Society*, October 1988, pp. 64–68.

4. Mello, O. A. F., "Numerical Simulation of Helicopter / Ship Airwake Interactions," Research Report submitted to Naval Air Warfare Center, School of Aerospace Engineering, Georgia Institute of Technology, Atlanta, July 1993.

5. Riaz, J., Prasad, J. V. R., Schrage, D. P., and Gaonkar, G. H., "New Method for Simulating Atmospheric Turbulence for Rotorcraft Applications," 47th Annual Forum of the American Helicopter Society, Phoenix, Arizona, 1991.

6. Riaz, Jamshed, "A Simulation Model of Atmospheric Turbulence for Rotorcraft Applications," Ph.D. Thesis, Georgia Institute of Technology, Atlanta, 1992.

7. Hess, J. L., and Smith, A. M. O., "Calculation of Potential Flow about Arbitrary Bodies," *Progress in Aeronautical Sciences*, Vol. 8. Edited by D. Küchemann. Pergamon Press, Oxford, England, 1967.

8. Press, W. H., Flannery, B. P., Teukolsky, S. A. and Vetterling, W. T., *Numerical Recipes — The Art of Scientific Computing (FORTRAN Version)*, Cambridge University Press, 1989.

9. U.S. Department of the Army — Aeroflightdynamics Directorate, "2GCHAS Theory Manual," (Second Generation Comprehensive Helicopter Analysis System, Version 2.1), Vol. II, Chapter 5 – Airloads and Induced Velocity, Ames Research Center, Moffett Field, CA, July 1992.

10. Sheridan, P. F., and Wiesner, W., "Aerodynamics of Helicopter Flight Near the Ground," 33rd Annual Forum of the American Helicopter Society, 1977.

11. Johnson, W., "A Comprehensive Analytical Model of Rotorcraft Aerodynamics and Dynamics, Part I: Analysis Development," NASA TM-81182, Part 1, June 1980.

F-16-1107
24

Progress Report
on
Aerodynamic Modeling of Ground Effect for Helicopter/Ship Interaction Studies
Period covered: January - February, 1995

During this period, we have worked on understanding the effect of advance ratio (forward speed) on the ship deck induced upwash at the rotor disk. Note that the forward speed here denotes the windspeed of the ship as the helicopter is assumed to be hovering with respect to the ship deck. Using the computer code previously developed and integrated into the GENHEL program as part of this research project, the helicopter was trimmed at different advance ratios. For the rotor height above the center of the ship deck equal to 1.2 R , the upwash induced by the ship deck was computed. The upwash was decomposed into uniform, first and second harmonic components using Fourier analysis of the numerical data. Then a suitable analytical formula for modeling of the advance ratio effect was arrived at through trial and error. The following relationship was found to be a reasonable representation of advance ratio effect on the ship deck induced upwash at the rotor disk.

$$\frac{(V_i)_{IGE@\mu}}{(V_i)_{IGE@\mu_0}} = a + b\mu + c\mu^2$$

where

μ is advance ratio

μ_0 is reference advance ratio

i represents 0, 1C, 1S, 2C or 2S corresponding to uniform, first and second harmonic components

With the above representation, the ship ground effect model is modified to include the advance ratio effect as

$$V_i(x,y,h,\mu)_{IGE} = (a + b\mu + c\mu^2)(V_i(x,y,h)_{IGE@\mu_0})$$

where an expression (model) for $V_i(x,y,h)_{IGE@\mu_0}$ has previously been developed as part of this research project. A paper describing these results has been accepted for presentation at the 1995 AIAA GNC, Flight Mechanics and Simulation Conference.

Also, during this period, we have continued our work on developing a theoretically based ground effect model by extending the generalized wake theory to include ground effect. Initial comparison of ground effect results with experimental results indicate that the theoretical model captures the ground effect very well as compared to previous models.

Currently work is in progress to check whether the above representation of advance ratio effect is valid for different heights. Also, work is in progress to predict off-the-rotor down wash and hence, the wake structure using the theoretical ground effect model.

Publications during this period:

1. Hong Zhang, O.A.F. Mello, J.V.R. Prasad, L.N. Sankar and J.D. Funk, "A Simulation Model of Ship Ground Effect for Rotorcraft/Ship Interaction Study," Paper to be presented at the 51st Annual of the American Helicopter Society.

2. Hong Zhang, " A New Ground Effect Model for Lifting Rotors," Ph.D. Proposal, School of Aerospace Engineering, Georgia Tech, January 1995. Advisor: Dr. J.V.R. Prasad

Progress Report
on
Aerodynamic Modeling of Ground Effect for Helicopter/Ship Interaction Studies
Period covered: March - April, 1995

During this period, we have continued the work on computing flow velocities using the analytical ground effect model. In this regard we ran into difficulties on the validity of our method in computing the flow velocities using integrals of pressure potential. The difficulty stems from the limitation in the dynamic inflow model for out-of-ground effect wherein the model assumes (the momentum theory value) twice the induced velocity at the rotor to be the value in the far wake and at infinity. In reality, due to unstable effects, the velocity in the far wake slowly decays. Hence the analytical ground effect model that has been developed in this study which is an extension of the original dynamic inflow theory by superposition of solutions using a rotor and its image system, the definition of wake for the rotor and/or for the image rotor across the ground plane has no meaning. This aspect is currently being studied to develop an alternate procedure for computing flow velocities off the disk using the in-ground effect model.

The work on developing ship ground effect model for the steady case is completed by including the effect of variation with advance ratio. The results from this effort have been presented at the AHS 51st Annual Forum and at the TTCP meeting held at NAWC, Lakehurst. A paper describing the ship ground effect methodology is currently being prepared which will be presented at the AIAA Flight Simulation Conference in August, 1995. Also, a Technical Note on the analytical ground effect model is being written to be submitted for publication in the AHS journal.

In addition to the issue of flow velocity computations off the rotor for the in-ground effect case, the next issue that is to be studied is to extend the analytical ground effect model for inclined ground effect. Such a model will be useful in helicopter inclined slope landing studies.

E- 16 - M07

#26

Progress Report
on
Aerodynamic Modeling of Ground Effect for Helicopter/Ship Interaction Studies
Period covered: May - June, 1995

During this period, the effort was directed towards carrying out the ship ground effect/vehicle simulations using the GENHEL program for hovering with respect to deck at different heights. Using CFD results, a simplified inflow model was obtained as a function of (x,y) location around the ship deck and height from the ship deck. The results were obtained for the case of the ship moving at a speed of 15 knots. A paper was written and was presented at the 1995 Annual Forum of the American Helicopter Society. A copy of the paper is attached. During the next progress report period, parametric studies will be conducted to include the effect of ship speed in the ship ground effect model.

The work on developing a theoretical ground effect model is continuing.

A SIMULATION MODEL OF SHIP GROUND EFFECT FOR ROTORCRAFT / SHIP INTERACTION STUDY

Hong Zhang* O.A.F.Mello* J.V.R.Prasad‡ L.N.Sankar † and John D. Funk,Jr.§

School of Aerospace Engineering
Georgia Institute of Technology
Atlanta, GA

Aero Analysis Division
Naval Air Warfare Center Aircraft Division
Warminster, PA

Abstract

A simple ground effect model for rotorcraft / ship dynamic interactions, which is suitable for implementation in flight simulators for real-time simulation purposes, has been extracted from the analysis of the aerodynamic interaction results obtained from a computationally intensive method that incorporates a rigid rotor wake and a panel representation of the ship with corresponding image systems. It is found that the ground effect is very sensitive to the helicopter position with respect to the ship deck, as well as the height above the deck. The inflow gain matrix in dynamic inflow model is modified as a function of the position (x,y,z) relative to the deck. Numerical results for a SH-60 helicopter flying above the deck of a moving FFG-7 class frigate at the same speed as the ship are presented and discussed in this paper. Results show that the ground effect model works well all over the deck. The ground effect model integrated with the airwake model which has already been developed at Georgia Tech provides the basis for the real-time simulation study for rotorcraft/ship interactions.

1. Introduction

Modern helicopters must routinely operate under various adverse weather conditions. Helicopter landing on a moving ship deck behind the superstructure is hazardous(10), and yet up to today, little knowledge about the flow characteristics is available due to the time dependent uncertainty nature of the flow, as well as the complicated and sensitive flow field over the deck behind the superstructure. Because the lack of a suitable ship airwake model and the still unsolved rotorcraft / ship dynamic interaction problem, any realistic simulation of helicopter take-off and landing on a ship deck is still impractical. Also, in real time implementation, these models have to be computationally simple. A series of studies of these effects and models have been carried on at Georgia Tech (1,2) for the past few years, and a suitable ship airwake model and a systematic simulation method have already been developed. Moreover, a method to analyze helicopter/ship aerodynamic interactions has been formulated recently by Georgia Tech researchers(3). It is found that the widely used traditional ground effect model, which basically introduces a factor to modify the uniform inflow of the helicopter rotor(8,9), is not accurate for a helicopter operating under a ship "ground effect".

A computationally intensive method, which combines a rigid rotor wake model and the well developed traditional potential flow theory, is formulated in Ref.(3) and the method is used here to generate the data base for the ground effect model identification. Our purpose in this paper, however, is to identify a simple ground effect model suitable for real-time simulation implementation.

2. Computational Fluid Dynamics (CFD) Model Used for Generating the Data Base

The ship "ground effect" is manifested by the changes of the flow field, so that the flow at the ship surface follows the motion of the ship surface. This effect is modeled by a panel representation of the ship surface, and the strength of the panel is determined by satisfying the boundary condition at the ship surface, i.e. there is no penetration of flow through the solid ship surface and/or ship deck. The velocity induced by the rotor wake on the ship surface is computed by using a rigid wake theory. The simulation of helicopter motion near the ship is carried out by the general helicopter simulation code GENHEL(8), which has been modified to incorporate a first-order dynamic inflow model(11). By taking into account the induced velocity or upwash at the rotor disk due to the ship panel system into the blade-element analysis, the ground effect is coupled into the simulation code. Through changing the collective pitch and cyclic pitch, the helicopter is retrimmed at the same location with the consideration of the ground effect. The total inflow at the rotor disk is outputted as the rotor blade rotates azimuthally, and this forms the data base for later analysis.

3. Dynamic Inflow Model

A generalized dynamic inflow theory exists in the literature in which air mass passing through the rotor is treated as a dynamic system. The dynamic inflow theory (4,5,6,7) has found wide applications in flight dynamics and aeroelastic studies. Peter's dynamic inflow model (6) is used in this investigation for simplicity, i.e. the induced inflow is assumed to have the following variations:

---

* Graduate Research Assistant
‡Associate Professor
† Professor
§ Aerospace Engineer

1995 AHS FORUM PAPER

$$\lambda(\bar{r},\bar{\psi}) = \lambda_0 + \lambda_s \frac{r}{R}\sin\psi + \lambda_c \frac{r}{R}\cos\psi \qquad (1)$$

where:

$\lambda_0, \lambda_s, \lambda_c$ are the uniform, lateral and longitudinal variations of the rotor inflow in tip path plane (tpp), respectively.

The dynamic inflow model is:

$$[M]\{\dot{\bar{\lambda}}\} + [\hat{L}]^{-1}\{\bar{\lambda}\} = \{\bar{C}\}_{aero} \qquad (2)$$

where

$$\lambda = (\lambda_0, \lambda_s, \lambda_c)^T$$
$$C = (CT, -C1, -C2)^T$$

$[M], [\hat{L}]$ are the apparent mass matrix and the inflow gain matrix and their explicit expressions for out-of-ground effect case can be found in Ref. [4]. CT is the thrust coefficient. C1,C2 are instantaneous aerodynamic rolling and pitching moment coefficients expressed in the tip path plane. Obviously, they are time dependent for unsteady flight.

The subscript "aero" denotes that only the aerodynamic contribution is considered and the inertial part is not included. The " • " denotes time derivative.

Due to the proximity of the rotor disk to the ship deck, the rotorcraft/ship interactions induce upwash at the rotor disk, thereby changing the total inflow and the inflow distribution over the whole rotor disk. Hence, it is not surprising that $[M]$ and $[\hat{L}]$ matrices are going to change due to the ground effect. Thus, the dynamic inflow model near the ground can be written as:

$$[M]_{ige}\{\dot{\bar{\lambda}}\}_{ige} + [\hat{L}]^{-1}_{ige}\{\bar{\lambda}\}_{ige} = \{\{\bar{C}\}_{aero}\}_{ige} \qquad (3)$$

where : $[M]_{ige}$, $[L]_{ige}$ are the apparent mass and the inflow gain matrices with ground effect.

Suppose

$$\left\{\bar{\lambda}\right\}_{ige} = \begin{bmatrix} \alpha_1 & 0 & 0 \\ 0 & \beta_1 & 0 \\ 0 & 0 & \gamma_1 \end{bmatrix} \left\{\bar{\lambda}\right\}_{oge} \qquad (4)$$

and

$$\left\{\bar{C}\right\}_{ige} = \begin{bmatrix} \alpha_2 & 0 & 0 \\ 0 & \beta_2 & 0 \\ 0 & 0 & \gamma_2 \end{bmatrix} \left\{\bar{C}\right\}_{oge} \qquad (5)$$

where:

$\alpha_i, \beta_i, \gamma_i \ (i = 1,2)$ are the correction factors to account for ground effect to the inflow and the forcing functions, which are functions of the helicopter position (x,y,z) relative to the deck.

Thus, for the steady case, i.e., trimmed flight condition,

$$\left[\hat{L}\right]_{ige} = \begin{bmatrix} \alpha_1/\alpha_2 & \alpha_1/\beta_2 & \alpha_1/\gamma_2 \\ \beta_1/\alpha_2 & \beta_1/\beta_2 & \beta_1/\gamma_2 \\ \gamma_1/\alpha_2 & \gamma_1/\beta_2 & \gamma_1/\gamma_2 \end{bmatrix} \left[\hat{L}\right]_{oge} \qquad (6)$$

All six factors $\{\alpha_1, \beta_1, \gamma_1, \alpha_2, \beta_2, \gamma_2\}$ can be obtained by conventional identification methods.

For trimmed flight (steady case), we have:

$$\{\bar{\lambda}\} = [\hat{L}]\{\bar{C}\}_{aero} \qquad (7)$$

Thus, for trimmed hovering with respect to the deck of the moving ship, since the forcing functions (CT,C1,C2) are approximately the same for out-of-ground case and in-ground case, Eq. (6) reduces to:

$$\left\{\hat{L}\right\}_{ige} = \begin{bmatrix} \alpha_1 & 0 & 0 \\ 0 & \beta_1 & 0 \\ 0 & 0 & \gamma_1 \end{bmatrix} \left\{\hat{L}\right\}_{oge} \qquad (8)$$

4. Identification Approach

For illustration purpose, the SH-60 Seahawk helicopter flying at 15kts above the deck of a FFG-7 class frigate, which is moving at the same velocity as the helicopter, is used in this investigation. To capture the ground effect, the rotorcraft/ship interactions are computed using the CFD code at all the grid points over the ship deck as shown in Figure 1(a) at eight heights ranging from 0.5R to 3R for each grid point (Figure 1(b))

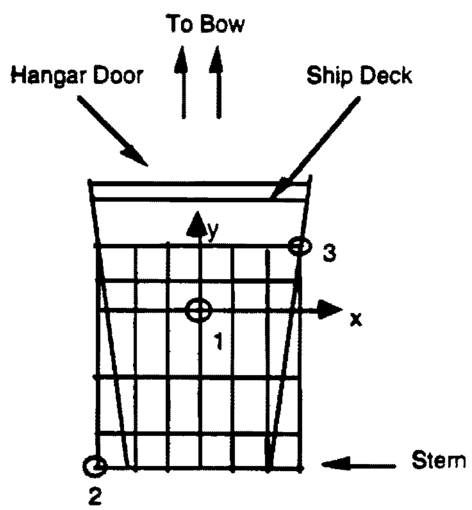

Figure 1(a): Positioning of helicopter above ship deck (top view)

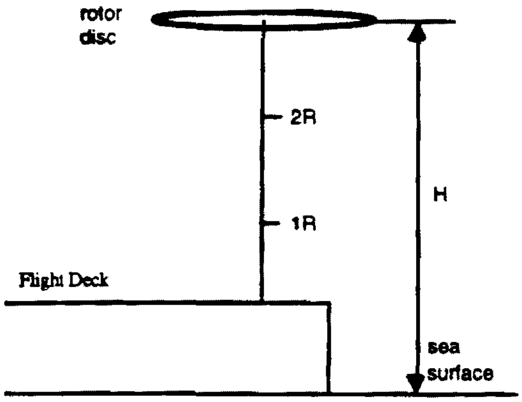

Figure 1(b): Helicopter Relative Position

It is recognized that the ground effect and the ship airwake effect are actually coupled when the helicopter is flying near the deck. However, only the ground effect part is considered in this study.

Figures 2(a) and 2(b) show how the nondimensional upwash at 80% radial station changes in one revolution above the center of the deck (location 1 in Figure 1(a)) and at the lower left corner of the deck (location 2 in Figure 1(a)) for different values of height above the deck.

It can be seen from Figure 2(a) that the upwash is almost constant at the fore part of the rotor for a given height (azimuth angle between 90 and 270 degrees), whereas at the rear part of the rotor (azimuth angle form 0 to 90, and 270 to 360 degrees), the upwash changes significantly. Also, we see that the effect of the height on upwash is different at different azimuth angles, hence it is not accurate to model this effect by using a simple constant factor. Because of the presence of the hanger, the rotor wake hits the deck differently at different locations.

For the case of the rotor hovering above the lower left corner of the deck, the upwash is much higher at advancing side and much lower at retreating side (see Fig. 2(b)). In order to incorporate the upwash in the dynamic inflow model, harmonic analysis of the upwash is carried out in order to extract the uniform and lateral and longitudinal variations due to the contribution of the upwash from the ground effect. It is seen from this analysis that terms up to second harmonic are required in order to account for the effect of ship deck on the rotor inflow variation.

$$\Delta w = -\Delta\lambda_0 - \Delta\lambda_s \frac{r}{R}\sin\psi - \Delta\lambda_c \frac{r}{R}\cos\psi - \Delta\lambda_{2s}\frac{r}{R}\sin(2\psi) - \Delta\lambda_{2c}\frac{r}{R}\cos(2\psi) \quad (9)$$

where

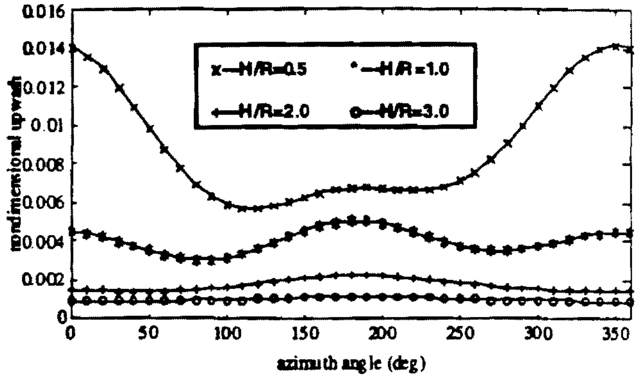

Figure 2(a): Effect of height on upwash at rotor disk at the center of the deck

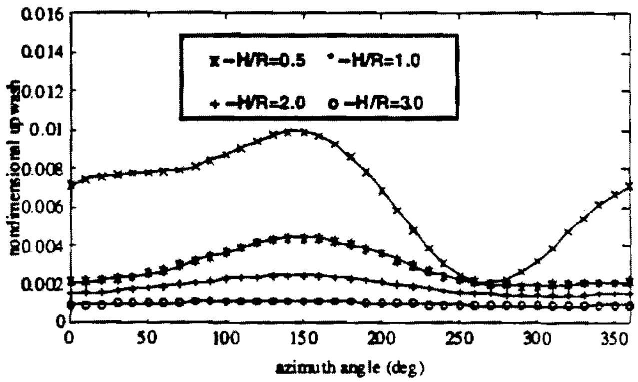

Figure 2(b): Effect of height on upwash at the rotor at the lower left corner of the deck

$\Delta\lambda_0$ is the upwash contribution to the uniform inflow

$\Delta\lambda_s$ is the lateral inflow changes due to the ground effect

$\Delta\lambda_c$ is the longitudinal inflow variation because of the ground presence

$\Delta\lambda_{2s}$ is the 2nd lateral inflow change

$\Delta\lambda_{2c}$ is the 2nd longitudinal inflow change

The analysis is carried out for different heights from 0.5 R to 3 R above the deck.

Figure 3 gives the effect of the height on the uniform inflow changes for location 1 (center of the deck, "*" in Fig.3--5) and for location 2 (left corner at the stern, "o" in Fig.3--5). The magnitude of total uniform inflow increases as the height increases. This is quite reasonable, because the ground cushion effect gets less and less as the rotor moves away from the deck, hence the upwash gets less and less. We see that at the deck center, the uniform inflow undergoes a maximum of 14% change due to "ground" effect.

Figures 4(a) and 4(b) give the effect of height on the first harmonic lateral inflow λ_s and first harmonic longitudinal inflow component λ_c

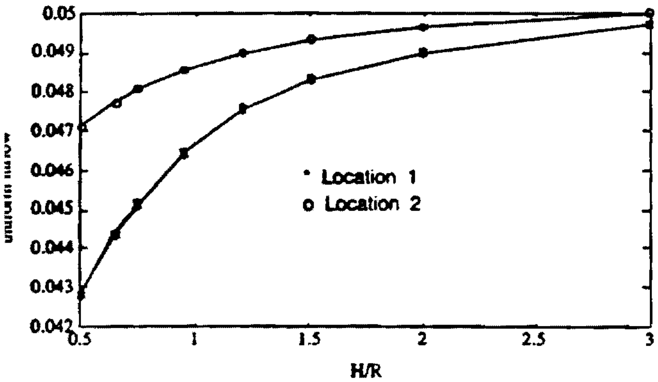

Figure 3: Effect of height on uniform inflow

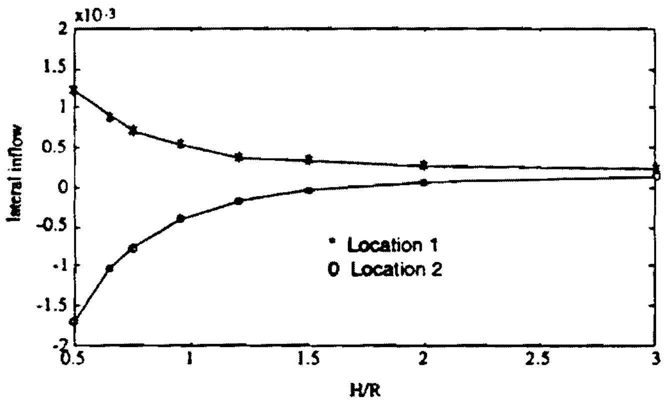

Figure 4(a) : Effect of height on lateral inflow
(First harmonic term)

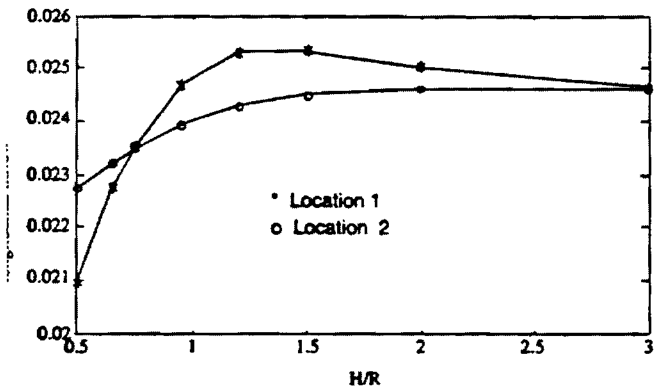

Figure 4(b): Effect of height on longitudinal inflow
(First harmonic term)

It is seen from Fig 4 that the longitudinal inflow change is not a linear function of height.
Figures 5(a) and 5(b) are the effect of height on the 2nd inflow terms λ_{2s} , λ_{2c}. Still, the ground effect gets less important as the distance between the helicopter and the deck gets larger. Also, the lateral component in the upwash is smaller than the longitudinal component.
From Figs 3,4 and 5, it can be seen that the ground effect is not a linear function of the height, and it is sensitive to the location of the rotor hub over the deck.

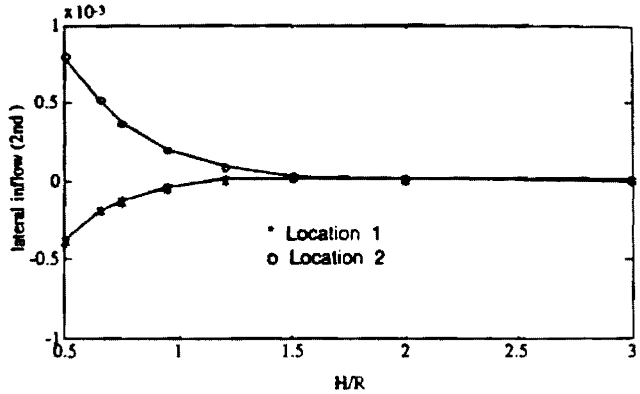

Figure 5(a): Effect of height on lateral inflow
(2nd harmonic term)

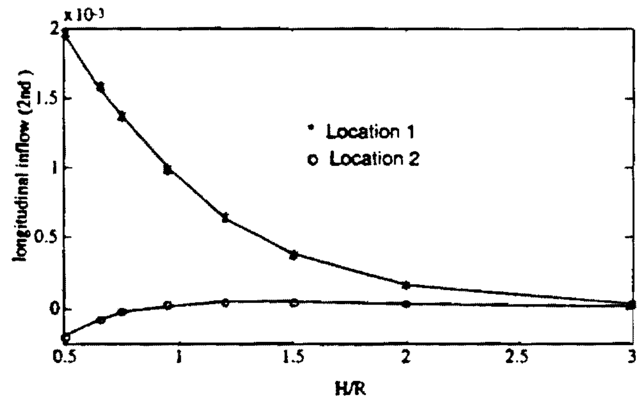

Figure 5(b): Effect of height on longitudinal inflow
(2nd harmonic term)

Several models are tried to represent these changes. By comparison of the **Pearson** correlation coefficient, the following model is seen to capture the variation with height:

$$\{\lambda_i\} = \{\lambda_i\}_{ref}\ [a+\frac{b}{h}+\frac{c}{h^2}+\frac{d}{h^3}] \qquad (10)$$

where :
a,b,c,d are constants for a given location w.r.t. the deck, h is the nondimensional (w.r.t. rotor radius R) height, and λ_{ref} is the corresponding value of the component out of ground effect.

Thus from (5) and (10),

$$\left\{\begin{array}{c}\alpha_1\\ \beta_1\\ \gamma_1\end{array}\right\} \Rightarrow a+\frac{b}{h}+\frac{c}{h^2}+\frac{d}{h^3} \tag{11}$$

Cheeseman and Bennett [9] derived an expression for the upwash at the rotor disk due to the ground:

$$\Delta w = \frac{\lambda_{0ref}}{16h^2} \tag{12}$$

i.e.

$$\lambda_0 = (1.-\frac{1}{16h^2})\lambda_{0ref} \tag{13}$$

Figure 6 shows the comparison of the uniform inflow predicted by the simple model Eq.(13) and the fitted model of Eq. (10) at several locations.

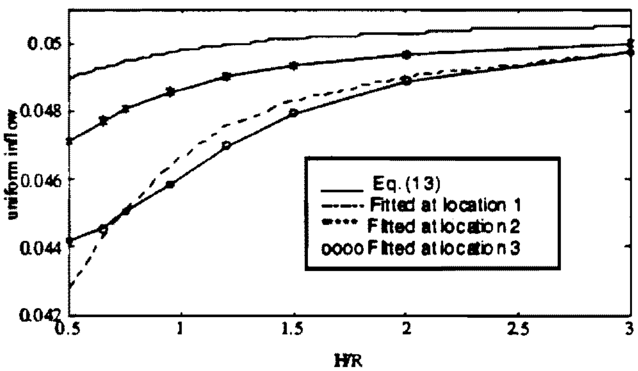

We see that the Cheeseman model is not accurate enough to capture the ship ground effect. First the ground effect is location dependent, and second it does not follow the h^{-2} law . Hence the ship ground effect model has to incorporate a function of location x and y, as well as the height.

5. Spline Fit

Having taken care of the effect of the height, we now move to the modeling of the location effect. Based on the data base, it is found that we can not use a simple function for f(x,y) to fit these data. Because spline fit has advantages of passing through every grid point, and yet it preserves the nice continuous property (up to 2nd derivatives), we use a two dimensional spline-fit to model the ground effect, i.e. a,b,c,d will be spline functions of x and y.

Suppose we have a set of data on the grid of X and Y as:

$X=\{X_i\}$, i=1,2,.....m+kx
$Y=\{Y_j\}$, j=1,2,..... n+ky
$F=\{ f(x_i,y_j)\}$

where: kx is the order of the spline in x direction, ky is the order of the spline in y direction. For cubic spline, the order is 4. For quadratic spline, the order is 3.

Let:

$$qx = m + kx$$
$$qy = n + ky$$

$N_{kx,i}(X,x)$ denotes the normalized B-spline of order kx in x direction with support $[X_{i-kx},X_i]$

$N_{ky,j}(Y,y)$ denotes the normalized B-spline of order ky in y direction with support $[Y_{j-ky},Y_j]$

Then any bivariate spline S(x,y) of order kx in x, and ky in y, has the following representation:

$$S(x,y)=\sum_{i=1}^{q}\sum_{j=1}^{q} C_{i,j}N_{kx,i}(X,x)N_{ky,j}(Y,y) \tag{14}$$

With the help of ***Mathematica*** [12], the coefficients C_{ij} are obtained for cubic spline fit. That is kx=ky=4.

Finally the total inflow with ground effect is modeled as:

$$\lambda = \lambda_0 + \frac{r}{R}(\lambda_s \sin(\psi) + \lambda_c \cos(\psi) + \lambda_{2s}\sin(2\psi)+\lambda_{2c}\cos(2\psi)) \tag{15}$$

and

$$\{\lambda_i\} = \{\lambda_i\}_{ref}[a(x,y)+\frac{b(x,y)}{h}+\frac{c(x,y)}{h^2}+\frac{d(x,y)}{h^3}] \tag{16}$$

where i may be 0,s,c,2s,2c.

For illustration purpose, the following is the spline fitted result for the uniform inflow:

$$\begin{aligned}\lambda_0 =\ & 0.994 - 0.0448x - 0.2993x^2 - 0.1752x^3 - 0.0355xy \\ & + 0.036x^2y + 0.040x^3y + 0.027xy^2 + 0.236x^2y^2 \\ & + 0.14x^3y^2 + 0.0177y^3 + 0.069xy^3 - 0.066x^2y^3 \\ & - 0.074x^3y^3 \\ & + (0.011 + 0.486x + 2.334x^2 + 1.3x^3 + 0.026y \\ & + 0.269xy - 0.298x^2y - 0.325x^3y - 0.0625y^2 \\ & - 0.2656xy^2 - 1.8x^2y^2 - 1.05x^3y^2 - 0.1358y^3 \\ & - 0.53xy^3 + 0.55x^2y^3 + 0.594x^3y^3)/h \\ & + (-0.2255 - 1.55x - 5.587x^2 - 3.02x^3 - 0.0389y \\ & - 0.6457xy + 0.7674x^2y + 0.815x^3y + 0.077y^2 \\ & + 0.76xy^2 + 4.25x^2y^2 + 2.42x^3y^2 + 0.327y^3 \\ & + 1.28xy^3 - 1.437x^2y^3 - 1.5x^3y^3)/h^2 \\ & + (-0.05999 + 1.21x + 3.9x^2 + 2.05x^3 + 0.01557y \\ & + 0.4987xy - 0.61x^2y - 0.639x^3y + 0.183y^2 \\ & - 0.534xy^2 - 3.x^2y^2 - 1.685x^3y^2 - 0.2448y^3 \\ & - 0.9727xy^3 + 1.157x^2y^3 + 1.17886x^3y^3)/h^3\end{aligned} \tag{17}$$

The computation with the above formula is quite fast when compared to the CFD code used to build the database. For comparison, CFD code takes about 30 minutes of CPU time in HP Apollo 700 Workstation to obtain a converged solution for a helicopter flying at one single height and single (x,y) location. Whereas using the above formula, the computation is carried out in a fraction of a second. Hence the formula is very useful for real-time simulation purposes. Figure 7 shows the variation of the uniform inflow over the whole deck at height h=0.75. Figures 8 and 9 display the variation of the harmonics of the inflow at h=0.75. It can be seen that the total inflow mainly consists of the uniform inflow and the longitudinal variation. This is from the fact that the reference flight is forward flight.

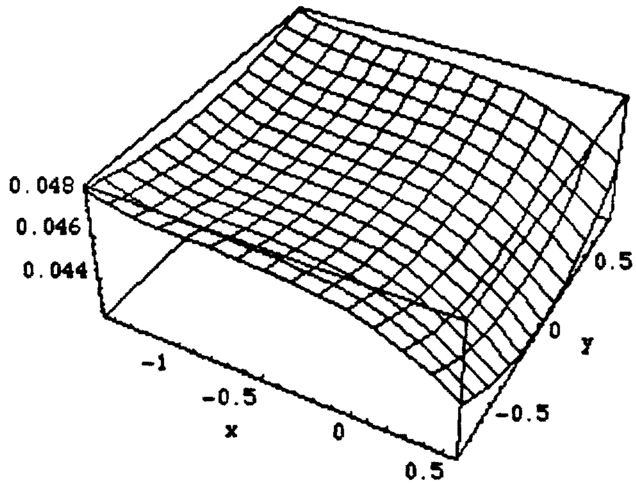

Figure 7: distribution of the uniform inflow over the deck

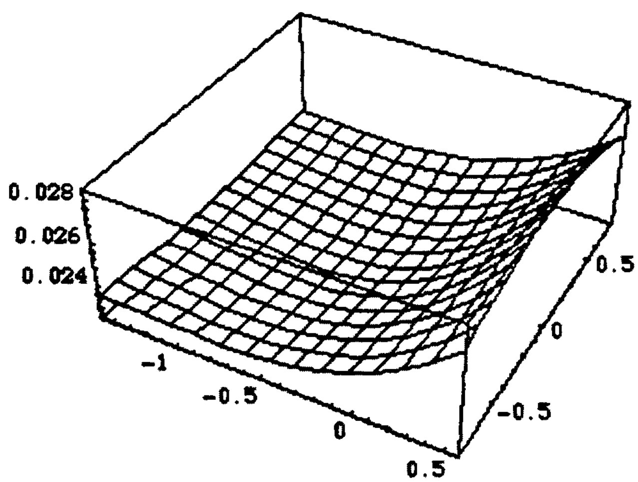

Figure 8: distribution of the longitudinal inflow over the deck

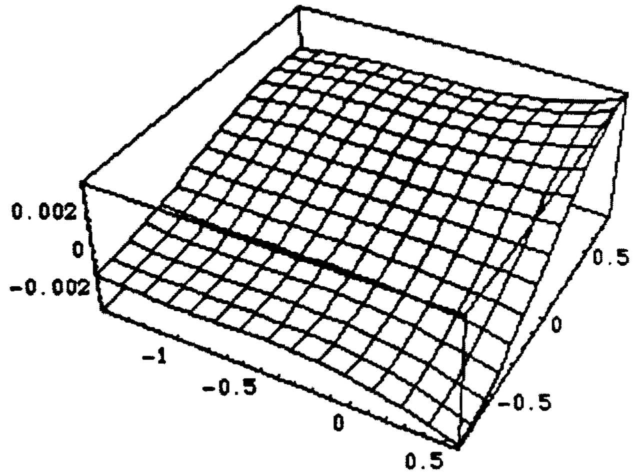

Figure 9: distribution of the lateral inflow over the deck

Figures 10(a) and 10(b) compare the results from the CFD code and from the formula at location x=-7.5/R, y=-5.5/R, h=0.75 and x=-25/R,y=15/R, h=1.75. We see that the fitted formula computes the inflow variation quite well.

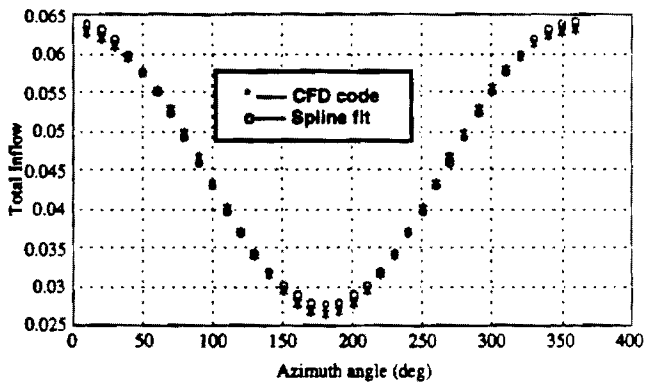

Figure 10 (a): comparison of the total inflow from CFD code and Spline fit formula at h=0.75

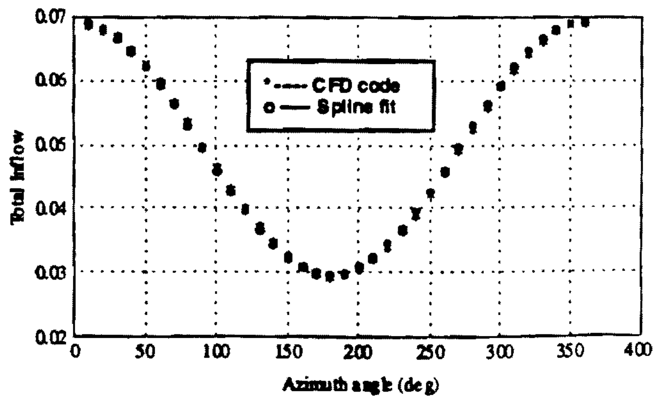

Figure 10 (b): comparison of the total inflow from CFD code and Spline fit formula at h=1.75

6. Conclusions

A ground effect model for rotorcraft/ship dynamic interface that is suitable for real time simulation purposes is developed in this paper. The gain matrix in the dynamic inflow model is identified as a function of the location of the rotor with respect to the ship deck, as well as the height of the rotor above the deck. However, the ship ground effect model developed in this study is applicable for trimmed flight above the deck. Further work is needed to capture the unsteady effects due to the rolling and/or pitching of the ship deck.

Acknowledgment

This work is funded by the Naval Air Warfare Center, Warminster, PA.

References

1.Prasad, J.V.R., Mavris, D.N., and Schrage, D.P., "Ship Airwake Modeling and Simulation, Phase I --- Methodology Development", Research Report submitted to Naval Air Warfare Center, School of Aerospace Engineering, Georgia Institute of Technology, Atlanta, Aug. 1992

2.Zhang, H., Prasad, J.V.R., and Mavris, D.N., "Ship Airwake Effects on Helicopter Rotor Aerodynamics", AIAA 94-3509, Arizona, August, 1994

3.Mello, O.A.F., Prasad, J.V.R., Sankar, L.N., and Tseng, W., "Analysis of Helicopter/Ship Aerodynamic Interactions," AHS Aeromechanics Specialists Conference, San Francisco, California, Jan. 1994.

4.Gaonkar, G.H., and Peters, D.A., "Review of Dynamic Inflow Modeling for Rotorcraft Flight Dynamics," Vertica, Vol. 12, No. 3, pp. 213-242, 1988.

5.Pitt, D.M., and Peters, D.A., "Theoretical Prediction of Dynamic Inflow Derivatives", Sixth European Rotorcraft and Powered Lift Aircraft Forum, Bristol, England, Sept. 1980

6.Peters, D.A., and HaQuang, N., "Dynamic Inflow for Practical Applications" J. of AHS, Oct. 1988.

7.He, Changjian, and Lewis, W.D., "A Parametric Study of Real Time Mathematical Modeling Incorporating Dynamic Wake and Elastic Blades", 48th Annual Forum of the AHS, Washington, DC, June 1992.

8.Howlett, J.J., "UH-60A Black Hawk Engineering Simulation Program: Volume I -- Mathematical Model", NASA CR-166309, 1981.

9.Cheeseman, I.C. and Bennett, W.E., "The Effect of the Ground on a Helicopter Rotor in Forward Flight", ARC R&M No.3021, Sept. 1955.

10. Healey, J. Val., "Prospects for Simulating the Helicopter/Ship Interface," Naval Engineers Journal, Vol. 99, No. 2, March 1987, pp. 45-63.

11. Mello, O. A. F., Numerical Simulation of Helicopter/Ship Aerodynamic Interactions," Research Report submitted to Naval Air Warfare Center, School of Aerospace Engineering, Georgia Institute of Technology, Atlanta, July 1993.

12. Wolfram, S., Mathematica: A System for Doing Mathematics by Computer, Addison-Wesley, Redwood City, Calif., 1988.

E-16-M07
#27

Progress Report
on
Aerodynamic Modeling of Ground Effect for Helicopter/Ship Interaction Studies

Period covered: July - August, 1995

During this period, the effort was directed towards carrying out the ship ground effect/vehicle simulations using the GENHEL program for hovering with respect to deck at different heights and for different ship speeds. Using CFD results, an inflow model was obtained as a function of (x,y) location around the ship deck, height from the ship deck and ship speed. Results from the model developed in this study were compared with results one would obtain by using the Cheeseman and Bennett formula. A paper was written and was presented at the 1995 AIAA Flight Simulation Conference. A copy of the paper is attached.

The work on development of theoretical ground effect model is continuing.

GROUND EFFECT SIMULATION MODEL FOR ROTORCRAFT/SHIP INTERACTION STUDY

Hong Zhang * J.V.R. Prasad† L.N. Sankar‡
School of Aerospace Engineering
Georgia Institute of Technology
Atlanta, GA 30332, USA

O.A.F. Mello§
Centro Técnico Aerocspacial
Instituto de Aeronáutica e Espaco
São José dos Campos-SP, BRAZIL

John D. Funk, Jr. ¶
Aircraft Division
Naval Air Warfare Center
Warminster, PA, USA

Abstract

In this paper, a real time simulation model of ship ground effect for rotorcraft/ship interactions is developed by combining computational fluid dynamics (CFD) analysis and finite state representation of rotor inflow. For CFD analysis, the ship is modeled by using a source panel representation and the rotor wake is modeled as rigid with prescribed geometry but unknown vorticity distribution. The sea surface is modeled by placing an image rotor wake and an image ship panel system below the sea surface. The CFD model is then combined with the batch version of a generic helicopter flight simulation program. Using trim solutions from the simulation program, the ship ground effects on rotor inflow for cases of helicopter hovering with respect to ship deck are identified and analyzed. With a finite state representation of rotor inflow, a real time simulation model of ship ground effect is developed using results from the CFD analysis.

1. Background

Due to complex flow interactions between the air flow surrounding the ship deck and rotor wake, the pilot workload during shipboard landing and take-off of a helicopter is significantly increased [1]. Also, When a helicopter is flying close to a ship deck, the rotor wake is modified due to the presence of ship deck, superstructure and sea surface [2-4]. An alternative, to extensive and time-consuming testing at sea for establishing safe operating envelopes for helicopter shipboard operations, is simulation. A prerequisite to simulation approach is the development of simulation models of ship airwake and ship ground effect. This paper addresses the development of a simulation model of ship ground effect model while a companion paper [5] addresses the development of a simulation model of ship airwake. The organization of the paper is as follows: First, the methodology used for the development of a real-time ship ground effect simulation model is described. Next, a detailed description of the CFD modeling used in this methodology is presented followed by parametric investigations of the CFD model. Then a brief description of the real-time simulation model which is obtained by modifying the gain matrix of an existing dynamic inflow model is given and results are presented to illustrate how the real-time simulation model captures the ship ground effect for different rotor heights above deck and at various forward speeds.

2. Methodology for Developing Ship Ground Effect Simulation Models

The methodology used for developing ship ground effect simulation models is given in Fig. 1. First, a comprehensive computational fluid dynamic model that takes into account interactions between rotor wake and ship deck, superstructure and sea surface is developed. The CFD model is then combined with a comprehensive non-real time helicopter simulation model and rotor inflow distribution for cases of helicopter trimmed at different positions (see Fig. 2) and at different heights (see Fig. 3) with different values of ship speed are obtained. Then a harmonic analysis of inflow distribution for each of the cases is carried out. Using results from the harmonic analysis, the gain matrix of the dynamic inflow model is modified by matching the inflow distribution predicted by the dynamic inflow model with CFD results.

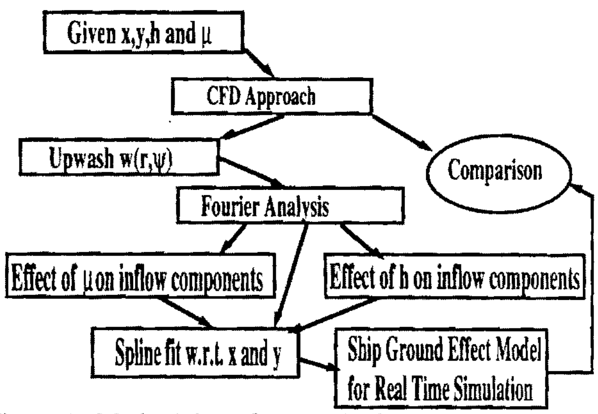

Figure 1. Methodology for Developing Ship Ground Effect Models

* Graduate Research Assistant
† Associate Professor, Member AIAA
‡ Professor, Member AIAA
§ Captain, Brazil Air Force
¶ Aerospace Engineer

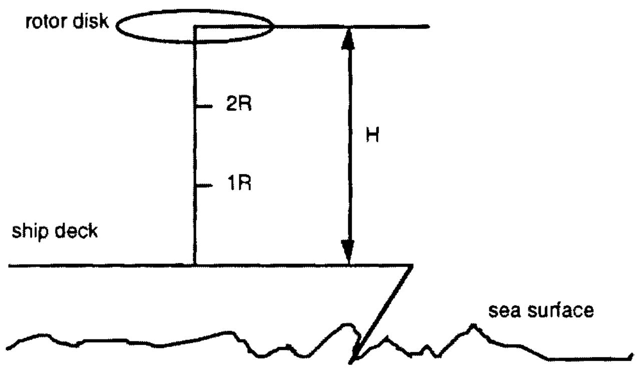

Figure 2. Helicopter Relative Position

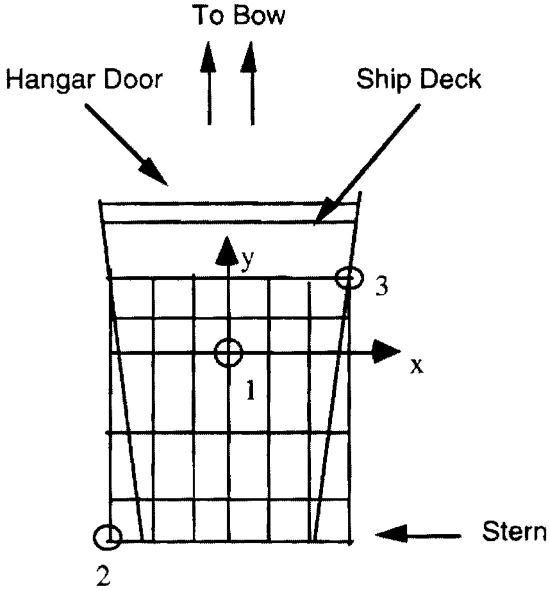

Figure 3. Positioning of Helicopter above Ship Deck (top view)

3. CFD Modeling

3.1 Ship Formulation

The ship surface is approximately represented by plane source panels with constant distributed strength. The strengths of the sources are determined by enforcing the non-penetration condition at the centroid of each panel. The normal component of the ship's motion and the normal component of the downwash induced by the rotor are taken into account in this formulation. The details of the source panel method can be found in Ref. 6 and therefore will not be repeated here. This formulation results in a linear system of equations to be solved for the ship panel source strengths σ:

$$[A]\{\sigma\} = [B] \tag{1}$$

where [A] is the matrix of influence coefficients, $\{\sigma\}$ is the vector of unknown source strengths and [B] is the RHS including the normal component of the velocities on the ship surface due to the free-stream and due to the rotor and its wake. The resulting source panel strengths are used to compute the velocities induced by the ship source panel system at the rotor disk.

3.2 Rotor Wake Formulation

A rigid wake model is used to compute the induced velocity due to the rotor and its wake on the ship and the vorticity distribution is computed from the blade section lift. In this study, the following assumptions are made:
(a) Blade flapping angles is small and high harmonic variation of blade flapping angle are negligible
(b) The rotor blade is modeled by a lifting line of bound vorticity, which is related to the blade section lift by Kutta-Joukowski's theorem.
(c) A classical skewed helical wake with a limited contraction is used, the wake is assumed to become flat near the ship deck as shown in Fig. 4.
(d) The wake is divided into a "near" wake, composed of trailing and shed vortices and a "far" wake composed of trailing tip vortices only. The strength of the far wake tip vortex is assumed to be equal to the maximum bound vorticity at the azimuthal location where the vortex filament leaves the blade.
(e) The rotor wake is convected downstream with a velocity which is equal to the vector sum of the free stream velocity and the averaged (momentum theory value) induced velocity over the disk.

3.2.1 Bound Vortices

The blade bound vorticity distribution is obtained through an iterative process from the blade section lift. Let the blade bound vorticity be $\Gamma_{b_{ij}} = \Gamma_b(r_i, \psi_j)$. From Kutta-Joukowski theorem:

$$\ell_{ij} = \rho V_{ij}\Gamma_{ij} = \rho(\Omega R)(\bar{r}_i + \mu \sin\psi_j)\Gamma_{b_{ij}} \tag{2}$$

i.e.

$$\Gamma_{b_{ij}} = \frac{\ell_{ij}}{\rho(\Omega R)(\bar{r}_i + \mu \sin\psi_j)} \tag{3}$$

From the computed bound vorticity distribution, the velocity induced by the blade bound vortices can be obtained by applying the Biot-Savart law.

3.2.2 Near Wake

The near wake is assumed to be composed of trailing and shed vortices, with strengths given by the radial and azimuth-wise variations of the bound vorticity respectively, at the azimuth location where the vortex filament leaves the blade. Let us first consider an element of a trailing vortex filament of length $r_i\Delta v$, which leaves the blade at the radial location r_i, and is located at a wake age v_k. This element had left the blade when it was at an azimuth location $\psi_j - \nu_k$, with ψ_j being the current azimuth location of the blade. Therefor, the vorticity of the element is given by $\Gamma_t(\bar{r}_i, \psi_j - \nu_k)\bar{r}_i\Delta\nu$, where

$$\Gamma_{t_{ijk}} = \Gamma_t(\bar{r}_i, \psi_j - \nu_k) = \frac{\partial \Gamma_b}{\partial \bar{r}} \qquad (4)$$

i.e.

$$\Gamma_{t_{ijk}} \approx \frac{\Gamma_b(\bar{r}_i, \psi_j - \nu_k) - \Gamma_b(\bar{r}_{i-1}, \psi_j - \nu_k)}{\bar{r}_i - \bar{r}_{i-1}} \qquad (5)$$

The velocity induced by the entire filament at a point is given by integration of elementary induced velocities obtained from the Biot-Savart law along the near wake only.

Now let us consider an element of a shed vortex filament of length Δr_i, which leaves the blade at the radial location r_i, and is located at a wake age ν_k. This element had left the blade when it was at an azimuth location $\psi_j - \nu_k$, with ψ_j being the current azimuth location of the blade. Therefore, the vorticity of the element is given by $\Gamma_s(\bar{r}_i, \psi_j - \nu_k)$, where $\Gamma_s(\bar{r}_i, \psi_j - \nu_k)\Delta r_i$ is the shed vortex vorticity, equal to the azimuthal variation of Γ_b:

$$\Gamma_{s_{ijk}} = \Gamma_s(\bar{r}_i, \psi_j - \nu_k) = \frac{\partial \Gamma_b}{\partial \psi} \qquad (6)$$

$$\Gamma_{s_{ijk}} \approx \frac{\Gamma_b(\bar{r}_i, \psi_j - \nu_k) - \Gamma_b(\bar{r}_i, \psi_{j-1} - \nu_k)}{\Delta\psi} \qquad (7)$$

Also, the velocity induced by the entire shed vortex system at a point is given by radial integration of the elementary induced velocities obtained from the Biot-Savart law along the "near" wake.

3.2.3 Far wake

The far wake is assumed to be only composed of trailing tip vortices, with strength equal to the maximum bound vorticity at the azimuth location where the vortex filament leaves the blade. Considering an element of wake filament of length $r_{tv}\Delta\nu$ (where r_{tv} corresponds to the radial location where the tip vortex has rolled up) and at a wake age ν_k. This element has left the blade when it was at an azimuth location $\psi_j - \nu_k, \psi_j$ being the current azimuth location of the blade. Therefore, the vorticity of the element is given by $\Gamma_{T_{jk}} r_{tv}\Delta\nu = \Gamma_T(\psi_j - \nu_k) r_{tv}\Delta\nu$, where $\Gamma_T(\psi_j - \nu_k)$ is the strength of the trailing tip vortex equal to the radial maximum of Γ_b:

$$\Gamma_{T_{jk}} = \Gamma_T(\psi_j - \nu_k) = \max_i(\Gamma_b(r_i, \psi_j - \nu_k)) \qquad (8)$$

3.2.4 Vortex Core Model

A Rankine vortex core model [7] with radius of one tenth (1/10) of the blade chord is used. This model is applied by scaling the induced velocity due to the elementary vortex filament by the square of the ratio between the distance to the filament and the core radius, whenever the point where the induced velocity is being calculated lies within the vortex core. The geometry of the far wake is modified by making it flat and parallel to the ship deck with assumed clearance between the wake and the deck (see Fig. 4).

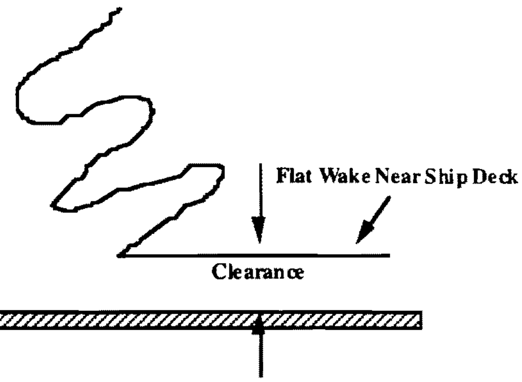

Figure 4. Modified Wake Geometry

In order to determine the number of rotor revolutions and clearance between the wake and the ship deck, the rotor wake model is combined with a generic helicopter simulation package [8]. Assuming a flat ground, the number of rotor revolutions in the wake geometry and wake clearance are adjusted by matching the rotor power required from analysis with experimental results. Figure 5 shows the effect of ground clearance on the rotor power required, whereas Fig. 6 illustrates the effect of number of revolutions in the wake geometry. It can be seen from Fig. 5, that the wake clearance has negligible effect on the rotor power. However, from Fig. 6, it is clear that the number of revolutions in the wake geometry has significant effect on rotor power. Also, from Fig. 6, it is seen that roughly 10 rotor revolutions of wake is needed in order to match with experimental data for the hover case. However, the results are less sensitive to number of revolutions for forward flight cases. It is felt that the value of 10 rotor revolution of wake geometry arrived at for the hover case is rather ad hoc as this value will be different for different heights of the rotor above the ground. Also, it is felt that a detailed investigation using , possibly, a free wake analysis is required to determine the wake geometry for the hover case. Hence, only forward flight cases are considered in the subsequent analysis.

4. Parametric Investigation

4.1 Effect of Locations

For illustration purpose, the SH-60 helicopter flying at 15kt above the deck of a FFG-7 class frigate, which is moving at the same velocity as the helicopter, is used in this investigation. The simulation of helicopter motion near the ship is carried out using the general helicopter simulation code [8]. By taking into account the induced velocity or upwash at the rotor disk due to the ship panel system into the blade-element analysis, the ground effect is coupled into the simulation code. Through changing the collective pitch and cyclic pitch, the helicopter is retrimmed at the same location with the consideration of the ground effect. Using the coupled ship ground effect CFD model and the generic flight simulation package, the helicopter is trimmed at different locations and different heights above the deck.

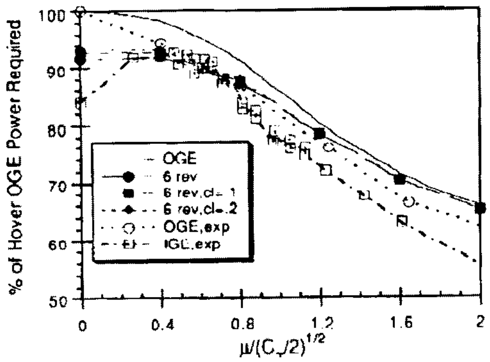

Figure 5. Clearance Effect on Power

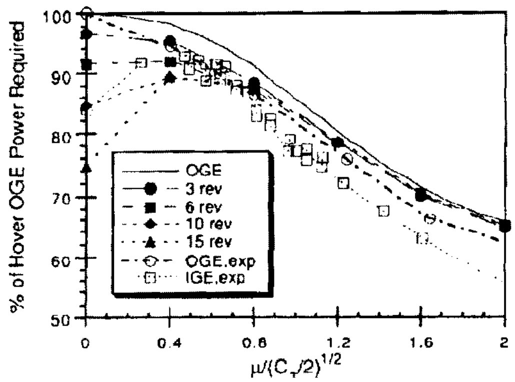

Figure 6. Effect of Number of Revolutions

Figure 7 shows the nondimensional upwash at 0.8R blade station for the rotor positioned at various heights above the center of the deck. It can be seen that the upwash is symmetric about the flight direction. The variation of the nondimensional upwash at the rotor at 0.8R blade station is shown in Fig. 8 for different heights of rotor from the ship deck for the helicopter above the lower left corner of the deck. It is seen from Fig. 8 that with an increase in rotor height above the deck, the ship ground effect diminishes. Also, the ship ground effect results in an increase in upwash on the advancing side of the rotor indicating, as one would expect, a "partial" ship ground effect.

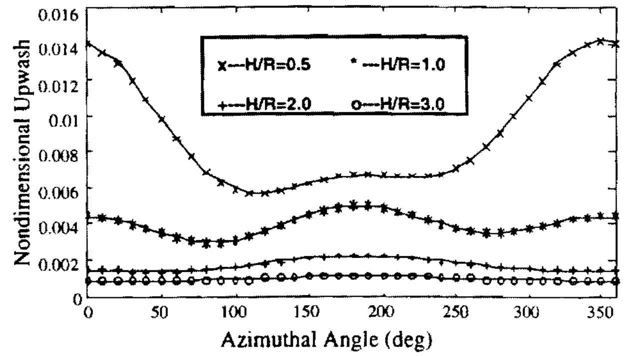

Figure 7. Effect of Height on Upwash at Rotor Disk at the Center of the Deck

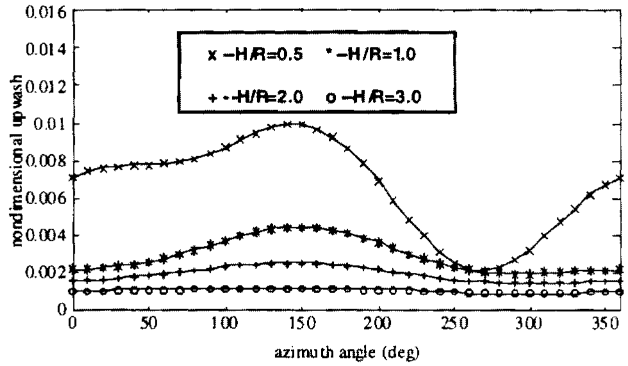

Figure 8. Effect of Height on Upwash at Lower Left Corner of the Deck

4.2 Effect of Advance Ratio

To study the advance ratio effect on the inflow distribution over the rotor disk when flying near the ship deck with the ship in motion, the helicopter is trimmed at 1.2 R above the ship deck at various speeds ranging from 10kt to 80kt. Figure 9 compares upwash due to the ship deck between the cases of helicopter flying at 15kt and 45kt

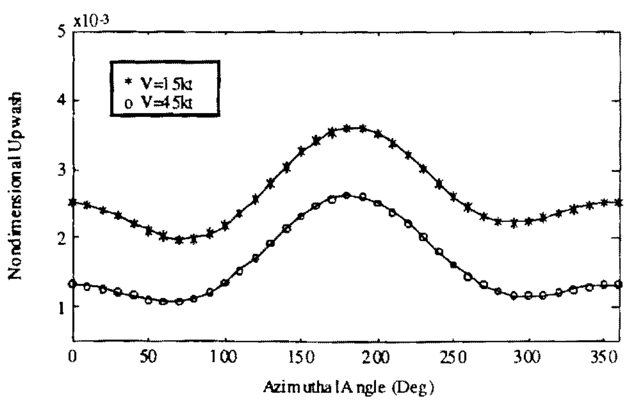

Figure 9. Upwash at Different Advance Ratio

cases. As expected, Fig. 9 shows that the upwash decreases as the helicopter speed is increased.

4. 3 Harmonic Analysis of the Inflow

Harmonic analysis is carried out for the upwash at various locations and advance ratios. It is found that up to second harmonic terms are needed to match the upwash from CFD results, i.e.:

$$\Delta w = -\Delta\lambda_0 - \Delta\lambda_s \frac{r}{R}\sin\psi - \Delta\lambda_c \frac{r}{R}\cos\psi$$
$$- \Delta\lambda_{2s} \frac{r}{R}\sin(2\psi) - \Delta\lambda_{2c} \frac{r}{R}\cos(2\psi) \qquad (9)$$

where

$\Delta\lambda_0$ is the upwash contribution to the uniform inflow

$\Delta\lambda_s$ is the lateral inflow changes due to the ground effect

$\Delta\lambda_c$ is the longitudinal inflow variation because of the ground presence

$\Delta\lambda_{2s}$ is the 2nd lateral inflow change

$\Delta\lambda_{2c}$ is the 2nd longitudinal inflow change

Thus, the inflow in ship ground effect can be modeled as,

$$(\lambda)_{ige} = (\lambda)_{oge} - \Delta w \qquad (10)$$

Figure 10 shows how the rotor height above the ship deck influences the uniform inflow at the rotor at two different locations. It is seen that the uniform inflow gets smaller when the rotor height above the ship deck increases, which is as expected. Figure 11 shows how the uniform inflow changes as the advance ratio varies. A nonzero value of advance ratio represents the case of the helicopter hovering with respect to the ship deck while the ship is in motion. The advance ratio effect on longitudinal inflow component is shown in Fig. 12. It is clear from Figs. 11 and 12 that the ship ground effect with advance ratio is not the same on average and the harmonic components. While the average component of inflow decreases with an increase of advance ratio, the longitudinal component of inflow first increases and then decreases as the advance ratio is increased.

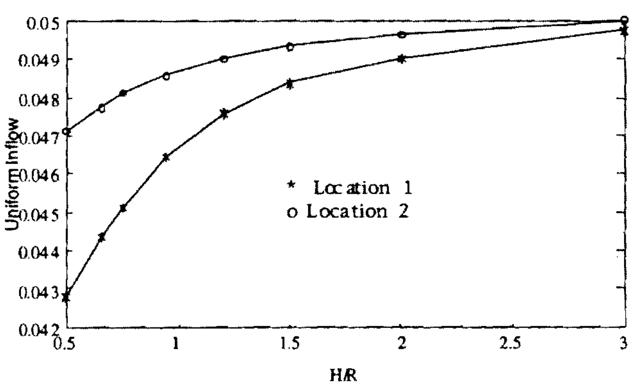

Figure 10. Effect of Height on Uniform Inflow Component

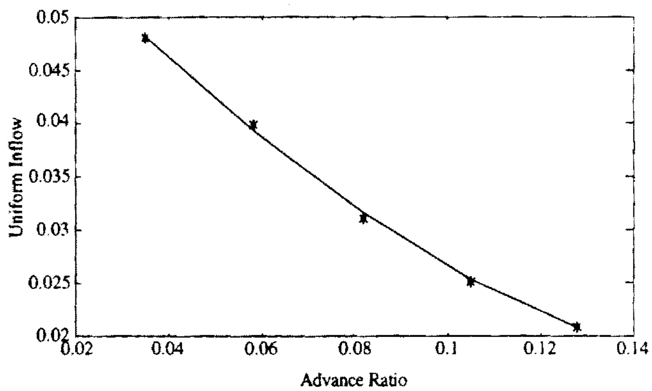

Figure 11: Effect of Advance Ratio on Uniform Inflow Component

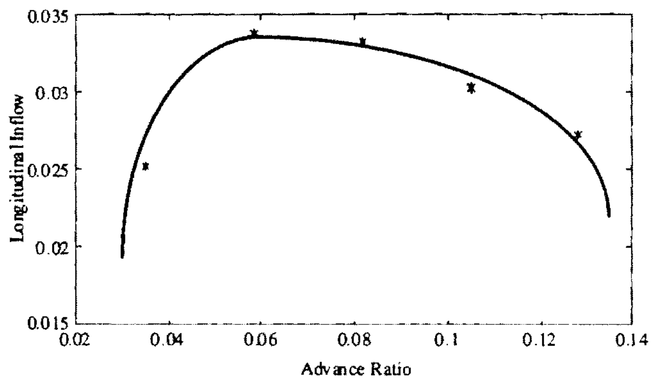

Figure 12. Effect of Advance Ratio on Longitudinal Inflow Component

5. Real Time Ship Ground Effect Model

As most of the current day flight simulation programs include a dynamic inflow representation for rotor inflow in order to account for the time-varying and distributed nature of inflow over the rotor disk, it is felt that a real time ship ground effect model can be obtained by appropriately modifying the parameters in the dynamic inflow model. The dynamic inflow model can be written as [9]:

$$[M]\{\dot{\bar{\lambda}}\} + [\hat{L}]^{-1}\{\bar{\lambda}\} = \{\bar{C}\}_{aero} \qquad (11)$$

where

$$\bar{\lambda} = (\lambda_0, \lambda_s, \lambda_c)^T$$
$$C = (CT, -C1, -C2)^T$$

$[M], [\hat{L}]$ are the apparent mass matrix and the inflow gain matrix and their explicit expressions for out-of-ground effect case can be found in Ref. 9. CT is thrust coefficient. C1, C2 are instantaneous aerodynamic rolling and pitching moment coefficients expressed in the tip path plane. Obviously, they are time dependent for unsteady flight. The subscript "aero" denotes that only the aerodynamic contribution is considered and the inertial part is not included. The "• " denotes time derivative.

Due to the proximity of the rotor disk to the ship deck, the rotorcraft/ship interactions induce upwash at the rotor disk, thereby changing the total inflow and the inflow distribution over the rotor disk. Hence, the dynamic inflow model for the case of in-ground-effect model can be written as:

$$[M]_{ige}\,\{\dot{\bar{\lambda}}\}_{ige} + [\hat{L}]^{-1}_{ige}\{\bar{\lambda}\}_{ige} = \{\{\bar{C}\}_{aero}\}_{ige} \qquad (12)$$

where : $[M]_{ige}$, $[\hat{L}]_{ige}$ are the apparent mass and the inflow gain matrices for the case of in-ground-effect. Suppose

$$\left\{\bar{\lambda}\right\}_{ige} = \begin{bmatrix} g_1 & 0 & 0 \\ 0 & g_2 & 0 \\ 0 & 0 & g_3 \end{bmatrix} \left\{\bar{\lambda}\right\}_{oge} \qquad (13)$$

and

$$\left\{\bar{C}\right\}_{ige} = \begin{bmatrix} h_1 & 0 & 0 \\ 0 & h_2 & 0 \\ 0 & 0 & h_3 \end{bmatrix} \left\{\bar{C}\right\}_{oge} \qquad (14)$$

Thus, for trimmed flight with rotor treated as a disk, and noticing that the forcing functions (CT, C1, C2) are approximately the same for out-of-ground effect case and in-ground effect case. From Eqs. (12)-(14) with $h_i = 1$, $i = 1,2,3$ and $\dot{\bar{\lambda}} = 0$, we get

$$\left\{\hat{L}\right\}_{ige} = \begin{bmatrix} g_1 & 0 & 0 \\ 0 & g_2 & 0 \\ 0 & 0 & g_3 \end{bmatrix} \left\{\hat{L}\right\}_{oge} \qquad (15)$$

Using results from CFD analysis for the ship ground effect cases of helicopter hovering over the ship deck at different positions and for different speeds, general expressions for g_i, $i = 1,2,3$ are obtained using curve fitting techniques. The resulting expression are obtained as

$$g_i = \frac{a_i(x,y) + \frac{b_i(x,y)}{h} + \frac{c_i(x,y)}{h^2} + \frac{d_i(x,y)}{h^3}}{k_{0_i} + k_{1_i}\mu + k_{2_i}\mu^2}, \; i = 1,2,3 \qquad (16)$$

where a_i, b_i, c_i, d_i are all cubic spline fitted functions of x and y. Thus, from equation (16), the correction factors g_1, g_2, g_3 that account for ground effect, are all functions of rotor position (x,y,z) with respect to ship deck and advance ratio. For comparison, the widely used Cheesemann & Bennett model [10] is of the form

$$g_i = 1. - \frac{1}{16h^2}\left(\frac{1}{1 + (\frac{\mu}{\lambda_{oge}})^2}\right), \; i = 1,2,3 \qquad (17)$$

Also, for comparison purpose, the variation of g_1 (for the uniform component) is shown in Fig. 13 as computed using the Cheesemann & Bennett model and the new model, for cases of helicopter hovering at three different locations above the ship deck. From Fig. 13, it is clear that ship ground effect is different for different positions around the ship deck as predicted by the new model.

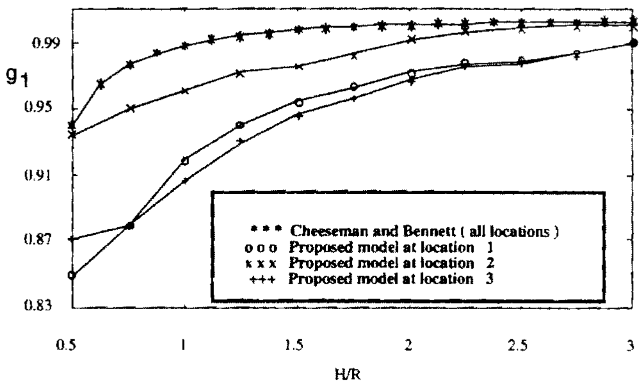

Figure 13. Comparison of Different Models

6. Conclusions

A ground effect model for rotorcraft/ship dynamic interface that is suitable for real time simulation purposes is developed in this paper. The gain matrix in the dynamic inflow model is identified as a function of the location of the rotor with respect to the ship deck, the height of the rotor above the deck and advance ratio. Also, the new model takes into account partial ground effect. However, the ship ground effect model developed in this study is only applicable for trimmed flight above the deck. Further work is needed to capture the unsteady effects due to heaving, rolling and/or pitching of the ship deck. Also, validation of the model using experimental data is needed.

Acknowledgment

This project is funded by the Naval Air Warfare Center, Warminster, PA.

References

1. Healey, J. Val., "Prospects for Simulating the Helicopter/Ship Interface," Naval Engineers Journal, Vol. 99, No. 2, March 1987, pp. 45-63.
2. Mello, O.A.F., Prasad, J.V.R., Sankar, L.N., and Tseng, W., "Analysis of Helicopter/Ship Aerodynamic Interactions," AHS Aeromechanics Specialists Conference, San Francisco, California, Jan. 1994.
3. Ferrir, B., and Semenza, J., "NATC Manned Flight Simulator VTOL Ship Motion Simulation and Application" 46th Annual Forum of AHS, Washington DC, 1990
4. Zhang H., Mello, O.A.F., Prasad, J.V.R., Sankar, L. N., and Funk, J. D. , "A Simulation Model of Ship Ground Effect For Rotorcraft/Ship Interaction Study," AHS 51st Annual Forum, Fort Worth, TX May 9-11,1995
5. Prasad, J.V.R., Manoj M., Mavris, D. and Zhang, H. , "Ship Airwake Simulation Models for Rotorcraft/Ship Interactions Study," AIAA 95-3406
6. Hess, J. L., and Smith, A. M O., " Calculation of Potential Flow About Arbitrary Bodies," Progress in Aeronautical Sciences, Vol. 8 Edited by D. Küchemann, Pergmon Press, Oxford, England, 1967
7. U.S. Department of Army-AFDD, " Second Generation Comprehensive Helicopter Analysis Systems, Version 2.1 " Vol. II, chapter 5, Moffett Field, CA July 1992
8. Kaplita,T.T., " UH-60A Black Hawk Engineering Simulation Method Validation and Proposed Modifications" Technical Report SER-70982, United Technologies Sikorsky Aircraft, June 1984.
9. Peters, D.A., and HaQuang, N., "Dynamic Inflow for Practical Applications" J. of AHS, Oct. 1988
10. Cheesemann, I.C. and Bennett, W.E., "The Effect of the Ground on a Helicopter Rotor in Forward Flight", ARC R&M No. 3021, Sept. 1955.

E - 16 - M07
#28

Progress Report
on
Aerodynamic Modeling of Ground Effect for Helicopter/Ship Interaction Studies
Period covered: September-October, 1995

During this period, the effort was directed towards completing the theoretical development of dynamic inflow model for ground effect for the forward flight case. The Peters-He generalized inflow theory is extended to include ground effect by syperimposing solutions from the rotor and its image. The inflow at the rotor disc including the effect of ground is represented as a series of normalized Legendre functions of radial station, and as a series of azimuth angle. The magnitude of each term is determined from first-order differential equations in time domain. The coefficients of the differential equations depend on the rotor height above the ground plane, rotor inclination and flight speed. The forcing functions are user-supplied, radial integrals of the blade loading. Initial validation with experimental results demonstrate the validity of the new ground effect model.

Ground Effect Modeling For Lifting Rotor In Forward Flight

It has been previously shown in the literature that the pressure distribution of a lifting rotor can be represented in ellipsoidal coordinates as :

$$\Phi(\nu,\eta,\overline{\psi},\overline{t}) = -\frac{1}{2}\sum_{m=0}^{\infty}\sum_{n=m+1,m+3,\cdots}^{\infty} \overline{P}_n^m(\nu)\overline{Q}_n^m(i\eta)\,[\tau_n^{mc}(\overline{t})\cos(m\overline{\psi}) + \tau_n^{ms}(\overline{t})\sin(m\overline{\psi})] \quad (1)$$

where $\overline{P}_n^m(.), \overline{Q}_n^m(.)$ are normalized associated Legendre functions of the first and second kind respectively, τ_n^{mc}, τ_n^{ms} are the disc loading coefficients corresponding to the cosine and sine harmonic distributions.

In order to model the ground effect using pressure potential idea, the following conditions must be met for the new pressure potential Φ:

(1) Φ must satisfy the basic governing equation (Laplace equation).

(2) Φ goes to zero at infinity (upstream and downstream).

(3) Φ will render the desired disk loading.

(4) Φ must be chosen in such a way that there will be no normal component of flow at the ground surface. Using image technique, the combined pressure potential can be written as:

$$\Phi_{Total}(\nu,\eta,\bar{\psi},\bar{t}) = -\frac{1}{2}\sum_{m=0}^{\infty}\sum_{n=m+1,m+3,\cdots}^{\infty} \bar{P}_n^m(\nu_1)\bar{Q}_n^m(i\eta_1)\,[\tau_{n\ 1}^{mc}(\bar{t})\cos(m\bar{\psi}_1)+\tau_{n\ 1}^{ms}(\bar{t})\sin(m\bar{\psi}_1)]$$

$$+\frac{1}{2}\sum_{m=0}^{\infty}\sum_{n=m+1,m+3,\cdots}^{\infty} \bar{P}_n^m(\nu_2)\bar{Q}_n^m(i\eta_2)\,[\tau_{n\ 2}^{mc}(\bar{t})\cos(m\bar{\psi}_2)+\tau_{n\ 2}^{ms}(\bar{t})\sin(m\bar{\psi}_2)] \tag{2}$$

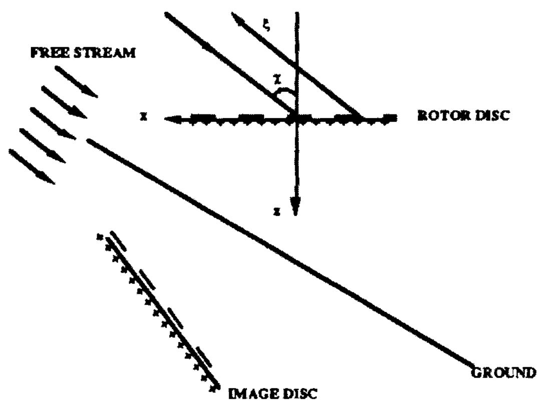

Figure 1: Ground Effect Modeling

In Fig. 1, assume the rotor hub is at height **h** above the ground and the wake skew angle is χ, the transformation matrix (**T**) can be written as:

$$\begin{Bmatrix} X \\ Y \\ Z \end{Bmatrix} = \begin{bmatrix} -\cos(2\alpha) & 0 & \sin(2\alpha) \\ 0 & 1 & 0 \\ -\sin(2\alpha) & 0 & -\cos(2\alpha) \end{bmatrix} \begin{Bmatrix} x2 \\ y2 \\ z2 \end{Bmatrix} + \begin{Bmatrix} 2h\cos(\alpha) \\ 0 \\ 2h\sin(\alpha) \end{Bmatrix} \tag{3}$$

where:

$$\alpha = \frac{\pi}{2} - \chi - a\tan(\frac{\lambda_m}{V_\infty}) \tag{4}$$

Suppose the inflow can be expanded in terms of a harmonic variation and a series of associated Legendre function of the first kind of radial position ν, i.e.:

$$W(\bar{r},\psi,\bar{t};h) = \sum_{m=0}^{\infty}\sum_{n=m+1,m+3,\cdots}^{\infty} \frac{\bar{P}_n^m(\nu)}{\nu}[\alpha_n^m(\bar{t};h)\cos(m\psi)+\beta_n^m(\bar{t};h)\sin(m\psi)] \tag{5}$$

where $\nu=\sqrt{1-(\frac{r}{R})^2}$, $\bar{r}=\frac{r}{R}$

Thus, the dynamic inflow equation can be formulated as:

$$[M]^{-1}\frac{\partial}{\partial \bar{t}}\left\{\begin{Bmatrix}\vdots\\ \{\alpha_j^k\}\\ \vdots\end{Bmatrix} \atop \begin{Bmatrix}\vdots\\ \{\beta_j^k\}\\ \vdots\end{Bmatrix}\right\}+V\begin{bmatrix}\tilde{L}^c & 0\\ 0 & \tilde{L}^s\end{bmatrix}^{-1}\left\{\begin{Bmatrix}\vdots\\ \{\alpha_j^k\}\\ \vdots\end{Bmatrix} \atop \begin{Bmatrix}\vdots\\ \{\beta_j^k\}\\ \vdots\end{Bmatrix}\right\}=\frac{1}{2}\left\{\begin{Bmatrix}\vdots\\ \{\tau_n^{mc}\}\\ \vdots\end{Bmatrix} \atop \begin{Bmatrix}\vdots\\ \{\tau_n^{ms}\}\\ \vdots\end{Bmatrix}\right\} \tag{6}$$

For steady situation, the model is decoupled to:

$$\left[\tilde{L}^c\right]^{-1}\begin{Bmatrix}\vdots\\ \{\alpha_j^k\}\\ \vdots\end{Bmatrix}=\frac{1}{2V}\begin{Bmatrix}\vdots\\ \{\tau_n^{mc}\}\\ \vdots\end{Bmatrix} \tag{7}$$

$$\left[\tilde{L}^s\right]^{-1}\begin{Bmatrix}\vdots\\ \{\beta_j^k\}\\ \vdots\end{Bmatrix}=\frac{1}{2V}\begin{Bmatrix}\vdots\\ \{\tau_n^{ms}\}\\ \vdots\end{Bmatrix} \tag{8}$$

A simple check is made for forward flight case (μ=0.08) at several heights above the ground. They are carried out for the UH60 Black Hawk helicopter using the general helicopter simulation package for trimming the helicopter. The comparison between predicted and measured inflow results for forward flight is shown in Figure 2.

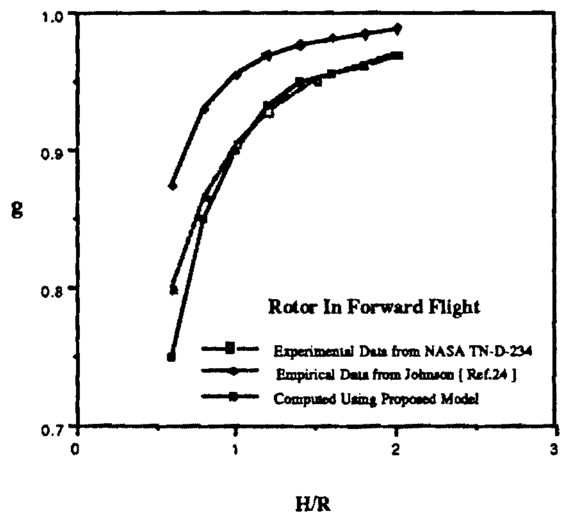

Figure 2: Uniform Inflow Ratio in Forward Flight

It is seen from Fig. 2 that results predicted from the new ground effect model match with experimental results better than results from empirical formula.

E-16-M07
#29

Progress Report
on
Aerodynamic Modeling of Ground Effect for Helicopter/Ship Interaction Studies
Period covered: November - December, 1995

During this period, the effort was directed towards the development of theoretical ground effect model for hover case.

Ground Effect Modeling For Lifting Rotor In Hover

It should be pointed out that since the dynamic inflow theory is good only in the vicinity of the rotor disk, it is not correct to use it to predict the inflow far away under the rotor disc. Apparently, if the inflow theory is applied, the inflow under rotor disc at infinity is twice the inflow at the rotor disc, which contradicts the fact that any disturbance must vanish at infinity. In our computations, an exponential decay function of the following form is used.

$$f_{decay}(h) = e^{-0.5h} \tag{1}$$

For near the rotor disc case:

$$\begin{aligned} w_Z &= \frac{1}{v}\{2\Phi_1|_{z=-h^-} - \Phi_1|_{z=0} - \Phi_2|_{z=0}\} \\ W_z &= 0 \end{aligned} \tag{2}$$

For far away from the rotor disc case:

$$\begin{aligned} w_Z &= \frac{1}{v}\{(2\Phi_1|_{z=-h^-} - \Phi_1|_{z=0}) * f_{decay}(h) - \Phi_2|_{z=0}\} \\ W_z &= 0 \end{aligned} \tag{3}$$

With the above modification in terms of a decay function, a new ground effect model for the hover case has been formulated.

An initial validation is carried out by simplifying the model and by comparing results predicted from this model with experimental data. For this purpose, only one radial function and only the first harmonic variations are considered in the dynamic inflow model. A comparison of results obtained from the new model with experimental data is shown in Fig. 1. The ratio of uniform inflow in-ground effect and out-of-ground effect is shown versus rotor height above the ground in Fig. 1. It is seen from Fig. 1 that results from the new model with the decay function correlate very well with experimental data. The effect of height on the first harmonic component as predicted using the new model is shown in Fig. 2. From Figs. 1 and 2, it is seen that as height is increased, the effect of ground on inflow decreases.

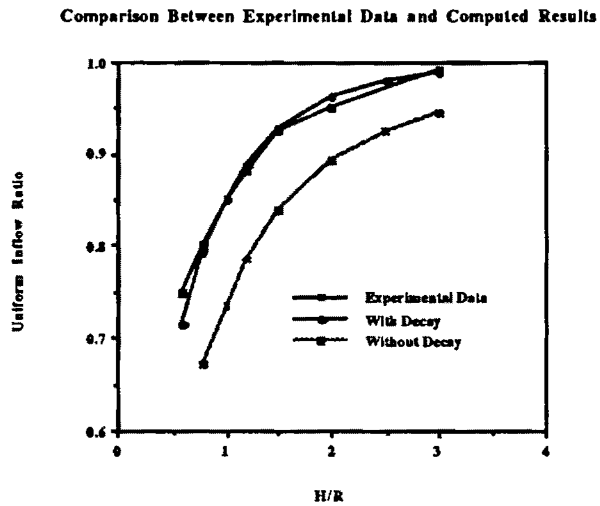

Figure 1. Effect of Height on Uniform Inflow

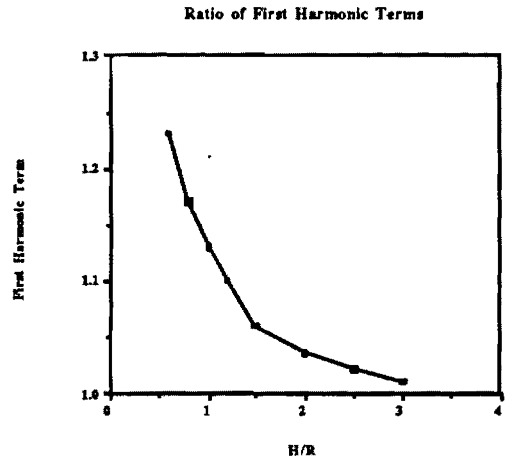

Figure 2 Effect of Height on First Harmonic Inflow

E-16-M07
30,31

GROUND EFFECT MODELS FOR ROTORCRAFT/SHIP DYNAMIC INTERFACE STUDY

J.V.R. Prasad
L.N. Sankar
School of Aerospace Engineering
Georgia Institute of Technology
Atlanta, GA 30332

Project Final Report
Contract #: N62269-90-C-0246

Submitted to:
Naval Air Warfare Center
Warminister, PA 18974-0591

April 1996

SUMMARY

A real time simulation model of ship ground effect for rotorcraft/ship dynamic interactions is developed by combining computational fluid dynamics (CFD) analysis and finite state representation of rotor inflow. For CFD analysis, the ship is modeled using a source panel representation and the rotor wake is modeled as rigid with prescribed geometry but unknown vorticity distribution. The sea surface is modeled by placing an image rotor wake and an image ship panel system below the sea surface. The CFD model is then combined with a batch version of a generic flight simulation program. From trim solutions using the simulation program, the ship ground effect on rotor inflow for cases of helicopter hovering with respect to ship deck at different points are identified and analyzed. With finite state representation of rotor inflow, a real time simulation model of ship ground effect is developed using in-ground effect inflow results from the CFD analysis.

INTRODUCTION

Modern helicopters must routinely operate from various naval ships under adverse weather conditions, including high winds, high seas, and low visibility. Under many combinations of such conditions, and for various ship orientations relative to the wind and waves, helicopter launch and recovery operations prove unsafe. Safe operating envelopes thus must be determined for each particular helicopter and ship combination. Current methodology to determine such envelopes involves extensive flight testing at sea. However, with an ever increasing number of rotorcraft and ship combinations, it has become prohibitive, both economically and operationally, to carry out testing at sea on the entire test matrix of U.S. Navy, Marine Corps, and Coast Guard rotorcraft aboard U.S. Navy and Coast Guard ships. It has been recognized for some time that an attractive alternative to full scale testing would be to perform the bulk of rotorcraft launch and recovery envelope expansion using real time piloted simulation.

An important ingredient of simulation models that can be used for rotorcraft/ship dynamic interface study is adequate representation of ground effect between the ship deck and the vehicle for simulation of shipboard landing and take off maneuvers. Current simulation models include empirically derived ground effect models which are basically quasi-steady in nature, i.e., the uniform part of the rotor downwash and the rotor thrust are modeled as functions of instantaneous vertical height from the ship deck. The ground effect model suitable for simulation of shipboard operations must include effects that result from rolling, pitching and heaving motions of the ship deck. Also, the ground effect model needs be computationally simple to be included in a real time rotorcraft flight simulation for man-in-the-loop simulation studies in order to determine handling qualities and pilot workload during shipboard operations. This report documents results from the research effort carried out in the School of Aerospace Engineering at the Georgia Institute of Technology on the development of a real time simulation model of ship ground effect.

MODEL DEVELOPMENT AND RESULTS

The general methodology used for developing a real time simulation model of ship ground effect is as follows. First, a comprehensive computational fluid dynamic (CFD) model that takes into account interactions between rotor wake and ship deck, super structure and sea surface is developed. The CFD model is then combined with a comprehensive non-real time helicopter simulation model. Rotor inflow distributions for cases of helicopter trimmed at different points with respect to ship deck with different values of ship speed are obtained. Then a harmonic analysis of inflow distribution for each of the cases is carried out. Using results from the harmonic analysis, the gain matrix of the dynamic inflow model is modified by matching the inflow distribution predicted by the dynamic inflow model with CFD results.

The general methodology was applied for the development of a real time ship ground effect simulation model of the SH-60 helicopter hovering over the deck of a FFG-7 class frigate. The models developed and the results obtained have been presented at various conferences and the same are included as Appendices.

Appendix 1: Mello, O.A.F., Prasad, J.V.R., Sankar, L.N. and Tseng, W., 'Analysis of Helicopter/Ship Aerodynamic Interactions," Paper presented at the 1994 AHS Aeromechanics Specialists Conference, San Francisco, January 1994.

This paper documents the CFD model development using a prescribed wake approach. Both the geometry and the vortex distribution in the rotor wake are prescribed. Results of inflow distributions and control positions required for trim are included.

Appendix 2: Zhang, H., Mello, O.A.F., Prasad, J.V.R., Sankar, L.N. and Funk, J.D., "A Simulation Model of Ship Ground Effect for Rotorcraft/Ship Interaction Study," Paper presented at the 1995 AHS Forum.

This paper modifies the CFD model by treating the vortex distribution as unknown and determined as part of the solution. Also, it documents the development of a real time ship ground effect simulation model using a finite state wake representation for the SH-60 helicopter hovering over the ship deck moving at a speed of 15 knots.

Appendix 3: Zhang, H., Prasad, J.V.R., Sankar, L.N., Mello, O.A.F. and Funk, J.D., "Ground Effect Simulation Model for Rotorcraft/Ship Interaction Study," Paper presented at the AIAA Flight Simulation Conference, August 1995.

This paper describes the general methodology used for the development of a real time ship ground effect simulation model and includes results for various values of ship speed. Also, it includes results on effects of wake parameters used in the CFD model (wake clearance and number of rotor revolutions of wake) on rotor power.

Appendix 4:

This appendix details the batch version of the ship ground effect simulation model computer code with details on mathematical model development.

CONCLUSIONS

The following conclusions can be made from the results of this study:

1. It is possible to develop a dynamic inflow model, which is applicable to in-ground effect flight conditions, by appropriately adjusting the parameters (of M and L matrices) of the dynamic inflow model.

2. The developed model is found to take into account of 'partial ground effect' as seen in the case of a rotor hovering over the edge of a ship deck.

FUTURE WORK

1. The present study addresses only steady state (trimmed flight) cases. Further work is needed for the unsteady case of heaving, pitching and rolling ship deck.

2. Validation of the model using experimental data is needed.

APPENDIX 1

ANALYSIS OF HELICOPTER / SHIP AERODYNAMIC INTERACTIONS

O. A. F. Mello*, Graduate Student
J. V. R. Prasad, Associate Professor
L. N. Sankar, Professor
School of Aerospace Engineering
Georgia Institute of Technology
Atlanta, Georgia

and

W. Tseng
Aerospace Engineer
Naval Air Warfare Center
Aircraft Division
Warminster, Pennsylvania

ABSTRACT

A method for analysis of the aerodynamic interactions between a helicopter and a ship is presented. The complex flow problem is decomposed into two: The first effect is the ship "ground effect", consisting of the changes in the helicopter-induced flowfield in the vicinity of the ship so that the airflow contours the ship surface. This effect is modeled by a panel representation of the ship surface, taking into account the downwash induced by the rotor and its wake. The second effect is the ship airwake effect, for which a recently developed model at Georgia Institute of Technology, derived from full-scale measurements, is used. This airwake model provides both mean and turbulent velocity components. Numerical results for a SH-60 helicopter trimmed at several locations near a FFG-7 class frigate are presented and these results indicate that both effects are quantitatively important and need to be considered in realistic simulations.

INTRODUCTION

Landing a helicopter on a ship deck can be a hazardous process. The determination of safe operating envelopes has been done at sea in a lengthy and expensive process[1]. The need to consider the many combinations of ships and helicopters aggravates the problem and suggests a demand for an appropriate helicopter/ship aerodynamic interaction model to be incorporated into rotorcraft simulation codes.

There are several aspects that contribute to the complexity of the problem, namely:

1. Sea and ship motions;
2. Atmospheric turbulence;
3. Ship aerodynamics;
4. Helicopter motion itself, in the presence of the ship.

The sea and ship motions can be modeled to a reasonable degree[2]. The only effect of the sea motion on the helicopter would be in the extent that it modifies the ground effect, but this change may be regarded as negligible with respect to the other factors involved. The ship motion will have a more significant effect on the ship/helicopter interference and has to be considered.

The ship aerodynamics is very complex. The flow around the superstructure is characterized by turbulence and vortex shedding. The turbulence level in the atmosphere also affects the flow. The knowledge about this type of flow is mostly empirical and based on building aerodynamics. During the past few years, there has been an increased activity in investigating the ship airwake through wind-tunnel[3–5] and full-scale[6–7] tests. A recent research effort by Prasad et al.[8] has used full-scale ship airwake measurements obtained by the Australian Aeronautical Research Laboratory[7] to construct a quantitative model of the ship airwake using system identification techniques.

In the present approach, the effects of ship aerodynamics on the helicopter are divided into the "ground effect" due to the proximity between the rotor and the ship surface, and the ship airwake effect. The ship "ground effect" is approximately modeled under the assumption of attached flow around the ship, which is subject to the velocity field induced by the rotor and its wake. For this purpose, a panel method representation of the ship surface is used, and the effect of the ship on the rotor is modeled by the induced velocity field produced by the ship's panels.

The ship airwake effect is included using the model developed by Prasad et al.[8], which gives both the mean and turbulent velocity components.

The simulation of helicopter motion near the ship can be carried out by a standard helicopter simulation code, if the effects discussed above are included. The simulation program used in the present work is a general helicopter flight simulation code[9], which uses a blade-element rotor model, suitable for the addition of induced velocity components due to the ship panel system and velocity components from the ship airwake model.

The remaining of this paper is organized as follows: First, a brief description of the mathematical formulation of the rotor wake and ship panel methods is given. Next, numerical results for a SH-60 helicopter trimmed at several

* On leave from Instituto de Aeronáutica e Espaço, Centro Técnico Aeroespacial, Brazil.

Presented at the American Helicopter Society Aeromechanics Specialists Conference, San Francisco, California, January 19–21, 1994.

locations near a FFG-7 class frigate are presented. The paper concludes with an assessment of the ship "ground" and airwake effects and directions for future work.

MATHEMATICAL FORMULATION

Rotor Wake Formulation

In order to compute the downwash on the ship surface due to the rotor, a rigid wake model is used. The rotor blade is modeled by a lifting line of bound vorticity, which is assumed to have a prescribed variation both radially and azimuth-wise. The wake has a prescribed geometry, which is basically a classical skewed helical wake, with a limited wake contraction model. The wake is divided into a "near" wake, composed of trailing and shed vortices and a "far" wake composed of trailing tip vortices only. The strength of the trailing and shed vortices are given by the radial and azimuth-wise variations of the bound vorticity, respectively, while the strength of the far wake tip vortex is assumed as equal to the maximum bound vorticity at the azimuth location where the vortex filament leaves the blade. The rotor wake is convected downstream with a velocity which is equal to the vector sum of the free stream velocity and the averaged (momentum theory value) induced velocity over the disk.

The blade bound vorticity distribution is assumed to be a known function of the non-dimensional radial location $\bar{r} = r/R$ and azimuth ψ. The radial variation is assumed to be of the form:

$$f(\bar{r}) = \bar{r}\sqrt{1-\bar{r}^2} \tag{1}$$

which is characteristic of a typical radial variation of circulation. The azimuth-wise variation is assumed to be such that no thrust offset is produced, by imposing the condition that the total blade moment be constant over the disk[10]. Under this assumption, the resulting azimuth-wise variation can be shown to be:

$$g(\psi) = \frac{1}{1+\frac{3}{2}\,k_T\,\mu\sin\psi} \tag{2}$$

where ψ is the azimuth, μ is the advance ratio and k_T is a constant which depends on the radial circulation distribution. It can be shown that for the radial variation assumed here, k_T has the value of $15\pi/16$ or approximately 0.982.

With the assumptions (1) and (2), the bound vorticity distribution along the blade and disk is of the form:

$$\Gamma_b(\bar{r},\psi) = \Gamma_0\,\bar{r}\sqrt{1-\bar{r}^2}\,\frac{1}{1+\frac{3}{2}\,k_T\,\mu\sin\psi} \tag{3}$$

The constant Γ_0 which appears in Eq. (3) may be related to the thrust coefficient C_T by applying the Kutta-Joukowski theorem for a section of the rotor blade and integrating over the rotor disk, which yields:

$$\tilde{\Gamma}_0 = \frac{\Gamma_0}{R(\Omega R)} = C_T\,\frac{\pi}{N_b}\,\frac{\sqrt{1-a^2}}{\frac{\pi}{16}+\frac{4}{9k_T}\left(\sqrt{1-a^2}-1\right)} \tag{4}$$

where $a = 1.5\,k_T\,\mu$ and N_b is the number of blades.

From Eq. (4), the trailing and shed vorticities in the near wake can be shown to be given respectively by:

$$\Gamma_t(\bar{r},\psi) = \frac{\partial\Gamma_b}{\partial\bar{r}} = \Gamma_0\,\frac{1-2\bar{r}^2}{\sqrt{1-\bar{r}^2}}\,\frac{1}{1+\frac{3}{2}\,k_T\,\mu\sin\psi} \tag{5}$$

and

$$\Gamma_s(\bar{r},\psi) = \frac{\partial\Gamma_b}{\partial\psi} = -\,\Gamma_0\,\bar{r}\sqrt{1-\bar{r}^2}\,\frac{\frac{3}{2}\,k_T\,\mu\cos\psi}{\left(1+\frac{3}{2}\,k_T\,\mu\sin\psi\right)^2} \tag{6}$$

while the far wake's single trailing tip vortex strength is given by

$$\Gamma_T(\psi) = \frac{1}{2}\,\Gamma_0\,\frac{1}{1+\frac{3}{2}\,k_T\,\mu\sin\psi} \tag{7}$$

Using the vorticity strengths given by Eqs. (3)–(7) and the assumed wake geometry, the velocities induced by the rotor and its wake on the ship surface are computed by applying the Biot-Savart law and integrating over the radial direction (bound vortices and near wake shed and trailing vortices) and over the wake[11]. The total induced velocities are then resolved for the component normal to the ship panel for input in the ship model.

A crude wake contraction model is applied, such that the near wake initially starts from the blade root cut-out location $\bar{r}_i$ and extends to the blade tip; after the wake shed and trailing vortices have traveled a specified helical angle denoted by ν_{ctr}, the wake is contracted such as to start from the hub (r=0) and extend to the radial location r_{tv}. Between ν=0° and $\nu=\nu_{ctr}$, a linear interpolation is used to determine the starting and end radial locations.

A Rankine vortex core model[12] with radius of one tenth of the blade chord is used. This model is applied by scaling the induced velocity due to the elementary vortex filament by the square of the ratio between the distance to the filament and the core radius, whenever the point where the induced velocity is being calculated lies within the vortex core.

Ship Formulation

The ship is modeled by a source panel method[13] common in aeronautical applications. The ship surface is approximately represented by plane source panels with constant distributed strength. The strengths of the sources are determined by enforcing the non-penetration condition at the centroid of each panel. A typical ship panel representation is shown in Fig. 1.

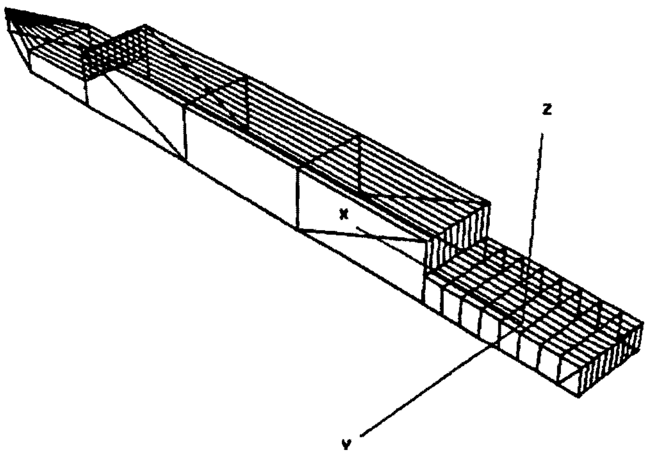

Fig. 1: Ship Panel Representation.

Since the ship airwake mean velocities are given by polynomial fitting of full-scale measurements, the ship's mean velocity is not considered for computation of the right-hand side of the system of equations, i.e., only the component of the downwash induced by the rotor normal to the ship panel and the normal component of the ship's oscillatory motion are taken into account in this implementation. This formulation results in a linear system of equations which is solved for the source strengths σ:

$$[A]\{\sigma\} = [B] \tag{8}$$

where [A] is the matrix of influence coefficients, $\{\sigma\}$ is the vector of unknown source strengths and [B] is the right-hand side which includes the normal component of the velocities on the ship surface due to ship oscillatory motion and due to the rotor and its wake. The system of equations (8) is solved by a standard LU decomposition for efficient backsubstitution at each time step. The resulting source panel strengths are then used to compute the velocities induced by the ship source panel system on the rotor disk.

Effect of Sea Surface

In order to model the ground effect due to the sea surface, the method of images is used. An image rotor wake and an image ship panel system are placed below the sea surface and the influence of these images is taken into account in the computation of the downwash induced by the rotor and in the computation of the coefficient matrix for the ship panel method.

RESULTS AND DISCUSSION

The above described helicopter/ship interaction method has been applied to a SH-60 Sea Hawk helicopter flying at 15 kts (7.72 m/s) and at a height of one rotor radius (26.83 ft or 8.18 m) above the landing deck of a FFG-7 class frigate. The helicopter was positioned above the center of the deck, above the edge of the deck and at the same height just outside the deck. These positions are illustrated in Fig. 2. The ship was moving forward at the same speed as the helicopter. These positions were chosen as representatives of configurations experienced during the final approach for landing[14]. The helicopter was trimmed at each of the above positions. Note that for trim only the mean component of the ship airwake is used, i.e., the results presented herein do not include the turbulent component.

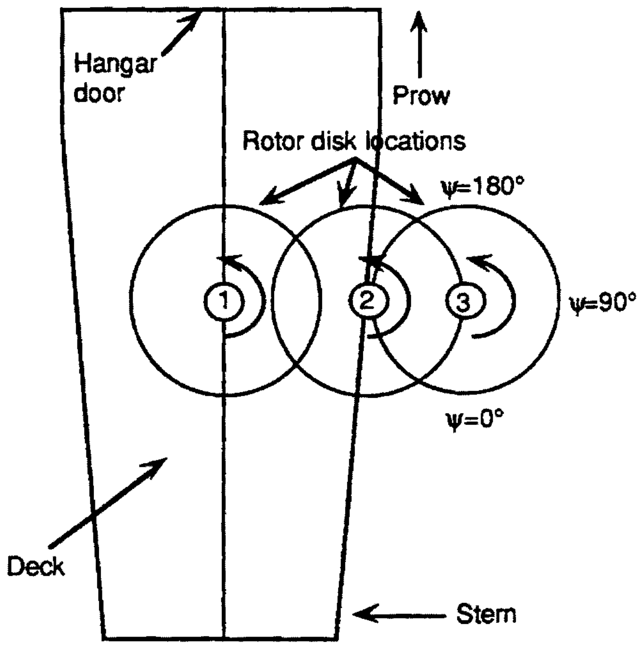

Fig. 2: Positioning of helicopter near ship (top view): Above center of deck (1), above edge of deck (2), and just outside deck (3).

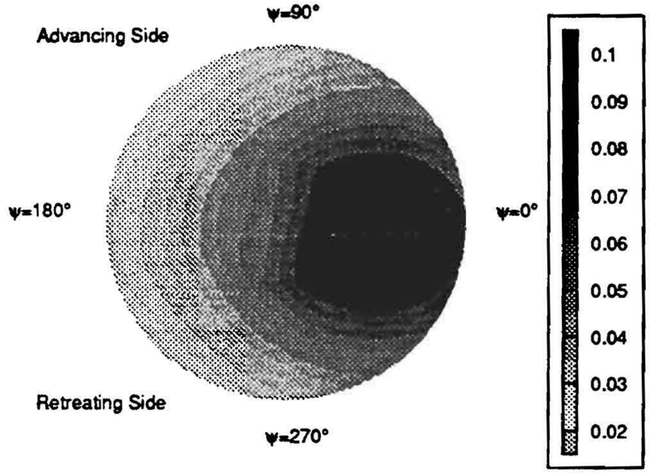

Fig. 3: Normalized upwash induced by ship panel system, helicopter above center of deck.

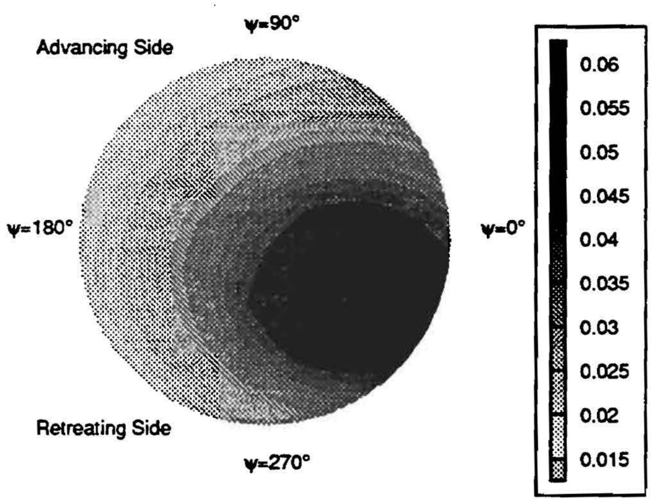

Fig. 4: Normalized upwash induced by ship panel system, helicopter above edge of deck.

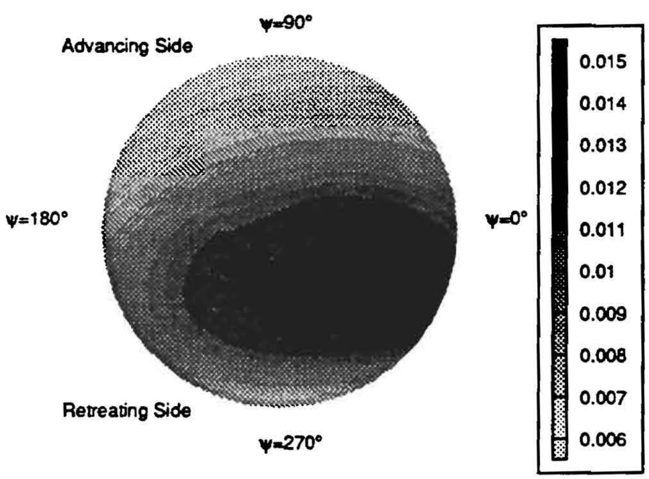

Fig. 5: Normalized upwash induced by ship panel system, helicopter outside deck.

Numerical results for the upwash induced by the ship panel system over the rotor disk, normalized by the mean induced inflow, are presented in Figs. 3–5 for each of the above described helicopter locations. It can be observed that the upwash is generally higher in the aft portion of the disk. This observation can be attributed to the rotor wake being washed aft and consequently the rear portion of the ship deck being more affected by the wake and thus resulting in higher upwash values near that region.

It can also be observed that the upwash is higher in the retreating side of the disk, when the helicopter is moved towards the edge of the deck. This is expected because this part of the rotor disk is closer to the ship deck for this configuration.

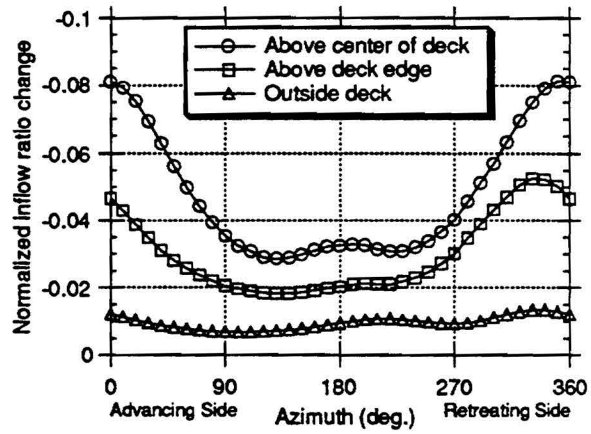

Fig. 6: Effect of helicopter position on ship "ground effect".

The ship "ground effect" can be further visualized in Fig. 6, where the inflow ratio due to the ship panel system, normalized by the mean induced inflow ratio, is presented for each of the above described positions at the radial station 80% and at azimuth locations corresponding to one rotor revolution. For the rotor located just outside the deck, the "ground effect" upwash is mostly uniform and about 1% of the mean induced inflow. As the helicopter moves inward with respect to the deck, the ground effect increases, as expected. It is also clear that the highest values of ship ground effect upwash occur around the aft portion of the disk, as mentioned before.

In current simulation codes[9], it is common to adopt a simple correction factor, based on the height above the ground, to account for the ground effect. While this may be acceptable in other situations, the helicopter-above-ship configuration poses the need for a more accurate local correction. This can be observed in Fig. 7, where the inflow ratio due to the ship panel system, divided by the local inflow ratio, is presented for each of the above described positions at the radial station 80%. It is clear that using a constant inflow correction factor cannot account for the significant variations involved.

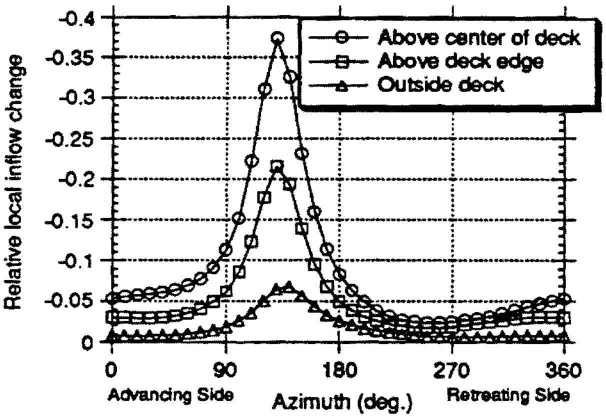

Fig. 7: Local inflow change due to ship "ground effect".

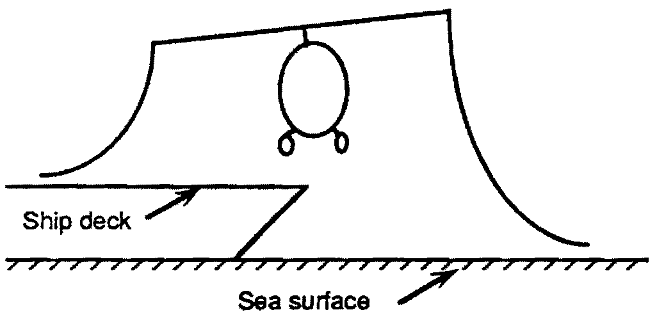

Fig. 8: "Partial" Ground Effect

The above discussed results indicate that the distribution of ship ground effect over the disk is very sensitive to the rotor disk location with respect to the deck when the helicopter moves inward for landing, while the magnitude of this effect depends directly on how much of the ship is "washed" by the rotor wake. These phenomena constitute what may be termed as "partial" ground effect, which is shown schematically in Fig. 8. It is clear that this effect should be adequately included in simulations in order to provide increased fidelity. The present method is a tool that can be used to represent this effect. However, during the course of this work it was observed that the computational times required for the current method (about 0.6 CPU sec per iteration in an HP Apollo 700 workstation) are not compatible with a real-time simulation. For example, the time step used in the present calculations was about 0.013 sec. This observation suggests a need for the development of an approximate method that can account for the above described "partial" ground effect. The present method can then be used for parametric studies which will lead to the definition of the important parameters to be included in the approximate real-time simulation method.

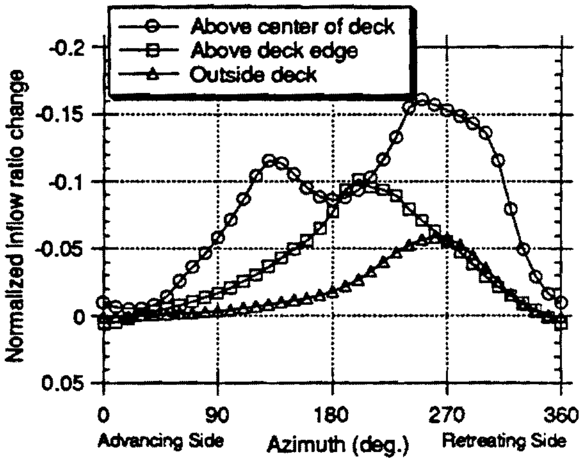

Fig. 9: Effect of helicopter position on normal velocities due to the ship airwake.

In order to compare quantitatively the ship "ground effect" with the ship airwake effect, the contribution of the mean ship airwake to the total inflow ratio, normalized by the mean induced inflow ratio, is presented in Fig. 9 for each of the above described positions at the radial station 80%. It can be observed that the ship airwake contribution is of the same order as the ship ground effect. It should be pointed out that the ship airwake semi-empirical model used here is strictly valid only within the spatial range of coordinates where the velocities were measured during the full-scale tests. Their extrapolation using the same polynomials outside the range is not valid. In order to estimate the effect of the ship airwake outside the valid range and therefore allow a comparison with the ship ground effect, an exponential decay was assumed.

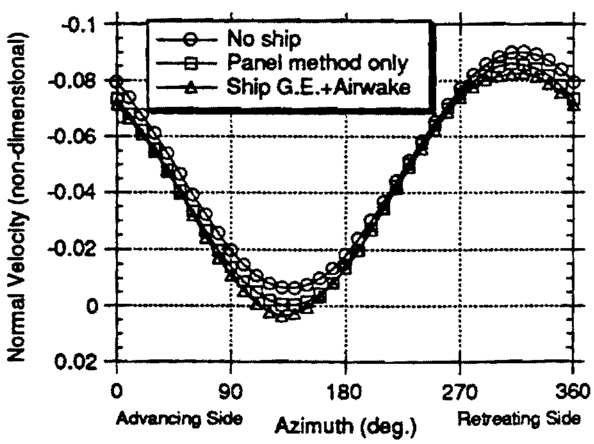

Fig. 10: Total normal blade velocities at r/R=0.8, helicopter above center of deck.

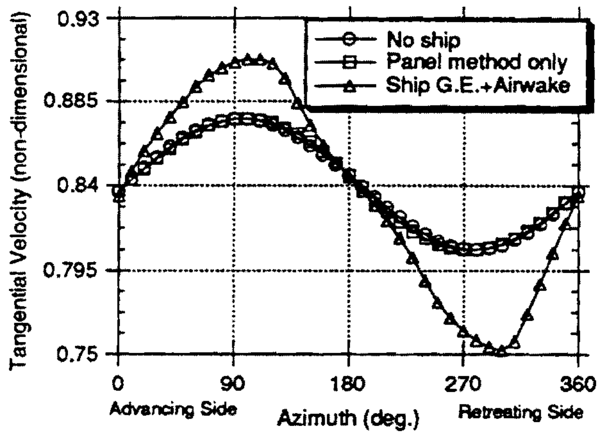

Fig. 11: Total tangential blade velocities at r/R=0.8, helicopter above center of deck.

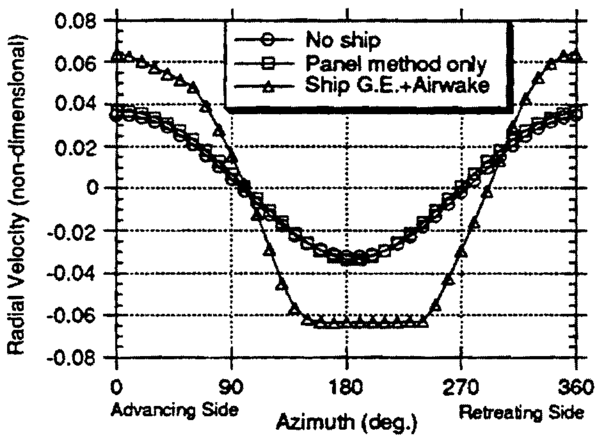

Fig. 12: Total radial blade velocities at r/R=0.8, helicopter above center of deck.

The effects of the ship airwake can be further illustrated by Figs. 10–12, where the total blade normal, tangential and radial velocities, respectively, are presented. The velocities were computed without the ship present, with the ship influence computed using a panel method only, i.e., including the ship free-stream velocity in the computation of the ship sources/sinks, and with the ship airwake in addition to the ship ground effect. While the previously discussed influence of ship ground effect and normal component of airwake is again clear in Fig. 10, the most dramatic effect appears in the tangential and radial components. In general, the ship airwake contributes with an overall increase in forward velocity, although its actual quantitative effect is somewhat localized, which is characteristic of the airwake.

It is clear from Figs. 11–12 that the ship airwake cannot be even crudely approximated by a panel method. Therefore, a ship airwake database is needed in order to provide a realistic simulation.

Table 1: Trimmed Control Positions (inches)

Config	Lat.Cyc.	Long.Cyc.	Collective	Pedal
1	4.595	4.466	5.137	2.008
2	4.595	4.469	5.135	2.010
3	4.563	4.196	4.946	2.084
4	4.622	4.301	5.083	2.072
5	4.599	4.414	5.138	2.037

The overall effect of the modified blade velocities is reflected in the trimmed control positions, as shown in Table 1, where the control positions are shown for five conditions: (1) no ship, no ground effect; (2) no ship, ground effect computed using simple inflow correction[9]; (3) helicopter above center of ship deck; (4) helicopter above edge of ship deck; and (5) helicopter just outside deck. The conventions for these control positions are as follows: full left lateral cyclic corresponds to zero, full right corresponds to 10 in; full forward longitudinal cyclic corresponds to zero, full aft to 10 in; full low collective pitch corresponds to zero, full high to 10 in; full left pedal corresponds to zero, full right to 5.38 in. The increased tangential velocity due to the ship airwake is felt as an addition to the forward velocity, resulting in additional forward longitudinal cyclic as the helicopter moves inward. The lateral cyclic and pedal are also adjusted. The combination of ship ground effect and normal airwake velocity results in decreased collective pitch, which is also more significant when the helicopter moves toward the center of the deck.

CONCLUDING REMARKS

A method for analysis of the aerodynamic interactions between a helicopter and a ship has been presented. This method divides the interaction problem into two effects: the ship "ground effect", modeled by a panel representation of the ship surface, which results in an upwash on the rotor disk, and the ship airwake effect, for which an existing semi-empirical model, derived from full-scale measurements, is used.

Numerical results for a SH-60 helicopter trimmed at three locations near a FFG-7 class frigate have indicated that the ship "ground effect" increases significantly as the helicopter moves toward the center of the ship deck, while its distribution over the disk is sensible to the helicopter location, with higher upwash in the rear portion of the disk and in the side near the ship. It is clear that this effect should be included in simulations in order to provide increased fidelity. The present method, however, is computationally intensive and thus inappropriate for real-time simulation. It can be used as a tool for building a modified dynamic inflow method which takes into account the ship ground effect.

The ship airwake effect has been shown to be quantitatively more important than the ship ground effect and somewhat localized. It cannot be even crudely approximated by a simple panel method and requires the availability of a ship airwake database in order to provide a realistic simulation.

Overall, the present work provided an insight into the relevant helicopter/ship aerodynamic interaction phenomena, and suggests additional parametric investigations, including simulation of approach flights where ship airwake turbulent components of velocity are included.

ACKNOWLEDGMENT

This work was partially supported by the Naval Air Warfare Center. The technical monitor was Dr. Wei Tseng. The first author was supported by the Conselho Nacional de Desenvolvimento Científico e Tecnológico (CNPq) and the Fundação de Amparo à Pesquisa do Estado de São Paulo (FAPESP), Brazil. The authors would like to thank Mr. Hong Zhang for his assistance with the implementation of the ship airwake model.

REFERENCES

1. Ferrier, B., and Semenza, J., "NATC Manned Flight Simulator VTOL Ship Motion Simulation and Application," 46th Annual Forum of the American Helicopter Society, Washington, DC, 1990.

2. Healey, J. Val., "The Prospects for Simulating the Helicopter/Ship Interface," *Naval Engineers Journal*, March 1987, pp. 45-63.

3. Hurst, D. W., and Newman, S. J., "Wind Tunnel Measurements of Ship Induced Turbulence and the Prediction of Helicopter Rotor Blade Response," *Vertica*, Vol. 12, No. 3, 1988, pp. 267-278.

4. Healey, J. Val., "Establishing a Database for Flight in the Wakes of Structures," *Journal of Aircraft*, Vol. 29, no. 4, July-August 1992, pp. 559-564.

5. Rhoades, M. M., and Healey, J. Val., "Flight Deck Aerodynamics of a Nonaviation Ship," *Journal of Aircraft*, Vol. 29, no. 4, July-August 1992, pp. 619-626.

6. Carico, D., Reddy, B., and Dimarzio, C., "Ship Airwake Measurements and Modeling Options for Rotorcraft Applications," In: Aircraft Ship Operations, AGARD CP-509, November 1991.

7. Arney, A. M., Blackwell, J., Erm, L. P., and Gilbert, N. E., "A Review of Australian Activity on Modelling the Helicopter/Ship Dynamic Interface," In: Aircraft Ship Operations, AGARD CP-509, November 1991.

8. Prasad, J. V. R., Mavris, D. N., and Schrage, D. P., "Ship Airwake Modeling and Simulation, Phase I — Methodology Development," Research Report submitted to Naval Air Warfare Center, School of Aerospace Engineering, Georgia Institute of Technology, Atlanta, August 1992.

9. Howlett, J. J., "UH-60A Black Hawk Engineering Simulation Program: Volume I — Mathematical Model," NASA CR-166309, 1981.

10. Stepniewski, W. Z. and Keys, C. N., *Rotary-Wing Aerodynamics*, Dover, 1984.

11. Mello, O. A. F., "Numerical Simulation of Helicopter / Ship Airwake Interactions," Research Report submitted to Naval Air Warfare Center, School of Aerospace Engineering, Georgia Institute of Technology, Atlanta, July 1993.

12. U.S. Department of the Army — Aeroflightdynamics Directorate, "2GCHAS Theory Manual," (Second Generation Comprehensive Helicopter Analysis System, Version 2.1), Vol. II, Chapter 5 – Airloads and Induced Velocity, Ames Research Center, Moffett Field, CA, July 1992.

13. Hess, J. L., and Smith, A. M. O., "Calculation of Potential Flow about Arbitrary Bodies," *Progress in Aeronautical Sciences*, Vol. 8. Edited by D. Küchemann. Pergamon Press, Oxford, England, 1967.

14. Westra, D. P., Sheppard, D. J., Jones, S. A., and Hettinger, L. J., "Simulator Design Features for Helicopter Shipboard Landing: II. Performance Experiments," Naval Training Systems Center, Orlando, FL, Report No. NTSC TR-87-041, July 1987.

APPENDIX 2

A SIMULATION MODEL OF SHIP GROUND EFFECT FOR ROTORCRAFT / SHIP INTERACTION STUDY

Hong Zhang* O.A.F.Mello* J.V.R.Prasad‡ L.N.Sankar † and John D. Funk,Jr.§

School of Aerospace Engineering
Georgia Institute of Technology
Atlanta, GA

Aero Analysis Division
Naval Air Warfare Center Aircraft Division
Warminster, PA

Abstract

A simple ground effect model for rotorcraft / ship dynamic interactions, which is suitable for implementation in flight simulators for real-time simulation purposes, has been extracted from the analysis of the aerodynamic interaction results obtained from a computationally intensive method that incorporates a rigid rotor wake and a panel representation of the ship with corresponding image systems. It is found that the ground effect is very sensitive to the helicopter position with respect to the ship deck, as well as the height above the deck. The inflow gain matrix in dynamic inflow model is modified as a function of the position (x,y,z) relative to the deck. Numerical results for a SH-60 helicopter flying above the deck of a moving FFG-7 class frigate at the same speed as the ship are presented and discussed in this paper. Results show that the ground effect model works well all over the deck. The ground effect model integrated with the airwake model which has already been developed at Georgia Tech provides the basis for the real-time simulation study for rotorcraft/ship interactions.

1. Introduction

Modern helicopters must routinely operate under various adverse weather conditions. Helicopter landing on a moving ship deck behind the superstructure is hazardous[10], and yet up to today, little knowledge about the flow characteristics is available due to the time dependent uncertainty nature of the flow, as well as the complicated and sensitive flow field over the deck behind the superstructure. Because the lack of a suitable ship airwake model and the still unsolved rotorcraft / ship dynamic interaction problem, any realistic simulation of helicopter take-off and landing on a ship deck is still impractical. Also, in real time implementation, these models have to be computationally simple. A series of studies of these effects and models have been carried on at Georgia Tech [1,2] for the past few years, and a suitable ship airwake model and a systematic simulation method have already been developed. Moreover, a method to analyze helicopter/ship aerodynamic interactions has been formulated recently by Georgia Tech researchers[3]. It is found that the widely used traditional ground effect model, which basically introduces a factor to modify the uniform inflow of the helicopter rotor[8,9], is not accurate for a helicopter operating under a ship "ground effect".

A computationally intensive method, which combines a rigid rotor wake model and the well developed traditional potential flow theory, is formulated in Ref.(3) and the method is used here to generate the data base for the ground effect model identification. Our purpose in this paper, however, is to identify a simple ground effect model suitable for real-time simulation implementation.

2. Computational Fluid Dynamics (CFD) Model Used for Generating the Data Base

The ship "ground effect" is manifested by the changes of the flow field, so that the flow at the ship surface follows the motion of the ship surface. This effect is modeled by a panel representation of the ship surface, and the strength of the panel is determined by satisfying the boundary condition at the ship surface, i.e. there is no penetration of flow through the solid ship surface and/or ship deck. The velocity induced by the rotor wake on the ship surface is computed by using a rigid wake theory. The simulation of helicopter motion near the ship is carried out by the general helicopter simulation code GENHEL[8], which has been modified to incorporate a first-order dynamic inflow model[11]. By taking into account the induced velocity or upwash at the rotor disk due to the ship panel system into the blade-element analysis, the ground effect is coupled into the simulation code. Through changing the collective pitch and cyclic pitch, the helicopter is retrimmed at the same location with the consideration of the ground effect. The total inflow at the rotor disk is outputted as the rotor blade rotates azimuthally, and this forms the data base for later analysis.

3. Dynamic Inflow Model

A generalized dynamic inflow theory exists in the literature in which air mass passing through the rotor is treated as a dynamic system. The dynamic inflow theory [4,5,6,7] has found wide applications in flight dynamics and aeroelastic studies. Peter's dynamic inflow model [6] is used in this investigation for simplicity, i.e. the induced inflow is assumed to have the following variations:

---

* Graduate Research Assistant
‡Associate Professor
† Professor
§ Aerospace Engineer

1995 AHS FORUM PAPER

$$\lambda(\bar{r},\bar{\psi}) = \lambda_0 + \lambda_s \frac{r}{R}\sin\psi + \lambda_c \frac{r}{R}\cos\psi \qquad (1)$$

where:

$\lambda_0, \lambda_s, \lambda_c$ are the uniform, lateral and longitudinal variations of the rotor inflow in tip path plane (tpp), respectively.

The dynamic inflow model is:

$$[M]\{\dot{\bar{\lambda}}\} + [\hat{L}]^{-1}\{\bar{\lambda}\} = \{\bar{C}\}_{aero} \qquad (2)$$

where

$$\lambda = (\lambda_0, \lambda_s, \lambda_c)^T$$
$$C = (CT, -C1, -C2)^T$$

$[M], [\hat{L}]$ are the apparent mass matrix and the inflow gain matrix and their explicit expressions for out-of-ground effect case can be found in Ref. [4]. CT is the thrust coefficient. C1,C2 are instantaneous aerodynamic rolling and pitching moment coefficients expressed in the tip path plane. Obviously, they are time dependent for unsteady flight.

The subscript "aero" denotes that only the aerodynamic contribution is considered and the inertial part is not included. The "•" denotes time derivative.

Due to the proximity of the rotor disk to the ship deck, the rotorcraft/ship interactions induce upwash at the rotor disk, thereby changing the total inflow and the inflow distribution over the whole rotor disk. Hence, it is not surprising that $[M]$ and $[\hat{L}]$ matrices are going to change due to the ground effect. Thus, the dynamic inflow model near the ground can be written as:

$$[M]_{ige}\{\dot{\bar{\lambda}}\}_{ige} + [\hat{L}]^{-1}_{ige}\{\bar{\lambda}\}_{ige} = \{\{\bar{C}\}_{aero}\}_{ige} \qquad (3)$$

where : $[M]_{ige}$, $[L]_{ige}$ are the apparent mass and the inflow gain matrices with ground effect.

Suppose

$$\left\{\bar{\lambda}\right\}_{ige} = \begin{bmatrix} \alpha_1 & 0 & 0 \\ 0 & \beta_1 & 0 \\ 0 & 0 & \gamma_1 \end{bmatrix} \left\{\bar{\lambda}\right\}_{oge} \qquad (4)$$

and

$$\left\{\bar{C}\right\}_{ige} = \begin{bmatrix} \alpha_2 & 0 & 0 \\ 0 & \beta_2 & 0 \\ 0 & 0 & \gamma_2 \end{bmatrix} \left\{\bar{C}\right\}_{oge} \qquad (5)$$

where:

$\alpha_i, \beta_i, \gamma_i$ $(i = 1,2)$ are the correction factors to account for ground effect to the inflow and the forcing functions, which are functions of the helicopter position (x,y,z) relative to the deck.

Thus, for the steady case, i.e., trimmed flight condition,

$$\left[\hat{L}\right]_{ige} = \begin{bmatrix} \alpha_1/\alpha_2 & \alpha_1/\beta_2 & \alpha_1/\gamma_2 \\ \beta_1/\alpha_2 & \beta_1/\beta_2 & \beta_1/\gamma_2 \\ \gamma_1/\alpha_2 & \gamma_1/\beta_2 & \gamma_1/\gamma_2 \end{bmatrix} \left[\hat{L}\right]_{oge} \qquad (6)$$

All six factors $\{\alpha_1, \beta_1, \gamma_1, \alpha_2, \beta_2, \gamma_2\}$ can be obtained by conventional identification methods.

For trimmed flight (steady case), we have:

$$\{\bar{\lambda}\} = [\hat{L}]\{\bar{C}\}_{aero} \qquad (7)$$

Thus, for trimmed hovering with respect to the deck of the moving ship, since the forcing functions (CT,C1,C2) are approximately the same for out-of-ground case and in-ground case, Eq. (6) reduces to:

$$\left\{\hat{L}\right\}_{ige} = \begin{bmatrix} \alpha_1 & 0 & 0 \\ 0 & \beta_1 & 0 \\ 0 & 0 & \gamma_1 \end{bmatrix} \left\{\hat{L}\right\}_{oge} \qquad (8)$$

4. Identification Approach

For illustration purpose, the SH-60 Seahawk helicopter flying at 15kts above the deck of a FFG-7 class frigate, which is moving at the same velocity as the helicopter, is used in this investigation. To capture the ground effect, the rotorcraft/ship interactions are computed using the CFD code at all the grid points over the ship deck as shown in Figure 1(a) at eight heights ranging from 0.5R to 3R for each grid point (Figure 1(b))

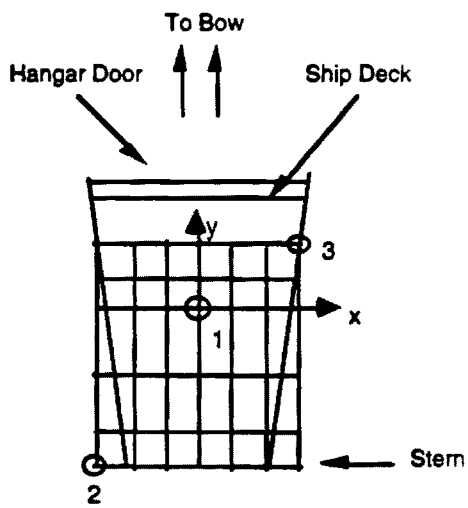

Figure 1(a): Positioning of helicopter above ship deck (top view)

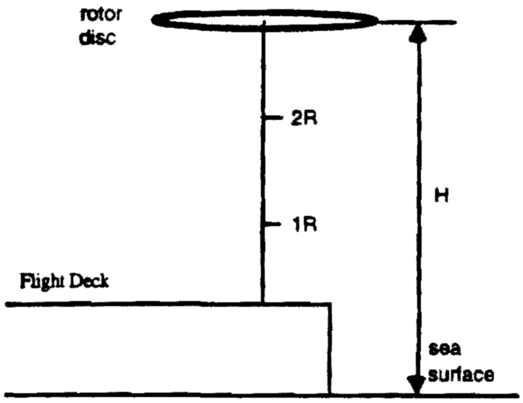

Figure 1(b): Helicopter Relative Position

It is recognized that the ground effect and the ship airwake effect are actually coupled when the helicopter is flying near the deck. However, only the ground effect part is considered in this study.

Figures 2(a) and 2(b) show how the nondimensional upwash at 80% radial station changes in one revolution above the center of the deck (location 1 in Figure 1(a)) and at the lower left corner of the deck (location 2 in Figure 1(a)) for different values of height above the deck.

It can be seen from Figure 2(a) that the upwash is almost constant at the fore part of the rotor for a given height (azimuth angle between 90 and 270 degrees), whereas at the rear part of the rotor (azimuth angle form 0 to 90, and 270 to 360 degrees), the upwash changes significantly. Also, we see that the effect of the height on upwash is different at different azimuth angles, hence it is not accurate to model this effect by using a simple constant factor. Because of the presence of the hanger, the rotor wake hits the deck differently at different locations.

For the case of the rotor hovering above the lower left corner of the deck, the upwash is much higher at advancing side and much lower at retreating side (see Fig. 2(b)). In order to incorporate the upwash in the dynamic inflow model, harmonic analysis of the upwash is carried out in order to extract the uniform and lateral and longitudinal variations due to the contribution of the upwash from the ground effect. It is seen from this analysis that terms up to second harmonic are required in order to account for the effect of ship deck on the rotor inflow variation.

$$\Delta w = -\Delta\lambda_0 - \Delta\lambda_s \frac{r}{R}\sin\psi - \Delta\lambda_c \frac{r}{R}\cos\psi - \Delta\lambda_{2s}\frac{r}{R}\sin(2\psi) - \Delta\lambda_{2c}\frac{r}{R}\cos(2\psi) \quad (9)$$

where

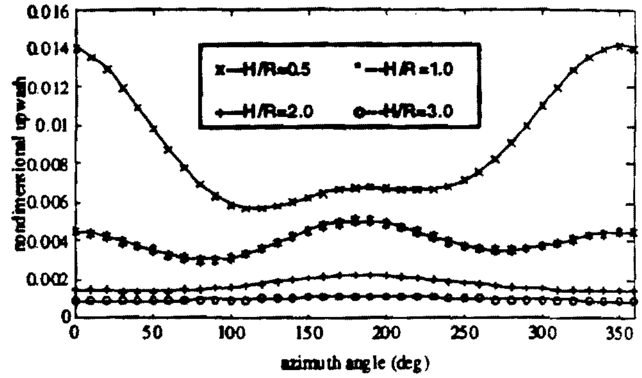

Figure 2(a): Effect of height on upwash at rotor disk at the center of the deck

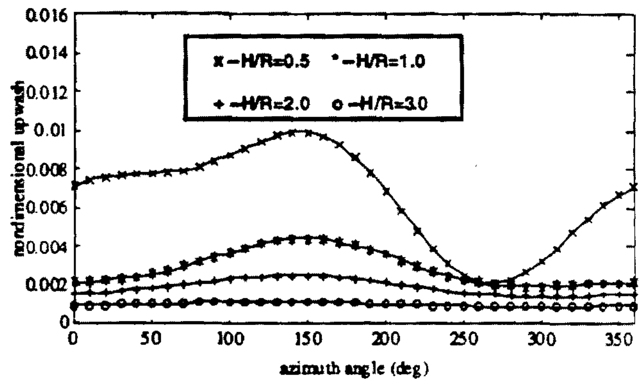

Figure 2(b): Effect of height on upwash at the rotor at the lower left corner of the deck

$\Delta\lambda_0$ is the upwash contribution to the uniform inflow

$\Delta\lambda_s$ is the lateral inflow changes due to the ground effect

$\Delta\lambda_c$ is the longitudinal inflow variation because of the ground presence

$\Delta\lambda_{2s}$ is the 2nd lateral inflow change

$\Delta\lambda_{2c}$ is the 2nd longitudinal inflow change

The analysis is carried out for different heights from 0.5 R to 3 R above the deck.

Figure 3 gives the effect of the height on the uniform inflow changes for location 1 (center of the deck, "*" in Fig.3--5) and for location 2 (left corner at the stern, "o" in Fig.3--5). The magnitude of total uniform inflow increases as the height increases. This is quite reasonable, because the ground cushion effect gets less and less as the rotor moves away from the deck, hence the upwash gets less and less. We see that at the deck center, the uniform inflow undergoes a maximum of 14% change due to "ground" effect.

Figures 4(a) and 4(b) give the effect of height on the first harmonic lateral inflow λ_s and first harmonic longitudinal inflow component λ_c

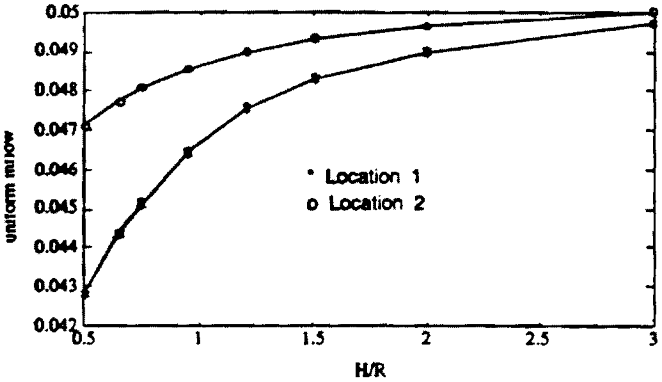

Figure 3: Effect of height on uniform inflow

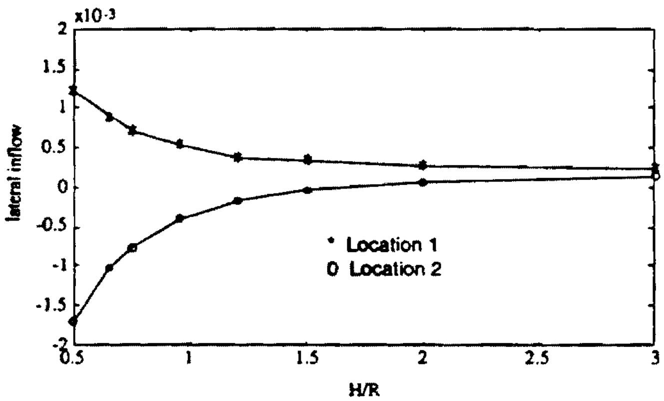

Figure 4(a) : Effect of height on lateral inflow
(First harmonic term)

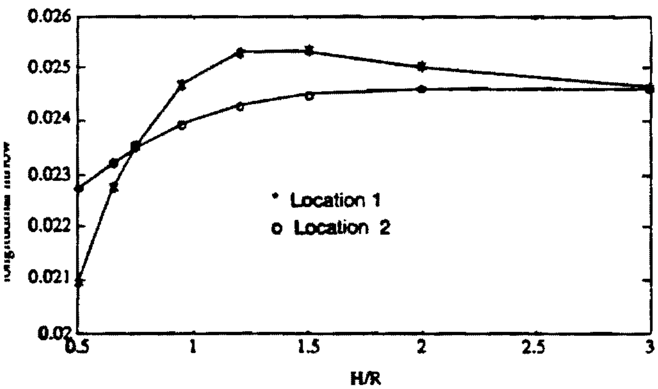

Figure 4(b): Effect of height on longitudinal inflow
(First harmonic term)

It is seen from Fig 4 that the longitudinal inflow change is not a linear function of height.
Figures 5(a) and 5(b) are the effect of height on the 2nd inflow terms λ_{2s} , λ_{2c}. Still, the ground effect gets less important as the distance between the helicopter and the deck gets larger. Also, the lateral component in the upwash is smaller than the longitudinal component.
From Figs 3,4 and 5, it can be seen that the ground effect is not a linear function of the height, and it is sensitive to the location of the rotor hub over the deck.

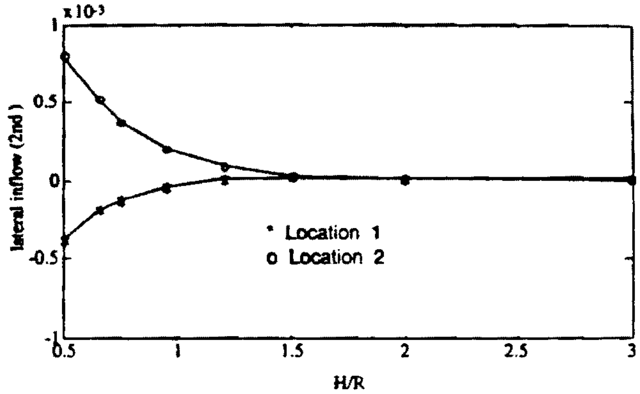

Figure 5(a): Effect of height on lateral inflow
(2nd harmonic term)

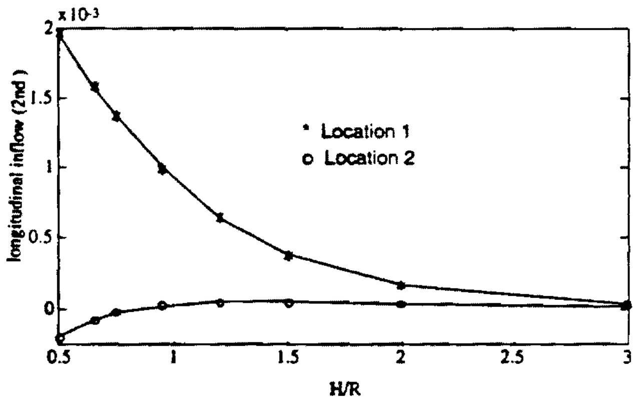

Figure 5(b): Effect of height on longitudinal inflow
(2nd harmonic term)

Several models are tried to represent these changes. By comparison of the **Pearson** correlation coefficient, the following model is seen to capture the variation with height:

$$\{\lambda_i\} = \{\lambda_i\}_{ref}\ [a + \frac{b}{h} + \frac{c}{h^2} + \frac{d}{h^3}] \tag{10}$$

where :
a,b,c,d are constants for a given location w.r.t. the deck, h is the nondimensional (w.r.t. rotor radius R) height, and λ_{ref} is the corresponding value of the component out of ground effect.

Thus from (5) and (10),

$$\begin{Bmatrix} \alpha_1 \\ \beta_1 \\ \gamma_1 \end{Bmatrix} \Rightarrow a+\frac{b}{h}+\frac{c}{h^2}+\frac{d}{h^3} \qquad (11)$$

Cheeseman and Bennett [(9)] derived an expression for the upwash at the rotor disk due to the ground:

$$\Delta w=\frac{\lambda_{0ref}}{16h^2} \qquad (12)$$

i.e.

$$\lambda_0=(1.-\frac{1}{16h^2})\lambda_{0ref} \qquad (13)$$

Figure 6 shows the comparison of the uniform inflow predicted by the simple model Eq.(13) and the fitted model of Eq. (10) at several locations.

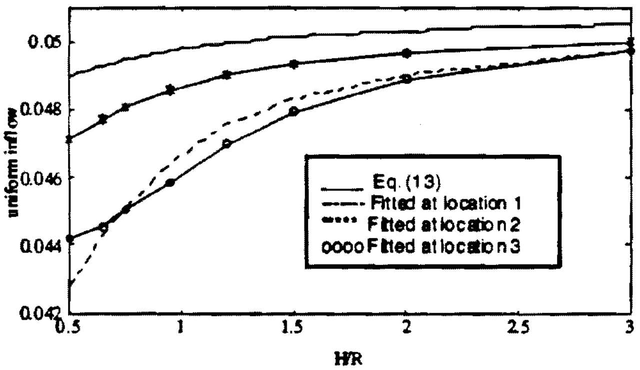

We see that the Cheeseman model is not accurate enough to capture the ship ground effect. First the ground effect is location dependent, and second it does not follow the h^{-2} law . Hence the ship ground effect model has to incorporate a function of location x and y, as well as the height.

5. Spline Fit

Having taken care of the effect of the height, we now move to the modeling of the location effect. Based on the data base, it is found that we can not use a simple function for f(x,y) to fit these data. Because spline fit has advantages of passing through every grid point, and yet it preserves the nice continuous property (up to 2nd derivatives), we use a two dimensional spline-fit to model the ground effect, i.e. a,b,c,d will be spline functions of x and y.

Suppose we have a set of data on the grid of X and Y as:

$X=\{X_i\}$, $i=1,2,.....m+kx$
$Y=\{Y_j\}$, $j=1,2,.....\ n+ky$
$F=\{\ f(x_i,y_j)\}$

where: kx is the order of the spline in x direction, ky is the order of the spline in y direction. For cubic spline, the order is 4. For quadratic spline, the order is 3.

Let:

$$qx=m+kx$$
$$qy=n+ky$$

$N_{kx,i}(X,x)$ denotes the normalized B-spline of order kx in x direction with support $[X_{i-kx},X_i]$

$N_{ky,j}(Y,y)$ denotes the normalized B-spline of order ky in y direction with support $[Y_{j-ky},Y_j]$

Then any bivariate spline S(x,y) of order kx in x, and ky in y, has the following representation:

$$S(x,y)=\sum_{i=1}^{qx}\sum_{j=1}^{qy}C_{i,j}N_{kx,i}(X,x)N_{ky,j}(Y,y) \qquad (14)$$

With the help of ***Mathematica*** [(12)], the coefficients C_{ij} are obtained for cubic spline fit. That is kx=ky=4.

Finally the total inflow with ground effect is modeled as:

$$\lambda=\lambda_0+\frac{r}{R}(\lambda_s\sin(\psi)+\lambda_c\cos(\psi)+ \\ \lambda_{2s}\sin(2\psi)+\lambda_{2c}\cos(2\psi)) \qquad (15)$$

and

$$\{\lambda_i\}=\{\lambda_i\}_{ref}[a(x,y)+\frac{b(x,y)}{h}+\frac{c(x,y)}{h^2}+\frac{d(x,y)}{h^3}] \qquad (16)$$

where i may be 0,s,c,2s,2c.

For illustration purpose, the following is the spline fitted result for the uniform inflow:

$$\begin{aligned}\lambda_0=&0.994 - 0.0448x - 0.2993x^2 - 0.1752x^3 - 0.0355xy \\ &+ 0.036x^2y + 0.040x^3y + 0.027xy^2 + 0.236x^2y^2 \\ &+ 0.14x^3y^2 + 0.0177y^3 + 0.069xy^3 - 0.066x^2y^3 \\ &- 0.074x^3y^3 \\ &+ (0.011 + 0.486x + 2.334x^2 + 1.3x^3 + 0.026y \\ &+ 0.269xy - 0.298x^2y - 0.325x^3y - 0.0625y^2 \\ &- 0.2656xy^2 - 1.8x^2y^2 - 1.05x^3y^2 - 0.1358y^3 \\ &- 0.53xy^3 + 0.55x^2y^3 + 0.594x^3y^3)/h \\ &+ (-0.2255 - 1.55x - 5.587x^2 - 3.02x^3 - 0.0389y \\ &- 0.6457xy + 0.7674x^2y + 0.815x^3y + 0.077y^2 \\ &+ 0.76xy^2 + 4.25x^2y^2 + 2.42x^3y^2 + 0.327y^3 \\ &+ 1.28xy^3 - 1.437x^2y^3 - 1.5x^3y^3)/h^2 \\ &+(-0.05999 + 1.21x + 3.9x^2 + 2.05x^3 + 0.01557y \\ &+ 0.4987xy - 0.61x^2y - 0.639x^3y + 0.183y^2 \\ &- 0.534xy^2 - 3.x^2y^2 - 1.685x^3y^2 - 0.2448y^3 \\ &- 0.9727xy^3 + 1.157x^2y^3 + 1.17886x^3y^3)/h^3\end{aligned} \qquad (17)$$

The computation with the above formula is quite fast when compared to the CFD code used to build the database. For comparison, CFD code takes about 30 minutes of CPU time in HP Apollo 700 Workstation to obtain a converged solution for a helicopter flying at one single height and single (x,y) location. Whereas using the above formula, the computation is carried out in a fraction of a second. Hence the formula is very useful for real-time simulation purposes. Figure 7 shows the variation of the uniform inflow over the whole deck at height h=0.75. Figures 8 and 9 display the variation of the harmonics of the inflow at h=0.75. It can be seen that the total inflow mainly consists of the uniform inflow and the longitudinal variation. This is from the fact that the reference flight is forward flight.

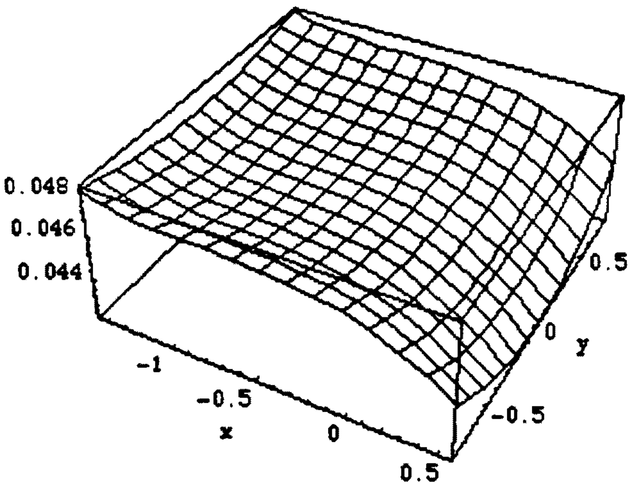

Figure 7: distribution of the uniform inflow over the deck

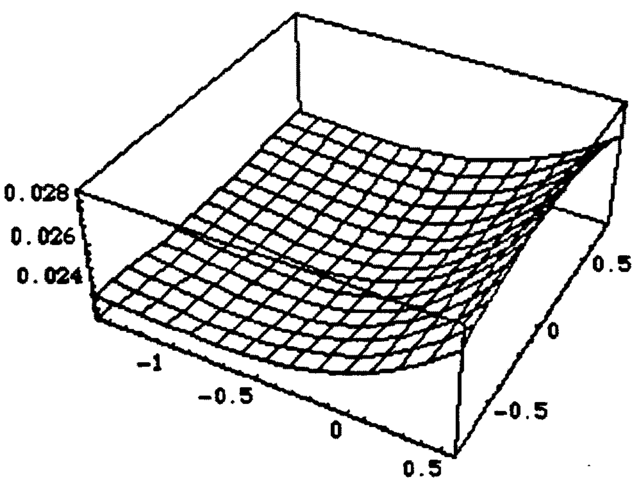

Figure 8: distribution of the longitudinal inflow over the deck

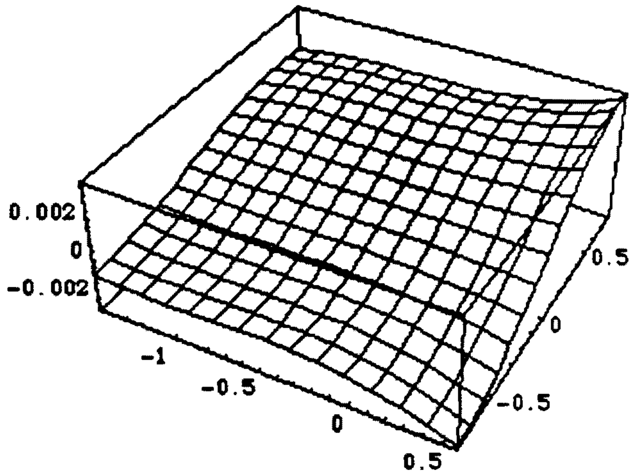

Figure 9: distribution of the lateral inflow over the deck

Figures 10(a) and 10(b) compare the results from the CFD code and from the formula at location x=-7.5/R, y=-5.5/R, h=0.75 and x=-25/R,y=15/R, h=1.75. We see that the fitted formula computes the inflow variation quite well.

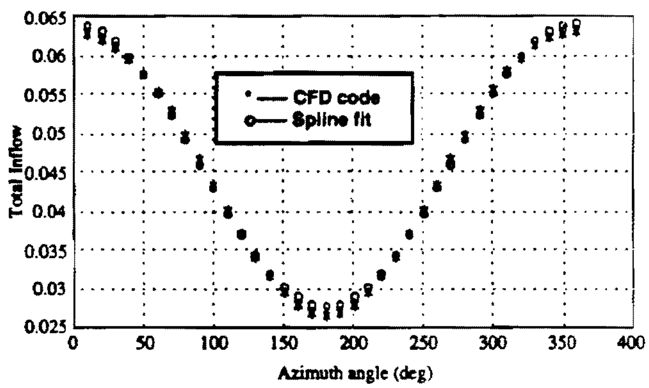

Figure 10 (a): comparison of the total inflow from CFD code and Spline fit formula at h=0.75

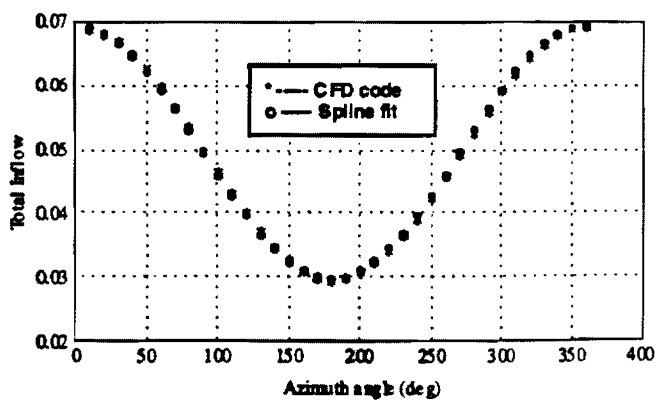

Figure 10 (b): comparison of the total inflow from CFD code and Spline fit formula at h=1.75

6. Conclusions

A ground effect model for rotorcraft/ship dynamic interface that is suitable for real time simulation purposes is developed in this paper. The gain matrix in the dynamic inflow model is identified as a function of the location of the rotor with respect to the ship deck, as well as the height of the rotor above the deck. However, the ship ground effect model developed in this study is applicable for trimmed flight above the deck. Further work is needed to capture the unsteady effects due to the rolling and/or pitching of the ship deck.

Acknowledgment

This work is funded by the Naval Air Warfare Center, Warminster, PA.

References

1.Prasad, J.V.R., Mavris, D.N., and Schrage, D.P., "Ship Airwake Modeling and Simulation, Phase I --- Methodology Development", Research Report submitted to Naval Air Warfare Center, School of Aerospace Engineering, Georgia Institute of Technology, Atlanta, Aug. 1992

2.Zhang, H., Prasad, J.V.R., and Mavris, D.N., "Ship Airwake Effects on Helicopter Rotor Aerodynamics", AIAA 94-3509, Arizona, August, 1994

3.Mello, O.A.F., Prasad, J.V.R., Sankar, L.N., and Tseng, W., "Analysis of Helicopter/Ship Aerodynamic Interactions," AHS Aeromechanics Specialists Conference, San Francisco, California, Jan. 1994.

4.Gaonkar, G.H., and Peters, D.A., "Review of Dynamic Inflow Modeling for Rotorcraft Flight Dynamics," Vertica, Vol. 12, No. 3, pp. 213-242, 1988.

5.Pitt, D.M., and Peters, D.A., "Theoretical Prediction of Dynamic Inflow Derivatives", Sixth European Rotorcraft and Powered Lift Aircraft Forum, Bristol, England, Sept. 1980

6.Peters, D.A., and HaQuang, N., "Dynamic Inflow for Practical Applications" J. of AHS, Oct. 1988.

7.He, Changjian, and Lewis, W.D., "A Parametric Study of Real Time Mathematical Modeling Incorporating Dynamic Wake and Elastic Blades", 48th Annual Forum of the AHS, Washington, DC, June 1992.

8.Howlett, J.J., "UH-60A Black Hawk Engineering Simulation Program: Volume I -- Mathematical Model", NASA CR-166309, 1981.

9.Cheeseman, I.C. and Bennett, W.E., "The Effect of the Ground on a Helicopter Rotor in Forward Flight", ARC R&M No.3021, Sept. 1955.

10. Healey, J. Val., "Prospects for Simulating the Helicopter/Ship Interface," Naval Engineers Journal, Vol. 99, No. 2, March 1987, pp. 45-63.

11. Mello, O. A. F., Numerical Simulation of Helicopter/Ship Aerodynamic Interactions,"
Research Report submitted to Naval Air Warfare Center, School of Aerospace Engineering, Georgia Institute of Technology, Atlanta, July 1993.

12. Wolfram, S., Mathematica: A System for Doing Mathematics by Computer, Addison-Wesley, Redwood City, Calif., 1988.

APPENDIX 3

GROUND EFFECT SIMULATION MODEL FOR ROTORCRAFT/SHIP INTERACTION STUDY

Hong Zhang * J.V.R. Prasad† L.N. Sankar‡
School of Aerospace Engineering
Georgia Institute of Technology
Atlanta, GA 30332, USA

O.A.F. Mello§
Centro Técnico Aerocspacial
Instituto de Aeronáutica e Espaco
São José dos Campos-SP, BRAZIL

John D. Funk, Jr. ¶
Aircraft Division
Naval Air Warfare Center
Warminster, PA, USA

Abstract

In this paper, a real time simulation model of ship ground effect for rotorcraft/ship interactions is developed by combining computational fluid dynamics (CFD) analysis and finite state representation of rotor inflow. For CFD analysis, the ship is modeled by using a source panel representation and the rotor wake is modeled as rigid with prescribed geometry but unknown vorticity distribution. The sea surface is modeled by placing an image rotor wake and an image ship panel system below the sea surface. The CFD model is then combined with the batch version of a generic helicopter flight simulation program. Using trim solutions from the simulation program, the ship ground effects on rotor inflow for cases of helicopter hovering with respect to ship deck are identified and analyzed. With a finite state representation of rotor inflow, a real time simulation model of ship ground effect is developed using results from the CFD analysis.

1. Background

Due to complex flow interactions between the air flow surrounding the ship deck and rotor wake, the pilot workload during shipboard landing and take-off of a helicopter is significantly increased [1]. Also, When a helicopter is flying close to a ship deck, the rotor wake is modified due to the presence of ship deck, superstructure and sea surface [2-4]. An alternative, to extensive and time-consuming testing at sea for establishing safe operating envelopes for helicopter shipboard operations, is simulation. A prerequisite to simulation approach is the development of simulation models of ship airwake and ship ground effect. This paper addresses the development of a simulation model of ship ground effect model while a companion paper [5] addresses the development of a simulation model of ship airwake. The organization of the paper is as follows: First, the methodology used for the development of a real-time ship ground effect simulation model is described. Next, a detailed description of the CFD modeling used in this methodology is presented followed by parametric investigations of the CFD model. Then a brief description of the real-time simulation model which is obtained by modifying the gain matrix of an existing dynamic inflow model is given and results are presented to illustrate how the real-time simulation model captures the ship ground effect for different rotor heights above deck and at various forward speeds.

2. Methodology for Developing Ship Ground Effect Simulation Models

The methodology used for developing ship ground effect simulation models is given in Fig. 1. First, a comprehensive computational fluid dynamic model that takes into account interactions between rotor wake and ship deck, superstructure and sea surface is developed. The CFD model is then combined with a comprehensive non-real time helicopter simulation model and rotor inflow distribution for cases of helicopter trimmed at different positions (see Fig. 2) and at different heights (see Fig. 3) with different values of ship speed are obtained. Then a harmonic analysis of inflow distribution for each of the cases is carried out. Using results from the harmonic analysis, the gain matrix of the dynamic inflow model is modified by matching the inflow distribution predicted by the dynamic inflow model with CFD results.

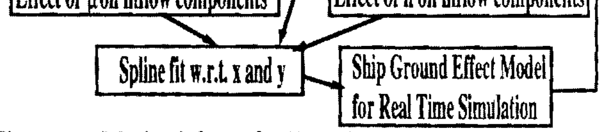

Figure 1. Methodology for Developing Ship Ground Effect Models

---

* Graduate Research Assistant
† Associate Professor, Member AIAA
‡ Professor, Member AIAA
§ Captain, Brazil Air Force
¶ Aerospace Engineer

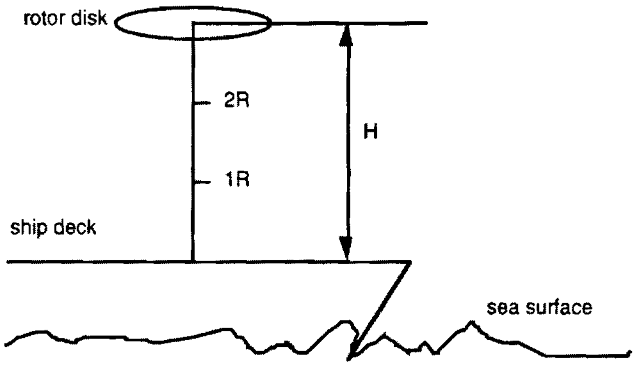

Figure 2. Helicopter Relative Position

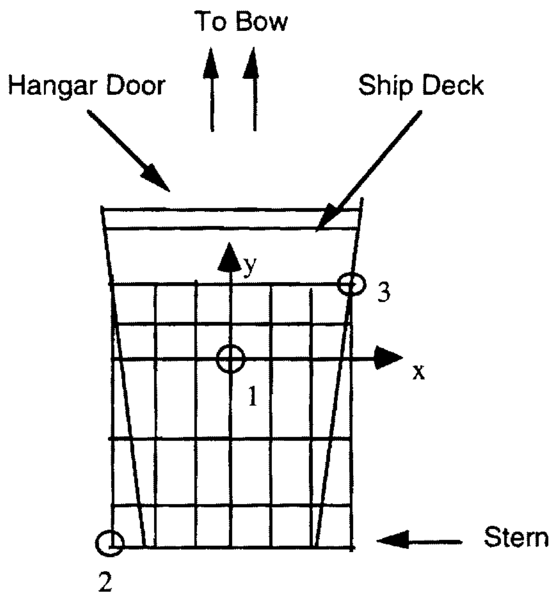

Figure 3. Positioning of Helicopter above Ship Deck (top view)

3. CFD Modeling

3.1 Ship Formulation

The ship surface is approximately represented by plane source panels with constant distributed strength. The strengths of the sources are determined by enforcing the non-penetration condition at the centroid of each panel. The normal component of the ship's motion and the normal component of the downwash induced by the rotor are taken into account in this formulation. The details of the source panel method can be found in Ref. 6 and therefore will not be repeated here. This formulation results in a linear system of equations to be solved for the ship panel source strengths σ:

$$[A]\{\sigma\} = [B] \tag{1}$$

where [A] is the matrix of influence coefficients, $\{\sigma\}$ is the vector of unknown source strengths and [B] is the RHS including the normal component of the velocities on the ship surface due to the free-stream and due to the rotor and its wake. The resulting source panel strengths are used to compute the velocities induced by the ship source panel system at the rotor disk.

3.2 Rotor Wake Formulation

A rigid wake model is used to compute the induced velocity due to the rotor and its wake on the ship and the vorticity distribution is computed from the blade section lift. In this study, the following assumptions are made:

(a) Blade flapping angles is small and high harmonic variation of blade flapping angle are negligible

(b) The rotor blade is modeled by a lifting line of bound vorticity, which is related to the blade section lift by Kutta-Joukowski's theorem.

(c) A classical skewed helical wake with a limited contraction is used, the wake is assumed to become flat near the ship deck as shown in Fig. 4.

(d) The wake is divided into a "near" wake, composed of trailing and shed vortices and a "far" wake composed of trailing tip vortices only. The strength of the far wake tip vortex is assumed to be equal to the maximum bound vorticity at the azimuthal location where the vortex filament leaves the blade.

(e) The rotor wake is convected downstream with a velocity which is equal to the vector sum of the free stream velocity and the averaged (momentum theory value) induced velocity over the disk.

3.2.1 Bound Vortices

The blade bound vorticity distribution is obtained through an iterative process from the blade section lift. Let the blade bound vorticity be $\Gamma_{b_{ij}} = \Gamma_b(r_i, \psi_j)$. From Kutta-Joukowski theorem:

$$\ell_{ij} = \rho V_{ij}\Gamma_{ij} = \rho(\Omega R)(\bar{r}_i + \mu \sin\psi_j)\Gamma_{b_{ij}} \tag{2}$$

i.e.

$$\Gamma_{b_{ij}} = \frac{\ell_{ij}}{\rho(\Omega R)(\bar{r}_i + \mu \sin\psi_j)} \tag{3}$$

From the computed bound vorticity distribution, the velocity induced by the blade bound vortices can be obtained by applying the Biot-Savart law.

3.2.2 Near Wake

The near wake is assumed to be composed of trailing and shed vortices, with strengths given by the radial and azimuth-wise variations of the bound vorticity respectively, at the azimuth location where the vortex filament leaves the blade. Let us first consider an element of a trailing vortex filament of length $r_i\Delta\nu$, which leaves the blade at the radial location r_i, and is located at a wake age ν_k. This element had left the blade when it was at an azimuth location $\psi_j - \nu_k$, with ψ_j being the current azimuth location of the blade. Therefor, the vorticity of the element is given by $\Gamma_t(\bar{r}_i, \psi_j - \nu_k)\bar{r}_i \Delta\nu$, where

$$\Gamma_{t_{ijk}} = \Gamma_t(\bar{r}_i, \psi_j - \nu_k) = \frac{\partial \Gamma_b}{\partial \bar{r}} \tag{4}$$

i.e.

$$\Gamma_{t_{ijk}} \approx \frac{\Gamma_b(\bar{r}_i, \psi_j - \nu_k) - \Gamma_b(\bar{r}_{i-1}, \psi_j - \nu_k)}{\bar{r}_i - \bar{r}_{i-1}} \tag{5}$$

The velocity induced by the entire filament at a point is given by integration of elementary induced velocities obtained from the Biot-Savart law along the near wake only.

Now let us consider an element of a shed vortex filament of length Δr_i, which leaves the blade at the radial location r_i, and is located at a wake age ν_k. This element had left the blade when it was at an azimuth location $\psi_j - \nu_k$, with ψ_j being the current azimuth location of the blade. Therefore, the vorticity of the element is given by $\Gamma_s(\bar{r}_i, \psi_j - \nu_k)$, where $\Gamma_s(\bar{r}_i, \psi_j - \nu_k)\Delta r_i$ is the shed vortex vorticity, equal to the azimuthal variation of Γ_b:

$$\Gamma_{s_{ijk}} = \Gamma_s(\bar{r}_i, \psi_j - \nu_k) = \frac{\partial \Gamma_b}{\partial \psi} \tag{6}$$

$$\Gamma_{s_{ijk}} \approx \frac{\Gamma_b(\bar{r}_i, \psi_j - \nu_k) - \Gamma_b(\bar{r}_i, \psi_{j-1} - \nu_k)}{\Delta\psi} \tag{7}$$

Also, the velocity induced by the entire shed vortex system at a point is given by radial integration of the elementary induced velocities obtained from the Biot-Savart law along the "near" wake.

3.2.3 Far wake

The far wake is assumed to be only composed of trailing tip vortices, with strength equal to the maximum bound vorticity at the azimuth location where the vortex filament leaves the blade. Considering an element of wake filament of length $r_{tv}\Delta\nu$ (where r_{tv} corresponds to the radial location where the tip vortex has rolled up) and at a wake age ν_k. This element has left the blade when it was at an azimuth location $\psi_j - \nu_k, \psi_j$ being the current azimuth location of the blade. Therefore, the vorticity of the element is given by $\Gamma_{T_{jk}} r_{tv}\Delta\nu = \Gamma_T(\psi_j - \nu_k) r_{tv}\Delta\nu$, where $\Gamma_T(\psi_j - \nu_k)$ is the strength of the trailing tip vortex equal to the radial maximum of Γ_b:

$$\Gamma_{T_{jk}} = \Gamma_T(\psi_j - \nu_k) = \max_i(\Gamma_b(r_i, \psi_j - \nu_k)) \tag{8}$$

3.2.4 Vortex Core Model

A Rankine vortex core model [7] with radius of one tenth (1/10) of the blade chord is used. This model is applied by scaling the induced velocity due to the elementary vortex filament by the square of the ratio between the distance to the filament and the core radius, whenever the point where the induced velocity is being calculated lies within the vortex core. The geometry of the far wake is modified by making it flat and parallel to the ship deck with assumed clearance between the wake and the deck (see Fig. 4).

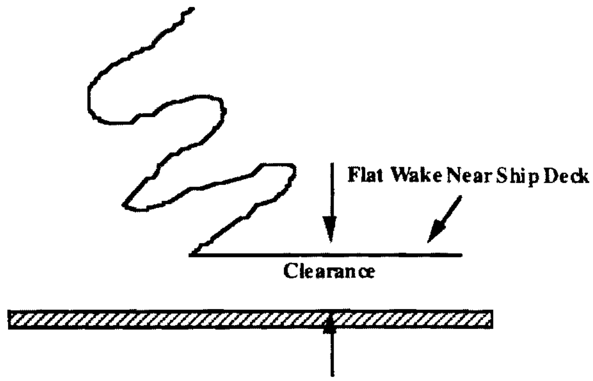

Figure 4. Modified Wake Geometry

In order to determine the number of rotor revolutions and clearance between the wake and the ship deck, the rotor wake model is combined with a generic helicopter simulation package [8]. Assuming a flat ground, the number of rotor revolutions in the wake geometry and wake clearance are adjusted by matching the rotor power required from analysis with experimental results. Figure 5 shows the effect of ground clearance on the rotor power required, whereas Fig. 6 illustrates the effect of number of revolutions in the wake geometry. It can be seen from Fig. 5, that the wake clearance has negligible effect on the rotor power. However, from Fig. 6, it is clear that the number of revolutions in the wake geometry has significant effect on rotor power. Also, from Fig. 6, it is seen that roughly 10 rotor revolutions of wake is needed in order to match with experimental data for the hover case. However, the results are less sensitive to number of revolutions for forward flight cases. It is felt that the value of 10 rotor revolution of wake geometry arrived at for the hover case is rather ad hoc as this value will be different for different heights of the rotor above the ground. Also, it is felt that a detailed investigation using , possibly, a free wake analysis is required to determine the wake geometry for the hover case. Hence, only forward flight cases are considered in the subsequent analysis.

4. Parametric Investigation

4.1 Effect of Locations

For illustration purpose, the SH-60 helicopter flying at 15kt above the deck of a FFG-7 class frigate, which is moving at the same velocity as the helicopter, is used in this investigation. The simulation of helicopter motion near the ship is carried out using the general helicopter simulation code [8]. By taking into account the induced velocity or upwash at the rotor disk due to the ship panel system into the blade-element analysis, the ground effect is coupled into the simulation code. Through changing the collective pitch and cyclic pitch, the helicopter is retrimmed at the same location with the consideration of the ground effect. Using the coupled ship ground effect CFD model and the generic flight simulation package, the helicopter is trimmed at different locations and different heights above the deck.

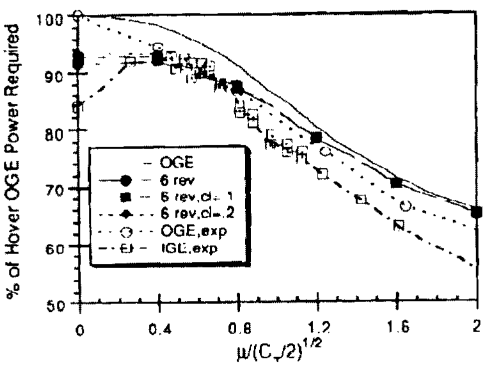

Figure 5. Clearance Effect on Power

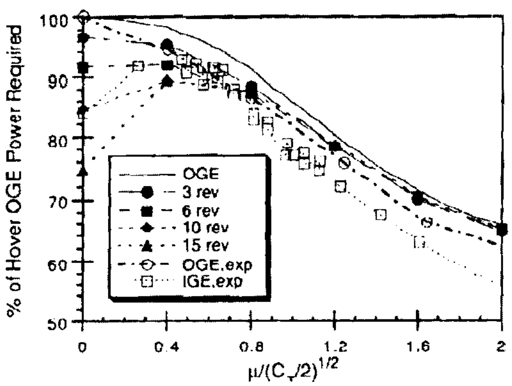

Figure 6. Effect of Number of Revolutions

Figure 7 shows the nondimensional upwash at 0.8R blade station for the rotor positioned at various heights above the center of the deck. It can be seen that the upwash is symmetric about the flight direction. The variation of the nondimensional upwash at the rotor at 0.8R blade station is shown in Fig. 8 for different heights of rotor from the ship deck for the helicopter above the lower left corner of the deck. It is seen from Fig. 8 that with an increase in rotor height above the deck, the ship ground effect diminishes. Also, the ship ground effect results in an increase in upwash on the advancing side of the rotor indicating, as one would expect, a "partial" ship ground effect.

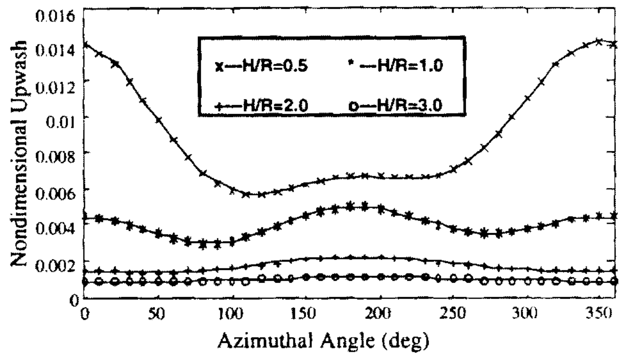

Figure 7. Effect of Height on Upwash at Rotor Disk at the Center of the Deck

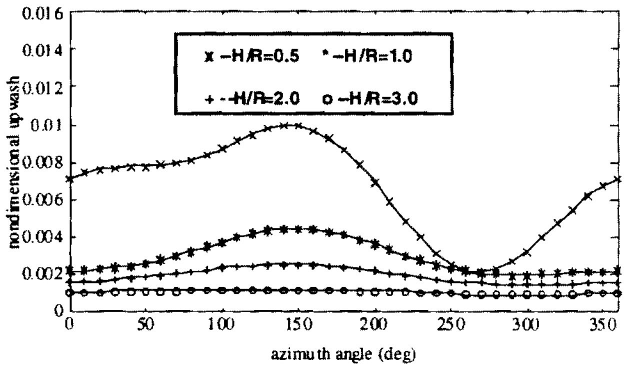

Figure 8. Effect of Height on Upwash at Lower Left Corner of the Deck

4.2 Effect of Advance Ratio

To study the advance ratio effect on the inflow distribution over the rotor disk when flying near the ship deck with the ship in motion, the helicopter is trimmed at 1.2 R above the ship deck at various speeds ranging from 10kt to 80kt. Figure 9 compares upwash due to the ship deck between the cases of helicopter flying at 15kt and 45kt

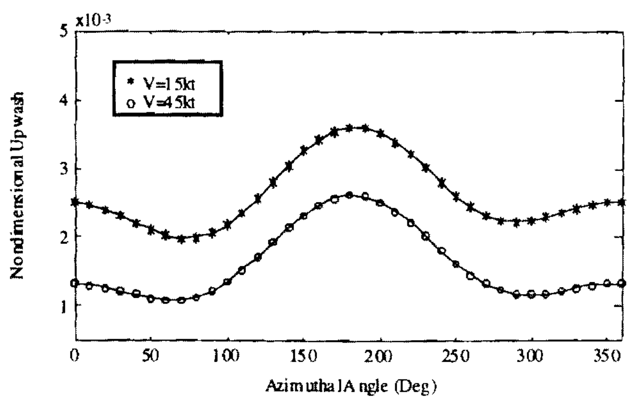

Figure 9. Upwash at Different Advance Ratio

cases. As expected, Fig. 9 shows that the upwash decreases as the helicopter speed is increased.

4. 3 Harmonic Analysis of the Inflow

Harmonic analysis is carried out for the upwash at various locations and advance ratios. It is found that up to second harmonic terms are needed to match the upwash from CFD results, i.e.:

$$\Delta w = -\Delta\lambda_0 - \Delta\lambda_s \frac{r}{R}\sin\psi - \Delta\lambda_c \frac{r}{R}\cos\psi - \Delta\lambda_{2s}\frac{r}{R}\sin(2\psi) - \Delta\lambda_{2c}\frac{r}{R}\cos(2\psi) \qquad (9)$$

where

$\Delta\lambda_0$ is the upwash contribution to the uniform inflow

$\Delta\lambda_s$ is the lateral inflow changes due to the ground effect

$\Delta\lambda_c$ is the longitudinal inflow variation because of the ground presence

$\Delta\lambda_{2s}$ is the 2nd lateral inflow change

$\Delta\lambda_{2c}$ is the 2nd longitudinal inflow change

Thus, the inflow in ship ground effect can be modeled as,

$$(\lambda)_{ige} = (\lambda)_{oge} - \Delta w \qquad (10)$$

Figure 10 shows how the rotor height above the ship deck influences the uniform inflow at the rotor at two different locations. It is seen that the uniform inflow gets smaller when the rotor height above the ship deck increases, which is as expected. Figure 11 shows how the uniform inflow changes as the advance ratio varies. A nonzero value of advance ratio represents the case of the helicopter hovering with respect to the ship deck while the ship is in motion. The advance ratio effect on longitudinal inflow component is shown in Fig. 12. It is clear from Figs. 11 and 12 that the ship ground effect with advance ratio is not the same on average and the harmonic components. While the average component of inflow decreases with an increase of advance ratio, the longitudinal component of inflow first increases and then decreases as the advance ratio is increased.

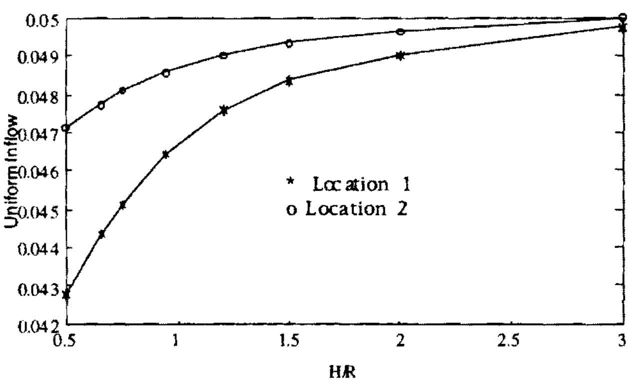

Figure 10. Effect of Height on Uniform Inflow Component

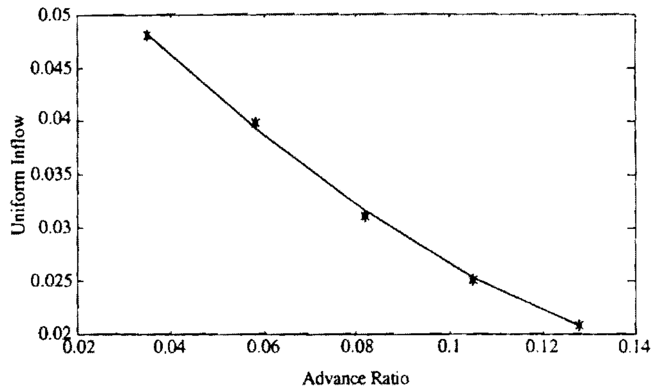

Figure 11: Effect of Advance Ratio on Uniform Inflow Component

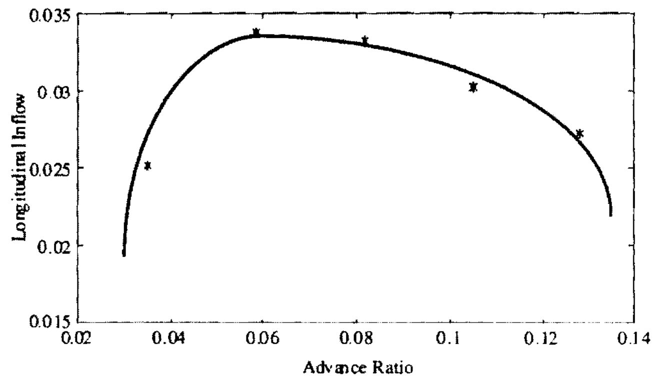

Figure 12. Effect of Advance Ratio on Longitudinal Inflow Component

5. Real Time Ship Ground Effect Model

As most of the current day flight simulation programs include a dynamic inflow representation for rotor inflow in order to account for the time-varying and distributed nature of inflow over the rotor disk, it is felt that a real time ship ground effect model can be obtained by appropriately modifying the parameters in the dynamic inflow model. The dynamic inflow model can be written as [9]:

$$[M]\{\dot{\bar{\lambda}}\} + [\hat{L}]^{-1}\{\bar{\lambda}\} = \{\bar{C}\}_{aero} \qquad (11)$$

where

$$\bar{\lambda} = (\lambda_0, \lambda_s, \lambda_c)^T$$
$$C = (CT, -C1, -C2)^T$$

$[M], [\hat{L}]$ are the apparent mass matrix and the inflow gain matrix and their explicit expressions for out-of-ground effect case can be found in Ref. 9. CT is thrust coefficient. C1, C2 are instantaneous aerodynamic rolling and pitching moment coefficients expressed in the tip path plane. Obviously, they are time dependent for unsteady flight. The subscript "aero" denotes that only the aerodynamic contribution is considered and the inertial part is not included. The "$\bullet$ " denotes time derivative.

Due to the proximity of the rotor disk to the ship deck, the rotorcraft/ship interactions induce upwash at the rotor disk, thereby changing the total inflow and the inflow distribution over the rotor disk. Hence, the dynamic inflow model for the case of in-ground-effect model can be written as:

$$[M]_{ige}\ \{\dot{\bar{\lambda}}\}_{ige} + [\hat{L}]^{-1}_{ige}\{\bar{\lambda}\}_{ige} = \{\{\bar{C}\}_{aero}\}_{ige} \qquad (12)$$

where : $[M]_{ige}$, $[\hat{L}]_{ige}$ are the apparent mass and the inflow gain matrices for the case of in-ground-effect. Suppose

$$\left\{\bar{\lambda}\right\}_{ige} = \begin{bmatrix} g_1 & 0 & 0 \\ 0 & g_2 & 0 \\ 0 & 0 & g_3 \end{bmatrix} \left\{\bar{\lambda}\right\}_{oge} \qquad (13)$$

and

$$\left\{\bar{C}\right\}_{ige} = \begin{bmatrix} h_1 & 0 & 0 \\ 0 & h_2 & 0 \\ 0 & 0 & h_3 \end{bmatrix} \left\{\bar{C}\right\}_{oge} \qquad (14)$$

Thus, for trimmed flight with rotor treated as a disk, and noticing that the forcing functions (CT, C1, C2) are approximately the same for out-of-ground effect case and in-ground effect case. From Eqs. (12)-(14) with $h_i = 1,\ i = 1,2,3$ and $\dot{\bar{\lambda}} = 0$, we get

$$\left\{\hat{L}\right\}_{ige} = \begin{bmatrix} g_1 & 0 & 0 \\ 0 & g_2 & 0 \\ 0 & 0 & g_3 \end{bmatrix} \left\{\hat{L}\right\}_{oge} \qquad (15)$$

Using results from CFD analysis for the ship ground effect cases of helicopter hovering over the ship deck at different positions and for different speeds, general expressions for g_i, $i = 1,2,3$ are obtained using curve fitting techniques. The resulting expression are obtained as

$$g_i = \frac{a_i(x,y) + \dfrac{b_i(x,y)}{h} + \dfrac{c_i(x,y)}{h^2} + \dfrac{d_i(x,y)}{h^3}}{k_{0_i} + k_{1_i}\mu + k_{2_i}\mu^2},\ i = 1,2,3 \qquad (16)$$

where a_i, b_i, c_i, d_i are all cubic spline fitted functions of x and y. Thus, from equation (16), the correction factors g_1, g_2, g_3 that account for ground effect, are all functions of rotor position (x,y,z) with respect to ship deck and advance ratio. For comparison, the widely used Cheesemann & Bennett model [10] is of the form

$$g_i = 1. - \frac{1}{16h^2}\left(\frac{1}{1 + \left(\dfrac{\mu}{\lambda_{oge}}\right)^2}\right),\ i = 1,2,3 \qquad (17)$$

Also, for comparison purpose, the variation of g_i (for the uniform component) is shown in Fig. 13 as computed using the Cheesemann & Bennett model and the new model, for cases of helicopter hovering at three different locations above the ship deck. From Fig. 13, it is clear that ship ground effect is different for different positions around the ship deck as predicted by the new model.

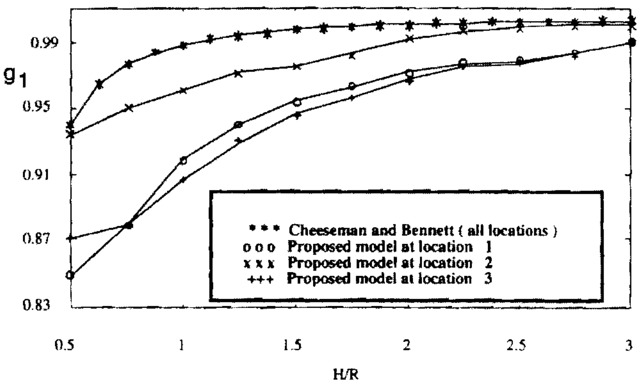

Figure 13. Comparison of Different Models

6. Conclusions

A ground effect model for rotorcraft/ship dynamic interface that is suitable for real time simulation purposes is developed in this paper. The gain matrix in the dynamic inflow model is identified as a function of the location of the rotor with respect to the ship deck, the height of the rotor above the deck and advance ratio. Also, the new model takes into account partial ground effect. However, the ship ground effect model developed in this study is only applicable for trimmed flight above the deck. Further work is needed to capture the unsteady effects due to heaving, rolling and/or pitching of the ship deck. Also, validation of the model using experimental data is needed.

Acknowledgment

This project is funded by the Naval Air Warfare Center, Warminster, PA.

References

1. Healey, J. Val., "Prospects for Simulating the Helicopter/Ship Interface," Naval Engineers Journal, Vol. 99, No. 2, March 1987, pp. 45-63.
2. Mello, O.A.F., Prasad, J.V.R., Sankar, L.N., and Tseng, W., "Analysis of Helicopter/Ship Aerodynamic Interactions," AHS Aeromechanics Specialists Conference, San Francisco, California, Jan. 1994.
3. Ferrir, B., and Semenza, J., "NATC Manned Flight Simulator VTOL Ship Motion Simulation and Application" 46th Annual Forum of AHS, Washington DC, 1990
4. Zhang H., Mello, O.A.F., Prasad, J.V.R., Sankar, L. N., and Funk, J. D. , "A Simulation Model of Ship Ground Effect For Rotorcraft/Ship Interaction Study," AHS 51st Annual Forum, Fort Worth, TX May 9-11,1995
5. Prasad, J.V.R., Manoj M., Mavris, D. and Zhang, H. , "Ship Airwake Simulation Models for Rotorcraft/Ship Interactions Study," AIAA 95-3406
6. Hess, J. L., and Smith, A. M O., " Calculation of Potential Flow About Arbitrary Bodies," Progress in Aeronautical Sciences, Vol. 8 Edited by D. Küchemann, Pergmon Press, Oxford, England, 1967
7. U.S. Department of Army-AFDD, " Second Generation Comprehensive Helicopter Analysis Systems, Version 2.1 " Vol. II, chapter 5, Moffett Field, CA July 1992
8. Kaplita,T.T., " UH-60A Black Hawk Engineering Simulation Method Validation and Proposed Modifications" Technical Report SER-70982, United Technologies Sikorsky Aircraft, June 1984.
9. Peters, D.A., and HaQuang, N., "Dynamic Inflow for Practical Applications" J. of AHS, Oct. 1988
10. Cheesemann, I.C. and Bennett, W.E., "The Effect of the Ground on a Helicopter Rotor in Forward Flight", ARC R&M No. 3021, Sept. 1955.

APPENDIX 4

1. INTRODUCTION

This report describes the modifications made in the helicopter simulation code GENHEL, in order to investigate helicopter/ship interactions. The theoretical formulation for the GENHEL code is given in Refs. 1 and 2 and will not be discussed here.

The effect of the ship proximity to the helicopter is modeled by using a standard panel method, based on the classical solution by Hess and Smith[7]. The ship is modeled by source panels which allow a good geometric representation. The effect of the ship on the rotor is given by the induced velocities on the rotor disk due to the ship panels. For the computation of the strengths of the sources, it is necessary to take into account both the ship velocity and the velocity field on the ship due to the rotor wake. This velocity field is computed using a rigid helical wake model. The strength of the rotor wake vortices depends on the circulation around the rotor blade, which, in turn, depends on the ship effects. Therefore, an iterative process would be needed. However, for the simulation problem, it may be assumed that changes in circulation around the blade and the flow about the ship are not too rapid and consequently the iterative process may be intrinsically performed during the simulation process.

For the computation of wake vorticity, two approaches have been employed: The first approach was to assume a prescribed vorticity distribution along the rotor disk. This allows all vorticity strengths on the disk and in the wake to be related to the thrust coefficient. Details on this approach were given in Ref. 4. The second approach was to compute the local vorticity at the rotor disk from the section lift. This approach requires numerical differentiation of the resulting vorticity distribution in order to obtain the wake vorticity strengths. Details on this latter approach are given in the Appendix.

In order to model the ground effect due to the sea surface, the method of images is used. An image rotor wake and an image ship panel system are placed below the sea surface and the influence of these images are taken into account in the computation of the downwash induced by the rotor and in the computation of the coefficient matrix for the ship panel method.

The remaining of this report is organized as follows: First, brief instructions on compiling and running GENHEL are given; Next the modifications and additions to GENHEL are described, including the first-order dynamic inflow model and the helicopter/ship interaction code using both the prescribed wake vorticity and computed wake vorticity models. Finally, an attempt to extend the rotor wake code to a free wake model is described.

2. COMPILING AND RUNNING GENHEL

The source code for the original version of GENHEL is divided into five FORTRAN files: bhawk.f, bhawka.f, bhawkb.f, bhawkc.f and bhawkd.f. The subroutine ROTOR is included in the file bhawkd.f and contains the blade-element model. In addition, several *.DAT files and a "Makefile" file are needed. The compilation is achieved by issuing the command Makefile twice to compile and link. This results in an executable file called bhawk. The execution is then performed by simply running bhawk. All the input files have their names pre-defined. The main input file is BHAWK.DAT. The input parameters in BHAWK.DAT are described in Ref. 1. Ref. 2 contains test cases that may be useful for validation of changes made to the original code.

3. FIRST-ORDER DYNAMIC INFLOW

The first order dynamic inflow model from Ref. 3 was implemented in GENHEL, as described in Ref. 4. These modifications were made mainly in the subroutines `ROTOR` and `RADIAL`, and a new subroutine called `DYNINF` was added. These changes were made in `bhawkd.f`, resulting in a new file called `bhawkd2.f`. Minor changes were made to the file `bhawkc.f`, for output of variables of interest, but this file was not renamed. A new `Makefile2` file was used to compile and link this dynamic inflow version. Note that these files also include the turbulence modifications made by Riaz (Refs. 5,6).

4. HELICOPTER/SHIP INTERACTION: PRESCRIBED VORTICITY VERSION

The first version of the helicopter/ship interaction model was developed using a rigid helical wake model with prescribed vorticity distribution in the wake, as described in Ref. 4. The ship model was the panel method of Ref. 7. The rotor wake and ship models were included in the file `bhawke.f`. Changes were made in the file `bhawkd2.f`, resulting in a new file `bhawkd3.f`. Minor changes were also made in `bhawk.f` and `bhawkb.f`, resulting in `bhawk2.f` and `bhawkb2.f`, respectively. This version should be compiled and linked by issuing the command `Makefile3` twice, which generates the executable file `bhawk2`. The changes are significantly commented (one can search for them by searching for the string `MELLO`).

4.1. Subroutines

The subroutines and function subprograms included in `bhawke.f` are as follows:

`RSHIP` Main module for computation of the interaction between the rotor and the ship; calls other needed routines.

`GETSHC` Reads ship coordinates and computes unit vectors.

`EUL3` Constructs a matrix of coordinate transformations after 3 Euler rotations α about y, β about z' and γ about x".

`MATMUL`, `MTMUL`, `MTMUL2` Subroutines for matrix multiplication.

`CONV` Contains the convergence procedure for the integration which gives the velocity induced by the rotor wake at a given point.

`AINTT` Function to be integrated along the wake coordinate to give total induced velocity due to wake tip vortex filaments.

GAMATV Functional variation of trailing vorticity as a function of the sine and cosine of blade azimuth when the filament left the blade.

AINTB Function to be integrated along the radius to give total induced velocity due to blade bound vortices on a given point.

GAMABV Functional variation of bound vorticity as a function of the radius and sine and cosine of blade azimuth.

AINTNW Function to be integrated along the near wake to give total induced velocity due to blade shed and trailing vortices on a given point; for a given wake age, it uses a radial integration of AINWR.

AINWR Function to be integrated along the radius to give total induced velocity due to a blade shed vortex filament and due to the sum of trailing vortex elements at that near wake location on a given point.

GSHEDV Functional variation of shed vorticity as a function of the radius and sine and cosine of blade azimuth.

GTRAV Functional variation of trailing vorticity as a function of the radius and sine and cosine of blade azimuth.

GAULEG Computes abscissas and weights for Gauss-Legendre quadrature (from Ref. 8).

QGAUS, QGAUSR Integrate a function using Gauss-Legendre quadrature (from Ref. 8).

PANEL Contains the panel method procedure; calls subroutines for the several coordinate transformations and induced velocity computations. It computes the influence coefficients for induced velocities due to a ship panel on other ship panels and due to a ship panel on the rotor blade elements.

PANVEL Computes the velocities induced by a ship panel, in the panel axes, on a point given in the same panel axes.

TRAFP Performs coordinate transformations from ship axes to panel axes.

TRAPF Performs coordinate transformations from panel axes to ship axes.

TRAFPM Performs coordinate transformations from ship axes to mirror panel axes.

TRAPFM Performs coordinate transformations from mirror panel axes to ship axes.

LUDCMP Performs an LU decomposition of the ship influence coefficient matrix (from Ref. 8).

LUBKSB Performs a back-substitution for solution of the system of equations, given the LU decomposition of the matrix of coefficients.

4.2. Input Parameters

The input parameters for the rotor/ship interaction computation are included in the file `BHAWK.DAT` and in a new file called `rship.dat`. The format of this latter file is as follows:

```
0.95  0.5   0.0   1.0   1.0  0.02  36  10  3    10
Rtv   Fnw   Xn0fr Fnctr Kt   Eps   Nqn Nqr Nmin Nmax
```

The above parameters have the following meaning:

Rtv	Radial location of the tip vortex
Fnw	Length of near wake, in number of revolutions
Xn0fr	Wake age for starting of integration
Fnctr	Wake age for wake contraction, in number of revolutions
Kt	Factor used in vorticity distribution (see Ref. 4)
Eps	Tolerance for convergence in wake integration
Nqn	Number of points along the wake for Gauss quadrature

Nqr Number of points along the radius for Gauss quadrature

Nmin Minimum number of revolutions for wake integration

Nmax Maximum number of revolutions for wake integration

The additions to BHAWK.DAT are as follows: The following flags are added to $RUNFLAG:

IGNDEF Ground effect flag (0 for no ground effect)

ISHIP Ship flag (0 for no ship)

IRRW Rotor induced velocity flag: If set to 1, rotor wake is used to compute inflow on rotor disk; if set to 0, dynamic inflow is used. Recommended setting is 0.

ISHMV Ship mean velocities flag: If set to 1, the ship airwake mean velocities are obtained from polynomial fitting of test data; if set to 0, the panel method is used. Recommended setting is 1.

and the following inputs are included in $RUNIC:

ALSHIP Ship attitude (deg)

PHSHIP Ship bank angle (deg)

VSHKT Ship velocity (knots)

XSHIP0, YSHIP0, ZSHIP0 Initial ship location in inertial reference frame.

VWIND Wind velocity (knots)

PSIWND Wind direction (deg)

NSS Number of blade elements (was fixed in the code in the original version).

5. HELICOPTER/SHIP INTERACTION: COMPUTED VORTICITY VERSION

Another version of the helicopter/ship interaction model was developed using the same rigid helical wake model as above, but with the vorticity distribution in the wake computed from the section lift coefficients. Details on this model are given in the Appendix.

The changes in the rotor wake model resulted in a new file `bhawke2.f`, which replaced `bhawke.f`. Changes were also made in `bhawkd3.f`, resulting in a new file `bhawkd4.f`, primarily to compute the section lift and pass it to the rotor wake code. This version should be compiled and linked by issuing the command `Makefile4` twice, which generates the executable file `bhawk3`.

For all versions of the helicopter/ship interaction code discussed so far, the rotor wake was simply truncated at a small height above the ship deck. It was observed that this procedure resulted in unrealistic ground effect modeling at very low heights. Consequently, a new version was developed in which the wake was not truncated, but assumed to be "flat", i.e., in a plane parallel to the ground, just above it, for wake ages above the wake age for which the vortex wake filaments were at a specified minimum distance from the deck (see Fig. 1). These changes were implemented in a new file `bhawke3.f`, which replaced `bhawke2.f`. This version should be compiled and linked by issuing the command `Makefile6` twice, which generates the executable file `bhawk6`. This is to be considered the current production version.

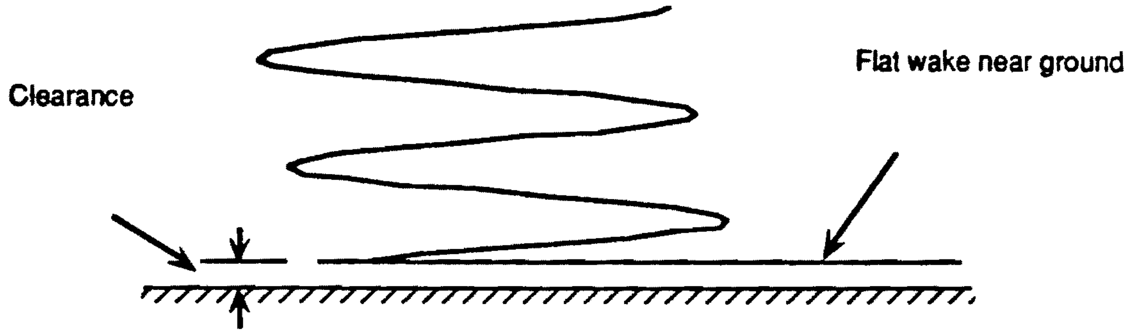

Fig. 1: Modified Wake Geometry

5.1. Subroutines

The subroutines and function subprograms in `bhawke2.f` and `bhawke3.f` are essentially the same as in `bhawke.f` and are listed below:

`RSHIP` Main module for computation of the interaction between the rotor and the ship; calls other needed routines.

`GETSHC` Reads ship coordinates and computes unit vectors.

`EUL3` Constructs a matrix of coordinate transformations after 3 Euler rotations α about y, β about z' and γ about x''.

`MATMUL`, `MTMUL`, `MTMUL2` Subroutines for matrix multiplication.

`GAMABV` Functional variation of bound vorticity as a function of the radius and sine and cosine of blade azimuth.

`GSHEDV` Functional variation of shed vorticity as a function of the radius and sine and cosine of blade azimuth.

`GTRAV` Functional variation of trailing vorticity as a function of the radius and sine and cosine of blade azimuth.

GAMATV Functional variation of trailing vorticity as a function of the sine and cosine of blade azimuth when the filament left the blade.

BVINT Subroutine for integration of bound vortices' contribution using trapezoidal rule.

AINTB Function to be integrated along the radius to give total induced velocity due to blade bound vortices on a given point.

NWINT Subroutine for integration along near wake.

AINTNW Function to be integrated along the near wake to give total induced velocity due to blade shed and trailing vortices on a given point; for a given wake age, it uses a radial integration of AINWR.

AINWR Function to be integrated along the radius to give total induced velocity due to a blade shed vortex filament and due to the sum of trailing vortex elements at that near wake location on a given point.

FWINT Subroutine for integration along far wake.

AINTT Function to be integrated along the wake coordinate to give total induced velocity due to wake tip vortex filaments.

CONV Integration routines not used in these versions
GAULEG,
QGAUS,
QGAUSR

PANEL Contains the panel method procedure; calls subroutines for the several coordinate transformations and induced velocity computations. It computes the influence coefficients for induced velocities due to a ship panel on other ship panels and due to a ship panel on the rotor blade elements.

PANVEL Computes the velocities induced by a ship panel, in the panel axes, on a point given in the same panel axes.

TRAFP Performs coordinate transformations from ship axes to panel axes.

TRAPF Performs coordinate transformations from panel axes to ship axes.

TRAFPM Performs coordinate transformations from ship axes to mirror panel axes.

TRAPFM Performs coordinate transformations from mirror panel axes to ship axes.

LUDCMP Performs an LU decomposition of the ship influence coefficient matrix (from Ref. 8).

LUBKSB Performs a back-substitution for solution of the system of equations, given the LU decomposition of the matrix of coefficients.

5.2. Input Parameters

As in the prescribed vorticity version, the input parameters for the rotor/ship interaction computation are included in the file BHAWK.DAT and in a new file called rship.dat. The format of this latter file is as follows:

```
0.95  0.5   0.0   1.0   1.0  0.02  36  10  3    10   0.1
Rtv   Fnw   Xn0fr Fnctr Kt   Eps   Nqn Nqr Nmin Nmax Gndclf
```

The above parameters have the following meaning:

Rtv Radial location of the tip vortex

Fnw Length of near wake, in number of revolutions

Xn0fr Wake age for starting of integration

Fnctr Wake age for wake contraction, in number of revolutions

Kt Factor used in vorticity distribution (not used in this version)

Eps Tolerance for convergence in wake integration (not used in this version)

Nqn Number of points along the wake for Gauss quadrature (not used in this version)

Nqr Number of points along the radius for Gauss quadrature (not used in this version)

`Nmin` Minimum number of revolutions for wake integration

`Nmax` Maximum number of revolutions for wake integration

`Gndclf` Wake clearance above deck (minimum distance between wake filaments and deck), non-dimensionalized by the rotor radius.

Note that the format of the input file is the same as in the previous version, with the addition of `Gndclf`. The unused input parameters were maintained for compatibility with the previous version.

The additions to `BHAWK.DAT` are as in the previous version: The following flags are added to `$RUNFLAG`:

`IGNDEF` Ground effect flag (0 for no ground effect)

`ISHIP` Ship flag (0 for no ship)

`IRRW` Rotor induced velocity flag: If set to 1, rotor wake is used to compute inflow on rotor disk; if set to 0, dynamic inflow is used. Recommended setting is 0.

`ISHMV` Ship mean velocities flag: If set to 1, the ship airwake mean velocities are obtained from polynomial fitting of test data; if set to 0, the panel method is used. Recommended setting is 1.

and the following inputs are included in `$RUNIC`:

`ALSHIP` Ship attitude (deg)

`PHSHIP` Ship bank angle (deg)

`VSHKT` Ship velocity (knots)

`XSHIP0`, `YSHIP0`, `ZSHIP0` Initial ship location in inertial reference frame.

`VWIND` Wind velocity (knots)

`PSIWND` Wind direction (deg)

`NSS` Number of blade elements (was fixed in the code in the original version).

5.3. Parametric Investigation

A limited parametric investigation was performed to determine the effect of number of revolutions and wake clearance above the ground on the ground effect modeling. Representative results are shown in Figs. 2 and 3. In these figures the power required is non-dimensionalized by the hover out-of-ground effect (OGE) power required and plotted as a function of the reduced advance ratio, $\mu/(C_T/2)^{1/2}$. These non-dimensionalizations allow a more meaningful comparison with the experimental data in Ref. 10, which were obtained for the Boeing-Vertol YUH-61, a helicopter of the same class as the UH-60.

From the parametric investigation, it may be concluded that the clearance above the ground is a minor factor, at least in the range investigated. The number of revolutions is a major factor at low speeds, and a minor factor at high speeds, because as the speed is increased, the wake is washed away from the deck.

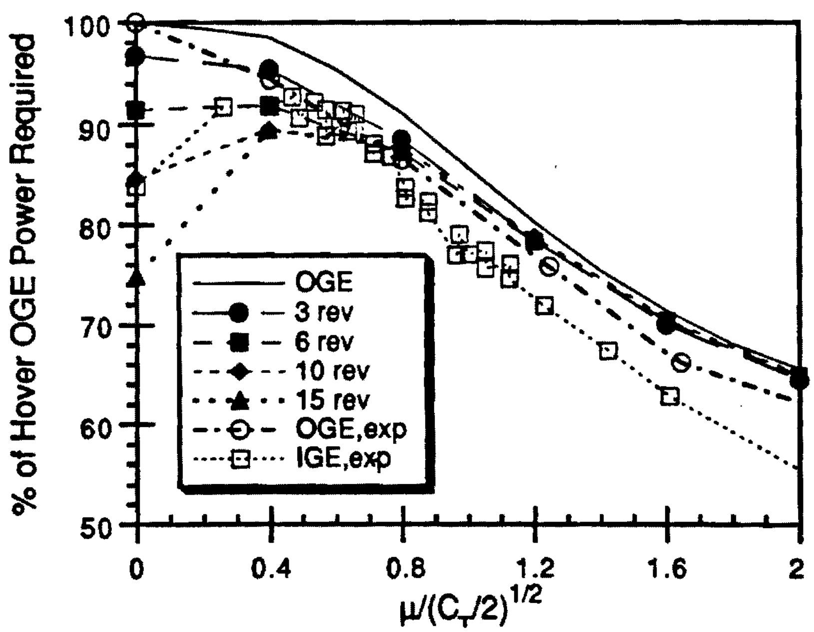

Fig. 2: Parametric Investigation: Effect of Number of Wake Revolutions.

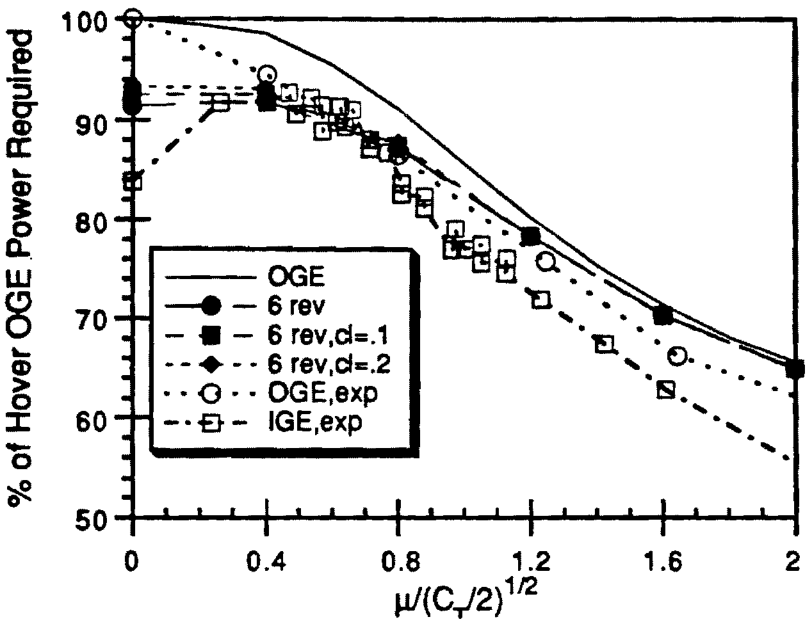

Fig. 3: Parametric Investigation: Effect of Clearance above Ground.

6. HELICOPTER/SHIP INTERACTION: FREE WAKE MODEL

In order to increase the code fidelity at very low speeds, an extension of the current code to a free wake model has been attempted. The changes in the rotor wake model resulted in a new file `bhawke4.f`. Preliminary runs showed that the wake was unstable, even though relaxation techniques were used. This is illustrated in Fig. 4, where side views of a wake filament from one blade is shown at four iteration levels. This unstable behavior has been observed during the development of other free wake codes. From these preliminary computations, it became apparent that the further development of a free wake code would require a substantial effort by itself, in a deviation from the main objective at hand, which is the helicopter/ship interaction study. Therefore, it is recommended that the emphasis be shifted towards the adaptation of the existing free wake module in CAMRAD for application to the helicopter/ship interaction study.

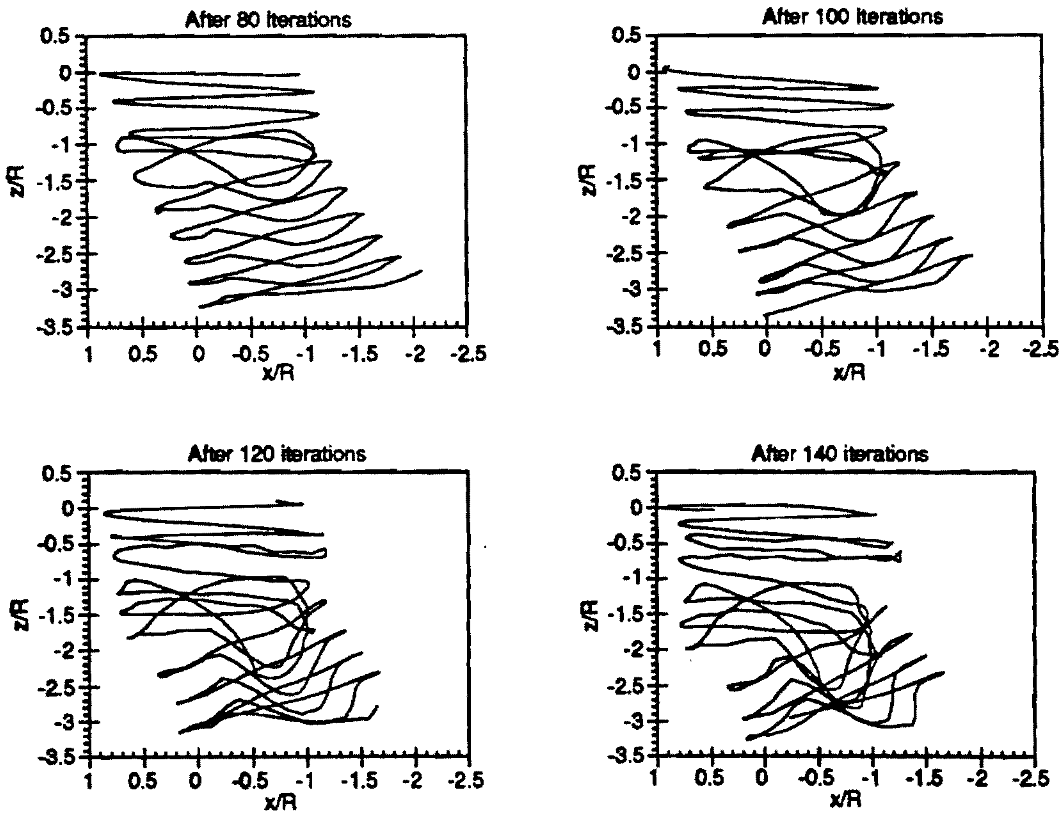

Fig. 4: Free Wake Instability

APPENDIX

SHIP GROUND EFFECT MODELING USING PRESCRIBED WAKE GEOMETRY WITH COMPUTED WAKE VORTICITY DISTRIBUTION

The effect of the ship proximity to the helicopter is modeled by using a standard panel method, based on the classical solution by Hess and Smith[7]. The ship is modeled by source panels which allow a good geometric representation. The effect of the ship on the rotor is given by the induced velocities on the rotor disk due to the ship panels. For the computation of the strengths of the sources, it is necessary to take into account both the ship velocity and the velocity field on the ship due to the rotor wake. This velocity field is computed using a rigid helical wake model. The strength of the rotor wake vortices depends on the circulation around the rotor blade, which, in turn, depends on the ship effects. Therefore, an iterative process would be needed. However, for the simulation problem, it may be assumed that changes in circulation around the blade and the flow about the ship are not too rapid and consequently the iterative process may be intrinsically performed during the simulation process.

In order to model the ground effect due to the sea surface, the method of images is used. An image rotor wake and an image ship panel system are placed below the sea surface and the influence of these images are taken into account in the computation of the downwash induced by the rotor and in the computation of the coefficient matrix for the ship panel method.

A.1. Ship Formulation

The ship surface is approximately represented by plane source panels with constant distributed strength. The strengths of the sources are determined by enforcing the non-penetration condition at the centroid of each panel. In this implementation, both the normal component of the ship's motion and the normal component of the downwash induced by the rotor are taken into account. The details of the ship source panel method are given in Ref. 7 and therefore will not be repeated here. This formulation results in a linear system of equations to be solved for the ship panel source strengths σ:

$$[A]\{\sigma\} = [B] \tag{A.1}$$

where [A] is the matrix of influence coefficients, $\{\sigma\}$ is the vector of unknown source strengths and [B] is the right-hand side which includes the normal component of the velocities on the ship surface due to the free-stream and due to the rotor and its wake. The system of equations (A.1) is solved by a standard linear equations solver. The resulting source panel strengths are then used to compute the velocities induced by the ship source panel system on the rotor disk.

A.2. Rotor Wake Formulation

In order to compute the induced velocity due to the rotor and its wake on the ship, as well the rotor disk inflow distribution in ground effect, a rigid wake model is used. This model is a modified version of the model described in Ref. 4 and allows the computation of the instantaneous induced velocities both on the rotor disk and on the ship surface. In Ref. 4 a prescribed vorticity distribution was assumed. In the current version, the vorticity distribution is computed from the blade section lift, as described in more detail in Section A.2.1. It should also be noted that in the present work the rotor wake model is used only for computation of the induced velocities on the ship surface. Numerical experimentation has shown that using the current model for computation of induced velocities on the rotor disk is computationally time-consuming while presenting no clear advantage over a dynamic inflow model.

The following assumptions are made:

1) Blade flapping angles are small and their higher harmonics are negligible;

2) The rotor blade is modeled by a lifting line of bound vorticity; this bound vorticity is related to the blade section lift by Kutta-Joukowski's theorem;

3) The wake has a prescribed geometry, which is basically a classical skewed helical wake, with a limited wake contraction model;

4) The wake is divided into a "near" wake, composed of trailing and shed vortices and a "far" wake composed of trailing tip vortices only. The strengths of the trailing and shed vortices are given by the radial and azimuth-wise variations of the bound vorticity, respectively, while the strength of the far wake tip vortex is assumed as equal to the maximum bound vorticity at the azimuth location where the vortex filament leaves the blade;

5) The rotor wake is convected downstream with a velocity which is equal to the vector sum of the free stream velocity and the averaged (momentum theory value) induced velocity over the disk.

A.2.1. Vorticity Distribution

The blade bound vorticity distribution is obtained through an iterative process from the blade section lift. Let the blade section bound vorticity be $\Gamma_{b_{ij}} = \Gamma_b(r_i,\psi_j)$. From Kutta-Joukowski theorem:

$$l_{ij} = \rho\, V_{ij}\, \Gamma_{ij} = \rho\, (\Omega R)(\bar{r}_i + \mu \sin \psi_j)\, \Gamma_{b_{ij}} \tag{A.2}$$

or:

$$\Gamma_{b_{ij}} = \frac{\ell_{ij}}{\rho(\Omega R)(\bar{r}_i + \mu \sin \psi_j)} \tag{A.3}$$

A.2.2. Velocity Induced by Blade Bound Vortices

From the computed bound vorticity distribution, the velocity induced by the blade bound vortices can be obtained by application of the Biot-Savart law:

$$v_b = \frac{1}{4\pi} \int_{\bar{r}=0}^{1} \Gamma_b \frac{d\vec{s}_b \times \Delta \vec{R}_{Pb}}{|\Delta \vec{R}_{Pb}|^3} \tag{A.4}$$

where $d\vec{s}_b$ is the elementary vector in the direction of the vortex filament and $\Delta\vec{R}_{Pb}$ is the position vector of the point in question with respect to the bound vortex element. Denoting by $\vec{R}_b$ the position vector of a blade bound vortex element as expressed in the tip-path-plane (TPP) reference frame:

$$\vec{R}_b = r\left\{\left[-\cos\psi\,\hat{i}_T - \sin\psi\,\hat{j}_T\right]\cos\beta_0 + \sin\beta_0\,\hat{k}_T\right\} \tag{A.5}$$

Then the elementary vector $d\vec{s}_b$ can be obtained from:

$$d\vec{s}_b = \frac{\dfrac{\partial\vec{R}_b}{\partial r}}{\left|\dfrac{\partial\vec{R}_b}{\partial r}\right|}\,dr \tag{A.6}$$

with

$$\frac{\partial\vec{R}_b}{\partial r} = \left[-\cos\psi\,\hat{i}_T - \sin\psi\,\hat{j}_T\right]\cos\beta_0 + \sin\beta_0\,\hat{k}_T = \frac{\vec{R}_b}{r} \tag{A.7}$$

Given a point with coordinates (x_P, y_P, z_P) in the tip-path-plane reference frame, the vector $\Delta\vec{R}_{Pb}$ is then:

$$\Delta\vec{R}_{Pb} = \vec{R}_P - \vec{R}_b = \left(x_P\,\hat{i}_T + y_P\,\hat{j}_T + z_P\,\hat{k}_T\right) - \vec{R}_b \tag{A.8}$$

The discretization of Eqs (A.5–A.8) is straightforward. Eq. (A.4) then reduces to a summation over the blade:

$$v_b\left(\psi_j,\vec{R}_P\right) = v_{b_j} = \frac{1}{4\pi}\sum_{i=1}^{N_r}\Gamma_{b_{ij}}\,\frac{\Delta\vec{s}_{b_j}\times\Delta\vec{R}_{Pb_{ij}}}{\left|\Delta\vec{R}_{Pb_{ij}}\right|^3} \tag{A.9}$$

A.2.3. Near Wake

As mentioned above, the near wake is assumed to be composed of trailing and shed vortices, with strength given by the radial and azimuth-wise variations of the bound vorticity, respectively, at the azimuth location where the vortex filament leaves the blade. Let us first consider an element of a trailing vortex filament of length $r_i \, \Delta v$, which left the blade at the radial location r_i, and is located at a wake age v_k. This element has left the blade when it was at an azimuth location $\psi_j - v_k$, ψ_j being the current azimuth location of the blade. Therefore, the vorticity of the element is given by $\Gamma_t(\bar{r}_i, \psi_j - v_k)\, r_i \, \Delta v$, where $\Gamma_{t_{i,j,k}} = \Gamma_t(\bar{r}_i, \psi_j - v_k)$ is the trailing vortex vorticity, equal to the radial variation of Γ_b:

$$\Gamma_{t_{ijk}} = \Gamma_t\left(\bar{r}_i, \psi_j - v_k\right) = \frac{\partial \Gamma_b}{\partial \bar{r}} \approx \frac{\Gamma_b\left(\bar{r}_i, \psi_j - v_k\right) - \Gamma_b\left(\bar{r}_{i-1}, \psi_j - v_k\right)}{\bar{r}_i - \bar{r}_{i-1}} \tag{A.10}$$

The velocity induced by the entire filament at a point is given by integration of elementary induced velocities obtained from the Biot-Savart law:

$$dv_t = \frac{1}{4\pi} \int_{v=0}^{v_{nw}} \Gamma_t \frac{d\vec{s}_t \times \Delta \vec{R}_{Pt}}{\left|\Delta \vec{R}_{Pt}\right|^3} \tag{A.11}$$

where $d\vec{s}_t$ is the elementary vector in the direction of the vortex filament and $\Delta\vec{R}_{Pt}$ is the position vector of the point in question with respect to the vortex element. Note that the integration is performed only along the "near" wake. Note also that Eq.(A.11) gives only the velocity induced by a single trailing vortex filament. To obtain the total induced velocity due to all trailing vortex filaments, one has to integrate Eq.(A.11) along the blade, i.e.:

$$v_t = \frac{1}{4\pi} \int_{\bar{r}=0}^{1} \int_{v=0}^{v_{nw}} \Gamma_t \frac{d\vec{s}_t \times \Delta \vec{R}_{Pt}}{\left|\Delta \vec{R}_{Pt}\right|^3} \tag{A.12}$$

Denoting by $\vec{R}_s$ the position vector of the trailing vortex element as expressed in the tip-path-plane (TPP) reference frame and using the assumption that the wake is convected downstream with a velocity which is equal to the vector sum of the free stream velocity and the averaged induced velocity over the disk, we have:

$$\vec{R}_s = r \left\{ \left[-\cos(\psi - v)\, \hat{i}_T - \sin(\psi - v)\, \hat{j}_T \right] \cos\beta_0 + \sin\beta_0 \, \hat{k}_T \right\} + \frac{\vec{v}_{i_0} - \vec{V}_{H_T}}{\Omega} v \tag{A.13}$$

where β_0 is the coning angle, Ω is the rotor rotational speed, $\vec{V}_{H_T}$ is the helicopter velocity vector in the TPP reference frame, $\hat{i}_T$, $\hat{j}_T$ and $\hat{k}_T$ are the unit vectors corresponding to the TPP axes, and $\vec{v}_{i_0}$ is the averaged induced inflow vector, given by:

$$\vec{v}_{i_0} = -\left(\Omega R\right) \lambda_{i_0} \hat{k}_T \tag{A.14}$$

where λ_{i_0} is the induced inflow ratio. The elementary vector in the direction of the filament, $d\vec{s}_t$, can be obtained as:

$$d\vec{s}_t = \frac{\dfrac{\partial \vec{R}_s}{\partial \nu}}{\left|\dfrac{\partial \vec{R}_s}{\partial \nu}\right|} r \, d\nu \tag{A.15}$$

with

$$\frac{\partial \vec{R}_s}{\partial \nu} = r \left[- \sin(\psi\text{-}\nu)\, \hat{i}_T + \cos(\psi\text{-}\nu)\, \hat{j}_T\right] \cos \beta_0 + \frac{\vec{v}_{i_0} - \vec{V}_{H_T}}{\Omega} \tag{A.16}$$

Given a point with coordinates (x_P, y_P, z_P) in the tip-path-plane reference frame, the vector $\Delta\vec{R}_{Pt}$ is then:

$$\Delta\vec{R}_{Pt} = \vec{R}_P - \vec{R}_s = \left(x_P\, \hat{i}_T + y_P\, \hat{j}_T + z_P\, \hat{k}_T\right) - \vec{R}_s \tag{A.17}$$

The discretization of Eqs (A.13–A.17) is straightforward. Eq. (A.12) then reduces to a double summation over the radial and wake coordinates along the near wake:

$$v_t\left(\psi_j, \vec{R}_P\right) = v_{t_j} = \frac{1}{4\pi} \sum_{k=1}^{N_{nw}} \sum_{i=1}^{N_r} \Gamma_{t_{ijk}} \frac{\Delta\vec{s}_{t_{ijk}} \times \Delta\vec{R}_{Pt_{ijk}}}{\left|\Delta\vec{R}_{Pt_{ijk}}\right|^3} \tag{A.18}$$

Now, let us consider an element of a shed vortex filament of length Δr_i, which left the blade at the radial location r_i, and is located at a wake age ν_k. This element has left the blade when it was at an azimuth location $\psi_j - \nu_k$, ψ_j being the current azimuth location of the blade. Therefore, the vorticity of the element is given by $\Gamma_s(\bar{r}_i,\psi_j-v_k)\,\Delta r_i$, where $\Gamma_s(\bar{r}_i,\psi_j-v_k)$ is the shed vortex vorticity, equal to the azimuthal variation of Γ_b:

$$\Gamma_{s_{ijk}} = \Gamma_s\left(\bar{r}_i,\psi_j-v_k\right) = \frac{\partial \Gamma_b}{\partial \psi} \approx \frac{\Gamma_b\left(\bar{r}_i,\psi_j-v_k\right)-\Gamma_b\left(\bar{r}_i,\psi_{j-1}-v_k\right)}{\Delta\psi} \tag{A.19}$$

The velocity induced by the entire shed vortex system at a point is given by radial integration of elementary induced velocities obtained from the Biot-Savart law, and subsequent integration along the wake to account for all the shed vortices:

$$v_s = \frac{1}{4\pi}\int_{v=0}^{v_{nw}}\int_{\bar{r}=0}^{1}\Gamma_s\,\frac{d\vec{s}_s\times\Delta\vec{R}_{P_s}}{\left|\Delta\vec{R}_{P_s}\right|^{\beta}} \tag{A.20}$$

Note that the integration is performed only along the "near" wake. The position vector of the shed vortex element, $\vec{R}_s$, is given again by Eq. (A.13), therefore the vector $\Delta\vec{R}_{P_s}$ is equal to $\Delta\vec{R}_{P_t}$ and is accordingly given by Eq. (A.17). The elementary vector in the direction of the shed vortex filament, $d\vec{s}_s$, can be obtained as:

$$d\vec{s}_s = \frac{\dfrac{\partial\vec{R}_s}{\partial r}}{\left|\dfrac{\partial\vec{R}_s}{\partial r}\right|}\,dr \tag{A.21}$$

with

$$\frac{\partial\vec{R}_s}{\partial r} = \left[-\cos(\psi-v)\,\hat{i}_T - \sin(\psi-v)\,\hat{j}_T\right]\cos\beta_0 + \sin\beta_0\,\hat{k}_T \tag{A.22}$$

The discretization of Eq (A.22) is straightforward. Eq. (A.20) then reduces to a double summation over the radial and wake coordinates along the near wake:

$$v_s\left(\psi_j,\vec{R}_P\right) = v_{s_j} = \frac{1}{4\pi}\sum_{k=1}^{N_{nw}}\sum_{i=1}^{N_r}\Gamma_{s_{ijk}}\,\frac{\Delta\vec{s}_{s_{ijk}}\times\Delta\vec{R}_{P_{s_{ijk}}}}{\left|\Delta\vec{R}_{P_{s_{ijk}}}\right|^{\beta}} \tag{A.23}$$

A.2.4. Far Wake

As mentioned above, the far wake is assumed to be composed of trailing tip vortices only, with strength assumed as equal to the maximum bound vorticity at the azimuth location where the vortex filament leaves the blade. Considering an element of
3 wake filament of length $r_{tv}\,\Delta\nu$ (where r_{tv} corresponds to the radial location where the tip vortex has rolled up) and at a wake age ν_k, this element has left the blade when it was at an azimuth location $\psi_j-\nu_k$, ψ_j being the current azimuth location of the blade. Therefore, the vorticity of the element is given by $\Gamma_{T_{jk}}\, r_{tv}\,\Delta\nu = \Gamma_T\,(\psi_j-\nu_k)\, r_{tv}\,\Delta\nu$, where $\Gamma_T\,(\psi_j-\nu_k)$ is the trailing tip vortex vorticity, equal to the radial maximum of Γ_b:

$$\Gamma_{T_k} = \Gamma_T\left(\psi_j - \nu_k\right) = \max_i \Gamma_b\left(\bar{r}_i, \psi_j - \nu_k\right) \tag{A.24}$$

The velocity induced by the wake at a point is given by integration of elementary induced velocities obtained from the Biot-Savart law:

$$v_T = \frac{1}{4\pi} \int \Gamma_T \frac{d\vec{s}_T \times \Delta\vec{R}_{PT}}{\left|\Delta\vec{R}_{PT}\right|^3} \tag{A.25}$$

where $d\vec{s}_T$ is the elementary vector in the direction of the vortex filament and $\Delta\vec{R}_{PT}$ is the position vector of the point in question with respect to the vortex element. Denoting by $\vec{R}_T$ the position vector of the tip vortex element as expressed in the tip-path-plane (TPP) reference frame and using the assumption that the wake is convected downstream with a velocity which is equal to the vector sum of the free stream velocity and the averaged induced velocity over the disk, we have:

$$\vec{R}_T = r_{tv}\left\{\left[-\cos(\psi-\nu)\,\hat{i}_T - \sin(\psi-\nu)\,\hat{j}_T\right]\cos\beta_0 + \sin\beta_0\,\hat{k}_T\right\} + \frac{\vec{v}_{i_0} - \vec{V}_{H_T}}{\Omega}\,\nu \tag{A.26}$$

The elementary vector in the direction of the tip vortex filament, $d\vec{s}_T$, can be obtained as:

$$d\vec{s}_T = \frac{\dfrac{\partial \vec{R}_T}{\partial \nu}}{\left|\dfrac{\partial \vec{R}_T}{\partial \nu}\right|} r_{tv}\, d\nu \qquad \text{(A.27)}$$

with

$$\frac{\partial \vec{R}_T}{\partial \nu} = r_{tv}\left[-\sin(\psi\text{-}\nu)\,\hat{i}_T + \cos(\psi\text{-}\nu)\,\hat{j}_T\right]\cos\beta_0 + \frac{\vec{v}_{i_0} - \vec{V}_{H_T}}{\Omega} \qquad \text{(A.28)}$$

Given a point with coordinates (x_P, y_P, z_P) in the tip-path-plane reference frame, the vector $\Delta\vec{R}_{PT}$ is then:

$$\Delta\vec{R}_{PT} = \vec{R}_P - \vec{R}_T = \left(x_P\,\hat{i}_T + y_P\,\hat{j}_T + z_P\,\hat{k}_T\right) - \vec{R}_T \qquad \text{(A.29)}$$

The discretization of Eqs (A.26–A.29) is straightforward. Eq. (A.25) then reduces to a summation over the wake coordinate along the far wake:

$$v_T\left(\psi_j, \vec{R}_P\right) = v_{T_j} = \frac{1}{4\pi}\sum_{k=N_{nw}+1}^{N_w} \Gamma_{T_k}\frac{\Delta\vec{s}_{T_{jk}} \times \Delta\vec{R}_{PT_{jk}}}{\left|\Delta\vec{R}_{PT_{jk}}\right|^{\beta}} \qquad \text{(A.30)}$$

A.2.5. Vortex Core Model

A Rankine vortex core model[9] with radius of one tenth of the blade chord is used. This model is illustrated in Fig. A.1, and is applied by scaling the induced velocity due to the elementary vortex filament by the square of the ratio between the distance to the filament and the core radius, whenever the point where the induced velocity is being calculated lies within the vortex core.

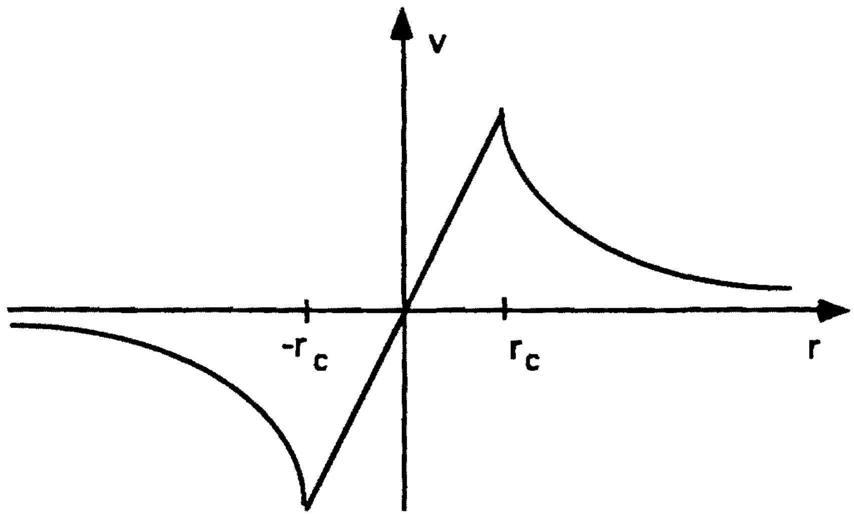

Fig. A.1: Rankine Vortex Core Model

REFERENCES

1. Howlett, J. J., "UH-60A Black Hawk Engineering Simulation Program: Volume I — Mathematical Model," NASA CR-166309, 1981.

2. Ballin, M. G., "Validation of Real-Time Engineering Simulation of the UH-60A Helicopter," NASA TM-88360, February 1987.

3. Peters, D. A., and HaQuang, N., "Dynamic Inflow for Practical Applications," *Journal of the American Helicopter Society*, October 1988, pp. 64–68.

4. Mello, O. A. F., "Numerical Simulation of Helicopter / Ship Airwake Interactions," Research Report submitted to Naval Air Warfare Center, School of Aerospace Engineering, Georgia Institute of Technology, Atlanta, July 1993.

5. Riaz, J., Prasad, J. V. R., Schrage, D. P., and Gaonkar, G. H., "New Method for Simulating Atmospheric Turbulence for Rotorcraft Applications," 47th Annual Forum of the American Helicopter Society, Phoenix, Arizona, 1991.

6. Riaz, Jamshed, "A Simulation Model of Atmospheric Turbulence for Rotorcraft Applications," Ph.D. Thesis, Georgia Institute of Technology, Atlanta, 1992.

7. Hess, J. L., and Smith, A. M. O., "Calculation of Potential Flow about Arbitrary Bodies," *Progress in Aeronautical Sciences*, Vol. 8. Edited by D. Küchemann. Pergamon Press, Oxford, England, 1967.

8. Press, W. H., Flannery, B. P., Teukolsky, S. A. and Vetterling, W. T., *Numerical Recipes — The Art of Scientific Computing (FORTRAN Version)*, Cambridge University Press, 1989.

9. U.S. Department of the Army — Aeroflightdynamics Directorate, "2GCHAS Theory Manual," (Second Generation Comprehensive Helicopter Analysis System, Version 2.1), Vol. II, Chapter 5 – Airloads and Induced Velocity, Ames Research Center, Moffett Field, CA, July 1992.

10. Sheridan, P. F., and Wiesner, W., "Aerodynamics of Helicopter Flight Near the Ground," 33rd Annual Forum of the American Helicopter Society, 1977.

11. Johnson, W., "A Comprehensive Analytical Model of Rotorcraft Aerodynamics and Dynamics, Part I: Analysis Development," NASA TM-81182, Part 1, June 1980.